XVII European Conference on Soil Mechanics and Geotechnical Engineering - Reykjavík, Iceland

1 – 6 of September 2019

Geotechnical Engineering,
foundation of the future

Conference proceedings

ECSMGE 2019
Reykjavík

Proceedings of the XVII European Conference on Soil Mechanics and Geotechnical Engineering, Reykjavík, Iceland

1 – 6 of September 2019

Geotechnical Engineering, foundation of the future

The Icelandic Geotechnical Society encompasses members interested in geotechnical engineering, engineering geology and rock mechanics. The members of the Society are simultaneously members of one or more of the international societies:

- ISSMGE - International Society for Soil Mechanics and Geotechnical Engineering
- IAEG - International Association of Engineering Geology and the environment
- ISRM - International Society for Rock Mechanics

Jarðtæknifélag Íslands / Icelandic Geotechnical Society

Website: www. jtfi.net

Preface

The Icelandic Geotechnical Society are pleased to welcome you to the XVII European Conference on Soil Mechanics and Geotechnical Engineering in Reykjavik, Iceland on the 1st - 6th of September 2019

The theme of the Conference is:

"Geotechnical Engineering, foundation of the future"

The themes of the conference embrace all aspects of geotechnical engineering, the foundation of current as well as future societies. The future relies on complex civil engineering infrastructures and mitigation of potential geo hazards. Geotechnical solutions are required to ensure safe and sustainable development, which are rooted in past experiences and enhanced by todays research and technology.

The aim of the conference is to share knowledge and experience with our colleagues and strengthen the relationship between members of the geotechnical society; introduce innovations, research and development, report on successful geotechnical constructions and application of design methods, as well as on mitigation and assessment of geohazards.

We hope that this conference exceeds your expectations with interesting papers, posters and exhibitions. We gratefully thank all the speakers, authors and reviewers, supporting committees, members of ISSMGE technical committees, chairs of sessions and exhibitors as well as all other participants making this conference a reality.

We hope you have a pleasant stay in Iceland and look forward to seeing you again.

Reykjavík, September 2019

On behalf of the XVII ECSMGE 2019 Organizing Committee
Haraldur Sigursteinsson

COMMITTEES & SECRETARY

The local Organizing Committee

Executive group:

Haraldur Sigursteinsson, *chairman*
- Icelandic Road and Costal Administration
Aldís Ingimarsdóttir
- Reykjavik University
Bjarni Bessason
- University of Iceland
Sigurður Erlingsson
- University of Iceland - VTI Sweden
Þorbjörg Sævarsdóttir
- EFLA consulting

Members:

Andrés Jónsson
- JÁVERK General Contractors
Fjóla Guðrún Sigtryggsdóttir
- NTNU Throndheim, Norway
Geraldine Andrea Sørum
- NGI Norway
Gunilla Franzén
- Geoverkstan Sweden
Margrét Elín Sigurðardóttir
- Mannvit consulting
Þorri Björn Gunnarsson
- Mannvit consulting

Conference Advisory Committee

Mario Manassero, *chairman*
 - Vice-President of the ISSMGE for Europe 2017-21
Charles Wang-wai Ng
 - President of the ISSMGE 2017-2021
Antonio Gens
 - Vice-President of the ISSMGE for Europe 2013-17
Roger Frank
 - President of the ISSMGE 2013-2017
Neil Taylor
 - Seretary General of the ISSMGE
Mike Winter
 - Chair of the XVI COC, Edinburgh 2015
Derek Smith
 - Secretary of the XVI COC, Edinburgh 2015
Haraldur Sigursteinsson
- Chair of the COC, Reykjavik 2019
Sigurður Erlingsson
 - Member of the the COC, Reykjavik 2019

Conference Scientific Committee

ALBANIA - *Luljeta Bozo*
AUSTRIA - *Helmut F. Schweiger*
BELGIUM - *Maurice Bottiau*
BOSNIA & HERZEGOVINA - *Mato Uljarević*
BULGARIA - *Lena Mihova*
CROATIA - *Predrag Miščević*
CYPRUS - *Dimitrios Loukidis*
CZECH & SLOVAK REPUBLICS - *Jana Frankovska*
DENMARK - *Morten Albjerg Liingaard*
FINLAND - *Leena Korkiala-Tanttu*
FRANCE - *Fabrice EMERIAULT*
GERMANY - *Juergen Grabe*
GREECE - *Michael Bardanis*
HUNGARY - *András Mahler*
ICELAND - *Aldís Ingimarsdóttir*
IRELAND - *Ronan Travers*
ITALY - *Nicola MORACI*
LATVIA - *Kaspars Bondars*
FYR MACEDONIA - *Jovan Br. Papić*
NETHERLANDS - *Maarten Profittlich*
NORWAY - *Vikas Thakur*
POLAND - *Katarzyna Zabielska-Adamska*
PORTUGAL - *Alexandre Pinto*
ROMANIA - *Sanda Manea*
RUSSIA - *Maxim Tupikov*
SERBIA - *Mirjana Vukicevic*
SLOVENIA - *Borut Macuh*
SPAIN - *Herminia Cano*
SWEDEN - *Christoffer With*
TURKEY - *Feyza Cinicioglu*
UK - *David Toll*

Conference Secretariat

Athygli Conferences
Ármúla 11, 108 Reykjavík
www.athygliradstefnur.is
Þorbjörg Þráinsdóttir, (Tobba)
Birna Björg Berndsen
Þórunn Dögg Harðardóttir

Table of contents

Exhibitors at the Conference

Following exhibitors were at the Conference Exhibition, see more on the website:
www.ecsmge-2019.com and https://www.ecsmge-2019.com/exhibition--sponsorship.html

A.P. Van den Berg	Holland
Allnamics Pile Testing Experts BV,	NL
Apageo	France
APS Antriebs_, Prued- und Steuertechnik	Germany
ArcelorMittal Commercial RPS S.á R.L	Luxemburg
Beaulieu Technical Textiles	Belgium
Bentley Geotechnical Analysis,	Netherlands
Cambridge Insitu Limited,	UK
Carmeuse	Belgium
CESAR, by itech & ifsttar	France
Concrete Canvas Ltd.	
Controls SPA	Italy
Diana Fea	Holland
EMerald Geomodelling	Norway
G & G Partners Srl – Italy	Italy
GDS Instruments a division of GDSL	UK
GEOBRUGG	Switzerland
Geofem	Cyprus
Geokon	USA
Geoslope International ltd	Canada
Geotomographie GmbH	Germany
Keller Holding	Germany
Leca Finland Oy	Finland
Mannvit-Consulting Engineers	Iceland
NAUE GmbH & Co. KG,	Germany
NGI - Norwegian Geotechnical	Norway
Oasys Ltd	UK
Platipus Anchors LTD	UK
Profound BV	Holland
Reinforced Earth	France
Rocscience	Canada
Studio Prof. Marchetti S.R.L	Italy
Taylor & Francis	UK
Terrasol	France
The Geological Society of London	UK
VERKÍS - Consulting Engineers	Iceland
VistaDataVision/VistaEngineering	Iceland
VJTech Ltd	UK

ISSMGE, Coming conferences

Technical Committees Workshops

Following technical committees arrange pre-conference workshops Sunday the 1st of September.

ERTC7 - Numerical Methods	TC 202 - Transportation
TC 104 - Physical Modelling	TC 205 - Safety and Serviceability
TC 201 - Dykes and Levees	TC 208 - Slope Stability
	TC 210 - Dams & Embankments

See more on the TC's workshops on the website: https://www.ecsmge-2019.com/tcs-workshops.html

Topics for Technical Papers

The main topics are divided in following six main categories and 22 subcategories:

A: Modelling and experimental assessment of geomaterials
   A.1. Investigation by laboratory tests
   A.2. Investigation by in situ tests
   A.3. Physical modelling and large scale tests
   A.4. Theoretical modelling
   A.5. Design parameters

B: Geotechnical construction and soil improvement
   B1. Foundations, excavations and earth retaining structure
   B.2. Slopes stabilization and earthworks
   B.3. Ground reinforcement and ground improvement
   B.4. Structures and infrastructure
   B.5. Near shore and offshore structures and the marine environment

C: Geohazards, earthquakes and mitigation
   C.1. Landslides and other solid flows
   C.2. Earthquake engineering and soil dynamics
   C.3. Floods, erosion and scours
   C.4. Hazard and risk management

D: Environment, water and energy
   D.1. Environmental geotechnics
   D.2. Groundwater and hydrology
   D.3. Energy, incl. geothermal energy

E: Historical heritage preservation
   E.1. Investigation, characterization and testing
   E.2. Case histories

F: Special and Specific Issues
   F.1. Problematic materials and environments
   F.2. Developments and innovations in geotechnical engineering, education and practice
   F.3. Forensic geotechnical engineering

Risk assessment and dams –
Recent developments and applications

Approche fiabiliste et barrages – Développements récents et applications

S. Lacasse
Norwegian Geotechnical Institute (NGI), Oslo, Norway

F. Nadim, Z.Q. Liu, U.K. Eidsvig, T.M.H. Le, C.G. Lin[1]
Norwegian Geotechnical Institute (NGI), Oslo, Norway
[1]NGI and Tongji University, Shanghai, China

ABSTRACT: Increasingly, society and standards require "risk-informed" decisions. The paper demonstrates the benefits of implementing reliability and risk concepts in dam engineering as a complement to conventional deterministic analyses. Reliability evaluations can range from qualitative estimates, to simple statistical evaluations, to full probabilistic modelling of the hazards and consequences for a system of dams. The paper gives an overview of basic concepts of reliability-based approaches and illustrates their use with three case studies. The paper discusses the strengths of reliability-based analyses and key issues such as tolerable and acceptable risk, the meaning of factor of safety, the targets for a margin of safety and the selection of characteristic value for analysis. Reliability-based approaches provide useful insight and complementary information. They enable the analysis of complex uncertainties in a systematic and more complete manner than deterministic analyses alone, both for the design of dams and for their safety evaluation during their lifetime. Reliability and risk-based approaches assist with preparing engineering recommendations and making decisions.

RÉSUMÉ: La société et les normes exigent de plus en plus de décisions "fondées sur le risque". L'article démontre les avantages de la mise en œuvre de concepts de fiabilité et du risque dans le dimensionnement de barrages comme un complément aux analyses déterministes classiques. Les évaluations de fiabilité peuvent être des estimations qualitatives, de simples évaluations statistiques, ou une modélisation probabiliste complète des aléas et des conséquences pour un système de barrages. L'article donne un aperçu des concepts de base des analyses fiabilistes et illustre leur utilisation avec des études de cas de trois barrages en remblai rocheux. Le document discute des points forts de l'approche fiabiliste et les questions clés telles que le risque tolérable et acceptable, la signification du facteur de sécurité, les objectifs pour une marge de sécurité et le choix de la valeur caractéristique pour l'analyse. L'article conclut que les approches basées sur la fiabilité fournissent des informations complémentaires utiles et permettent d'analyser des incertitudes complexes de manière systématique et plus complète que les analyses déterministes, tant pour la conception des barrages que pour leur évaluation pendant leur durée de vie. Des approches basées sur la fiabilité et le risque aideront à préparer les recommandations d'ingénierie et à prendre de bonnes décisions.

Keywords: Risk assessment, risk management, dams, reliability index, failure probability

1 INTRODUCTION

Karl Terzaghi (1929; 1961) wrote: *"Soil engineering projects require a vast amount of effort and labor securing only roughly approximate values for the physical constants that appear in the equations. The results of the computations are not more than working hypotheses, subject to confirmation or modification during construction. In the past, only two methods have been used for coping with the inevitable uncertainties: either adopt an excessively conservative factor of safety, or make assumptions in accordance with general, average experience. The first method is wasteful; the second is dangerous."*

Concepts of reliability and risk analyses are presented to illustrate the benefits of using reliability-based concepts for taking into account uncertainties and for the design and follow-up of dams. The paper discusses the significance of level of safety and the influence of uncertainties on the computed factor of safety. The need to use reliability-based approaches has risen because society and standards require more than before "risk-informed" design and "risk-informed" decision-making (ISO2394:2015). Reliability evaluations can range from qualitative estimates and simple statistical evaluations to full probabilistic modelling of the hazards and consequences for a system of dams.

The paper illustrates the use of the reliability-based approach with three case studies of embankment dams and summarizes the lessons learned. Key issues such as tolerable and acceptable risk and targets for a margin of safety are discussed. Reliability-based approaches provide useful insight and complementary information, and enable the analysis of complex uncertainties in a more systematic manner than deterministic analyses alone, both for the design of dams and for the safety evaluation during their lifetime. Reliability and risk-based approaches assist with the preparation of engineering recommendations and with making decisions.

2 A PRACTITIONER'S APPROACH TO UNCERTAINTY

During a design, the engineer always looks at the safety to know whether or not the foundation or the geotechnical structure can fail to perform adequately under the applied loads. The many uncertainties affecting geotechnical calculations need to consider their effect on the performance.

Silva *et al* (2008) combined historical and subjective probabilities (Fig. 1) to establish an approximate correlation between safety factor and failure probability. The diagram was devised for engineering practice. The figure is updated from Lambe (1985) and Baecher and Christian (2003), and compiles data from over 75 projects spanning over 4 decades. The projects include zoned and homogeneous earth dams, tailings dams, natural and cut slopes and earth retaining structures. The annual probabilities of failure for the different case studies were quantified iteratively, through experience, engineering judgment and published (historical) statistics.

Figure 1 cannot be used to either establish annual probabilities of failure in a design or verification situation or a relationship between factor of safety and probability of failure. It illustrates clearly, however, the effect of the uncertainties on the perceived factor of safety. Silva *et al* (2008) classify the structures into categories based on a judgment of the level of engineering. The level of engineering was established subjectively on the basis of the design practices (investigation, testing and analysis), documentation, construction, operation and monitoring:

Category I:
Facilities designed, built, and operated with state-of-the-practice engineering;
Category II:
Facilities designed, built, and operated using standard engineering practice;
Category III:
Facilities without site-specific design and substandard construction/operation;
Category IV:
Facilities with little or no engineering.

The family of curves were anchored on two sets of coordinates: a factor of safety of 1.5 for an annual probability of failure of 10^{-4} based on the historical performance of earth dams designed and constructed with conservative engineering practice (Baecher *et al* 1980; Whitman 1984; Christian *et al* 1992); and a 50% annual probability of failure for a safety factor of unity, based on a normally distributed uncertainty in the factor of safety (Vick 1994).
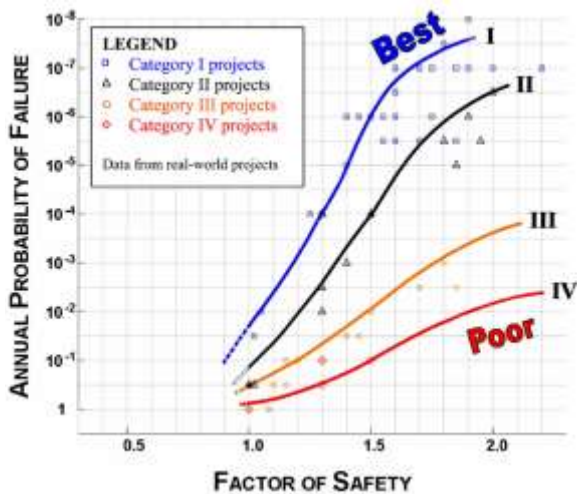

Figure 1. Practitioners' view of how factor of safety varies with uncertainty (Silva et al 2008)

Figure 1 suggests that, in the view of three practitioners (Silva *et al 2008*), a factor of safety of 1.5 can have an annual failure probability between 10^{-7} and 10^{-2} depending on the uncertainties, and a factor of safety of 1.3 an annual failure probability between 10^{-4} and 50%. The range of perceived failure probability for a "given" factor of safety is extremely wide.

3 UNCERTAINTIES AND EVENT PROBABILITIES

A statistical distribution is a practical tool to quantify uncertainty (Fig. 2), with a mean μ, a standard deviation (*SD*) and a coefficient of variation, *CoV*, which is an expression of the size of the standard deviation with respect to the mean ($CoV = SD/\mu$).
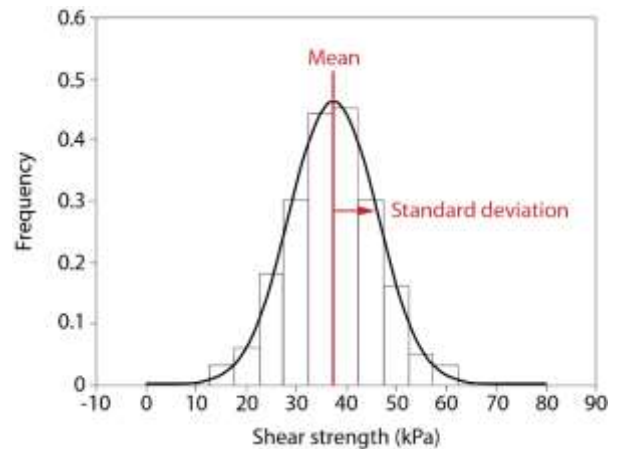

Figure 2. Uncertainty in a parameter

Uncertainties are either aleatoric or epistemic. *Aleatoric* uncertainty (also known as variability) is the natural randomness of a property or a load, e.g. soil strength or rainfall. The aleatoric uncertainty cannot be reduced. *Epistemic* uncertainty is the uncertainty due to lack of knowledge, e.g. measurement and method uncertainty. The epistemic uncertainty can be reduced by, e.g. increasing the number of tests or measurements, improving the measurement method and/or verifying the calculation procedure with model tests. Since the uncertainty is never zero, there is always a finite, even if small, probability that a failure may occur.

Both load and resistance have uncertainties (Fig. 3). Failure probability relates to the overlap of the two uncertainty distributions. Høeg and Murarka (1974) illustrated how uncertainties influence the probabilistic design of a retaining wall based on partial safety factors.

Uncertainties, their sources and their treatment could be a paper in itself. The quantification of uncertainties is not part of this paper. The reader can refer to several books and papers on this subject, including Ang and Tang (2007), Baecher and Christian (2003), Keaveny *et al* (1990), Lacasse and Nadim (1996), Lacasse *et al*

(2017), Nadim (2015), Tang (1973; 1984; 1987) and Uzielli *et al* (2006). This paper concentrates on risk-based approaches and the insight they bring to improve the design and safety of dams. The use of risk-based approaches is illustrated with case studies of dams.
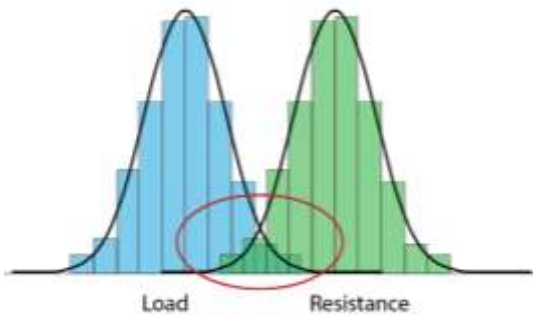

Figure 3. Potential overlap of load and resistance

The engineering literature (*e.g*., Morgenstern 1995; Vick 1994) identifies three ways of estimating annual event probabilities: (1) based on the frequency calculated from observations (historical data); (2) derived from probability theory (reliability-based design with some mathematical modelling); and (3) using and quantifying, where possible, expert judgment (subjective probabilities).

Benjamin and Cornell (1970) stated that *"the sources of the probability [estimates] may include observed frequencies, deductions from mathematical models, and in addition, measures of an engineer's subjective degree of belief regarding the possible states of nature"*.

4   SAFETY FACTOR

Figure 4 shows that a design with a high factor of safety can have higher annual failure probability than another with a lower factor of safety. A higher safety factor, as commonly calculated, does not necessarily imply a smaller risk, because it is affected by the uncertainties in the analysis. The curves in Figure 1 reflect the concept in Figure 4: a design with a high factor of safety can

have a higher probability of failure than another with a lower factor of safety. A higher factor of safety does not imply a smaller risk. Duncan (2000) pointed out that: *"Through regulation or tradition, the same value of safety factor is applied to conditions that involve widely varying degrees of uncertainty. This is not logical"*.

Safety factor is therefore not a sufficient indicator of safety because it does not account for the uncertainties in the analysis.

Soil properties and quality of engineering are not the only sources of uncertainty. The methods used to calculate stability, displacements or bearing capacity have themselves significant uncertainties. Nadim and Lacasse (1992) gave an example where stability analyses were done with the so-called effective stress and total stress approaches on a 'contractant' and a 'dilatant' soil. The computed failure probability differed significantly for each approach, although the computed factors of safety for the dilatant material were nearly the same. The differences in the calculated safety factors and the nominal failure probabilities were due to the different uncertainties in soil parameters and calculation methods.
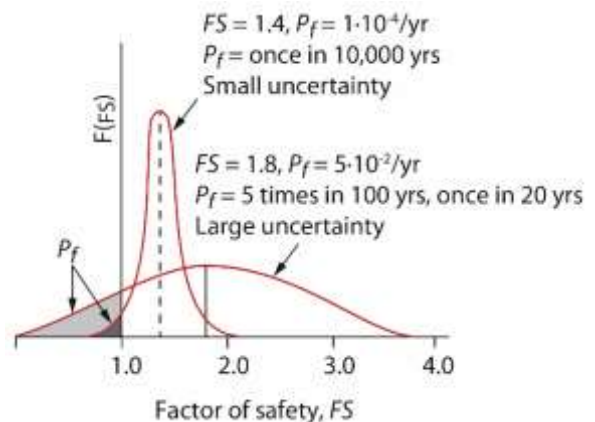

Figure 4. Safety factor and failure probability (P_f) of a slope (Lacasse and Nadim 1996)

5 RELIABILITY CONCEPTS

The terminology in this paper is consistent with the recommendations of ISO 31000:2018:

Danger (Threat):
Phenomenon that could lead to damage.
Hazard:
Probability that a danger (threat) occurs within a given period of time.
Exposure:
The circumstances of being exposed to a threat.
Vulnerability:
The degree of loss to a given element or set of elements affected by a hazard.
Risk:
Measure of probability and severity of an effect to life, health, property or environment.

Risk is the product of the probability of an event occurring (hazard) with the consequences due to this event. The consequences depend on exposure and vulnerability of the elements at risk. ISO 31000:2018 defines risk as the "*effect of uncertainty on objectives*". Consequences can be positive or negative and risk can be positively or negatively affected by changing circumstances.

5.1 Deterministic and probabilistic analysis

The terms "deterministic" analysis and "probabilistic" analysis are used.

− A deterministic system is one in which no randomness is involved in the estimate of future states of the system. A deterministic analysis aims at demonstrating that a facility is tolerant to identified faults or hazards within a "design basis", and evaluates a "nominal" performance. The approach does not consider the full range of possible outcomes nor quantify the likelihood of each of the outcomes. Deterministic scenario(s) may underestimate the risk.

− A probabilistic analysis aims at providing an estimate of the risk associated with a facility, and an estimate of the uncertainties involved. Probabilistic risk assessments help understand and account for the uncertainties.

Discussing the uncertainties will, in any case, usually promote a debate that should lead to more insight and robust decisions.

While a deterministic analysis considers the impact of a single scenario (and a single set of input data), a probabilistic analysis attempts to include all possible scenarios, their likelihood and impact. A probabilistic analysis is comparable to series of sensitivity analyses (many thousands, even millions, of analyses).

5.2 Margin of safety

The objective of a safety assessment is to demonstrate that the risk associated with a facility is acceptable. The conventional way is to use a "deterministic" safety factor, FS. A safety factor of 1.5, for example, is often used to account for the combination of uncertainties in the ground, in the analysis parameters and the calculation method. There is a general perception that a design with a safety factor FS $\geq$ 1.5 has to be "safe".

Reality is not so simple. A safety factor 1.5 represents a spectrum of failure probabilities, which depend on the uncertainties in the analysis.

In a safety assessment, the engineer aims to quantify the margin of safety (M). Margin of safety is defined as:

$$M = Resistance - Load \qquad (1)$$

With $M > 0$, the structure is safe; if $M \leq 0$, the structure is not safe. There is also an uncertainty in the safety margin (Fig. 5), and the failure probability, P_f, is the zone under the probability distribution of M where $M \leq 0$.

5.3 Reliability-based design

There are three approaches to design:

− The "Working stress" design (WSD) is the traditional approach based on an overall factor of safety, and has been used for a long time.

− Modern design codes are based on partial safety factors (or coefficients): the LRFD

approach (Load and Resistance Factor Design) in North America and the characteristic values and "partial safety factors" approach in Europe. The partial safety factors (also in the LRFD approach) are used to reflect the level of uncertainty and/or the relative importance of a particular parameter in design.

− Reliability-based design (RBD) using a target annual failure probability or target reliability index to verify margin of safety.
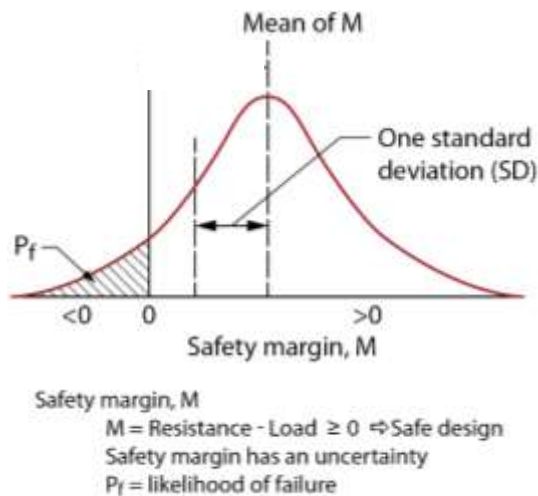

Figure 5. Safety margin and failure probability

5.3.1 Reliability index and failure probability

An alternative to using failure probability is to express the safety target in terms of an annual reliability index, β. Reliability index has a more positive connotation than failure probability and the two terms are directly correlated. Reliability index refers to the number of standard deviations between the mean safety margin and failure (M=0) in Figure 5. Reliability index is defined as:

$$\beta = \frac{M_{mean}}{SD} \qquad (2)$$

Figure 6 gives the relationship between failure probability and reliability index for a normally

distributed safety margin. For example, a reliability index (β-value) of 3.7 corresponds to a failure probability (P_f) of 10^{-4} and a β-value of 4.3 to a P_f of 10^{-5}. Similar curves exit for other distributions, e.g. the lognormal and triangular distributions.

Practice should use the concept of reliability index. Failure probability reminds of failure, reliability index refers to the reliability of a dam ("*Fiabilité*" in French, which is a synonym for "trustworthiness").
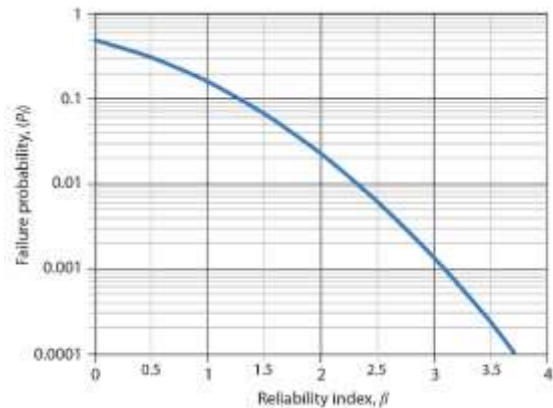

Figure 6. Relationship between probability of failure, P_f, and reliability index β (normal distribution)

5.3.2 Deterministic or probabilistic safety target

For large dams, there are often discussions of the safety target to achieve, and whether the safety target should remain the same during the entire life. The individuals downstream of a dam should not be exposed to a higher risk with time, and any potential environmental damage should not increase with time.

What should be the safety target during the life of a dam? Is a fixed deterministic safety factor sufficient to ensure the same safety margin throughout the lifetime of a dam? A safety level can be reflected in a constant annual failure probability, but not necessarily in a constant safety factor, because the uncertainties are not the same during the life of a dam, the likelihood of events

may change and the consequences change with the downstream development.

A target annual failure probability, on the other hand, allows a more consistent comparison of the safety margin at different times of the life of a dam. A dam in operation for 50 years, represents 50 years of evaluated experience, not unlike a prototype test on site for 50 years under operation and environmental loads. In most cases, the uncertainties under design and construction will have reduced with time as more information and data become available, and as the performance of the dam is experienced over 50 years. The reliability-based approach can account for the observations and experiences during the course of operation of the dam.

5.4   Risk assessment and management

Risk management is the process of identifying, analysing and assessing risks to enable informed decisions on accepting or treating and controlling risks to minimize them. Risk management integrates the recognition and assessment of risk with the development of appropriate risk mitigation strategies.

Risk management comprises six main tasks: (a) Danger or hazard identification; (b) Causal analysis of the dangers or hazards; (c) Consequence analysis, including vulnerability analysis; (d) Risk assessment combining hazard, consequence and uncertainty assessments; (e) Risk evaluation of whether the risk is acceptable or not; and (f) Risk treatment (or risk mitigation).

Risk management has been formalised into a framework by ISO 31000:2018, with an integrated process involving communication and consultation on the one hand, and monitoring and review on the other hand. The process systemizes knowledge and uncertainties, to evaluate the significance of risk and for comparing options. In 2018, ISO added a "recording and reporting" requirement, and the entire risk assessment and management process is assimilated to a revolving circle.

There are several methods to do risk assessment, from simple qualitative risk matrices to more advanced numerical tools. Lacasse and Nadim (2007) summarized many of the methods in detail, and the methods are only briefly mentioned herein.

5.4.1 Qualitative methods

The most common tool is the "traffic-light" matrix (Fig. 7). Such qualitative matrices are very useful, especially when assessed through the consensus of several individuals with different expertise. Over the years, the 5x5 matrix has become more popular than the original 3x3 matrix. In the matrix, green designates "Low risk", red "High risk" and orange a situation in between, "Medium risk". Such qualitative estimates are useful, even recommended, as a first pass tool to establish whether or not a more detailed analysis is needed (if scenarios fall in the red or orange
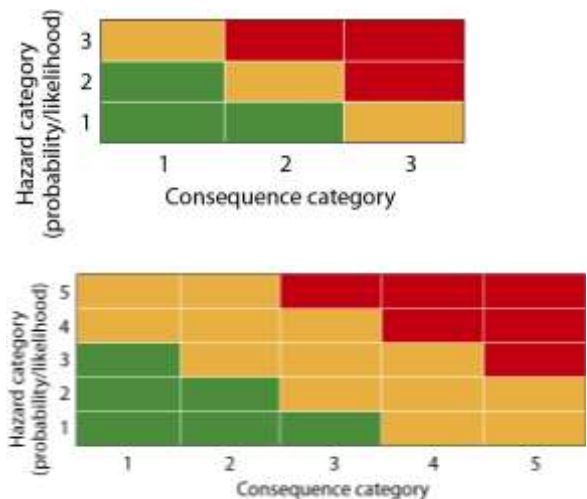
zones).

Figure 7. Qualitative 3 × 3 and 5 × 5 risk matrix: Hazard categories 1 to 3 or 1 to 5 (Very Low to Very High hazards); Consequence categories 1 to 3 or 1 to 5 (Very Small to Very Large consequences)

Such matrices can be implemented in e.g. a macro-operated Excel sheet (Langford *et al* 2019). It is important in such qualitative evalu-

ation to define and use unambiguously and consistently the definitions of 'very low', 'low', 'medium', 'high' and 'very high' hazards and of 'very small', 'small', 'medium', 'large' and 'very large' consequence (or impact). Other qualitative methods, devised mainly for large dams and other critical facilities, include the Life Cycle Inventory and Life Cycle Assessment, also known as "Cradle to Grave" analysis (US EPA 2010) and the "Failure Modes and Effects Analysis" (FMEA) and the Failure Modes, Effects and Criticality Analysis (FMECA) (USACE 2011; USACE 2014; FEMA 2015).

5.4.2 Quantitative methods

In a quantitative probabilistic analysis, the same equation for load and resistance is used as for the deterministic calculation. The difference is that the material and load properties are described by a probability distribution function with a mean and standard deviation, that an additional variable is introduced, the method uncertainty.

Quantitative methods include: Event tree analysis, Fault tree analysis, Bayesian updating and the First Order Second Moment (FOSM) method. More complex tools are: Monte-Carlo simulations, Bayesian networks, the First and Second Order Reliability Method (FORM and SORM) and system reliability analysis, such as SYSREL Schneider (1997) and Lacasse and Nadim (2007) summarized many of the methods in detail. One can also combine two or several approaches to obtain reliability estimates, e.g. a probabilistic analysis of slope stability with an event tree analysis covering all plausible breach scenarios.

5.5 Acceptable and tolerable risk

Risk acceptance criteria are difficult to set, for both deterministic and probabilistic analyses. Acceptable risk refers to the level of risk requiring no further reduction, and is the level of risk society desires to achieve. Tolerable risk refers to the risk level reached by compromise in order to gain certain benefits. A construction with tolerable

risk requires no action or expenditure for risk reduction, but it is desirable to control and reduce the risk if the economic and/or technological means for doing so are available.

A Frequency-Consequence chart (*F-N* chart) is a practical way to present risk level and compare different facilities. The *F-N* curves relate the annual probability *F* of an event to the number of fatalities *N*. The term "*N*" can be replaced by other measures of consequences such as costs. Figure 8 presents the Whitman (1984) *F-N* chart.
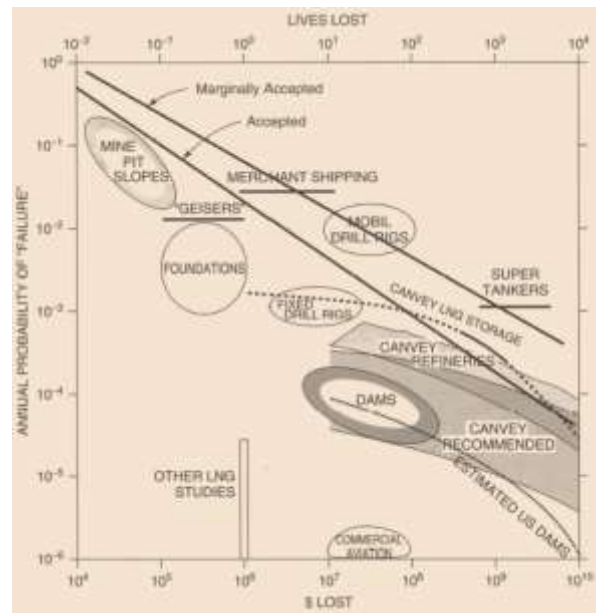

Figure 8. Whitman (1984) curves of acceptable and marginally acceptable risk (adapted by Baecher and Christian 2003) (note: 1984 US dollars).

Guidelines have been suggested by several countries. Some are for dams, some for man-made slopes, some more general (Fig. 9). Although there are differences, the annual acceptable risk level centres around 10^{-4} for ten fatalities. Figure 10 illustrates the range of published guidelines and the Hong Kong criterion for man-made slopes, which is one of the most frequently used criteria. The F-N diagram in Figure 9 is more stringent than Whitman's. The area to the right where the number of fatalities is greater than

1000 requires detailed assessment and reflects risk aversion in cases of very high number of fatalities.

The demarcation between acceptable and unacceptable risk is usually a gradual transition (Fig. 11). In Figure 11, the zone for F between 10^{-3} and 10^{-4} and 1 to 8 mortalities seems to belong to two categories. If a risk estimate should fall in that zone, the most severe action (red line) should be applied.
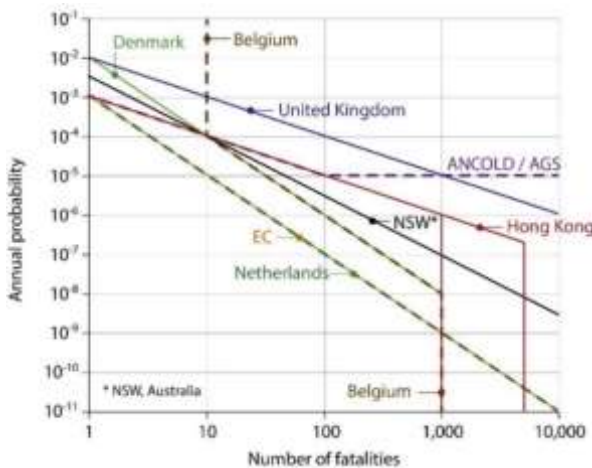

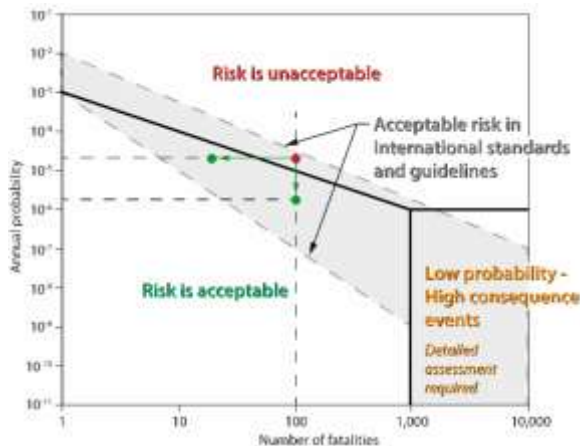*Figure 9. F-N risk guidelines in different countries (K. Ho Pers. comm. Hong Kong Nov. 2008)*

Figure 10. Range of risk guidelines (green dots illustrate how to reduce risk)

Hypothetical reductions of the failure probability for the same consequence of the consequences or for the same failure probability are illustrated with circles in Figure 10. It is not possible to show such evolution with a fixed factor of safety used as safety target. One can also define an *ALARP* zone on the F-N chart, where the risk level is to be kept "As Low As Reasonably Practicable". The *ALARP* zone describes a level of risk that cannot be reduced further without efforts and cost being disproportionate to the benefit gained or where the solution is impractical to implement.
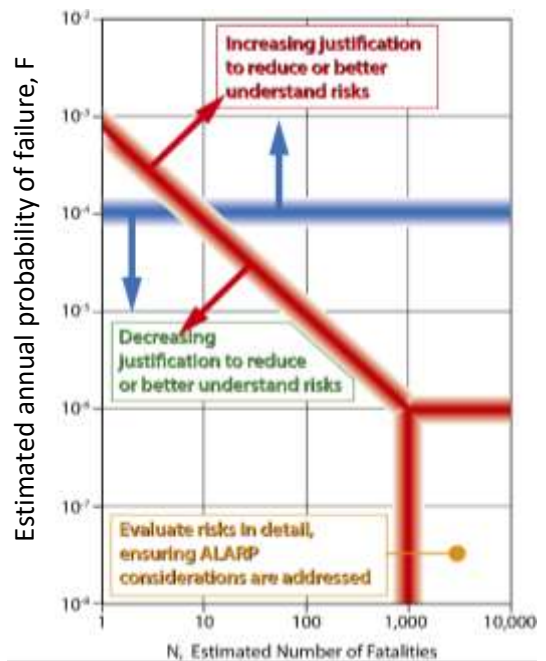

Figure 11. US Bureau of Reclamation 2011 guidelines

An annual failure probability of 10^{-4} has an actual significance. Figure 12 shows the mortality rate in Canada, due to all causes, as a function of age (https://www150.statcan.gc.ca/). At age 5-10, the probability of dying in the next year is 1/10,000 or 10^{-4}. At age 40, the probability increases to 1‰, at age 65 to 1%. As we reach a respectable age of 90, the probability of dying in the next year is close to 10%.
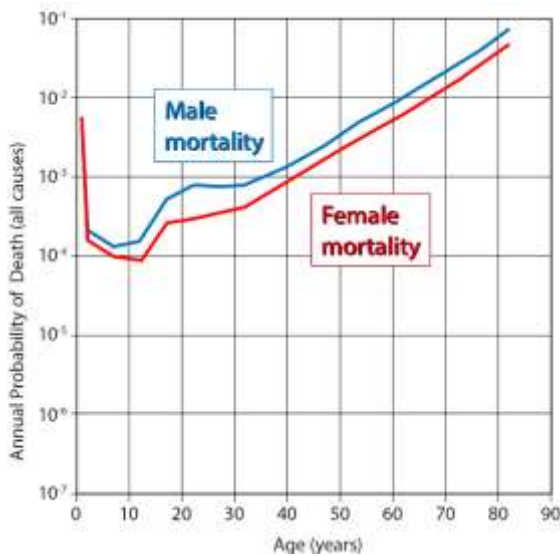
Figure 12. Annual probability of dying (Statistics Canada)

6 CASE STUDY: EMBANKMENT DAM UNDER WINTER CONDITIONS

6.1 Dravladalen Dam

The 340-m long rockfill embankment Dravladalen Dam has a height of 29 m and a reservoir of $58 \cdot 10^6$ m^3. The dam, built in 1971−1972, is founded on rock and has a till core. The dam is designed for a 1,000-year flood. Leakage was observed from the early stages of impoundment, but only small deformations were recorded. The "normal" seepage through the till core, based on laboratory seepage measurements, was 3 to 8 l/s. In 1994, the recorded leakage was 11 to 13 l/s. In 2016, the leakage under full reservoir was on average 5 to 6 l/s, and the leakage water was clear (no discernible fines). The dam is classified in the highest consequence class in Norway.

6.2 Reliability approach

The probabilistic analyses were carried out with two approaches: (1) event tree analysis, and (2) Bayesian network[1] combined with Monte Carlo simulations. The techniques are described in e.g. Hartford and Baecher (2004), Baecher and Christian (2003) and Lacasse *et al* (2017). Each of the methods uses nine steps (modified after Vick 2002; Høeg 1996):

1. Review of field performance and history.
2. Dam site inspection and data review.
3. Failure mode screening.
4. Agreement on descriptors of uncertainty.
5. Event tree construction.
6. Probability estimate at each node of the tree.
7. Calculation of annual probability of breach.
8. Evaluation of results.
9. Iteration and documentation.

The analyses were done in a workshop mode by bringing together 18 "experts" with knowledge about the dam, the hazards and risks involved, the dam construction and dam behaviour in general. The participants included dam owners, engineers responsible for the dam operation, hydrologists, earthquake specialists, reliability specialists, consultants and regulatory bodies. One person in charge of the day-to-day follow-up of the dam was at the dam site and available to answer questions. The format of a workshop was very useful to assess and discuss the estimates of probability. The probability estimates for the event tree and Bayesian analyses were set with the help of (1) statistical estimates based on past observations (actual data); (2) engineering models based on physical processes, e.g. stability analyses (including parameter uncertainties); and (3) expert judgment based on knowledge and evaluated experience. Vick (2002) suggested that: *"The collective judgment of experts, structured within a process of debate,*

---

[1] Bayesian network is an emerging method for reasoning and modelling under conditions of uncertainty. The method has been applied to avalanche risk, design of early warning system for landslide hazard mitigation, rock slope failure, dam risk analysis, earthquake risk management and multi-hazard, multi-risk assessment. Liu *et al* (2015) presented a summary of the uses so far.

can yield as good an assessment of probabilities as mathematical analyses".

The process of hazard and risk assessment for dams in a workshop format, where event trees are constructed for different plausible failure scenarios, helps identify the weak points in a complex system and/or in a reasoning and enables one to make the system more robust through, for example, hypothetical remediation measures for discussion sake. The probabilities assigned to each node in the event trees was extensively discussed in plenum at the workshop initially. There was often disagreement in the values assigned. Consensus was reached through argumentation, verification of hypotheses, consultation of additional information and discussion. The event tree analyses went through two or three iterations before the event probabilities on the tree branches and the final failure probabilities were determined.

6.3 Failure mode screening

One of the essential parts of a review of the possible failure modes before the construction of event trees. After discussion, the following mechanisms and triggers were examined:

Weaknesses in the dam or dam system:
− Internal erosion
− Slides in upstream and downstream slope
− Rockslide in reservoir causing overtopping
− Plane of weakness in bedrock foundation
− Operator error

External triggers:
− Flood
− Extreme snow/ice in the winter
− Earthquake
− Melting of glacier causing flood in reservoir
− Sabotage/terror
− Meteors or plane crashing into the dam

Before the workshop, NGI (2004) had checked that the safety was more than adequate against a rock slide triggering a tsunami in the Dravladalen Dam reservoir. The stability of the rock foundation was also checked for the high quality gneiss and granite rock foundation, with foliation dips upstream and no weakness planes downstream. Meteors and plane crash at the location of Dravladalen Dam were estimated to have occurrence probability of less than 10^{-7}/ year.

6.4 Results of analyses

Tables 1 and 2 present the results of two series of analyses, the first in 1996, the second in 2016, in terms of the annual probability of failure, $P_{f\,annual}$. The probabilistic analyses in 1996 led to the identification of an unforeseen mode of failure, which turned out to be the most critical failure mode (Johansen *et al* 1996). Remediation measures were completed during the subsequent years. The rehabilitation included: new toe for the dam to increase drainage capacity; new slope protection downstream, with gentler slope; new dam crest; new concrete shelter for the approach channel to the spillway tunnel; new leakage monitoring system; and instrumentation of upstream slope and dam crest.

The 2016 analyses looked at each of the failure modes and at the effectiveness of the remediation measures in the period 1996-2016. Table 3 compares the event tree reliability results from the analyses in 1996 and 2016. For1996, the results of the two iterations are shown. In 2016, three iterations were done, and each gave approximately the same results. The Bayesian network analyses, combined with over 500 Monte Carlo simulations, gave essentially the same 'mean' annual probability of failure as the event tree analyses in 2016. The Bayesian network analyses provided in addition the distribution of the failure probabilities, with a mean value of P_f, maximum value and minimum value of P_f, as illustrated in Figure 13 for the scenario of 'ice and hard-packed snow blocking the spillway tunnel'.

Table 1. Results of event tree analyses of Dravladalen Dam in 1996

Scenario	Most probable failure mechanism	$P_{f\,annual}$ **(it. 1)**	$P_{f\,annual}$ **(it. 2)**
Earthquake	Overtopping due to settlement of dam	$< 1.5 \cdot 10^{-6}$	$< 1.5 \cdot 10^{-6}$
Winter flood	Overtopping due to plugging of spillway tunnel	$3 \cdot 10^{-3}$	$4 \cdot 10^{-4}$
Int. erosion	Failure in downstream slope and toe *	$P_{f\,life} = 5 \cdot 10^{-4}$	$P_{f\,life} = 5 \cdot 10^{-5}$
Sabotage	Overtopping	$< 1 \cdot 10^{-5}$	$< 1 \cdot 10^{-5}$
All scenarios	$P_{f\,annual}$ without internal erosion	$< 3 \cdot 10^{-3}$	$< 4 \cdot 10^{-4}$

* In 1996, the lifetime probability of failure was calculated for the internal erosion case.

Table 2. Results of event tree analyses of Dravladalen Dam in 2016

Analysis		$P_{f\,annual}$ **(last iteration)**
Internal erosion		$4.7 \cdot 10^{-6}$
Flood	*Winter*: Ice and hard-packed snow blocking tunnel	$2.4 \cdot 10^{-7}$
	Summer: Glacier melting in reservoir	$5.4 \cdot 10^{-6}$
Earthquake		$9.0 \cdot 10^{-8}$
All geotechnical and natural hazards scenarios		$1.0 \cdot 10^{-5}$
Sabotage/terror		$2 \cdot 10^{-7}$

Table 3. Comparison of the results of event tree analyses in 1996 and 2016

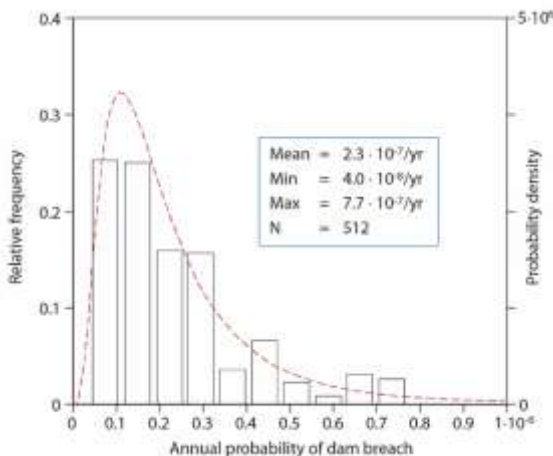| Analysis		$P_{f\,annual}$ **- 2016**	$P_{f\,annual}$ **- 1996**
Internal erosion		$4.7 \cdot 10^{-6}$	$5 \cdot 10^{-5}$ (life)
Flood	*Winter:* Ice and hard-packed snow blocking tunnel	$2.4 \cdot 10^{-7}$	$4 \cdot 10^{-4}$
	Summer: Glacier melt in reservoir	$5.4 \cdot 10^{-6}$	--
Earthquake		$9.0 \cdot 10^{-8}$	$< 1,5 \cdot 10^{-6}$
All geotechnical and natural hazards scenarios		$1.0 \cdot 10^{-5}$	$< 4,2 \cdot 10^{-4}$
Sabotage/terror		$2 \cdot 10^{-7}$	$< 1 \cdot 10^{-5}$

Figure 13. Dam Dravladalen: Annual failure probability from Bayesian Network and Monte Carlo analysis

Figure 13 gives the histogram of annual probabilities of failure and the best lognormal distribution fit, and gives the number (N) of Monte Carlo simulations done. The new risk assessment in 2016 showed that the annual failure probability for this failure mode was reduced by two to three orders of magnitude because of the implementation of the mitigation measures.

6.5 Summary

The application of reliability concepts can be useful for ensuring safe and cost-effective dam design and rehabilitation. The annual probability of failure for Dravladalen Dam in 2016 was estimated as 10^{-5} (once in 100,000 years). The annual probability of failure had been estimated as $0.4 \cdot 10^{-3}$ in 1996. The 1996 analyses identified a

new failure scenario ('ice and hard-packed snow blocking spillway tunnel'), which had been over-looked in the deterministic design. The probabilistic analyses demonstrated the effectiveness of the mitigation measures implemented in the period 1996-2012.

An annual probability of failure of 10^{-5} is lower than the statistical annual probability of failure values reported by ICOLD and the published values for acceptable risk for dams. A consequence analysis, not reported herein, established that 200 to 300 persons could be affected by a dam breach, but no lives would be lost in the case of a dam breach, due to the long warning time for this dam built in a remote area.

When all the breach scenarios were examined together, the consensus was that the most probable scenario that could lead to a breach was the sabotage/terror scenario, because it included larger uncertainties than the other scenarios and because there are today no security measures on Dravladalen Dam. The situation is however not believed to be critical because the dam is located in a very remote area with very difficult access, summer and winter. A recommendation was made (1) to maintain the leakage and displacement observations as they provide useful information for future evaluation of risk and (2) to establish measures to limit and control access to the dam.

7 CASE STUDY: 40 YEARS OF SATISFACTORY PERFORMANCE

7.1 Nyhellervatn Dam

The 650-m long rockfill embankment Nyhellervatn Dam with till core is 82.5 m high and has a reservoir capacity of $450 \cdot 10^6$ m^3. The dam, built in the period 1975−1979, is founded on bedrock. The dam is designed for a 1,000-year flood. The main Nyhellervatn Dam is classified in the highest consequence class in Norway. The stability analysis of the downstream slope gave a deterministic safety factor less than the required 1.5

after 40 years of operation. Throughout these 40 years, the dam has behaved satisfactorily, with no unexpected leakage, pore pressure increase or displacements. Leakage is monitored continuously, and reported in real time.

7.2 Reliability approach

The reliability analyses used the same approaches as for Dravladalen Dam. The three iterations gave essentially the same results. In addition, Monte Carlo analyses with the "SLOPE/W" were used to verify the stability of the upstream and downstream slopes.

7.3 Failure mode screening

After discussion during the workshop, the following mechanisms and triggers were considered:

Weaknesses in the dam or dam system:
− Internal erosion
− Slides in upstream and/or downstream slope
− Leakage at rock foundation undermining the core
− Plane of weakness in bedrock foundation
− Rockslide in reservoir causing overtopping
− Operator error

External triggers:
− Flood
− Extreme snow/ice in the winter
− Earthquake
− Wave and ice loading upstream on rip-rap
− Melting of glacier causing flood in reservoir
− Sabotage/terror
− Meteors or plane crashing into the dam

7.4 Results of analyses

7.4.1 Failure probability

Table 4 presents the results of the probabilistic event tree analyses in terms of the annual probability of failure, $P_{f\,annual}$.

The Bayesian network analyses, combined with 1000 Monte Carlo simulations, gave the same 'mean' annual probability of failure as the event tree analyses. The maximum and minimum annual P_f (mean=$3.7 \cdot 10^{-7}$/year, minimum of

$1.0 \cdot 10^{-8}$/year and maximum of $1.2 \cdot 10^{-5}$/year respectively) were obtained for the scenario of 'Leakage through cracks in the rock foundation causing erosion of the core' (row 2 in Table 4).

Table 4. Annual failure probability for Nyhellervatn Dam

Scenario	$P_{f\,annual}$
Internal erosion	$1.5 \cdot 10^{-6}$
Leakage through cracks in rock foundation causing erosion of the core	$3.7 \cdot 10^{-7}$
Flood	$6.5 \cdot 10^{-9}$
Wave loading on upstream slope	$1.0 \cdot 10^{-8}$
Ice loading on upstream slope	$1.0 \cdot 10^{-8}$
Earthquake	$2.7 \cdot 10^{-7}$
All geotechnical and natural hazards scenarios	$2.2 \cdot 10^{-6}$

7.4.2 Stability of downstream slope

The deterministic analyses of the stability of the downstream slope suggested two potential critical slip surfaces, a very shallow slip surface A, and a deeper slip surface B (Fig. 14). The following values were used for the deterministic analysis in design (φ' is effective friction angle, c' is effective cohesion and γ is total unit weight) (carefully assessed "representative" values for the entire rockfill were used at the time):

Till core: $\varphi' = 33°$, $c' = 10$ kPa, $\gamma = 23$ kN/m^3
Rockfill: $\varphi' = 45°$, $c' = 0$ kPa, $\gamma = 20.5$ kN/m^3

There is, however, a large uncertainty in the friction angle of the rockfill, as illustrated in Figure 14. The strength of a rockfill depends on many factors, including the effective stress on the slip surface, compacted rockfill porosity and quality of the rockfill material. Figure 15 (upper) presents the available data on the shear strength of rockfill, based on Leps' data (1970) and additional experimental data (EBL 2003/NGI 2002). Figure 15 (lower) shows NGI's recommendation and the requirement in Norway for the design of rockfill dams, as imposed by Norwegian regulatory body NVE (The Norwegian Water Resources and Energy Directorate, www nve.no).

Probabilistic analyses were run to include the effect of the uncertainty in the friction angle of various types of rockfill. The probabilistic analyses used a lognormal distributed random variable for the friction angle of the rockfill, with a best estimate mean (not a careful assessment) and minimum and maximum values (thus a truncated lognormal distribution). The range of values used for slip surfaces A and B is shown with the green arrows in Figure 15. The values selected for the analyses were well within the recommendation by EBL/NGI.

Table 5 compares the results of the deterministic and probabilistic stability analyses of the downstream slope under stationary conditions (stability under rapid drawdown, flood and earthquake loading was also verified). The probabilistic analyses showed that, using a plausible range of frictions angles shown in Figure 15, the downstream slope safety was adequate, even though the deterministic analysis gave a safety factor somewhat less than 1.5.

Table 5. Analysis of stability of downstream slope under stationary conditions ($FS_{required} = 1.5$)

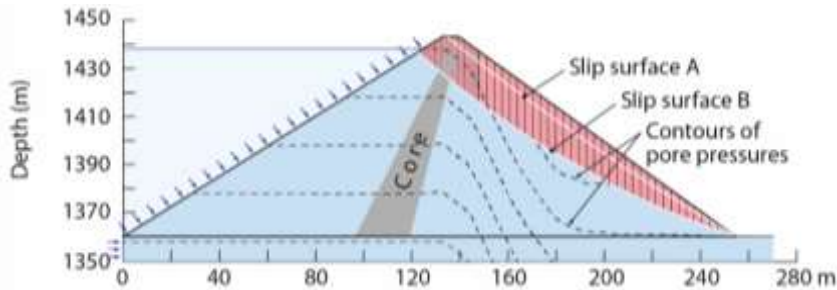| Slip surface	Deterministic FS	Probabilistic FS_{mean}	Failure probability
A	1.51	1.58	$P_f < 10^{-7}$
B	1.42	1.32	$P_f = 7 \cdot 10^{-7}$

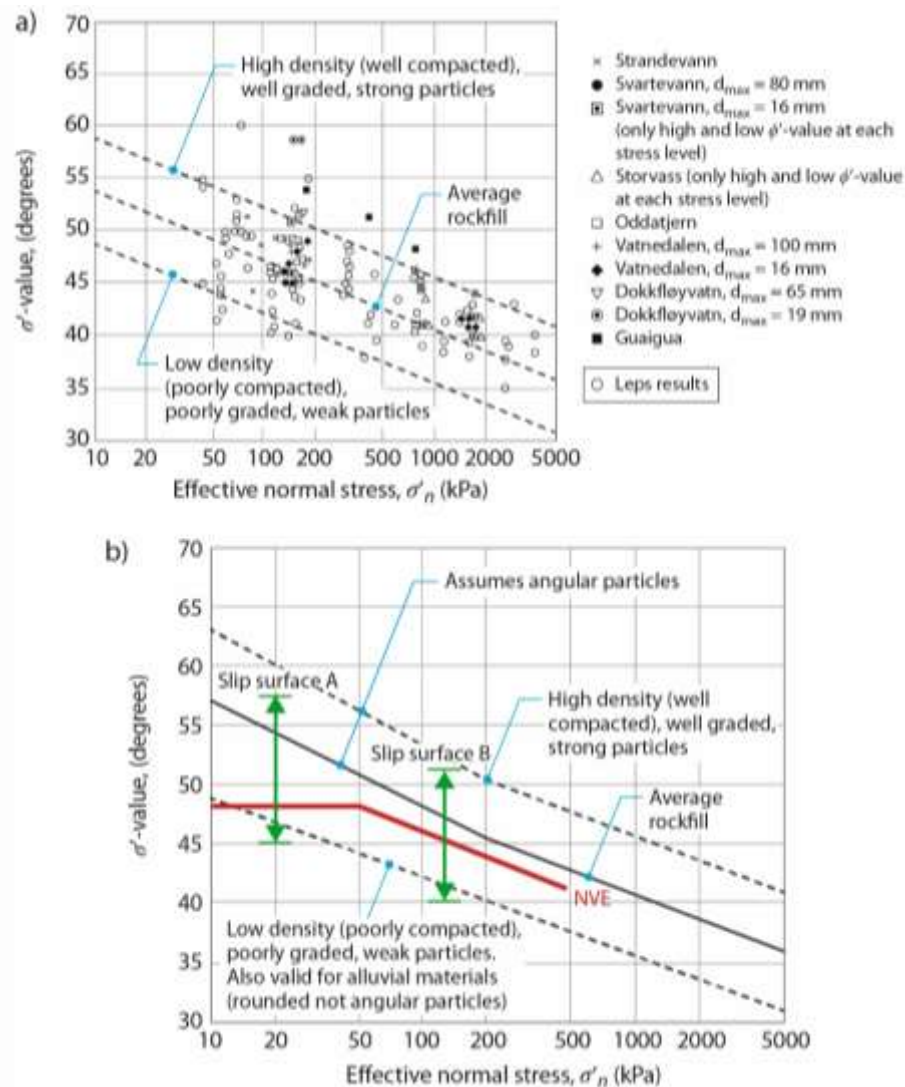*Figure 14. Stability analyses of downstream embankment, Nyhellervatn Dam*

Figure 15. a) Data underlying recommendation in Lower diagram (EBL 2003/NGI 2002); b) Recommended friction angle values for rockfill materials (Høeg, K. Pers. comm. Bucuresti Inaugural Lecture 2008)
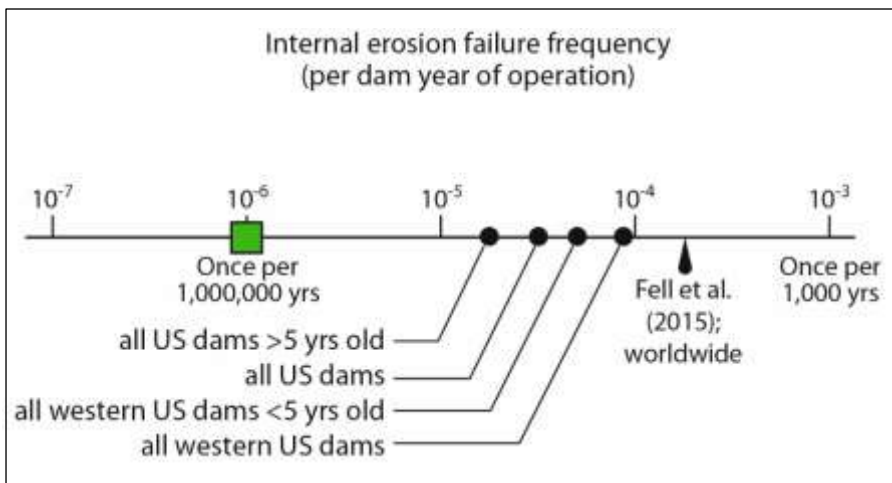
Internal erosion failure frequency
(per dam year of operation)

Figure 16. Comparison of failure frequency of Dam Nyhellervatn (green square) with statistics of breach due to internal erosion

7.4.3 Summary

The best estimate of the annual failure probability for Nyhellervatn Dam in 2017 was $2 \cdot 10^{-6}$ or lower, or a breach frequency of about once in one million years. The calculated failure probability is considerably lower than the breach frequency reported for dams in the literature, e.g. ICOLD's statistics. Figure 16 compares the failure probability with international statistics for dam breach due to internal erosion.

Nyhellervatn Dam is a solid, robust and safe dam. It is therefore important to pose the question of whether or not the dam should be rehabilitated to increase the safety factor of the downstream slope to meet the requirement of a constant safety factor, $FS \geq 1.5$. The dam has been in operation for over 40 years, undergoing multiple drawdown and filling cycles, and experiencing very harsh as well as very mild summer and winters, and flooding events. Nyhellervatn Dam has not shown any signs of distress or unexpected behaviour. The 40 years of operation are in fact 40 years of a dam under full scale loading. The added knowledge should be taken into account in the deterministic analysis, but there is no mechanism to do this. Statistics for embankment dams (e.g. Fell *et al* 2015) also show that the majority of the failures occur in the first five operative years of the dam.

8 CASE STUDY: SYSTEM OF DAMS

8.1 The Nesjen Dams

The system of dams at Nesjen consists of one main rockfill embankment dam with till core, 50 m high, four secondary (saddle) dams (of much lower heights) and a separate spillway. The dams are briefly characterized in Table 6. All the dams are rockfill dams, except for Saddle Dam 1 which is a concrete buttress dam. The Main Nesjen Dam, built in the period 1966−1968, is founded on bedrock, and is designed for a 1,000-year flood. The Main Dam and Saddle Dams 2 and 3 are classified in the highest consequence class in Norway. The reliability analyses were done to evaluate the effects of different rehabilitation measures.

8.2 Reliability approach

The reliability analyses used for the Nesjen dams were the same approaches as for Dravladalen Dam. The three event tree iterations gave essentially the same results. In addition, first-order and second-order (FORM and SORM) probabilistic analyses were run to verify the stability of the concrete buttress Secondary Dam 1, but these

Table 6. Brief description of the dams at Nesjen

Characteristics	Main Dam	Saddle Dam 2	Saddle Dam 3	Saddle Dam 4	Saddle Dam 1
Dam length (m)	675	225	170	75	500
Volume (1000 m³)	560	148	61	--	--
Maximum dam height (m)	50	19	15	15	10
Consequence class*	4	4	4	3	2

* Consequence class 4 is most severe consequence class in Norway

analyses are not reported herein. Failure probability of the concrete buttress was very low, and the consequence of a failure was much smaller than for the other dams (Consequence Class 2).

8.3 Failure mode screening

After discussion at the workshop, the following mechanisms and triggers were considered:

Weaknesses in the dam or dam system:
- Internal erosion
- Slides in upstream and/or downstream slope Leakage at rock foundation undermining the core
- Plane of weakness in bedrock foundation
- Rockslide in reservoir causing overtopping

Operator error *External triggers:*
- Flood
- Extreme snow/ice in the winter
- Earthquake
- Wave and ice loading upstream on rip-rap
- Melting of glacier causing flood in reservoir
- Sabotage/terror
- Meteors or plane crashing into the dam

8.4 Results of analyses

Table 7 and 8 present the results of the probabilistic analysis in terms of the annual failure probability, $P_{f\ annual}$, for the Main Dam before rehabilitation, and Table 8 the Main Dam after rehabilitation. Figure 17 compares the annual failure probability with the failure probability statistics for dam breach due to internal erosion. Even before rehabilitation, the Main Dam has a

low failure probability. The different rehabilitation measures decreased importantly the annual probability of a breach.

For the Nesjen system of dams, it was important to not only analyse each dam separately but to also look at the risk associated with the dams in a system of one large dam and several smaller secondary dams. During the reliability analyses under extreme flooding, it was concluded that it was desirable to reduce the reservoir water level increase due to flooding at the Main Dam by allowing some damage due to overtopping of Saddle Dam 4. The consequences of an overtopping of Saddle Dam 4 are significantly smaller (no life loss) that the consequences of an overtopping of the Main Dam. There is also ample warning time downstream, with a planned overtopping of Saddle Dam 4.

Originally, the rehabilitation required that the core and the crest be raised equally for all dams. After the reliability analyses, the dam core and the dam crest of Saddle Dam 4 should be left at a lower elevation than the other 'Consequence Class 4' dams, such that the dam owner can plan for a controlled overtopping under an extreme flood event. On the basis of the reliability analyses, recommendations were made on the most effective rehabilitation measures for reducing the risk of internal erosion (Table 8), on warning systems in the case of a controlled overtopping of Saddle Dam 4, and the interrelationship between risk at the Main Dam and the raising of all secondary dams at the same level as that of the main dam.

Table 7. Annual failure probability for Nesjen Main Dam, before rehabilitation (last iteration)

Scenario	Annual failure probability, $P_{f\,annual}$
Internal erosion (iteration 1 and iteration 2))	$7.6 \cdot 10^{-5}$
Flood	$2.9 \cdot 10^{-7}$
Earthquake	$1.0 \cdot 10^{-8}$
Erosion in rock foundation	$5.0 \cdot 10^{-6}$
Total failure probability	$5.5 \cdot 10^{-5}$

Table 8. Annual failure probability for Nesjen Main Dam, after rehabilitation (last iteration)

Scenario	Annual failure probability $P_{f\,annual}$
Internal erosion (toe reinforcement, fibre cable in till and leakage monitoring)	$8.4 \cdot 10^{-6}$
Flood, raising dam crest and core	$1.8 \cdot 10^{-7}$
Flood, improving spillway	$2.0 \cdot 10^{-8}$
Earthquake	$1.0 \cdot 10^{-8}$
Erosion in rock foundation	$1.5 \cdot 10^{-6}$
Total failure probability	$9.1 \cdot 10^{-6}$
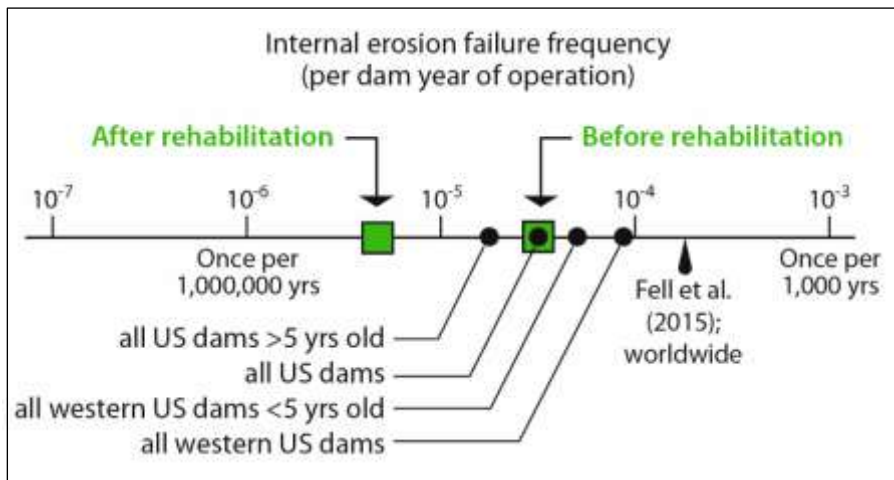
Figure 17. Comparison of failure frequency of the Main Nesjen Dam (two green squares) with statistics of breach due to internal erosion

8.5 Summary

The calculated best estimate of the annual failure probability for the Main Dam at Nesjen before the implementation of rehabilitation measures was $5 \cdot 10^{-5}$ (or about once per 50,000 years), and $1 \cdot 10^{-5}$ (or once per 100,000 years) after selected rehabilitation measures were implemented. The calculated probabilities were lower than the annual probabilities of dam breach compiled in international statistics for embankment dams (e.g. Fell *et al* 2015).

The reliability analyses shed light on the benefit of allowing overtopping of Saddle Dam 4 to reduce the failure probability of a breach of the Main Dam. In the case of an extreme flood situation, an overtopping of Saddle Dam 4 will reduce

the reservoir water level at the Main Dam and immediately reduce the risk of a breach of the Main Dam. The consequences of a dam breach at the Saddle Dam 4 are significantly lower than for the Main Dam, and would not cause loss of human life. Also there is ample warning time for the people downstream.

Originally, the rehabilitation required that the core and the crest be raised equally for all dams. Rather, after the reliability analyses, the recommendation is that the dam core and the dam crest of Saddle Dam 4 should be left at a lower elevation than the other 'Consequence Class 4' dams at Nesjen, such that the dam owner can plan for a controlled overtopping of Saddle Dam 4, if necessary under an extreme flood event.

9 RECENT DEVELOPMENTS

9.1 Use of machine learning algorithms

Artificial intelligence techniques, like machine learning, can be used to predict soil behaviour.

The Three Gorges Dam reservoir is a landslide-prone area and the construction of the Three Gorges Dam dramatically increased landslide hazard in the area. A reliable early warning system would help reduce the risk associated with landslides. Such systems can be successful if one can forecast an imminent landslide.

Yang et al (2019a; b) proposed a novel machine learning model to predict landslide displacement in dam reservoirs, and applied the model to the Three Gorges reservoir. The machine learning model uses time series analysis and the Long Short Term Memory (LSTM)" neural network approach.

Long Short-Term Memory (LSTM) neural networks are a type of "Recurrent Neural Networks (RNN)" designed to model temporal sequences and time dependency more accurately than conventional RNNs. In simple words, LSTM has a memory block, which relates one

time step to another. The memory block can retain or forget information. The 'Input gate' controls the flow of input activations into the memory cell. The 'Forget gate' controls whether the information from the previous time step is remembered or forgotten. During the process, the LSTM model learns rules from historical information and makes full use of this information. Yang *et al.* (2019a) described in more detail the architecture of the LSTM neural network used.

The displacement was decomposed into three components: a trend (T), a periodic (P) and system noise (N) components. The accumulated total displacement corresponds to $T + P + N$:
- The long term displacement (trend), controlled by 'internal' geological conditions such as lithology, geological structure and progressive weathering.
- The periodic short term displacement, influenced by two 'external' factors: rainfall and reservoir water level.
- The system error covering systematic errors during the deformation monitoring process.

The trend displacement was predicted using a cubic polynomial function.

The periodic displacement was predicted by a multivariate LSTM model based on the relationship among landslide displacement, rainfall and reservoir water level: seventy percent of the data were used to develop the model. To verify the performance of the new model, the latter 30% of the displacements were predicted by the model and compared with the measurements.

The performance of the LSTM model was validated with the observations of three typical "step-wise" colluvium landslides in the Three Gorges Dam Reservoir, and compared with other machine learning prediction models.

Figure 18 presents the results of the fitting of the model and the prediction if the periodic displacements for two of the validation landslides. Figure 19 presents the same comparison for the total accumulated prediction. The predicted values fitted well with the measured values during

the training of the model and can then be used to predict the future behaviour. The model was able to reflect the dynamic evolution of landslide deformation by relating observations from one time step to the next, thus introducing a dynamic component in the analysis.

The application of the model to the three landslides demonstrates that the LSTM model gave a more reliable prediction of the observed landslide displacement than a static model. It was concluded that the new model can be used to effectively predict the displacement of colluvium landslides in the Three Gorges Reservoir area. Such reliable predictive models can become an essential component for implementing an early warning system and reducing landslide risk.

Overall, the proposed dynamic modelling approach, based on time series analysis and LSTM, can achieve a good prediction of displacements for slow and step-wise deformations. This dynamic method has the potential for broad application to predict landslide displacement in landslide-prone regions.
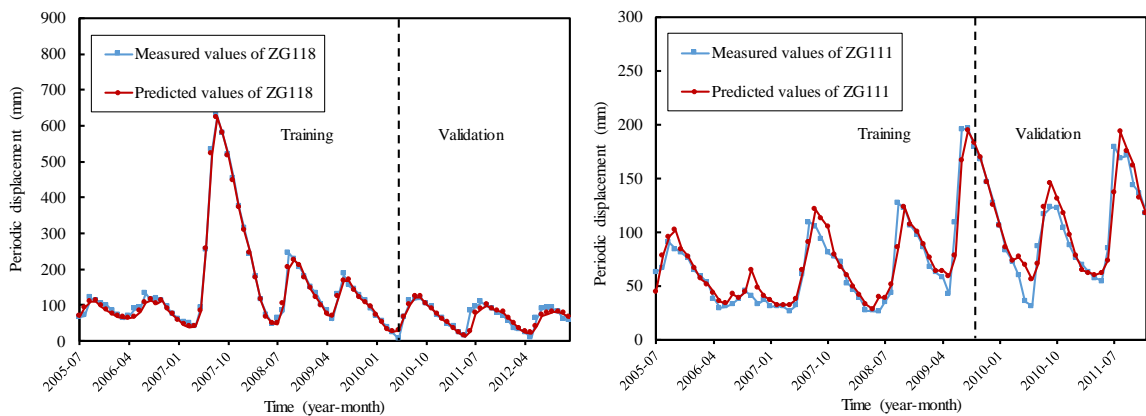
Figure 18. Periodic displacement for Baishuihe (left) and Bazimen (right) landslides (Yang et al 2019a; b)
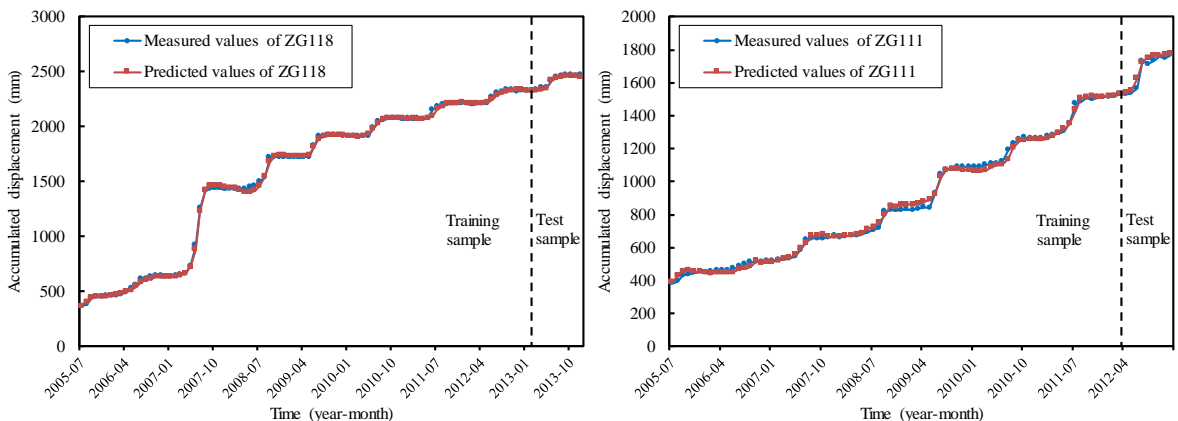
Figure 19. Total accumulated displacement for Baishuihe (left) and Bazimen (right) landslides (Yang et al 2019a: b)

9.2 The Observational Method

Terzaghi's and Peck's Observational Method should be used to greater extent for the design and the follow-up of dams on sites with complex geological conditions. The Observational Method (Peck 1969) includes several aspects of uncertainty and risk in geotechnical design, by looking at the mean and the uncertainty (*assessment of the most probable conditions and the most unfavourable conceivable deviations from these conditions[2]*), evaluating the hazards (*calculation of values of the same quantities under the most unfavourable conditions*) and preparing mitigation measures (*selection in advance of a course of action or modification of design for every foreseeable significant deviation of the observational findings from those predicted on the basis of the working hypothesis and modification of design to suit actual conditions*). Peck gave in 1996 the reason he published the Observational Method: *"My real interest, instead* [of theoretical research] *was in the ways our existing knowledge could be applied more effectively".*

ICOLD (1993) strongly suggested that the Observational Method is desirable, even required, for seepage control and drainage treatment in a dam foundation. Information gained during foundation excavation and further investigations may significantly modify and improve the original design. The implementation of the Observational Method and stabilization measures helped reduce considerably the risk of instability for the Zelazny Most tailings dam in Poland on a geologically very complex foundation (Jamiolkowski 2014: Jamiolkowski *et al* 2008). The application of the Observational Method resulted in measures such as moving the dam crest upstream to flatten the average downstream slope, constructing stabilizing berms at the dam toe, and installing relief wells in the foundation to reduce pore water pressures. Other examples of the benefit of the monitoring and the Observational Method are presented in Table 9 for three Norwegian dams.

Table 9. Benefits of monitoring program for three dams in Norway (Lacasse and Höeg 2019)

Type of dam/Dam height/Year/Core	Benefit of monitoring program
Moravatn Dam Rockfill dam 77-m/1968 Moraine core	Confirmed need for rehabilitation from the high pore pressure in the dam foundation: - Drove a drainage gallery into the downstream foundation. - Installed a system of drainage and observation holes. Checked that the drainage was efficient. Checked the drop in pore pressures. Pore pressures have remained stable ever since
Svartevann Dam Rockfill dam 129m/1976 Zoned dam Moraine core	Documented satisfactory behaviour during construction and operation - Total settlement was somewhat larger than predicted. - Pore pressures in core measured during early construction to check stability: low pore pressures allowed steeper upstream slope than initially designed. - Small leakage.
Storvatn Dam Rockfill dam 90m/1987 Inclined asphalt core	Documented the deformation behaviour of asphaltic core Used the observations to calibrate the analytical models Provided useful information for future dams of this type

---

[2] Texts in italics are quotes from Peck's (1969).

There is a potential for combining the Observational Method (OM) with the Bayesian updating approach (Christian and Baecher, 2011; Lacasse and Höeg 2019). The OM is a practical way to deal with uncertainty. Bayes' theorem provides a framework that enables updates of first estimates with new information. Bayes' theorem is the essential means of adjusting one's opinion in the light of new evidence. In fact, it is a tool made for geotechnics, as most of what geotechnical engineers do is Bayesian! Most often, the estimates of soil profiles, soil properties, model uncertainties and predictions are based on both measurements and earlier experience and engineering judgment. Bayesian thinking was, for instance, used by Alan Turing in solving the German *Enigma* code during WWII (the movie *The Imitation Game*).

Two sets of data (or predictions), in this case the mean value and the standard deviation, can be combined by Bayes theorem, assuming both datasets are normally distributed, to yield an updated estimate:

$$\mu_{updated} = (\mu_1/\sigma_1^2 + \mu_2/\sigma_2^2)/(1/\sigma_1^2 + 1/\sigma_2^2) \quad (2)$$

$$\sigma_{updated} = (\sigma_1^2 \cdot \sigma_2^2)/(\sigma_1^2 + \sigma_2^2) \quad (3)$$

where μ_1 and σ_1 are the mean and standard deviation of the first estimate (prior), μ_2 and σ_2 are the mean and standard deviation of the measurements (likelihood/new knowledge), and $\mu_{updated}$ and $\sigma_{updated}$ are the updated (posterior) estimates of the mean and the standard deviation. The result is an updated average weighted by the inverse of the standard deviations.

The Observational Method and the field monitoring during dam operation could be "complemented" with a Bayesian updating formulation in the assessments. In this way, one could associate uncertainties and outcomes with probabilistic estimates (probability of occurrence and consequences) and quantify the scenarios for making

decisions. A dynamic updating of the risk picture (means and standard deviations) with the help of continuous real-time measurements and prepared response scenarios would be an easy way to make designs safer and provide support for "risk-informed" decision-making.

Bayesian updating has been applied to continuously update the latest knowledge of the unknown parameters with the knowledge of new observations. For dams, two examples of successful applications of the Bayesian updating approach are: (1) in an uncertainty analysis of overtopping of a flood mitigation dam, Michailidi and Bacchi (2017) improved information on the flood peaks from historical observations by incorporating supplementary knowledge from different sources, including their associated uncertainty and errors; (2) Andreini *et al* (2019) developed probabilistic models to predict the internal erosion rate in embankment dams. They did reliability analysis of earth dams in terms of the critical shear stress and a coefficient of internal erosion. The Bayesian updating approach was used to quantify the uncertainty of the uncertain model parameters on the basis of observations in situ jet erosion tests.

Folayan *et al* (1970) were the first to introduce the application of Bayes' theorem to geotechnical engineering. They used Bayesian updating to predict the settlements of a marshland development analysed the associated economic consequences. The approach was also used to illustrate the optimal number of samples to improve the reliability of the prediction. Figure 7 illustrates the overconfidence that can occur in prior subjective estimates of probability distributions, in this case for the compressibility of San Francisco Bay mud.

10 INSIGHT FROM STATISTICAL AND RELIABILITY ANALYSES

For each of the case studies herein and other case studies in Norway and other countries, the relia-

bility analyses have provided useful, but different, insight and formation. For each of the cases reported herein:

- For Dravladalen Dam, the failure mode screening and reliability considerations led to the identification of a so far unidentified, but significant, failure mode. Rehabilitation was required. The analyses documented the important risk reduction through the rehabilitation.
- For Nyhellervatn Dam, the continuous leakage monitoring provided considerable information that confirmed no indication of internal erosion. Nyhellervatn Dam is perceived as solid, robust and well-behaved. Consideration of the failure probability of the downstream slope suggests that there is no need for rehabilitation, even if the traditional deterministic analysis suggest the need for rehabilitation.
- The analyses of the Nesjen Main Dam also suggest a safe and robust dam. Internal erosion is the critical failure mechanism. Rehabilitation measures may further reduce the risk. The analyses show that an optimal solution is achieved if one plans for controlled overtopping of Secondary Dam 4 in the case of an extreme flood event. Overtopping of Secondary Dam 4 has relatively smaller consequences, and water discharge would reduce considerably the risk of a breach at the Main Dam.

Another rockfill dam in Norway, which had been subjected to internal erosion during its first 20 years (the dam is now 50 years old), looked into the failure probability associated with further internal erosion and possible overtopping due to a massive rock slide in the dam reservoir. The analyses quantified the risk reduction potential of different rehabilitation measures and documented that the most expensive measures are not necessarily the most risk-reducing ones.

An additional benefit of reliability-based approaches, although not illustrated herein, lies in the fact that the process of calculating probability of failure reveals which uncertainties are the most significant for the calculated failure probability, and which are unimportant. This additional information provides an effective guide to what improvements in knowledge will reduce the overall uncertainty and failure probability. Although the number calculated is never highly precise, the range of failure probabilities provide a valuable supplement to other measures of safety. For this reason alone, calculating reliability index and/or failure probability adds value to geotechnical engineering analyses

11 SUMMARY AND CONCLUSIONS

This paper aimed at illustrating that a reliability-based approach is more rigorous and more "complete" than the deterministic approach alone because it accounts for the uncertainty in the analysis parameters, their correlation, and therefore leads to a more robust design, and a more rational assessment of safety of existing structures. The reliability-based approach is not meant to replace the traditional deterministic approach. Instead, it should be used as a complement to deterministic analyses. Examples illustrate the complementary information and value added of probabilistic analyses. Recommendations are made for acceptable risk level and on exploiting the seminal Observational Method during dam construction and drawing benefit from continued monitoring during dam operation.

An analysis that allows for both deterministic and probabilistic modelling provides an improved understanding of the potential range of behaviour under various uncertainties. The design criterion in reliability-based design is best defined in terms of a target annual reliability index or failure probability.

There is an increasing demand to adopt a reliability-based approach for the design of geotechnical structures. The techniques have considerably evolved in past years, and the probabilistic analysis software packages are accessible and

easy to use. Probability and risk concepts have now reached maturity for our profession. Most owners and operators understand the concept of risk. They expect engineers to provide probability and risk information and/or quantification to help them make risk-informed decisions.

A reliability-based estimate is not necessary for all dam engineering problems, but such estimates should be used to a greater extent when there are significant uncertainties that could influence the result or lead to decisions other than those based on deterministic results alone. All levels of reliability analyses qualitative or quantitative, are useful to gain insight and help make better engineering and management decisions.

There is today a cultural shift in civil engineering practice and the social perception of the engineer's work. Table 10 compares the earlier focus (first column) with the new directions (second column).

Table 10. Cultural shift in civil engineering practice

Earlier focus	To new direction
Hazard	Consequence
Response	Preparedness and Risk Reduction
Reactive	Proactive
Science-driven	Multi-disciplinary
Response Management	Risk Management
Planning *for* communities	Planning *with* communities
Decision-making	Risk-informed decision-making

Science and engineering help us to predict hazards and their probability of occurrence. Knowing the hazards and the risk helps making risk-informed decisions. The time to implement the tools that enable us to qualify or quantify the risk is now. In the future, the dam engineering profession will need to show that the key decisions were "risk-informed" (ISO2394:2015).

12 ACKNOWLEDGMENTS

13 REFERENCES

Andreini, M., Gardoni, P., Pagliara, S., Sassu, M. 2019. Probabilistic models for the erosion rate in embankments and reliability analysis of earth dams. *Reliability Engineering and System Safety*. 181: 142–155.

Ang, A, H-S., Tang, W.H. 2007. *Probability concepts in engineering. Emphasis on applications to civil and environmental engineering.* 2nd Ed., Wiley and Sons. 406 pp.

Baecher, G. B., Christian J. T. 2003. *Reliability and Statistics in Geotechnical Engineering.* Chichester, West Sussex, England; Hoboken, NJ, J. Wiley. 618 pp.

Benjamin, J. R., Cornell, C. A. 1970. *Probability, statistics, and decision for civil engineers*. McGraw-Hill, New York. 704 pp.

Christian J.T., Baecher G.B. 2011. Unresolved Problems in Geotechnical Risk and Reliability. State-of-the-Art. ASCE Georisk 2011. Atlanta https://doi.org/10.1061/41183(418)3.

EBL 2003/NGI 2002. Stability and Breaching of dams. Shear Strength of Rockfill and Stability of Dam Slopes. Oslo. Publ.123-20033.

FEMA 2015. Federal Guidelines for Dam Safety Risk Management. Federal Emergency Management Agency. P-1025.

Folayan, J.I., Hoeg, K.. Benjamin, J.R. 1970. Decision theory applied to settlement predictions. ASCE *Journal of Soil Mechanics and Foundation*. **96**(4): 1127–1141.

Geotechnique 1996. *The observational method in geotechnical engineering.* The Inst. of Civil Engineers. Thomas Telford London. 332 pp.

Hartford, D.N.D., Baecher G.B. 2004. *Risk and uncertainty in dam safety.* T. Telford. 391 pp.

Høeg, K. 1996. Performance Evaluation, Safety Assessment and Risk Analysis for Dams. *Hydro-power and Dams.* **6** (3): 8 pp.

Høeg, K., Murarka, R.P. 1974. Probabilistic analysis and design of a retaining wall. *ASCE JGGE.* Proc. **100** (GT3): 349−366.

ICOLD 1993. *Rock Foundations for Dams.* ICOLD Bulletin 88.CIGB. Paris. 241 pp.

ISO 31000:2018. Risk management. Guidelines. ISO 31000 2nd edition 2018-02. 16 pp.

ISO 2394:2015. General principles on reliability for structures. ISO/TC 98/SC 2. 111 pp.

Jamiolkowski, M. 2014. Soil Mechanics and the observational method: challenges at the Zelazny Most copper tailings disposal facility. *Géotechnique.* **64** (8) 590–619.

Jamiolkowski, M, Carrier, WD, Chandler, RJ, Høeg, K, Swierczynski, W, Wolski, W 2010. The geotechnical problems of the second world largest copper tailings pond at Zelazny Most, Poland. Proc. 17th SEAGC Southeast Asian Geotech. Conf. Taipei, Taiwan (eds J.C.C. Li and M.L. Lin). **2**: (12–27).

Johansen, P.M. Vick, S.G., Rikartsen, C. 1997. Risk analyses of three Norwegian rockfill dams. Proc. Intern. Conf. on Hydropower. Hydropower'97. Trondheim. pp. 431−442.

Keaveny, J.M., Nadim, F., Lacasse, S. 1990. Autocorrelation functions for offshore geotechnical data. ICOSSAR 1990. Intern. Conf. Structural Safety and Reliability. Perth. Australia. 263−270.

Lacasse, S., Nadim, F. 1996. Uncertainties in characterizing soil properties. *Uncertainty in the Geologic Environment: From Theory to Practice (Uncertainty '96),* ASCE GSP **158** (49−75).

Lacasse, S., Nadim, F. 2007. Probabilistic geotechnical analyses for offshore facilities. *Georisk*, **1**(1): 21−42.

Lacasse, S., Nadim, F., Liu, Z.Q., Eidsvig, U.K. 2017. Reliability Analysis of Embankment Dams. Geotechnical Frontiers 2017: Geotechnical Materials, Modelling and Testing. ASCE GSP **280** (910−920).

Lacasse, S, Hoëg, K. 2019. In praise of monitoring and the Observational Method for increased dam safety, ICOLD 2019 Annual Meeting/Symposium. Ottawa. 12 pp.

Langford, J. Norén-Cosgriff, K, Lacasse, S., Soergjerd, T., Brekke, A., Koelsch, G. 2019. Risk assessment of vibrations caused by groundworks. 19th ECSMGE. Reykjavik, Iceland.

Leps. T.M. 1970. Review of shearing strength of rockfill. *ASCE Journal of Soil mechanics and Foundation Engineering.* 96(4): 1159−1170.

Liu, Z.Q., Nadim, F., Garcia-Aristizabal, A., Mignan, A., Fleming, K., Luna, B. Q. 2015. A three-level framework for multi-risk assessment, *Georisk: Assessment and Management of Risk for Engineered Systems and Geohazards.* **9**(2): 59−74.

Michailidi, E.M., Bacchi, B. (2017). Dealing with uncertainty in the probability of overtopping of a flood mitigation dam. *Hydrology and Earth System Sciences.* **21**(5): 2497–2507.

Morgenstern, N. R. 1995. Managing risk in geotechnical engineering. 10th Panamerican Conf. Soil Mechanics and Foundation Eng, **4**:102–126. Guadalajara, Mexico.

Nadim, F., Lacasse, S. 1992. Probabilistic Bearing Capacity Analysis of Jack-Up Structures. *Can. Geotech. J.*, **29**, 580–588.

Peck, R.B. 1969. Advantages and Limitations of the Observational Method in Applied Soil Mechanics. *Géotechnique.* **19**(1): 171–187.

Schneider, J. 1997. Introduction to Safety and Reliability of Structures, Intern. Assoc. for Bridge and Structural Engineering. Structural Engineering documents **5**. 138 pp.

Tang, W.H. 1973. Modelling, Analysis and Updating of Uncertainties. *Proc., ASCE National Meeting on Structural Engineering,* San Francisco.

Tang, W.H. 1984. Principles of probabilistic

characterization of soil properties. *Probabilistic Characterization of Soil Properties: Bridge Between Theory and Practice,* ASCE, 4−89.

Terzaghi, K. 1929. Effect of minor geologic details on the safety of dams. American Inst. Mining and Metallurgical Eng. **215**: 31–44.

Terzaghi, K. 1961. Engineering geology on the job and in the classroom: Past and future of applied soil mechanics. Harvard soil mechanics series. **62**.

US EPA. 2010. Defining Life Cycle Assessment (LCA) US Environmental Protection Agency. 17 October 2010. Web.

USACE 2011. US Army Corps of Engineers. Engineering and Design. Safety of Dams – Policy and Procedures. Engineer Regulation ER 1110-2-1156. Washington DC. USACE. http://publications.usace.army.mil/publications/eng-regs/ER_1110-2 1156/ER_1110-2-1156.pdf.

USACE 2014. Engineering and Design. Safety of dams – policy and procedures, Department of the Army, ER 1110-2-1156, US Army Corps of Engineers, Washington, DC 20314-1000. 31 March 2014.

US Bureau of Reclamation 2011. Dam Safety Public Protection Guidelines. Dam Safety Office, Denver, Colorado. August. http://www.usbr.gov/ssle/damsafety/documents/PPG201108.pdf

Uzielli, M., Lacasse, S., Nadim, F., Phoon, K.K. 2007. Soil variability analysis for geotechnical practice. In Tan *et* al (eds.), Proc. 2nd Intern. Workshop Characterization and Engineering Properties of Natural Soils. **3**:1653−1752. Singapore, Taylor and Francis.

Vick, S. 1994. Geotechnical risk and reliability-From theory to practice in dam safety. Proc., Earth, Engineers and Education. Symp. in Honor of R.V. Whitman, MIT, Cambridge, MA. 45–58.

Vick, S. 2002. *Degrees of Belief. Subjective Probability and Engineering Judgment*. ASCE Press. 405 pp.

Whitman, R.V. 1984. Evaluating calculated risk in geotechnical engineering. *ASCE JGE* **110**(2): 143−188.

Yang, B.B. Yin, K.L., Lacasse, S., Liu, Z. 2019a. Time series analysis and long short-term memory neural network to predict landslide displacement. *Landslides.* Journal of the International Consortium on Landslides. doi:10.1007/s10346-018-01127-x.

Yang, B.B., Yin, K.L., Liu, Z., Lacasse, S. 2019b. Machine learning to predict landslide displacement in dam reservoir. Proc ICOLD 2019. Eds J.P. Tournier *et al*. International Commission on Large Dams. Symposium, Sustainable and Safe Dams Around the World. Paper #485. CRC Press. 8 pp.

XVII European Conference
ECSMGE 2019
Reykjavik
on Soil Mechanics
and Geotechnical Engineering

Geotechnical Challenges in Iceland
Challages de geotechnices d'Islande

S. Erlingsson

Faculty of Civil and Environmental Engineering, University of Iceland, Reykjavik, Iceland

VTI – The Swedish National Road and Transport Research Institute, Sweden.

ABSTRACT: The geotechnical challenges in Iceland are in many aspects unusual. The geological setting of the country is unique and has a great influence on the local geotechnical conditions. Iceland lies on the divergent boundary between the Eurasian plate and the North American plate formed by the Mid-Atlantic Ridge. This has created a landmass with active volcanoes, geothermal areas and zones of high seismicity. The bedrock is relatively young and mainly basaltic. It has been built up of relatively thin lava layers during eruptions. It is frequently highly jointed with irregular interlayers. The horizontal stresses in the rock mass are furthermore very low. The soil layers consist mainly of non-cohesive materials, often created in catastrophic events such as glacial floods, and are therefore often loosely packed. This paper gives a short overview of the geotechnical conditions in the country and additionally describes several geotechnical engineering projects. Some geotechnical challenges due to climate change will also be briefly discussed.

RÉSUMÉ: Les défis géotechniques en Islande sont à bien des égards inhabituels. Le cadre géologique du pays est unique et a une grande influence sur les conditions géotechniques locales. L'Islande se trouve sur la frontière divergente entre la plaque eurasienne et la plaque nord-américaine formée par la dorsale médio-atlantique. Cela a créé une masse continentale avec des volcans actifs, des zones géothermiques et des zones de haute sismicité. Le substratum rocheux est relativement jeune et principalement basaltique. Il a été construit de couches de lave relativement minces pendant les éruptions. Il est souvent très joint avec des intercouches irrégulières. Les contraintes horizontales dans la masse rocheuse sont en outre très faibles. Les couches du sol sont principalement constituées de matériaux non cohésifs, souvent créés lors d'événements catastrophiques tels que les inondations glaciaires, et sont donc souvent emballés. Cet article donne un bref aperçu des conditions géotechniques dans le pays et décrit en outre plusieurs projets d'ingénierie géotechnique. Certains défis géotechniques dus au changement climatique seront également brièvement.

Keywords: Geotechnical engineering, geology, Iceland, rock mass, soils, material properties.

1 INTRODUCTION

Geotechnical engineering is a relatively young discipline in Iceland. Until the last decade of the nineteenth century the country was poor and isolated. Construction activities had been only minor and had not required any civil engineering knowledge. The first bridges for river crossings were made in the southern part of the country in

the 1890's. In the early twentieth century, the government started to investigate the possibilities of building a harbour in the capital area. The main pressure came from the traders and merchants who needed better and more secure quays for their loading and unloading their ships (Friðriksson 2013). In 1913 the construction of the Reykjavík harbour finally started. Four years later the first three piers that made up what is now called the Old Harbour had been erected. The earth and rock materials needed for the construction were transported about 3 km on specially built rail lines from quarries in nearby Öskjuhlíð and Skólavörðuholt. The harbour was the country entry to modern times for more secure export of fish products, improved trading and efficient transportation (Friðriksson 2013).

The next large engineering project was the construction of irrigation canals in the South Iceland lowland area between 1923 and 1930 to mitigate and control the discharge over agricultural land. It was at that time an engineering achievement requiring precise surveying followed by hydrological and hydraulic design based on a thorough understanding of fundamental geotechnical conditions. It was a successful project and benefitted farming in the area for many decades (Þórðarson 2002).

The beginning of exploitation of domestic energy resources started in 1920's, first and foremost to generate electricity from hydropower. The first power plant of any importance was the Elliðarárstöð, inaugurated in 1921, after only two years of construction time, providing almost one MW of electricity to the fast-growing city of Reykjavik (Þórðarson 2002). The location of the Elliðarár station was in the outskirts of the Reykjavík area, requiring only short transmission lines. The next phase in harnessing hydropower in Iceland was the construction of three hydropower stations by the River Sog, built in 1935 – 1960 about 50 km east of Reykjavík (Bjarnason et al. 2019). The third phase of hydropower utilisation began in the late 1960's on the River Þjórsá in South Iceland with

several relatively big dams and associated reservoirs culminating with the Kárahnjúkar hydropower plant (690 MW) in East Iceland completed in 2009 (Bjarnason et al. 2019). Another pioneering engineering project during the last century was the utilisation of the geothermal energy which today is used to heat over 90% of houses in Iceland and produces about 27% of the electricity (Flóvenz 2019). This of course required good geotechnical skills as well as accountable and responsible construction practices. About 85% of the total primary energy supply in the country comes from domestically produced renewable energy sources. This is the highest share of renewable energy in any national total energy budget (Bjarnason et al. 2019).

The modern roads and bridge building era started in 1891 when the first suspension bridge over the River Ölfusá was erected. The bridge collapsed in 1944 due to overloading from two trucks transporting dairy products to the capital area (Þórðarson 2002). Gravel roads were thereafter gradually extended out from the capital area. In the 1960's construction was started of more permanent pavements with concrete or asphaltic surfaces. In 1974 the Icelandic ring road was completed. The construction of the last section of the ring road was a considerable challenge to geotechnical and hydraulic engineering due to the proximity to the Vatnajökull glacier and huge glacial floods.

The objective of this paper is to give a brief overview of the geotechnical and rock mechanical conditions in Iceland. As they are highly influenced by geological and geophysical processes, these are addressed as well. Examples of some typical challenges are given.

Finally, new challenges that we are facing within the field, such as climate change, will be discussed.

2 GEOLOGICAL SETTINGS

The geological setting of Iceland is unique. Iceland lies on the divergent boundary between

two tectonic plates, the Eurasian plate and the North American plate located squarely on the Mid-Atlantic Ridge (MAR) (Einarsson 2008, Thordarson and Höskuldsson 2014). Furthermore, the island is situated on a hotspot, the Iceland plume. The plume has probably, through its activity, caused the formation of the island with its first appearance over the ocean surface about 16 to 18 m years ago (Flóvenz 2019). The MAR enters the island from the south-west on the Reykjanes Peninsula and departs from the north-east coast. As the spreading axis crosses the island, it manifests a zone of active spreading and volcanism, the axial volcanic zones (AVZ) (Flóvenz 2019).
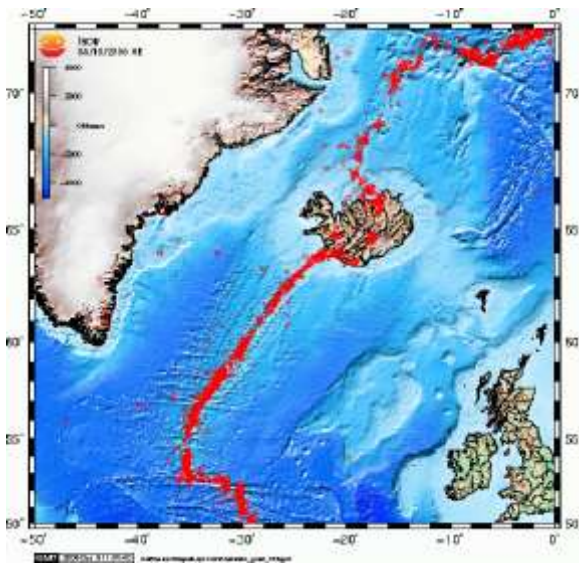
Figure 1. Epicentres of earthquakes in the Atlantic Ocean 1964–2006. Data are from the epicentre list of the NEIC, US Geological Survey. Figure courtesy of P. Einarsson.

As the AVZ passes through the country, it forms an irregular pattern. It has shifted about 150 km eastwards, close to the southern shoreline, forming the South Icelandic Seismic Zone (SISZ) and back north-west through the Tjörnes Fracture Zone (TFZ) on the northern cost. Between the two fracture zones (FZ), two parallel spreading segments are active but join into one segment north of the Iceland plume. There is active volcanism along the AVZ associated with this geological anomaly. Additionally there is earthquake activity, both along the ridges themselves and the two FZ (SISZ and TFZ) and geothermal fields along the rift zones as well as on both its flanks.

Figure 1 shows the epicentres of earthquakes on the Mid-Atlantic Ridge during the period 1964 – 2006. It shows that the epicentres form a narrow deformation zone south and north of the country, but as it crosses the Iceland plateau the zone becomes wider. This can also be seen in Figure 2.
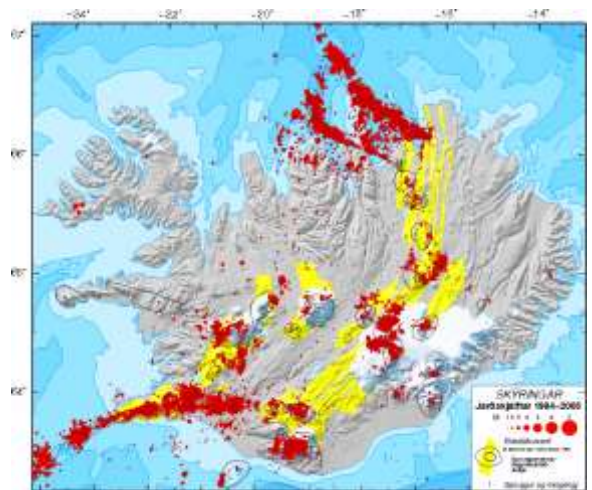
Figure 2. Earthquake epicentres, 1994 – 2007 and volcanic systems of Iceland. Epicentres are from the data bank of the Icelandic Meteorological Office. Figure courtesy of P. Einarsson.

A simplified geological map of Iceland is shown in Figure 3 where all the main geological subdivisions are indicated (Thordarson and Höskuldsson 2014).
.
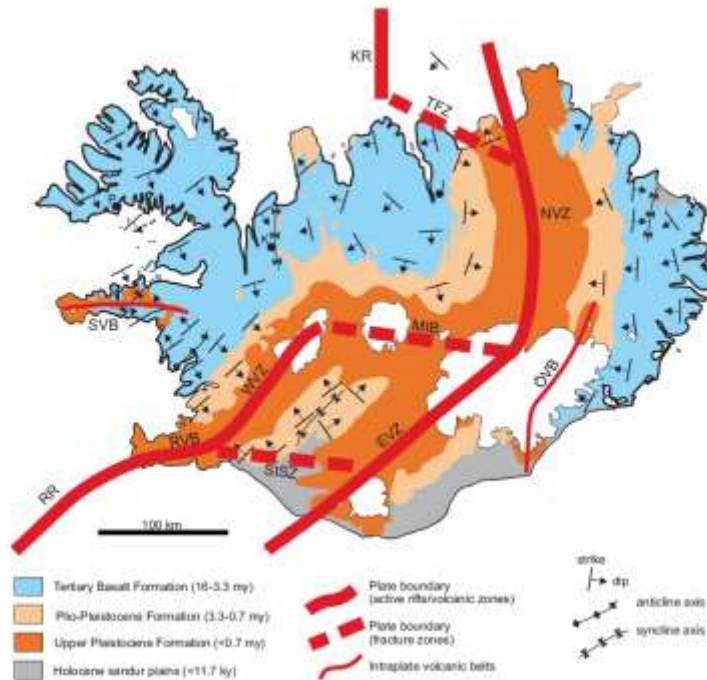
Figure 3. Simplified geological map of Iceland showing the main geological subdivisions as the fault structures, volcanic zones and belts. RR is the Reykjanes Ridge, RVB Reykjanes Volcanic Belt, WVZ West Volcanic Zone, MIB Mid-Iceland Belt, EVZ East Volcanic Zone, NVZ North Volcanic Zone, SISZ South Iceland Seismic zone, TFZ Tjörnes Fracture Zone, KR Kolbinsey Ridge, ÖVB Öræfi Volcanic Belt, SVB Snæfellsnes Volcanic Belt. Figure courtesy of Á. Höskuldsson.

The AVZ follows the divergent plate boundary where hot magma wells up vertically from the mantle and the two plates diverge horizontally. The new material then fills in the gap between the plates, thus increasing the overall size of the main island. This lateral movement can be observed on the surface (Árnadóttir et al. 2009). Figure 4 shows the observed lateral movements of the surface measured during the period 2004 – 2016 with the GPS technique (Valsson 2019). On average, this gives a movement of 19 mm/year (stations close to the SISZ earthquake in 2008 and to the volcanic eruption in Holuhraun in 2014 ignored).
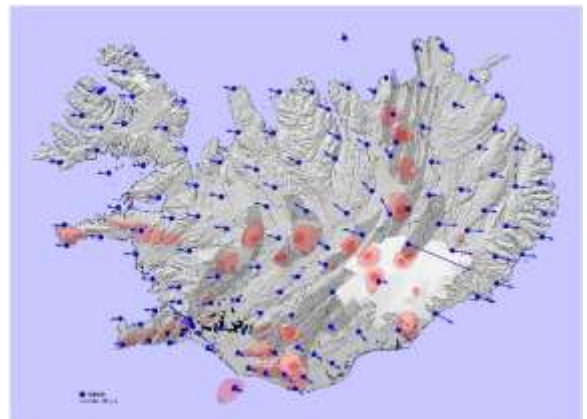
Figure 4. Observed lateral displacement measured with the GPS technique in Iceland during 2004 to 2016. Figure courtesy of G. Valsson.

Figure 5 shows a simplified overview of the geothermal fields of Iceland. The high temperature areas follow the AVZ. On both flanks of the AVZ, an irregular band of low temperature areas is formed. However, at a considerable number of locations low temperature fields have been observed further away from the AVZ.
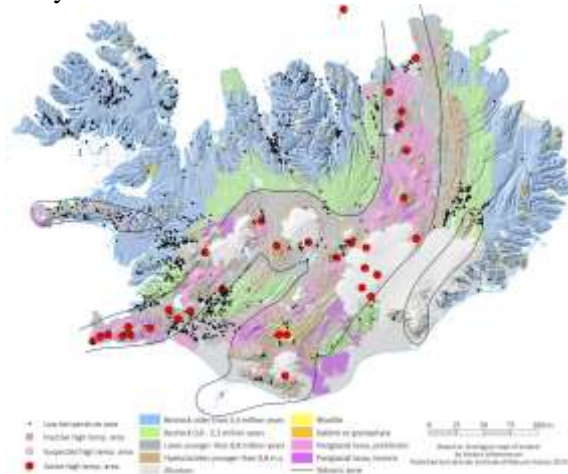
Figure 5. Geothermal fields in Iceland. Figure courtesy of H. Bjarnason.

Figure 6 shows typical temperature logs in boreholes in Iceland outside the AVZ (high temperature geothermal areas) (Flóvenz 2019). The figure shows that the temperature in the uppermost five hundred metres can vary from very low temperatures to almost 80°C. Thus, from a geotechnical point of view, at very many locations the risk of encountering high temperatures in the ground needs to be considered.

3 ROCK ENGINEERING

The geological and geophysical settings have a major impact on the local rock engineering characteristics and therefore their applications in engineering such as foundations, dam and bridge abutments, stability of underground openings and aggregate productions.
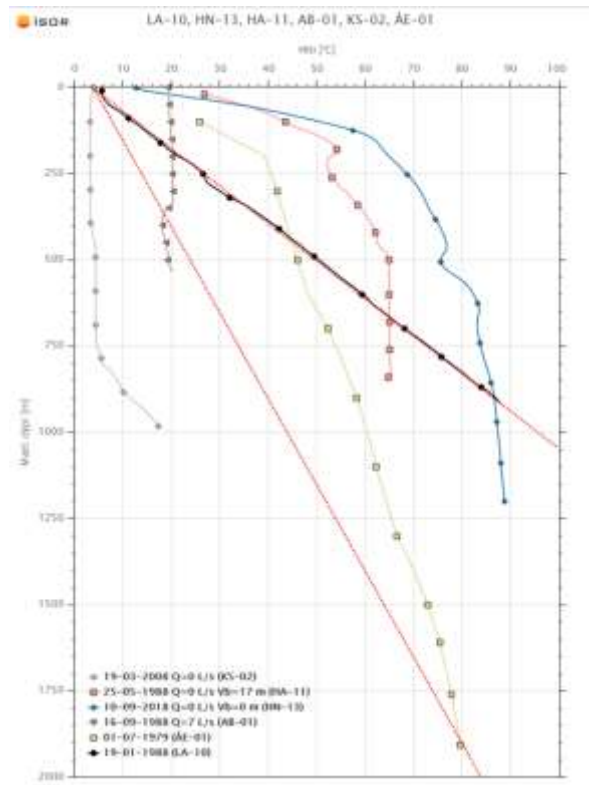
Figure 6. Temperature logs in a few boreholes in Iceland. Figure courtesy of Ó. Flóvenz.

As stated before, Iceland is a volcanic island created by volcanism on the MAR during the last approximately 18 million years. Most of the rock formations in Iceland are therefore of volcanic origin from the late Tertiary to the present time. The oldest rock is in the extreme east and west of Iceland where the rock mass is in general built up of sub-horizontal strata of regional basalt layers, most often with scoriaceous interfaces between the adjacent basaltic layers and sedimentary interbeds (Loftsson et al. 2005). Inclined dikes or other discontinuities appear frequently. The basaltic lava can be highly fractured. Figure 7 gives a schematic overview of a melted lava stream running over existing land. The lava cools off from the surface and the bottom, creating highly fractured zones. With time the inner part cools off as well, creating shrinkage joints in the rock mass.
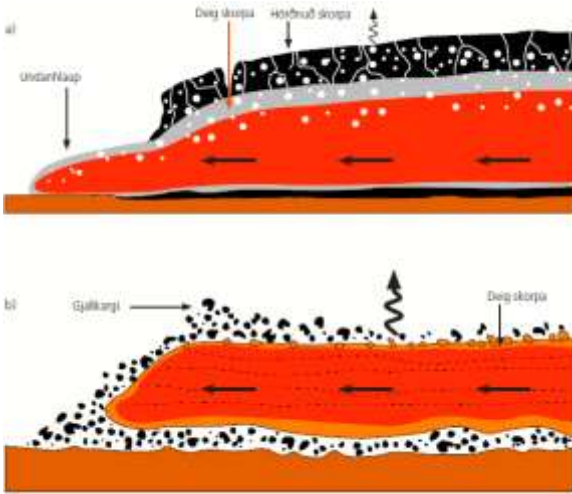
Figure 7. Melted lava flowing over existing land. The moving lava cools off from the surface and the bottom, creating highly fractured zones. Sólnes et al. 2013 (Þ. Þórðarson).

Figure 8 shows a typical Icelandic lava stratum.

Figure 8. Cross section of typical Icelandic rock mass. Horizontal lines can be seen, forming boundaries between different lava layers. The layers are usually a few to tenths of metres in thickness.

3.1 Mechanical properties

The main engineering properties of intact rock samples are strength and deformation. An example of a measurement of the stiffness and

Poisson's ratio from a uniaxial compression test of basalt and scoria is given in Figure 9 (Jóhannsson 1997). The samples were from the Hvalfjörður tunnel that was completed in 1998.
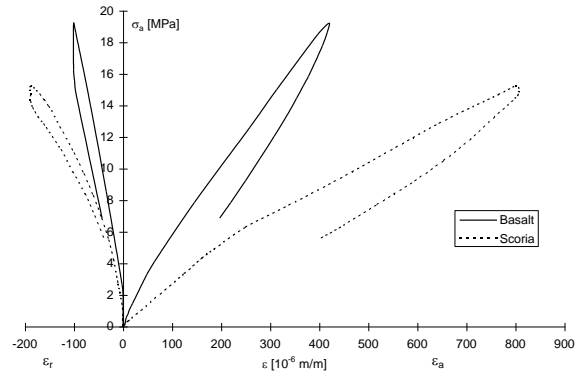
Figure 9. Stress-strain relationship of basalt and scoria in one-dimensional compression test. The indices a and r refer to the axial and radial directions, respectively.

3.2 In situ rock mass stress

Measurements of rock stresses have been made in combination with various underground projects throughout the country during the last 50 years with the hydraulic fracturing and overcoring methods (Loftsson et al. 2006, Hemmingsen 2016). The vertical stress components can be assumed to follow the worldwide trend with an increasing slope of $0.027 \, \text{MN/m}^3$ with depth. The horizontal stresses, on the other hand, are unconventional. The horizontal stresses are usually expressed as the rock stress coefficient k defined as

$$k = \frac{\frac{1}{2}(\sigma_h + \sigma_H)}{\sigma_v} \tag{1}$$

where σ_h, σ_H and σ_v are the minor and major horizontal and vertical stress components, respectively. The results of the rock stress coefficient measurements as a function of depth are shown in Figure 10.

Table 1. Some typical technical properties of common Icelandic bedrock (based on Guðmundsson et al. 1991).

Porperty	Basalt	Scoria	Sedim. rock Fine-grained	Sedim. rock Coarse-grained	Fault Breccia
UCS [MPa]	100 – 300	20 – 60	5 – 30	5 – 80	1 - 20
E [GPa]	20 – 60	2 – 20	2 – 10	2 – 15	?
Q – value [-]	4 -12	3 – 10	0.1 – 3	0.5 – 4	0.01 1.0
Typical strata thickness [m]	2 – 15	0.5 – 5	0.2 – 5.0	1 – 10	0.1 – 2

UCS is the Uniaxial Compression Strength of intact rock specimens of 50 mm in diameter.
E is the Young modulus (stiffness) of intact rock specimens.
Q-value is the NGI Quality value (https://www.ngi.no/eng/Services/Technical-expertise-A-Z/Engineering-geology-and-rock-mechanics/Q-system)
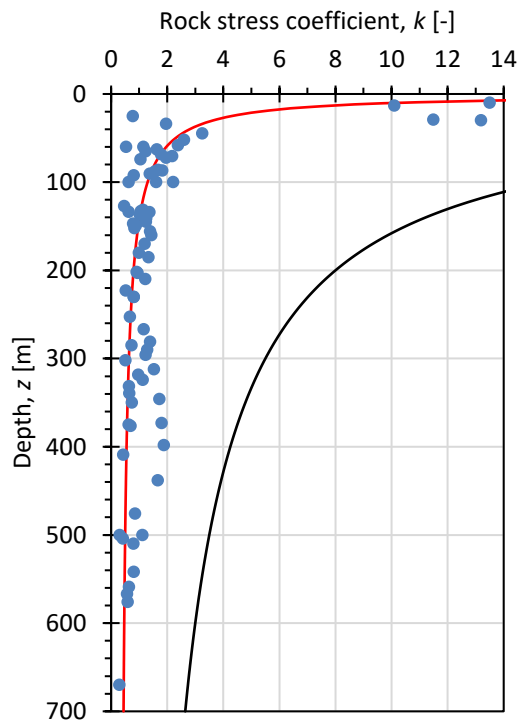
Figure 10. Rock stress coefficient as a function of depth from 17 stress measurement locations in Iceland. The black and red lines represent the upper and lower boundaries based on worldwide trends.

The red and black lines represent the worldwide lower and upper limit trends (Hudson and Harrison 2002) expressed as

$$\frac{100}{z} + 0.3 < k < \frac{1500}{z} + 0.5 \qquad (2)$$

where z is in metres.

As can be seen in Figure 10 the rock stress coefficient is generally very low and many measurements reveal values that are even lower than the lower boundary trend implicates. The reason for these low horizontal stresses is probably due to the divergent plate movements at the MAR which generate a pulling force in the crust that reduces horizontal compression.

A simple relationship between the k-value and the horizontal deformation modulus E_h exist as

$$k = 0.25 + 7E_h\left(0.001 + \frac{1}{z}\right) \qquad (3)$$

where E_h is given in GPa and z in m (Sheory 1994). The previously obtained results are shown in Figure 11 along with three E_h values.

Based on Figure 11 it is clear that the deformation moduli in the country lie mainly between 4 and 35 GPa, particularly at depths shallower than 300 m. At one location in the oldest bedrock (furthest away from the rift zone) a deformation modulus as high as 70 GPa was observed at depths greater than 300 meters.

3.3 Underground openings

There are basically two types of underground openings constructed in the country, i.e. as a part of hydropower schemes (access, headrace- & tailrace tunnels, vertical shafts, power houses) and road tunnels. The building of underground openings began in 1948 with the 30m long Arnardalshamar road tunnel and culminated in 2004 – 2008 with the construction of the Kárahnjúkar hydropower plant where all together 73 km of tunnels were built, of which around 48

km were full face TBM bored tunnels (Loftsson et al. 2005; Bjarnason et al. 2019).
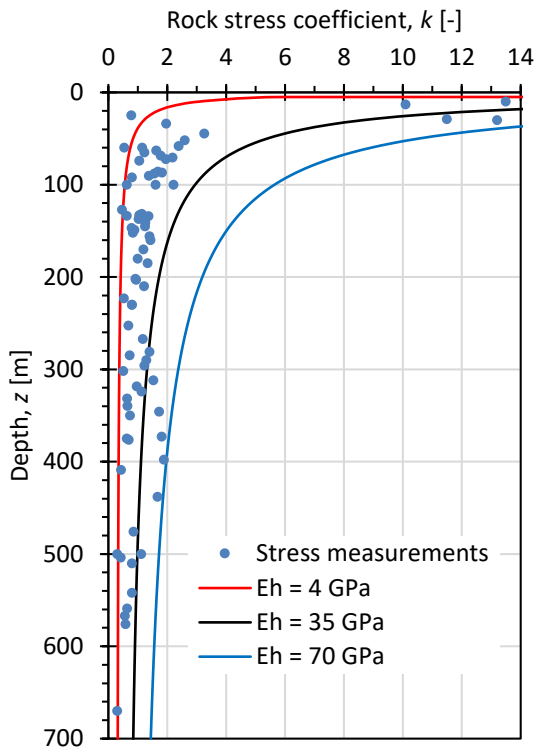
Figure 11. Rock stress coefficient as a function of depth. The lines represent three values of the horizontal deformation modulus.

The structural stability design of the underground openings has almost solely been based on the *Q*-system (NGI 2015). The reinforcement strategy presented there works well over the entire range of *Q*-values. i.e. from spot bolting in extremely good conditions through systematic bolting and fibre reinforced shotcrete to rib reinforcements in very or extremely poor conditions.

The main problems that occur in rock mass underground openings are usually related to:

Water leakage
Geothermal heat
Layered strata
Sedimentary layers

The rock mass is often highly fractured, with thin layers and irregularly directed dikes and other weakness planes. Furthermore, the horizontal stresses are low. The permeability of the rock mass can therefore be expected to be high. In areas with high groundwater table a large inflow of water has occurred that has been difficult to control.

In areas where the heat gradient is high, the rock mass can in some areas have a temperature up to 70 – 80 °C at depths of just a few hundred metres. Where water inflow has also taken place, this has caused difficult working conditions.

The fact that the strata are built up of thin layers ranging from a few tens of cm to a few metres or tens of metres that frequently further dip from horizontal, means that tunnels are always crossing new layer interfaces. The rock face consists therefore frequently of mixed layers of materials with different mechanical properties. Stress concentrations can therefore be observed at the layers´ boundaries, and if a weak layer appears in the crown the risk of instability is high.

4 SOIL CONDITIONS

The local soil conditions consist mostly of normally consolidated Holocene soils of basaltic origin. The soils have been created by glacial or weather erosion and transported by aerial or fluvial processes, usually from the central plateau towards the coast. Some soil movement occurred in catastrophic events, such as in volcanic eruptions or by glacial floods. This means mostly that the local soils are coarse-grained aggregates (coarse silty particles and coarser grains) that are often loosely compacted. The finer fractions, which settle in low streams, are transported to the sea. An example of typical soil conditions is shown in Figure 12 where a newly constructed bridge over the River Morsá is shown in the foreground and the Öræfajökull Glacier (part of the Vatnajökull) in the background. The soils shown are fluvial sandy or gravelly soils and have been transported mainly in catastrophic events originated from volcanic or geothermal activity under the Vatnajökull Glacier.

Figure 12. Thick sediments of loosely compacted sandy and gravelly soils in the forefront that have been piled up mainly in catastrophic events such as volcanic eruptions or glacial flow. Figure courtesy of by V. A. Ingólfsson.
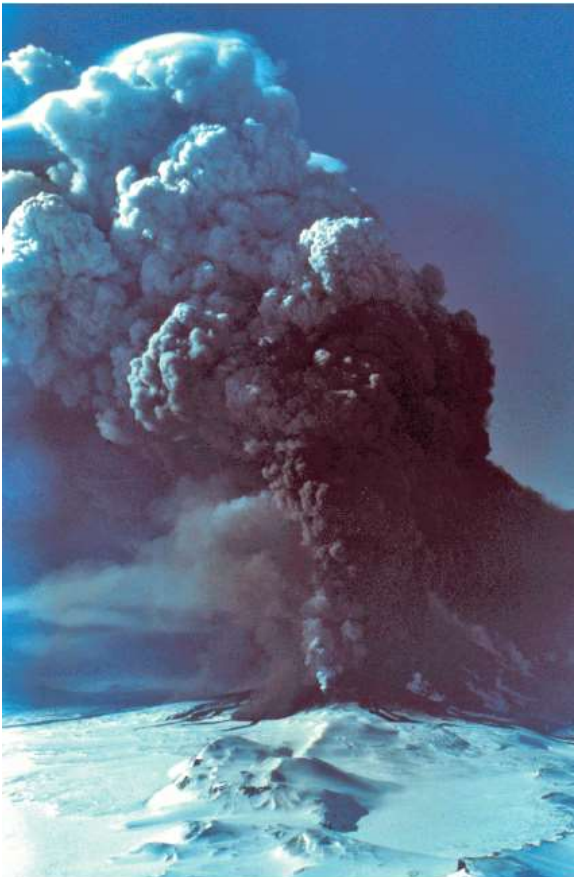
Figure 13. Mt. Hekla has created thick sediments of pumice in prehistoric eruptions. Sólnes et al. 2013 (Pálmi Hannesson/Sólarfilma).

Additionally there are soils that have been created in volcanic eruptions. Ash and pumice from Holocene volcanic eruptions can be found in some areas such as near some of the active volcanoes. Pumice is a lightweight and highly porous material of low strength. However, it also has good thermal properties and has been used in mortar or as thermal isolation layers in construction (see Figure 13).

As in many northern European countries and in North America peat deposits can be found in some places in Iceland. The local climate, geography and environment favour bog and peat bog formations. The peat is usually lightly decomposed with a high void content and water content as high as a few hundred to one thousand per cent. Figure 14 shows a thin road structure resting on peaty land. The pavement structure was damaged in the June 17, 2000, earthquake (M_w 6.5) due to liquefaction of the underlaying soft peat.

Figure 14. A pavement structure resting on a peaty subgrade in Holt, South Iceland that liquefied in the June 17, 2000 earthquake (M_w 6.5). Figure courtesy of V. A. Ingólfsson.

The main soil categories according to the Unified Soil Classification System (USCS) are gravel (G), sand (S) and silt (M) or mixtures of these fractions, as well as organic soils (peat). The fine particles (diameter < 63 μm) consist mostly of silt size fractions (between 2 and 63

μm); thus hardly any clayey soils can be found in the country.

4.1 Deformation properties

The deformation characteristics of the soils, for settlement predictions, are usually estimated with Janbu's Modulus Method (Janbu 1970). The load-deformation relationship is therefore estimated by a one-dimensional compressional (oedometer) test where the slope of the curve in the stress strain plot, the tangent modulus M_t, can be expressed as:

$$M_t = \frac{d\sigma'}{d\varepsilon} \quad (4)$$

where $d\sigma'$ and $d\varepsilon$ are the increments of effective stress and strain, respectively. The tangent modulus can be assumed to follow the relationship:

$$M_t = m\sigma_a \left(\frac{\sigma'}{\sigma_a}\right)^{1-a} \quad (5)$$

where m and a are material parameters and σ_a is a reference stress (100 kPa). By rewriting equation (4) and integrating, the strain can be estimated by

$$\varepsilon = \int_{\sigma'_0}^{\sigma'_0+\Delta\sigma'} \frac{1}{M_t} d\sigma' \quad (6)$$

giving

$$\varepsilon = \frac{1}{ma}\left[\left(\frac{\sigma'_0+\Delta\sigma'}{\sigma_a}\right)^a - \left(\frac{\sigma'_0}{\sigma_a}\right)^a\right] \text{ if } a\neq 0 \quad (7)$$

or

$$\varepsilon = \frac{1}{m}\ln\left(\frac{\sigma'_0+\Delta\sigma'}{\sigma'_0}\right) \text{ if } a = 0 \quad (8)$$

Based on a large amount of testing (Skúlason 1978) the two parameters, the modulus number m and the stress exponent a for saturated samples, have been estimated for different soil types (see Figures 15 – 17). The stress exponent can be assumed as 1.0 for coarse gravel, 0.5 for silt and sandy materials, and 0.0 for clay and organic (peaty) soils.
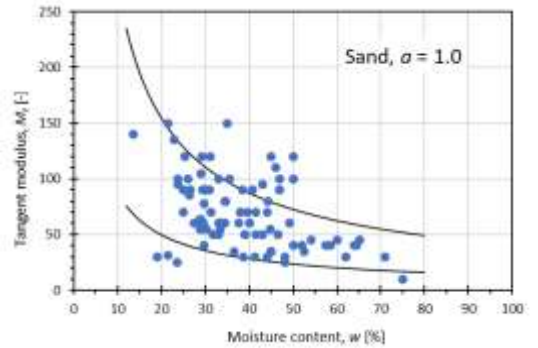
Figure 15. Tanget modulus M_t ($M_t = m\sigma_a$ as $a = 1.0$) of saturated sandy materials as a function of moisture content.
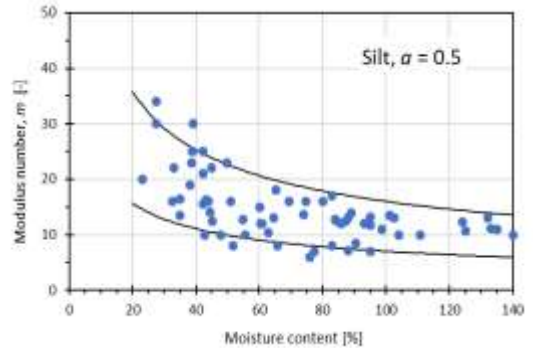
Figure 16. Modulus number m of saturated silty materials as a function of moisture content.
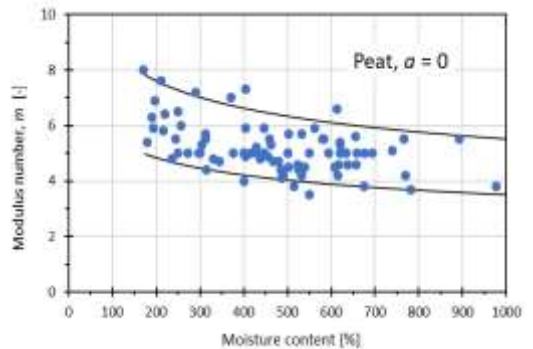
Figure 17. Modulus number m of saturated peat as a function of moisture content. Note that the moisture content is high, ranging from 150 – 1000%.

Furthermore, the soil types exhibit time dependent deformations that are not stress

dependent. Again, the soil parameter, the time resistance R, is usually estimated according to Janbus method (Janbu 1970), i.e.

$$R = \frac{dt}{d\varepsilon} = r_s\left(t - t_r\right) \quad t > t_r \tag{9}$$

where r_s is the time resistance coefficient and t_r is a reference time (for most soils it can be assumed that $t_r = 0$) (Skúlason 1978). The induced strain as a function of time can now be estimated as

$$\varepsilon_s = \frac{1}{r_s}\ln\left(\frac{t}{t_p}\right) \tag{10}$$

where t_p is the time for the primary consolidation.

The time resistance coefficient r_s for the three soil groups of sand, silt and peat are shown in Figures 18 – 20.
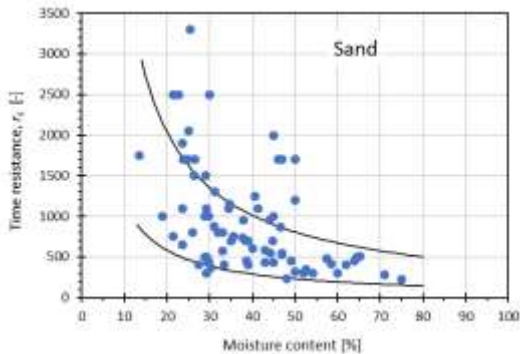
Figure 18. Time resistance coefficient r_s for sand as a function of moisture content.
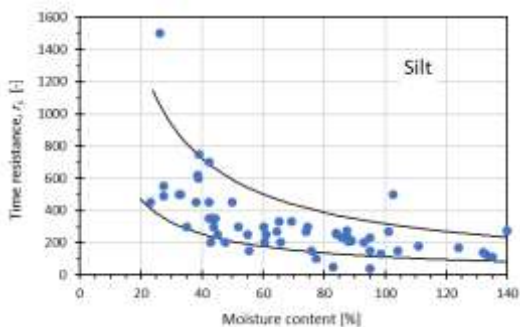
Figure 19. Time resistance coefficient r_s for silt as a function of moisture content.
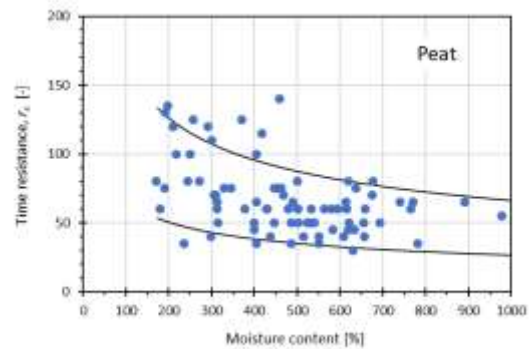
Figure 20. Time resistance coefficient r_s for peat as a function of moisture content. Note the high in-situ moisture content.

4.2 Strength characteristics

Most soils in Iceland are coarse-grained with a low fine content. Hence they are non-cohesive with no or little plasticity. The main strength parameter is therefore consequently the friction angle ϕ' and the cohesion c can be ignored. The friction angle in a compacted state is, however, relatively high as compared to many other regions. The reason for this is probably linked to the surface characteristics of the grains that are frequently angular with fresh surfaces and sharp corners that show good interlocking effects in a compacted state.
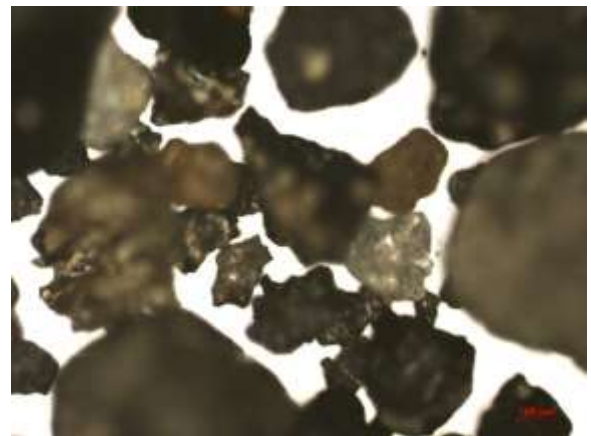
Figure 21. Magnified image of sand particles from a sample from test pit at the proposed Urridafoss HE project site (Wells 2009).

Common values of friction angles of well compacted materials are given in Table 2 (Skúlason et al. 2002, Pálmason 2018).

Table 2. Common friction angles for well compacted soils in Iceland.

Soil type	Friction angle [°]
Gravelly soil	50 – 65
Sandy soil	42 – 48
Silty moraine	40 – 47

4.3 Classification of soils

For soil exploration, dynamic sounding and rotary/percussion sounding have frequently been used successfully. They both suit well for coarse-grained materials and as the cone head or crown is robust, there is little risk of damaging during testing. In both methods, the rod can both be pushed downwards and rotated and can therefore penetrate through all soil types, ranging from fine-grained to very coarse- grained soils or rock. The interpretation of the data for soil classification is however somewhat difficult, although depth to firm ground (bedrock) can be estimated.

A Standard Penetration test (SPT) or Cone Penetration test (CPT) is further used. An example of CPT test results on the south coast at a location close to Þorlákshöfn is given in Figure 22. This is a site consisting of typical non-cohesive material with particle sizes ranging from silty particles and larger. Although the site deposit is very thick, the test was terminated at 8.3 m depth due to high resistance and consequently risk of damage to the CPT cone. This was probably due to the fact that the cone hit larger boulders that fequently occur in the local soils.
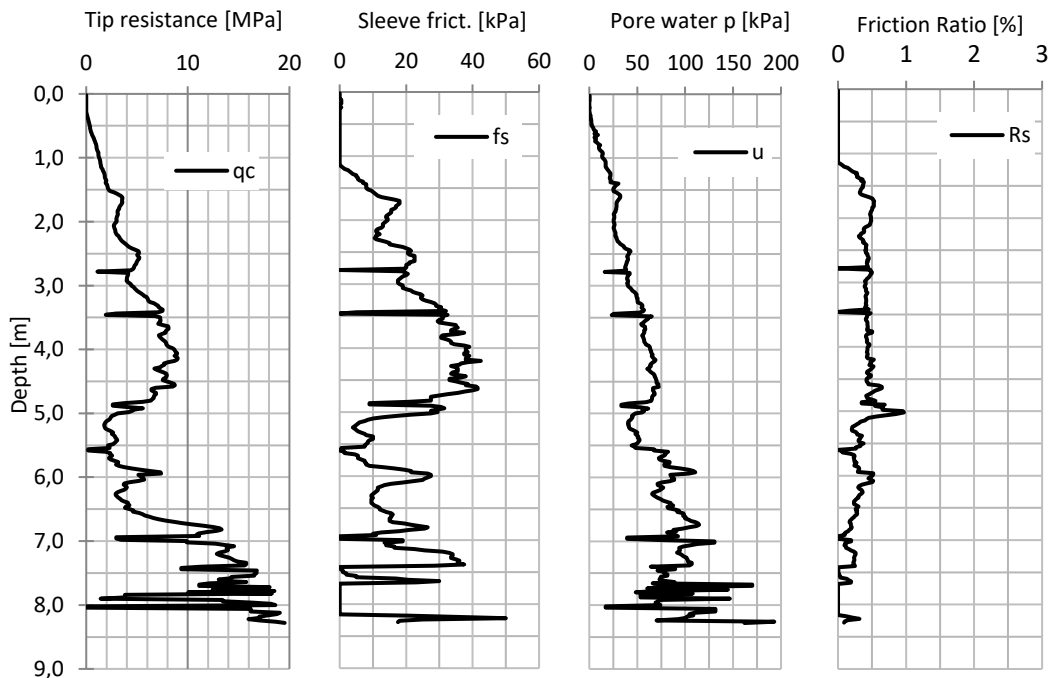
Figure 22. CPT results from a sandy site on the south coast close to Þorlákshöfn.

The results of the CPT measurements were then used to classify the deposit using the normalized soil behaviour type (SBTn) chart (Robertson 1990 and 2009) (see Figure 23). Most of the data points are classified as soil behaviour type 6 "sands – clean sand to silty sand". However, some data points, mainly in the depth range of 5.0-5.7 m, are classified as type 5 "sand mixtures – silty sand to sandy silt".

Depth: 0-4.98 m
Depth: 5.00-5.70 m
Depth: 5.72-8.28 m

Soil Behaviour Type
1. Sensitive, fine grained
2. Organic soils - clay
3. Clays - silty clay to clay
4. Silt mixtures - clayey silt to silty clay
5. Sand mixtures - silty sand to sandy silt
6. Sands - clean sand to silty sand
7. Gravelly sand to dense sand
8. Very stiff sand to clayey sand*
9. Very stiff, fine grained*
   * Heavily overconsolidated or cemented
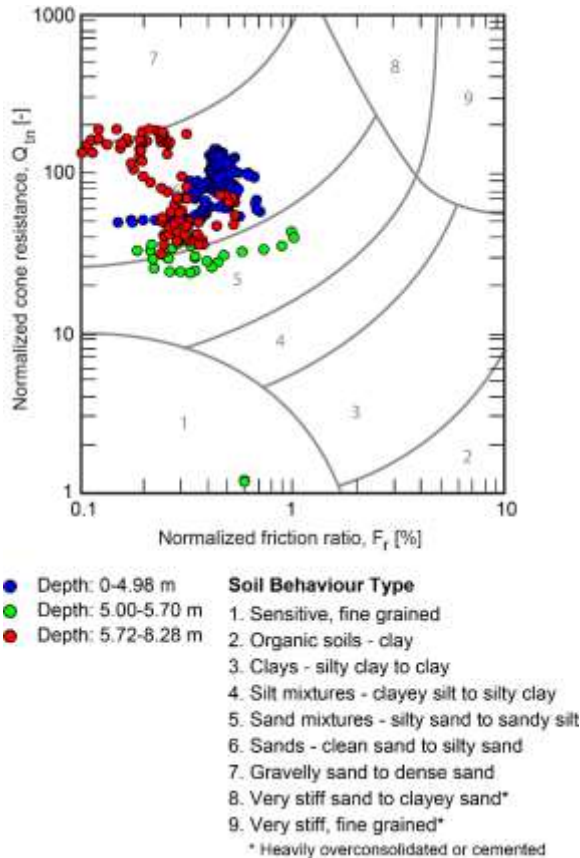
Figure 23. Normalized soil behaviour type (SBTn) chart with results of CPT measurements at the Þorlákshöfn site.

Multichannel Analysis of Surface Waves (MASW) measurements have subsequently been conducted at the site. The method is non-invasive and it is suitable on soft as well as coarse-grained soils. The method gives the shear wave velocity of the soil stratum (Park et

al. 1999, Ólafsdóttir et al. 2018). Various correlation equations exist between shear wave velocity *Vs* and different CPT-related parameters, such as cone resistance (q_c), corrected cone resistance (q_t), sleeve friction (f_s), overburden stress (σ_{v0}), effective stress (σ'_{v0}) and depth (z). Examples of CPT-V_S correlations, either intended for sands or for all soil types, are provided in Table 3 (Ólafsdóttir et al. 2019b, Erlingsson et al. 2017).

Table 3. Examples of CPT-V_S correlation equations.

$V_S \approx 17.48 q_c^{0.13}(\sigma'_{v0})^{0.27}$	Baldi et al. (1989)
$V_S \approx (10.1 \log(q_c) - 11.4)^{1.67} \left(\frac{100 f_s}{q_c}\right)^{0.3}$	Hegazy and Mayne (1995)
$V_S \approx 118.8 \log(f_s) + 18.5$	Mayne (2007)
$V_S \approx 32.3 q_c^{0.089} f_s^{0.121} z^{0.215}$	Piratheepan (2002)
$V_S \approx 134.1 + 0.0052 q_c$	Sykora and Stokoe (1983)

q_c, q_t, f_s, σ_{v0} and σ'_{v0} in kPa and z in meters. $p_a = 100$ kPa.

The CPT-V_S correlations in Table 3 were applied to the acquired CPT data. Figure 24 compares the V_S-profiles predicted based on the CPT-V_S correlation equations and the profile that was obtained by the MASW method.

MASW
Baldi et al. (1989)
Hegazy and Mayne (1995)
Mayne (2007)
Piratheepan (2002)
Sykora and Stokoe (1983)
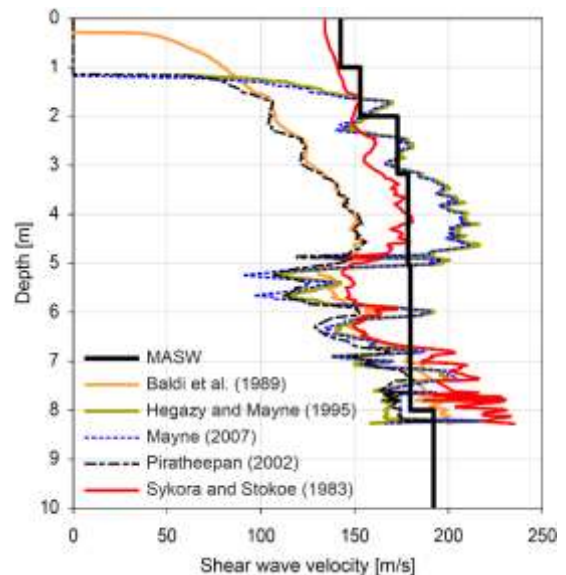
Figure 24. V_S-profiles for the Þorlákshöfn site predicted based on selected CPT-V_S correlations and obtained by MASW.

One can see in Figure 24 that the proposed equation by Sykora and Stokoe (1983) fits the data relatively nicely. It is necessary, however, to bear in mind that this is a relatively shallow profile. Further validation is needed.

5 INFRASTRUCTURE PROJECTS

Geotechnical engineering and engineering rock mechanics have played a major roll in forming modern Iceland, in building the road infrastructure, and harnessing of hydropower and geothermal energy, as well as in the construction of the ports and harbours along the coast.

Here are a few examples of projects to give the reader insight into problems that we have been facing.

5.1 Rock tunnels

As of today, 14 road tunnels are part of the road network for a total of over 65 km of tunnels. Most tunnels include two lanes, giving a cross-sectional area of around 55 m². In addition, the total length of tunnels associated with hydropower utility is around 85 km with a cross-section area that varies from 6 to over 150 m² (Loftsson et al. 2005) Reinforcement is mainly designed according to the Q-system and on average around 3 rockbolts (3 m long) are used per metre for tunnels with ~8 m span (cross section around 54 m²) and 2.5 m³/m of fibre-reinforced shotcrete. If conditions are very poor shotcrete ribs or lattice girders provide additional support that has been proven to be both economic and durable. An example of using lattice girders is shown in Figure 25.

Due to the Tertiary volcanic activity the local bedrock is piled up in thin layers, frequently with interlayers. An example of a tunnel face from the Vaðlaheiði road tunnel is shown in Figure 26. In the crown a basaltic layer can be seen with a thin layer of scoria underneath. Below this there is a soft red sedimentary layer resting on a thin scora/basalt layer on top of another thin brownish

sedimentary layer. Finally, in the insert a new scoria and basalt layer can be seen.

Figure 25. Lattice girders as a support in the 2-lane Vaðlaheiði road tunnel. Figure courtesy of B. A. Harðarson.

Figure 26. Drilling into a layered face at the Óshlíð road tunnel. Figure courtesy of B. A. Harðarson.

The general low horizontal stresses and frequently fractured rock mass with irregular interbeds can lead to major water inflow into tunnels if excavation takes place under the groundwater table in the rock mass. This has happened in some tunnel excavations such as the Vestfjörður tunnel, Héðinsfjarðar tunnel and Vaðlaheiði tunnel, leading to delays and increased cost. An example of a water inflow into the Héðinsfjörður tunnel is shown in Figure 27.

Figure 27. Water inflow into the Héðinfjörður tunnel. Figure courtesy of B. A. Harðarson.

5.2 Hydropower utility and dams

Iceland's numerous rivers are relatively short but with a large head and high run-off. This makes them very suitable for generating electricity. As of today hydropower accounts for almost 73% of all electricity production in Iceland (Bjarnason et al. 2019). Harvested electricity comes mainly from glacial rivers that have a seasonally varied flow rate. Water reservoirs with associated dams are therefore necessary. Today 29 dams in Iceland meet the criteria set by ICOLD (International Commission on Large Dams) for large dams. The oldest one is the Skeiðfoss dam, a concrete buttress structure constructed in 1945, and the most recent one is the Sporðalda dam commissioned in 2013 (Bjarnason et al. 2019). Most dams are earth-rockfill dams with a central impervious moraine core (23 dams), abutted by gravel filters, supporting fills and riprap for erosion and wave protection. Other types of large dams in Iceland are two concrete-faced rock fill dams (CFRD), one asphalt concrete-faced dam, one gravity dam and two buttress dams. A cross section of Búrfell dam is given in Figure 28.
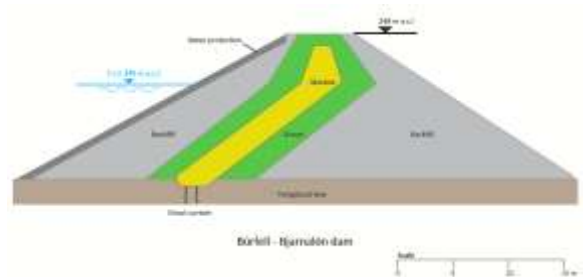
Figure 28. Cross section of the 5.9 km long and 33 m high Búrfell dam. The core consists of local loessic soil with alluvial gravel filter material and rock-fill shells. Figure courtesy of H. Bjarnason.

Many of the hydropower stations are located in the Þjórsá-Tungná-Kaldakvísl area in the outskirts of the SISZ. Seismic aspects need therefore to be taken into account in the design process. An attempt was made in 2018 to assess the shear stiffness of three dam structures (Ólafsdóttir et al. 2019a) using the MASW technique (see Figure 29). The purpose was to estimate their structural health and to create a base in order to be able to observe potential changes in the future.
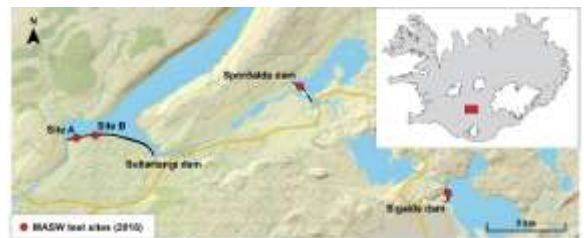
Figure 29. Location of MASW test sites at Sigalda dam, Sporðalda dam and Sultartangi dam. [The map is based on data from the National Land Survey of Iceland.].

Results from the two MASW measurments at the Sultartangi dam are shown in Figure 30.

.
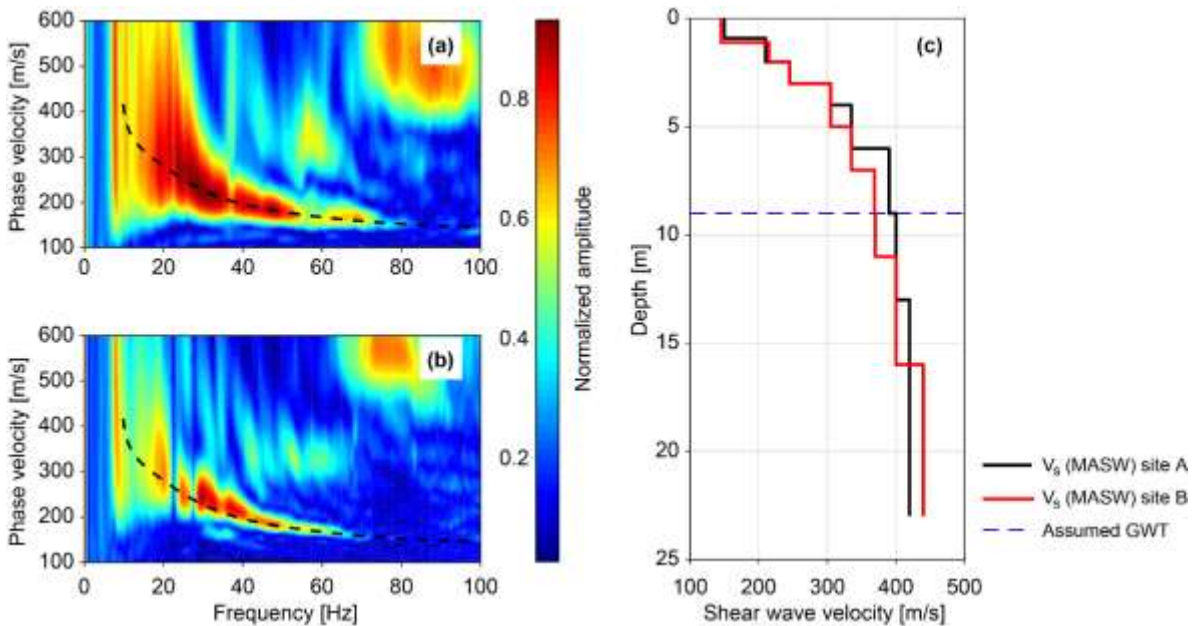
Figure 30. Results of MASW measurements at two locations on the crest of the Sultartangi dam (site A and B). Dispersion images obtained at Sultartangi site A by using survey profiles of length (a) 11.5 m and (b) 23 m. Estimated (c) shear wave velocity (V_S). The theoretical dispersion curve corresponding to the V_S-profile for site A is shown using a black dashed line in (a) and (b). The assumed location of the groundwater table (GWT) within the central core of the dam is shown using a blue dashed line in (c).

A simple model proposed by Seed and Idriss was therafter used to estimate the small-strain shear modulus of the dams

$$G_{max} = 1000 K_{2,max} \sqrt{\sigma'_m} \qquad (11)$$

where $K_{2,max}$ (kPa$^{0.5}$) is an empirical coefficient (Gazetas 1991, Kramer 1996).

The results are presented in Figure 31. They indicate that the experimentally evaluated small-strain shear stiffness profiles can in general be fitted adequately with the empirical model. A value of $K_{2,max}$ in the range of 30-35 seems to provide the best fit between the experimental and empirical stiffness profiles for the Sigalda and Sporðalda dams. However, for the two test sites on the crest of the Sultartangi dam (where the central core was primarily made of loess), a slightly lower value of $K_{2,max}$, or between 25-30, appears to provide the closest match. It can be further noted that a $K_{2,max}$ in the range $25-40$ is classified as very dense sand and gravel (Gazetas 1991).

.
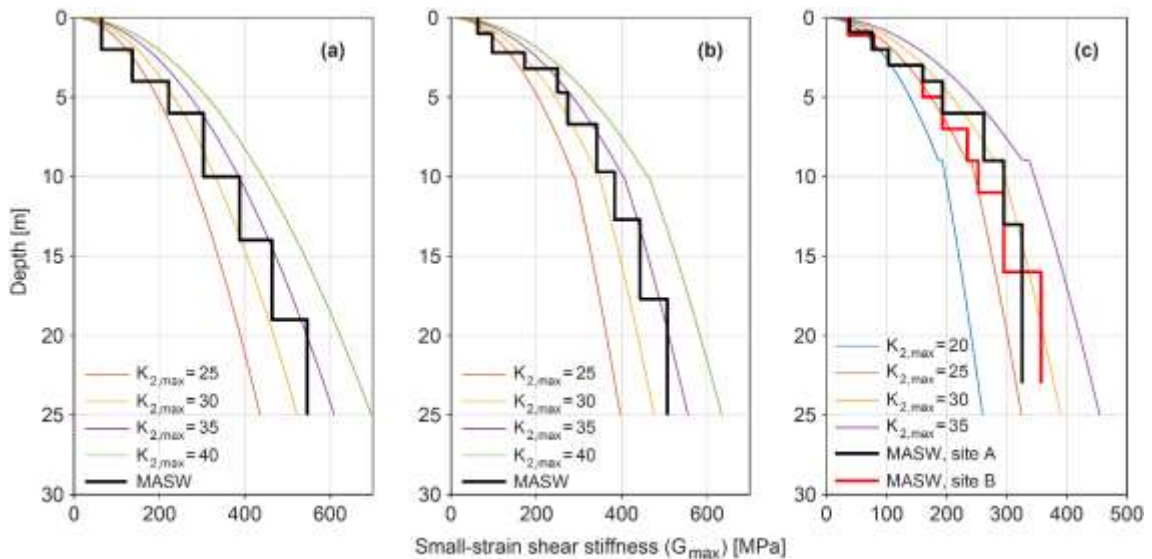
Figure 31. Comparison of empirical and experimental stiffness profiles for the (a) Sigalda dam site, (b) Sporðalda dam site and (c) Sultartangi dam sites. The empirical profiles were obtained by the model of Seed and Idriss using four different $K_{2,max}$ values.

In 2009 the Kárahnjúkar hydropower project (690 MW) was completed. It included the creation of the Hálslón reservoir (2100 Gl) by construction of three dams: two earth-rock-fill dams, the Desjará Dam and the Sauðárdalur Dam, and the concrete-faced rock fill (CFRD) Kárahnjúkar Dam that is the highest CFRD of its kind in Europe, 198 m (Bjarnason et al. 2019).

Kárahnjúkar Dam, the Desjará Dam and the Sauðárdalur Dam are shown in Figure 32.

5.3 Sesimic Hazard

In 2000 two earthquakes occurred within the SISZ with only a 4 day interval, on the 17th and 21st of June. Their magnitudes were both M_w6.5. Eight years later on May 29, 2008, the third earthquake hit the area (M_w6.3). Considerable damage was observed but no casualties (Einarsson 2008, Sigbjörnsson et al. 2009). Liquefaction was observed at Arnarbæli in the western part of the SISZ where sand boils were found on the bank of the River Ölfusá (Fig. 33).

Figure 32. Hálslón Reservoir area; the Desjará Dam to the left, the Kárahnúkar Dam and spillway in the middle, the Sauðárdalsstífla Dam to the right. The Brúarjökull Glacier (part of the Vatnajökull Glacier) in the background. Figure courtesy of H. Bjarnason.

The Arnarbæli site is located less than 1 km from the active fault that ruptured in the 2008 earthquake. The estimated peak ground acceleration (PGA) for the site a_{max} was in the range of 0.6–0.7g. The soil at the Arnarbæli site consists of loosely compacted glaciofluvial volcanic sand. The soil stratum is uniform down

to a great depth with the groundwater table close to the surface. Soil samples were collected at the Arnarbæli site by Green et al. (2012). The fine content of the material is around 7% and its grain size distribution lies well within the boundaries for potentially liquefiable soils, and partially within the boundaries identified as "most liquefiable soils" (Green et al. 2012; Tsuchida 1970).

Figure 33. Sand boils (liquefaction) on the bank of the River Ölfus close to the epicentre of the 29 May 2008 $M_w6.3$ earthquake. Figure courtesy of O. Sigurðsson.

A liquefaction resistance curve (V_{S1} – CRR curve) scaled to account for the effects of an $M_w6.3$ earthquake is presented in Fig. 34. The cyclic stress ratio and the normalized shear wave velocity were calculated for reference points at a depth ranging from $0.3 – 20.7$ m and compared to the liquefaction resistance curve. The PGA of the site was estimated as 0.65g. The results presented in the figure indicate that liquefaction had occurred at the site down to around a 4 m depth.

The complex local lava bedrock piles additionally show some unexpected behaviour. One such example is reported in Bessason and Kanyia (2002). In the June 17, 2000, earthquake (M_w 6.5) strong ground motion was recorded at both abutment piers of the 83 m long Thjórsá bridge, which is located in the SISZ. The east pier of the bridge is resting on bedrock but the west pier is resting on a 9 m thick Tertiary laval layer resting on a 20 m alluvial sand deposit on top of the bedrock (Figure 35).
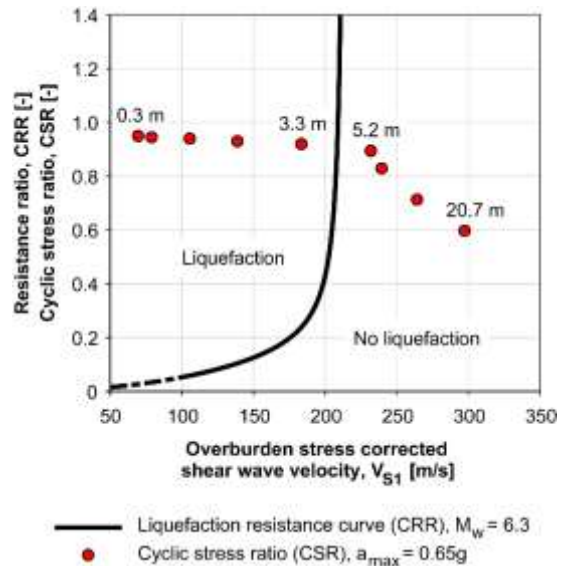
Figure 34. Liquefaction evaluation chart for the Arnarbæli site.
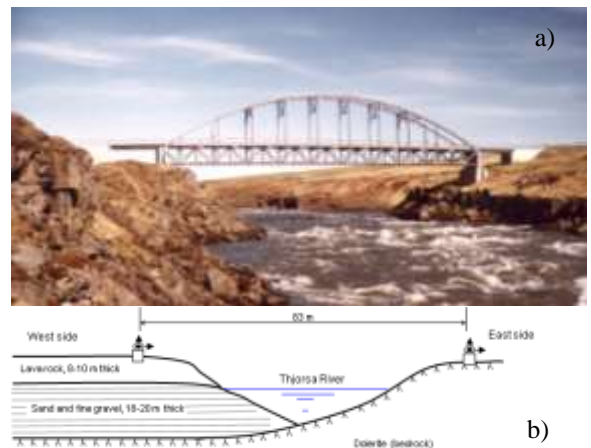
Figure 35. a) The Thjórsá bridge. The left pier is resting on lava rock but the right pier is resting on bedrock. b) schematic cross section of the Thjórsá bridge. Figure courtesy of B. Bessason.

The three recorded acceleration time histories from the west and east abutments during the earthquake are shown in Figure 36.

The observed peak ground acceleration (PGA) was 53% and 120% higher respectively in the N_S versus E_W components on the western abutment compared to the eastern abutment.
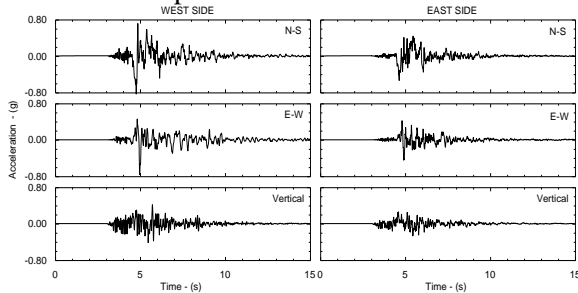
Figure 36. Recorded acceleration time histories at the Thjórsá bridge abutments. Figure courtesy of B. Bessason.

This was further seen clearly in the elastic response spectra of the two sides, as shown in Figure 37 where the sesimic coefficient (horizontal over vertical spectral values) are shown.
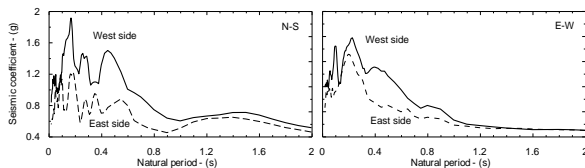
Figure 37. Elastic response spectra (ς=5%) on each side of the Thjorsa River canyon for the earthquake occurring on 21 June 2000 (M=6.5, PGA=0.84g). Figure courtesy of B. Bessason.

The complex lava strata of the western side show some considerable amplification compared to the simpler eastern side where the abutment rests directly on bedrock. The western side fits poorly in the soil categories defined in Eurocode 8.

5.4 Road structures

Large parts of the Icelandic road network consist of thin flexible pavements with either a Hot Mix Asphalt layer or Bituminous Surface Treatments as the surface course over unbound base course and subbase layers. These structures are highly dependent on the performance of the unbound layers. Two typical structures were tested in a full scale Accelerated Pavement Testing (APT) using a Heavy Vehicle Simulator (HVS) testing facility for improving our understanding of the behaviour and the degradation of the structures under heavy loading. In the test over 500,000 rolling wheel load repetitions were applied (Erlingsson & Ingason 2004; Erlingsson 2005 and 2007). The structures were instrumented with deformation sensors, strain gauges and soil pressure cells. A cross section of one of the tested structures is shown in Figure 38.
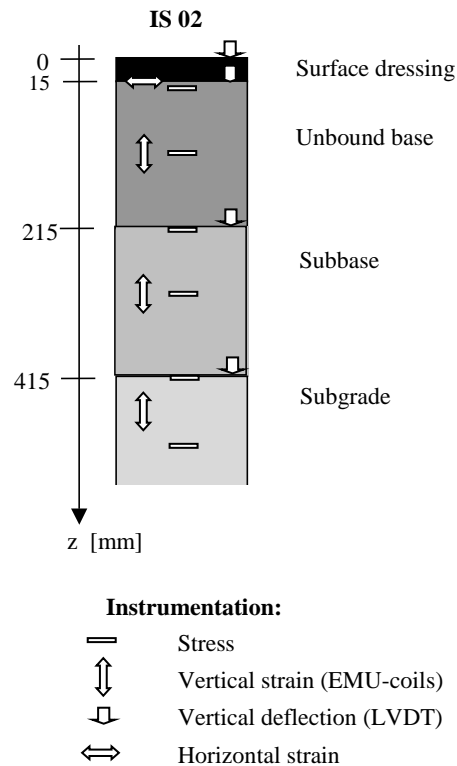
Figure 38. A thin pavement structure tested in an HVS testing facility.

The heavy traffic loading imposes a significant loading in the unbound base and subbase layers of such thin pavement structures. The nonlinear stiffness characterization of these layers is therefore of importance (see Figure 39), where both linear stiffness and non-linear stress dependent stiffness have been used. The stress dependent stiffness M_R has been assumed to follow

$$M_R = k_1 \left(\frac{3p}{p_a} \right)^{k_2} \tag{12}$$

where p is the mean principal stress level, p_a is a reference stress (100 kPa) and k_1 and k_2 are material parameters.
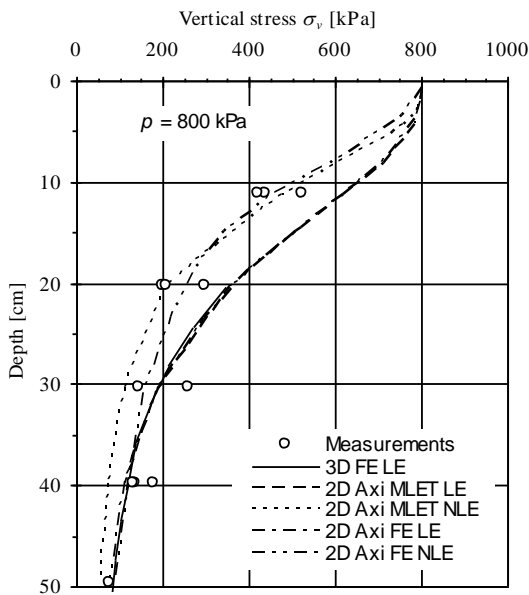
Figure 39. Induced vertical stress under the centre of a single tyre as a function of depth. The axle load was 120 kN and the tyre pressure 800 kPa. 3D = three dimensional analysis, 2D Axi = two dimensional axisymmetric analysis, MLT = Multilayer theory, FE = finite element, LE = linear elastic, NLE non-linenar stress dependent elastic.

Rutting predictions were then carried out using a simple power law function that gave a good agreement with actual measurements of permanent deformation development (see Figure 40).
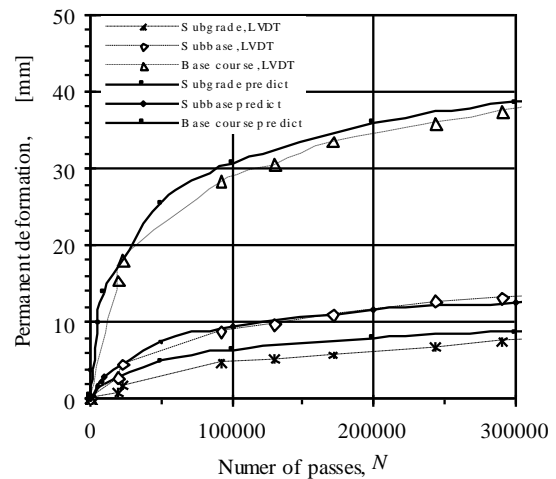
Figure 40. Rutting prediction versus measurements of permanent deformation development as a function of load repetition. The permanent deformation development of each layer is shown (subgrade, subbase, base course) as well as their sum (top line) which is manifested on the surface as rutting. LVDT= Linear Variable Deflectometer Transducers at the top of each layer, predict = prediction based on the numerical anlyses.

A new pavement design method and performance prediction scheme has been developed based on this. For further details, see Erlingsson and Ahmed (2013 and 2019) and Saevarsdottir and Erlingsson (2015).

6 NEW CHALLENGES

The effects of climate changes have created new geotechnical challenges. Two of them are related to retreats of the glaciers and sea level risings. They will be mentioned here briefly. Furthermore, ongoing development of a greenhouse gas mitigation method will be described.

6.1 Glacial retreats

Glaciers cover about 11% of the country (Björnsson and Pálsson, 2008; Hannesdóttir et al. 2014). Since 1995, the glacier mass loss due to climate warming has been continuous, and between 1995 and 2010 the largest ice cap, the Vatnajökull Glacier, lost almost 4% of its volume (Björnsson et al., 2013). This has caused significant changes on and around the present-day outlet glaciers.

The rapidly retreating outlet glaciers often leave steep valley sides behind which may become unstable because of loss of buttressing by the glacier, permafrost degradation and other factors (Stoffel, 2012).

One example of such mass movements has taken place at Svínafellsheiði due to the retreat of the Svínafellsjökull (part of the Vatnajökull Glacier). In 2014, over a100 m long and up to 30 cm wide fracture in bedrock was discovered in the Svínafellsheiði mountain slope. The fracture is located at 850 m a.s.l. in the uppermost part of a 500 m high, almost vertical mountainside (Sæmundsson et al. 2019).

Figure 41. The Svínafellsheiði mountain slope. The solid black line marks the boundary between the topmost basalt layer and underlying móberg/hyaloclastite, the dotted black line shows the observed fracture, and the transparent red polygons shows the overhangs in the basaltic area. Figure courtesy of Þ. Sæmundsson.

6.2 Sea level rising

Due to the complex geological activity and tectonic movements of the country as well as the retreat of the large icecaps, irregular vertical displacement continues to take place on the Iceland plateau. Figure 42 shows the uplift measurements in Iceland during the period 2004 – 2016. On average the land rise is about 1 cm per year, but with high spatial variations (Valsson 2019). These vertical movements affect the design of sea portals and other near- coast structures. In the south-east the uplift is about 3.5 cm/year and probably to a large extent due to the large mass reduction of the Vatnajökull icecap. In other areas hardly any uplift has been measured or even sinking movements observed. For the capital area an average sinking movement of 0.6 mm/y has been observed during these 12 years. For the period 1993 – 2004 the sinking movements were about 2 mm per year.
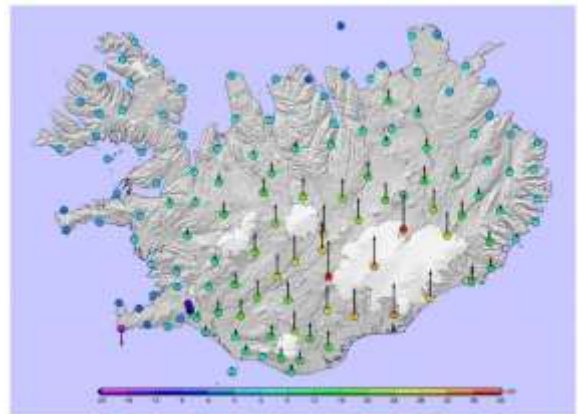
Figure 42. Vertical movements during the period 2004 – 2016 observed by GPS measurements. Figure courtesy of G. Valsson.

6.3 Turning gas into rock by fixation

Five major geothermal plants (> 50 MW) exist in Iceland, of which the Hellisheiði Power station is the biggest (303 MW). Like all other geothermal power plants, the Hellisheiði power plant emits geothermal gases such as the greenhouse gas carbon dioxide (CO_2), but also hydrogen sulfide (H_2S). The CO_2 emission is, however, only a fraction of that stemming from fossil-fuel generation. A new method has been under

development to mineralize the carbon- dioxide and hydrogen-sulphide by turning gas into rock, referred to as mineralization (www. carbfix.com). The CO_2-H_2S gases emitted from the power plant are captured into condensate water from the power plant in a scrubber and the gas-charged water injected deep into the hot basaltic rocks (>700m and >250°C) close to the power plant (Gunnarsson et al. 2018). Basalt plays an important role in this mineralization process as it contains a high amount of calcium, magnesium and iron which interact with the CO_2 and H_2S to form minerals like calcite ($CaCO_2$) and pyrite (fool's gold; FeS_2) (see Figure 43). The mineralization has proven to take less than a year at elevated temperatures and less than two years at 20-50°C, and the minerals can be stable for over centuries or even millions of years (Gislason and Oelkers 2014, Matter et al. 2016). The method can be utilized wherever carbon-dioxide is emitted in the vicinity of basaltic rock and close to water or sea-water sources.
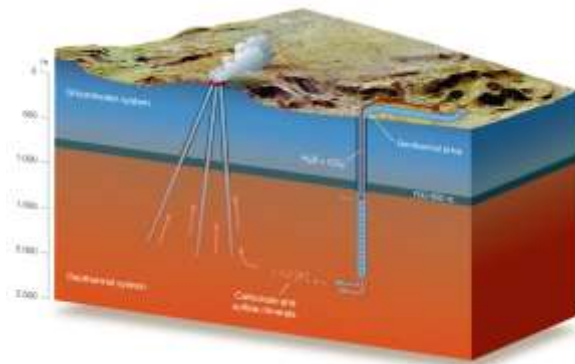
Figure 43. Schematic cross section of the CarbFix2 injection site. Gas-charged and effluent water are injected separately to a depth of 750 m and then allowed to mix until they enter the aquifer at a depth of 1900–2200 m. This combined fluid flows down a hydraulic pressure gradient to monitoring wells. Figure courtesy of S. R. Gislason.

7 CONCLUSION

During the last 100 years, the Icelandic society has gone through extreme changes from being one of the poorest in Europe to a wealthy country with well functioning infrastructure. Geotechnology and related fields have played an important role in this transition related to construction and maintenance of portals, roads, bridges and tunnels, and harvesting of the hydropower as well as of geothermal energy. This paper has given a short overview of the geotechnical conditions in the country. Furthermore, some geotechnical engineering projects have been described. Finally, some new geotechnical challenges due to climate changes have been briefly introduced.

8 ACKNOWLEDGEMENT

9 REFERENCES

Árnadóttir, Th., Lund B., Jiang, W., Geirsson, H., Björnsson, H., Einarsson, P., Sigurdsson T. 2009. Glacial rebound and plate spreading: Results from the first countrywide GPS observations in Iceland. *Geophys. J. Int*., 177(2), 691-716, doi: 10.1111/j.1365-246X. 2008.04059.x.

Baldi, G., Bellotti, R., Ghionna, V.N., Jamiolkowski M., LoPresti D.C.F. 1989. Modulus of sands from CPTs and DMTs. *Proceedings of the 12th International Conference on Soil Mechanics and Foundation Engineering,* 13-18 August 1989, Rio de Janeiro, Brazil, Vol. 1, pp. 165-170.

Bessason, B., Kaynia, A.M. (2002). Site amplification in lava rock on soft sediments, *Soil Dynamics and Earthquake Engineering*, 22(7);525-540.

Bjarnason, H., Palmason, P.R, Arnalds, S.S., Adalsteinsson, H. 2019. *Hydropower and Large Dams in Iceland*. Icelandic Committee on Large Dams (ISCOLD), Reykjavik.

Björnsson, H., Pálsson, F. 2008. Icelandic glaciers. *Jökull*, 58, 365–386.

Björnsson, H., Pálsson, F., Guðmundsson, S., Magnússon, E., Aðalgeirsdóttir, G., Jóhannesson, T., Berthier E., Sigurðsson, O., Thorsteinsson T. 2013. Contribution of Icelandic ice caps to sea level rise: Trends and variability since the Little Ice Age. *Geophysical Research Letters*, 40, 1546–1550, doi:10.1002/grl.50278.

Einarsson, P. 2008. Plate boundaries, rifts and transforms in Iceland. *Jökull*, 58, 35-58.

Erlingsson, S. 2005. Numerical modelling of unbound granular materials in thin pavement structures. *Proceedings of the 16th International Conference on Soil Mechanics and Geotechnical Engineering*, Osaka, Japan, 12 – 16 September, pp.1699-1702.

Erlingsson, S. 2007. Numerical modelling of thin pavements behaviour in accelerated HVS tests. *Road Materials and Pavement Design, an International Journal*. Vol. 8/4, pp. 719 - 744.

Erlingsson, S., Ahmed, A. W. 2013. Fast layered elastic response program for the analysis of flexible pavement structures, *Road Materials and Pavement Design*, Vol. 14, No. 1, pp. 196-210. DOI:10.1080/14680629.2012. 757558.

Erlingsson, S., Ahmed, A.W. 2019. Mechanistic rutting modelling of a LTPP road structure. In

Crispino, M. (Ed.) *Pavement and Asset Management*. CRC Press/Balkema Taylor, 2019 Taylor & Francis Group, London, UK. ISBN 978-0-367-20989-6, pp. 241-249.

Erlingsson, S., Ingason, Th. 2004. Performance of Two Thin Pavement Structures During Accelerated Pavement Testing Using a Heavy Vehicle Simulator. *Proceedings of the 2nd International Conference on Accelerated Pavement Testing*, Minnesota, 26 – 29 September, 15 pp.

Erlingsson, S., Olafsdottir, E.A., Bessason, B. 2017. Stiffness of sandy sites using the Multichannel Analysis of Surface Waves method. *Proceedings of the 19th International Conference on Soil Mechanics and Geotechnical Engineering,* Seoul, Korea, 17 – 22 Sept. 2017.

Flóvenz, Ó.G. 2019. Geothermal exploitation in Iceland – Success and Challenges. *Proceedings of the 17th European Conference on Soil Mechanics and Geotechnical Engineering*, 1 – 6 September, Reykjavík.

Friðriksson, G. 2013. *Hér heilsast skipin, fyrra bindi* (In Icelandic). Uppheimar.

Gazetas, G. 1991. Foundation Vibrations. *Foundation Engineering Handbook, 2nd edition* (Ed. Fang, H.-Y.), 553–593. Van Nostrand Reinhold, New York, NY.

Gislason S.R., Oelkers, E.H. 2014. Carbon storage in basalt. *Science* 344, 373-374.

Green, R.A., Halldorsson, B., Kurtulus, A., Steinarsson, H., Erlendsson, O.A. 2012. Unique liquefaction case study from the 29 May 2008, M_w6.3 Olfus earthquake, Southwest Iceland. In: *15th World Conference on Earthquake Engineering*, Lisbon, Portugal.

Guðmundsson, Á., Jóhannesson, H., Harðarsson, B.A. 1991. Hvalfjörður Tunnel, Geological report, *Stratigraphy and Structure*. Reykjavík, October, 51 p.

Gunnarsson, I., Aradóttir, E.S., Oelkers, E.H., Clark, D.E., Arnarson, M.Þ., Sigfússon, B., Snæbjörnsdóttir, S.Ó., Matter, J.M., Stute M., Júlíusson, B.M., Gíslason, S.R. 2018. The rapid and cost-effective capture and

subsurface mineral storage of carbon and sulfur at the CarbFix2 site. *International Journal of Greenhouse Gas Control* 79, 117-126.

Hannesdóttir, H., Björnsson, H., Pálsson, F., Aðalgeirsdóttir, G., Guðmundsson, S. 2014. Area, volume and mass changes of southeast Vatnajökull ice cap, Iceland, from the Little Ice Age maximum in the late 19th century to 2010. *The Cryosphere Discuss*., 8, 4681–4735.

Hegazy, Y.A., Mayne, P.W. 1995. Statistical correlations between V_S and cone penetration data for different soil types. *Proceedings of the International Symposium on Cone Penetration Testing, CPT '95*, 4-5 October 1995, Linköping, Sweden, Vol. 2, pp. 173-178.

Hemmingsen, P.K. 2016. *Spennur í íslensku bergi – samantekt á bergspennumælingum á Íslandi* (In Icelandic). MS thesis. Faculty of Civil and Environmental Engineering, University of Iceland.

Hudson, J., Harrison, J. 2002. *Engineering Rock Mechanics: An Introduction to the Principles*. Oxford.

Janbu, N. 1970. *Grunnlag i Geoteknikk* (In Norwegian). Tapir Forlag. Trondheim.

Jóhannsson, Æ. 1997. *Mechanical Properties of Rock in Icelandic Lava Stratum*. M.Sc. thesis. Dept. of Civil and Environmental Engineering University of Iceland.

Kramer, S.L. 1996. *Geotechnical Earthquake Engineering*, Prentice-Hall, Inc., Upper Saddle River, NJ.

Loftsson, M., Ingimarsson, A.K., Jóhannesson, Æ. 2006. In situ rock mass stresses in Iceland and rock mass deformation of underground caverns in the Kárahnjúkar and Blanda Hydroelectric Projects. *ISRM In Situ Rock Stress Conference*, June 2006.

Loftsson, M., Jóhannesson, Æ., Erlingsson, E. 2005. Kárahnjúkar Hydroelectric Project – Powerhouse Cavern. Successful excavation despite complex geology and stress induced stability problems: *26.1-26.25*, *Proceedings Fjellsprengningskonferansen*, Oslo, 24-25 November 2005.

Matter, J.M., Stute M., Snæbjörnsdóttir, S.Ó., Oelkers, E.H., Gíslason, S.R., Aradóttir, E.S., Sigfusson, B., Gunnarsson, I., Sigurdardóttir H., Gunnlaugsson, E., Axelsson, G., Alfredsson, H.A., Wolff-Boenisch, D., Mesfin, K., Fernandez de la Reguera Taya, D., Hall, J., Dideriksen K., Broecker, W.S. 2016. Rapid carbon mineralization for permanent disposal of anthropogenic carbon dioxide emissions. *Science* 352, 1312-1314.

Mayne, P.W. 2007. *Cone Penetration Testing State-of-Practice*. NCHRP Project 20-05, Topic 37-14, Synthesis 368 on Cone Penetration Testing, February 2007.

NGI. 2015. *Using the Q-system, Rock Mass Classification and Support Design*. NGI, Oslo.

Ólafsdóttir, E.Á., Bessason, B., Erlingsson, S. 2019a. Stiffness profiles of earth dams based on the MASW technique. *Proceedings of the XVII European Conference on Soil Mechanics and Geotechnical Engineering*, Reykjavík, Iceland.

Ólafsdottir, E.Á., Bessason, B., Erlingsson, S. 2019b. Application of MASW in the South Iceland Seismic Zone. Chapter 5 in: Rupakhety R., Olafsson, S. and Bessason B. (eds.) *Proceedings of the International conference on Earthquake Engineering and Structural Dynamics*, Springer, pp. 53 – 66.

Ólafsdóttir, E.Á., Erlingsson, S., Bessason, B. 2018. Tool for analysis of multichannel analysis of surface waves (MASW) field data and evaluation of shear wave velocity profiles of soil, *Canadian Geotechnical Journal* **55**(2), 217-233.

Pálmason, P.R. 2018. *Embankment dam design in Iceland – conceptual considerations*. Landsvirkjun, National Poweer Company of Iceland, Report no.: LV-2018-091. 27 pp.

Park, C.B., Miller, R.D., Xia, J. 1999. Multichannel analysis of surface waves. *Geophysics, 64*(3), 800–808. doi:10.1190/1.1444590.

Piratheepan, P. 2002. *Estimating Shear-Wave Velocity from SPT and CPT Data*. (Master of Science Thesis). Clemson University, Clemson, SC.

Robertson, P.K. 1990. Soil classification using the cone penetration test. *Canadian Geotechnical Journal 27* (1), 151-158.

Robertson, P.K. 2009. Interpretation of cone penetration tests - unified approach. *Canadian Geotechnical Journal* 46 (11), 1337-1355.

Saevarsdottir, Th., Erlingsson, S. 2015. Modelling of responses and rutting profile of a flexible pavement structure in an HVS. *Road Materials and Pavement Design*. Vol. 16/1, pp 1-18. DOI: 10.1080/14680629.2014.939698.

Sæmundsson, Þ., Helgason, J.K., Ben-Yehoshua, D., Bergsson, B. H., Ófeigsson, B., Magnússon, E., Hjartardóttir, Á.R., Drouin, V., Belart, J.M-C., Grímsdóttir, H., Pedersen, G.B.M., Pálsson, F., Guðmundsson, S., Geirsson, H. 2019. Risk of major rock slope failure at the Svínafellsheiði mountain, SE Iceland. *Geophysical Research Abstracts,* Vol. 21, EGU2019-9650, EGU General Assembly.

Sheory, P.R. 1994. A theory for in situ stresses in isotropic and transversely isotropic rock. *Int. J. Rock Mech. Min. Sci. & Geomech. Abstr*. **31**(1), 23-34.

Sigbjörnsson, R., Snæbjörnsson,·J.Th., Higgins, S.M., Halldórsson, B., Ólafsson, S. 2009. A note on the Mw 6.3 earthquake in Iceland on 29 May 2008 at 15:45 UTC. *Bulletin of Earthquake Engineering, 7*, 113–126. doi:10.1007/s10518-008-9087-0.

Skúlason, J. 1978. *Rannsóknir á sigeiginleikum efna ákvörðuðum í ödometer* (in Icelandic). Vegagerð ríkisins, 26 pp.

Skúlason, J., Júlíusson, E., Þórðarson, O. Hilmarsson, H. 2002. *Eiginleikar íslenskra jarðefna gagnvart sveifluálagi* (In Icelandic). Rannsóknastofnun Byggingariðnaðarins. Reykjavík.

Sólnes, J., Sigmundsson, F., Bessason, B. (Eds) 2013. *Náttúruvá á Íslandi Eldgos og jarðskjálftar*, University of Iceland Press and Natural Catastrophe Insurance of Iceland (in Icelandic).

Stoffel, M., Huggel, C. 2012. Effects of climate change on mass movements in mountain environments. *Progress in physical geography,* 36(3), 421–439.

Sykora, D.W., Stokoe, K.H. 1983. *Correlations of In Situ Measurements in Sands With Shear Wave Velocity. Geotechnical Engineering Report GR83-33*. The University of Texas, Austin, TX.

Thordarson, T., Höskuldsson, Á., 2014. Iceland. Dunedin Academic Press, 2nd edition. *Classic Geology in Europe series*, 192 pp. ISBN: 978-1-780-46-021-5.

Þórðarson, S. 2002. *Frumherjar í verkfræði á Íslandi* (In Icelandic). Verkfræðingafélag Íslands.

Tsuchida, H. 1970. Prediction and countermeasure against the liquefaction in sand deposits. In: *Abstract of the Seminar in the Port and Harbor Research Institute*, Yokohama, Japan, pp. 3.1-3.33

Valsson, G. 2019. *Endurmæling ISNET 2016 grunnstöðvanetsins og nýjar viðmiðanir fyrir landmælingar og kortagerð á Íslandi* (In Icelandic). Akranes: Landmælingar Íslands.

Wells, H. 2009. *Liquefaction Potential at a Proposed Hydroelectric Site in Iceland: Urridafoss Case Study Using Cone Penetration Data*. MS thesis, Faculty of Civil and Environmental Engineering University of Iceland, 119 pp.

XVII European Conference
ECSMGE 2019
Reykjavik
on Soil Mechanics
and Geotechnical Engineering

Hydraulic fills with special focus on liquefaction
Remblais hydrauliques en dédiant une attention particulière à la liquéfaction

A. Gens
Technical University of Catalonia (UPC), Barcelona, Spain

ABSTRACT: Hydraulic fills are often deposited in a loose state making them susceptible to liquefaction. The paper focuses on flow/static liquefaction, a phenomenon that has led to a number of catastrophic failures. The current understanding of flow/static liquefaction, based on the concepts of critical/steady state and state parameter, is reviewed. Theoretical concepts such as that of controllability lead to a more rigorous definition of the undrained instability phenomena associated with flow liquefaction. Hydraulic fills are often characterised by in situ tests. Advanced numerical analyses of the piezocone penetration test (CPTu) on soils exhibiting undrained softening are presented and discussed. Two case histories involving the liquefaction of hydraulic fills are described. The first one concerns a tailings dam where hydraulic fill liquefaction was a consequence of an independent foundation failure. Tailings liquefaction, however, was the major contributor to the devastating consequences of the failure. The second case is the failure of a harbour quay where backfill liquefaction was the immediate cause of the failure and its consequences. Some general considerations on the liquefaction of hydraulic fills close the paper.

RÉSUMÉ: Les remblais hydrauliques sont souvent déposés dans un état lâche, ce qui les rend vulnérables à la liquéfaction. L'article se concentre sur la liquéfaction statique, un phénomène qui a conduit à un certain nombre de ruptures catastrophiques. La compréhension actuelle de la liquéfaction statique, basée sur les concepts d'état critique ou stationnaire et de paramètre d'état, est examinée. Des concepts théoriques tels que celui de contrôlabilité conduisent à une définition plus rigoureuse des phénomènes d'instabilité non drainée associés à la liquéfaction statique. Les remblais hydrauliques sont souvent caractérisés par des essais in situ. Des analyses numériques avancées de l'essai de pénétration du piézocône (CPTu) sur des sols présentant un radoucissement non drainé sont présentées et discutées. Deux cas historiques impliquant la liquéfaction de remblais hydrauliques sont décrits. Le premier concerne une digue de résidus miniers où la liquéfaction du remblai hydraulique était la conséquence d'une rupture indépendante de la fondation. La liquéfaction des résidus a toutefois été le principal facteur des conséquences dévastatrices de cette rupture. Le deuxième cas se réfère à la faillite d'un quai de port où la liquéfaction du remblai était la cause immédiate de la rupture et de ses conséquences. Quelques considérations générales sur la liquéfaction des remblais hydrauliques sont exposées à la fin de l'article.

Keywords: Hydraulic fills; liquefaction; brittleness; tailing dams; quays

1 INTRODUCTION

Hydraulic fills are deposited in place by a flowing stream of water (Figure 1). They are used widely in different types of civil and mining engineering projects. Although the use of hydraulic fills in embankment dams has largely lapsed, posibly as a consequence of the Fort Peck dam failure (Davies et al. 2002), they are frequently used in land reclamation projects or in the construction of harbour quays and esplanades where dredged material is often available (van't Hoff and van der

Kolff 2012). Tailings from mining operations are also often deposited hydraulically in ponds although, as a result of some recent devastating failures, dry stacking is becoming more common. The particle size and grading of hydraulic fills can be very variable depending on the source material and the velocity of the deposition flow. Often, hydraulic fills exhibit significant particle-size segregation and a high degree of heterogeneity within the same area.

Figure 1. Deposition of a hydraulic fill

Hydraulic fills are often deposited in a loose state and are prone to liquefaction for a wide range of gradings from coarse sands to silts and any combination in between these limits. Although much liquefaction research has focused on sand, there is convincing evidence that presence of non-plastic fines may actually increase the potential for liquefaction (e.g. Lade and Yamamuro 1997).

Although, for a considerable period, there was a certain amount of confusion in liquefaction terminology, it is now generally accepted that it is useful to distinguish the phenomenon of flow/static liquefaction from that of cyclic liquefaction or cyclic mobility.

Flow/static liquefaction is associated with undrained softening behaviour and it often leads to catastrophic failures. Herein, the term flow liquefaction will be preferentially used because this type of liquefaction can also be triggered by cyclic loading. Carrera et al. (2011) have proposed the term 'true (or complete) liquefaction' for the extreme case when the deviator stress becomes zero at the end of undrained softening.

Cyclic liquefaction is not dependent on undrained softening and results from the accumulation of pore pressures during cyclic loading. Earthquake loading and storm loading on offshore structures are common examples of cyclic loading. The generation of pore pressures is enhanced if cyclic loading involves shear stress reversal. If, as a result of cyclic loading, very low effective stress states are reached, large deformations can occur although they largely stop once cyclic loading ends. The term cyclic mobility is usually applied to cases where zero effective stress is not approached and only limited deformations are produced.

The typical undrained behaviour of non-plastic soils (including sands) is summarised in Figure 2 in a somewhat idealized manner. When the material is very loose, a frequent state in hydraulic fills, undrained softening occurs with a significant loss of strength after the peak is reached (A). The soil exhibits a compressive behaviour with a significant generation of pore pressures. In contrast, when the material is very dense, dilatant behaviour is obtained (C). An intermediate behaviour (B) is also observed sometimes where the final dilatant behaviour is preceded by a compressive phase with limited undrained softening. This intermediate behaviour will not generally lead to very large displacements and catastrophic failures. In this paper, only flow liquefaction is considered corresponding to the behaviour depicted as A in Figure 2. As discussed below, the terms loose or dense have proper meaning only in the context of a particular stress level.

Because flow liquefaction often results in catastrophic failures (Olson & Stark 2002, Jefferies & Been 2006, 2016), the phenomenon has been associated with many landmark cases involving hydraulic fills such as Fort Peck Dam (US) in 1938 (Casagrande, 1965), Lower San Fernando Dam (US) in 1971 (Seed et al. 1975,

Castro et al. 1989) and Nerlerk Berm (Canada) in 1982-1983 (Sladen et al. 1985b). Tailing dams have also provided many instances of flow liquefaction failures (Davies et al. 2002, Santamarina et al. 2019), e.g. the cases of Stava Fluorite Mine in 1985 (Chandler and Tosatti 1995), Sullivan Mine (Canada) in 1991 (Davies et al. 2002), Merriespruit Harmony Mine (South Africa) in 1994 (Fourie et al. 2001), Aznalcóllar tailings dam (Spain) in 1997 (Alonso and Gens 2006a) and Fundão Tailings Dam in 2015 (Morgenstern et al. 2016).
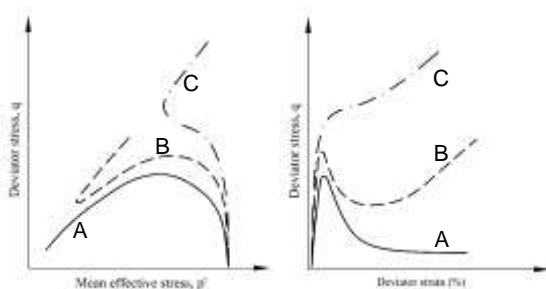
Figure 2. Typical modes of undrained behaviour

Naturally, flow liquefaction affects materials other than hydraulic fills. Important examples are Wachusett dam (US) in 1907 involving a sand fill placed (and lightly compacted) by carts (Olson et al. 2000), the failure of Aberfan spoil Tip No7 in Wales in 1966 involving uncompacted colliery waste (Bishop et al. 1969) and the dredged slopes of the guide bunds of the Jamuna bridge in Bangladesh (Yoshimine et al. 1999). The Aberfan case was significant not only due to the high number of casualties but also because it led to a significant advance in the understanding of flow liquefaction (Bishop et al. 1973). The Jamuna bridge case brought to the fore the unfavourable behaviour of micaceous sands compared to more conventional siliceous sands (Hight et al. 1999).

This paper focuses on flow liquefaction in hydraulic fills although many of the concepts used are also applicable to other soils undergoing undrained softening. Given the importance and frequent catastrophic consequences, a large amount of research has been performed on flow liquefaction. This contribution is by no means intended as a state-of-the-art of the topic, it simply presents and discusses some selected aspects that have been considered relevant. Because of space/time limitations, remedial and mitigation measures are not dealt with here.

The paper starts with an account of the current understanding of the mechanisms underlying the phenomenon of flow/static liquefaction, based on the concepts of critical/steady state and state parameter. It is shown that theoretical concepts such as that of controllability lead to a more rigorous definition of the undrained instability phenomena associated with flow liquefaction. The various forms of flow liquefaction triggering are presented next. Given that hydraulic fills are often characterised by in situ tests, some advanced numerical analyses of the piezocone test (CPTu) on soils exhibiting undrained softening are presented and discussed. Attention is given to the description of the constitutive law selected to represent undrained brittle behaviour. In order to provide context and relevance to the topic, two case histories involving the liquefaction of hydraulic fills are described: the failure of Aznalcóllar tailings dam and the failure of the Prat quay in Barcelona harbour. Some general considerations on the liquefaction of hydraulic fills close the paper.

2 MECHANISM OF FLOW LIQUEFACTION

2.1 Critical states and state parameter

The mechanism of flow liquefaction is now reasonably well understood although there are still some uncertainty and controversy regarding some of its specific aspects. Here, only a summary description is given. Flow liquefaction mechanism is best examined in the context of the notion of critical state. The concept was introduced by Casagrande (1936) who observed that, in shear box tests, loose sands contracted

and dense stands dilated until reaching approximately the same void ratio after large displacements (Figure 3). This final void ratio was called the critical void ratio. No further volume change was observed once the sand had reached this final state. Critical void ratio turned out to be stress dependent (Taylor 1948).
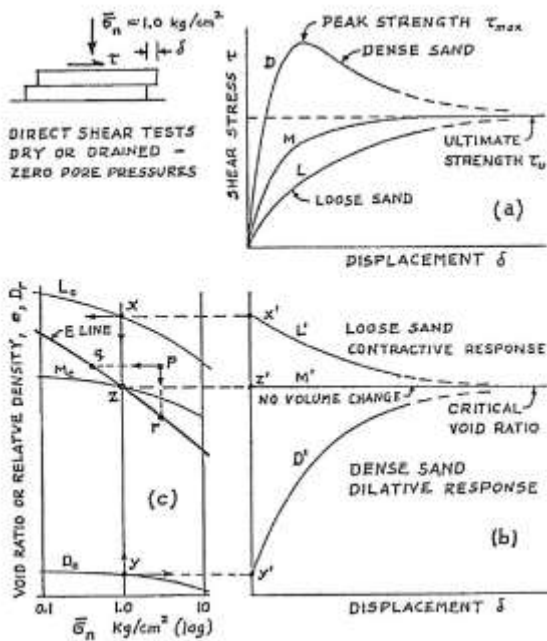
Figure 3. Critical void ratio from direct shear tests (Casagrande 1975)

More generally, the condition of a soil undergoing shear strains under constant stress and with no volume change is called the critical state of the soil and it is a key element of the critical state frameworks and models (Schofield and Wroth 1968). The relationship between critical void ratio and effective stress (usually the mean effective stress is selected) is the critical state line or critical state locus, CSL (Figure 4). Sometimes the line is alternatively called the steady state line (SSL) although the definitions of steady state and critical state are slightly different, as discussed below. Although, the critical state locus is often approximated as a straight line in semi-log space, in fact the line is

often bilinear or curved (e.g. Figure 5). The increase of the slope of the CSL at high stresses is often attributed to particle crushing although it is debatable whether, in the case of evolving materials, a single plane is more appropriate than a single line (Muir Wood 2007, Ciantia et al. 2019). It is interesting to note that early applications of critical state or critical void ratio concepts were made in the investigation of the flow liquefaction of Fort Peck dam; flow liquefaction and critical states appear to have been associated from the start.
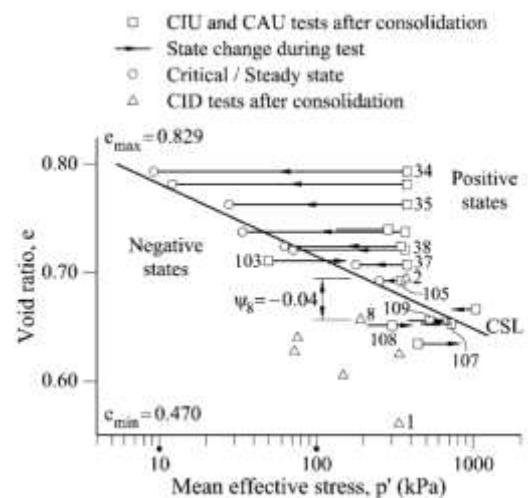
Figure 4. Critical state line for Kogyuk 350/2 sand (modified from Been and Jefferies 1985)
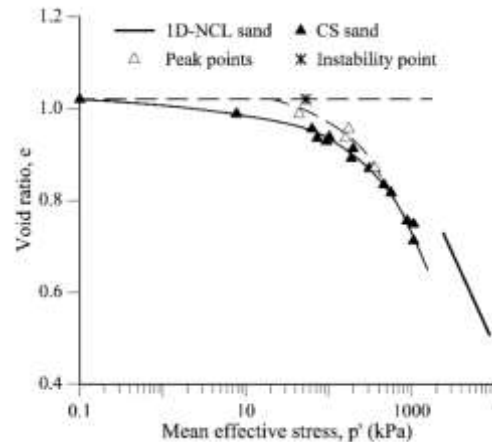
Figure 5. Critical state line for Stava tailings (modified from Carrera et al. 2011)

An important contribution to the characterisation of the behaviour of soils has been the concept of state parameter, ψ. It was anticipated in Wroth and Basett (1965) but it has been incorporated into the mainstream of soil mechanics though the work of Been, Jefferies and co-workers. In their seminal paper (Been and Jefferies 1985), the state parameter is simply defined as the difference between the current void ratio and the void ratio at critical state for the same mean effective stress (Figure 6). In this way, the character of a soil, loose or dense, is automatically related to the magnitude of the effective stress. An advantage of referring the state of the soil to its critical state is that the natural alternative, the normal consolidation line, is difficult to identify in some materials (especially granular ones) and it may be strongly dependent on the initial conditions of the specimen. Been and Jefferies (1985) showed that the state parameter provided a more unified perspective of soil behaviour, especially for sands. Naturally, the behaviour of the soils cannot depend uniquely on the state parameter; other parameters such as fabric and anisotropy are required (Been et al. 1991). It is again interesting to note that the development of the state parameter concept was made in the context of providing a rational engineering approach to the construction of structures using undensified hydraulic sand fills.

2.2 Undrained softening

The mechanism underlying flow liquefaction is illustrated by the undrained stress path and stress-strain curve of Figure 7; it corresponds to behaviour type A of Figure 2. The key feature is that the deviatoric stress reaches a peak (sometimes called instability point) and the material softens afterwards, i.e. the undrained shear strength reduces. The stress path and stress-strain curve finally reach a point where no further pore pressure develops and deviatoric strains increase indefinetely, i.e. the critical state (CS) has been reached. Accordingly, the end point will

be basically controlled by void ratio and effective stress magnitude following the CSL relationship. Large positive pore pressures develop corresponding to the compressive nature of the soil; hence development of flow liquefaction is closely related to positive values (or even slightly negative) of the state parameter. If the void ratio is very high and plots above the critical state value at very low mean effective stress (see Figure 5), then the stress path will go all the way down to zero deviator stress (Carrera et al. 2011, Yamamuro and Lade 1998). As indicated above, this case has been named 'true liquefaction' on the basis that the shear strength of the soil now truly becomes zero (Carrera et al. 2011). However, as undrained softening (without reaching zero strength) can also lead to flow liquefaction and, consequently, to catastrophic outcomes, no distinction will be made in this paper between undrained softening and true liquefaction although, naturally, the consequences of a failure would be more drastic if a soil does reach a zero shear strength value.
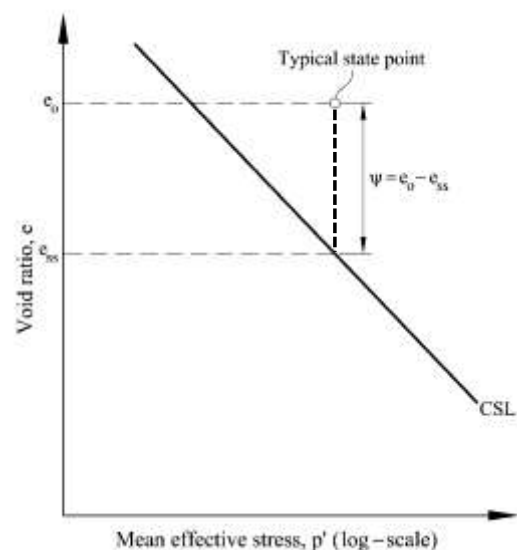
Figure 6. Definition of state parameter, ψ (modified from Been et al. 1991)

a)

b)
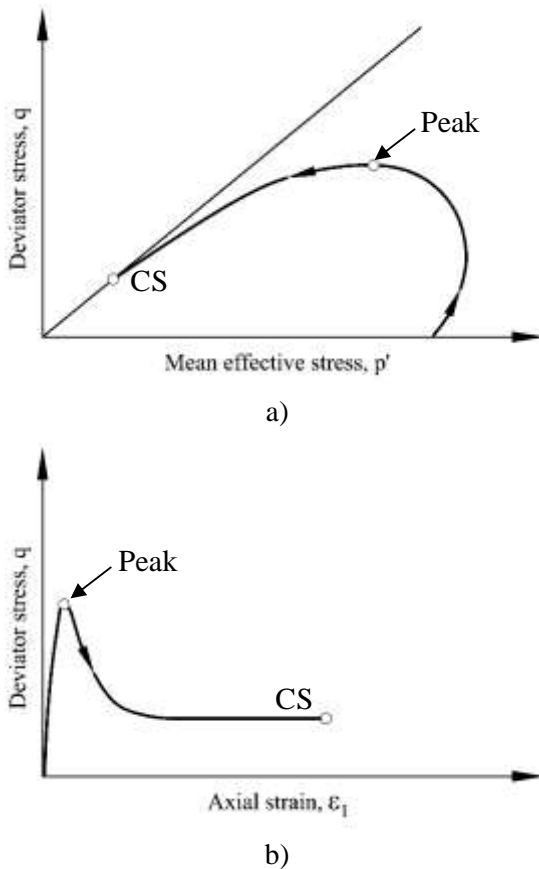
Figure 7. Undrained softening: a) effective stress path; b) stress-strain curve

The association of flow liquefaction with undrained softening and pore pressure increase was already clearly identified in the stress-controlled tests carried out by Castro (1969) (Figure 8). It should be noted that, because of the stress-controlled nature of the tests, the strain rate after peak is several orders of magnitude larger than the strain rate before the peak, raising some questions about potential rate effects. The same undrained softening mechanism was also recognized by Bishop et al. (1969) and Bishop (1973) as the ultimate cause underlying the Aberfan disaster. To quantify the magnitude of softening, Bishop (1973) proposed the definition of a brittleness index that, for an undrained case, reads:

$$I_B = \frac{(c_u)_f - (c_u)_r}{(c_u)_f} \qquad (1)$$

where $(c_u)_f$ is the peak undrained shear strength and $(c_u)_r$ is the residual (critical state) undrained shear strength. The peak point and the critical state have in fact very different characteristics as discussed in the next two subsections.
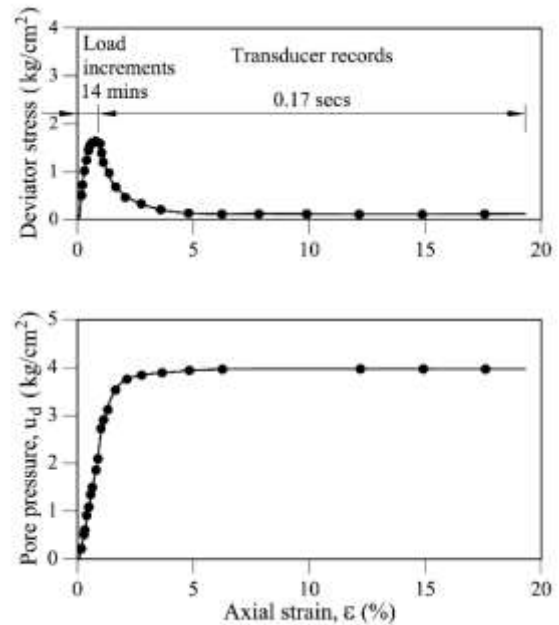
Figure 8. Results of a stress controlled test on loose Banding sand (modified from Bishop 1973, data from Castro 1969): deviator stress-axial strain curve and pore pressure-axial strain curve

2.3 Critical/steady state

As indicated above, the final state of the soil after undrained softening corresponds closely to the definition of critical state (Jefferies and Been 2006). In terms of effective stress, the mobilised friction angle corresponds to that of critical state (or constant volume). In the context of flow liquefaction, the final state has also been called steady state. It has been defined by Poulos (1981) as follows: 'the steady state of deformation of any mass of particles is that state in which the mass is

continuously deforming at constant volume, constant normal effective stress, constant shear stress and constant velocity'. Thus, the main difference compared to critical state is that a constant velocity is additionally prescribed. The notion of steady state has been central to the development and application of the steady state approach to liquefaction evaluation (Poulos et al. 1985). Often, however, critical state and steady state are used interchangeably. The final strength after softening has also been called liquefied strength or residual strength.

Been et al. (1991) found the same critical state for Erksak sand independently of strain rate even when comparing strain-controlled and stress-controlled tests. However, they acknowledge that different results may be obtained testing other materials such as finer silty sands. In fact, the issue of the uniqueness or otherwise of the critical state line has a long history. Casagrande (1975) and Alarcon et al. (1988) distinguished between "S" and "F" lines. The "S" line would correspond to drained triaxial tests whereas the "F" line would correspond to undrained triaxial tests. In fact, this distinction cannot be considered correct within the framework of the effective stress principle, as drained/undrained situations are boundary conditions that should not affect the fundamental behaviour of the soil.

However, at observational level, the question of uniqueness of the critical state line remains largely unresolved. Some studies have found a unique critical state line (e.g. Been et al 1991, Ishihara 1993, Fourie and Papageorgiou 2001, Carrera et al. 2011, Li et al. 2018) whereas non uniqueness has been reported from other sources (Konrad 1993, Kuerbis and Vaid 1988, Vaid et al. 1990, Hird and Hassona 1990). Coop (2015) has identified a range of soils (named 'transitional soils') where the critical state framework faces significant limitations.

In any case, account should be taken of the experimental difficulties of determining the critical state accurately. They arise from different causes: the limitation of the axial strain that can be achieved in the triaxial apparatus, the need for area and membrane penetration corrections, accounting for volume changes during backpressure saturation, the effects of strain localisation, and incorporating inertial effects in the interpretation of stress-controlled tests. Probably, more research is required on this topic especially at the very high strain rates involved in field liquefaction phenomena.

2.4 Peak strength

Whereas the final state after undrained softening is reasonably well established based on critical state considerations, there are less conceptual constraints concerning the point of maximum (peak) strength that signals the onset of instability. It can be noted that peak strength is reached with a mobilised friction angle well below the critical state one. Because peak strength values increase in an approximately linear manner with mean effective stress, it is tempting to join the different peak state points to establish a kind of failure criteria in terms of effective stresses. Two different proposals have been made (Figure 9): a collapse line that passes through the steady state point (Sladen et al. 1985a, Ishihara 1993) and a flow liquefaction line that passes through the origin (Vaid and Chern 1985, Lade 1993). Yang (2002) puts forward a proposal, based on the state parameter, to reconcile the two concepts. Probably, the different existing approaches just reflect the variability and lack of conceptual restrictions for this soil state. It has been observed, for instance, that peak strength is dependent on strain rate and consolidation stress path (Gens 1982). From both a fundamental and practical viewpoint, peak conditions are better considered based on undrained shear strength considerations rather than on effective stress parameters.

An important factor that has not been sufficiently attended to, concerns the effect of anisotropic consolidation. For instance, the tests performed by Castro (1969) show a clear dependence of undrained sand behaviour on the nature of the initial stress state (Figure 10).

However, much of the laboratory experimental work on flow liquefaction has been performed on isotropically consolidated samples. Obviously, this condition does not correspond to the in situ stress state of a hydraulic fill where normally consolidated Ko conditions (and therefore anisotropic stresses) should prevail.

a)

b)
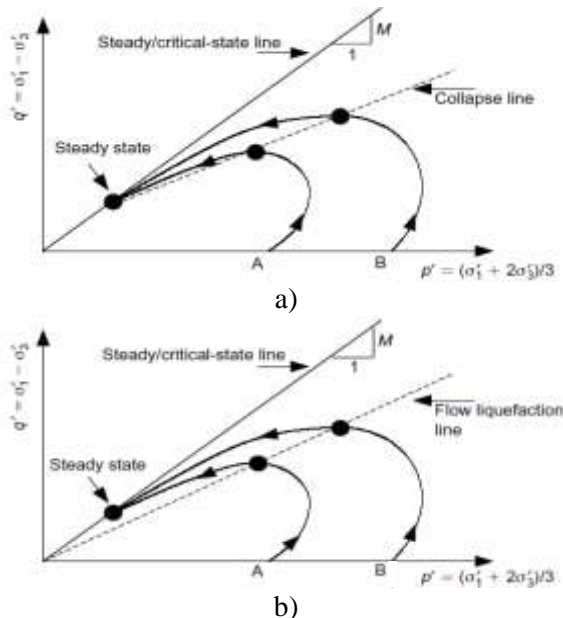
Figure 9. Schematic diagram for peak strength envelopes (Yang 2002): a) collapse line concept; b) flow liquefaction line
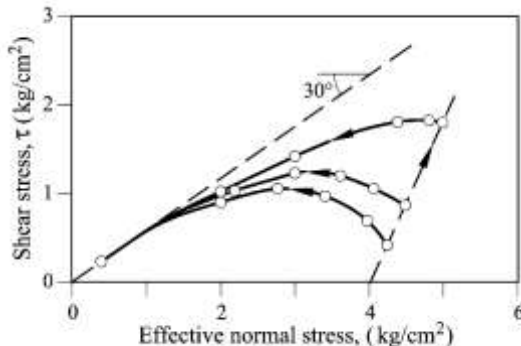
Figure 10. Stress paths for anisotropically consolidated undrained tests on saturated Banding sand (modified from Bishop 1973, data from Castro 1969)

Strong evidence of the effect of the initial state is provided by Fourie and Tshabalala (2005). They performed undrained triaxial tests on specimens of Merriespruit gold tailings and examined the results for each value of fines content. As an example, Figure 11 shows the results from samples with 20% fines consolidated isotropically and anisotropically. The differences are apparent especially concerning the peak strength and the possible flow liquefaction line. Thus the stress ratio ($\eta=q/p'$) at which peak is reached is about 0.6 for the isotropically consolidated samples but it rises to 0.9 for the anisotropically consolidated ones. A proper consideration of peak strength and associated undrained softening behaviour should be based on tests that adopt the correct initial stress state. Indeed, a general perspective should ideally also include the effect of principal stress orientation and intermediate principal stress (Symes et al. 1984).

2.5 Instability conditions

Much work has been done to deal with material instability from a rigorous theoretical mechanics perspective (e.g. Nova 1989, 1994, Darve 1994, Borja, 2006, Nicot et al. 2007, Andrade 2009). It is interesting to examine, from this general point of view, the instability event that takes place when the deviator stress reaches the value of peak strength. At that point (point P in Figure 12), there is an apparent inconsistency. When an undrained test reaches its peak strength, the material softens and collapses, especially under stress-controlled conditions. However, if the test is performed drained, the material crosses point P without any visible instability.

This paradox is usefully explored using the important concept of controllability developed by Nova and co-workers (Nova 1994, Imposimato and Nova 1998). The concept addresses the role of control conditions in the onset of failure. The response of a material can be expressed as (Buscarnera and Whittle 2013):

$$\Phi = \mathbf{X}\,\Psi \qquad (2)$$

where Φ is the combination of control stresses and strains whereas Ψ is the combination of stresses and strains that define the material response. $\mathbf{X}$ expresses the relationship between the applied variables and the material response. Stresses and strains in Φ and Ψ must be work-conjugate. Loss of controllability arises when:

$$\det \mathbf{X} = 0 \qquad (3)$$
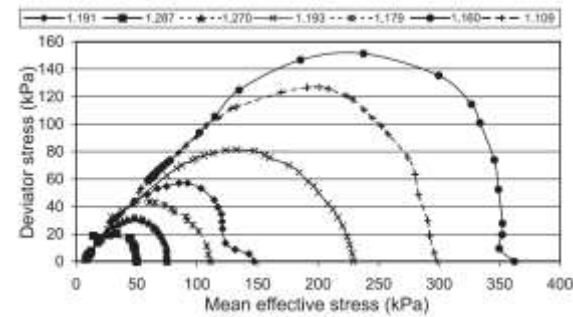
a)
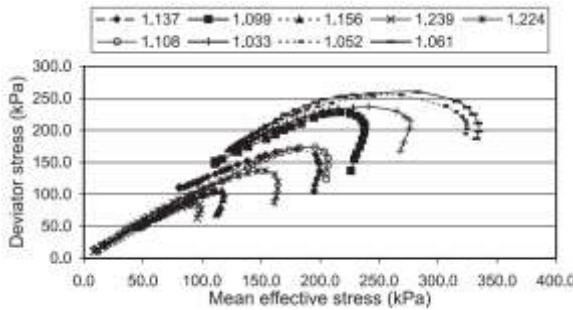
b)

Figure 11. Stress paths from undrained triaxial compression tests on Merriespruit gold tailings with 20% fines (Fourie and Tshabalala 2005): a) isotropically consolidated specimens; b) anisotropically consolidated specimens

The basic difference between a drained and undrained test lies in their different control variables. Specifically, in an undrained test a negligible volume change conditions is prescribed. Under those conditions, it is possible to define, within an elastoplastic framework, a critical liquefaction modulus as:

$$H_{LIQ} = -\frac{\partial f}{\partial p'} K \frac{\partial g}{\partial p'} \qquad (4)$$

where f is the current yield surface, g the plastic modulus and K the elastic volumetric modulus.
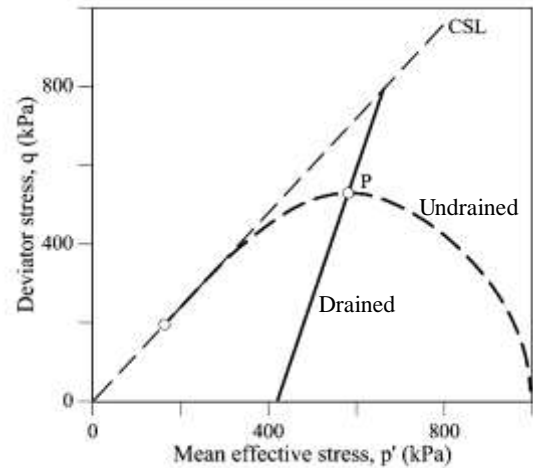
a)
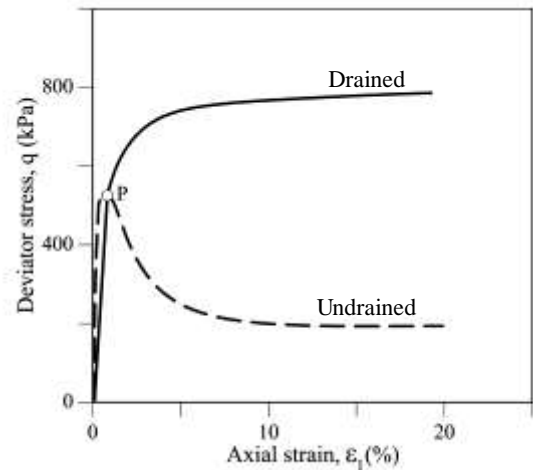
b)

Figure 12. Drained and undrained behaviour of a soil exhibiting undrained softening: a) effective stress paths; b) stress-strain curves

Controllability is lost when the difference between hardening modulus and the critical liquefaction modulus (Λ)

$$\Lambda_{LIQ} = H - H_{LIQ} \qquad (5)$$

becomes zero or negative.

This situation corresponds to the onset of liquefaction and Λ has been called stability index because it constitutes a scalar measure of stability (Buscarnera and Whittle 2013). In fact, Buscarnera et al. (2011) have shown that that it is possible to consider together controllability, uniqueness and existence of the incremental response of the material depending on the sign of the stability index.

Instability can now be re-examined with reference to Figure 13 that shows the simulation of an undrained triaxial test on a loose sample of Toyoura sand using the elastoplastic model MIT-S1 (Pestana and Whittle 1999). Figure 13a presents the stress-strain curve together with the evolution of the stability index. It can be noted that the stability index becomes zero when the material reaches the peak undrained strength and it has a negative value during the softening branch of the test. The index goes back to zero on reaching critical state. The two components of the stability index, plastic modulus and critical liquefaction modulus, are plotted separately in Figure 13b. It is interesting to note that the plastic modulus is positive (i.e. strain hardening) throughout the test even during softening. Therefore, the drained test (that uses a different set of control variables) can remain stable in a strain hardening regime although there is obviously a latent instability present that can be triggered by a change of control conditions.
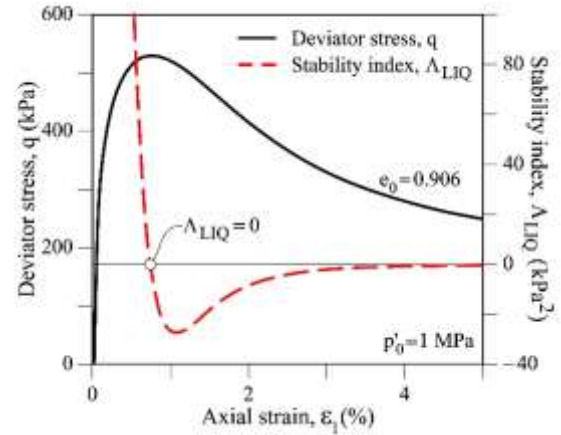
a)
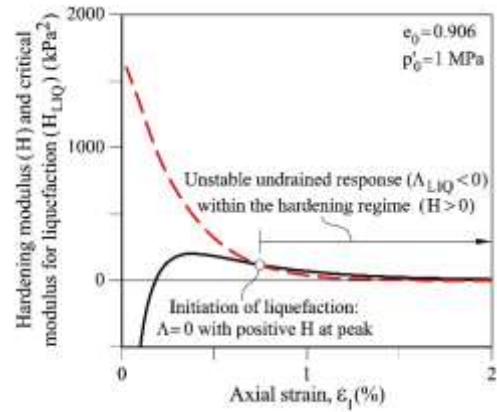
b)

Figure 13. MIT-S1 simulations of loose Toyoura sand (modified from Buscarnera and Whittle 2013): a) evolution of deviator stress and stability index; b) evolution of hardening modulus and critical modulus for liquefaction

3 TRIGGERING FLOW LIQUEFACTION

If a loose material is deposited along a slope, liquefaction may occur with minimum disturbance if the inclination is large enough (e.g. di Prisco et al. 1995). This phenomenon probably corresponds to the concept of 'spontaneous liquefaction' introduced by Terzaghi (1957). However, in other circumstances, a triggering

event is required to set off liquefaction. Consider for instance the undrained stress path of a specimen of a flow liquefaction-prone material after Ko consolidation (Figure 14a). It is necessary to apply an additional deviator stress to reach peak strength and start the softening regime. The additional deviator may arise from an undrained increase in vertical stress (total stress path A), a reduction in horizontal stress (total stress path B) or a combination of the two. It should be noted that, in terms of effective stress paths, the different undrained loading types are all equivalent. A drained lateral stress reduction may also lead to instability and liquefaction (Figure 14 b). Liquefaction can also be triggered by an increase of pore pressure that may be due to changes in hydraulic conditions (Figure 14 c) or to the effects of cyclic loading (Figure 14d). The latter case should not be confused with cyclic liquefaction. In all the three latter cases (14b, c, d), soil behaviour becomes undrained once the instability point has been reached.

b)

c)

a)

d)
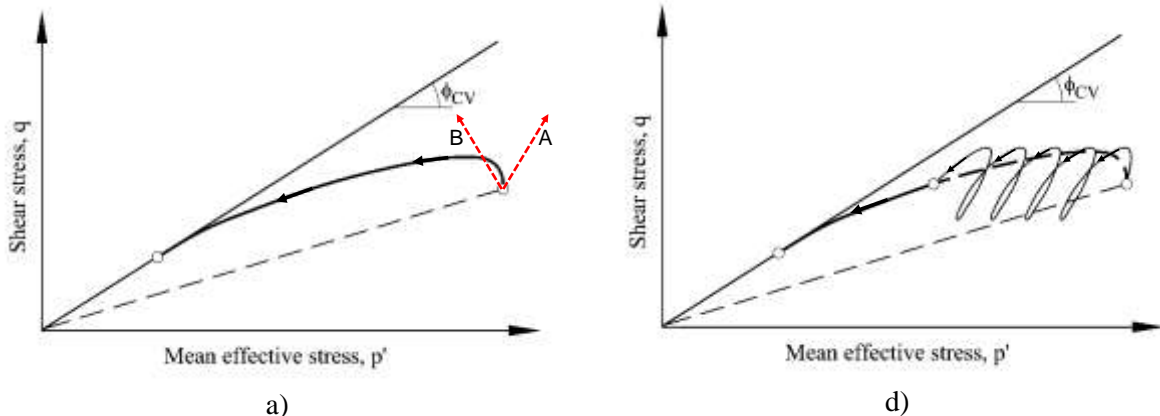
Figure 14. Triggering mechanisms for flow liquefaction: a) undrained increment of deviator stress; b) drained unloading; c) pore pressure increase due to change in hydraulic conditions; d) pore pressure increase due to cyclic loading

A number of different physical triggering mechanisms for flow liquefactions have been identified (e.g. Martin and Mc Roberts 1999). They can be classified in the following manner:

a) Load increase due to emplacement of the material or other construction activities on the surface. The placing of the material cannot be uniform as Ko conditions, by definition, will never lead to static failure. (Figure 14 a, path A).

b) Lateral stress reduction due to foundation sliding, dam overtopping, toe erosion or excavation. In this unloading case, triggering may be undrained if those events are rapid (Figure 14a, path B) or drained if they occur very gradually (Figure 14b).

c) Changes in pore pressures due to increased pond levels, unfavourable weather conditions or pore pressure redistribution (Figure 14c).

d) Vibrational loads due to earthquakes, construction traffic or blasting (Figure 14 d).

Lateral stress reduction due to basal sliding is a very common trigger of flow liquefaction. It has been identified in the cases of Fort Peck Dam, Mount Polley dam, Kingston fly ash dike and Fundão dam. In the failure of Aberfan spoil tip, the immediate cause was also a sliding on a pre-existing shear surface that triggered the liquefaction of the colliery waste that had been taken close to saturation by rainfall. In Merriespruit dam, the lateral stress release was brought about by overtopping and rapid erosion of the dam. In the well-known case of Lower San Fernando dam, the triggering mechanism was not foundation failure and lateral stress reduction but the increase of pore pressures that resulted from the redistribution of pore pressures set up during the preceding earthquake.

4 ANALYSIS OF THE CPTU TEST IN UNDRAINED SOFTENING MATERIALS

4.1 General

It is difficult to extract really undistorted samples from most materials that are prone to flow liquefaction (clean sands, silty sands, sandy silts and silts). For this reason, soil characterization is usually based on in situ tests (Viana da Fonseca 2013); currently, cone penetration tests (CPT and CPTu) are probably the most dominant ones. Normalized parameters based on cone penetration records have been used as a screening tool to assess whether a particular soil deposit is potentially flow-liquefiable. The most commonly used ones are:

$$Q_t = (q_t - \sigma_{vo}) / \sigma'_{vo} \qquad (6)$$

$$F = f_s / (q_t - \sigma_{vo}) \qquad (7)$$

$$B_q = (u_2 - u_o) / (q_t - \sigma_{vo}) \qquad (8)$$

$$Q(1 - B_q) + 1 = (q_t - u_2) / \sigma'_{vo} \qquad (9)$$

where q_t is the total cone penetration resistance, u_2 is the pore pressure measured at the shoulder of the cone in CPTu tests, u_0 is the initial pore pressure, and σ'_{v0} and σ_{v0} are the initial effective and total vertical stresses respectively.

Thus, Robertson (1990, 2009. 2010a, 2012, 2016) used a Q_t - F space to map regions of different soil type behaviour; potential flow liquefaction is associated materials with contractive behaviour. Alternatively, the potential for flow liquefaction can be evaluated by determining the state parameter, ψ, from the cone penetration data (Been et al. 1986, 1987, Jefferies and Been 2006, Robertson 2010b, Reid 2015, Been 2016). The relationship between the state parameter and cone penetration resistance is not however unique but it is affected by a number of other soil properties that, ideally, should be

taken into account (Shuttle and Jefferies 1998). The availability of G_0, independently measured with the seismic cone, can provide additional useful information for a more accurate estimation of the state parameter (Schnaid and Yu 2007).

Undrained shear strength at the critical state (normalised by the initial effective vertical stress) have been estimated from backanalysed case histories (Olson and Stark 2002, Robertson 2010). They fall in the range of 0.05 to 0.15. Empirical relationships have been developed relating those strength values (sometimes supplemented with laboratory test results) with cone penetration data (Yoshimini et al. 1999, Robertson 2010). The evaluation depends strongly on the specific value of the soil behaviour type (SBT) leading to some significant uncertainty. Critical state undrained strength can also be derived from the value of the state parameter (Jefferies and Been 2006); in this case, uncertainties arise from the method of state parameter estimation.

In any case, interpretation of the cone penetration test is difficult and a satisfactory outcome would ideally require the combination of physical tests (calibration chambers or centrifuges), case histories and numerical analyses. There are a significant number of calibration chamber results but they are usually limited to clean sands leaving unexplored the important case of silts and silty materials. Interpretation of case histories is always approximate because relevant information is often missing or incomplete.

The challenges for the numerical analysis of cone penetration are considerable. Shuttle and Jefferies (1998) and Shuttle and Cunning (2007) have performed large deformation analysis assimilating cone penetration to a spherical cavity expansion but, obviously, this approach, while providing important insights, can only be considered a first approximation. A more realistic simulation of cone penetration requires the incorporation of the actual geometry and dealing with the nonlinearities associated with large deformations, appropriate soil constitutive models and cone/soil interface characteristics. Advanced numerical procedures currently exist that allow the performance of such analyses with a reasonable degree of success. Examples are the various formulations of Arbitrary Lagrangian-Eulerian procedures (ALE) (Wang et al. 2015) such as the Remeshing and Interpolation Technique by Small Strain (RITSS) (Zhou and Randolph 2009), the efficient ALE (EALE) approach (Nazem et al. 2006) and the Coupled Eulerian-Lagrangian (CEL) method (Pucker et al. 2013). Other possibilities are the Material Point Method (MPM) (Solowski and Sloan 2015) or the Particle Finite Element Method (PFEM) (Oñate et al. 2004, Zhang et al. 2028). Applications of those methods to the cone penetration test have been reported in a number of cases (e.g. Lu et al. 2004, Nazem et al. 2012, Walker and Yu 2006, Ceccato et al. 2016, 2017, Gens et al. 2016, Monforte et al. 2017a, 2018) although they do not address the case of undrained softening.

In this section, selected results of numerical analyses of the cone penetration test in an undrained softening material are presented. They are part of a systematic exploration of the effects of brittleness on the interpretation of the cone penetration test, currently under way.

4.2 Features of the PFEM analyses

The CPTu test has been analysed using the PFEM to examine the effect of increasing brittleness on the results of the cone penetration test. A coupled PFEM formulation (Monforte et al. 2017b, 2018) has been used in order to obtain not only the total cone resistance but also the pore pressure field developed during penetration. The PFEM can be summarised in the following points:

- The nodes of the domain of analysis are treated as particles whose motion is tracked during the solution process
- The particles are used as nodes of a Finite Element mesh.

- The FE discretization is periodically re-meshed (h-adaptive techniques are used) by Delauney tessellation, new nodes are included if necessary, and element smoothing is performed
- The continuum is modelled using an Updated Lagrangian formulation
- Interpolation algorithms are applied to transfer information between successive meshes
- Although it is not strictly required, well-shaped low order elements are used

The computational procedure sequence is illustrated in Figure 15.
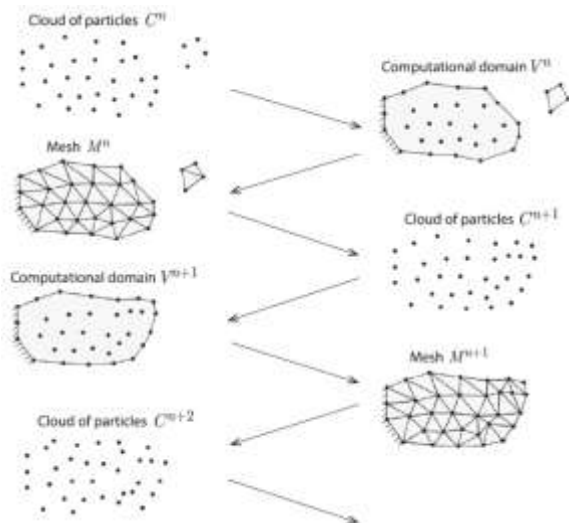
Figure 15. Scheme of a PFEM analysis

However, because the simulation of flow-liquefiable materials requires the representation of undrained softening, an additonal important development is required. It is well-known that conventional finite element analyses of softening materials rend to deliver non-objective results that exhibit a pathological dependence on mesh size (Bazant and Pijaudier-Cabot 1988, De Borst et al. 1993). In order to obtain correct results, it is necessary to use one of a number of existing regularization techniques (Bazant and Jirasek 2002). For these analyses, a non-local formulation (Manica et al. 2018) based on the

weighting function of Galavi and Schweiger (2010) has been incorporated into the PFEM procedure. The essence of the formulation is the assumption that the state of a particle point depends not only on the variables of the point itself but also on the variables of neighbouring points (Figure 16).
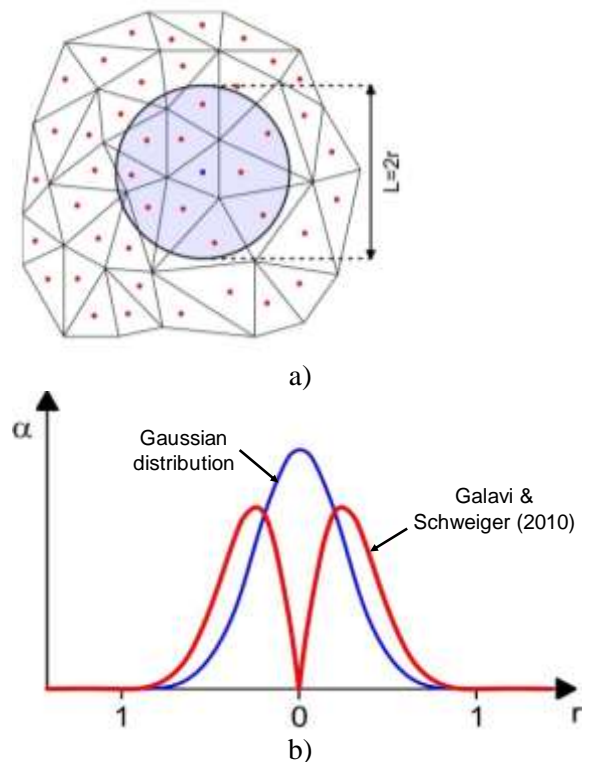
Figure 16. a) Stress points considered in the neighbourhood of a point in a nonlocal formulation; b) Weighting functions

4.3 Constitutive model

There are significant number of constitutive models available that are capable of simulating the undrained softening that underlie flow liquefaction phenomena (e.g. Jefferies 1993, Manzari and Dafalias 1997, Yu 1998, Pestana and Whittle 1999, Gajo and Muir Wood 1999, Imam et al. 2005). Most are isotropic but the MIT–S1 model can account for anisotropic

behaviour (Pestana et al. 2002). In the analyses presented here, a somewhat modified version of the CASM model (Yu 1998) has been used and is briefly presented here. The CASM model has been selected because i) it is relatively simple having a single yield surface, ii) it is based on the state parameter concept, iii) it uses non-associated plasticity allowing for instability phenomena to be reproduced, and iv) selecting appropriate parameters, it can mimic classical critical state models. Naturally, there are shortcomings associated with simplicity: the model is isotropic and the simulated behaviour inside the yield surface is quite simplistic. It has sufficient flexibility, however, to model a range of behaviour spanning from loose to dense states, including, naturally, the softening behaviour underlying flow liquefaction.

A schematic summary of the model is presented in Figure 17 where the concept of state parameter, ξ, is illustrated. The reference state parameter, ξ_r, defines the spacing, r, between the reference consolidation line and the critical state line, CSL. The model is based on a general expression for the state boundary surface of the following form:

$$\left(\frac{\eta}{M}\right)^n = 1 - \frac{\xi}{\xi_r} \tag{10}$$

where η is the stress ratio (q/p'), M is the slope of the CSL in q-p' space and n is a model parameter.

From geometrical considerations (Figure 17):

$$\frac{\xi}{\xi_r} = 1 + \frac{\ln(p'/p'_0)}{\ln r} \quad ; \quad r = \frac{p'_0}{p'_x} \tag{11}$$

and the following expression for the state boundary surface results:

$$\left(\frac{\eta}{M}\right)^n = -\frac{\ln(p'/p'_0)}{\ln r} \tag{12}$$

Through the variation of n and r, a wide variety of yield surface shapes can be obtained making the model very suitable for application to a wide range of materials.

The original CAM model used Rowe's dilatancy rule for the plastic potential but for the applications reported here, the following flow rule has been preferred (Yu 2006, Gonzalez 2011):

$$\frac{d\varepsilon_v^p}{d\varepsilon_q^p} = \frac{M^n - \eta^n}{m\eta^{n-1}} \tag{13}$$

where $d\varepsilon_v^p$ and $d\varepsilon_q^p$ are plastic volumetric and shear strains respectively and m is a parameter that controls the value of Ko for normally consolidated states. It can be noted that when $\eta=M$ (critical state), dilatancy is zero. The hardening law is the classical isotropic volumetric strain rule of critical state soil models.

Often, it is required that the model is defined in terms of the undrained shear strength, $(s_u)_{SS}$ at critical (steady) state conditions. In that case, parameter r is expressed as (Gonzalez 2011):

$$r = \left(\frac{M}{2}\frac{p_e'}{(s_u)_{SS}}\right)^{\frac{1}{\Lambda}} \tag{14}$$

where p_e' is the equivalent pressure and $\Lambda = (1-\kappa/\lambda)$ (Figure 17).

Figure 18 shows the capability of the model for simulating dense and loose behaviour under undrained conditions. More details on the model is given in Yu (1998, 2006) and Gonzalez (2011). It should be pointed out that, in this model, the undrained softening behaviour takes place under strain hardening conditions as discussed in section 2.5.
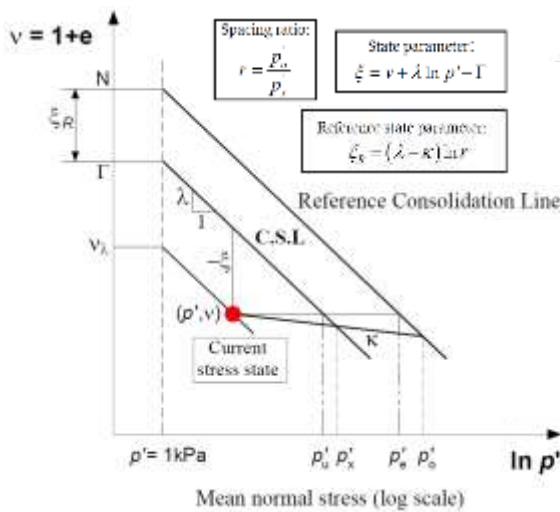
Figure 17. Definition of the CASM model (modified from Yu (1998)

4.4 Results

As indicated above, a systematic exploration of the effects of brittleness on the interpretation of the cone penetration tests is currently under way, only some illustrative results are shown here. For the set of analyses selected, appropriate values of n and r have been chosen in order to obtain the series of undrained stress paths and stress-strain curves of Figure 19. It can be observed that the undrained peak strength is the same in all cases but the degree of brittleness varies. Case A exhibits the lowest critical state undrained shear strength and, consequently, the maximum brittleness whereas case G corresponds to the minimum degree of brittleness.

The geometry and boundary conditions of the analyses are shown in Figure 20. The cone is pushed into the soil at the standard rate of 2 cm/s. Because of the low permeability adopted for the soil (a silty material has been assumed), penetration is basically undrained. The initial effective vertical and horizontal stresses are 96 kPa and 56 kPa, respectively, i.e. a Ko value of 0.58 has been assumed. Note that, because of the CASM model formulation, all results of the analyses can be normalized by the value of initial effective stresses.
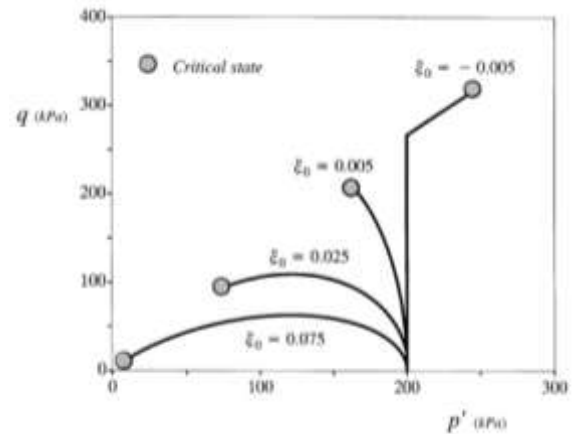
a)
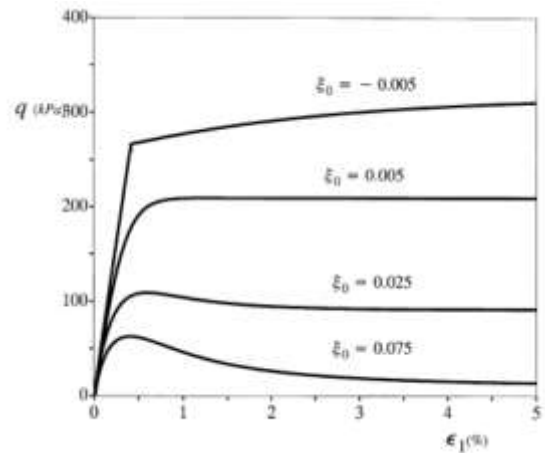
b)

Figure 18. Range of soil behaviour simulated by the CASM model (Yu 1998). Effect of state parameter in an undrained triaxial test: a) effective stress path; b) stress-strain curves

Figure 21 shows the results of the analyses in terms of net cone resistance (q_n), i.e. the total cone resistance minus the total vertical stress, the excess pore pressure at the cone face (Δu_1) and the excess pore pressure measured at the cone shoulder (Δu_2) whereas Figure 22 shows the same results in terms of the normalised parameters Q_t, B_q and $Q_t(1 - B_q) + 1$. As expected, although all the cases have the same peak undrained shear strength, the degree of brittleness has a very

strong influence on the results. This is illustrated in Figure 23 where Q_t, and B_q are plotted against Bishop's brittleness index. The effect of brittleness on the development of pore pressures is apparent in Figure 24 where the pore pressures around the cone (normalised by the net cone resistance) are compared for cases A (maximum brittleness) and G (minimum brittleness).
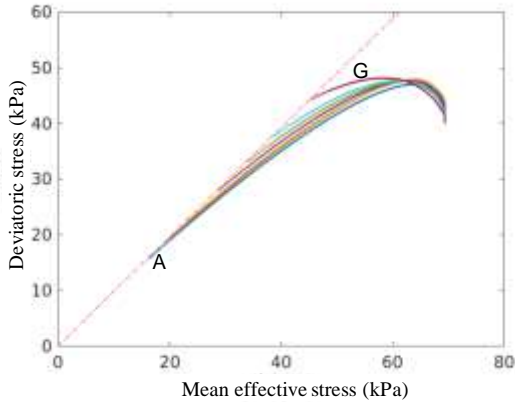
a)
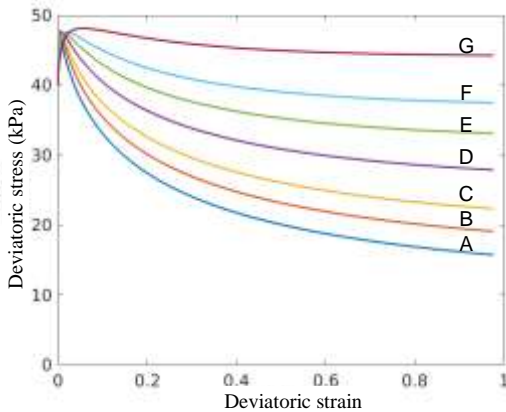
b)

Figure 19. Simulated soil behaviour for the analyses of the CPTu test: a) effective stress path; b) stress-strain curves
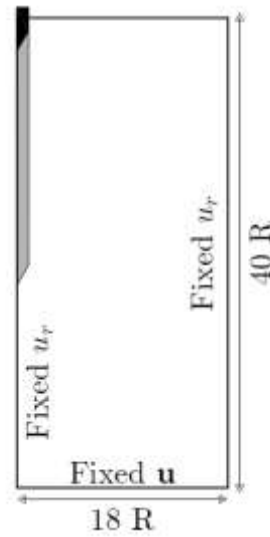
Figure 20. Analysis of the CPTu test. Geometry and boundary conditions
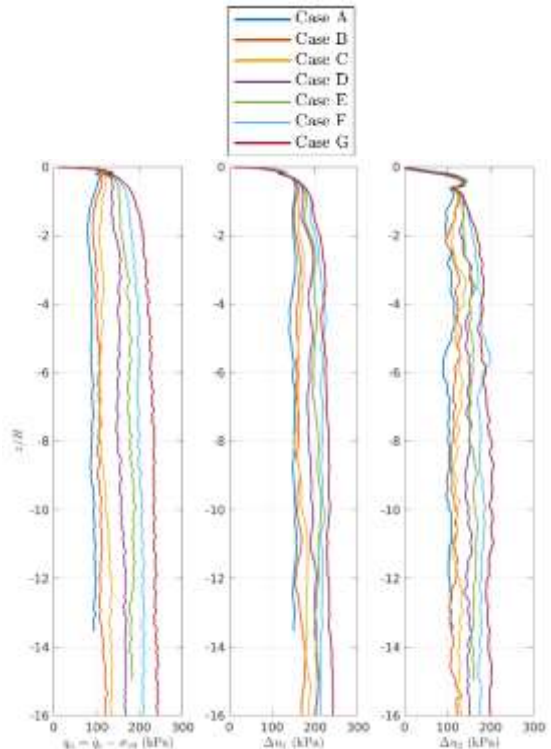
Figure 21. Results of the simulations of the CPTu test: net cone resistance (q_n), excess pore pressure at the cone face (Δu_1) and excess pore pressure at the cone shoulder (Δu_2)
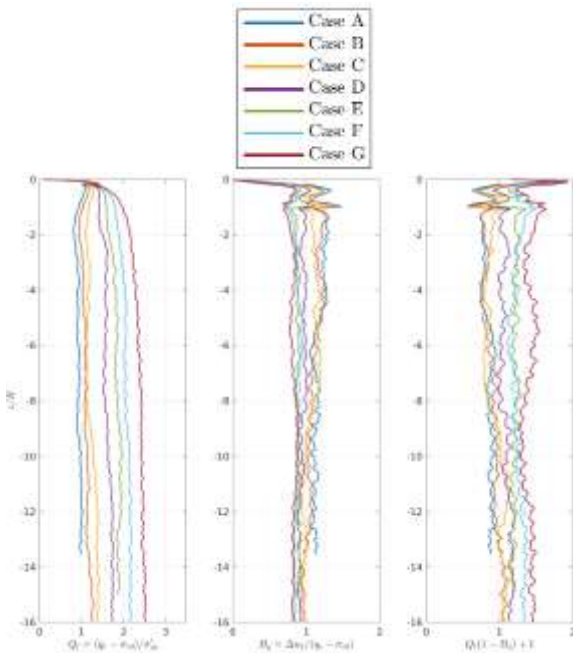
Figure 22. Results of the simulations of the CPTu test in terms of the normalised parameters Q_t, B_q and $Q_t(1-B_q)+1$.
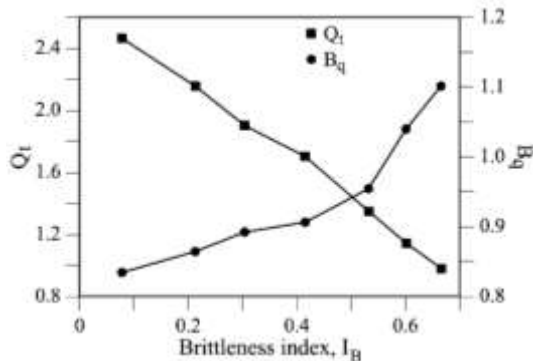
Figure 23. Variation of normalized parameters Q_t, and B_q with brittleness index

a)   b)
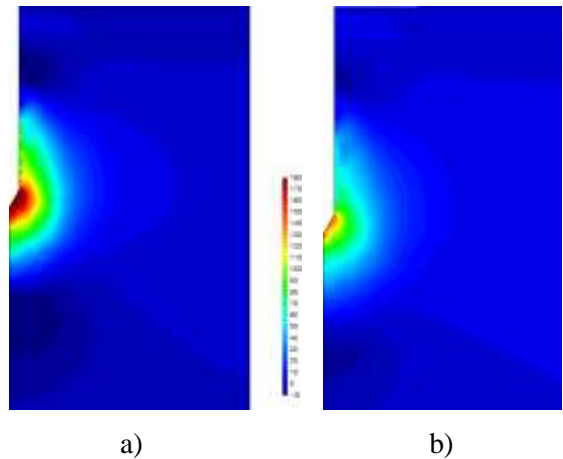
Figure 24. Contours of pore pressures (normalised by the net cone resistance): a) case A, maximum brittleness; b) case G, minimum brittlenes

5 CASE HISTORY 1: AZNALCOLLAR DAM

Aznalcóllar tailings dam failed catastrophically in April 1998 (Figure 25) when the top of the dam had reached a height of 28 m above foundation level. The case has been described in detail in Alonso and Gens (2006a) and Gens and Alonso (2006b). In this instance, tailings were not used to form the retaining structure but a rockfill dam with an upstream clay blanket was designed and built. The dam failed by sliding on the foundation; the failure surface was located in the blue Guadalquivir clay that underlie the site. Figure 26 shows the mechanism of failure. The foundation clay exhibited the classical brittle behaviour associated with many stiff clays that led to the development of progressive failure. Failure resulted in a maximum quasi-horizontal displacement of over 50 meters. The dam and the upper part of the foundation moved downstream as a rigid body. This large movement allowed the opening of a breach in the dam that in turn made possible the spillage of water and tailings. Water and tailings caused the visible erosion of the dam that allowed more material to be released into the

environment. In total, it is estimated that the 7 million m^3 spillage was composed of 5.5 million m^3 of contaminated water, 1.3 million m^3 of tailings and 0.2 million m^3 of dam materials. Tailings were mainly dragged away by water erosion, most of the tailings remained inside the basin because they had a small degree of cementation and therefore a modest amount of cohesion. There were no casualties due to the failure but the environment damage was enormous. Acording to the multi-criteria ranking used by the worldminetailingsfailures.org. website, the Azanalcóllar failure is one of the twenty worst mine tailings disasters in history.

Figure 25. View of Aznalcóllar dam after failure
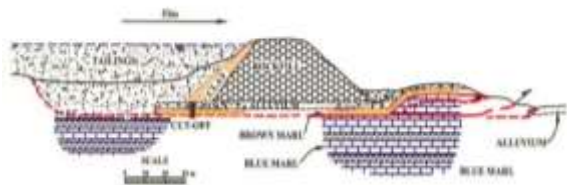
Figure 26. Mechanism of failure

The tailings had been deposited hydraulically in the lagoon; the material involved in the sliding failure were silt-size pyrite tailings. Coarser materials (pyroclastic tailings) had been deposited in the adjacent basin but they were not involved in the foundation failure. The pyrite tailings had a quite uniform grading (average D_{50}: 10 microns). The material was non-plastic, with high density (3-3.3 g/cm^3), a high friction angle

(around 40º) and low permeability (about 10^{-6} - 10^{-7} m/s). There was clear evidence after the failure that the tailings close to the failed section of the dam had undergone liquefaction (Figure 27). However, the liquefaction of the tailings was not the cause of the failure but a consequence. When the dam started to move on the slip surface, lateral stress reduced and deviatoric stress increased so that the undrained stress path went over the peak strength (similarly to stress path B in Figure 14a). Liquefaction followed from that moment on.

Figure 27. Evidence of tailings liquefaction

The study of the dynamics of the failure of Aznalcóllar dam was reported in Alonso and Gens (2006b). Because of the simple failure mechanism involved, it was possible to represent realistically the problem as a rigid body motion of the dam and upper part of the foundation materials (Figure 28). The moving body (mass *M*) is subjected to thrust (F_T) and resisting (F_R) forces. If they are not in equilibrium, an acceleration, *a*, will result (equation 15).

$$\sum F = \sum F_T + \sum F_R = Ma \qquad (15)$$
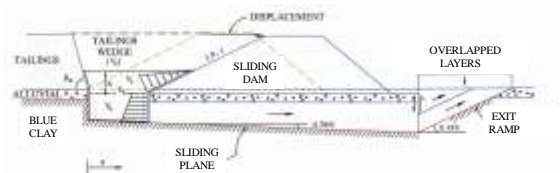
Figure 28. Scheme of the motion analysis of Aznalcóllar dam slide (Alonso and Gens 2006b)

The thrust force F_T is exerted by the tailings whereas there are two main components of the resisting forces, the friction along the sliding force F_{RF} and the passive resistance of the ground at the toe of the dam, F_{RF}. If the acceleration is computed using equation (16), a single integration in time provides the velocity of the dam and a double integration, the displacement.

$$\sum F = F_T + \left(F_{RF} + F_{RP} \right) = M \frac{d^2 x}{dt^2} \quad (16)$$

It has proved possible to make quite reasonable estimates of those forces and their variation with dam displacement (Alonso and Gens 2006b). The results are shown in Figure 29. It can be noted that the base resistance of the sliding plane reduces because the strength of the blue clay is decreasing towards the residual value. In contrast, the passive resistance provided by the ground at the toe of the dam increases because the sediments located there rise as a consequence of the movement of the dam. However, the most important contribution to the failure dynamics is provided by the tailings. Once they liquefy (due to the initial movement of the dam), they provide a very large additional thrust that is decisive for increasing drastically the acceleration of the dam and, consequently, the velocity and final displacement. Tailings also provide the braking mechanism because they fill the volume left by the sliding mass, their height reduces and their thrust diminishes accordingly. The variation of the resulting force with time is also plotted in Figure 29.

The resulting evolutions of velocity and displacement are plotted in Figure 30. It can be seen that the computed total displacement is of the same order as that observed in the field. The duration of the motion is 15.5 s, the maximum speed 5.5 m/s and the maximum computed acceleration 0.14g. Unfortunately, the only observations available are the final displacements of the dam; the failure occurred at about 2:30 in the morning and there were no eyewitnesses.

Although computations included a number of uncertain variables, sensitivity analyses showed that the final outcome of the calculations was very robust with only modest variations in the computed final dam displacement.
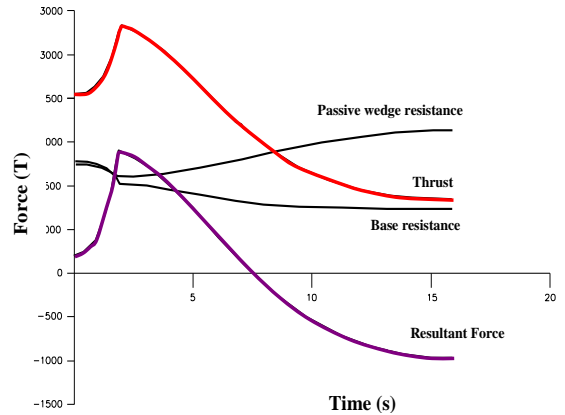
Figure 29. Variation of thrust, resistance and resultant forces with time
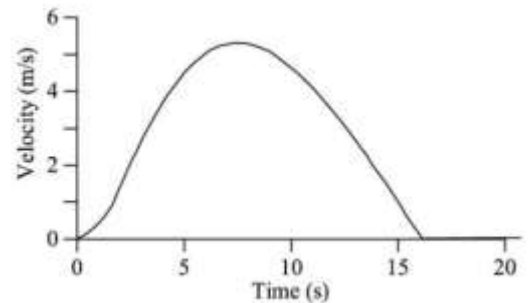
a)
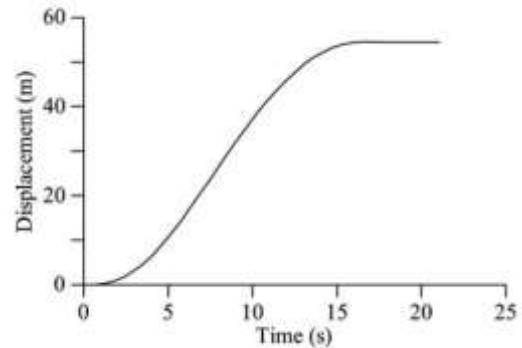
b)

Figure 30. a) Evolution of dam velocity with time; b) evolution of dam displacement with time

6 CASE HISTORY 2: PRAT QUAY

6.1 Background

Prat quay provides the platform for a new container terminal, part of the latest development of Barcelona Harbour. It has a total length of 1,580 m and its construction was divided in two phases, Phase 1, 1000 m long, and Phase 2, 580 m long. Caissons were used to construct the quay wall; 25 units for Phase 1 and 12 for Phase 2 (Figure 31). On January 1st 2007, the Phase 1 quay wall failed catastrophically over a length of 600 m (Figures 32 and 33). Figure 34 shows the distanced travelled by the 15 caissons involved in the failure. It can be observed that some of the caissons travelled long distances, up to 90 m in one case.
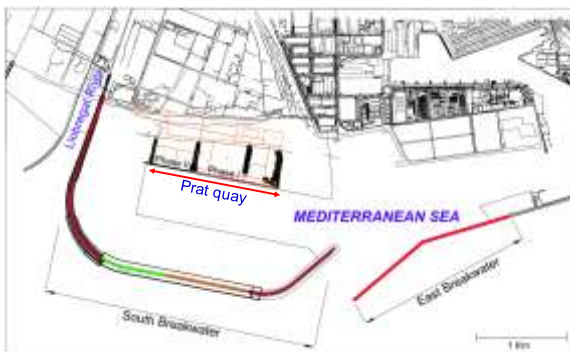
Figure 31. Location of the Prat quay

Figure 32. View of the Prat quay failed section

Figure 33. Length of the Prat quay failure and maximum distance travelled by the caissons
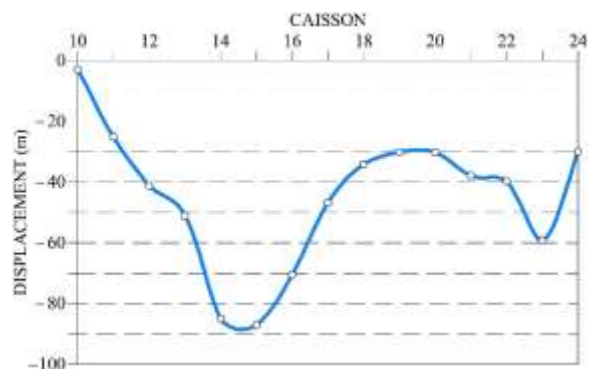
Figure 34. Displacements travelled by the caissons involved in the failure

The process of construction was as follows: i) dredging of the natural soil from an elevation of approximately -8.0 m to elevation -25.0 m, ii) construction of a rubble mound to elevation -16 m, iii) emplacement of the caisson on the rubble mound, iv) filling of the caisson cells with sand, and v) placement of the hydraulic fill at the back of the caissons. Hydraulic backfill was placed by rainbowing (Figure 1). The quay wall and the hydraulic backfill sit on the natural ground that, in this particular area, is made up of soft silty clay down to depths of 60-70 m below sea level.

The state of the quay at the moment of failure is illustrated in Figure 35. The caisson is 17.5 m high (emerging 1.5 m above mean sea level) and 18.5 m wide. The width of the caisson is larger than in most designs, the reason being that the caisson was designed to withstand storm forces

while the South breakwater (Figure 31) was being completed. In addition, at the time of failure, two embankments were being constructed (South and East embankments, see Figure 33) on top of the the backfill. The aim was to isolate an area for preloading. The embankments were constructed by simply dumping rockfill on the hydraulic backfill.
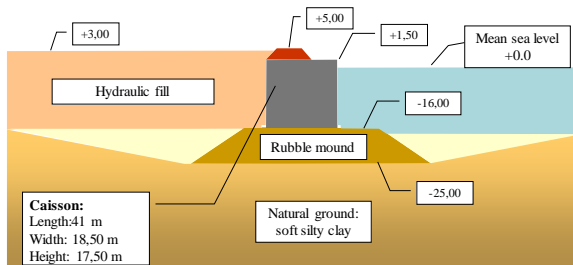
Figure 35. Cross-section of the Part quay before failure

Prior to failure, a 3.5 m high bund had been constructed on top of the caisson in order to allow the construction of the backfill to a higher elevation with the aim of accelerating preloading and reducing construction time. Naturally, this increased the pressures on the caisson wall. Backfill was rapid, it started in May 2006 and it was largely completed at the time of failure, eight months later. Failure occurred when the hydraulic backfill had reached an elevation of approximately +3.00 m and the water level behind the caissons an elevation of +3.50 m. At the moment of failure, the only site activity was hydraulic backfilling close to the area that failed.

Investigations after the failure clearly revealed that the underlying natural soft silty clay had not been involved. The rubble mound was in place and largely intact with perhaps only a small local failure at the seaward edge. Caisson sliding on the rubble mound was evidently the failure mechanism. The hydraulic fill liquefied and provided the necessary thrust to move the caissons the large distances observed. The largest movements were centred on caissons 14 and 15 close to the centreline of the South embankment. After investigation, it is strongly suspected that

failure of the South embankment started the backfill liquefaction that subsequently spread to other locations. The failure could well have been triggered by release of air trapped in the backfill (Hight 2007); an eyewitness reported five or six air discharges in the relevant area minutes before the failure.

The fill involved in the failure had flowed and dispersed widely in the basin and therefore it was not available for investigation. The knowledge on the state and properties of the hydraulic fill before the failure has been based on the information provided by the remaining fill in Phase 1 and the fill in Phase 2 that had been placed in exactly the same way. The grading of a hydraulic fill is generally dependent on the location of a particular area with respect to the discharge point and on the distance that the soil particles have travelled before sedimentation. Therefore, it is not surprising that there was quite a significant span in the grading of the fill ranging from silty sands to clayey silts. In any case, the proportion of fines was generally high. Figure 36 shows an example of the particle size distributions obtained from the samples recovered from a particular borehole.
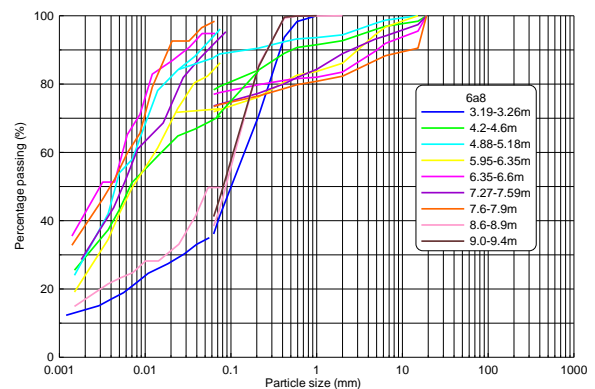
Figure 36. Particle size distributions from samples recovered from borehole 6a8.

A large campaign of CPTu tests was performed in both the failed and non-failed sections of the Prat quay covering both land and sea sides. Figure 37 shows the CPTu results in an unfailed section of Phase 1 on the land side. It is

apparent that the cone resistances are very small in the hydraulic fill, the transition to the natural ground clearly visible in most cases. It cannot be discarded that some excess pore water pressures were present in backfill areas of lower permeability. Figure 38 shows in more detail the CPTu observations of cone resistance, pore pressure and sleeve friction for a particular sounding. In Figure 39, the observations in the hydraulic fill of two representative CPTu tests are plotted in the SBT (soil behaviour type) charts proposed by Robertson (2016). It can be noted that there is a significant spread from sand-like to clay-like materials but practically all points indicate contractive behaviour and therefore with a potential for flow liquefaction.
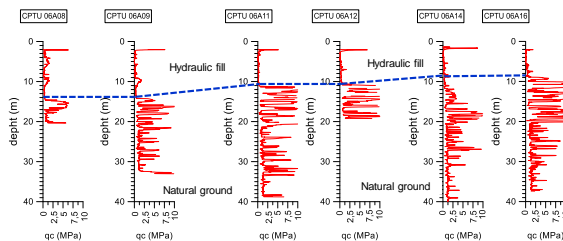
Figure 37. Cone resistance in a non-failed section of Phase 1
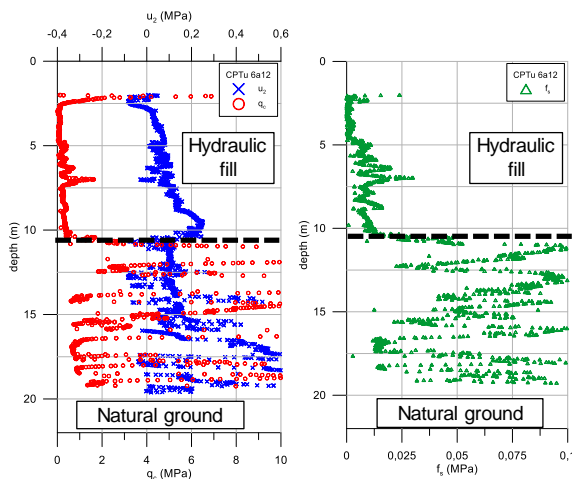
Figure 38. CPTu results of sounding 6a12
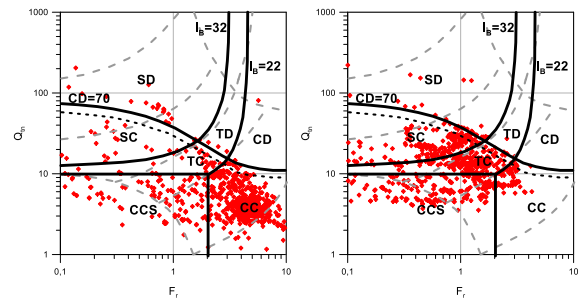
Figure 39. Location of the observations in two CPTu tests in Robertson (2016) SBT charts: a) CPTu 6a12 (Phase 1); b) CPTu 3b11 (Phase 2)

6.2 Analysis of failure

Ideally, a proper understanding of the failure and failure mechanism, including flow liquefaction, should be demonstrated by the performance of an analysis (Shuttle 2016) that, while incorporating the basic features of the case and of the behaviour of the materials involved, it proves capable of reproducing field observations and the failure characteristics in an adequate manner. In this particular case, a plane-strain numerical analysis has been performed simulating the history of construction up to the moment of failure. The behaviour of the hydraulic fill has been modelled using the CASM constitutive law in the manner described in section 4. Figure 40 shows the computed construction settlements compared with the observed settlements of all Phase 1 caissons. The agreement is quite satisfactory. Full details of the numerical analysis performed are provided in Tarragó (2019).

The triggering of the failure was simulated by assuming that a limited area of the backfill in the area of the South embankment and close to the surface liquefied. In that case, on reaching a backfill elevation of +3.0 m, the numerical analyses predicted failure with the mechanism shown in Figure 41, i.e. the caisson sliding on the rubble mound due to the backfill pressure. The development of failure after the initial liquefaction is clearly illustrated in Figure 42. It can be observed how the displacements associated with failure spread from the initial

liquefaction region until producing the complete failure of the caisson wall.
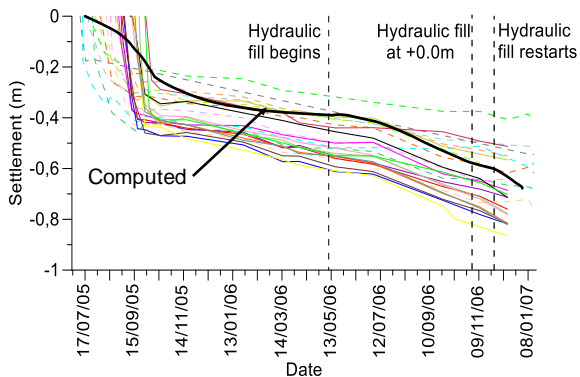
Figure 40. Caisson settlements before failure. Computed results vs. observations
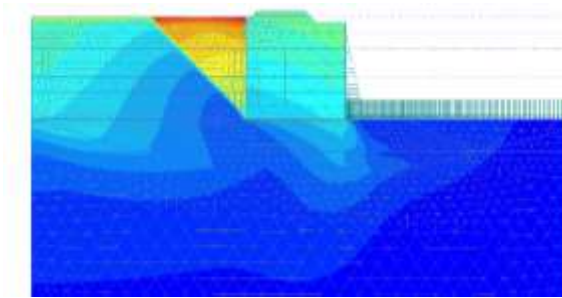
Figure 41. Computed failure mechanism

The subsequent development of caisson movements cannot be modelled with a conventional finite element analysis, a 3D PFEM analysis was performed (Celigueta et al. 2007). Because of the much larger complexity of the model (Figure 43), a simplified constitutive model had to be used where the strength drop was instantaneous coupled to an established rate of liquefaction propagation. Several hypothesis of liquefaction initiation were tried. The only analysis that resulted in caisson displacements similar to those observed in the field was the case in which liquefaction was initiated close to the tip of the South embankment followed by a second liquefaction episode close to the East embankment (Figure 44). The final computed

position of the caissons are shown in Figure 45. Figure 46 shows the development of the computed displacements of the caissons during the analysis. It can be seen that the final situation is achieved after 41 seconds. The observed displacements are also plotted for reference.

a) b)

c) d)

e) f)
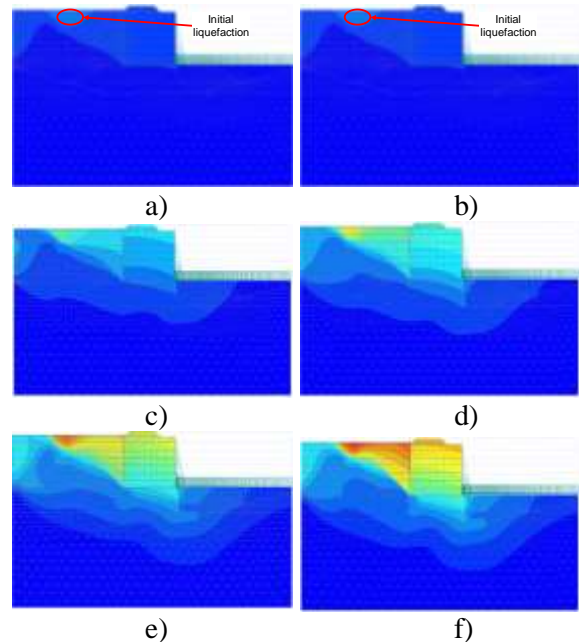
Figure 42. Succession of computed displacements contours during failure
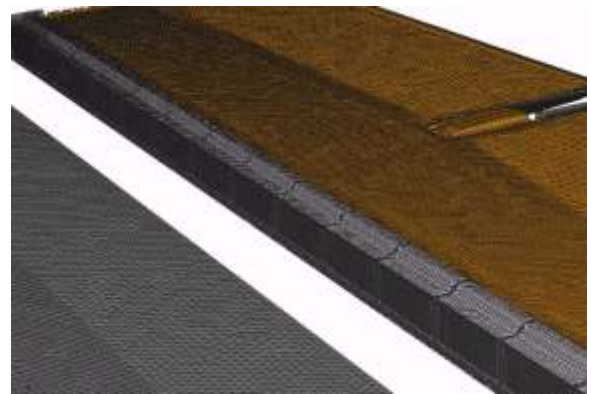
Figure 43. Mesh employed in the 3D PFEM analysis
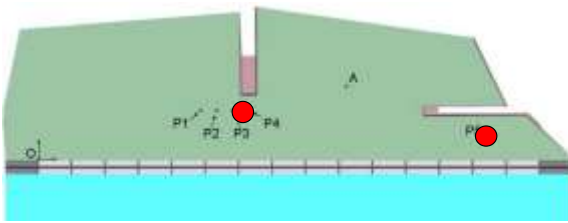
Figure 44. Assumed locations of succesive liquefaction initiation
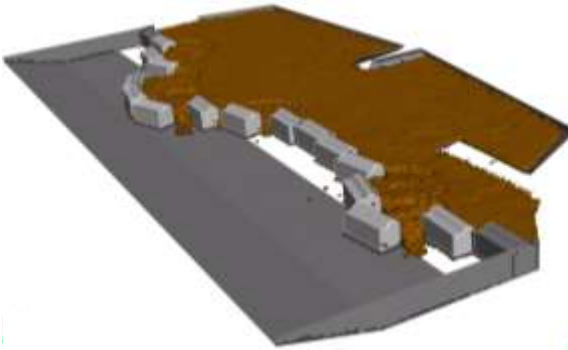
Figure 45. Computed caisson locations at the end of failure from the PFEM analysis
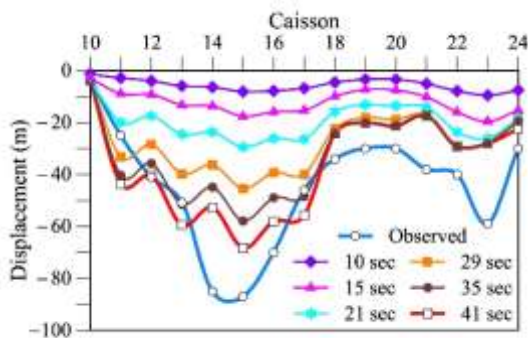
Figure 46. Evolution of computed caisson displacements with time. Observed caisson displacements are added for reference

The post-failure analysis appears to confirm that the initial liquefaction of the backfill was triggered by the failure of the south embankment. It also suggests that, when liquefaction reached the zone of the East embankment, an additional failure provided a new liquefaction focus. It should be noted however, that the analyses performed are necessarily quite simplified. Nevertheless, they appear capable of reproducing the basic traits of the post-failure phenomena.

In contrast to many previous cases, liquefaction of the hydraulic fill was not triggered in this instance by a conventional sliding failure underlying the site or by a pore pressure increase. On this occasion, it was the fill liquefaction that initiated the horizontal sliding of the caissons. Subsequently, the propagation of liquefaction and the associated loss of strength of a large amount of fill provided the unbalanced thrust force required to transport the large and heavy caissons considerable distances.

7 SUMMARY AND CONCLUDING REMARKS

Hydraulic fills are often deposited in a loose state making them susceptible to flow liquefaction, a phenomenon that has led to a number of catastrophic failures. Although some details are still uncertain, there is now a reasonable understanding of the fundamental mechanism of flow liquefaction grounded in a framework that incorporates the concepts of critical state and state parameter. Soils undergoing flow liquefaction exhibit undrained softening and therefore brittle behaviour. The conceptual framework allows distinguishing the very different character of peak strength and critical or steady state. New theoretical concepts such as that of controllability lead to a more rigorous definition of the undrained instability phenomena associated with flow liquefaction. A number of triggering factors exist that may lead to the onset of instability: additional loading, reduction of lateral stresses, increase of pore pressure, cyclic effects. They have all been documented in the literature although it seems that loss of lateral support is one of the most frequent triggering events.

Hydraulic fills and other materials prone to flow liquefaction are difficult to sample; they are usually characterized by means of in situ tests.

The CPTu test is one of the most commonly used ones. The interpretation of the CPTu test is generally of an empirical nature; the question arises, however, whether the information gathered mostly from conventional soils is readily applicable to materials that exhibit undrained softening. Some results of a systematic exploration of this issue by numerical analysis have been presented. The use of advanced numerical formulations are inevitably required to account for large deformations, highly nonlinear constitutive models and softening behaviour. The results demonstrate the large effect of the degree of brittleness on pore pressure response and, especially, on cone resistance.

Two case histories involving flow liquefaction of hydraulically deposited materials have been presented. The first one involved the failure of a tailings dam due to shear sliding of the foundation clay. In this case, liquefaction of the tailings was a consequence of the foundation failure; it was caused by the movement downstream of the dam reducing lateral support. However, analysis has demonstrated that tailings liquefaction was the prime cause of the catastrophic consequences of the failure. The additional thrust provide by liquefaction constituted the main driving force for the large displacements of the dam. In the absence of this additional thrust, a dam breach would not have opened and the catastrophic outcome would have been avoided.

The second case history concerns the failure of a harbour quay. In this case, the hydraulic fill liquefied before failure probably as a consequence of some construction activities on site. The initial liquefaction spread through the backfill causing the failure of the caisson wall without affecting the natural soil in the foundation. The unbalanced force resulting from the strength loss of the backfill was capable of moving the heavy caissons considerable distances, up to 90 m in one case. Analysis has been able to simulate quite satisfactorily the initial quay wall failure and the subsequent post-failure movements of the caissons.

It is evident that most hydraulic fills, like other brittle materials, constitute a serious potential risk on many occasions and that their use require especial caution. Failures due to liquefaction are generally unannounced and often have catastrophic consequences. In addition, there is a large variety of triggering events that can lead to liquefaction; some of them may prove difficult to prevent in practice. Naturally, there is a wide range of remedial measures that can be applied to reduce or eliminate the risk of liquefaction; indeed a number of them have been used in the reconstruction of the Part quay. Remediation measures are, however, outside the scope of this paper.

8 ACKNOWLEDGEMENTS

9 REFERENCES

Alarcon-Guzman, A., Leonards, G.A., Chameau, J.L. 1988. Undrained monotonic and cyclic strength of sands. *Journal of Geotechnical Engineering, ASCE*, **114**, 1089–1110.

Alonso, E.E., Gens, A. 2006a. Aznalcóllar dam failure. Part 1: Field observations and

material properties, *Géotechnique* **56**, 165-183.

Alonso, E. E., Gens, A. 2006b. Aznalcóllar dam failure. Part 3: Dynamics of the motion, *Géotechnique* **56**, 203–210.

Andrade, J.E. 2009. A predictive framework for liquefaction instability, *Géotechnique* **59**, 673–682.

Bažant ZP, Jirásek M. 2002. Nonlocal integral formulations of plasticity and damage: survey of progress. *Journal Engineering Mechanics* **128**, 1119–1149.

Bažant, Z.P., Pijaudier-Cabot, G. 1988. continuum damage, localization instability and convergence. *Journal Applied Mechanics* **55**, 287–93.

Been, K. 2016. Characterizing mine tailings for geotechncial design. *Geotechnical and Geophysical Site Characterization 5* (Eds. Lehane, Acosta-Martínez, Kelly), 41-55. Australian Geomechanics Society, Sydney.

Been, K., Crooks, J.H.A., Becker, D.E, Jefferies M.G. 1986. The cone penetration test in sands: Part 1, State parameter interpretation. *Géotechnique* **36**, 239-249.

Been, K., Jefferies M.G., Crooks J.H.A., Rothenberg, L, 1987. The cone penetration test in sands: Part II, general inference of state. *Géotechnique* **37**, 285-299.

Been, K., Jefferies, M. G. 1985. A state parameter for sands. *Géotechnique* **35**, 99–112.

Been, K., Jefferies, M.G., Hachey, J. 1991. The critical state of sands, *Géotechnique* **41**, 365–381.

Bishop, A. W. 1973. The stability of tips and spoil heaps, *Quaterly Journal of Engineering Geology* **6**, 335–376.

Bishop A.W., Hutchinson, J.N., Perman, A.D.M., Evans, H.E. 1868. *Geotechnical Investigation into the Causes and Circumstances of the Disaster of 21st October , 1966*. A Selection of Technical Papers submitted to the Aberfan Tribunal, 1-80. Welsh Office, H.M.S.O., London.

Borja, R.I. 2006. Condition for liquefaction instability in fluid saturated granular soils, *Acta Geotechnica* **1**, 211–224.

Buscarnera, G., Dattola, G., and di Prisco, C. 2011. Controllability, uniqueness and existence of the incremental response: a mathematical criterion for elastoplastic constitutive laws. *International Journal of Solids and Structures* **48**, 1867–1878

Buscarnera, G., Whittle, A.J. 2013. Constitutive modelling approach for evaluating the triggering of flow slides, *Canadian Geotechnical Journal* **49**, 499–511.

Carrera, A., Coop, M.R., Lancellotta, R. 2011. The influence of grading on the mechanical behaviour of Stava tailings. *Géotechnique* **61**, 935–946.

Casagrande, A. 1936. Characteristics of cohesionless soils affecting the stability of earth fills. *J. Boston Society of Civil Engineers* **23**, 257–276.

Casagrande, A. 1965. Second Terzaghi lecture: role of the "calculated risk" in earthwork and foundation engineering. *Journal of the Soil Mechanics and Foundations Division*, *ASCE* **91**, 1-40.

Casagrande, A. (1975) Liquefaction and cyclic deformation of sands: A critical review. *Proceedings of the Fifth Pan-American Conference on Soil Mechanics and Foundation Engineering* **5**, 79-133. Buenos Aires, Argentina,

Castro, G. 1969. *Liquefaction of sands*. Harvard Soil Mechanics Series, No. 81. Cambridge, MA: Harvard University.

Castro, G., Keller, T.O., Boynton, S.S. 1989. *Re-evaluaiton of the Lower San Fernando Dam. An investigation of the February 9, 1971 slide*. Contract Report GL-89-2. US Army Corps of Engineers, Washington DC..

Ceccato, F., Beuth, L., Vermeer, P.A., Simonini, P. 2016. Two-phase Material Point Method applied to the study of cone penetration. *Computers and Geotechnics* **80**, 440-452.

Ceccato, F., Simonini, P. 2017. Numerical study of partially drained penetration and pore

pressure dissipation in piezocone test. *Acta Geotechnica* **12**, 195-209.

Celigueta, M.A., Oñate, E., Suárez, B. 2007. *Trabajos realizados por CIMNE en relación con la rotura del muelle del Prat del puerto de Barcelona (in Spanish)*. Informe Técnico, CIMNE IT-514. CIMNE, Barcelona.

Chandler R.J., Tosatti, G. 1985. The Stava tailings dams failure, Italy, Proceedings of the *Institution of Civil Engineers-Geotechnical Engineering* **113**, 67-79.

Ciantia, M.O., Arroyo, M., O'Sullivan, C., Gens, A., Liu T. 2019. Grading evolution and critical state in a discrete numerical model of Fontainebleau sand. *Géotechnique* **69**, 1-15.

Coop, M. 2015. Limitations of a Critical State Framework Applied to the Behaviour of Natural and "Transitional" Soils. *Advances in Soil Mechanics and Geotechnical Engineering* (Eds. Rinaldi, V.A., Zeballos, M.E., Claria, J.J.), 115-155. IOS Press, Amsterdam.

Darve, F., 1994. Liquefaction phenomenon: modelling, stability and uniqueness. *Verification of Numerical Procedures for the Analysis of Soil Liquefaction Problems.* (Eds: Arulanandan, K., Scott, R.F.), 1305–1319. Balkema, Rotterdam.

Davies, M., McRoberts, E., Martin, T. 2002. Static liquefaction of tailings – Fundamentals and case histories. *Tailings Dams 2002*. ASDSO/USCOLD, Las Vehgas, Nevada.

De Borst, R., Sluys, L.J., Mühlhaus, H.-B., Pamin, J. 1993. Fundamental issues in finite element analyses of localization of deformation. *Engineering Computations* **10**, 9–121

di Prisco, C., Matiotti, R., Nova, R. 1995. Theoretical investigation of the undrained stability of shallow submerged slopes. *Géotechnique* **45**, 479–496.

Fourie, A.B., Blight, G.E., Papageorgiou, G. 2001. Static liquefaction as a possible explanation for the Merriespruit tailings dam failure. *Canadian Geotechnical Journal* **38**, 707–719.

Fourie, A.B., Papageorgiou, G. 2001. Defining an appropriate steady state line for Merriespruit gold tailings. *Canadian Geotechnical Journal 38*, 695–706.

Fourie, A.B., Tshabalala, L. 2005. Initiation of static liquefaction and the role of K0 consolidation. *Canadian Geotechnical Journal* **42**, 892–906

Gajo, A., Muir Wood, D. (1999) Severn-Trent sand, a kinematic hardening constitutive model: The q-p formulation. *Géotechnique* **49**, 595- 614.

Galavi, V., Schweiger, H.F. 2010. Nonlocal multilaminate model for strain softening analysis. *Int. Journal of Geomechanics* **10**, 30–44

Gens, A. 1982. *Stress–strain and strength of a low plasticity clay*. Ph.D. Thesis. Imperial College, London.

Gens, A., Alonso, E. E., 2006. Aznalcóllar dam failure. Part 2: Stability conditions and failure mechanism, *Géotechnique* **56**, 185–201.

Gens, A., Arroyo, M., Butlanska, J., Carbonell, J.M Ciantia, M., Monforte, L., O'Sullivan, C. 2016. Simulation of the cone penetration test: discrete and continuum approaches, *Australian Geomechanics* **51**, 169-182.

González, N.A. 2011. *Development of a family of constitutive models for geotechnical applications.* Ph.D. Thesis. Universitat Politècnica de Catalunya, Barcelona.

Hight, D.W. 2002. Personal communication.

Hight, D.W., Georgiannou, V.N., Martin, P.L., Mundegar, A.K. 1999. Flow slides in micaceous sands. In *Proceedings of the International Symposium on Problematic Soils*, (Eds. Yanagisawa, E., Moroto, N. & Mitachi, T.), 945–958. Balkema, Rotterdam.

Hird, C.C., Hassona, F. 1990. Some factors affecting the liquefaction and flow of saturated sands in laboratory tests. *Engineering Geology* **28**, 149-170.

Imam, S.M.R., Morgenstern, N.R., Robertson, P.K., Chan D.H. 2005. A critical-state constitutive model for liquefiable sand.

Canadian Geotechnical Journal **42**, 830-855.

Imposimato, S., Nova, R. 1998. An investigation on the uniqueness of the incremental response of elastoplastic models for virgin sand, *Mechanics of Cohesive-Frictional Materials* **3**, 65–87.

Ishihara, K. 1993. Liquefaction and flow failure during earthquakes, *Géotechnique* **43**, 351–451.

Jefferies, M.G. 1993. Nor-Sand: a simple critical state model for sand, *Geotechnique* **43**, 91–103.

Jefferies, M.G., and Been, K. 2006. *Soil liquefaction: a critical state approach*. Taylor and Francis, New York.

Jefferies, M.G., and Been, K. 2016. *Soil liquefaction: a critical state approach (2nd edition)*. Taylor and Francis, Boca Raton.

Konrad, J.-M. 1993. Undrained response of loosely compacted sands during monotonic and cyclic compression tests. *Géotechnique* **43**, 69–89.

Kuerbis, R.H., Vaid, Y.P. 1988. Sand sample preparation - The slurry deposition method. *Soils and Foundations* **28**, 107-118.

Lade, P.V. 1993. Initiation of static instability in the submarine Nerlerk berm. *Canadian Geotechnical Journal* **30**, 895–904.

Lade, P.V., Yamamuro, J.A. 1997. Effects of nonplastic fines on static liquefaction of sands. *Canadian Geotechnical Journal* **34**, 918-928.

Li, W., Coop, M.R., Senetakisc, K.,. Schnaid, F. 2018. The mechanics of a silt-sized gold tailing. *Engineering Geology* **241**, 97-108.

Lu, Q., Randolph, M.F., Hu, Y., Bugarski, I.C. 2004. A numerical study of cone penetration in clay, *Géotechnique* **54**, 257–67.

Manica, M., Gens, A., Vaunat, J., Ruiz, D.F. 2018. Nonlocal plasticity modelling of strain localisation in stiff clays. *Computers and Geotechnics* **103**, 138–150.

Manzari, M.T., Dafalias, Y.F. 1997. A critical state two-surface plasticity model for sands. *Géoteclmique* **47**, 255-272.

Martin, T.E., McRoberts E.C. 1998. Some considerations in the stability analysis of upstream tailings dams 287-302. *Tailings and Mine Waste '99*, Fort Collins, Colorado,

Monforte, L., Arroyo, M., Carbonell, J.M., Gens, A. 2018. Coupled effective stress analysis of insertion problems in geotechnics with the Particle Finite Element Method, *Computers and Geotechnics* **101**, 114–129.

Monforte, L., Arroyo, M., Carbonell, J.M., Gens, A. 2017a. Numerical simulation of undrained insertion problems in geotechnical engineering with the particle finite element method (PFEM), *Computers and Geotechnics* **82**, 44–156

Monforte, L., Carbonell, J.M., Arroyo, M., Gens, A. 2017b. Performance of mixed formulations for the particle finite element method in soil mechanics problems, *Computational Particle Mechanics* **4**, 269-284.

Morgenstern, N.R., Vick, S.G., Viotti, C.B., Watts, B.D. 2016. *Report on the Immediate Causes of the Failure of the Fundão Dam*. Fundão Tailings Dam Review Panel

Muir Wood, D. 2007. The magic of sands – the 20th Bjerrum Lecture presented in Oslo, 25 November 2005. *Canadian Geotechnical Journal 44*, 1329–1350.

Nazem, M., Sheng, D., Carter, J.P. 2006. Stress integration and mesh refinement for large deformation in geomechanics, *Int J Numer Meth Eng* **65**, 1002–1027.

Nazem, M., Carter, J.P., Airey, D.W., Chow, S.H. 2012. Dynamic analysis of a smooth penetrometer free-falling into uniform clay, *Géotechnique* **62**, 893–905.

Nicot, F., Darve, F., Khoa, H.D.V., 2007. Bifurcation and second-order work in geomaterials. *International Journal for Numerical and Analytical Methods in Geomechanics* **31**, 1007–1032.

Nova, R. 1989. Liquefaction, stability, bifurcations of soil via strainhardening plasticity. In *Numerical Methods for Localisations and Bifurcations of Granular*

Bodies, Proceedings of an International Workshop.(Eds. Dembicki, E., Gudehus, G. & Sikora Z.), 117–132. Technical University of Gdansk, Gdansk

Nova, R. 1994. Controllability of the incremental response of soil specimens subjected to arbitrary loading programmes, *Journal of the Mechanical Behavior of Materials* **5**, 193–202.

Olson, S. M., and Stark, T. D. 2002. Liquefied strength ratio from liquefaction flow failure case histories. *Canadian Geotechnical Journal* **39**, 629–647.

Olson, S.M., Stark, T.D., Walton, W.H., and Castro, G. 2000. 1907 Static liquefaction flow failure of the North Dike of Wachusett Dam. *Journal of Geotechnical and Geoenvironmental Engineering*, *ASCE* **126**, 1184-1193.

Onate, E., Idelsohn, S.R., Del Pin, F., Aubry, R. 2004. The particle finite element method: an overview, *Int J. Comput Meth*. **1**, 267–307.

Pestana, J.M., Whittle, A.J. 1999. Formulation of a unified constitutive model for clays and sands, *International Journal for Numerical and Analytical Methods in Geomechanics* **23**, 1215–1243.

Pestana, J.M., Whittle, A.J., Salvati, L. 2002. Evaluation of a constitutive model for clays and sands: Part I Sand behavior, *International Journal for Numerical and Analytical Methods in Geomechanics* **26**, 1097–1121.

Poulos, S.J. 1981. The steady state of deformation, *Journal of the Geotechnical Engineering Division, ASCE 107*, 553–562.

Poulos, S.J., Castro, G., France, J. 1985. Liquefaction evaluation procedure, *Journal of the Geotechnical Engineering Division, ASCE* **111**, 772–792.

Pucker., T., Bienen, B., Henke, S. 2013. CPT based prediction of foundation penetration in siliceous sand, *Appl Ocean Res*. **41**, 9–18.

Reid, D. 2015. Estimating slope of critical state line from cone penetration test – an update. *Canadian Geotechnical Journal* **52**, 46 - 57

Robertson, P.K., 1990. Soil classification using the cone penetration test. *Canadian Geotechnical Journal* **27**, 151-158.

Robertson, P.K. 2009. Interpretation of cone penetration tests a unified approach. *Canadian Geotechnical Journal* **46**, 1337-1355

Robertson, P.K. 2010a. Evaluation of flow liquefaction and liquefied strength using the cone penetration test. *Journal of Geotechnical and Geoenvironmental Engineering, ASCE* **136**, 842-853.

Robertson, P.K. 2010b. Estimating in-situ state parameter and friction angle in sandy soils from the CPT. *2nd International Symposium on Cone Penetration Testing*, Paper No. 2-43. CD-Rom.

Robertson, P.K. 2012. In situ soil testing: from mechanics to interpretation. 5th J.K. Mitchell Lecture. *Geotechnical and Geophysical Site Characterization 4* (Eds. Coutinho, Mayne), 3-24. Taylor & Francis Group, London

Robertson, P.K. 2016. Cone penetration test (CPT)-based soil behaviour type (SBT) classification system - an update. *Canadian Geotechnical Journal* **53**, 1910-1927.

Santamarina J.C., Torres-Cruz, L.A., Bachus, R.C. 2019. Why coal ash and tailings dam disasters occur. Knowledge gaps and management shortcomings contribute to catastrophic dam failures. *Science*, **364**, 526-528.

Schnaid, F., Yu, H. S. 2007. Theoretical interpretation of the seismic cone test in granular soils. *Géotechnique*, **57**, 265–272.

Schofield, A. N., Wroth, C. P. 1968. *Critical state soil mechanics,* McGraw-Hill, London.

Seed, H.B., Lee, K.L., Idriss, I.M., Makdisi, F.I. 1975. The slides in the San Fernado Dams during the earthquake of February 9, 1971. *Journal of the Geotechnical Engineering Division, ASCE* **101**, 651-688.

Shuttle, D.A., Cunning, J. 2007. Liquefaction Potential of Silts from CPTu. *Canadian Geotechnical Journal* **44**, 1-19.

Shuttle, D.A., Jefferies, M.G. 1998. Dimensionless and unbiased CPT interpretation in sand. *International Journalof Numerical and Analytical Methods in Geomechanics* **22**, 351-391.

Shuttle, D.A. 2016. Chapter 8 in *Jefferies, M.G., and Been, K. Soil liquefaction: a critical state approach (2nd edition)*. Taylor and Francis, Boca Raton.

Sladen, J.A., D'Hollander, R.D., Krahn, J. 1985a. The liquefaction of sands, a collapse surface approach, *Canadian Geotechnical Journal* **22**, 564–578.

Sladen, J.A., D'Hollander, R.D., Krahn, J., Mitchell, D.E. 1985b. Back analysis of the Nerlerk berm Liquefaction slides, *Canadian Geotechnical Journal* **22**, 579–588.

Solowski, W. T., Sloan, S. W. 2015. Evaluation of material point method for use in geotechnics. *International Journal for Numerical and Analytical Methods in Geomechanics* **39**, 685-701.

Symes, M.J., Gens, A. Hight, D.W. 1984. Undrained anisotropy and principal stress rotation in saturated sand. *Géotechnique*. **34**, 11-27.

Tarragó, D. 2019. *Hydraulic fills liquefaction. Effect on quay stability*. Ph.D. Thesis. Universitat Politècnica de Catalunya, Barcelona.

Taylor, D.W. 1948. *Fundamentals of Soil Mechanics*. John Wiley, New York.

Terzaghi, K. 1957. *Varieties of submarine slope failure.* Norwegian Geotechnical Institute, Publication no. 25, 1–16.

Vaid, Y. P., Chern, J. C. 1985. Cyclic and monotonic undrained response of saturated sands. *Advances in the Art of Testing Soils under Cyclic Conditions*, 120–147. American Society of Civil Engineers.

Vaid, Y.P., Chung, E.K.F., Kuerbis, R.H. 1990. Stress path and steady state. *Canadian Geotechnical Journal* **27**, 1–7.

van't Hoff J., van der Kolff, A.N. (eds.) 2012. *Hydraulic fill Manual*. CRC Press Balkema, Leiden, the Netherlands.

Viana da Fonseca, A. 2013. Application of in situ testing in tailing dams, empahsis on liquefaction. *Geotechnical and Geophysical Site Characterization 4* (Eds. Coutinho, Mayne), 181-203. Taylor & Francis Group, London.

Wroth, C.P., Bassett, R.H. 1965. A stress–strain relationship for the shearing behaviour of a sand. *Géotechnique* **15**, 32–56

Walker, J., Yu, H.S. 2006. Adaptive finite element analysis of cone penetration in clay, *Acta Geotechnica* **1**, 43–57.

Wang, D., Bienen, B., Nazem, M., Tian, Y., Zheng, J., Pucker, T., Randolph M.F. 2015 Large deformation finite element analyses in geotechnical engineering. *Computers and Geotechnics*, **65**,104–14.

Yamamuro, J. A., Lade, P. L. 1998. Steady-state concepts and static liquefaction of silty sands. *J. Geotechmical Geoenvironmental Engineering ASCE* **124**, 868–877.

Yang,,]. 2002. Non-uniqueness of flow liquefaction line for loose sand. *Géoteclmique* **52**, 757-760

Yoshimine, M., Robertson, P.K., Wride, C.E. (Fear) 1999. Undrained shear strength of clean sands to trigger flow liquefaction, *Canadian Geotechnical Journal* **36,** 891–906

Yu, H.S. 1998. CASM: A unified state parameter model for clay and sand. *International .Journal for Numerical and Analytical Methods in Geomechanics* **22**, 621-653.

Yu, H.S. 2006. *Plasticity and Geotechnics*. Springer Science, New York.

Zhang, X., Sloan, S.W., Oñate, E. 2018. Dynamic modelling of retrogressive landslides with emphasis on the role of clay sensitivity, *International Journal for Numerical and Analytical Methods in Geomechanics* **42**, 1806-1822.

Zhou, H., Randolph, M.F. 2009. Numerical investigation into cycling of full-flow penetrometers in soft clay, *Géotechnique,* **59**, 801–12.

XVII European Conference
ECSMGE 2019
Reykjavik
on Soil Mechanics
and Geotechnical Engineering

The Mercer Lecture

The series was established in 1992 to provide individuals who have made significant technical contributions to the advancement of geosynthetics the opportunity to present their work at international conferences around the world. They are held in honour of the late Dr Brian Mercer, the inventor of geogrids and a strong advocate for innovation, research and development.

Mercer Lecture:

Stabilization of Roadways using Geosynthetics

Jorge G. Zornberg, Ph.D., P.E., F.ASCE

Professor, The University of Texas at Austin, Austin, TX 78705; zornberg@mail.utexas.edu
Immediate Past-President, International Geosynthetics Society (IGS)

SUMMARY:

Stabilization of pavement system involves placing a geosynthetic at the bottom or within the pavement base course in order to increase its load-carrying capacity. The base mechanical properties are improved because of the lateral restraint induced by the geosynthetic by minimizing deformations of the unbound granular material. There is clear evidence that geosynthetic stabilization has led to an increased design life of pavements for a given base thickness as well as to a decreased base course thickness for a given pavement design life. In addition, geosynthetic stabilization has been observed to result in significantly improved performance for pavements founded on problematic soils (e.g. on expansive clay subgrades).

Significant advances are being made towards identifying and quantifying the parameters that govern the stabilization of paved roads. This lecture provides an overview and discussion of current methodologies used in the design of geosynthetic-stabilized pavement systems. An overview is also presented of experimental, analytical and field monitoring evaluations that have been conducted to assess the geosynthetic stabilization of paved roads. The confined stiffness of the soil-geosynthetic composite under small displacements is identified as a parameter that provides good basis for the design of geosynthetic-stabilized pavements. Proper quantification of the parameters governing the behavior of geosynthetic-stabilized pavements is expected to trigger a significant increase in the adoption of geosynthetic stabilization of paved roads.

Geosynthetics have been used as reinforcement inclusions to improve pavement performance. While there are clear field evidences of the benefit of using geosynthetic reinforcements, the specific conditions or mechanisms that govern the reinforcement of pavements are, at best, unclear and have remained largely unmeasured.

Significant research has been recently conducted with the objectives of: (i) determining the relevant properties of geosynthetics that contribute to the enhanced performance of pavement systems, (ii) developing appropriate analytical, laboratory and field methods capable of quantifying the pavement performance, and

(iii) enabling the prediction of pavement performance as a function of the properties of the various types of geosynthetics.

Geosynthetics have been used in pavement design to address the functions of separation, filtration, lateral drainage, sealing, and reinforcement. Specifically, geosynthetics have been used for separation in pavement projects to minimize intrusion of subgrade soil into the aggregate base or sub-base. Also, geosynthetics have been used to perform a filtration function by restricting the movement of soil particles from the subgrade while allowing water to move to the coarser adjacent base material. In-plane drainage function of a geosynthetic can provide lateral drainage within its plane. In addition, geosynthetics have been used to mitigate the propagation of cracks by sealing the asphalt layer when used in pavement overlays. Finally, geosynthetics have been used in flexible pavements for reinforcement, which is the main focus of this paper. While the reinforcement function has often been accomplished using geogrids, geotextiles have also been used as reinforcement inclusions in transportation applications. The geosynthetic reinforcement is often placed at the interface between the base and sub-base layers or the interface between the sub-base and subgrade layers or within the base course layer of the flexible pavement. This leads to lower stresses over the subgrade than in unreinforced flexible pavements.

The improved performance of the pavement due to geosynthetic reinforcement has been attributed to three mechanisms: (1) lateral restraint, (2) increased bearing capacity, and (3) tensioned membrane effect. The primary mechanism associated with the reinforcement

function for flexible pavements is lateral restraint or confinement. The name of this mechanism may be misleading as lateral restraint develops through interfacial friction between the geosynthetic and the aggregate, thus the mechanism is one of a shear-resisting interface. When an aggregate layer is subjected to traffic loading, the aggregate tends to move laterally unless it is restrained by the subgrade or by geosynthetic reinforcement. Interaction between the base aggregate and the geosynthetic allows transfer of the shearing load from the base layer to a tensile load in the geosynthetic. The tensile stiffness of the geosynthetic limits the lateral strains in the base layer. Furthermore, a geosynthetic layer confines the base course layer thereby increasing its mean stress and leading to an increase in shear strength. Both frictional and interlocking characteristics at the interface between the soil and the geosynthetic contribute to this mechanism. Consequently, the geogrid apertures and base soil particles must be properly sized. A geotextile with good frictional capabilities can also provide tensile resistance to lateral aggregate movement.

The aforementioned mechanisms require different magnitudes of deformation in the pavement system to be mobilized. In the case of unpaved roads, significant rutting depths (in excess of 25 mm) may be tolerable. The increased bearing capacity and tensioned membrane support mechanisms have been considered for paved roads. However, the deformation needed to mobilize these mechanisms generally exceeds the serviceability requirements of flexible pavements. Thus, for the case of flexible pavements, lateral restraint is considered to contribute the most for their improved performance.

The results of field, laboratory and numerical studies have demonstrated the benefits of using geosynthetics to improve the performance of pavements. However, selection criteria for geosynthetics to be used in reinforced pavements are not well established yet. The purpose of this paper was to summarize information generated so far to quantify the improvement of geosynthetics when used as reinforcement inclusions in flexible pavement projects.

A Pullout Stiffness Test (PST) was recently developed at the University of Texas, Austin in order to quantify the soil-geosynthetic interaction in reinforced pavements. The equipment involves a modified large-scale pullout test modified to capture the stiffness of the soil-geosynthetic interface under small displacements. Research conducted using the PST has shown that monotonic pullout tests aimed at characterizing the soil-geosynthetic interaction under low displacements are promising. Although these pullout tests did not replicate the cyclic nature of traffic load conditions, it simulated the interface transfer mechanisms between soil and geosynthetic reinforcements that are expected in the field.

An analytical model was proposed to predict the confined load-strain characteristics of soil-geosynthetic systems under small displacements using the results obtained from the PST. This approach takes into account both the confined stiffness (Jc) and ability of geosynthetic to mobilize shear or interlock (τy), which are two important parameters governing the performance of geosynthetic interfaces. The two parameters can be combined to define a unique coefficient of soil-geosynthetic composite (KSGC) that characterizes the soil-reinforcement interface. This coefficient is computed as:

$$K_{SGC} = 4.\tau_y.J_C$$

(1)

A comprehensive field monitoring program is under way to relate the field performance to laboratory PST results for a number of geosynthetic reinforcements. While ongoing field monitoring is still in progress, good agreement has been obtained so far between the field performance and the properties defined from PST testing. Thus, a new performance-based test method in the form of a pullout stiffness test is promising as a performance-based test to evaluate the soil-geosynthetic confinement.

An overall assessment of the various tests developed so far for geosynthetic-reinforced pavements indicates that unconfined tests are simple, economical and expeditious, although they do not capture the important aspects associated with confinement and the type of soil. Also, unconfined tests have provided only index measures of the actual mechanisms, requiring subsequent correlations with field performance. It should be noted that field studies sometimes led to performance trends that contradicted the trends obtained using properties from unconfined tests. Accordingly, and based on the current body of literature, unconfined tests are considered inadequate for assessment of the performance of geosynthetic-reinforced pavements.

Previous research has led to a reasonably good understanding of the benefits achieved with the use of geosynthetics in pavement design but, for the most part, only from the empirical point of view. That is, while methods have been

developed for designing geosynthetic-reinforced flexible pavements, quantification of the reinforcement mechanisms, identification of properties governing the pavement performance and, ultimately, acceptable design guidelines are yet unavailable.

Efforts are currently under way in the US to develop design models consistent with the AASHTO and mechanistic-empirical (M-E) approaches. The TBR and BCR ratios have been used in the AASHTO approach but are limited because the approaches are specific to the products and test conditions under which these ratios have been calibrated. Thus, M-E methods are considered more generic and, consequently, more promising as framework to incorporate the use of geosynthetics in current pavement design. However, due to the complex nature of flexible pavements, research to identify and quantify the properties governing the performance of reinforced pavements and its incorporation into M-E design is still under way.

The available literature involving field and laboratory test results is conclusive in that the mechanical properties of the geosynthetics used for pavement applications are improved under the confinement provided by the soil. Field test sections showed improved performance in the reinforced sections over the unreinforced sections in terms of reduced surface deflections. Overall, available experimental evidence indicates that the improved performance of geosynthetic-reinforced pavements can be attributed to lateral restraint mechanisms. Attempts have been made to quantify the lateral restraint in terms of the interface shear stiffness property of the soil-geosynthetic system.

A number of confined laboratory tests have been recently developed with the objective of quantifying the interface shear stiffness of the soil-geosynthetic system. Several of these tests have applied cyclic loads to the soil-geosynthetic system in an attempt to simulate the dynamic nature of traffic-induced loading. However, probably due to the fact that measurements are sensitive to small changes in displacements, currently available methods have resulted in significant scatter in test results. This has compromised the repeatability of the approaches and has made it difficult to differentiate the performance among different geosynthetics. Ongoing research focusing on confined testing under low displacements using monotonic loading pullout stiffness test appears promising to quantify relevant mechanisms in pavement reinforcement design.

Overall, it may be concluded that significant advances have been made in the area of geosynthetic reinforcement of pavements. While the state of practice is rapidly improving, further research is still needed to provide a better theoretical basis to the currently available empirical design approaches.

Energy geostructures: a new era for geotechnical engineering practice

Géotstructures énergétique: une nouvelle ère pour la pratique de l'ingénierie géotechnique

L. Laloui
Swiss Federal Institute of Technology in Lausanne (EPFL), Lausanne, Switzerland

M. Sutman
Swiss Federal Institute of Technology in Lausanne (EPFL), Lausanne, Switzerland

ABSTRACT: Energy geostructures provide low carbon, cost-effective and local energy solutions to structures and infrastructures, which opens a new era for the geotechnical engineering practice, by extending the conventional role of geotechnical design to the one of addressing acute energy challenges of our century. The paper initially goes over the idea behind energy geostructures by highlighting its scope and applications to various geostructures for structural support and energy supply of built environments. Aspects of primary importance for maximizing the energy, geotechnical and structural performance of energy geostructures and solutions to address this challenge are presented. Moreover, analytical solutions and design tools, as well as performance-based design of energy geostructures are introduced. The goal of the paper is to uncover the great potential of energy geostructures on the path of less dependency on fossil fuels and to emphasize the new critical role of geotechnical engineers to take full advantage of this technology.

RÉSUMÉ: Les géostructures énergétiques fournissent aux structures et infrastructures des solutions énergétiques faibles en carbone, rentables et locales, et ouvrent une nouvelle ère pour la pratique de l'ingénierie géotechnique en élargissant le rôle conventionnel de la conception des fondations pour relever les défis énergétiques critiques de notre siècle. Le travail traite, d'une part, du principe des géostructures énergétiques en soulignant sa portée et ses applications dans diverses géostructures pour le soutien structurel et l'approvisionnement en énergie de l'environnement construit. Les aspects primordiaux visant à maximiser les performances énergétiques, géotechniques et structurelles des géostructures énergétiques sont alors présentés. D'autre part, des solutions analytiques et des outils de dimensionnement, ainsi que le principe de la conception de géostructures énergétiques sont introduits. L'objectif de cet article est de mettre en évidence le potentiel considérable des géostructures énergétiques sur la voie de l'indépendance des combustibles fossiles, et de souligner le nouveau rôle crucial des ingénieurs géotechniciens pour tirer pleinement parti de cette technologie.

Keywords: energy geostructures; renewable energy; thermo-mechanics; design; application

1 INTRODUCTION

This paper has been compiled on the keynote lecture of the first author at XVII European Conference on Soil Mechanics and Geotechnical Engineering in Reykjavik, Iceland.

Residential sector was responsible for 25.4% of final energy consumption in Europe in 2016, of which space heating and hot water production represented 82.6% in total (Eurostat, 2018). Fossil fuel based and conventional electric equipment still dominates the global building

market, accounting for more than 70% of space heating and 90% for hot water production, which is also responsible for 28% of global energy-related CO_2 emissions in 2017 (IEA, 2019). Moreover, due to global warming, economic growth and urbanization, the use of energy for space cooling more than tripled between 1990 and 2016 (IEA, 2018), which is mainly covered by electricity. Yet, global energy needs are expected to expand by 30% by 2040 as a result of a global economy growth with an annual rate of 3.4%, a projected population increase by 1.6 billion, as well as an inevitable growing urbanization (IEA, 2017).

Several initiatives and policies at national and international levels are being established in the construction sector (ASHRAE, 2008 and European Directive 2010/31/EU, 2010) for the implementation of zero- or nearly zero-energy buildings. As an example, ASHRAE Vision (2008) presents requirements to enable buildings to produce as much energy as they use by 2030. Furthermore, European Directive 2010/31/EU (2010) requires all new public buildings to be nearly zero-energy by 2018 and all new buildings by the end of 2020. Therefore, the development and the diffusion of reliable, economically viable and environmental-friendly technologies to satisfy a noteworthy part of the energy needs of building sector is an important challenge.

Energy geostructures concept is a technology enabling the use of renewable energy sources for efficient space heating and cooling. In this technology, any geostructure in contact with the soil and already required for structural support are equipped with geothermal loops, for heat exchange operations to exploit the near surface geothermal energy. The idea behind the energy geostructures comes from the fact that the temperature of the ground remains the same throughout the year below 6-8 meters. Therefore, with the integration of the geothermal loops and the water-antifreeze mixture circulating within

them, the heat is extracted from the ground to heat the buildings during winter. Similarly, during summer, the extra heat is injected into the ground to cool them. In this system, ground source heat pumps (GSHP) are often required which works intermittently in order to adapt the temperature of the circulating fluid to meet the energy demands from the building side.

The heat energy that can be provided by the energy geostructures depends on various factors, including, but not limited to, the thermal and hydraulic properties, and mean temperature of the ground, geothermal and geotechnical design of the geostructures, and the energy demand from the building side. 40-150 W/m, 20-40 W/m^2 and 20-60 W/m^2 are achievable energy extraction or withdrawal amounts from energy piles, energy walls and energy tunnels, respectively. A recent numerical investigation was performed, considering a five-storey office building, with net heat heated/cooled area of 2400 m^2, bearing on 32 piles with 0.5 m in diameter and 20 m length which were used as energy piles. The results of the analysis show that the energy piles can supply 100% of the heating demands and most of the cooling demands of the office building in Sevilla, Spain. An auxiliary air conditioning system was required only during July and August, to provide the remaining 11% and 6% of the cooling demand (Sutman et al., 2019).

2 ENERGY ASPECT

2.1 Typical energy problem

Operation of energy geostructures to meet the heating and cooling demands from the building side involves heat exchange within the three components of the GSHP system, being the primary circuit, the GSHP and the secondary circuit (Figure 1).
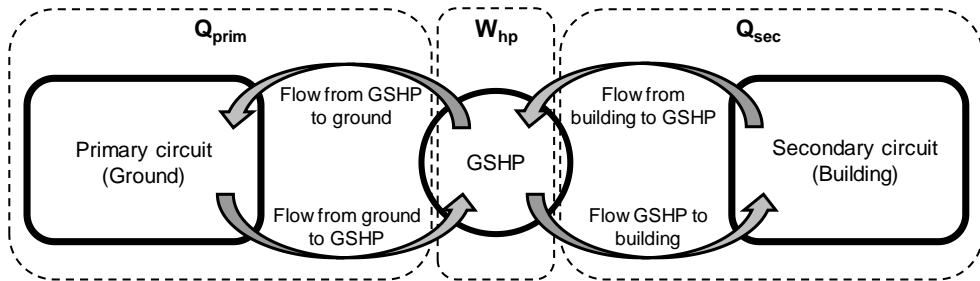
Figure 1. Heat exchange within the three components of ground source heat pump system

In the primary circuit, the heat exchange occurs between the ground and the GSHP, where the heat is extracted from or withdrawn into the ground for heating or cooling the building side, respectively. The heat exchange mechanism that occurs between the ground and the energy geostructure is shown in Figure 2, through the example of an energy pile, for both building heating and cooling purposes.
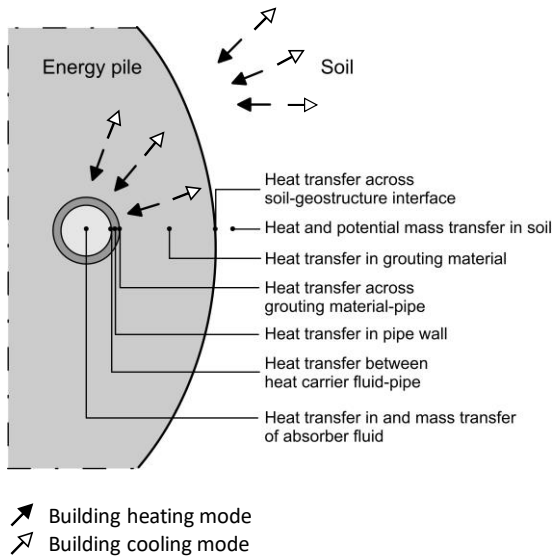
Figure 2. Heat exchange between the energy pile and the ground

Regarding the building cooling mode, shown by the white arrows, the temperature of the circulating fluid returning from the building side is warmer than the ground temperature, which results in a thermal gradient.

The circulating fluid exchanges heat with the ground loop wall through convection, which is followed by a heat conduction through the wall of the ground loop and the pile until reaching the pile-soil interface. Finally, the heat is transferred within the ground mainly by conduction and partially with convection if a moisture migration takes place. Similarly, during the building heating mode, the returning fluid temperature is colder than the ground temperature and the heat exchange occurs in the reverse direction, as shown by the black arrows. Assuming pure thermal conductivity within the energy pile and the ground, the energy conservation equation reads:

$$\rho c \frac{\partial T}{\partial t} - \text{div}(\lambda \mathbf{grad}\text{T}) = 0 \qquad (1)$$

where ρ (kg/m^3) is the density, c (J/(kg·K)) and λ (W/(m·K)) are the specific heat capacity and thermal conductivity, respectively, including both fluid and solid components, T (K) is the temperature, and div and **grad** are the divergence and gradient operators, respectively. The energy conservation equation for the incompressible circulating fluid within the loops can be written as:

$$\rho_f A_p c_f \frac{\partial T_f}{\partial t} + \rho_f A_p c_f \boldsymbol{u_{f,i}} \cdot \mathbf{grad}T_f = \text{div}(A_p \lambda_f \mathbf{grad}\text{T}_f) + \frac{1}{2} f_D \frac{\rho_f A_p}{d_h} |\boldsymbol{u}|^3 + q'_w \qquad (2)$$

where ρ_f (kg/m^3), c_f (J/(kg·K)), and λ_f (W/(m·K)) are the density, specific heat capacity, and thermal conductivity of the fluid,

respectively; A_p (m^2) and d_h (m) are the cross-sectional area and hydraulic diameter of the pipe, respectively; T_f (K) is the temperature of the fluid; $u_{f,i}$ (m/s) is the velocity vector; and f_D (-) is the Darcy friction factor.

In the secondary circuit, the heat is transfer to or from the building side for heating or cooling purposes, respectively. In between the two circuits, there exists the GSHP to transfer the heat between the two circuits. The efficiency of the GSHP is quantified by the coefficient of performance (COP) through examining the amount of energy input to operate the GSHP (W_{hp}) and the energy that can be supplied to the building side (Q_{sec}), as shown below:

$$COP = \frac{Q_{sec}}{W_{hp}} \qquad (3)$$

2.2 State of the art on the application of energy geostructures

Figure 3 presents the state of the art on energy piles, based on the integration of the information from 157 energy pile projects.
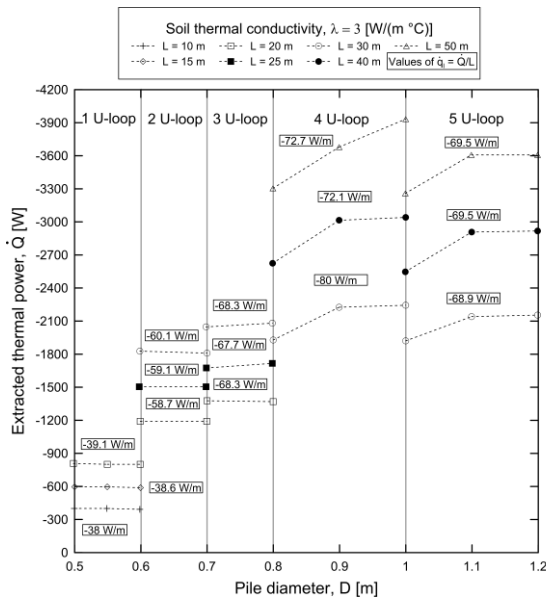
Figure 3. State of the art on application of operational energy piles (Laloui and Rotta Loria, 2019)

The data is the outcome of a comprehensive investigation to reveal the actual energy performance of energy geostructures from (i) a survey targeting international construction companies involved in energy geostructures, (ii) available literature on operational energy geostructures and (iii) complementary results by Di Donna et al. (2017). Figure 4.a and Figure 4.b show the state of the art for energy walls (from 17 projects) and energy tunnels (from 11 projects), respectively.
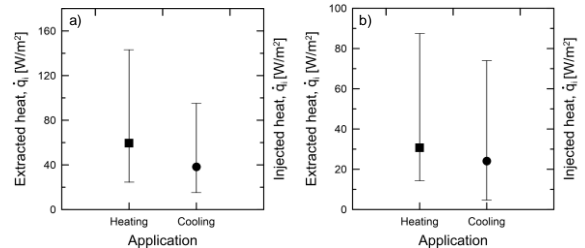
Figure 4. State of the art on application of a) energy walls and b) energy tunnels (Laloui and Rotta Loria, 2019)

3 GEOTECHNICAL ASPECT

As shown in the previous section, energy geostructures concept, a technology capable of exploiting geothermal sources for both space heating and cooling, is undoubtedly an outstanding candidate to cut down the governance of unsustainable resources. Yet, the use of conventional geostructures for heat exchange purposes is associated with temperature changes, hence thermal loads and displacements, along the geostructures and within the surrounding soil, which needs to be taken into consideration in addition to the typical geotechnical design.

In order to understand the extent of temperature change effects on energy geostructures, several in-situ tests were performed on single (Laloui et al., 2006; Bourne-Webb et al., 2009; You et al., 2016; Loveridge et al., 2016; McCartney and Murphy, 2017; Sutman et al., 2017; Sutman et al., 2019) and group of

energy piles (Mimouni et al., 2015; Rotta Loria et al., 2016), energy walls (Xia et al., 2012) and energy tunnels (Adam and Markiewicz, 2009; Frodl et al., 2010; Nicholson et al., 2014; Barla et al., 2019). Moreover, several models or tools with varying complexity were developed for the analysis and design of energy piles (Knellwolf et al., 2011; Bourne-Webb et al., 2014; Salciarini et al., 2013; Rotta Loria and Laloui, 2016; Makasis et al., 2018, Sutman et al., 2018), energy walls (Kürten et al., 2015; Sterpi et al., 2017; Sailer et al., 2019) and energy tunnels (Barla and Di Donna, 2018; Bidarmaghz and Narsilio, 2018). The previous research answered the most fundamental questions on the mechanisms governing the thermal and structural behavior of energy geostructures. These efforts opened a new era for the geotechnical engineering practice, by extending the conventional role of geotechnical design to the one of addressing acute energy challenges of our century.

3.1 Full-scale experimental analysis on energy piles

The two pioneering full-scale in-situ tests on energy piles performed at Swiss Federal Institute of Technology in Lausanne (EPFL), investigating (i) the response of a single energy pile to combinations of thermal and mechanical loads and (ii) the response of a group of closely spaced energy piles to thermo-mechanical loads are presented in this section. Compressive stresses and upward shaft resistance mobilization are considered positive, according to the adopted sign convention.

3.1.1 Single energy pile (Laloui et al., 2003)

A pioneering in-situ test was performed at EPFL campus, on a single energy pile, with a diameter of 0.88 m and length of 25.8 m, under a newly constructed 5-storey building. The single energy pile was one of the 97 bored piles constructed under the building. Along the test pile, polyethylene (PE) tubes were installed vertically on the reinforcing structure with a U-shaped

configuration to permit the passage of the heat-carrying fluid. The test pile was instrumented by a considerable amount of sensors to enable the measurement of temperature, strain and toe load variations during the thermal load applications. The soil profile at the site is consisted of alluvial soil at the first 12 m which is followed by a sandy gravelly moraine and bottom moraine until around 25 m. Finally, a molasse layer is found under the moraine. The ground water table at the test site is located at ground surface. Further information on soil and soil-pile interaction, as well as the test pile and instrumentation can be found in Laloui et al., 2003.

A heating and passive cooling cycle was applied to the test pile following the completion of each storey of the building with the purpose of evaluating the influence of structural load on the development of thermally induced axial stresses and displacements. Figure 5.a shows the results of the last test which was performed after the construction had been finalized. The distribution of the mechanical load profile shows the absence of toe resistance which implies that the structural load was entirely carried by the mobilized shaft resistance. The following temperature increase, with a magnitude of 13.4°C, resulted in generation of thermally induced compressive axial loads with a significant mobilization of the toe (2000 kN) and thermally induced axial loads at the pile head (1000 kN).
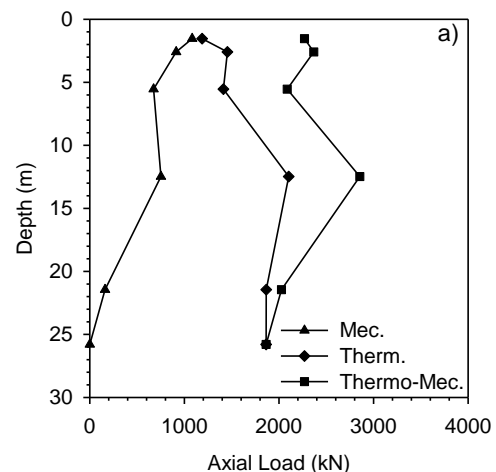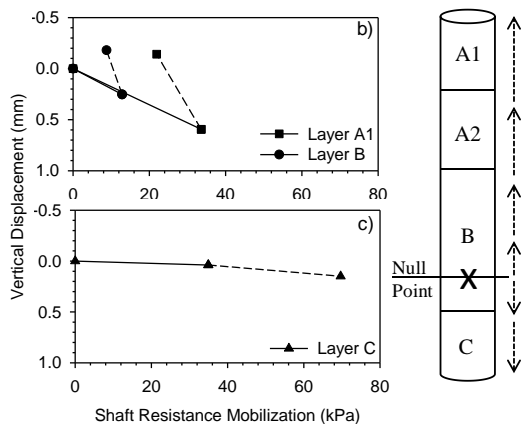
Figure 5. a) Mechanical, thermal and combined thermo-mechanical loads b, c) Shaft resistance mobilization along the test pile

Shaft resistance mobilization due to mechanical and thermal loads along the same test pile is shown in Figure 5.b and Figure 5.c. The mechanical load application resulted in downward displacement of the pile which is associated with positive shaft resistance mobilization. The subsequent temperature increase caused the portion of the pile, above the null point to possess an upward displacement, resulting in a decrease in corresponding shaft resistance (Figure 5.b). On the other hand, the portion below the null point displaced downward, further mobilizing the positive shaft resistance (Figure 5.c).

3.1.2 Group of closely-spaced energy piles (Mimouni and Laloui, 2015; Rotta Loria and Laloui, 2017)

A second field test was implemented at EPFL campus by equipping four out of 20 piles under a water retention tank within Swiss Tech Convention Center to evaluate the thermally induced group effects among closely-spaced energy piles. The test piles were 0.9 m in diameter and 28 meters in length.

Each test pile was equipped with four 24 m long U-loops connected in series of which were installed 4 m below the pile heads. The test piles were instrumented with vibrating wire strain gages at every 2 meters along the length, a pressure cell at the toe and radial optical fibers. Moreover, thermistors and piezometers were installed within boreholes at close proximity of the test piles to monitor the temperature and power water pressure changes during the field test. The field test site is 200 m away from the single energy pile test location, resulting in similar stratigraphic characteristics (Mimouni and Laloui, 2015).

Heating with maximum temperature increase of 20˚C and passive cooling cycles were applied to single (EP1) and group of four energy piles (EPall) (Rotta Loria and Laloui, 2017). Figure 6 shows (i) thermally induced axial strains and stresses along EP1 being the only operating pile among the group of four piles (20EP1) and (ii) average thermally induced axial strains and stresses along the length of all four piles during full geothermal activation of the group (EPall).

The comparison of tests 20EP1 and 20EPall shows that the presence of thermally induced group effects governs the higher development of axial strain when more energy piles operate as geothermal heat exchangers in a closely spaced pile group than when only one energy pile serves this purpose (Figure 6.a). Figure 6.b shows the comparison in terms of thermally induced axial stresses where an opposite behavior was attained corresponding to a decrease in thermally induced axial stresses as the number of thermally active energy piles increases. This phenomenon is associated with the increased deformation of energy piles operating in a group (Figure 6.a) which results in lower thermally induced blocked strains, since the temperature change and hence the free thermal strains are the same for Test 20EP1 and 20EPall, and therefore lower observed axial stresses.
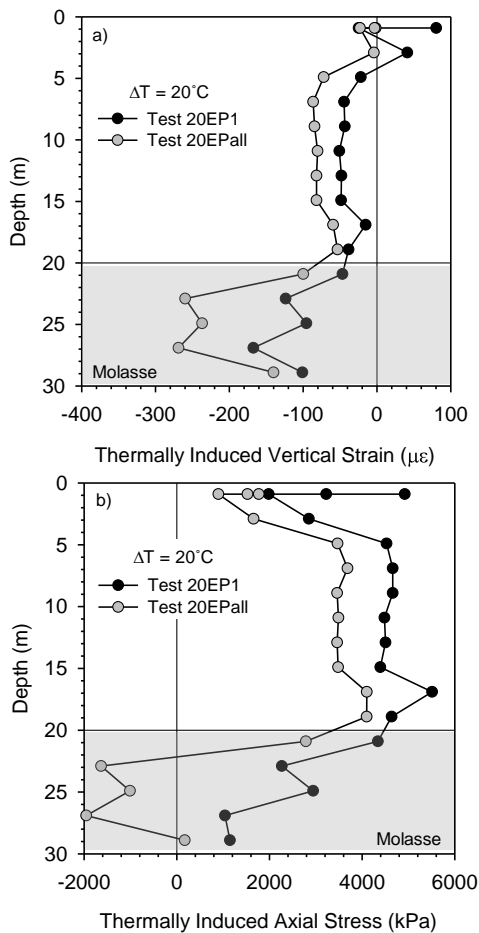
Figure 6. a) Thermally induced axial strains, b) Thermally induced axial stresses

Figure 7. Thermally induced group effects in terms of a) Axial strains and b) Axial Stresses (Redrawn after Rotta Loria, 2019)

Comparison of thermally induced strains and axial stresses per unit temperature change for the geothermal operation of a single energy pile (Test 20EP1) and a group of energy piles (Test 20EPall) is presented in Figure 7.a and Figure 7.b, respectively, which are average values along the active length of the piles. The figures clearly show greater average vertical strains and lower average axial stresses with increasing number of active energy piles. In terms of design aspects, analysis of a single pile in a closely-spaced group will lead to a conservative estimate of vertical stresses that can be employed during the preliminary design stages, which is not the case for the vertical strains.

3.2 Analytical methods for the analysis of energy piles

Full-scale in-situ tests provided the most fundamental information regarding the response of single and group of energy piles to thermo-mechanical actions. Moreover, finite-element methods, majority of which have been validated by the results of the in-situ tests, were developed, which are considered to be the most rigorous approaches for the analysis of energy piles. However, these comprehensive methods require considerable number of geotechnical parameters, as well as high computational efforts, which renders them more suitable for research purposes rather than for practical piling problems. For the design and wider application of energy piles, a reasonable balance between excessive

complexity and unsatisfactory simplicity should be established for which the development of practical analytical models plays undoubtedly the most essential role. Therefore, several simplified analytical methods have been developed to serve preliminary design of single and group of energy piles.

3.2.1 *Load-transfer approach for single and group of energy piles (Knellwolf et al., 2011; Ravera et al.)*

Load-transfer approach, where the soil-pile interaction is represented by springs distributed along the pile shaft and toe by neglecting the continuity of the soil domain, is one of the most common analytical methods employed for the analysis of conventional piles (Seed and Reese, 1957; Coyle and Reese, 1966). In this approach, numerous analytical and empirical methods have been proposed to define the load-transfer curves (Coyle and Suleiman, 1967; Randolph and Wroth, 1978; Frank and Zhao, 1982; Kraft et al, 1981). Later on, considering that most piles are implemented in groups in practice, the load-transfer curves have been modified to consider group effects (Randolph and Clancy, 1993; Comodromos et al., 2016). Given the great potential of load-transfer approach in providing a practical tool for the analysis of axial loaded conventional piles, the approach has been implemented for the analysis of single and group of energy piles.

Load-transfer approach has first been modified for single energy piles by Knellwolf et al. (2011), where the pile is divided into rigid elements that are connected to each other and to the surrounding soil by the springs (Figure 8.a). In order to define the relationships between the mobilized shaft friction/toe resistance and displacement, the method from Frank and Zhao (1982) was utilized, relating the shaft and toe stiffness to Menard pressuremeter modulus.

In this approach the load-transfer curve is divided into three main sections being (i) initial linear part characterizing the elastic response, (ii) second linear part associated with the elastoplastic response and (iii) final plateau referring to perfectly plastic response as represented in Figure 8.b by full lines for single isolated piles. The presence of a slab above energy piles was considered in a simplified way by introducing an additional spring linked to the pile head. The analytical model is validated by the results of both EPFL single pile in-situ test (Laloui et al., 2006) and Lambeth College in-situ test (Bourne-Webb et al., 2009) and has also been implemented in the Thermo-Pile Software developed by Laboratory of Soil Mechanics for the analysis and design of energy piles.

Following the same logical sequence as the one of conventional piles, the load-transfer approach for single energy piles has subsequently been extended to characterize the response of group of energy piles to thermo-mechanical loads in a simplified, yet rational manner (Ravera et al.,). To represent the interaction between a group of energy piles, a displacement ratio (R_d) was introduced adapting the displacement response of a single isolated energy pile to the one of an energy pile in a group.

As in the case of the approach proposed for conventional piles (Comodromos et al., 2016), the displacement ratio depends on the geometric configuration as well as the variations in the displacement field introduced by thermal and mechanical loads. In this approach, the ultimate shaft resistance of an energy pile in a group is considered to be the same as the one of a single isolated energy pile, while the displacement ratio is applied to adapt the displacement necessary to mobilize it. The load-transfer curve attained for a single energy pile in a group is represented by dashed lines in Figure 8.b and is determined as follows:

$$w_{gr} = R_d w_{is} \tag{4}$$
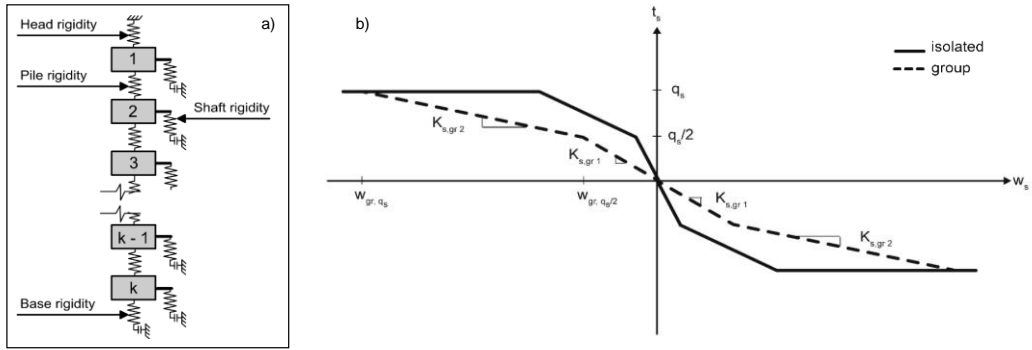
Figure 8. a) Load-transfer relationship for single isolated energy pile and energy pile in a group, b) Modeling approach

$$t_{s,gr} = t_{s,is} \tag{5}$$

where w_{gr} (m) and $t_{s,gr}$ (kPa) are the displacement and shaft resistance of an energy pile in a group, and w_{is} (m) and $t_{s,is}$ (kPa) are the displacement and shaft resistance of a single isolated energy pile, respectively. The load-transfer curve in Figure 8.b is determined using the method proposed by Frank and Zhao (1982), yet, any method developed for single conventional piles can be employed provided that a displacement factor is applied. Finally, since the behavior of a pile in the group highly depends on its location, the displacement ratio may also be corrected by introducing a location weighting factor (Comodromos et al., 2016).

The proposed method has been implemented in Comsol Multiphysics Software and its competence in analyzing the behavior of a group of energy piles has been investigated through the results of the full-scale in-situ test performed at EPFL campus, on a group of four energy piles. The material properties considered in the analysis as well as the development of the load-transfer curves are explained in detail by Ravera et al. Comparison of experimental data from the full-scale in-situ test (Rotta Loria and Laloui, 2017) and the numerical results obtained through the implemented method is presented in Figure 9.a and Figure 9.b, in terms of thermally induced axial stress and mobilized shaft resistance, respectively at 20˚C temperature increase.

The numerical results were attained employing two sets of parameters for the molasses layer in compliance with the ones presented in Knellwolf et al. (2011). The comparison presented in Figure 9 corresponds only to the geothermal activation of the group of energy piles, excluding the stresses generated by the body load and structural loads. The stress variation corresponds to the average value of the mean temperature variations along the uninsulated portions of all four energy piles in the group and the mobilized shaft resistance is determined by employing the stress variations. A good agreement between the experimental and numerical results is observed in the figure, despite the simplifications inherent in the theory.

102
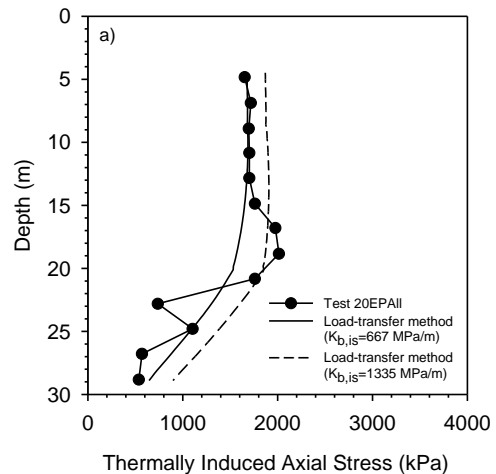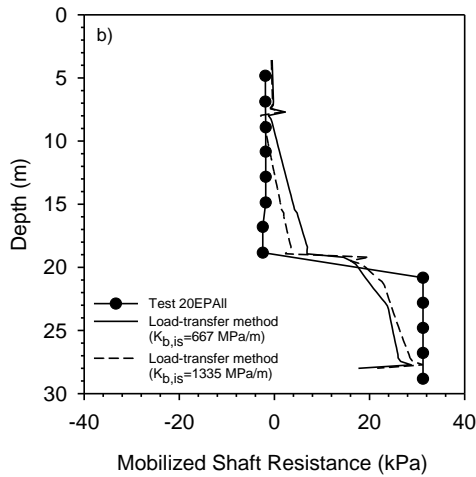
Figure 9. Comparison between experimental data and numerical results for a) Thermally induced axial stresses and b) Mobilized shaft resistance.

It was previously shown in Figure 7 that thermally induced vertical stresses decrease for the same temperature change as the number of geothermally active energy piles increases due to increased vertical strains caused by group interactions. The agreement between experimental and numerical results corroborates the additional value of this method, which allows determination of the thermally induced vertical stress along the depth of an energy pile in a group in a simplified and rational manner.

3.3 Interaction Factor Method for Group of Energy Piles (Rotta Loria and Laloui, 2016; Ravera et al.)

A second analytical method was extended from the interaction factor method in framework of conventional pile groups (Poulos, 1968) to the one of energy pile groups in order to provide a simplified analysis tool for estimating the vertical displacement of energy pile groups subjected to thermal loads (Rotta Loria and Laloui, 2016). The method allows the estimation of the head displacement of any energy pile in a group by employing the interactions between two energy piles and the superimposition of the individual effects of adjacent piles in the group as follows:

$$w_k = w_i \sum_{i=1}^{i=n_{EP}} \Delta T_i \Omega_{ik} \qquad (6)$$

where w_i (m) is the vertical head displacement of a single isolated pile per unit temperature change, ΔT_i (°C) is the applied temperature change to pile i, and Ω_{ik} is the interaction factor for two piles corresponding to the center-to-center distance between pile i and k. Interaction factor charts, characterizing a group of two energy piles and taking into consideration pile slenderness ratio and spacing, pile-soil stiffness ratio, Poisson's ratio and non-uniform moduli of the soil have been developed to determine Ω_{ik} (Rotta Loria and Laloui, 2016).

The formulation above provides solutions regarding the displacement interaction for free standing energy pile groups or energy pile groups with a perfectly flexible slab. However, in practice piles are often rigidly attached to a pile cap which stands on the soil (Poulos, 1968). Therefore, it is essential to consider thermally induced mechanical interactions which are governed by the changes in deformation field, due to the interplay between the energy pile-slab-soil responses. With this purpose, the interaction factor method was further extended to take into account the presence of the pile cap (Ravera et al.). 3D steady state finite element simulations were carried out employing Comsol Multiphysics Software to propose a formulation of the interaction factor for energy pile groups under a slab and to propose design charts for the analysis compatible with the former study. The influence of the rigid pile cap is expressed in terms of pile-cap displacement ratio as follows:

$$R_c = \frac{displacement\ of\ pile\ with\ cap}{displacement\ of\ free\ standing\ pile} \qquad (7)$$

Employing the pile-cap displacement ratio, displacement determined in free standing conditions can be adjusted to consider the contacting slab as follows:

$$w_k = R_c w_i \sum_{i=1}^{i=n_{EP}} \Delta T_i \Omega_{ik} \qquad (8)$$
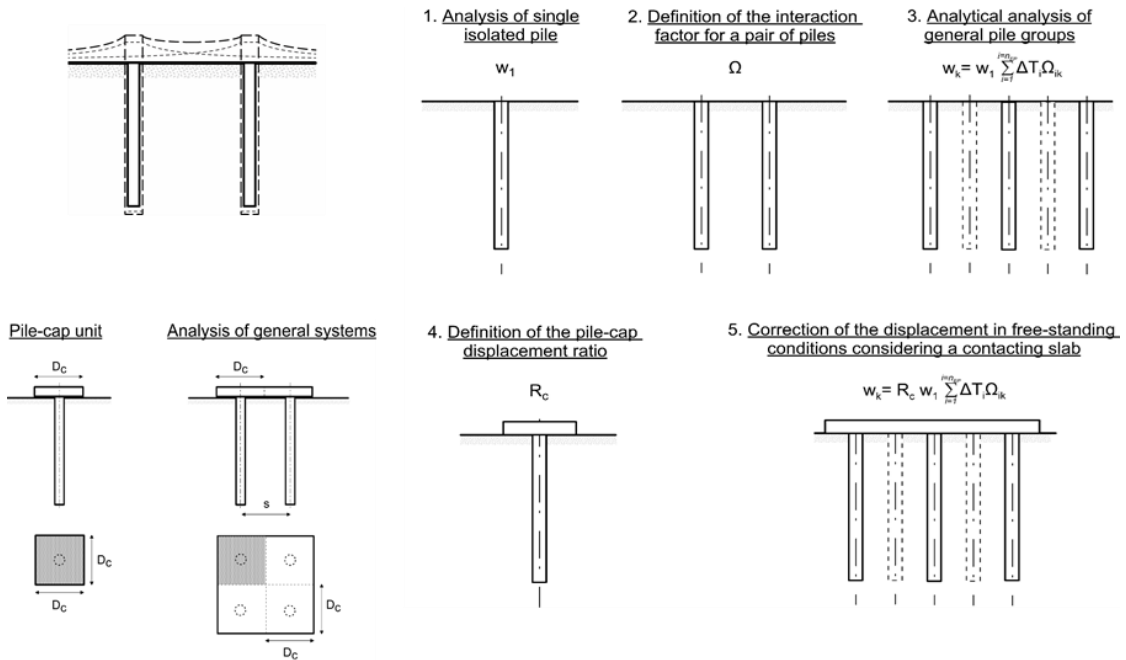
Figure 10. Steps of interaction factor method for the analysis of energy piles with contacting slab
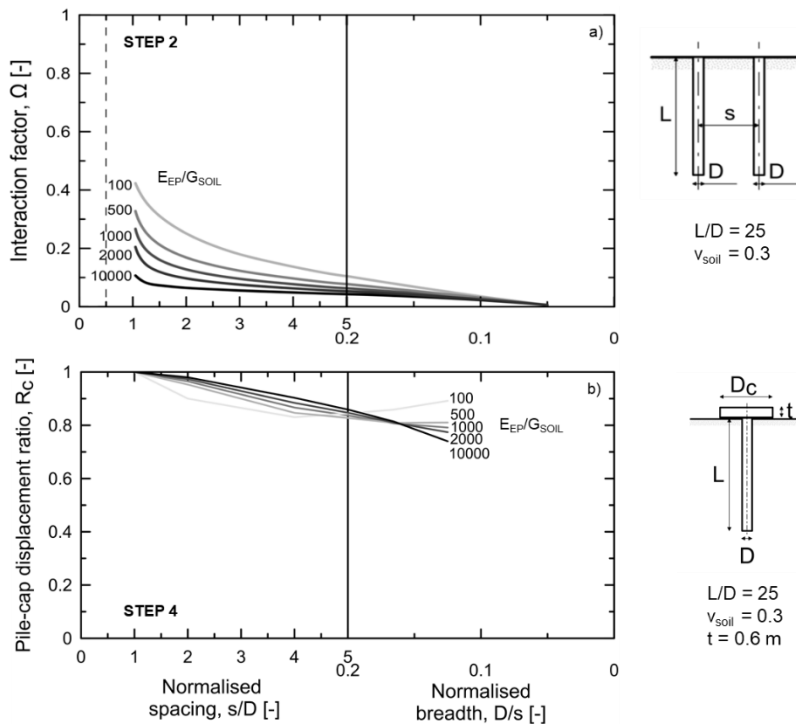
Figure 11. a) Interaction factors, b) Pile-cap displacement ratio for L/D = 25.

The combination of the two methodologies (1) interaction factor method for free standing energy piles and (2) extension of the method to consider the presence of the slab yields the following ultimate methodology illustrated in Figure 10. The first three steps belonging to the original methodology (Rotta Loria and Laloui, 2016) and the following two steps corresponding to the extension of the method (Ravera et al.), are as follows:

Step 1: Displacement of an isolated energy pile is computed by employing any suitable practical or sophisticated method as long as it returns representative displacement values for the considered case.

Step 2: Interaction factor is determined for a pair of two energy piles employing the design charts provided by Rotta Loria and Laloui (2016). A sample design chart regarding an energy pile with a slenderness ratio of twenty-five bearing in a soil with a Poisson's ratio of 0.3 is presented in Figure 11.a, for various soil-pile stiffness and normalized displacement.

Step 3: Vertical head displacement of any pile in the group in free standing conditions is calculated employing Equation (6).

Step 4: Pile-cap displacement ratio is determined referring to the design charts presented by Ravera et al. A sample design chart, compatible with the one presented for Step 2, is shown in Figure 11.b for pile cap thickness of 0.6 m.

Step 5: Displacement determined in Step 3 for free standing conditions is corrected by employing Equation (8).

The rather approximate yet rational methodology presented above enables the estimation of the head displacement of any energy pile group configuration with a slab supported on soil through the displacement of a single isolated energy pile and superimposition of the individual effects of adjacent piles and the slab in the group, providing a practical tool to perform displacement analysis of energy pile groups in the early stages of the design process.

4 DESIGN OF ENERGY PILES

Full-scale in-situ tests performed on energy piles, as well as the numerical and analytical tools developed since more than two decades by our group revealed the most fundamental information finally leading to the recommendations regarding the design of energy piles. According to these findings the design of energy piles at ultimate limit states can be considered as a conventional process by considering that the reactions provided by the soil above and below the null point compensate for each other ensuring equilibrium and provided that the structural elements are characterized by adequate ductility and rotation capacity (Rotta Loria et al.). However, regarding the serviceability limit states, the effects of both mechanical and thermal loads should be examined by taking into consideration the vertical displacement of single and group of energy piles, as well as the deflection.

Regarding the combinations of actions, Rotta Loria et al. recommended $\psi_0 = 0.60$, $\psi_1 = 0.50$ and $\psi_2 = 0.50$ for the combination, frequent and quasi-permanent values of variable actions, respectively. Regarding the consideration of thermal loads during cooling of the building side (i.e. temperature increase along the energy piles), two design combinations must be considered, assuming the effects of the thermal loads make them the dominant load ($\Delta Tk = Q_{k,1}$, where $Q_{k,1}$ is the dominant variable load) or not ($\Delta Tk = Q_{k,i}$, where $Q_{k,i}$ is the ith general variable load), since it is not known originally if the thermal loads are dominant with respect to the mechanical ones. Regarding the heating of the building side (i.e. temperature decrease along the energy piles) a single design combination must be considered ($\Delta Tk = Q_{k,1}$).

Finally, when the influence of thermal loads is analyzed during the design of energy piles, (i) piles free at the head and (ii) piles that are fully restrained should be considered to attain conservative estimations of vertical displacement and stress, respectively.

5 CONCLUSIONS

The fundamental research in the field of energy geostructures, compiled and expanded by our group since more than two decades, revealed that this emerging technology provides low carbon, cost-effective and local energy solutions to structures and infrastructures, which opens a new era for the geotechnical engineering practice.

The research activities performed in this field has exclusively covered various elements related to energy geostructures, including but not limited to energy, geotechnical, structural and design aspects. Related to the energy aspect, it has been revealed that typically, 40-150 W/m heat energy can be extracted from and withdrawn into the ground with the use of energy piles while 20-40 W/m^2 and 20-60 W/m^2 are achievable energy extraction and withdrawal amounts, respectively. Furthermore, two state-of-the-art in-situ tests have been performed on single and group of energy piles, which not only revealed the most fundamental knowledge regarding their thermo-mechanical behavior but have also provided invaluable information for the validation of numerical models and analytical tools developed in the area.

To provide satisfactory tools for the design and wider application of energy piles, several practical analytical tools have been developed for energy piles including load-transfer method for the assessment of axial stress, displacement and mobilized shaft resistance along single and group of energy piles, as well as interaction factor method for the estimation of vertical displacement of energy pile groups with and without a rigid slab. Incremental research efforts performed in the area, from both experimental and analytical points of view, have eventually led to development of recommendations for the design of energy piles for both ultimate and serviceability limit states. Overall, research outcomes, achieved in more than two decades revealed that energy geostructures concept is a mature and ready-to-be-employed technology.

The questions remained to be answered now are no longer on how an energy geostructure responds to thermal actions but rather on how the energy performance, as well as geotechnical and structural adaptations should be assessed to maximize its cost efficiency.

6 ACKNOWLEDGEMENTS

7 REFERENCES

Adam, D., Markiewicz, R. 2009. Energy from earth-coupled structures, foundations, tunnels and sewers. *Géotechnique* **59**(3): 229-236.

ASHRAE. 2008. ASHRAE Vision 2020. https://www.isiaq.org/docs/sponsor%20material/ASHRAE%20Strategic%20Plan%20Jun08.pdf. Last accessed May 2019.

Barla, M., Di Donna, A. 2018. Energy tunnels: concept and design aspects. *Underground Space* **3**(4): 268-276.

Barla, M., Di Donna, A., Insana, A. 2019. A novel real-scale experimental prototype of energy tunnel. *Tunnelling and Underground Space Technology* **87**, 1-14.

Bidarmaghz, A., Narsilio, G. A. 2018. Heat exchange mechanisms in energy tunnel systems. *Geomechanics for Energy and the Environment* **16**, 83-95.

Bourne-Webb, P. J., Amatya, B., Soga, K., Amis, T., Davidson, C., Payne, P. 2009. Energy pile test at Lambeth College, London: geotechnical and thermodynamic aspects of pile response to heat cycles. *Géotechnique* **59**(3): 237-248.

Bourne-Webb, P., Pereira, J. M., Bowers, G. A., Mimouni, T., Loveridge, F. A., Burlon, S., Olgun, C., McCartney, M., Sutman, M. 2014. Design tools for thermoactive geotechnical

systems. *DFI Journal-The Journal of the Deep Foundations Institute* **8**(2): 121-129.

Bourne-Webb, P. J., Freitas, T. B., da Costa Gonçalves, R. A. 2016. Thermal and mechanical aspects of the response of embedded retaining walls used as shallow geothermal heat exchangers. *Energy and Buildings* **125**: 130-141.

Comodromos, E. M., Papadopoulou, M. C. Laloui, L. 2016. Contribution to the design methodologies of piled raft foundations under combined loadings. *Canadian Geotechnical Journal* **53** (4): 559–577.

Coyle, H.M., Reese, L.C. 1966. Load transfer for axially loaded piles in clay. *Journal of the Soil Mechanics and Foundation Division, American Society of Civil Engineers* **92** (2): 1–26.

Di Donna, A., Cecinato, F., Loveridge, F., Barla, M. 2017. Energy performance of diaphragm walls used as heat exchangers. *Proceedings of the Institution of Civil Engineers-Geotechnical Engineering* **170**(3): 232-245.

Eurostat. 2018 https://ec.europa.eu/eurostat/statistics-explained/index.php/Energy_consumption_in_households (last updated March 2018)

Frank, R., Zhao, S. R. 1982. Estimation par les paramètres pressiométriques de l'enfoncement sous charge axiale de pieux forés dans des sols fins. *Bulletin de Liaison Laboratoires des Ponts et Chaussees* No. 119: 17–24.

Frodl, S., Franzius, J. N., Bartl, T. 2010. Design and construction of the tunnel geothermal system in Jenbach. *Geomechanics and Tunnelling* **3**(5): 658-668.

International Energy Agency, I. E. A. 2019 https://www.iea.org/tcep/buildings/ (last updated 25 January 2019)

International Energy Agency, I. E. A. 2018, The Future of Cooling, OECD Publishing, Paris/IEA, Paris, 92 pp.

International Energy Agency, I. E. A. 2017, World Energy Outlook 2017, OECD Publishing, Paris/IEA, Paris, https://doi.org/10.1787/weo-2017-en.

Knellwolf, C., Peron, H., Laloui, L. 2011. Geotechnical analysis of heat exchanger piles. *Journal of Geotechnical and Geoenvironmental Engineering* **137**(10): 890-902.

Kraft, L.M., Ray, R.P., Kagawa, T. 1981. Theoretical T-Z curves. *Journal of Geotechnical Engineering, American Society of Civil Engineers* **107** (11): 1543–1561.

Kürten, S., Mottaghy, D., Ziegler, M. 2015. Design of plane energy geostructures based on laboratory tests and numerical modelling. *Energy and Buildings* **107**: 434-444.

Laloui, L., Moreni, M., Vulliet, L. 2003. Comportement d'un pieu bi-fonction, fondation et échangeur de chaleur. *Canadian Geotechnical Journal* **40**(2): 388-402.

Laloui, L., Nuth, M., Vulliet, L. 2006. Experimental and numerical investigations of the behaviour of a heat exchanger pile. *International Journal for Numerical and Analytical Methods in Geomechanics* **30**(8): 763-781.

Laloui L., Rotta Loria A.F. 2019. Analysis and design of energy geostructures, ISBN: 9780128206232, Elsevier.

Loveridge, F. A., Powrie, W., Amis, T., Wischy, M., Kiauk, J. 2016. Long term monitoring of CFA energy pile schemes in the UK. *Energy Geotechnics*: 585-592.

McCartney, J. S., Murphy, K. D. 2017. Investigation of potential dragdown/uplift effects on energy piles. *Geomechanics for Energy and the Environment* **10**: 21-28.

Makasis, N., Narsilio, G. A., Bidarmaghz, A. 2018. A machine learning approach to energy pile design. *Computers and Geotechnics* **97**: 189-203.

Mimouni, T., Laloui, L. 2015. Behaviour of a group of energy piles. *Canadian Geotechnical Journal*, **52**(12): 1913-1929.

Nicholson, D. P., Chen, Q., de Silva, M., Winter, A., Winterling, R. 2014. The design of thermal tunnel energy segments for

Crossrail, UK. *Proceedings of the Institution of Civil Engineers-Engineering Sustainability* **167** (3): 118-134.

Poulos H.G. 1968. Analysis of the settlement of pile groups. *Géotechnique* **18** (4): 449-471.

Poulos H.G. 1968. The influence of a rigid pile cap on the settlement behaviour of an axially-loaded pile. *Civ. Eng. Trans., Inst. Engrs. Aust.* **CE10** (2): 206-208.

Randolph, M. F., Wroth C. P. 1978. Analysis of deformation of vertically loaded piles. *Journal of Geotechnical Engineering, American Society of Civil Engineers* **104** (2): 1465–1488.

Randolph, M. F. Clancy, P. 1993. Efficient design of piled rafts. *Proceedings of 5th International Conference on Deep Foundations on Bored and Auger Piles*, 1-4 June, Ghent, Belgium: 119-130.

Ravera, E., Sutman, M., Laloui, L.. Load-transfer method for energy piles in a group with pile-soil-slab-pile interaction. Under review.

Ravera, E., Sutman, M., and Laloui, L. Analysis of the interaction factor method for energy pile groups with slab. Under review.

Recast, E. P. B. D. 2010. Directive 2010/31/EU of the European Parliament and of the Council of 19 May 2010 on the energy performance of buildings (recast). *Official Journal of the European Union* **18** (6).

Rotta Loria, A. F., Laloui, L. 2016. Thermally induced group effects among energy piles. *Géotechnique* **67**(5): 374-393.

Rotta Loria, A. F. Laloui, L. 2016. The interaction factor method for energy pile groups. *Computers and Geotechnics* **80**: 121-137.

Rotta Loria, A. F., Bocco, M., Garbellini, C., Muttoni, A. Laloui, L. The role of thermal loads in the performance-based design of energy piles. Under review.

Sailer, E., Taborda, D. M., Zdravković, L., Potts, D. M. 2019. Fundamentals of the coupled thermo-hydro-mechanical behaviour of thermo-active retaining walls. *Computers and Geotechnics*, **109**: 189-203.

Salciarini, D., Ronchi, F., Cattoni, E., Tamagnini, C. 2013. Thermomechanical effects induced by energy piles operation in a small piled raft. *International journal of Geomechanics* **15**(2): 04014042.

Seed, H. B., Reese, L. C. 1957. The action of soft clay along friction piles. *T. Am. Soc. Civ. Eng.* **122** (1): 731–754.

Sterpi, D., Coletto, A., Mauri, L. 2017. Investigation on the behaviour of a thermo-active diaphragm wall by thermo-mechanical analyses. *Geomechanics for Energy and the Environment* **9**: 1-20.

Sutman, M., Olgun, G., Laloui, L. Brettmann, T. 2017. Effect of end-restraint conditions on energy pile behavior. *Geotechnical Frontiers*:165–174.

Sutman, M., Olgun, C. G., Laloui, L. 2018. Cyclic Load–Transfer Approach for the Analysis of Energy Piles. *Journal of Geotechnical and Geoenvironmental Engineering* **145**(1): 04018101.

Sutman, M., Brettmann, T., Olgun, C. G. 2019. Full-scale in-situ tests on energy piles: Head and base-restraining effects on the structural behaviour of three energy piles. *Geomechanics for Energy and the Environment* **18**: 56-68.

Sutman, M., Speranza, G., Ferrari, A., Larrey-Lassalle, P., Laloui, L. 2019. Long-term performance and life cycle assessment of energy piles in three different climatic conditions. *Renewable Energy*. https://doi.org/10.1016/j.renene.2019.07.035 In press.

Xia C, Sun M, Zhang G, Xiao S, Zou Y. 2012. Experimental study on geothermal heat exchangers buried in diaphragm walls. *Energy and buildings* **52**: 50-5.

You, S., Cheng, X., Guo, H., Yao, Z. 2016. Experimental study on structural response of CFG energy piles. *Applied Thermal Engineering* **96**: 640-651.

XVII European Conference
ECSMGE 2019
Reykjavik
on Soil Mechanics
and Geotechnical Engineering

Recent developments in laboratory testing of geomaterials with emphasis on imaging

Développements récents de la géomécanique expérimentale de laboratoire : focus sur l'imagerie

Gioacchino Viggiani & Alessandro Tengattini
Univ. Grenoble Alpes, CNRS, Grenoble INP, 3SR, F-38000 Grenoble, France

ABSTRACT: This paper presents a review of some recent technical developments and scientific accomplishments in laboratory experimental testing of geomaterials – with a special focus on imaging. Full-field techniques such as x-ray and neutron tomography have had a particular impact over the last two decades, and allowed the understanding of the micro scale processes ultimately driving the behavior at the macroscopic scale. Two other very recent, advanced experimental tools are briefly discussed: rheography and diffraction. These two modern techniques have shown increasing potential to further expand the portfolio of possibilities of experimental geomechanics, by expanding temporal resolution, and giving direct access to intra-granular strains, respectively. This contribution concludes by outlining the broader impact that this panoply of techniques has had and is expected to have in geomechanics and geotechnics at large.

RÉSUMÉ: Cet article présente quelques développements techniques et réalisations scientifiques récents en matière d'expérimentation en laboratoire sur les géomatériaux – avec un accent particulier sur l'imagerie. Les techniques de mesure de champs telles que la tomographie à rayons x et la tomographie à neutrons ont eu un impact important au cours des deux dernières décennies et ont permis de comprendre les processus à l'échelle micro qui déterminent finalement le comportement des sols à l'échelle macroscopique. L'article examine également deux autres méthodes expérimentales avancées, la rhéographie et la diffraction. Ces deux techniques modernes ont le potentiel pour élargir davantage la gamme des possibilités expérimentales en géomécanique, en améliorant la résolution temporelle, et en permettant la mesure des déformations intra-granulaires, respectivement. Finalement, cet article souligne l'impact plus large que cette panoplie de techniques a eu et devrait avoir en géomécanique et en géotechnique en général.

Keywords: Experimental geomechanics; full-field methods; tomography; x-rays; neutrons; review paper

1 INTRODUCTION

During the last few decades, laboratory experimental geomechanics has experienced a tremendous – and perhaps unprecedented – leap forward, thanks to major technological advances along with a matching computational power. Besides the availability of new and powerful tools, the increased intertwining of neighboring domains in material science has enabled the diffusion of techniques previously unknown in soil and rock mechanics, *e.g.*, nanoindentation (Daphalapurkar *et al*. 2011, Hu & Zongjin 2015) and diffraction (Hall *et al*. 2018) – to mention but two.

Of particular interest and impact are the so-called non-contact measurement techniques, which over the last two decades have passed from

relatively niche to well-established tools (*e.g.*, Hild & Espinosa 2012, Viggiani & Hall 2012). Such techniques are often referred to as *full-field*, in contrast to more conventional "point-wise" or "bulk-averaged" measurement techniques, which are based on the use of transducers positioned at the specimen boundaries.

In conventional material testing, in fact, the measured response can at best be seen to represent an overall, averaged material response. Consequently, only in the case of a perfectly homogeneous material undergoing perfectly uniform deformation will the response measured from the test reflect true material (*i.e.*, constitutive) behavior. Obviously, neither are materials truly homogeneous at the scale of a laboratory specimen, nor are boundary conditions perfect. Furthermore, even when starting from "perfectly" homogeneous conditions, processes (*e.g.*, deformation) can eventually localize into more or less narrow zones (shear and compaction bands, tensile and shear cracks or fractures) at some stage of a test. In the presence of localized strains, it is clear that the meaning of stress and strain variables derived from boundary measurements of loads and displacements is only nominal, or conventional. Measuring the full field of deformation in the specimen is in this case the only way in which test results can be appropriately interpreted.

A number of full-field techniques (thermal, wave-based, optical) have been – and are being – used in laboratory testing of soil and rock: ultrasonic tomography (*e.g.*, Hall & Tudisco 2012, Tudisco *et al*. 2015), electrical resistivity tomography (*e.g.*, Comina *et al*. 2008, 2011, Derfouf *et al*. 2019), magnetic resonance imaging (*e.g.*, Sheppard *et al*. 2003, Yu *et al*. 2019, Xu *et al*. 2019), infrared thermography (*e.g.*, Luong 1990, 2007, Salami *et al*. 2017) – to mention but a few. A remarkable example is represented by the techniques based on ionizing radiation: x-rays and neutrons. This paper will focus on these two techniques, as we believe that they are at the center of a veritable revolution in experimental soil and rock mechanics – besides, they are those that we are most familiar with. X-ray and neutron imaging

have a few limitations, notably spatial and temporal resolution, and the difficulty to directly access the intra-granular strains (hence inter-granular forces). An emerging technique that can help to assess them is *diffraction* (either using x-rays or neutrons), which will also be discussed. In terms of temporal resolution, rapid processes such as granular flow would require temporal resolutions incompatible even with the most performant synchrotron – not to mention that the rotation speed required would cause centripetal forces comparable to or larger than gravity (depending on the sample size). A very recent solution to this problem is x-ray *Rheography* (Baker *et al*. 2018), which allows the direct assessment of the probability distribution of velocities at high rates.

Even with synchrotrons, the spatial resolution of x-ray imaging is not good enough for investigating the mechanics of fine-grained geomaterials (*i.e.*, clays and clay rocks) at the particle scale. However, synchrotron x-ray tomography has been successfully applied, in combination with Digital Image Correlation, to investigate strain localization in clay rocks – at a scale that is much larger than the scale of clay particles, though (Lenoir *et al*. 2007, Bésuelle & Andò 2014). To access the scale of the clay particles, a suitable technique is *Broad Ion Beaming* (BIB), which allows, when coupled with Scanning Electron Microscopy (SEM), achieving a resolution of a few nanometers. BIB is used as a "knife", to cut and expose cross-sections that are then imaged by SEM. Cross-sections with an area of a few square millimeters can be obtained, which are relatively "large" as compared to those that can be obtained with *Focused* Ion Beaming (FIB) – of only a few square micrometers. See Desbois *et al*. (2017) and references quoted therein.

The structure of this paper is as follows. The next two sections (2 and 3) give an overview of x-ray and neutron imaging, respectively. For each of these two imaging techniques, the basic physics is outlined, an historical review of their use in geomechanics is given, and finally some selected examples are presented, with particular emphasis to the more recent and promising applications. Sec-

tion 4 focuses on two comparatively new applications: diffraction and rheography. Through all these examples our aim is to present the tremendous possibilities now available and the new avenues opening up for research in geomechanics.

The paper concludes with a critical review of the impact these techniques had (or could have) on geomechanics, and a discussion about their practicality (*i.e.*, how these methods might be practically employed in a "standard" geomechanics laboratory), as well as some foreseen avenues of future development. It should be noted that in this work we adopt the broader definition of geomaterials, which besides soils and rocks also includes concrete – which after all is nothing but an artificial conglomerate.

2 X-RAY IMAGING

2.1 Fundamentals

X-rays were discovered in 1895 by W.C. Röntgen, when the radiations emitted by a vacuum tube affected a barium platinocyanide screen across the room despite the obstacles interposed. Röntgen temporarily named them using the mathematical designation (x) for something unknown. The value of this non-destructive imaging technique for medical applications was immediately recognized.

X-radiation is a form of electromagnetic radiation composed of x-rays, with wavelengths ranging from 0.01 to 10 nanometers, lying between UV and gamma rays. One common way to produce x-rays is to accelerate with sufficient energy charged particles (electrons and ions) to hit a material. The deceleration of a charged particle causes the moving particle to lose kinetic energy, which is converted into a photon (braking radiation or Bremsstrahlung), this is for example the approach used in most laboratory scanners, whereas in Synchrotrons the braking radiation is produced by magnetically undulating or deviating electrons. In both cases, the upper boundary of the emitted x-rays is defined by the energy of the incident particle. X-rays interact with the outer electron shells of the atoms through different mechanisms (*e.g.*, Compton Scattering, Refraction and Reflection, Pair Production, Rayleigh Scattering).

For geomaterials, and for the energy of x-ray radiation normally used for their investigation, the predominant mechanism is photoelectric absorption (surpassed by Compton scattering as we approach higher energies). The attenuation by absorption of the x-ray intensity I (in photons per unit area and time) along an axis z can be expressed through the Beer-Lambert law for monochromatic beam as:

$$I(z) = I_0 e^{-\mu z} \tag{1}$$

where I_0 is the initial beam intensity. The coefficient of linear absorption μ can be expressed as:

$$\mu = \left(\frac{\rho_m N_A}{M}\right) \sigma_a \tag{2}$$

where ρ_m is the material density, N_A is Avogadro's number and M the molar mass. The absorption cross-section coefficient σ_a relates the number of absorption events with the atoms per unit area. This coefficient scales roughly with the fourth power of the atomic number Z, although it presents a strong discontinuity when the work provided by the radiation becomes insufficient to eject an electron belonging to the level closer to the nucleus.

X-rays are normally detected by employing special chemical compounds, named 'scintillators' which can absorb them while emitting visible light, which is then captured by cameras sometimes with the addition of optical focusing elements.

In laboratory scanners, x-rays are often times generated in conical beams, and the detectors are composed of scintillators and detector chips right behind them. In this case, the level of zoom is determined by the relative distance between the source, detector and sample. In Synchrotrons, the x-ray beam is parallel, and the detector additionally includes optical elements (*e.g.*, camera

lenses) and the zoom is determined by the optics chosen.

These elements allow acquiring bi-dimensional projections of the attenuation to x-rays of the object, named *radiographies*. To acquire then a *tomography*, several hundred projections are acquired over a range of relative angles between object and imaging axis. So-called "reconstruction" algorithms, based on the Radon transform, are then employed to obtain a 3D matrix of absorption values, which are representative – as aforementioned – of the material density and its cross-section coefficient σ_a.

2.2 Historical perspective

The use of x-ray imaging in experimental geomechanics dates back to the 1960s. To our knowledge, the earliest examples are the works of Hamblin (1962) and Calvert & Veevers (1962) for the study of the structure of sandstones – see Figure 1. In the same period, x-ray radiography was also used in Cambridge for measuring strain fields in soil (Roscoe *et al*. 1963, Roscoe 1970). The radiographs revealed extremely interesting effects associated with local changes in the soil density, namely narrow dilation bands forming in the soil models (see Figure 2). Similar observations were made by other authors (*e.g.*, Kirkpatrick & Belshaw 1968, Arthur & Dunstan 1982, Vardoulakis & Graf 1982, Bransby & Blair-Fish 1975). In all these examples, x-rays were used to obtain radiographs, *i.e.*, 2D images produced by x-ray radiation on photographic plates. As explained above, radiographs represent maps of attenuation accumulated through the complete soil mass in the direction perpendicular to the image, which is related to soil density.

The above studies provided valuable qualitative information on localization patterning. However, they all suffered from two major limitations: (i) lack of quantitative data on the observed density changes, and (ii) limitation to 2D images. Both limitations are overcome by x-ray Computed Tomography (CT). The principle of CT measurement consists of recording x-ray radiographs

of a specimen at many different angular positions around the object. From these different projections, a three dimensional image of the object can be reconstructed with appropriate algorithms (usually based on a back projection principle); see for example Baruchel (2000) for a thorough description of the technique. X-ray CT is therefore a non-destructive imaging technique that allows quantification of internal features of an object in 3D. First developed for medical imaging, x-ray CT is now widely used in material sciences and proved its interest in various domains of geosciences, including geomechanics (see, *e.g.*, the review paper by Cnudde & Boone (2013) and the several references quoted therein).
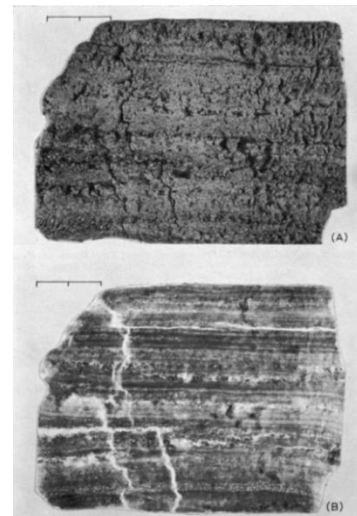
Figure 1. X-ray radiography of the structure and failure patterns in a sandstone (Calvert & Veevers 1962)

A pioneering application of x-ray CT to experimental geomechanics is due to Desrues and coworkers in Grenoble, who started from the early 1980s to use x-ray CT as a quantitative tool for experimental investigation of strain localization in sand (see Desrues *et al*. 1996, and Desrues 2004 for a review). As an example, Figure 3 shows horizontal slices through a three dimensional CT image of a specimen of dry dense Hostun sand (at a stage towards the end of a triaxial compression test). Patterns of localized density variations are

revealed as different intensities of the recorded x-ray radiation. The 3D mechanism that appears has some clear structure, which would be otherwise hidden (*i.e.*, invisible from just looking at the specimen, which to external viewing just had a barrel shape at the end of the test). Similar structures are shown in Figure 4, obtained from another triaxial test on Hostun sand (Desrues *et al.* 1996). The localization pattern in this case involves a cone and multiple sets of planes associated in pairs, each pair intersecting along a diameter at the top of the specimen. Figure 4b shows Desrues' interpretation of these patterns of localization, including a cross-section close to the top platen, and a section parallel to the axis (compare with Figure 4a).

Using x-ray tomography in a quantitative way requires a calibration of CT values to obtain absolute values of density or void ratio. With such a calibration, Desrues was able to show that global measurements of volume change in such tests only give an averaged picture, and in fact density variation (dilation for dense sand) occurs predominantly within the zones of localized shear. These quantitative analyses of density changes provided experimental confirmation that, for a given stress level, a unique limit void ratio is in fact reached, irrespective of the initial density of the sand being tested (the well-known concept of a critical state, as conjectured already by Casagrande & Watson (1938). However, this is only true locally, *i.e.*, within the shear zones (see Figure 4c).

Figure 2. Dilation bands in dense sand over a displacing trapdoor observed with x-ray radiography (Roscoe et al. 1963)
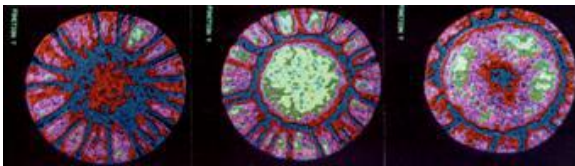
Figure 3. Horizontal slices through a CT image volume of a triaxial compression specimen of dry dense Hostun sand showing complex patterns of density variations (image was acquired near the end the test) (courtesy of J. Desrues).
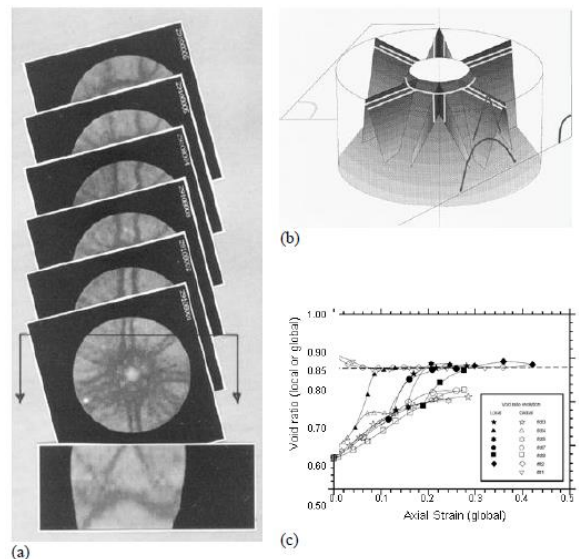
Figure 4. (a) patterns of localized density variations revealed in slices through a CT image volume of a specimen of dry dense Hostun sand near the end of a triaxial compression test (note this is a different test to Fig. 3). (b) suggested 3D interpretation of the patterns of localization in Fig. 4a. (c) local (solid symbols) and global (open symbols) variation of void ratio in loose and dense specimens of Hostun sand during triaxial compression with 60 kPa effective confining pressure (from Desrues et al. 1996).

2.3 Recent results, challenges and perspectives

This section presents recent and ongoing work where granular assemblies are deformed "in-situ" (*i.e*., inside an x-ray tomography machine), allowing multiple states to be imaged in 3D. It is important to note that we have deliberately chosen to present examples predominantly from our personal experience at Laboratoire 3SR in Grenoble. Obviously, in so doing, we do not claim that these are necessarily the best or the most advanced examples available – they are just those that we are most familiar with. In fact, this is a technique that has become extremely popular in materials science, and in particular for granular materials, also the work of Alshibli and coworkers in the USA (*e.g*., Druckery *et al*. 2018, just to mention their most recent publication on the subject) and the group at ANU in Australia (*e.g*., Saadatfar *et al*. 2013) must be mentioned. The main focus of these studies is on the grain-scale investigation of shear banding, with results from triaxial tests.

The triaxial tests used in this work differ significantly from standard to allow x-ray scanning of the specimen in various stages of deformation – to this end experiments are entirely performed within the Laboratoire 3SR x-ray microtomograph. Given that the D_{50} of the grains studied is in the order of 300μm, the pixel size necessary for sufficient information for grain has been set to 15.56μm/px, meaning that an average particle will have around 20 pixels across a diameter. This choice limits the field of view and consequently the size of the specimen is reduced to 22mm height and 11mm diameter. Despite this extreme miniaturization, the specimen is composed of more than 50,000 grains of sand.

Furthermore, since x-ray tomography requires the rotation of the specimen, the steel tie bars that usually take the return force from the compression of the specimen would severely degrade the scan. To avoid this, the pressure cell (which is made in x-ray transparent Plexiglas or polycarbonate) takes this extra load. Specimens are prepared dense (through dry pluviation through a 1m tube),

and are tested dry. This would normally mean that no volume changes can be measured; however these are obtained from the different 3D images. Triaxial testing is done under strain control at a strain rate of 0.1%/min, and loading is interrupted at various points during the test to scan the specimen (acquiring around a thousand radio-graphs as the specimen rotates through 360°). When loading is stopped the specimen relaxes – the majority of the relaxation happens in a few minutes after loading is stopped. Axial force and imposed displacement are measured externally.

The 3D images coming from each scan contain around 1000×1000×1600 voxels, each voxel representing a reconstructed value of x-ray attenuation (which is roughly related to density, meaning that grains have "high" and pores have "low" greyvalues). From such an image, a local field of porosity can easily be defined, for example by defining the greyvalues representing pore and grain, and measuring the average greyvalue in a suitably defined subvolume. However, the preferred technique for the low-pressure tests where grains do not break, is to define a threshold greyscale value, above which voxels are considered to be grain and below which they are considered to be pore – the value is chosen to obtain the solid volume of grains measured by weighing at the end of the test. Porosity is then easy to define in a subvolume in such an image: the volume of voids and solids are simply counted.

Binary images where the solid and void phases are defined are the starting point for the definition of individual grains: the solid phase is split into individual grains using a watershed as described in Andò *et al*. (2012a). Each grain (*i.e*., all the voxels making up an individual grain) are then each given a unique number, and properties of these 3D sets of voxels (position, volume) can be measured. The splitting and labelling procedure is repeated for each imaged state, and since grains will not have the same unique number, labels are reconciled by tracking grains from increment to increment using a specifically developed technique called ID-Track (Andò *et al*. 2012a). Following the change in the center-of-mass of each

grain over an increment gives a very precise evaluation of the displacement of the particle (with an error less than 0.1 pixels).

The measurement of rotations is more challenging: at this resolution the grain shapes are not detailed enough for the long and short axes of the moment of inertia tensor to be stable. To overcome this problem, a discrete DIC technique has been proposed in Andò *et al*. (2012b), where tracked grains are matched based on their images – this combined with ID-Track gives the full rigid body motion of the grains.
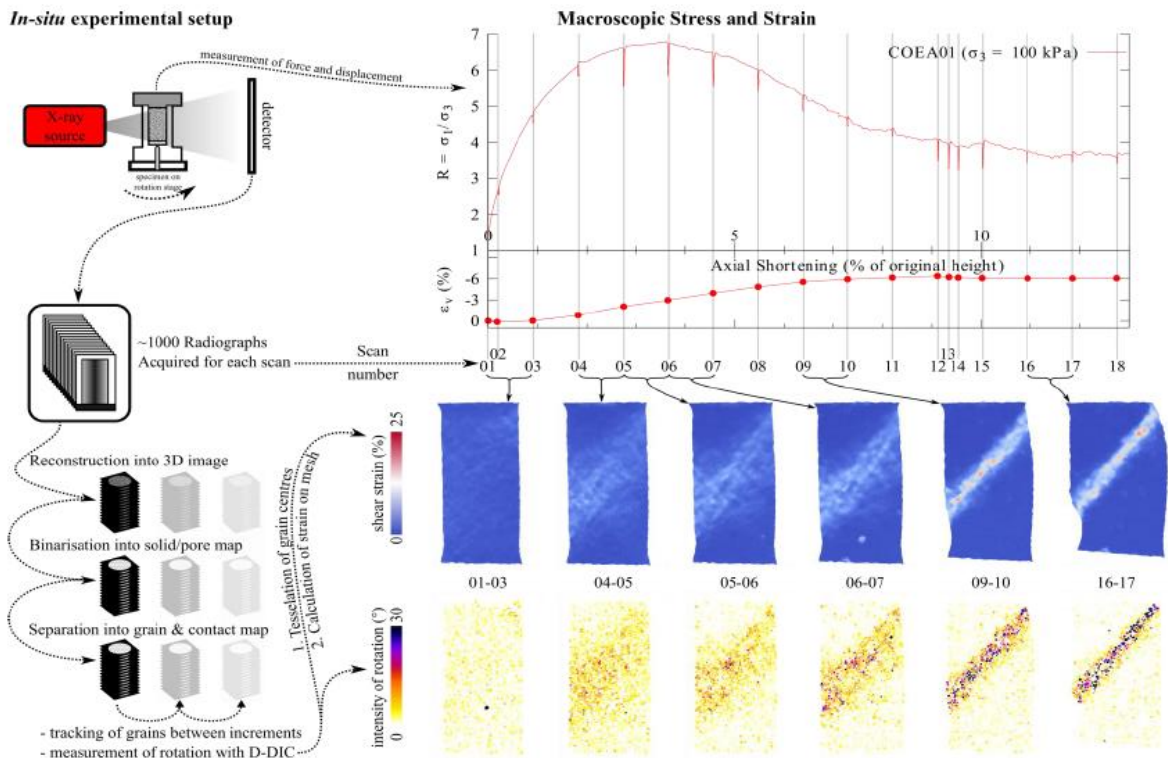
Figure 5. Illustration of the procedure for the analysis of in-situ experiments, with some highlighted results obtained on Caicos Ooids (after Andò et al. 2012a).

The measurements that can be obtained with the combination of tools detailed above are shown, for an example test, in Figure 5. In the top of the figure, a schematic of the in-situ setup is shown, along with the macroscopic measurements coming from the force and displacement measurements from the test.

In the bottom left of Figure 5, again very schematically, are shown the steps of image processing required to reconstruct a 3D image, and then to define and follow grains between imaged states, allowing measurement of their kinematics.

The series of images presented at the bottom right of the figure shows vertical slices taken through the specimen at points during the test, where all grains are colored by their incremental rotations. Above these maps of discrete quantities, is a map of a continuum mechanics quantity of shear strain, measured on tetrahedra defined by tessellating grain centers.

It is clear that this kind of discrete 3D information available all the way through a mechanical test represents an experimental revolution in geomechanics. Ongoing work focuses on two areas:

solving current measurement challenges for the subject presented above, as well as elucidating new phenomena using 3D images and data processing tools similar in spirit as those presented.

The rotations of grains, as well as the shear strain maps derived from grain displacements highlight some interesting phenomena. Especially before the macro-peak, there are some interesting chains of rotating grains that can even be seen in the vertical section shown (in 3D the chains are clear to see, but unfortunately analyzing this structure in 3D as well as showing it in print also remains an open challenge). The emergence of a wide band of rotating grains that concentrates into a final shear band is also very interesting, and the grain-scale reasons for this collective behavior are doubtlessly to be found in the way that forces are transmitted from grain to grain. Looking at the grain maps, we can see that a specimen with significantly fewer grains would not have had the degrees of granular freedom in order to exhibit such

a shear band. Unfortunately, having sufficient resolution to study grain kinematics does not appear, using standard tools, to offer enough to study grain-to-grain contacts, as shown in Andò *et al.* (2013) – the number of voxels describing the contact between the two objects is simply insufficient.

Problems appear both in the counting of contacts (they are systematically overestimated – see Wiebicke *et al.* (2017), as well as the extremely poor definition of their orientation.

Some work in collaboration with discrete mathematicians has allowed this measurement to be made in some idealized cases using a Random Walker (see Viggiani *et al.* 2013, the base of this algorithm is now implemented in the python toolkit skimage – see Van Der Walt *et al.* 2014), and the application of this sort of tool is part of the ongoing PhD work of M. Wiebicke, with the objective of obtaining a fabric tensor from such measurements (see Wiebicke *et al.* 2019a, 2019b).
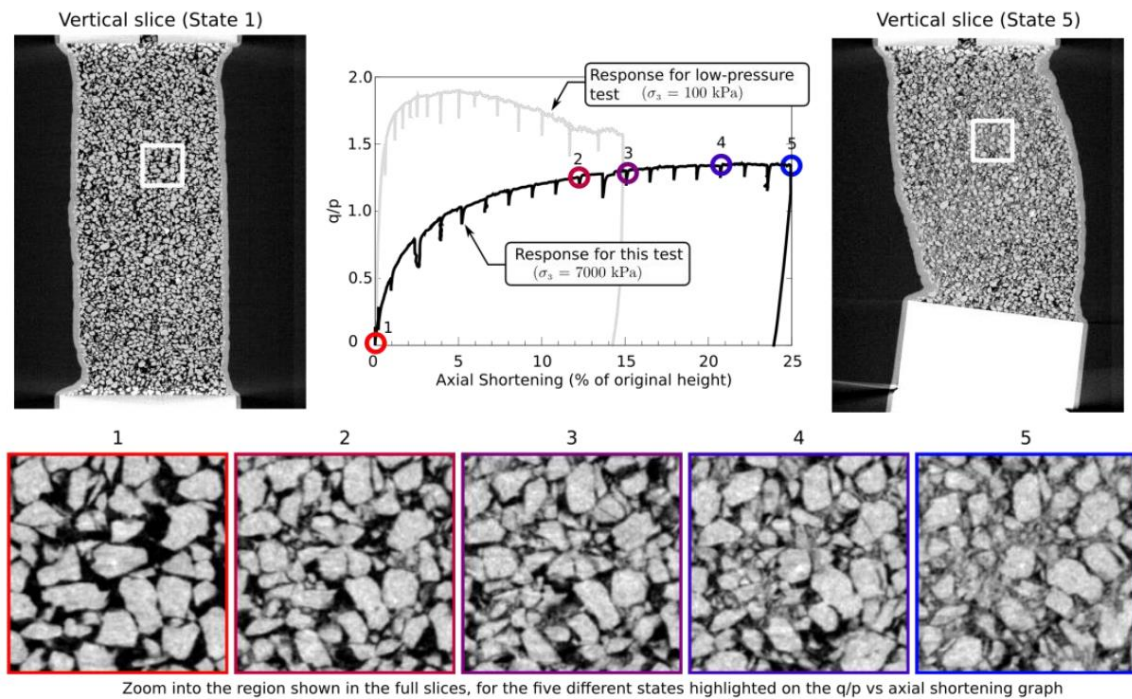
Figure 6. Some observations of grain breakage in triaxial compression of Hostun sand (after Andò et al. 2013)

Another approach to compensate for the scarcity of information is to use geometrical models to capture grain shapes, either in the style of level sets (Andrade *et al*. 2012, Kawamoto *et al*. 2018), or in the style of spherical harmonics (see Zhou *et al*. 2015). Work on all fronts is extremely important to get further in the characterization of the complex phenomenon of shear banding.

The ability to non-destructively image multiple states of a granular medium in 3D offers tremendous possibilities in the quantification of many phenomena in granular materials. In Grenoble, a number of different phenomena have been (and are being) investigated. The three-phase interaction of soil-water-air mix with a focus on the water-retention behavior of soil is an important area of focus (Kaddhour *et al*. 2018, with important work also done by other groups such as Sheel *et al*. 2008 and Higo *et al*. 2011, 2013). One of the main challenges here is the "trinarization" of such a volume to distinguish all three phases without errors; this is a particular challenge in the case of water, since its density is low compared to sand grains.

Furthermore, the quantification of cement is also an important area of research work, be it "bio-cemented" materials such as those produced in U.C. Davis (DeJong *et al*. 2006) which have been studied with x-ray tomography (Tagliaferri *et al*. 2011), or artificially cemented material (see Das *et al*. 2013 as well as Tengattini *et al*. 2014). Challenges here include the difficult quantification of cement and its evolution between grains (since both can be of similar grey-scale values).

One last major area of work is grain breakage (as illustrated in Figure 6), where the challenge is to quantify the process of breakage, even when particle shapes are evolving, and particle sizes are becoming small. When particles fall below the resolution of the measurement, only their average mass can be followed, and taking this into account in an algorithm is certainly a big challenge. Recent work by Karatza *et al*. (2019) propose two bespoke image analysis algorithms, which allow breakage to be tracked in 3D images of a dry granular assembly undergoing crushing, and con-

tacts prior to breakage to be identified. Finally, it is worth noting that recent work using synchrotron based x-ray tomography indicates that even *creep* of sand can in fact be the result of rather pronounced fracturing at the individual grain scale (Andò *et al*. 2019) – see Figure 7.
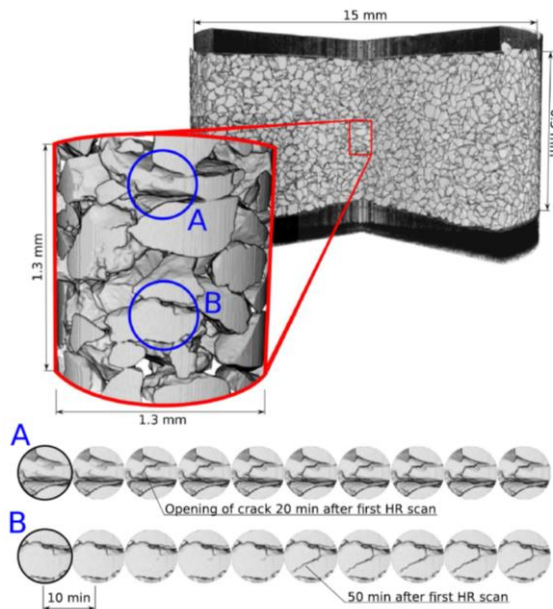
Figure 7. X-ray imaging of creep experiments on sand. Positions labelled A and B are tracked through time (after Andò et al. 2019)

3 NEUTRON IMAGING

3.1 Fundamentals

Neutrons were discovered in 1932 by J. Chadwick, while trying to understand the origin of the theoretical imbalance of the energy necessary to contain the electrons in the atom, which could not be justified by the protons alone.

Unlike x-rays, neutrons are fundamental particles which have mass and, as the name suggests, carry no electric charge. Two of the most common ways to produce neutrons is through *nuclear fission*, *e.g.,* by bombarding with one neutron a Uranium 235 atom, which splits into a Barium and a

Kripton atom plus three neutrons, with a net gain of two neutrons and about 180 MeV of energy. Alternatively, *spallation* can be adopted: protons are magnetically accelerated onto a heavy metal target as Lead, which releases about 15 to 20 neutrons per proton. The energy of neutrons is in both cases usually too high for imaging purposes, which is why they are generally slowed down by making them pass through water or heavy water tanks at low temperatures.

Unlike x-rays, neutrons interact with the nucleus of the atom, which is why they are sensitive to the different isotopes of the matter. A relevant example is provided by Hydrogen and Deuterium: they are both composed by one proton and one electron, but the latter also contains a neutron in its nucleus. As a result, their interaction with neutrons is an order of magnitude different, while being chemically and physically nearly identical. Like x-rays, neutrons interact with matter in a variety of ways, but the dominant ones in the context of geomaterials are *absorption* and *scattering*. While x-ray attenuation increases proportionally with the atomic number of the material, neutron interaction is far less obvious, as highlighted in Figure 8. One interesting example is hydrogen (and its compounds, such as water and hydrocarbons), which is nearly invisible to x-rays while highly opaque to neutrons. Similar considerations can be done for some salts (*e.g.*, the Chlorine in NaCl is highly visible), Lithium (for batteries), as well as Aluminum or Titanium, which are nearly transparent to neutrons and can thus be used to build sample environments imposing extreme conditions.
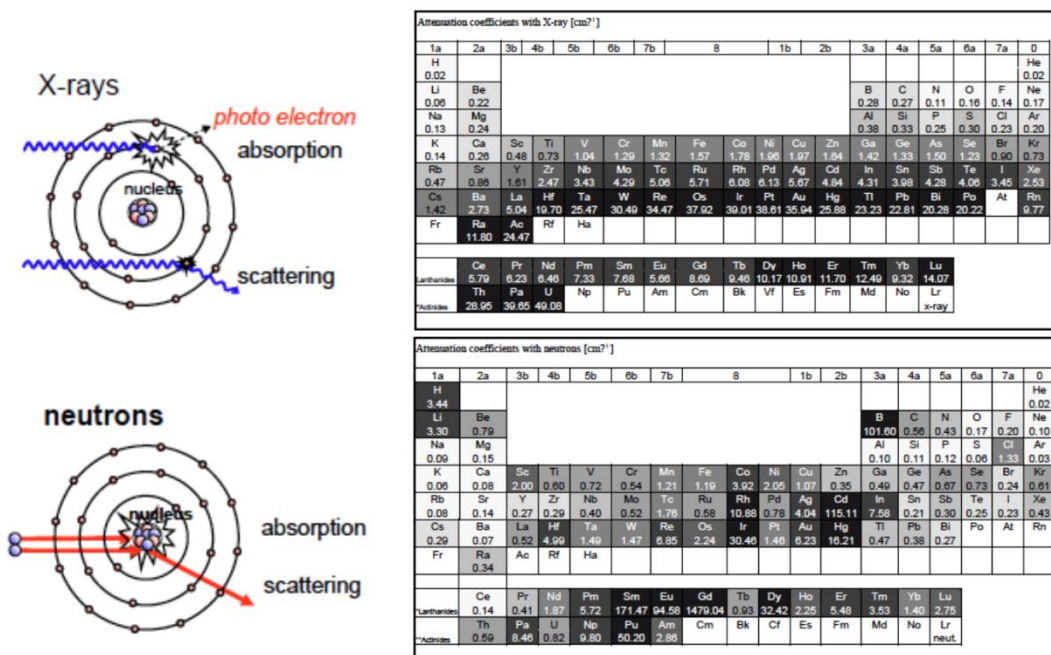
Figure 8. Interaction of x-rays and neutrons with matter: top: x-rays interact with the outer electron shells of atoms (left), which yields an increasing attenuation with increasing atomic number as highlighted by the periodic table (right). Conversely, neutrons (bottom) interact with the nuclei – hence their isotope sensitivity – and their attenuation does not depend on the atomic number.

The detection of neutrons follows the same principles as for x-rays, except that different scintillation compounds are sometimes required to convert neutrons into visible light. Producing neutrons

generally requires large-scale nuclear reactors (*e.g.*, Institut Laue-Langevin (ILL) in France, Helmholtz-Zentrum Berlin and Technische Universität München in Germany) or spallation sources (*e.g.*, European Spallation Source in Sweden and Paul Scherrer Institut in Switzerland), whereas laboratory sources are still substantially underdeveloped. The beams in these facilities are nearly parallel, so the zoom is, like in synchrotron x-rays, determined by the optical components employed. The Beer-Lambert law detailed for x-rays (Equation 1) is also generally valid for neutrons, although in some cases special attention is needed to account for the larger fraction of diffracted neutrons. The tomographic acquisition, reconstruction and data processing algorithms developed for x-rays are otherwise identical for neutrons.

3.2 Historical perspective

Neutrons were first used for geomaterials in the early 1950s, for measuring the water content in soil (Gardner & Kirkham 1952) by studying the thermalization of "fast" neutrons from a source probe. We must nonetheless wait for twenty years to see the first examples of neutron imaging applied to rocks (Subramanian & Burkhart 1973, see Figure 9), concrete (Reijonen & Pihlajavaara 1972) and soils (Wilson *et al*. 1975, Lewis & Krinitzsky 1976). The first attempt to quantitatively analyze dynamic processes in geomaterials is perhaps due to Jasti *et al*. (1987), where radiographies of water moving in rock pores were acquired. It isn't until the 1990s (Kupperman *et al*. 1990), though, that the first tomographies of a rock are reported – with the objective of characterizing water in tuff samples for permanent disposal of radioactive wastes (see Figure 10). This significant delay with respect to x-ray imaging is due to the aforementioned lower availability of neutron facilities, but also to the lower flux in most of these facilities (the most powerful of which is the one available at ILL in France), which makes the acquisition more cumbersome.

Past review papers on neutron imaging are quite broad in scope (*e.g.*, Lehmann *et al*. 2004, Win-

kler 2006, Banhart *et al*. 2010, Kardjilov *et al*. 2011, Kardjilov *et al*. 2018). Comparatively few review papers focus on geosciences and porous materials (Wilding *et al*. 2005, Hess *et al*. 2011, Perfect *et al*. 2014). Hereafter, we will focus on the more recent developments of neutron imaging, in particular those that are most relevant for the mechanics of geomaterials.
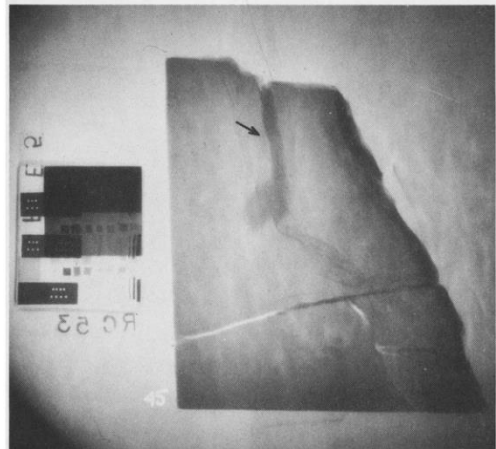
Figure 9. First neutron radiography of rock: polymer in shale (Subramanian and Burkhart 1973)
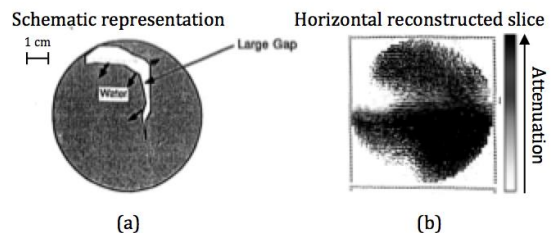
Figure 10. First neutron tomography of rock: water in tuff (Kupperman et al. 1990)

3.3 Neutron imaging for fluids

One of the key questions that neutron imaging can address is the distribution of fluids in geomaterials – thanks to the high attenuation of hydrogen to neutrons. The aforementioned pioneering work of Jasti *et al*. (1987) was followed by a number of radiographic studies of the evolving water distribution for a range of soils, rocks and concrete (de Beer *et al*. 2004, 2005, de Beer & Middleton 2006, El Abd *et al*. 2005) and even bricks

(Pleinert *et al*. 1998) and ceramics (Prazak *et al*. 1990). Some such studies (Middleton & Pàzsit 1998 and Sváb *et al*. 2000) used hydrogen isotopes such as deuterium (and the corresponding water molecule, informally named "heavy water") to obtain neutron contrast between two otherwise very similar – at least from a physico-chemical standpoint – fluids. A similar method can also be used to distinguish (heavy) water and any other fluid such as oil.

While these dynamic radiography experiments allow the observation of rapid processes of imbibition and fluid flow, their bi-dimensional nature fails to capture complex three-dimensional structures – whether intrinsic to the material or induced, for example by strain localization. In this direction, in Tudisco et *al.* (2017a) the effect of localization on fluid flow is studied by repeating a series of alternated flushes of heavy and normal water while performing the in-situ loading of a sandstone sample, highlighting the limits of radiography.

Tomography is in these cases essential, but so far the lower neutron flux available has limited most studies to static conditions, for example post-injection (Lopes *et al*. 1999, Solymar *et al*. 2003), or quasi-static conditions , *e.g.,* the determination of water retention curves in soils (Deinert *et al*. 2004, Tumlinson *et al*. 2008, Kim *et al*. 2012).

Explorations at acquisition speeds compatible with the speed of the process under investigation were generally performed at relatively low spatial resolutions. Masschaele *et al*. (2004) and Dierick et *al*. (2005), for example, acquired 10 s tomographies at a resolution of 8 pixels, or 1.5 mm.
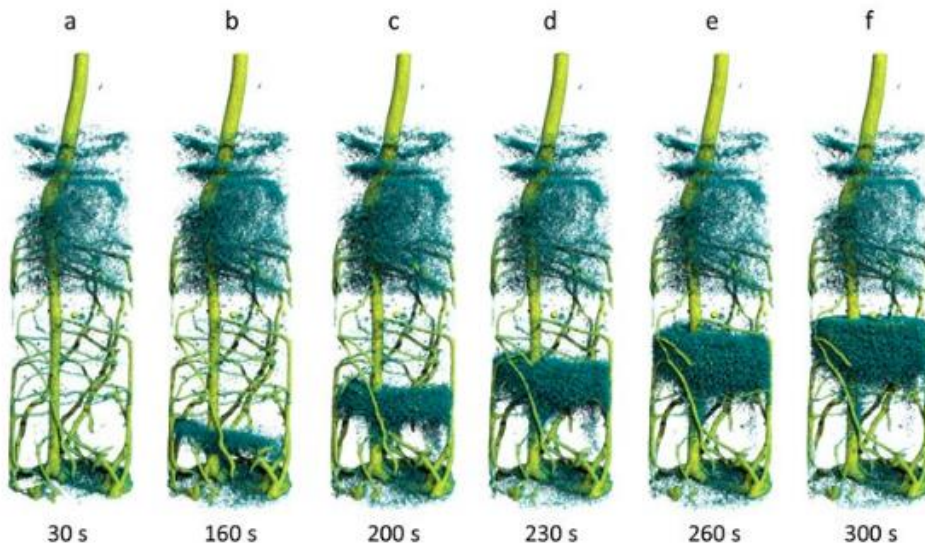
Figure 11. 3D renderings of the water uptake in Lupine roots captured through high speed (10 second) neutron tomography (after Tötzke et al. 2017)

It isn't until very recently that developments in detector technology allowed experimental campaigns that optimize resolution for a given process. A notable example is the study by Tötzke *et al*. (2017), where a series of 10 second neutron tomographies where performed on loose sand at a resolution sufficient to study the effect that lupine roots have on the hydraulic properties of granular media and most notably on the Rhizosphere (see Figure 11). A few experimental campaigns are currently being performed on rocks (sandstones and limestones) with the specific objective of investigating the influence of strain and damage localization on fluid flow (Extegarai *et al*. 2017, Lewis *et al*. 2017, Tudisco et *al*. 2019). While not

(yet) conclusive, the results obtained so far open new tantalizing perspectives.

In terms of future developments for high speed neutron tomography, the opening of imaging instruments in uniquely high flux centers (NeXT at ILL, see Tengattini *et al.* 2017, 2019) and the ongoing development of high flux centers (the European Spallation Source, ESS) will prove essential to further these efforts.

There are cases in which the experiments require relatively high confinement (cell pressure) – say several tens of MPa. This is for example the case when imaging fluid flow in concrete for understanding the durability and behavior of dams and infrastructures. In this respect, neutrons have the unique advantage over x-rays of a high penetration capability to metals, which allows the construction of high confinement vessels over sizes compatible with the intrinsic length scales of real concrete (and reinforcements), *i.e.,* several centimeters. One such testing rig, capable of withstanding 50 MPa pressure, has been recently developed by Yehya *et al.* (2018). This allowed the water flow in a concrete sample cured in heavy water to be imaged, revealing the dominant influence of local heterogeneities even at very high confinement. Besides the intrinsic interest for concrete, this also opens new interesting venues for all geomaterials at extreme conditions.

formances as well as to study the effect of fluid in the initiation of earthquakes. A recent example of the utility of neutrons in this domain is provided by Roshankhah *et al.* (2018), where shales were hydraulically fractured *in-operando* at site conditions (equivalent to 3 km depth, in plane strain) and rapid neutron imaging allowed for following the initiation process as well as the essential role of natural shale heterogeneities such as its bedding planes (see Figure 12).

Figure 12. 3D Renderings of natural and water-injection-induced features in Marcellus Shale (after Roshankhah et al. 2018)

Comparably high pressures are for example also necessary to hydraulically fracture rocks, *e.g*, for gas extraction, to enhance geothermal energy per-
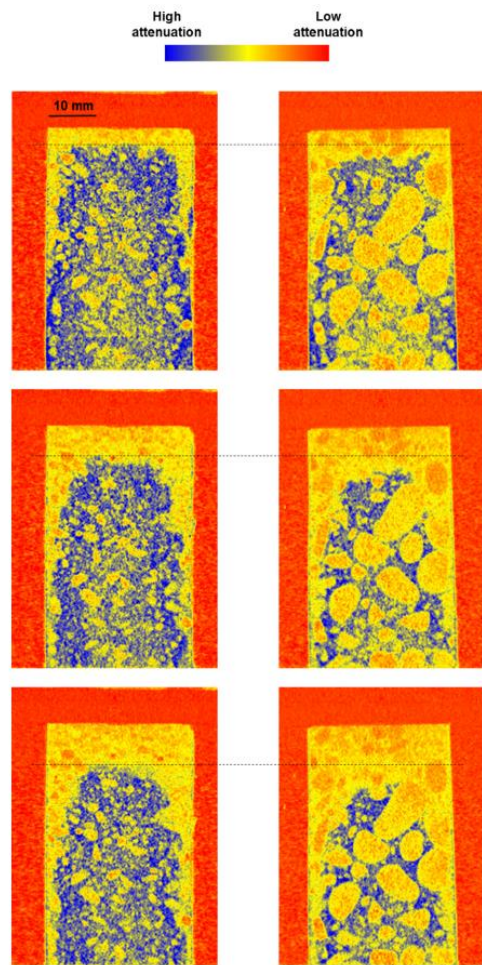
Figure 13. Vertical slices of rapid (1 minute) neutron tomographies capturing drying and moisture migration in concrete heated in operando – 4mm (left) and 8mm (right) aggregates. Top row at 38 mins, mid row at 48 mins, and bottom row at 58 mins (after Dauti et al. 2018)

A converse problem to that of fluid injection is the one of drying. A key engineering problem in this domain is moisture migration in construction materials in the event of a fire, which is at the root of explosive spalling, which in turn is a known precursor to structural collapse. In the study by Dauti *et al.* (2018), rapid (1 minute) tomographies of concrete samples heated at 500˚ were acquired. The comparison of samples with different aggregate grading revealed a significantly different hydraulic response despite a nearly identical thermal profile (Figures 13 and 14). Additionally, indicators of moisture accumulation ahead of the heating front (so far only *hypothesized* as a possible origin of spallation) were identified.
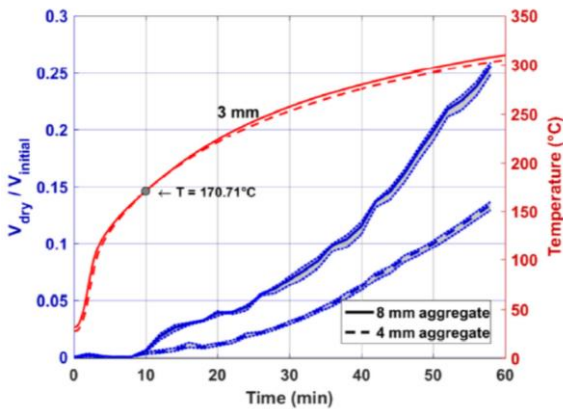
Figure 14. Comparison of the effect of aggregate size on temperature (in red) and moisture migration (in blue) as captured by neutron tomography (after Dauti et al. 2018)

All the aforementioned examples focus on the capability of neutrons to detect hydrogen and its compounds. The full potential of this technique for the broader scope of geomechanics is likely to be as of yet untapped, notably because of its less pervasive diffusion and less known potential in this domain. As highlighted in Figure 8 above in this paper (Section 3.1), a number of elements are far more (or less) visible in neutron than in x-ray imaging. So, for example, salts such as NaCl or pollutants containing Cadmium are highly visible in neutrons.

3.4 Neutron plus x-ray imaging

Besides individual advantages of x-ray over neutrons or *vice-versa*, Figure 8 highlights the extreme degree of complementarity of these two techniques. A noteworthy example of this is concrete: Figure 15 shows a scan of a concrete sample acquired with both ionizing radiations. X-rays are clearly effective in distinguishing pores from the rest of the matrix but, because of their comparable density, aggregates and mortar are barely distinguishable. Conversely, the low neutron attenuation of the SiO_2 aggregates makes them stand out with respect to the cement matrix, whereas it brings them too close to the average attenuation values of the pores to allow their straightforward segmentation. It is therefore evident that it is the *combination* of these two techniques which makes it possible to rigorously segment the essential phases. Recent theoretical developments (Tudisco *et al*. 2017b) allow not only for accurately aligning neutron and x-ray tomographies, but also for automatic segmentation of the phases – by analyzing the joint x-ray and neutron histogram. A recent paper by Roubin *et al.* (2019) presents the technical details of the algorithm proposed by Tudisco *et al*. (2017b) and applies it to neutron and x-ray tomographies of concrete (those shown in Figure 15). This yields a registered neutron image that matches the x-ray image with subpixel accuracy.

The combination of x-ray and neutron information allows also for compensating the lower neutron flux, as for example in the work by Stavropoulou *et al.* (2019a), which combines x-ray and neutrons to study the complex hydro-mechanical interactions in Callovo-Oxfordian claystone, used for the storage of nuclear pollutants. The higher speed of the x-rays and its high sensitivity to density variations can be exploited to study in 3D the evolving fracture network, whereas neutron *radiography* proves essential in determining their hydraulic origin – see Figure 16. The same authors have recently combined neutron and x-ray tomography modalities to characterize the dynamics of water absorption in Callovo-Oxfordian claystone

by comparing material deformation as well as water arrival (Stavropoulou *et al.* 2019b). Neutron and x-ray datasets are registered pairwise into a common coordinate system, meaning that a vector-valued field (*i.e.*, neutron and x-ray reconstructed values) is available for each time step, essentially making this a 5D dataset. The ability to cross-plot each field into a joint histogram allows an improved identification of mineral phases in this complex material. Material deformation obtained from the application of 3D DIC on the x-ray time series data is locally compared to changes in water content available from the neutrons, opening the way towards a quantitative description of the hydro-mechanics of this process.
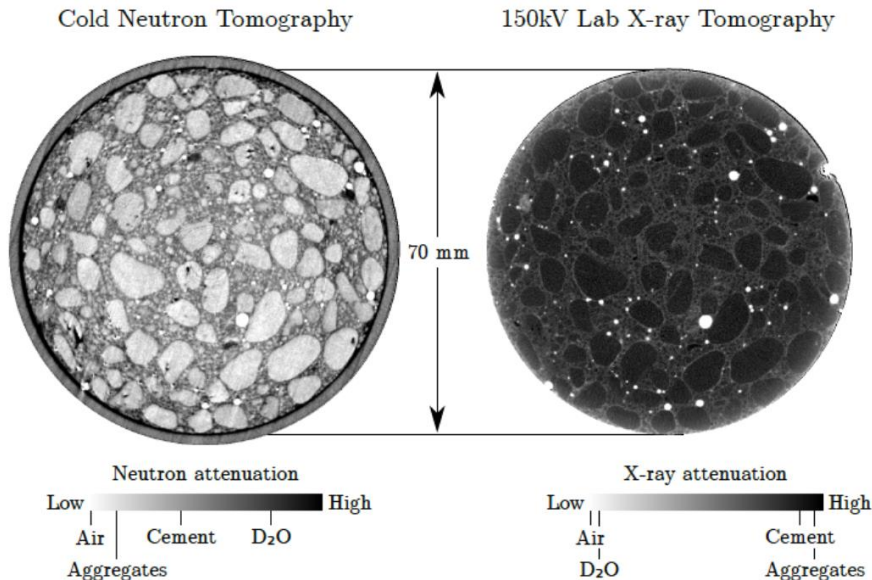
Figure 15. Example of an horizontal slice of a neutron (left) and x-ray (right) tomography of a sample of concrete, emphasizing the high complementarity of the two techniques, essential for rigorously analysing / segmenting the images (after Yehya et al. 2018). Please note that for compatibility with a white background in print, the color map has been inverted compared to the conventional for reconstructed volumes, such that low attenuation is white and high attenuation is black.

The combination of x-ray and neutron imaging for the study of geomaterials is relatively recent (*e.g.*, Kim *et al.* 2012, 2016, investigating partial saturation in granular media), albeit it is only in the last three years that some centers have started combining x-ray and neutron imaging to allow for *simultaneous* dual mode acquisitions: NeXT-Grenoble in ILL, France; ICON in PSI, Switzerland, and NeXT-NIST an NIST, USA.

Not unlike in x-ray imaging, technological developments grow along an ever growing portfolio of image processing toolboxes. While most techniques such as DIC can be used interchangeably between the two radiation types (*e.g.*, Tudisco et al. 2015) a number of problem-specific tools for example to track fluid fronts have been developed for neutron imaging (*e.g.*, Hall 2013, Jailin *et al.* 2018, Tudisco *et al.* 2019).

4 TWO OTHER ADVANCED X-RAY TECHNIQUES

4.1 3D X-ray Diffraction (3DXRD)

A full understanding of the grain-scale mechanisms that are responsible for the mechanical be-

havior of granular soils (*i.e.*, sand) requires the ability to measure *both* the grain kinematics (particle displacements and rotations) as well as the distribution of intergranular forces through the granular assembly – in fact, it is by them that the boundary forces are transmitted through the soil mass. Valuable insight can be (and has been) gained from discrete element simulations, but these are just models and, therefore, only help in the absence of real experimental data. Photoelasticity experiments are also very insightful (*e.g.*, Majmudar & Behringer 2005), but, whilst "real", they are highly simplified – they are restricted to 2D materials.
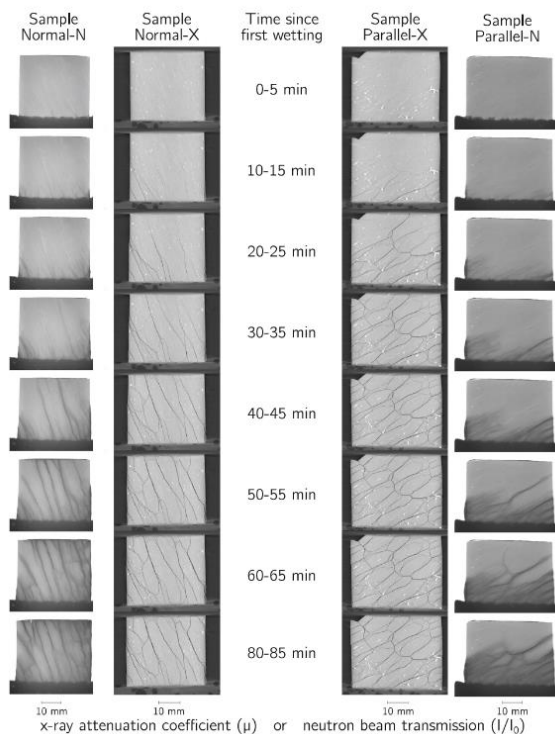
Figure 16. Comparison of x-ray tomographies and neutron radiographies of a sample of COX claystone in contact with a water reservoir, for two different orientations of the depositional layers. Water uptake is perfectly captured by neutrons, which complements the information about the fracture opening induced by it, highlighted by x-rays (after Stavropoulou et al. 2019a).

For real sand, full grain kinematics characterization has now become possible using x-ray tomography and adapted image analysis procedures – as seen in Sect. 2.3. Much fewer studies have tackled the second challenge, *i.e.*, measuring intergranular force distributions. Unfortunately, intergranular forces cannot be *directly* measured; however, they can be inferred from intragranular strains. Each grain essentially acts as a local 3D strain gauge or, for elastic deformations, a force gauge. This is in fact the basic principle of 3D x-ray diffraction (3DXRD), which has been recently proposed as a new tool that, in combination with x-ray tomography, enables force transfer networks to be studied in 3D (Hall et al. 2011, Alshibli *et al.* 2013, Cil *et al.* 2014, Hall & Wright 2015, Hurley *et al.*, 2016, 2017, 2018a, Hall *et al.* 2018).

The method is based on coherent elastic x-ray diffraction, *i.e.*, the interaction of x-rays with the electron cloud around an atom leading to diffraction of waves, which interfere to produce diffraction patterns characteristic of the arrangement of atoms in the scattering crystal. The basic equation describing this scattering is Bragg's law, which can be used to infer the mean strain tensor in each individual grain from the changes in diffraction patterns – provided the position of the grain is known (see Hurley *et al.* 2017 for details).

As an example, Figure 17 shows results obtained by Hurley, Hall and coworkers (Hurley *et al.* 2017) with 3DXRD for a sample consisting of 1099 single crystal ruby grains subjected to 1D compression. In the figure, (a) is a rendered image of the sample before loading, and (b) shows the stress-strain curves using stresses based on (i) the load cell of the device and (ii) the grain stresses from the 3DXRD data. Load step/scan numbers are indicated in (b). For one specific load step (step 14), (c) shows the grain vertical stresses derived from the 3DXRD data, (d) the local vertical strains in each tetrahedron of a Delaunay triangulation, and (e) shows the contact force network.

It should be noted that all the studies cited above employed spherical single-crystal grains. However, in the very recent contribution by Hurley *et al.* (2018b), 3DXRD has been used for ex-

periments on angular quartz grains. Therefore, 3D x-ray diffraction can be now used to study the mechanics of natural granular particles, *e.g.*, sand. In our opinion, the data from this type of experiments have the potential to enable improved calibration and/or validation of models aiming to describe the details of grain-scale characteristics and deformation mechanisms.
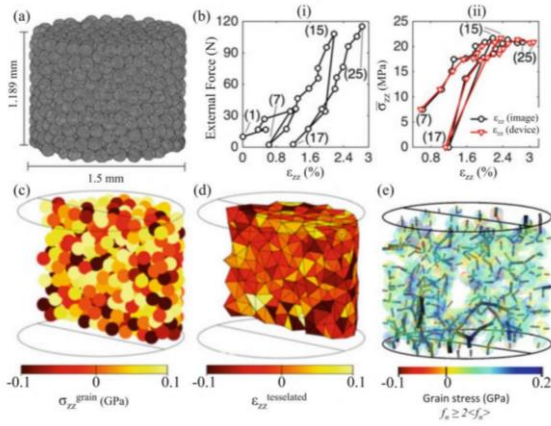
Figure 17. Example results from 3DXRD – 1D compression of a sample consisting of 1099 single crystal ruby grains. In (e) only forces greater than twice the average are shown with corresponding grains. Forces are shown as lines, centered at the corresponding contact points, scaled linearly in width and length magnitude, while grains are colored by principal stresses and given 70% transparency. Only half of the sample is shown to reveal the interior of the field (after Hall et al. 2018).

4.2 X-ray Rheography

As discussed above in the paper, one of the major limitations of tomography is temporal resolution. In most of the examples detailed in Sections 2 and 3, tomographies are acquired in quasi-static conditions. While in the most performant synchrotrons it has recently become possible to acquire images at MegaHertz rates (*e.g.*, Olbinado *et al.* 2017), their applicability in tomography for geomechanics is relatively limited. While this would allow several hundreds of tomographies per second, the centripetal forces on geomechanics-compatible samples would reach or surpass gravity, thus

irrecoverably affecting the mechanical representativity of the tests.
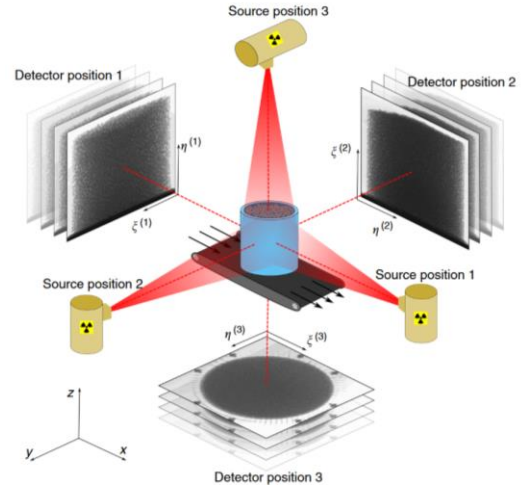
Figure 18. Schematic of the experimental set-up for rheography. Confined granular material lies inside the blue cylinder, which is sheared from below in the direction indicated. The three x-ray source positions are shown in yellow, with red indicating the approximate extent of beams, and grayscale images representing radiographic acquisition at the corresponding detector positions (after Baker et al. 2018).
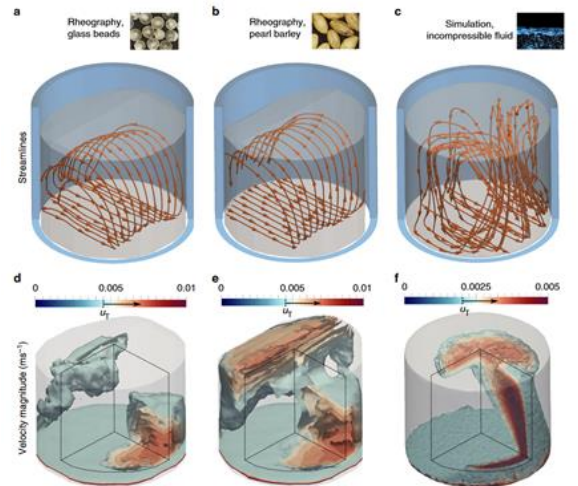
Figure 19. X-ray rheography experimental results for glass beads (a, d) and pearl barley (b, e), contrasted with the output of an incompressible Newtonian fluid simulation (after Baker et al. 2018).

A solution to this problem was recently proposed in Sydney by Einav and coworkers (Guillard *et al.* 2017, Baker *et al.* 2018). The technique was named *Rheography*, from the greek rhéō, "flow" and tomos, "slice, section". Very much like tomography, rheography allows to see the inside of the sample, however differently from tomogra-phy, it provides information about the internal flow. The scheme is illustrated in Figure 18: radiographic projections along the three cardinal axes are acquired by three x-ray source-detector pairs. Each radiography allows to evaluate the in-plane velocity. Auto- and cross-correlation functions on a regular grid can in fact be deconvolved to compute the probability density functions (PDFs) of in-plane displacements in that window. This does not nonetheless give the position of a given velocity along the x-rays although the other two source-detector pairs provide the analogous information along the other two orthogonal axes. An optimisation procedure (not unlike a Sudoku game) can then be adopted to estimate the (unique) set of velocities on a regular three-dimensional grid which can produce the distributions measured along the cardinal axes. In the work of Baker *et al.* (2018), steady state flow is imposed thanks to a conveyer belt on two granular materials with different degrees of sphericity. Representative results of the stream-lines and velocity magnitudes are reported in Figure 19, revealing a highly planar flow (unlike the simulated results for a fluid), which is then successfully matched to DEM simulations.

5 DISCUSSION AND CONCLUDING REMARKS

5.1 Potential for geomechanics

Imaging techniques of the type illustrated in the previous sections allow for unprecedented observations and a renewed understanding of geo-materials and processes – as stated by Viggiani *et al.* (2014), they "allow old questions to be revisited with relatively low experimental effort yet with the promise of gaining great insight and the potential for surprising observations of unexpected structures". Furthermore, these techniques provide, when combined with appropriate image analysis tools, *quantitative* information – images are experimental *data*. As such, they open new opportunities for theoretical and computational developments. In fact, the basis for constitutive models for geomaterials has historically been phenomenology: observations at the laboratory specimen level, and establishing a correlation between stress and strain. The goal has been to fit observable experimental data (stress-strain) by making use of models that depend on material properties or variables in order to explain the observed macroscopic behavior. In our opinion, the advances in experimental geomechanics that have been discussed in this paper have the potential to transform the way macroscopic stress-strain relations are developed, treated and used in practice. The road is now open for developing and *micro-inspired (continuum) constitutive models*, equipped with measurable micro-mechanics-based variables describing the evolution of the dominant inelastic processes. In other words, it is now possible to think of models possessing a direct and clear link between the macroscopic mechanical behavior and the statistically averaged evolution of the micro-structure – see, *e.g.*, the work by Tengattini *et al.* (2014) and Das *et al.* (2014).

For granular geomaterials (*i.e.*, sand and sandstone), the ability to acquire 3D images with a resolution of a few microns allows the grain-scale to be experimentally accessed, and phenomena to be characterized at this scale. This kind of measurement opens many doors: to treat particles discretely and analyze their collective behavior with complex networks (*e.g.*, Tordesillas *et al.*, 2013), as well as discrete particle-by-particle simulations (see the recent *Level Set DEM* by Andrade and coworkers: Lim *et al.* 2016, Kawamoto *et al.* 2016, 2018). It should be noted that many open metrological questions remain, since the development of accurate and well-characterized image analysis tools is a careful procedure (see Wiebicke *et al.* 2017), however the tempting prospect of an-

swering longstanding macro-questions at the micro-scale makes the challenge worth facing.

5.2 X-rays and physical modeling

This paper has mainly discussed the application of imaging to *element testing*. However, imaging is also of interest when applied to small-scale laboratory models, *i.e.*, *physical modeling*. Physical models can be defined as "physical idealizations of all or part of an envisioned geotechnical system" (White *et al.* 2013). They may provide qualitative and quantitative insights into soil-structure interaction and geotechnical behavior – particularly where simulation by numerical methods is problematic. Given the complexity of soil constitutive behavior and the complex deformations and processes in some construction technologies, physical modeling provides a basis to assess fundamental modes of behavior in controlled conditions – a more convenient method of gaining knowledge than observing or simulating the full geotechnical system. Physical models use well-characterized soil and known boundary conditions, thus providing reliable performance data for a given idealized problem. Of course, proper application of scaling laws is vital when interpreting physical model tests. In other terms, in order to link physical model test data to a field scale prototype, correct account must be made of the influence of size and timescale effects. In general, test conditions are admittedly not representative of true field, real engineering conditions. In fact, some of the results obtained from such physical models cannot (*and should not*) be directly extrapolated to field cases. However, due to well-defined and fully known testing conditions, physical models provide valuable results, which can be used to validate theoretical solutions or numerical models.

Otani and coworkers at the University of Kumamoto have pioneered the use of x-ray imaging in physical modeling. They have studied a number of geotechnical problems, including soil arching in a reinforced embankment with a rigid pile foundation system (Eskişara *et al.* 2012), compaction grouting (Takano *et al.* 2013), laterally loaded piles (Otani *et al.* 2006), the interaction behavior between soil and face bolts in tunnels (Takano *et al.* 2006a, 2006b, 2009, 2010), and cavity generation in soils subjected to sewerage defects (Mukunoki *et al.* 2010).
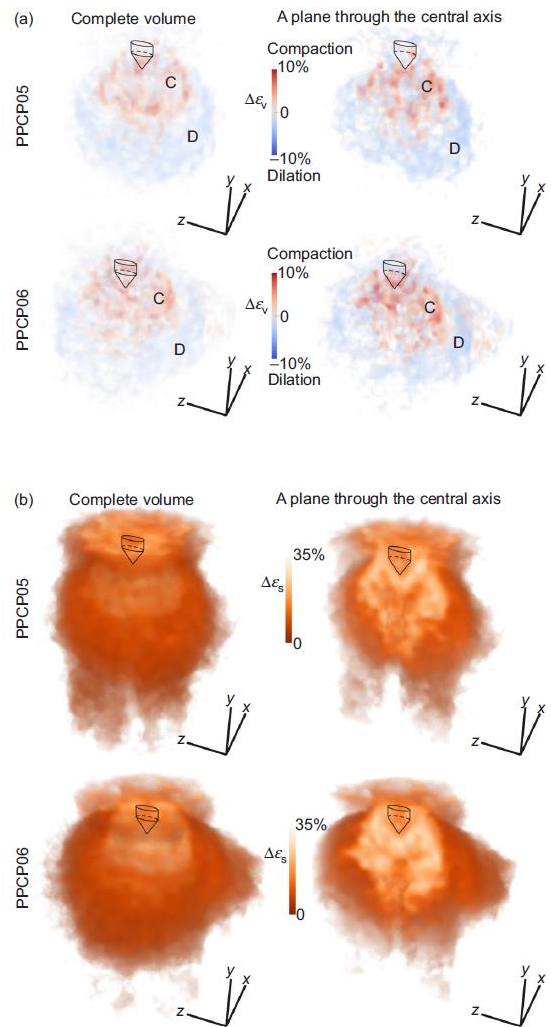
Figure 20. Incremental volumetric (a) and deviatoric (b) strains on the influence area of the cone during a 5mm penetration step of two cone penetration tests in silt (after Paniagua et al. 2013).

More recently, a few model-scale studies investigated the penetration of a probe (simulating either a penetrometer or a pile) into a soil, by means of

mini calibration chambers specifically designed to be tested inside an x-ray tomograph. Paniagua *et al*. (2013) performed cone penetration tests in silt, and used 3D DIC to quantify the evolution of displacement and strain fields in the soil. During insertion of the instrumented probe, they identified a contractant bulb of silt close to the tip of the probe surrounded by a larger bulb of dilating material – see Figure 20.
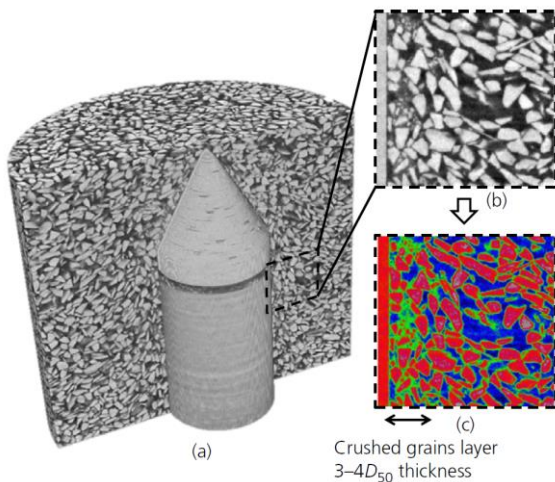
Figure 21. (a) 3D reconstructed volume after pile installation; (b) zoom on the interface; (c) detection of different phases (blue = pores, red = intact grains, and green = fines) (please note that, for practical reasons, the pile is installed from the bottom of the cell, i.e., it moves upwards) (after Doreau-Malioche et al. 2013).

The results obtained (in particular the failure mechanisms observed) shed new light on the mechanics of cone penetration in silt and consequently reflect on the interpretation of in situ CPTs. The mechanisms occurring at the grain scale at sand–pile interface under (displacement controlled) axial cyclic loading were analyzed quantitatively in a mini calibration chamber by Doreau-Malioche *et al*. (2017), again using x-ray tomography and 3D DIC. *Individual* grain kinematics and porosity evolution are followed along with the macroscopic mechanical response of the interface. Different phases in the evolution of shaft resistance during cyclic loading were observed, with a non-negligible increase of shaft resistance in the latter

phase. A layer of crushed grains (about $4D_{50}$ wide) was observed at the interface – see Figure 21. The powder resulting from grain crushing is highly packed and fills the pores between intact grains. Most of particle crushing occurred during pile installation.

Alcarez-Borges *et al*. (2018) explored the use of x-ray imaging to determine the changes in bulk density associated with chalk crushing and remolding during the penetration of a mini-pile into chalk. They observed the remolded chalk annulus and measured its thickness. Thanks to 3D imaging, they found out that pile installation in the radially confined chalk specimen took place, primarily, by crushing and densification of the chalk under the pile tip.

A final thought concerns centrifuge modeling, which is widely used in geotechnical engineering research (*e.g*., the series of the International Conferences on Centrifuge Modelling in Geotechnical Engineering – ICCMGE – the last of which took place in UK in August this year). As it is well-known, the purpose of spinning physical models on the centrifuge is to increase the g-forces on the model so that stresses in the model are equal to stresses in the prototype. Geotechnical centrifuges are typically equipped with high-speed digital cameras that take on-the-fly images of one or more sides of the model. Although the experiments do not necessarily need to be in 2D, in fact the recorded photographs are (by definition) in 2D. It would be of course of extreme interest to couple geotechnical centrifuge testing and x-ray radiography – or even tomography, *i.e*, 3D (volume) imaging. Technological advances are so fast these days that one cannot exclude this is going to become possible in the near future.

5.3 Availability / practicality

A crucial issue is practicality: clearly the methods discussed in this paper are of interest, but which can reasonably be used in a "standard" geomechanics laboratory and which require large investments?

The technology of laboratory x-ray tomographs is relatively simple, accessible, and readily adoptable for geotechnical applications. In fact, in recent years there has been a rapid proliferation of laboratory x-ray imaging facilities of ever increasing quality and decreasing cost, also thanks to the large demand – recent estimates place the overall number of tomographs to several tens of thousands including hospital and industrial scanners. This broad availability, coupled with the tremendous insight they allow, is certainly at the core of the ever increasing scientific interest, also testified by the ever growing dedicated conferences and workshops (*e.g.*, the series of the biennial International Conferences on Tomography of Materials and Structures – ICTMS – the last of which took place in Australia in July this year).

When the spatial and temporal resolutions of lab scanners is insufficient, forty to fifty synchrotron sources (*e.g.*, ESRF in France, DESY in Germany, PSI in Switzerland, DIAMOND in the UK, APS in the USA, SPring-8 in Japan, and ANSTO in Australia) are also available for free, although accessing them requires the successful submission of scientific proposals which are then ranked in rather competitive rounds. However, as shown by Viggiani *et al.* (2014), insightful, high-impact findings can be made with relatively modest x-ray lab devices without having to resort to limited-access synchrotron sources.

As for neutron tomography, it clearly requires large scale facilities, such as ILL in France, TUM in Germany, ISIS in the United Kingdom, and PSI in Switzerland. Laboratory neutron scanners are also available, but their cost and flux is still not competitive with that of x-ray scanners, albeit the unique properties of neutrons still make them of great interest for some specific research applications.

6 ACKNOWLEDGEMENTS

7 REFERENCES

Alshibli, K., Cil, M.B., Kenesei, P., Lienert, U. 2013. Strain tensor determination of compressed individual silica sand particles using high-energy synchrotron diffraction. *Granular Matter*, **15**, 5, 517-530.

Alvarez-Borges, F.J., Richards, D.J., Clayton, C.R.I., Ahmed, S.I. 2018. Application of X-ray computed tomography to investigate pile penetration mechanisms in chalk. In: *Engineering in Chalk*, Proceedings of the Chalk 2018 Conference, ICE, 565-570.

Andò, E., Hall, S. A., Viggiani, G., Desrues, J., Bésuelle, P. 2012a. Grain-scale experimental investigation of localised deformation in sand: a discrete particle tracking approach. *Acta Geotechnica*, **7**, 1, 1-13.

Andò, E., Dijkstra, J., Roubin, E., Dano, C., Boller, E. 2019. A peek into the origin of creep in sand. *Granular Matter*, **21**, 11.

Andò, E., Hall, S. A., Viggiani, G., Desrues, J., Bésuelle, P. 2012b. Experimental micromechanics: grain-scale observation of sand deformation. *Géotechnique Letters*, **2**, 3, 107-112.

Andò, E., Viggiani, G., Hall, S. A., Desrues, J. 2013. Experimental micro-mechanics of granular media studied by X-ray tomography: recent results and challenges. *Géotechnique Letters*, **3**, 142-146.

Andrade, J.E., Vlahinić, I., Lim, K.W., Jerves, A. 2012. Multiscale 'tomography-to-simulation' frame-work for granular matter: the road ahead. *Géotechnique Letters*, **2**, 135-139.

Arthur, J.R.F., Dunstan, T. 1982. Rupture layers in granular media. *Proceedings of IUTAM Conference on Defects and Failure in Granular Media*, Balkema, 453-459.

Baker, J., Guillard F., Marks, B., Einav, I. 2018. X-ray rheography uncovers planar granular flows despite non-planar walls. *Nature communications* **9**, 5119.

Banhart, J., Borbély, A., Dzieciol, K., Garcia-Moreno, F., Manke, I., Kardjilov, N., Kaysser-Pyzalla, A.R., Strobyl, M., Triemer, W. 2010. X-ray and neutron imaging – complementary techniques for materials science and engineering. *Int. J. Mater. Res.,* **101**, 1069-1079.

Baruchel, J. 2000. *X-ray Tomography in Materials Science*. Paris: Editions Hermes.

Bransby, P.J., Blair-Fish, P.M. 1975. Deformation near rupture surfaces in flowing sand. *Géotechnique*, **25**, 2, 384-389.

Bésuelle, P., Andò, E. 2014. Characterization of the mechanisms of deformation at the small scale in a clay rock by in-situ X-ray micro tomography. In: *International Symposium on Geomechanics from Micro to Macro*, Cambridge, UK.

Calvert, S., Veevers, J. 1962. Minor structures of unconsolidated marine sediments revealed by x-ray radiography. *Sedimentology*, **1**, 4, 287-295.

Casagrande, A., Watson, J.D. 1938. Compaction tests and critical density investigations of cohesionless materials for Franklin Falls Dam, Merrimack Valley flood control. *Corps of Engineers, U.S. Army Engng Office*, BII-7.

Cil, M.B., Alshibli, K., Kenesei, P., Lienert, U. 2014. Combined high-energy synchrotron X-ray diffraction and computed tomography to characterize constitutive behavior of silica sand. *Nuclear Instruments and Methods in Physics Research Section B*, **324**, 11-16.

Cnudde, V., Boone, M.N. 2013. High-resolution X-ray computed tomography in geosciences: a review of the current technology and applications. *Earth-Science Reviews*, **123**, 1-17.

Comina, C., Cosentini, R.M., Della Vecchia, G., Foti, S., Musso, G. 2011. 3D-electrical resistivity tomography monitoring of salt transport in homogeneous and layered soil samples. *Acta Geotechnica*, **6**, 195-203.

Comina, C, Foti, S, Musso, G, Romero, E 2008. EIT oedometer – an advanced cell to monitor spatial and time variability in soil. *Geotechnical Testing Journal*, ASTM, **31**, 5, 404-412.

Daphalapurkar, N., Wang, F., Fu, B., Lu, H., Komanduri, R. 2011. Determination of Mechanical Properties of Sand Grains by Nanoindentation. *Experimental Mechanics*, **51**, 719-728.

Das, A., Nguyen, G.D., Einav, I. 2013. The propagation of compaction bands in porous rocks based on breakage mechanics. *Journal of Geophysical Research: Solid Earth*, **118**, 2049-2066.

Das, A., Tengattini, A., Nguyen, G.D., Viggiani, G., Hall, S.A., Einav, I. 2014. A thermomechanical constitutive model for cemented granular materials with quantifiable internal variables. Part II – Validation and localization analysis. *Journal of the Mechanics and Physics of Solids*, **70**, 382-405.

Dauti, D., Tengattini, A., Dal Pont, S., Toropovs, N., Briffaut, M., Weber, B. 2018. Analysis of moisture migration in concrete at high temperature through in-situ neutron tomography. *Cement and Concrete Research*, **111**, 41-55.

de Beer, F.C., Middleton, M.F. 2006. Neutron radiography imaging, porosity and permeability in porous rocks. *S. Afr. J. Geol.*, **109**, 541-550.

de Beer, F.C., Middleton, M.F., Hilson, J. 2004. Neutron radiography of porous rocks and iron ore. *Appl. Radiat. Isot.*, **61**, 487–495.

de Beer, F.C., le Roux, J.J., Kearsley, E.P. 2005. Testing the durability of concrete with neutron radiography. *Nucl. Instrum. Methods Phys. Res. A* **542**, 226-231.

Deinert, M.R., Parlange, J.-Y., Steenhuis, T., Throop, J., Ünlü, K., Cady, K.B. 2004. Measurement of fluid contents and wetting front profiles by real-time neutron radiography. *J. Hydrol.*, **290**, 192-201.

DeJong, J.T., Fritzges, M.B., Nüsslein, K. 2006. Microbially induced cementation to control sand response to undrained shear. *J. Geotech. Geoenviron. Eng.*, **132**, 1381-1392.

Derfouf, F., Li, Z., Abou-Bekr, N., Taibi, Z., Fleureau, J. 2019. A New Osmotic Oedometer with Electrical Resistivity Technique for Monitoring Water Exchanges. *Geotechnical Testing Journal*, **43**.

Desbois, G., Höhne, N., Urai, J.L., Bésuelle, P., Viggiani, G. 2017. Deformation in cemented mudrock (Callovo–Oxfordian Clay) by micro-cracking, granular flow and phyllosilicate plasticity: insights from triaxial deformation, broad ion beam polishing and scanning electron microscopy. *Solid Earth*, **8**, 291-305.

Desrues, J. 2004. Tracking Strain Localization in Geomaterials Using Computerized Tomography.

Proc. Int. Workshop on X-ray CT for Geomaterials, Kumamoto, Japan, Balkema, Lisse, The Netherlands, 15-41.

Desrues, J., Chambon, R., Mokni, M., Mazerolle, F. 1996. Void ratio evolution inside shear bands in triaxial sand specimens studied by computed tomography. *Géotechnique*, **46**, 3, 527-546.

Dierick, M., Vlassenbroeck, J., Masschaele, B., Cnudde, V., van Hoorebeke, L., Hillenbach, A. 2005. High-speed neutron tomography of dynamic processes. *Nucl. Instrum. Methods Phys. Res. A*, **542**, 296-301.

Doreau-Malioche, J., Combe, G., Viggiani, G., Toni, J.B. 2018. Shaft friction changes for cyclically loaded displacement pile: an x-ray investigation. *Géotechnique Letters*, **8**, 1-7.

Druckrey, A., Alshibli, K.A., Al-Raoush, R. 2018. Discrete Particle Translation Gradient Concept to Expose Strain Localization in Sheared Granular Materials using 3D Experimental Kinematic Measurements. *Géotechnique*, **68**, 2, 162-170.

El Abd, A.E., Czachor, A., Milczarek, J.J., Pogorzelski, J. 2005. Neutron radiography studies of water migration in construction porous materials. *IEEE Trans. Nucl. Sci.*, **52**, 229-304.

Eskişara, T., Otani, J., Hironaka, J. 2012. Visualization of soil arching on reinforced embankment with rigid pile foundation using X-ray CT. *Geotextiles and Geomembranes*, **32**, 44-54.

Etxegarai, M., Tudisco, E., Tengattini, A., Hall, S.A., Viggiani, G. 2017. Hydromechanical behavior of porous rock studied with neutron tomography. *Proceedings 3rd Int. Conf. on Tomography of Materials and Structures*, Lund, Sweden.

Gardner, W., Kirkham, D. 1952. Determination of soil moisture by neutron scattering. *Soil Science*, **73**, 5, 391-402.

Guillard, F., Marks, B., Einav, I. 2017. Dynamic X-ray radiography reveals particle size and shape orientation fields during granular flow. *Scientific Reports*, **7**, 8155.

Hall, S.A. 2013. Characterization of fluid flow in a shear band in porous rock using neutron radiography. *Geophysical Research Letters*. **40**, 11, 2613-2618.

Hall, S.A., Wright, J., Pirling, T., Andò, E., Hughes, D.J., Viggiani, G. 2011. Can intergranular force transmission be identified in sand? *Granular Matter*, **13**, 251-254.

Hall, S.A., Wright, J. 2015. Three-dimensional experimental granular mechanics. *Géotechnique Letters*, **5**, 4, 236-242.

Hall, S.A., Hurley, R.C., Wright, J. 2018. Micromechanics of Granular Media Characterised Using X-Ray Tomography and 3DXRD. In: *Micro to Macro Mathematical Modelling in Soil Mechanics*, Birkhäuser, Cham, 169-176.

Hall, S.A., Tudisco, E. 2012. Full-field ultrasonic measurement (ultrasonic tomography) in experimental geomechanics. In: *Advanced experimental techniques in geomechanics*, G. Viggiani, S.A. Hall and E. Romero Eds., 103-124.

Hamblin, W. K. 1962. X-ray radiography in the study of structures in homogeneous sediments. *Journal of Sedimentary Research*, **32**, 2, 201-210.

Hess, K.-U.A., Flaws, M.J., Mühlbauer, B., Schillinger, A., Franz, M., Schulz, E., Calzada, D.B., Dingwell, Bente, K. 2011. Advances in high-resolution neutron computed tomography adapted to the earth sciences. *Geosphere*, **7**, 1294-1302.

Higo, Y., Oka, F., Kimoto, S., Sanagawa, T., Matsushima, Y. 2011. Study of strain localization and microstructural changes in partially saturated sand during triaxial tests using microfocus X-ray CT. *Soils and Foundations,* **51**, 95-111.

Higo, Y., Oka, F., Sato, T., Matsushima, Y., Kimoto, S. 2013. Investigation of localized deformation in partially saturated sand under triaxial compression using microfocus X-ray CT with digital image correlation. *Soils and Foundations*, **53**, 181-198.

Hild, F., Espinosa, H.D. (Editors) 2012. Full field measurements and identification in Solid Mechanics. Special Issue of *IUTAM Procedia*,**4**, 1-226.

Hu, C., Zongjin, L. 2015. A review on the mechanical properties of cement-based materials measured by nanoindentation. *Construction and Building Materials*, **90**, 80-90.

Hurley, R.C., Hall, S.A., Andrade, J.E., Wright, J. 2016. Quantifying interparticle forces and heterogeneity in 3D granular materials. *Physical Review Letters*, **117**, 098005.

Hurley, R.C., Hall, S.A., Wright, J. 2017. Multi-scale mechanics of granular solids from grain-resolved x-ray measurements. *Proceedings of the Royal Society A*, **473**, 0491.

Hurley, R.C., Lind, J., Pagan, D.C., Akin, M.C., Herbold, E.B. 2018a. In situ grain fracture mechanics during uniaxial compaction of granular

solids. *Journal of the Mechanics and Physics of Solids*, **112**, 273-290.

Hurley, R.C, Herbold, E.B., Pagan, D.C. 2018b. Characterization of the crystal structure, kinematics, stresses and rotations in angular granular quartz during compaction. *Journal of Applied Crystallography*, **51**(4), 021-1034.

Jailin, C., Etxegarai, M., Tudisco, E., Hall, S.A., Roux, S. 2018, Fast Tracking of Fluid Invasion Using Time-Resolved Neutron Tomography. *Transport in Porous Media*, **124**, 1, 117-135.

Jasti, J.K., Lindsay, J.T., Fogler, H.S. 1987. Flow imaging in porous mediausing neutron radiography. *SPE Annual Technical Conf. and Exhibition*, Dallas, SPE **16950**, 175-182.

Karatza, Z., Andò, E., Papanicolopulos, S.A., Viggiani, G., Ooi, J.Y. 2019. Effect of particle morphology and contacts on particle breakage in a granular assembly studied using x-ray tomography. *Granular Matter*, **21**, 44.

Kardjilov, N., Manke, I., Hilger, A., Strobl, M., Banhart, J. 2011. Neutron imaging in materials science. *Materials Today*, **14**, 248-256.

Kardjilov, N., Manke, I., Woracek, R., Hilger, A., Banhart, J. 2018. Advances in neutron imaging. *Materials Today*, **21:6**, 652-672.

Kawamoto, R., Andò, E., Viggiani, G., Andrade, J. 2016. Level set discrete element method for three-dimensional computations with triaxial case study. *Journal of the Mechanics and Physics of Solids*, **91**, 1-13.

Kawamoto, R., Andò, E., Viggiani, G., Andrade, J. 2018. All you need is shape: predicting shear banding in sand with LS-DEM. *Journal of the Mechanics and Physics of Solids*, **111**, 375-392.

Khaddour, G., Riedel, I., Andò, E., Charrier, P., Bésuelle, P., Desrues, J., Viggiani, G., Salager, S. 2018. Grain-scale characterization of water retention behaviour of sand using X-ray CT. *Acta Geotechnica*, **13**, 497-512.

Kim, F.H., Penumadu, D., Gregor J., Kardjilov, N., Manke, I. 2012. High-resolution neutron and X-ray imaging of granular materials. *J. of Geotechnical and Geoenvironmental Engineering*, **139**, 5, 715-723.

Kim, F., Penumadu, D., Kardjilov, N., Manke, I. 2016. High-resolution X-ray and neutron computed tomography of partially saturated granular materials subjected to projectile penetration. *International Journal of Impact Engineering*, **89**, 72-82.

Kirkpatrick, W.M., Belshaw, D.J. 1968. On the interpretation of the triaxial test. *Géotechnique*, **18**, 3, 336-350.

Kupperman, D.S., Hitterman, R.L., Rhodes, E., 1990. Energy dependent neutron imaging. *Review of Progress in Quantitative NDE Conference*, La Jolla, CA.

Lehmann, E.H., Vontobel, P., Kardjilov, N., 2004. Hydrogen distribution measurements by neutrons. *Appl. Radiat. Isot.*, **61**, 503-509.

Lenoir, N., Bornert, M., Desrues, J., Bésuelle, P., Viggiani, G. 2007. Volumetric digital image correlation applied to X-ray microtomography images from triaxial compression tests on argillaceous rocks. *Strain, International Journal for Experimental Mechanics*, **43**, 3, 193-205.

Lewis, J.T., Krinitzsky, E.E. 1976. Neutron radiation in the study of soil and rock. In: Berger, H. (Ed.), *Practical applications of neutron radiography and gaging*. ASTM STP 586. American Society for Testing and Materials, West Conshohocken, PA, 241-251.

Lewis, M.H., Tengattini, A., Couples, G.D., Tudisco, E., Charalampidou, E.M., Hall, S.A., Etxegarai, M., Edlmann, K. 2017. Neutron radiography and tomography used to characterise water flow through a low permeability carbonate altered by experimentally induced fracture. *Proceedings 3rd Int. Conf. on Tomography of Materials and Structures*, Lund, Sweden.

Lim, K.W., Kawamoto, R., Andò, E., Viggiani, G., Andrade, J.E. 2016. Multiscale characterization and modeling of granular materials through a computational mechanics avatar: a case study with experiment. *Acta Geotechnica*, **11**, 243-253.

Lopes, R.T., Bessa, A.P., Braz, D., de Jesus, E.F.O. 1999. Neutron computerized tomography in compacted soil. *Appl. Radiat. Isot.*, 50, 451-458.

Luong, M.P. 1990. Infrared thermovision of damage processes in concrete and rock. *Engineering Fracture Mechanics*, **35**, 1–3, 291-301.

Luong, M.P. 2007. Introducing infrared thermography in soil dynamics. *Infrared Physics & Technology*, **49**, 3, 306-311.

Majmudar, T.S., Behringer, R.P. 2005. Contact force measurements and stress-induced anisotropy in granular materials. *Nature*, **435**, 1079–1082.

Masschaele, B., Dierick, M., van Hoorebeke, L., Cnudde, V., Jacobs, P. 2004. The use of neutrons and

monochromatic X-rays for non-destructive testing in geological materials. *Environ. Geol.*, **46**, 486-492.

Middleton, M.F., Pàzsit, I. 1998. Neutron radiography: a technique to support reservoir analysis. *Explor. Geophys*., **29**, 512-515.

Mukunoki, T., Otani, J., Nonaka, S., Horii, T., Kuwano, R. 2010. Evaluation of Cavity Generation in Soils Subjected to Sewerage Defects using X-ray CT. In: *Advances in X-ray Tomography for Geomaterials*, J. Desrues et al. Eds, ISTE, 365-371.

Olbinado, M.P., Just, X., Gelet, J.L., Lhuissier, P., Scheel, M., Vagovic, P., Sato, T., Graceffa, R., Schulz, J., Mancuso, A., Morse, J., Rack, A. 2017. MHz frame rate hard X-ray phase-contrast imaging using synchrotron radiation. *Opt Express*, **25**(12), 13857-13871.

Otani, J., Pham, K.D., Sano, J. 2006. Investigation of failure patterns in sand due to laterally loaded pile using X-ray CT. *Soils and Foundations*, **46**, 4, 529-535.

Paniagua, P., Andò, E., Silva, M., Emdal, A., Nordal, S., Viggiani, G. 2013. Soil deformation around a penetrating cone in silt. *Géotechnique Letters*, **3**, 185-191.

Perfect, A., Cheng, C.-L., Kang, M., Bilheux, H.Z., Lamannad, J.M., Gragge, M.J., Wright, D.M. 2014. Neutron imaging of hydrogen-rich fluids in geomaterials and engineered porous media: A review. *Earth Science Reviews*, **129**, 120-135.

Pleinert, H., Sadouki, H., Wittmann, F.H. 1998. Determination of moisture distributions inporous building materials by neutron transmission analysis. *Mater. Struct*., **31**,218-224.

Prazak, J., Tywoniak, J., Peterka, F., Slonc, T. 1990. Description of transport of liquid in po-rous media—a study based on neutron radiography data. Int. J. *Heat Mass Transfer*, **33**, 1105-1120.

Reijonen, H., Pihlajavaara, S. 1972. On the determination by neutron radiography of the thickness of the carbonated layer of concrete based upon changes in water content. *Cement and Concrete Research*, **2**, 5, 607-615.

Roscoe, K.H. 1970. The influence of strains in soil mechanics, 10th Rankine Lecture, *Géotechnique*, **20** (2), 129-170.

Roscoe, K.H., Arthur, J.R.F., James, R.G. 1963. The determination of strains in soils by an x-ray method. Civ. Eng. Public Works Rev., **58**, 873-876 and 1009-1012.

Roshankhah, S., Marshall, J.P., Tengattini, A., Andò, E., Rubino, V., Rosakis, A.J., Viggiani, G., Andrade, J. 2018. Neutron Imaging: A New Possibility for Laboratory Observation of Hydraulic Fracture in Shale? *Géotechnique Letters*, **8**, 4, 1-23.

Roubin, E., Andò, E., Roux, S. 2019. The colours of concrete as seen by X-rays and neutrons. *Cement and Concrete Composites*, **104**.

Saadatfar, M., Francois, N., Arad, A., Madadi, M., Sheppard, A., Senden, T., Knackstedt, M. 2013. Grain-based characterisation and acoustic wave propagation in a sand packing subject to triaxial compression. *AIP Conference Proceedings* 1542, 571-574.

Salami, Y., Dano, C., Hicher, P.Y. 2017. Infrared thermography of rock fracture. *Géotechnique Letters*, **7**, 1-5.

Scheel, M., Seemann, R., Brinkmann, M., Di Michiel, M., Sheppard, A., Breidenbach, B., Herminghaus, S. 2008. Morphological clues to wet granular pile stability. *Nature Materials*, **7**, 189-193.

Sheppard, S., Mantleb, M.D., Sedermanb, A.J., Johnsb, M.L., Glad-den, L.F. 2003. Magnetic resonance imaging study of complex fluid flow in porous media: flow patterns and quantitative saturation profiling of amphiphilic fracturing fluid displacement in sandstone cores. *Magnetic Resonance Imaging*, **21**, 365-367.

Solymar, M., Fabricius, I., Middleton, M. 2003. Flow characterization of glauconitic sandstones by integrated dynamic neutron radiography and image analysis of backscattered electron micrographs. *Pet. Geosci*. **9**, 175-183.

Stavropoulou, E., Andò, E., Tengattini, A., Briffaut, M., Dufour, F., Atkins, D., Armand, G. 2019a. Liquid water uptake in unconfined Callovo-Oxfordian Clay-rock studied with neutron and x-ray imaging. *Acta Geotechnica*, **14**, 1, 19-33.

Stavropoulou, E., Andò, E., Roubin, E., Lenoir, N., Tengattini, A., Briffaut, M., Bésuelle, P. 2019b. Dynamics of water absorption in Callovo-Oxfordian Clayrock revealed with multimodal x-ray and neutron tomography. *Frontiers*, under review.

Subramanian, R., Burkhart, D. 1973. Determination by Neutron Radiography of the Location of Polymeric Resins Injected in Rock Fissures. *Nuclear Technology*, **17**, 2, 184-188.

Sváb, E., Balaskó, M., Kõrösi, F. 2000. Dynamic neutron radiography in petrophysical application. *Physica B*. 276–278, 916–917.

Tagliaferri, F., Waller, J., Andò, E., Hall, S.A., Viggiani, G., Bésuelle, P., DeJong, J.T. 2011. Observing strain localisation processes in bio-cemented sand using x-ray imaging. *Granular Matter*, **13**, 247-250.

Takano, D., Otani, J., Fukushige, S., Natagani, H. 2010. Investigation of interaction behavior between soil and face bolts using X-ray CT. In: *Advances in X-ray Tomography for Geomaterials*, J. Desrues et al. Eds, ISTE, 389-395.

Takano, D., Otani, J., Mukunoki, T., Date, K., Yokota, Y. 2006a. Reinforcing effect of face bolts for tunneling - application of X-ray CT and centrifuge model test. *Proceedings 17th ICSMGE*, 2469-2472.

Takano, D., Morikawa, Y., Nishimura, S., Takehana, K. 2013. Experimental study on compaction routing method for liquefiable soil using centrifuge test and X-ray tomography. *Proceedings 18th ICSMGE*, Paris, 965-968.

Takano, D., Nagatani, H., Otani, J., Mukunoki, T. 2006b. Evaluation of auxiliary method in tunnel construction using X-ray CT. *Proceedings of 6th Int. Conf. on Physical Modelling in Geotechnics*, Hong Kong, 1189-1194.

Tengattini, A., Das, A., Nguyen, G.D., Viggiani, G., Hall, S.A., Einav, I. 2014. A thermomechanical constitutive model for cemented granular materials with quantifiable internal variables. Part I – Theory. *Journal of the Mechanics and Physics of Solids*, **70**, 281-296.

Tengattini, A., Atkins, D., Giroud, B., Andò, E., Beaucour, J., Viggiani, G. 2017. NeXT-Grenoble, a novel facility for neutron and x-ray tomography in Grenoble. *Proceedings 3rd Int. Conf. on Tomography of Materials and Structures,* Lund, Sweden.

Tengattini, A., Lenoir, N., Andò, E., Giroud, B., Atkins, D., Beaucour, J., Viggiani, G. 2019. NeXT-Grenoble, the neutron and x-ray tomograph in Grenoble. U*nder review*.

Tordesillas, A., Walker, D.M., Andò, E., Viggiani, G. 2013. Revisiting localised deformation in sand with complex systems. *Proceedings of the Royal Society A: Mathematical, Physical & Engineering Sciences*, **469**, 2152, 20120606.

Tötzke, C., Kardjilov, N., Manke, I., Oswald, S.E. 2017. Capturing 3D Water Flow in Rooted Soil by Ultra-fast Neutron Tomography. *Scientific Reports*, **7**, 6192.

Tudisco, E., Hall, S.A., Charalampidou, E.M., Kardjilov, N., Hilger, A., Sone, H. 2015. Full-field measurements of strain localisation in sandstone by neutron tomography and 3D-volumetric digital image correlation. *Physics Procedia - 10th World Conf. on Neutron Radiography*. Kaestner, A. (ed.). Elsevier, **69**. 509-515..

Tudisco, E., Hall, S.A., Athanasopoulos, S., Hovind, J. 2017a. Neutron imaging and digital volume corre-lation to analyse the coupled hydro-mechanics of geomaterials. *Rivista Italiana di Geotecnica*, **51**:4, 60-68.

Tudisco, E., Jailin, C., Mendoza, A., Tengattini, A., Andò, E., Hall, S.A., Viggiani, G., Hild, F., Roux, S. 2017b. An extension of digital volume correlation for multimodality image registration. *Measurement Science & Technology*, **28**, 9, 095401.

Tudisco, E., Etxegarai, M., Hall, S.A., Charalampidou, E.M., Couples, G.D., Lewis, H., Tengattini, A., Kardjilov, N. 2019. Fast 4-D Imaging of Fluid Flow in Rock by High-Speed Neutron Tomography. *Journal of Geophysical Research: Solid Earth*. **124**, 4, 3557-3569.

Tudisco, E., Roux, P., Viggiani, G.M.B., Hall, S.A., Viggiani, G. 2015. Timelapse ultrasonic tomography for measuring damage localisation in geomechanics laboratory tests. *The Journal of the Acoustical Society of America*, 137 (3), 1389-1400.

Tumlinson, L.G., Liu, H., Silk, W.K., Hopmans, J.W. 2008. Thermal neutron computed tomography of soil water and plant roots. *Soil Sci. Soc. Am. J.*, **72**, 1234-1242.

Van der Walt, S., Schönberger, J.L., Nunez-Iglesias, J., Boulogne, F., Warner, J.D., Yager, N., Gouillart, E., Yu, T. & the scikit-image contributors, 2014. "scikit-image: Image processing in Python", *PeerJ* 2:e453.

Vardoulakis, I., Graf, B. 1982. Imperfection sensitivity of the biaxial test on dry sand. *Proceedings IUTAM Symposium on Deformation and Failure of Granular Materials*, Balkema, 485-491.

Viggiani, G., Andò, E., Jaquet, C., Talbot, H. 2013. Identifying and following particle-to-particle contacts in real granular media: An experimental challenge. In Powders and Grains 2013, *Proceedings of the 7th International Conference on Micromechanics of Granular Media*, AIP Publishing, 1542, 1, 60-65.

Viggiani, G., Andò, E., Takano, D., Santamarina, J.C. 2015. X-ray tomography: a valuable experimental tool for revealing processes in soils. *Geotechnical Testing Journal*, ASTM, **38**, 1, 61-71.

Viggiani, G., Hall S.A. 2012. Full-field measurements in experimental geomechanics: historical perspective,

current trends and recent results. In: *Advanced experimental techniques in geomechanics*, G. Viggiani, S.A. Hall and E. Romero Eds., 3-67.

White, D.J., Gaudin, C., Take, W.A. 2013. General report for TC104 physical modelling in geotechnics. *Proceedings 18th ICSMGE*, Paris, IOS Press, Vol. 2, 867-873.

Wiebicke, M., Andò, E., Herle, I., Viggiani, G. 2017. On the metrology of interparticle contacts in sand from x-ray tomography images. *Measurement Science and Technology*, **28**, 12, 124007.

Wiebicke, M., Andò, E., Šmilauer, V., Herle, I., Viggiani, G. 2019a. A benchmark strategy for the experimental measurement of contact fabric. *Granular Matter*, 21-54.

Wiebicke, M., Andò, E., Viggiani, G., Herle, I. 2019b. Measuring the evolution of contact fabric in shear bands with x-ray tomography. *Acta Geotechnica*, under review.

Wilding, M., Lesher, C.E., Shields, K. 2005. Applications of neutron computed tomographyin the geosciences. *Nucl. Instrum. Methods Phys. Res. A*. **542**, 290-295.

Wilson, N.E., Harms, A.A., Emery, J.J. 1975. A neutron radiographic in vitro examination of soils. *Canadian Geotechnical Journal*, **12**, 152-156.

Winkler, B. 2006. Applications of neutron radiography and neutron tomography. *Rev. Mineral. Geochem.*, **17**, 459-471.

Xu, L., Li, Q., Myers, M., Chen, Q., Li, X. 2019. Application of nuclear magnetic resonance technology to carbon capture, utilization and storage: a review. *Journal of Rock Mechanics and Geotechnical Engineering*, **11**, 892-908.

Yehya, M., Andò, E., Dufour, F., Tengattini, A. 2018. Fluid-flow measurements in low permeability media with high pressure gradients using neutron imaging: Application to concrete. *Nuclear Instruments and Methods in Physics Research Section A*, **890**, 35-42.

Yu, H., Sun, D., Tian, H. 2019. NMR-based analysis of shear strength of weakly expansive clay in sodium chloride solution. *Magnetic Resonance Imaging*, 58, 6-13.

Zhou, B., Wang, J., Zhao, B. 2015. Micromorphology characterization and reconstruction of sand particles using micro X-ray tomography and spherical harmonics. *Engineering Geology*, **184**, 126-137.

XVII European Conference

ECSMGE 2019
Reykjavík

on Soil Mechanics
and Geotechnical Engineering

Extending the life of existing infrastructure
Prolonger la durée de vie des infrastructures existantes

L. Zdravković

Imperial College London, London, United Kingdom

D. M. Potts

Imperial College London, London, United Kingdom

T. M. Bodas Freitas

CERIS, Instituto Superior Técnico, Universidade de Lisboa, Lisboa, Portugal

ABSTRACT: Contemporary geotechnical design is increasingly faced with a demand for extending the life of ageing infrastructure. Typical examples are foundation systems for re-development projects in congested urban environments, road and rail infrastructure and flood defences. The latter structures in particular are also projected to have to sustain rising sea-levels due to the effects of climate change. To enable such a design, the changes in the mechanical behaviour of the foundation soil over the period from first construction to the current state must be quantified. This transient period is governed by the time-related process of consolidation and creep in the ground. Considering examples of earthfill embankments, this paper discusses the facets of soil behaviour governing both the short- and long-term design of existing infrastructure embankments, using advanced numerical analysis.

RÉSUMÉ: La domaine de la géotechnique contemporaine est de plus en plus confrontée à la nécessité de prolonger la durée de vie d'infrastructures vieillissantes. Des exemples typiques sont les systèmes de fondations pour les projets de re-développement dans les environnements urbains encombrés, les infrastructures routières et ferroviaires et les défenses contre les inondations. Ces dernières structures, en particulier, devraient également faire face à l'élévation du niveau de la mer en raison des effets du changement climatique. Pour pallier de telles contraintes, les changements dans le comportement mécanique du sol de fondation au cours de la période allant de la première construction à l'état actuel doivent être quantifiés. Cette période transitoire est régie par le processus temporel de consolidation et de fluage du sol. À l'aide d'exemples de remblais en terre, ce document de recherche traite des aspects du comportement du sol régissant la conception à court et à long terme des remblais d'infrastructures existants, à l'aide d'une analyse numérique avancée.

Keywords: earth embankment; anisotropy; creep; numerical analysis;

1 INTRODUCTION

Earthfill embankments are common geotechnical structures for supporting networks of road and rail infrastructure and serving as flood defences along river banks and coastlines. They are often erected on soft clay deposits whose undrained strength limits the construction height of a single-stage embankment to 3 to 4 m. Bjerrum (1973) postulated that the strength anisotropy of soft clay deposits may be the key parameter for the short-term embankment design, as its structure imposes large rotations of principal stresses in the foundation soil, promoting the mobilisation of variable soil strength along the potential failure surface.

The effect of strength anisotropy can only be reasonably quantified through the application of advanced numerical analysis which employs appropriate constitutive models (e.g. Karstunen et al., 2005; Zdravković et al., 2002; Kavvadas & Amorosi, 2000; Whittle & Kavvadas, 1994).

During the transient post-construction period the foundation soil is subjected to time-related processes of consolidation and creep, the former dissipating the construction-generated pore water pressures in the ground and the latter accounting for changes in the soil fabric. These processes can induce large settlements, thus requiring the raising of the embankment height so that it can continue to fulfil its purpose. The reduction of void space in the foundation soil leads to an increase of its undrained strength. Again, advanced numerical analysis and appropriate soil constitutive models are needed to quantify the likely gain in undrained strength and the likely height to which an embankment can be raised without failing (e.g. Yin & Graham, 1999; Bodas Freitas et al., 2011, 2015; Karstunen & Yin, 2010).

Using numerical analysis and a number of case studies, this paper demonstrates the effect that the soil strength anisotropy has on the short-term design of soft-ground embankments, and the effect of creep on its long-term behaviour and ability for subsequent life extension. All analyses were performed using the Imperial College Finite Element Program (ICFEP; Potts & Zdravković, 1999), employing a hydro-mechanically coupled formulation, with appropriate time steps to simulate realistic construction sequences.

2 SHORT-TERM DESIGN

Faced with the need to build road embankments on soft Champlain deposits in east Canada, researchers at Laval University developed in the 1970s a large research programme that involved construction and monitoring of a number of trial embankments on Champlain clays at the Saint-Alban site in Quebec. The test embankment 'A' (Fig. 1) was brought to failure and was the subject of the numerical study by Zdravković et al. (2002) which quantified the effect of strength anisotropy on the short-term design of this embankment.
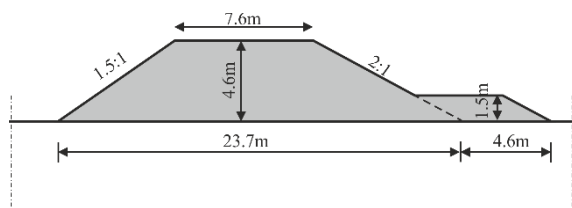
Figure 1. Cross-section of Saint-Alban embankment

2.1 Ground conditions

The soil investigation programme comprised a number of field and laboratory experiments on Champlain clays (e.g. Lefebvre et al., 1988; Leroueil et al., 1983), revealing highly anisotropic undrained strength, S_u, profiles. A typical desiccated crust exists up to 2 m depth, below which the clay is lightly overconsolidated, with $OCR = 2.2$ and $K_0^{OC} = 0.65$. The ground water level was found at 0.7 m depth and the permeability of the clay is in the range of 10^{-10} to 10^{-9} m/s, which indicates that undrained conditions are likely to exist in the foundation soil during embankment construction. The angle of shearing resistance was found to be $\phi'_{TXC} = 27°$ and $\phi'_{TXE} = 25°$, in triaxial compression and extension, respectively.

The embankment fill was a uniform medium to coarse sand, containing about 10% gravel, with an angle of shearing resistance $\phi'_{TXC} = 44°$.

2.2 Numerical modelling

A limit equilibrium analysis by the research team at Laval University predicted that the embankment A, with its cross-section depicted in Fig. 1, would fail at 4.6 m height, on the side of the steeper slope (1.5:1 horizontal to vertical). In the actual event the failure height was 3.9 m.

The main aspect of the finite element analyses conducted by Zdravković et al. (2002) was the choice of a constitutive model to represent the

foundation soil. The measured profiles of S_u in Fig. 2 are obtained from undrained triaxial compression (TXC) tests on isotropically-consolidated clay samples (CIU) and from a range of vane tests that were shown to give S_u values similar to direct simple shear (DSS) strengths (Lefebvre et al., 1988). The inclination of the major principal stress, σ'_1, in the former tests is vertical (i.e. $\alpha = 0^o$), while in the latter tests the σ'_1 is thought to be at around $\alpha = 45^o$ to the vertical. Consequently, there is a significant strength anisotropy in the soil from the profiles in Fig. 2.
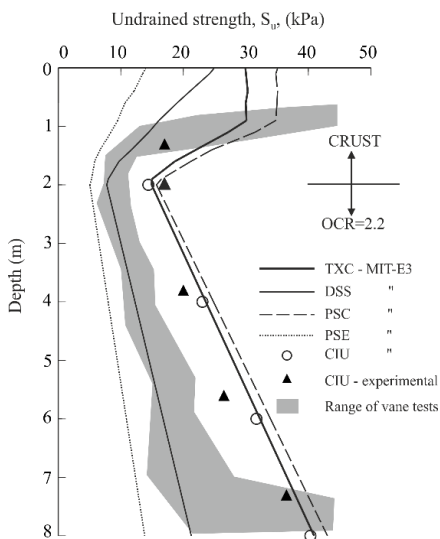
Figure 2. S_u profiles for the Champlain clay deposit

A critical state-based Modified Cam Clay (MCC) constitutive model (Roscoe & Burland, 1968) may be an obvious choice for modelling the behaviour of soft clays on the wet side of the critical state. However, this model can simulate only an isotropic undrained strength and in this study it was calibrated to reproduce either a TXC or a DSS S_u profile from Fig. 2. The former is most likely to be available from any site investigation, whereas the latter strength was recommended by Bjerrum (1973) as an appropriate average strength for the design of soft clay embankments. Conversely, an anisotropic MIT-E3 model (Whittle & Kavvadas, 1994), devel-

oped in the framework of bounding surface plasticity, was also employed in this investigation and calibrated to simulate the observed anisotropic nature of the soil's undrained strength. The calibrated MIT-E3 S_u profiles in Fig. 2 correspond to TXC (agreeing well with the measured CIU profile) and DSS (ploting in the range of vane tests) strengths. Also shown are the plane strain compression (PSC) and extension (PSE) profiles as limiting values (at $\alpha = 0^o$ and 90° respectively) of S_u that bound the strengths that the foundation soil can mobilise during embankment construction. The calibration process and parameters derived for both models are given in Zdravkovic et al. (2002).

2.3 Implications for short-term design

Fig. 3 shows the variation of the normalised horizontal movement, u, at the toe, with increase in embankment height, indicating also the predicted failure heights. Recalling that the trial embankment failed when reaching 3.9 m height, none of the analyses that modelled the foundation soil as isotropic (MCC) were able to predict the correct failure. Adopting the TXC profile of S_u is clearly unsafe, predicting that the embankment can be 1 m higher. Conversely, the DSS-based design is overly conservative, predicting a 0.6 m lower failure height from that observed in the field.
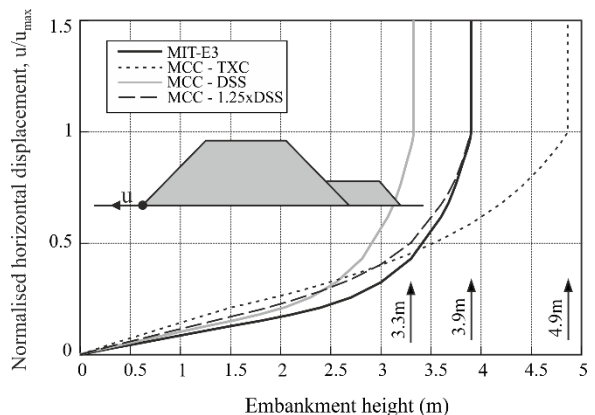
Figure 3. Predicted failure of St Alban embankment

The MIT-E3 model, calibrated only from the soil data (i.e. not back-calculating any of the parameters using the observed failure) predicts accurately the failure height. An accurate prediction of the failure height with the MCC model was obtained for an S_u profile that is 25% larger than the DSS strength profile (Fig. 3). Zdravković et al. (2002) further demonstrated that using such a back-calculated isotropic strength to predict the failure height of a different shape embankment built on the same foundation soil (e.g. adding another berm as in Fig. 4), did not produce the same result as the analysis of the same embankment using the originally calibrated MIT-E3 model. The isotropic prediction was again unsafe, giving 4.9 m failure height, compared to 4.4 m predicted when simulating anisotropic strength (Fig. 4).
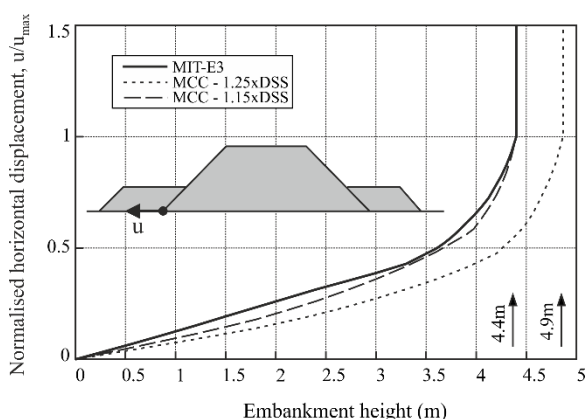
Figure 4. Predictions of modified embankment

3 LONG-TERM BEHAVIOUR

Having established in the previous study that the anisotropy of the undrained strength in soft clay foundation soils has a governing effect on the short-term design of earth embankments, the next step was to apply the established modelling procedure to the assessment of the long-term behaviour of embankments. A case study of a trial embankment constructed at the Mucking Flats test site in the Thames Estuary in the UK is used for this purpose, as it was subjected to a period of post-construction monitoring.

3.1 Ground conditions

Extensive laboratory and field characterisation of the site and the behaviour of the Mucking clay were reported in Pugh (1978) and Wesley (1975). Profiles of measured S_u in Fig. 5 indicate a desiccated crust, similar to the soft Champlain clays, to about 1.5 m depth. The clay beneath is lightly overconsolidated with an $OCR = 1.35$ and a $K_0^{OC} = 0.55$, while the permeability was characterised as anisotropic, with $k_h = 1.3 \cdot 10^{-9}$ m/s and $k_v = 2.6 \cdot 10^{-9}$ m/s.

The embankment material was a clean sand with $\phi'_{TXC} = 38^o$.
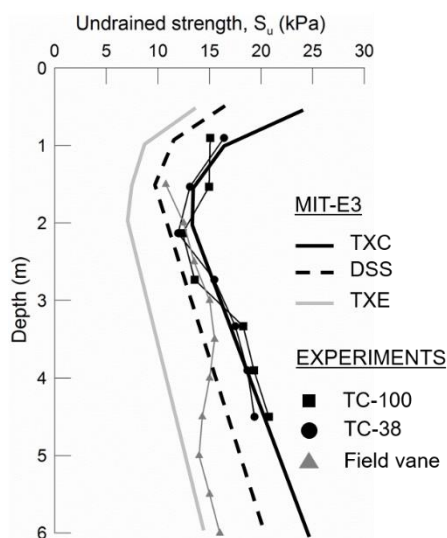
Figure 5. S_u profiles for the Mucking clay deposit

3.2 Numerical modelling

The same MIT-E3 constitutive model used in the Saint-Alban study was selected for the simulation of the Mucking clay behaviour. The calibration process and derived model parameters are given in Sheehy (2005). Fig. 5 shows that the strength anisotropy of the Mucking clay is less well defined experimentally compared to Champlain clays. However, the TXC S_u profiles are reasonably well reproduced by the model.

The embankment, termed Bank 2, was selected for this analysis, as it was erected to 2.8 m height

and then monitored for a limited period post-construction. A set of settlement gauges was placed at a 1 m deep horizontal level underneath the embankment body. Their measurements are compared with numerical predictions in Fig. 6.
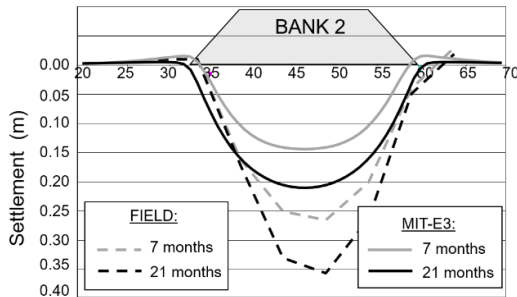
Figure 6. Post-construction settlements of Bank 2; predictions accounting for consolidation

Fig. 6 shows substantial embankment settlements measured at 7 and 21 months post-construction. However, the settlements predicted in the analysis employing the MIT-E3 model, which in the transient stage accounts only for consolidation (i.e. dissipation of excess pore water pressures), are significantly smaller, by some 40%, than measured. Adjusting the model parameters within the scatter of experimental data and repeating the analysis did not alter notably these predictions. It was evident that, for the transient/long term modelling of the embankment, additional facets of time-dependent soil behaviour, such as creep or viscosity, need to be considered.

A number of constitutive models have been proposed to simulate the time-dependent behaviour of soils (mainly clays) that follow isotach viscosity (Liigaard et al., 2004). Most of these are elastic-viscoplastic models, based on Perzyna (1963) overstress theory. The model selected for the current study adopts the same concept, in combination with the Yin (1999) equivalent time (ET) framework. Details of the model, termed IC-ET, its generalisation in stress space and its implementation in ICFEP are given in Bodas Freitas et al. (2011, 2012).

Calibration of the IC-ET model for the behaviour of Mucking clay is given in Losacco (2007).

The model is isotropic and was therefore calibrated to reproduce the TXC S_u profile in Fig. 5, which is similar to that reproduced by the MIT-E3 model. The main difference is that in the time-dependent framework the S_u profile has to be consistent with the strain rate at which the shearing in the experiments was conducted, which was 0.33 %/hour (Wesley, 1975).
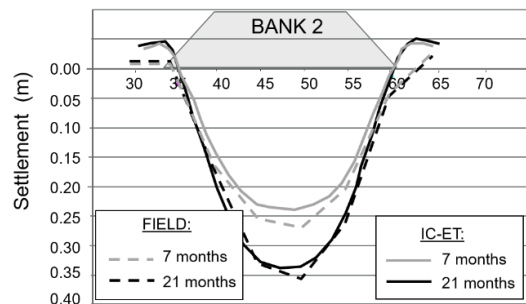
Figure 7. Post-construction settlements of Bank 2; predictions accounting for creep and consolidation

The finite element analysis of the Mucking Flat embankment Bank 2 was repeated, with the IC-ET model now simulating the behaviour of the foundation soil and accounting for both consolidation and creep. The predictions of its settlement at the same time instances of 7 and 21 months are shown in Fig. 7. The agreement with field measurements is excellent.

3.3 Life extension

One option for extending the life of ageing infrastructure embankments, in particular those that serve as flood defences, is to raise the embankment height. The issue is then to determine how high can the embankment be raised before it fails, which depends on the current S_u distribution that is altered by the time-dependent processes in the soil discussed above. This distribution is difficult to quantify empirically, hence standard methods of analysis cannot be used.

Having shown in Fig. 7 that, taking account of consolidation and creep reproduces accurately the time-dependent response of soft-clay foundations (albeit over a limited time-span, as available

in the case study), the finite element analysis of Bank 2 was extended to allow a period of 30 years to pass from the end of its construction. Both consolidation and creep were allowed to take place during this time, although pore water pressures stabilised after about 5 years. Bank 2 was then subjected to two hypothetical, but realistic, raising schemes shown in Fig. 8.
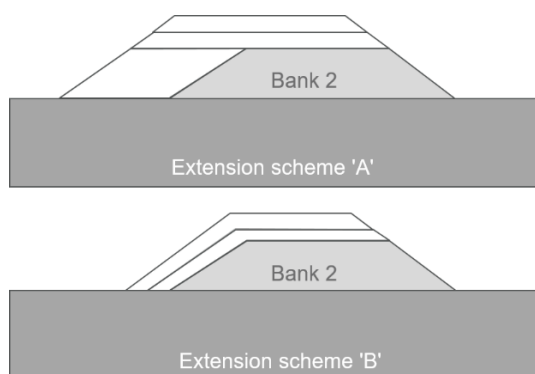
Figure 8. Raising schemes applied to Bank 2

The predicted raised height of Bank 2 just before failure was 5.3 m and 5.6 m for schemes 'A' and 'B', respectively, from the analyses that employed the IC-ET constitutive model for the foundation soil. This is nearly 100% increase of the height of the original embankment). The same extension exercises were applied in the analysis that employed the MIT-E3 model, although the transient soil behaviour was not well reproduced by this model (Fig. 6). The predicted raised heights, just before failure, were 3.9 m and 4.7 m for schemes 'A' and 'B', respectively.

4 VALIDATION

The soundness of the finite element predictions discussed above was demonstrated by comparisons of analyses results with available field measurements from the two case studies on infrastructure embankments. The analysis employing the MIT-E3 model was shown to reproduce accurately the soft-clay embankment construction to failure, emphasising the importance of strength anisotropy in the short-term design. The analysis that employed the IC-ET model demonstrated the accuracy in predicting the transient, post-construction behaviour of soft clay foundations. However, the raising of the embankment following the latter analysis was not possible to verify as this was not done in the field and hence the data is not available.

Consequently, to gain confidence in the ability of the IC-ET model to predict accurately the changes in the mechanical behaviour of the foundation soil that would enable life extension of infrastructure, a case study of two footings constructed on the soft Bothkennar clay (Jardine et al., 1995; Lehane & Jardine, 2003) is considered in this section.

4.1 Geometry and ground conditions

The footing experiment comprised two identical square footings (2.2 x 2.2 m) constructed at the Bothkennar site in the UK and instrumented to measure displacements, stresses and pore water pressures in the ground. The footing 'A' was loaded to failure (undrained) immediately after construction in 1990 (test A), as shown by the load-displacement curve in Fig. 9. The ultimate foundation pressure was estimated at 138 kPa. Footing 'B' was also loaded in 1990 (test B), but only to 89 kPa (equivalent to a factor of safety of about 1.5 applied to the bearing capacity) and was then left under this load for 11 years. In 2001 footing 'B' was further loaded to failure (test C), mobilising 204 kPa of ultimate pressure. The gain in capacity of footing 'B' after 11 years of consolidation and creep in the soil was 48% compared to the capacity of the virgin soil. The solid lines in Fig. 9 represent experimental data.

The behaviour of the Bothkennar clay was extensively examined through laboratory and field experiments in the 1990s and reported in the special issue of *Géotechnique* in 1992. The profile of undrained strength from TXC tests in Fig. 10 shows consistent data from samples obtained with different sampling techniques. The angle of shearing resistance is $\phi'_{TXC} = 37^{\text{o}}$ and $\phi'_{TXE} =$

42º and the permeability is about $5 \cdot 10^{-9}$ m/s. The clay is lightly overconsolidated with $OCR = 1.5$ and $K_0 = 0.65$.
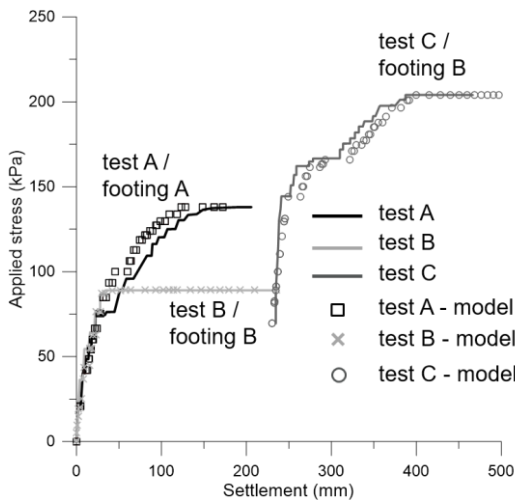
Figure 9. Load tests on footings at Bothkennar

4.2 Numerical modelling

The IC-ET model is employed in these analyses to simulate the behaviour of the Bothkennar clay. The calibration of the model and characterisation of ground conditions are detailed in Bodas Freitas et al. (2011, 2015). Fig. 10 shows that the calibrated TXC S_u profile, derived for the experimental shearing strain rate of 4.5 %/day, matches well the test data. This profile is marked as 'virgin strength' that exists in the soil before the construction of the footings and their loading.

The symbols in Fig. 9 show the predicted load-displacement curves from numerical analysis. Excellent reproduction of the experimental load-displacement curve in test A demonstrates consistency between the model calibration and characterisation of the initial ground conditions. The simulation of test B also shows excellent agreement with the test, mobilising a similar amount of settlement under the maintained load as experimentally observed. This is shown in more detail in Fig. 11, depicting the evolution of settlement with time. It was noted in the experimental study that consolidation was completed within a year under maintained load, implying that measured

total settlement after 11 years is a combination of both consolidation and creep processes in the ground. A slight discrepancy between the predicted and measured settlements at 11 years is attributed to the observation that many instruments had stopped working since the previous reading at 2 years post-initial loading, as discussed in Lehane & Jardine (2003), thus questioning the interpretation of that last measurement.
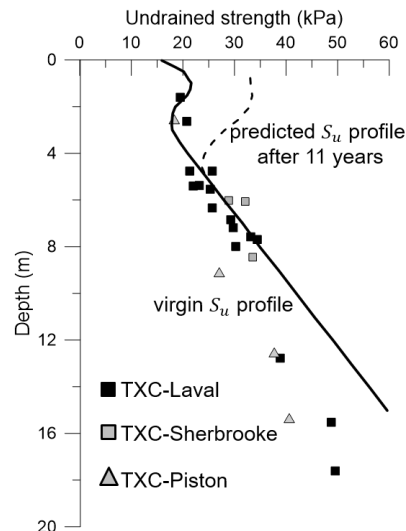
Figure 10. S_u profile for Bothkennar clay
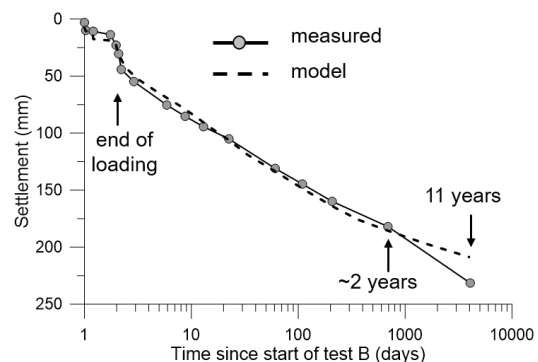
Figure 11. Evolution of settlement under the footing

The simulated further loading of the footing in test C, Fig. 9, is also in excellent agreement with test data, reproducing accurately the ultimate load and the gain in undrained capacity of the footing after 11 years of maintained load. This test demonstrates that the model was capable of

accurately predicting the gain in strength due to consolidation and creep over those 11 years. The S_u profile under the footing at 11 years post-initial construction and loading is shown as a dashed line in Fig. 10. This verification therefore gives confidence that the predictions of raised embankment heights with the IC-ET model, after 30 years of maintained load, are likely to be correct.

5 CONCLUSIONS

The studies of earth embankments discussed here indicate that the short-term design of this structures needs to consider the anisotropy in the foundation soil induced by principal stress rotation during construction. For the long-term design it would appear that creep in the soil is more dominant than strength anisotropy. The applied equivalent time constitutive model is able to accurately predict the long-term changes in the soils mechanical behaviour.

6 REFERENCES

Bjerrum, L. 1973. Problems of soild mechanics and construction on soft clays and structurally unstable soils, *8th ICSMFE Moscow* **3**, 109-159.

Bodas Freitas, T.M., Potts, D.M., Zdravkovic, L. 2011. A time dependent constitutive model for soils with isotach viscosity, *Comp. & Geotech.* **38**, 809-820.

Bodas Freitas, T.M., Potts, D.M., Zdravkovic, L. 2012. Implications of the definition of the Φ function in elastic-viscoplastic models, *Géotechnique* **62** (7), 643-648.

Bodas Freitas, T.M., Potts, D.M., Zdravkovic, L. 2015. Numerical study on the response of two footings at Bothkennar research site, *Géotechnique* **65** (3), 155-168.

Jardine, R.J., Lehane, B.M., Smith, P.R., Gildea, P.A. 1995. Vertical loading experiments on rigid pad foundations at Bothkennar, *Géotechnique* **45** (4), 573-597.

Karstunen, M., Krenn, H., Wheeler, S.J., Koskinen, M., Zentar, R. 2005. Effect of anisotropy and destructuration on the behaviour of Murro test embankment, *Int. Jnl. Geomechanics* **5** (2), 87-97.

Karstunen, M., Yin, Z.Y. 2010. Modelling time-dependent behaviour of Murro test embankment, *Géotechnique* **60** (10), 735-749.

Kavvadas, M.J., Amorosi, A. 2000. A constitutive model for structured soils, *Géotechnique* **50** (3), 263-273.

Lefebvre, G., Ladd, C.C., Pare, J.J. 1988. Comparison of field vane and laboratory undrained shear strength in soft sensitive clays. *ASTM STP 1014*, 233-246. ASTM, Philadelphia.

Lehane, B.M., Jardine, R.J. 2003. Effects of long-term preloading on the performance of a footing on clay, *Géotechnique* **53** (8), 689-695.

Leroueil, S., Tavenas, F., Samson, L., Morin, P. 1983. Preconsolidation pressure of Champlain clays. *Can. Geotech. Jnl.* **20**, 803-816.

Liigaard, M., Augustesen, A., Lade, P.V. 2004. Characterisation of models for the time-dependent behaviour of soils, *Int. Jnl. Geomech.* **4** (3), 157-177.

Lossaco, N. 2007. *Raising of embankments on soft clay*, MSc Thesis, Imperial College London.

Perzyna, P. (1963). The constitutive equations for work-hardening and rate sensitive plastic materials, *Proc. of vibrations problems*, Warsaw, **4**, 281-290.

Potts, D.M., Zdravković, L. 1999. *Finite element analysis in geotechnical engineering: theory*, Thomas Telford, London.

Pugh, R.S. 1978. *The strength and deformation characteristics of a soft alluvial clay under full scale loading conditions*. PhD Thesis, Imperial College, University of London.

Sheehy, W. 2005. *On the rising of embankments on soft clays*, MSc Thesis, Imperial College London.

Wesley, L.D. 1975. *Influence of stress path and anisotropy on the behaviour of soft clay*. PhD Thesis, Imperial College, University of London.

Whittle, A.J., Kavvadas, M.J. 1994. Formulation of MIT-E3 constitutive model for overconsolidated clays, *ASCE Jnl. Geotech. Engng.* **120** (1), 173-198.

Yin, J-H., Graham, J. 1999. Elastic viscoplastic modelling of the time-dependent stress-strain behaviour of soil, *Can. Geotech. Jnl.* **36**, 736-745.

Zdravković, L., Potts, D.M., Hight, D.W. 2002. The effect of strength anisotropy on the behaviour of embankments on soft ground, *Géotechnique* **52** (6), 447-457.

XVII European Conference
ECSMGE 2019
Reykjavík
on Soil Mechanics
and Geotechnical Engineering

Recent advances in pile design, construction, monitoring and testing

Avancées récentes en matière de dimensionnement, d'exécution, de monitoring et d'essais sur pieux

M. Bottiau
ISSMGE-ETC3 chairman & Franki Foundations Belgium

N. Huybrechts
Belgian Building Research Institute BBRI & KU Leuven, Belgium

ABSTRACT: In this contribution an overview is given about the recent evolution in the harmonization of codes and standards that apply for the design of piles, in particular the Eurocode 7. Based on the results of some design exercises, it is shown that differences between the output of the different national approaches remain huge. Several discrepancies of pile design standards and codes are identified.

The authors then give an overview of some recent technical progresses with regard to piling equipment, testing, instrumentation and monitoring methods. They try to analyse how those advances can be taken into account in the codes and design practice. The concrete example of the recent evolution of the Belgian practice is explained, where an attempt is made to reward testing and proper monitoring.

RÉSUMÉ: Dans cette contribution, les auteurs donnent un aperçu des évolutions récentes au niveau de l'harmonisation des codes et normes qui s'appliquent pour le dimensionnement des pieux, en particulier l'Eurocode 7. Sur base d'exercices de dimensionnement, il est démontré que les différences, en termes de résultats obtenus selon les différentes approches nationales, restent énormes. Certaines divergences entre codes et normes sont identifiées.

Les auteurs donnent ensuite un aperçu de quelques progrès techniques récents au niveau des équipements d'installation, des essais, de l'instrumentation et des méthodes de monitoring. Ils essayent d'analyser comment ces avancées peuvent être prises en compte dans la pratique des codes et normes. L'exemple concret de l'évolution récente de la pratique belge, où l'on tente de récompenser les essais et un monitoring approprié, est expliqué.

Keywords: Piles, Design, Execution, Testing, Monitoring

1 INTRODUCTION

Many evolutions took place in Europe over the last decades with regard to pile foundations, in the different areas of design, execution and testing.

Design:

- The Eurocode 7 was implemented throughout Europe, giving a common framework where design methods should fit in. As we discussed during the recent ETC3 Conference in Leuven (2016), this didn't result in a real harmonisation, but at least it helps designers and practitioners in the different countries to better

understand design practices in the other countries.

- As a result, more detailed guidelines and prescriptions have been drafted in some countries, whereas others just tried to translate the "old" design rules into the framework of the EC7.

- The second generation of Eurocodes are currently being established with a publication expected in 2022. The aim is a.o. to foster harmonisation in Europe and increase the ease of use. the steel bars.

Execution:

- The last decades have seen a huge evolution with regard to machines capacity resulting in significantly deeper and larger foundation elements than before.

- Innovations in equipment and larger dissemination of information have created new possibilities but time to market has shortened so that detailed knowledge of the systems sometimes comes after their use in the field.

- Piling rigs are now equipped with all kind of electronic measurement devices, allowing for better information over the installation parameters and even offering interactive ways to automate installation procedure. Interconnectivity with BIM systems will be on the agenda of the coming years.

- The industry constantly requests increasing loads and higher strength materials. In the same time, recent research on materials such as tremie concrete, support fluids or Soilmix have shown how adequate material selection, prescriptions and testing is part of a successful installation process.

Testing:

- Because of the standardization exercise required by the introduction of the EC7 and facilitated by the easier access to miniaturized and accurate testing equipment, instrumented load tests have been more widely adopted giving better understanding of pile behaviour.

- In the same time, as expressed earlier, advances in instrumentation equipment also give new insights with regard to pile performance although the use of the provided information is currently usually only limited to the guarantee of a better pile documentation.

Based on what precedes, one might expect that theoretical advances and progress in norms and codes have made it easier to predict the pile's performance in given circumstances. However, as we will demonstrate, the scatter between different theoretical approaches remains very important, and still, the major factors determining real pile performance are the correct knowledge of local soil conditions, and the understanding of the exact impact of the pile installation in these particular soil conditions. Contractor's proven skill, repeatable process and previous experience is key in the final result. As systems and equipment capacities evolve, it is important to link expected pile capacity to measured pile performance. Modern testing and monitoring equipment can help to make this effective in the field.

A first section will be dedicated to the review of the remaining discrepancies in codes. A second section will give a few examples of recent technological advances and though outstanding issues. In a third chapter, we will look at the progresses which were made in the field of testing. And finally we will try to look at the main question we have: how can we improve the fit between predicted capacity using the codes and the installed capacity in the field.

2 CODES AND EVOLUTION OF DESIGN PRACTICE

2.1 The purpose of codes

In recent years, under the pressure of a stricter regulation and contractual base of our profession, new or revised codes have been drafted. Eurocodes, in particular, have been forcing many

European countries to have a fresh look on their local regulations. They have also been serving as a reference for many other regions in the world.

Codes are obviously important, because they are supposed to (Peter Day, 2017):

- Establish the norms of the profession, and provide protection against legal action based on negligence,

- Represent a distillation of existing knowledge on which there is consensus,

- Should ensure fair competition.

On the other hand, many practitioners dislike them as they present the risk to refrain innovation and inhibit engineering judgement.

As we all like to say, "the practice of geotechnical engineering is a skill rather than a science. It involves perception and judgement, both of which are difficult to encapsulate in a code", (Peter Day, 2017). It is largely based on experience, a correct understanding of the basics behind it, and local knowledge. One of the main dangers is that the codes give the illusion of clarity and standardization. The code user's, however, can:

- miss practical knowledge of the adequate construction method in specific circumstances,

- base his interpretation on insufficient or inadequate data,

- have insufficient background for a correct interpretation of specific requirements or prescriptions.

2.2 The accuracy of codes

2.2.1

During the International Symposium organized by the European Technical Committee 3 Piles of the ISSMGE (ETC3) in Leuven "Design of Piles in Europe-How did Eurocode 7 change daily practice", (De Vos et al., 2016), the members of the different countries were invited to submit National reports on the design of piles in their countries, since the introduction of the EC7. Three design examples were also distributed to the members, asking them to provide solutions for these "simple" and well documented examples involving the design of driven, bored, screw, and CFA piles in different ground conditions. Trevor Orr accepted to analyse and compare the different solutions received. We show hereunder the details of two cases, bored piles and screw piles related to Example 2, in clayey soil.

Example 2 concerned the design of twenty piles for a stiff building in Belgium as part of a Belgian Building Research Institute (BBRI) research project on a site 36 m x 18 m. Two types of piles were to be considered: 900 mm bored piles with bentonite suspension and a temporary casing over the first 3 m, and 410 mm displacement (no soil excavation) screw piles. The soil consists of 1.0 m of fill over a deep deposit of stiff over-consolidated Boom clay. No additional surface load was to be considered and hence no downdrag.

The ground investigation involved three CPT, two SPT and two pressuremeter (PMT) tests well distributed over the site. Boring with undisturbed soil sampling and laboratory tests were carried out centrally on the site. The CPT q_c and SPT N values are plotted in Fig. 1. The results of the triaxial tests gave a c' value of 22 kPa and a φ' value of 28.2°.The groundwater was at a depth of 1.0 m.

The objective of this example was to predict the compressive resistance of the bored pile and the screw pile, stating what ground investigation information was used. Ten solutions were transmitted for the bored pile and eight for the screw piles. Seven of the ten solutions were based on the results of the three CPT tests. Figures 2a and 2b give the results for both examples.
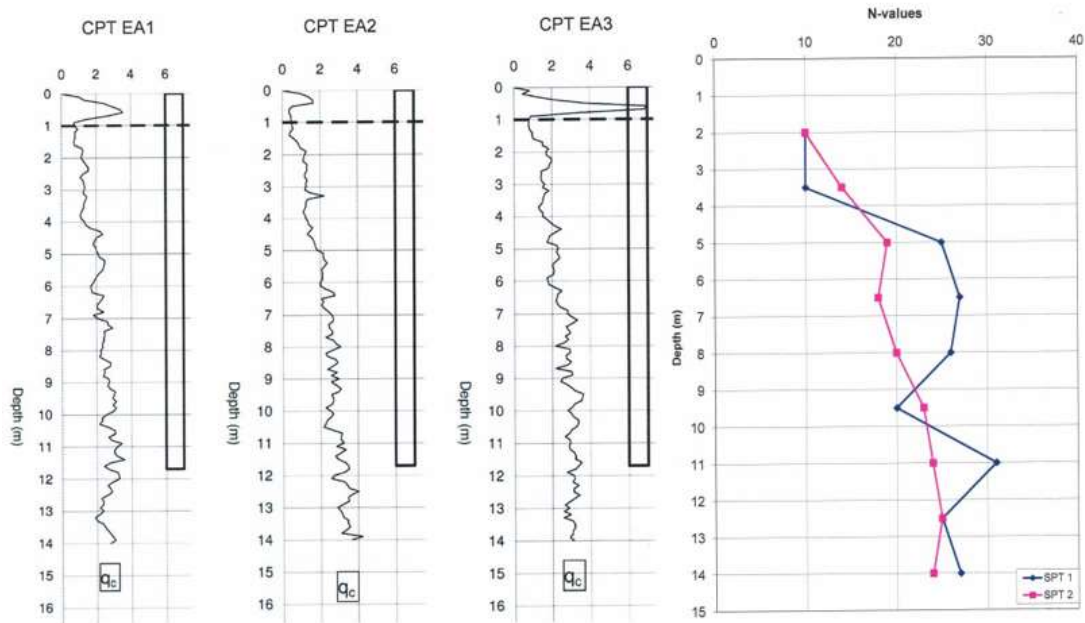
Figure 1. Example 2 (Bored and screw piles) – CPT and SPT plots
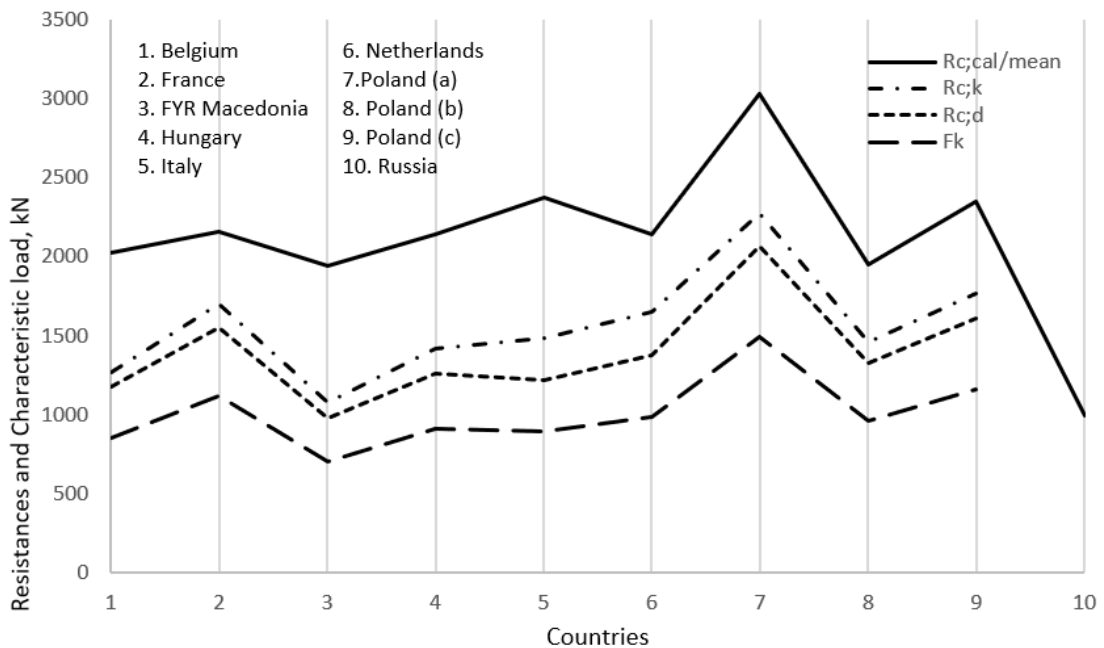
Figure 2a. Example 2 – Bored pile (T. Orr, 2016) – Resistances and characteristics loads
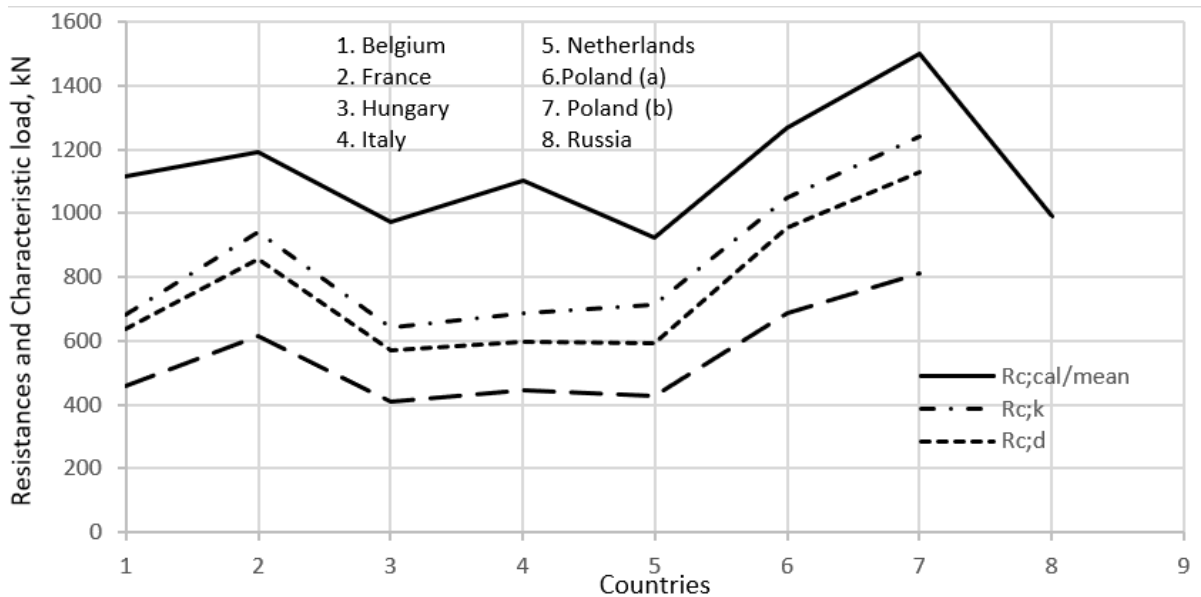
Figure 2b. Example 2 – Screw pile (T. Orr, 2016) – Resistances and characteristics loads

The graphs in Fig. 2a and 2b show that the calculated pile resistances and resulting characteristic loads are very variable, with coefficients of variation of 14% for the calculated resistance and a COV value of 22% for both the characteristic resistance and the characteristic load. The highest resistance was obtained by Poland using laboratory test data while the lowest value was obtained by Russia.

The OFS value (overall safety factor) is close to 1.5 in the case of all the solutions and theTSF values (total safety factors) range from 1.9 to 2.7.

The further analysis of all the design examples showed that (according to T.Orr, 2016):

- Harmonisation has occurred in the design method and consistent overall factors of safety are used. The outcome of the design, however, is far from being similar.

- Since Eurocode 7 does not provide any calculation models for pile design, different methods, mostly presented in national standards or guides, are used to calculate the pile resistances. Many of the national methods to calculate pile resistance involve additional factors or requirements to those in Eurocode 7, for example factors relating to pile type or pile shape.

- For more harmonisation to occur, there must be more agreement on the models to calculate pile resistance, but is that possible considering the different soil conditions, testing methods, pile types, installation methods and experiences that exist in Europe.

This last conclusion is not certain. In his conclusion, T.Orr also refers to a comparison exercise for retaining walls at an International Workshop on the Evaluation of the Eurocode 7 in Dublin (2005) by Simpson, showing again a considerable scatter in the results, even when calculated by authors using nominally the same method! This obviously brings us back to the fundamental comments raised under point 2.1.

2.2.2

Another interesting comparison exercise was organised in Bolivia by Bengt Fellenius and Mario Terceros as part of a prediction event related to a research study on construction and

static and dynamic testing of four instrumented bored and screw piles (DFI Stockholm, 2014).

Geotechnical studies comprising SPT,CPT and tests with routine laboratory analysis on recovered soil samples were performed. CPTU soundings were performed at a later stage and were not available for the participants in the prediction event.

Figures 3a and 3b show diagrams of the SPT N-indices and the distribution of water content in the three boreholes, as well as the CPTU diagrams from CPT-1; measured cone stress, sleeve friction, and pore pressure on the cone shoulder (U2), and calculated friction ratio. As one can see from the SI data, the soil density is compact. The average water content is about 15 % plus-minus a few percent.

The test piles were bored and screw piles described as follows (see Fig. 4).

TP1: a nominally 400 mm diameter pile, 17.5 m long, bored under bentonite ("standard pile").

TP2: a nominally 360 mm diameter pile, 11.6 m long, built as a FDP (Full Displacement Pile) which is constructed without removing any soil (but for nearest the ground surface on starting the pile).
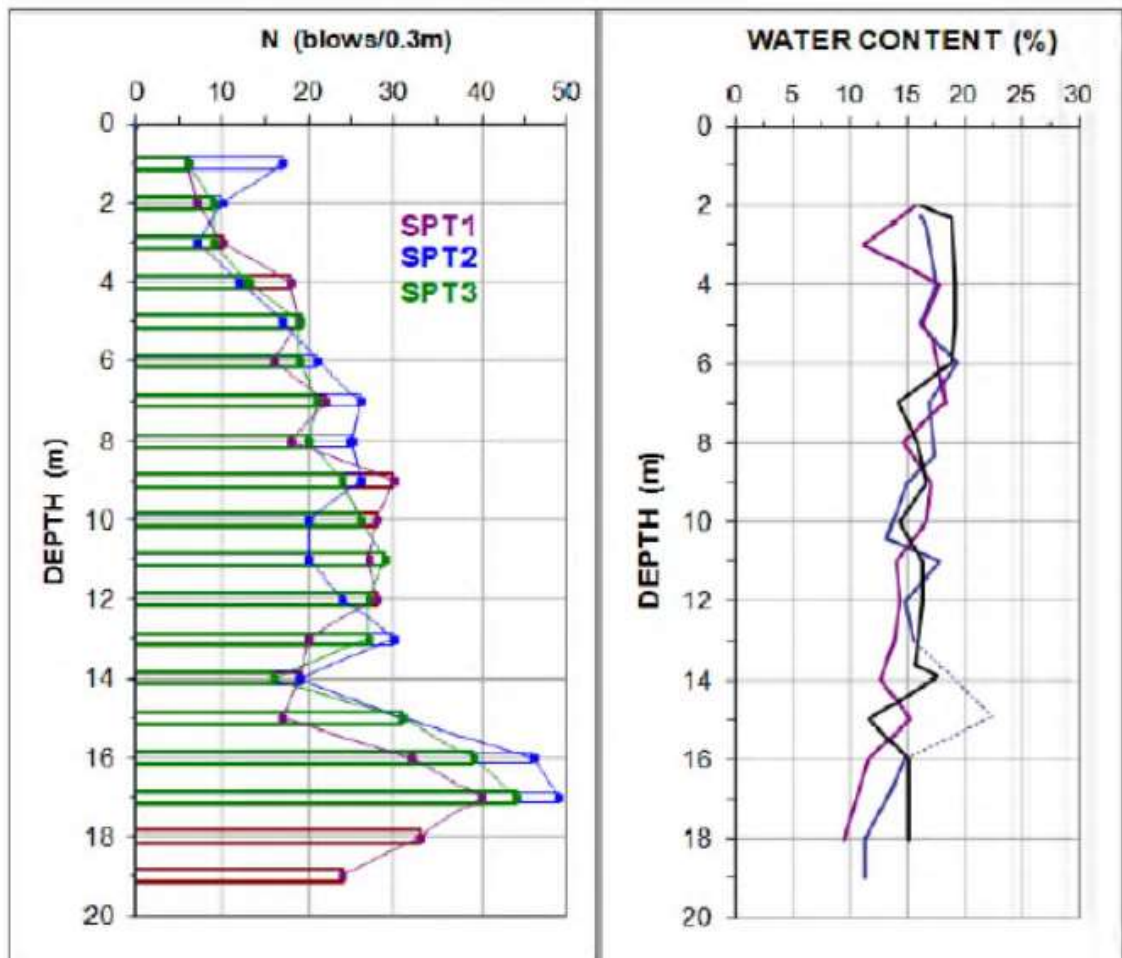
Figure 3a. Bolivian site (Fellenius et al, Stockholm, 2014) SPT N-indices and Water Contents
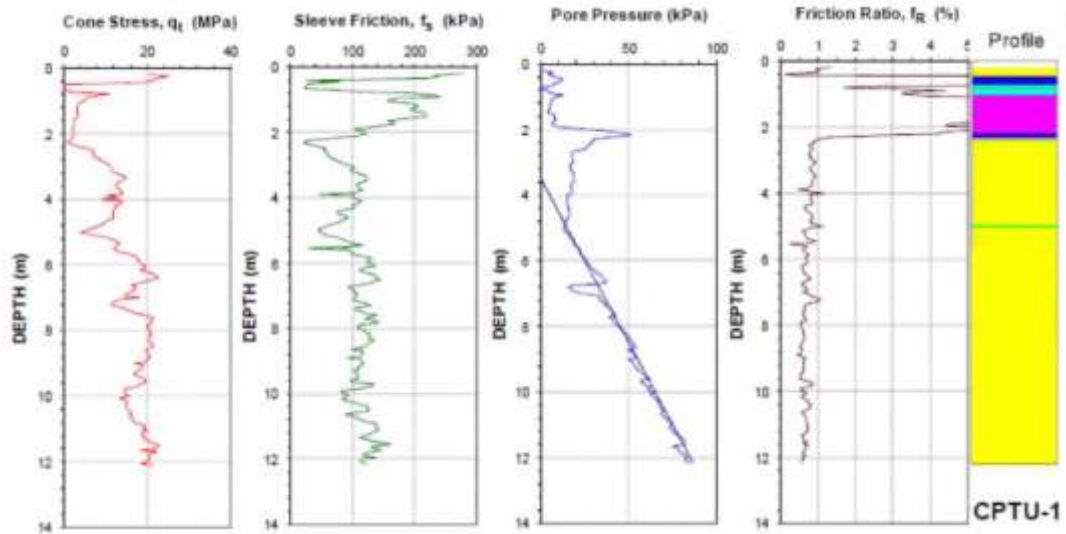
Figure 3b. Bolivian site (Fellenius et al, Stockholm, 2014) CPTU diagrams
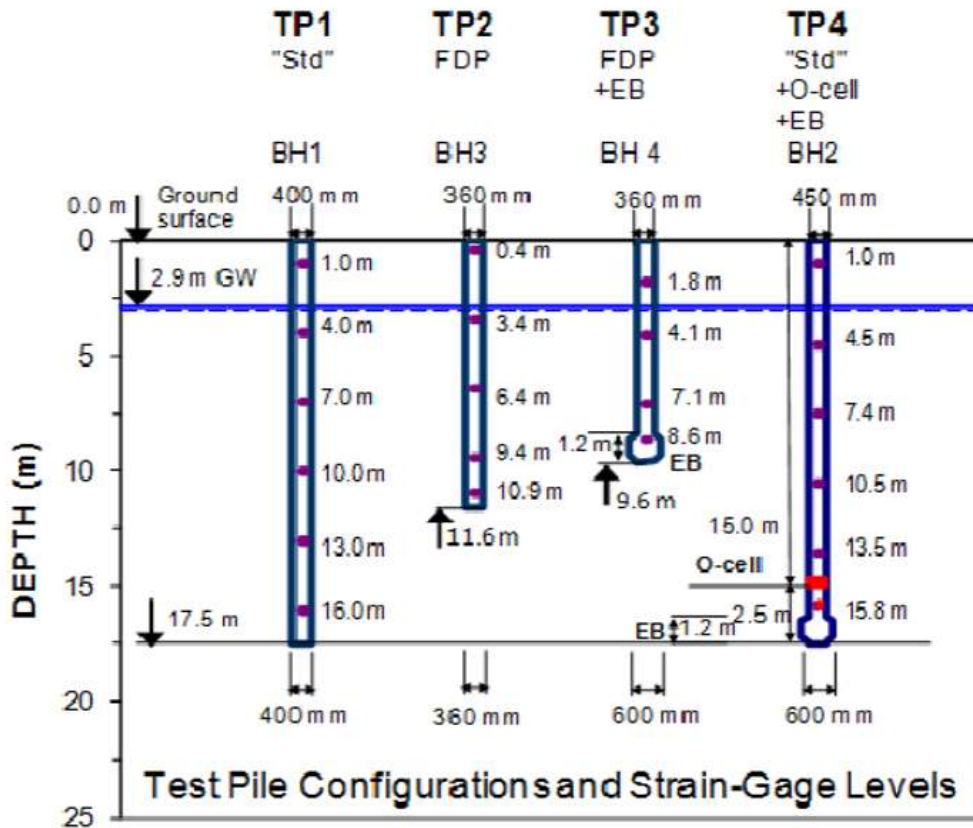
Figure 4. Bolivian site (Fellenius et al, Stockholm, 2014): test setup

TP3: a nominally 360 mm diameter pile, 9.6 m long, built as a FDP (Full Displacement Pile) and with a 600 mm diameter Expander Body, placed at the pile toe.

TP4: a nominally 450 mm diameter pile, 17.5 m long, bored under bentonite and with a 600 mm diameter Expander Body, EB, placed at the pile toe and with an Osterberg cell above the EB.

A total of 50 predictions were received from 63 individuals in 19 countries and all continents. Most predictions only addressed Pile TP1. Figure 5 shows a compilation of the submitted load-movement curves and the evaluated capacities.

Only one of the participants had experience from the Bolivian soil and piling conditions. According to Fellenius et al (2014), it is therefore no surprise that the upper and lower boundaries of the load-movement curves and the capacities are wide apart. They consider more surprising, that the range of pile head movements at the evaluated capacities is even wider.

Fellenius et al (2014): "Most geotechnical engineers would, we believe, accept an allowable load of half a capacity occurring at a movement of about 15 to 20 mm. But would they be equally willing to accept that same allowable load determined from a capacity that took 50+ mm movement to develop? Indeed, the main outcome of the prediction event is that the geotechnical community has very diffuse definitions of capacity as determined from the results of a static loading test. Few text books, guidelines, codes, and standards, if any, define how to determine the capacity that serves as reference to the proclaimed factors of safety or resistance factors, often with two-decimals precision. We consider

this to be a definite weakness in the geotechnical practice."

We could not have said it better.

2.2.3

When looking at these two examples, and many others published in the literature, we need to address the reasons of such a large variation:

- Codes sometimes miss a clear definition and approach to what is meant by ultimate/allowable/characteristic pile resistance. We believe this is a major achievement of EC7, that these concepts are usually better understood, at least by European practitioners.

- The distinction between the installation effect of a specific piling system and the reliability of the pile installation process is not always clear, and sometimes (large) global factors account for both.

- Calculation methods in codes are often based on empirical data (load-tests) which were performed decades ago. In many cases, insufficient data is (locally) available for adequate calibration of installation/model/safety factors resulting in a varying degree of sophistication/conservatism of the code and/or the calculation method.

- The correct understanding of the specific pile behaviour and the measured impact of the pile installation on the surrounding soil may be insufficient. Even more, the variation in pile equipment capacity and local construction practice can affect the (local) pile performance and result in irrelevant installation coefficients for other soils and/or other practices. This is why in-situ monitoring and testing is so important.
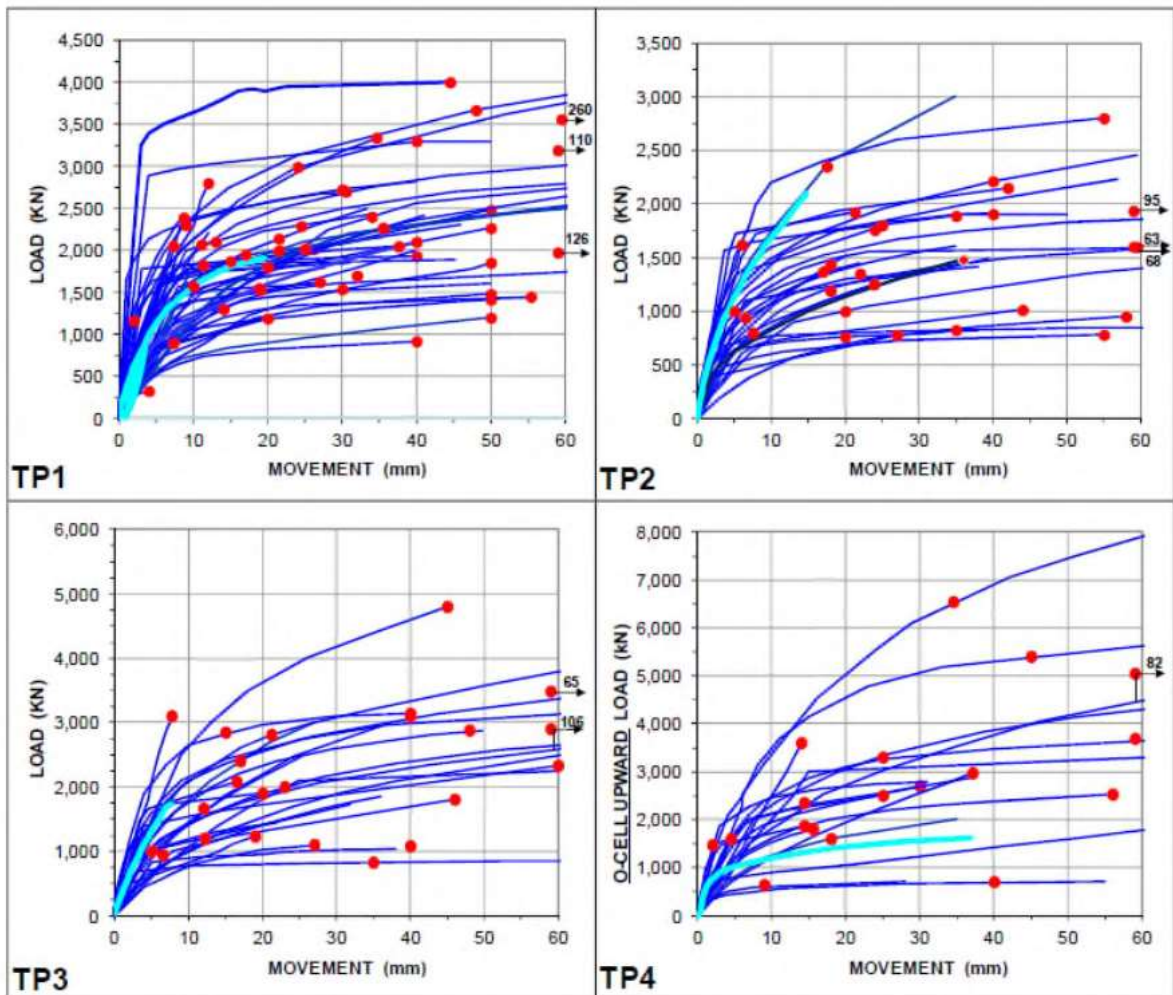
Figure 5. Bolivian site (Fellenius et al, Stockholm, 2014) - Piles TP1 - TP4 Capacities and Predicted Load-Movement Curves - Light Blue Curves are from the actual static loading tests

2.3 Codes and pile construction

We have shown how the simple definition of the theoretical pile capacity can differ in function of the code, the calculation method, the local experience or even the skill of the designer. The problem is: there is more, the installed pile capacity can largely vary as well! In the next chapters, we will try to show how system details and local circumstances or variable soil characteristics can alter the installed pile capacity.

In nearly all the models and codes, the effect of the pile execution on the stress state of the soil is accounted for by introducing a specific installation factor or a reduced fraction of the available shear and base resistance. Bored piles and CFA piles are often considered as less reliable than driven piles and affected by lower installation factors which can sometimes be very low.

It is the authors' opinion that the problem is more complex than usually addressed in the codes (Bottiau, 2014; Day, 2017):

- Influence of the pile installation and reliability of the pile installation should be treated separately, as all installation methods may prove to be inadequate in function of the soil conditions, and depending of the level of monitoring and testing of their installation.

- The different aspects governing the pile installation should all be considered: system details, equipment capacity, monitoring during and after pile installation.

- The correct interplay between pile installation and the surrounding soil is of predominant importance. In this respect, soil type exerts a major role. Codes usually limit soil categories to two or three main types of soils: sands, silts and clay, sometimes chalk, and/or weathered rock. In some cases, this classification is totally insufficient because the response of some types of soils to the solicitation of pile installation procedure, can be dramatically different than expected. In these cases, real scale load testing can prove to be the only adequate method to get the truth.

- Systems are in constant evolution, and small details are sometimes changed resulting in major differences. Too often, systems are classified into generic groups without paying enough attention for execution details. Moreover, modern alternative execution techniques (vibro-driving, jetting, grouting,…) are applied more regularly whereas their result in term of bearing capacity is not necessarily well understood.

- New knowledge or developments are only incorporated into codes and standards after they have been proven in practice and generally accepted. In this sense, codes and standards lag behind the introduction of new developments in the industry.

3 RECENT ADVANCES IN (THE UNDERSTANDING OF) DEEP FOUNDATIONS CONSTRUCTION

3.1 Evolution of the piling techniques

Based on a worldwide survey we update regularly (last update in 2016), the figure 6 shows the split between the different techniques used in Europe for pile foundations. It is obvious that new factors and challenges will drive the choice of one or another system, among which environmental considerations (vibrations, noise and/or production of spoil) will play a still larger role. Bored piles or assimilated represent a growing portion of piles installed: 59% in 2016. Equipment evolve dramatically, and quicker, and consequently, our profession pushes its limits further, sometimes reaching the limits of the existing design models. This evolution results in an increasing complexity of systems and execution details, but also in dimensions and ranges of depths or capacities which were never reached before. Moreover, the type of equipment and capacity available locally varies considerably, which can result in an extremely variable interaction with local soil type, and hence with totally different installed capacities. These are all areas which are difficult to account for in codes.

3.2 Examples and recent cases

3.2.1 Large diameter CFA (Augercast) piles

CFA are widely used worldwide. In Europe, they represent 24 % of the piles installed. The type of equipment used varies considerably from one end to the other of the spectrum, making it very difficult to predict the installed capacity. The system also gets acceptance to install larger diameters and longer piles. It becomes current practice to install piles down to 30 m, with diameters of 800 mm or 1000 mm. Soletanche-Bachy recently introduced a rig capable of installing Starsol piles of 50 m with a maximal diameter of 1500 mm (see Fig. 7).
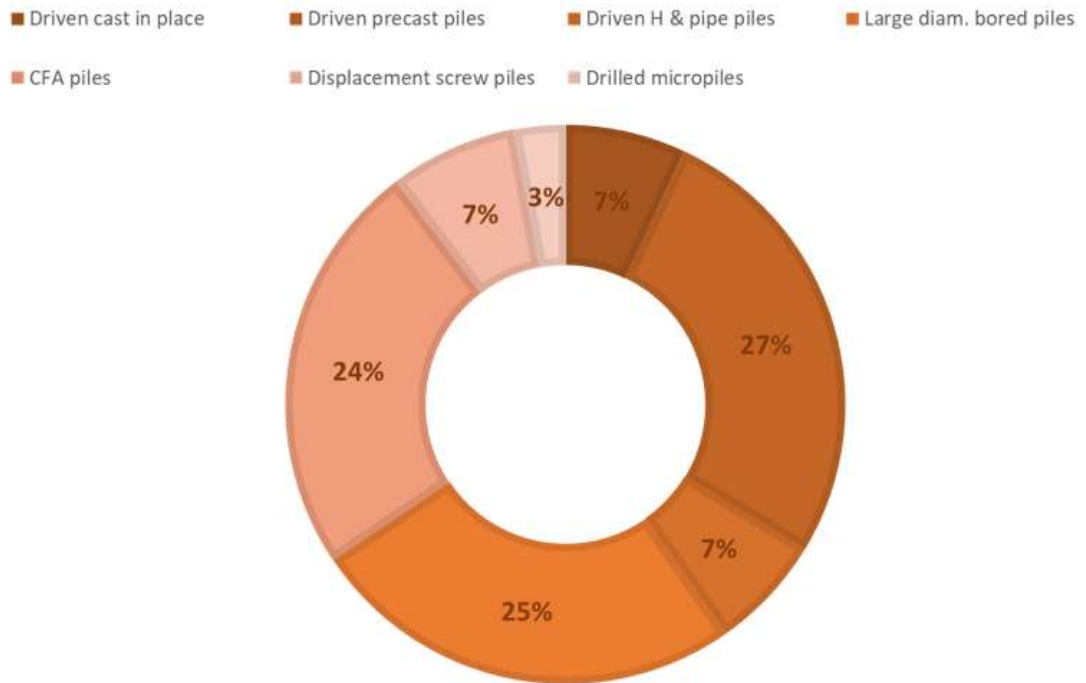
Figure 6. Distribution of piling construction methods across Europe (Bottiau, Leuven, 2016)

Figure 7. Soletanche-Bachy Starsol rig F5000

Even without reaching such records, the installation of CFA (augercast) piles remain a delicate matter, particularly in non-cohesive soils. As stated by many authors (Van Weele, 1988 and 1993; Viggiani, 1993; Van Impe, 1994) and recalled by Bustamante (2003), the complexity of the soil response to drilling is such that the ideal non disturbance conditions of the original soil conditions are far from being fulfilled in practice. The risk of over-augering and loosening of the soil is present, and is much dependent of different parameters, among which the installed power of the equipment plays a predominant role. This is particularly the case with large diameters CFA piles (> 600 mm).

Ideally, the vertical downward speed (potentially enhanced by an additional thrust) should be sufficient in order to avoid the scraping effect (over-augering). In other words, the importance of controlling the screwing ratio is governing the successful installation of augercast piles:

$$SR = \text{n}.\rho/V \tag{1}$$

where n is the revolution rate of the auger (rpm), ρ is the pitch of the auger (meter p round) and V is the rate of penetration of the auger (m/min).

Viggiani (1993) states that SR should ideally be equal to 1, what means that the auger is screwed in the soil without any soil removal. In real conditions, SR largely exceeds 1 and can even exceed 3, depending on soil and equipment conditions. There are not enough data available on SR values obtained in the field, and no consensus on a target value.

Based on recent advances in monitoring though, it is possible to get a real time value of SR based on the recorded n, p and V. On a recent job in Antwerp, we tried to analyse the SR ratio of large diameter CFA piles in very dense sands,

and the correlation with the results of SLT on selected piles. CFA piles of diameter 1000 mm and 1200 mm were to be installed down to 18 m with a penetration of several meters of a sand layer with qc values in excess of 15 MPa (see Fig. 8). Four piles were subject to control Load Tests up to 1.5 x the working load. Control CPT tests were performed at chosen locations after pile installation in order to check the possible decompaction.

The piles were installed using IHC rigs F2800 (piles diam. 1000 mm) and F3500 (piles diam. 1200 mm) with the following characteristics:
- Maximum torque : limited to 300 kN.m
- Maximum rotation speed 20 T/m
- Pull-down capacity : 15 T.

Figure 9 gives SR recorded during installation of test pile TP1 (diam. 1000 mm) and test pile TP2 (diam. 1200 mm). SR ratios of 5 to 7.5 (occasionally 9) were reached. It must be mentioned that very variable SR ratios between 4 and 10 in the dense sand layers were observed throughout the jobsite with no direct relation with local soil condition. Additional CPT's were performed after pile installation showing a decrease in qc-value. Again, this decrease was variable and no direct correlation could be found between local soil conditions or equipment-related information.

During execution, several attempts were made to influence the SR positively, by modifying one or another execution parameter (torque vs rotation or vice-versa; increased pull-down, decreased pull-down).

The results of the PLT are given in Fig. 10, as well as the matching of the αs value (installation factor for the assessment of the friction) used in the Belgian code using hyperbolic functions. The recommended αs value for CFA piles with specific provisions in order to limit soil relaxation is 0.6 in sands.
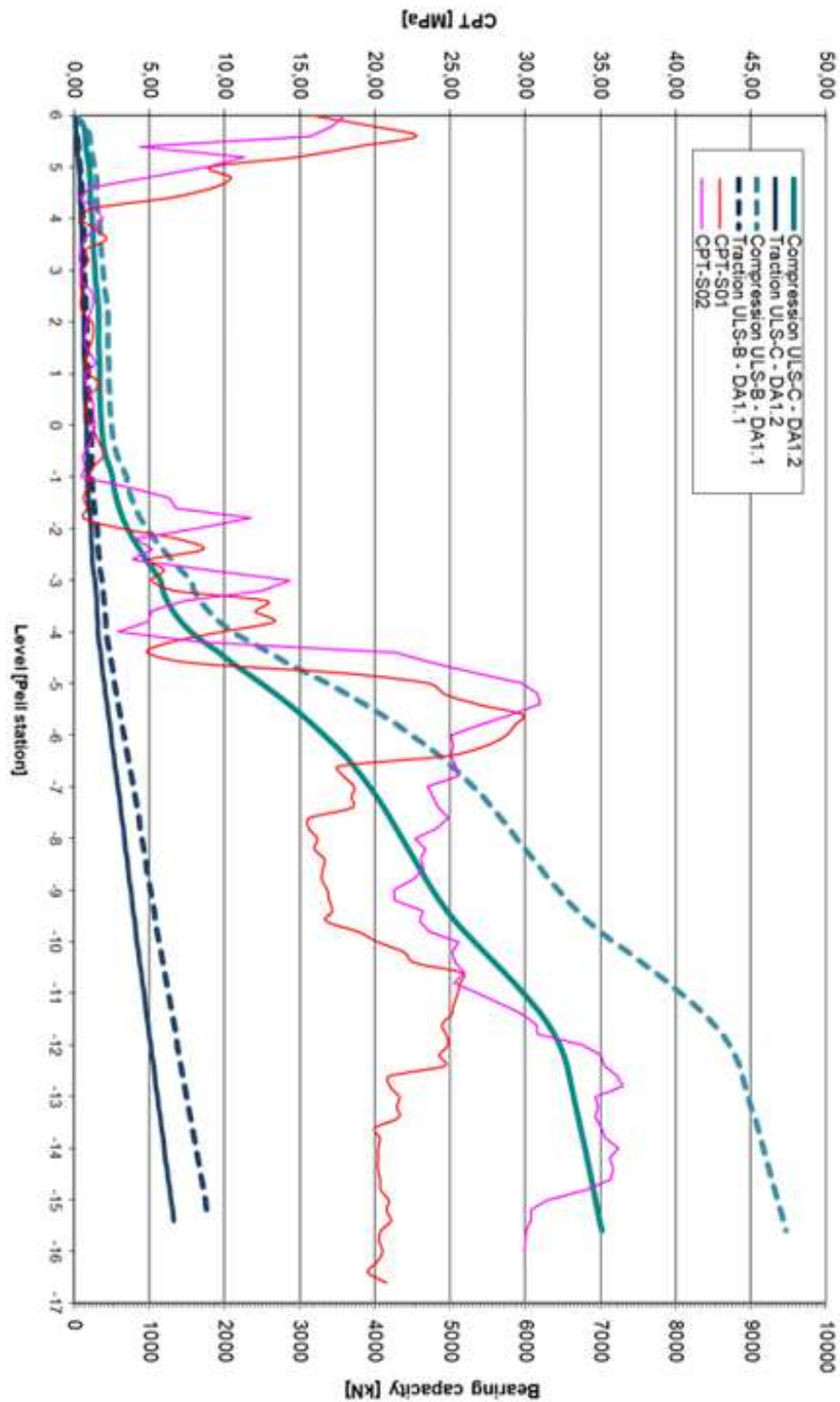
Figure 8. Antwerp jobsite – CPT tests
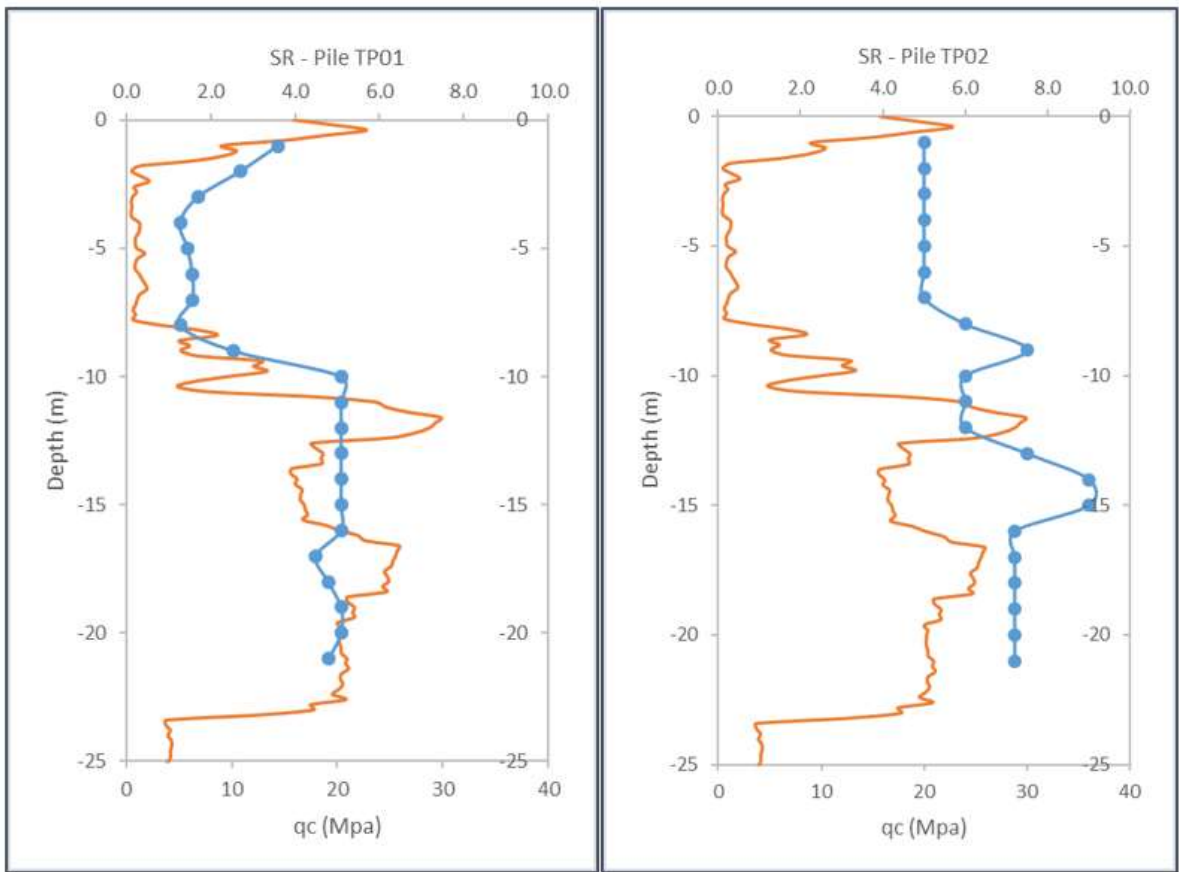
Figure 9. Antwerp jobsite – SR measured for TP1 and TP2
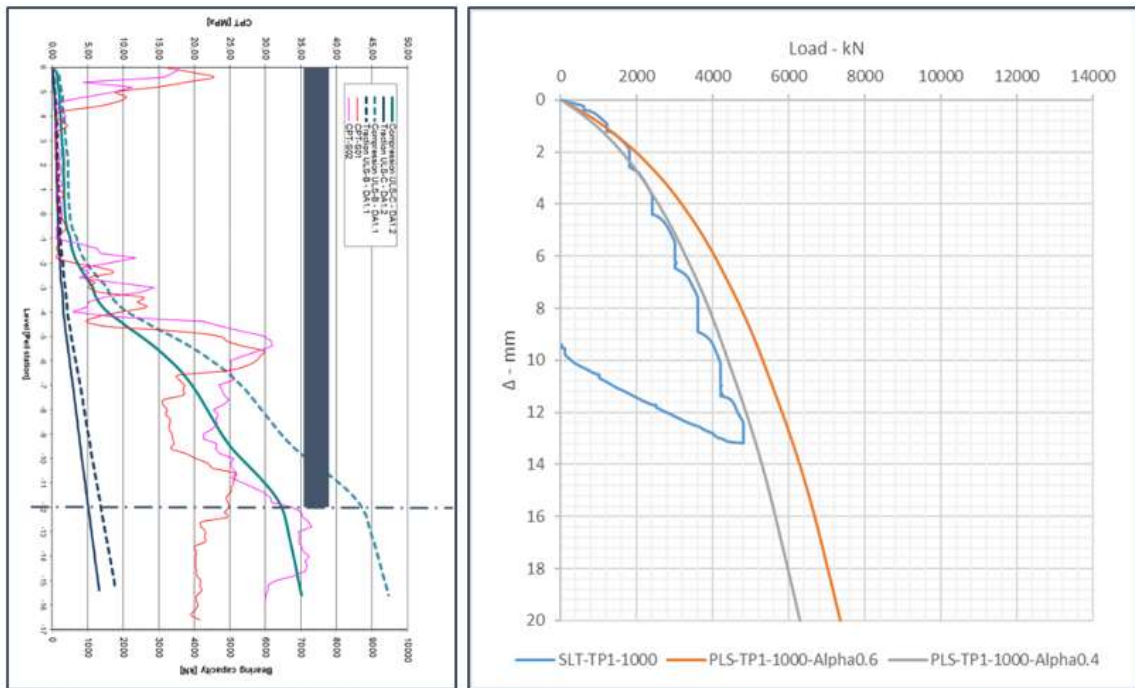
a)
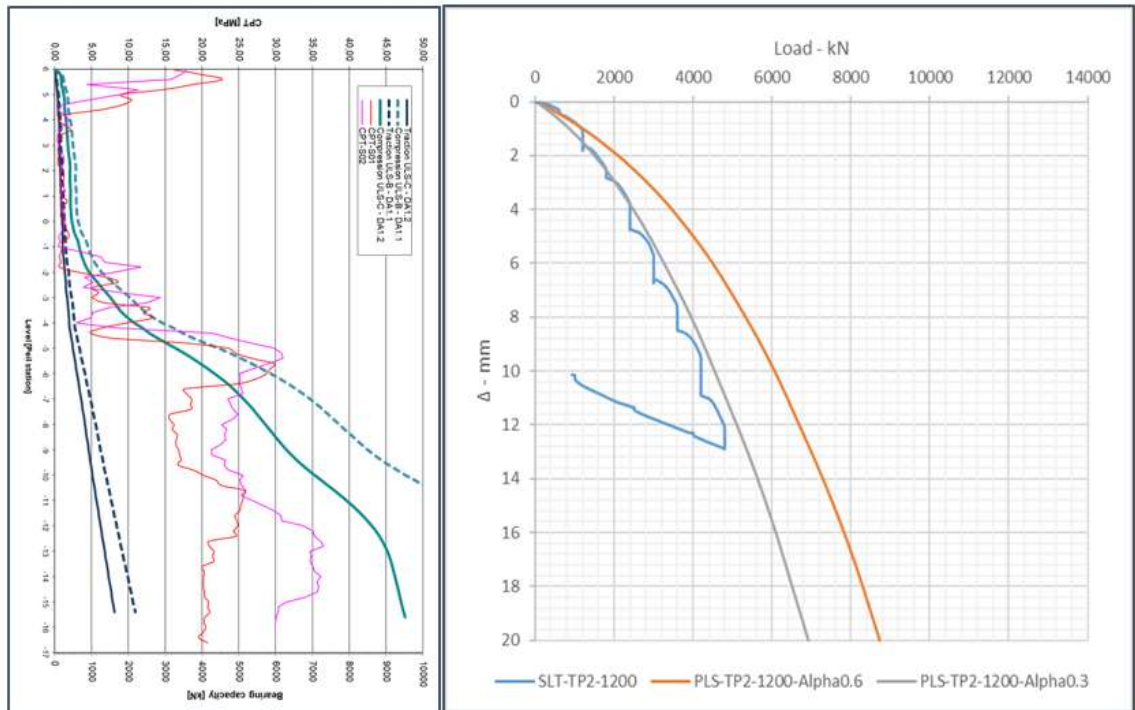
b)

Figure 10. Antwerp jobsite: a) Pile Load Test results for TP1 – diam. 1000 mm; b) Pile Load Test results for TP2 – diam. 1200 mm

The friction values were found as matching the values recommended for bored piles (and not the ones recommended for CFA piles), with a α_s close to 0.4 (TP1-1000 mm) and 0.3 (TP2-1200 mm) which we believe is not surprising considering the diameter of the piles, and the deep penetration into dense sands.

Further research is needed in order to better understand:

- If it is possible to establish a relationship between SR ratio and installation factor in a given soil

- How the diameter of the pile should be taken into account in the assessment of the pile capacity.

3.2.2 Displacement auger (screw) piles

The initial cast in place industrial application of Displacement Auger Piles appeared in the 1960's in Belgium and The Netherlands. The typical alluvial soils in the "low lands" are ideal for this type of pile and to a large extent explain their quick success in the area. To date the capacity and range of piling equipment (available power, torques of the rotary drives, pull downs…) has been increased along with differing auger configurations to allow the application of Displacement Auger Piles in more soil conditions.

Because of the technological evolution, a range of systems, types and labels have emerged (Van Impe (1988, 1989, 1994), Bustamante (1988, 1993), Huybrechts (2001), Basu et al(2010)). The term "Screw Pile" is used at times because the finished cast in place pile takes the shape of a conventional screw at others because the pile is "screwed" into the ground and at others because the pile resembles a large screw. An understanding of systems, types and labels is required.

Today, it is recognized that screw pile performance will depend on the key parameters defining the system:

- Shape of the auger – movement of the spoil
- Shape of the auger – effect on end bearing,
- Shape of the auger – shape of the final pile,
- Power of the piling rig to Rotate,
- Power of the piling rig to Push – force auger penetration,
- Casting method (pressure) of the concrete placement,
- Control of auger extraction – effect on the shape of the final pile.

A combination of the above governs the reliability and repeatability of the pile construction.

Screw piles (Displacement auger piles) can benefit of very interesting installation factors. Extensive research has been conducted in Belgium in the early years 2000, on the main systems used at that time. This research can be viewed as pioneering as screw piles are extensively used in Belgium, which gathers probably the largest experiences in this field. One can in this respect refer to the proceedings of the two Symposia on Screw piles, Brussels, (Holeyman, 2001) and Maertens and Huybrechts (2003). These campaigns and previous research illustrated some particularities associated with each system, and varying installation factors ranging between 0.65 and more than 1.00. The major differences can be observed for the end-bearing resistance. Finally, a global installation factor was prudently adopted in the Belgian code.

In recent years, though, new systems or variations on existing systems have been introduced, sometimes with important differences as shown in Fig. 12, showing a screw auger with an oversized portion of the extraction auger. In the same time, the detailed analyses of recent load tests have been providing ground for a more specific approach, with specific installation factors validated for each system. We will come back on this recent evolution in the last section.
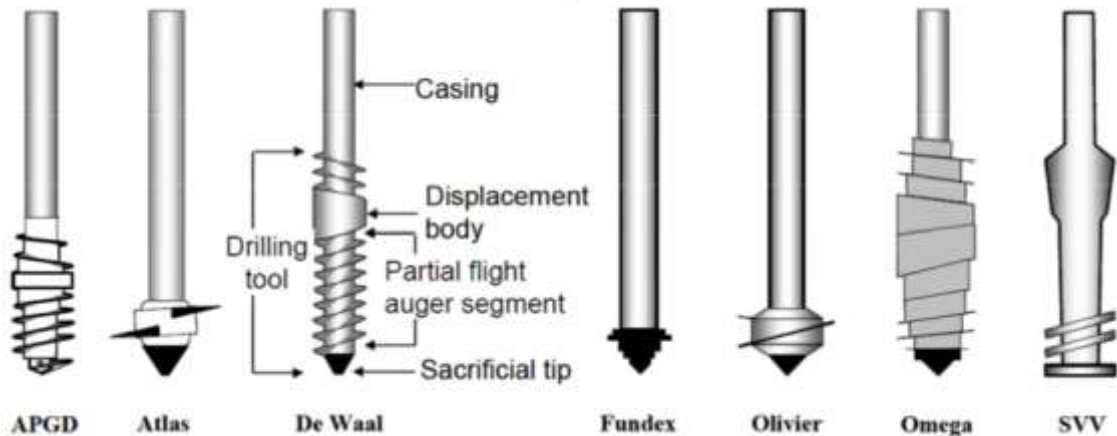
Figure 11. Drilled Displacement Piles – Current Practice and Design (Prasenjit Basu, Monica Prezzi and Dipanjan Basu, 2010)

Figure 12. Screw pile with oversized portion of excavation auger at the bottom (Bottiau, 2014)

In parallel, the use of injection in order to facilitate the penetration of displacement piles into dense sands or alternate loose and dense sands, as is encountered often in The Netherlands is getting more and more popular.

In this system, a tube corresponding to the pile concrete shaft and closed at its bottom by a prefabricated lost steel pile tip, with a diameter of the base diameter to be realized, is screwed in. During screwing-in phase simultaneous grout injection occurs at the bottom of the screw tip, in order to facilitate the penetration. The grout injection is mixed by the screw flanges with the in-situ soil and finally results in a grout shell around the concrete shaft. This shell can reach the outer diameter of the pile equal to the base diameter in sandy soils, although in clayey soils, the final diameter can be less. It is usual, in absence of other information, to take into account an intermediate diameter between the temporary tube and the pile tip.

This piling system proves to be very effective in difficult soil conditions. Recent applications in The Netherlands led to the application of larger dimensions reaching a combined diameter of more than 800 mm.

The exact effect of the grout injection, though, is not fully evaluated. For his reason, on major projects, SLTs are often required in order to control both the applicability and the pile capacity. This was the case on the jobsite in Brussels for the Railway Authorities, where displacement piles of diameter 540/660 had to be installed into relatively dense sands at a depth of 16.40 m.

Figure 13 illustrates the installation of the test piles and the results of a CPTE that was carried out in the axis of the test pile.

One fully instrumented SLT load test was performed by the BBRI. Instrumentation was installed after pile installation by integrating fibre optic extensometer sensors in reservation tubes that had been attached to the reinforcement cages (see Fig. 14).

The test load had been defined at 4800 kN, corresponding to 1.2 times the geotechnical bearing capacity of 4000 kN, (pile base settlement = 10% pile base diameter), which was estimated with the principles of Belgian design methodology according to EC7.

Figures 15 to 17 show the test results.

Results were very satisfactory showing a very stiff behaviour of the pile, certainly up to the predicted pile capacity. The test proved that, in the given soil conditions, the installation factors of DA piles could be safely used for the design of DA-piles with grout injection.

While, as mentioned before, a lot of experience exists in the low lands with displacement auger piles in their typical alluvial soils, the experience in particular soil as chalk e.g. is limited.

For a recent job site in the Mons area in Belgium, the pile foundation of a building needed to be installed at a relative large depth in order to obtain sufficient resistance for the high building loads. Several piles of the foundation had therefore to penetrate a chalk layer that is encountered on the site at a quite constant absolute level of ± 11.8 m TAW, which corresponds with a depth of about 18.5 m below soil surface level. A typical CPTE, illustrating the soil profile at the test location, is given in Fig. 18. The chalk layer shows in general cone resistance values between 3 and 10 MPa, with occasionally some higher peak values. The chalk layer is overlaid with sand, soft clay and peat layers with a variable thickness at different locations on the site.
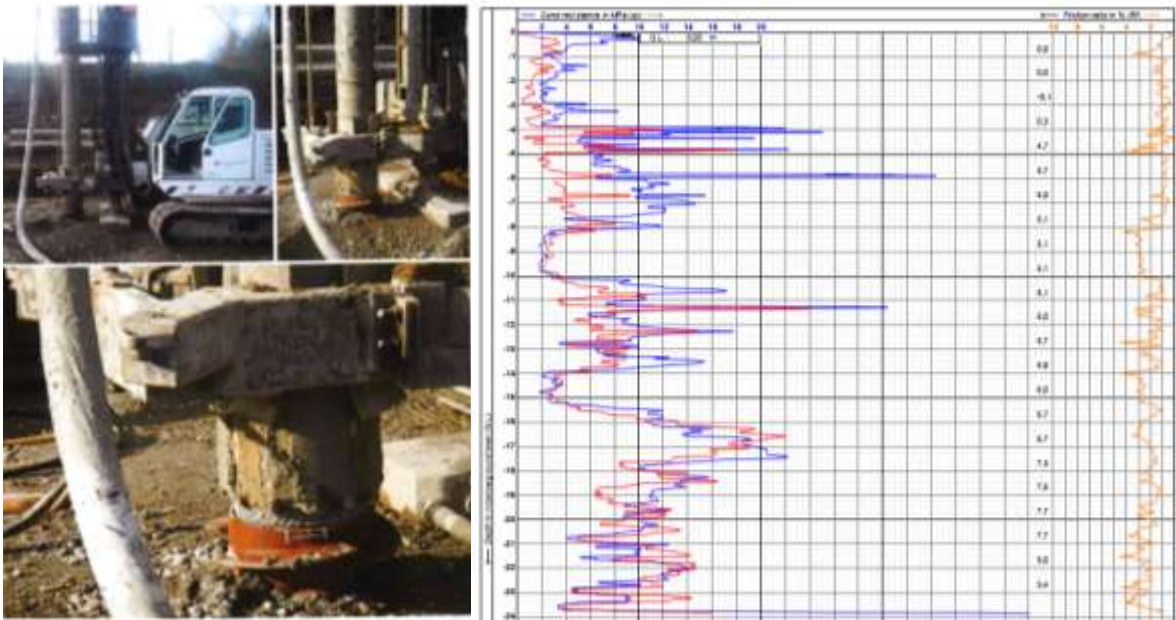
Figure 13. Haren test site - Illustration of the execution of a DA pile with grout injection (left) and results of the CPTE performed in the axis of the test pile

Figure 14. Haren test site - Illustration of the reinforcement cage provide with reservation tubes for the extensometer system
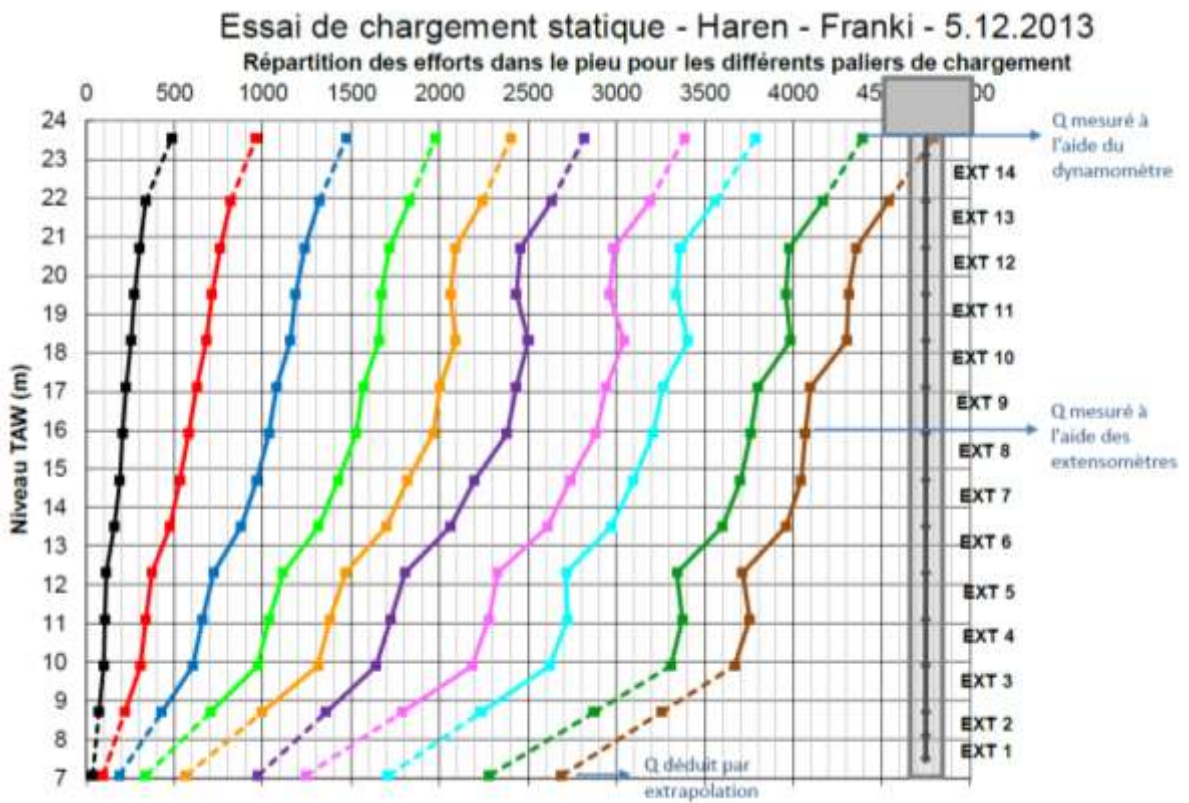
Figure 15. Haren test site - Normal load distribution in the test pile
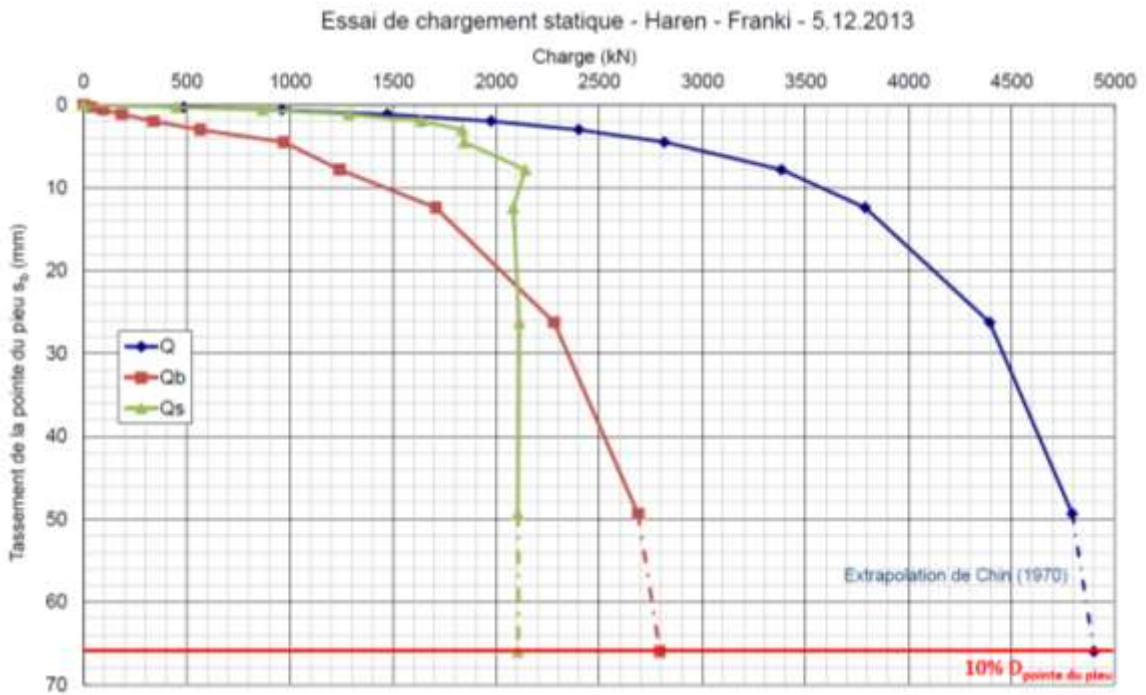
Figure 16. Haren test site - Load-settlement split up in pile base and shaft resistance
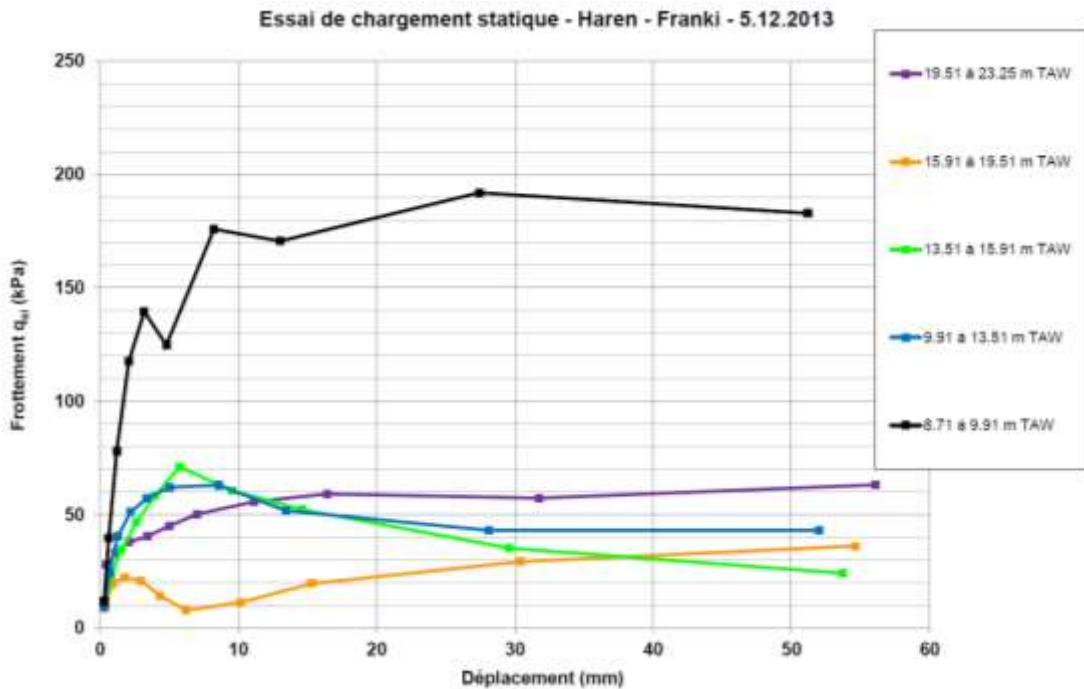
Figure 17. Haren test site - Mobilisation curves of the unit shaft friction in the relevant soil layers
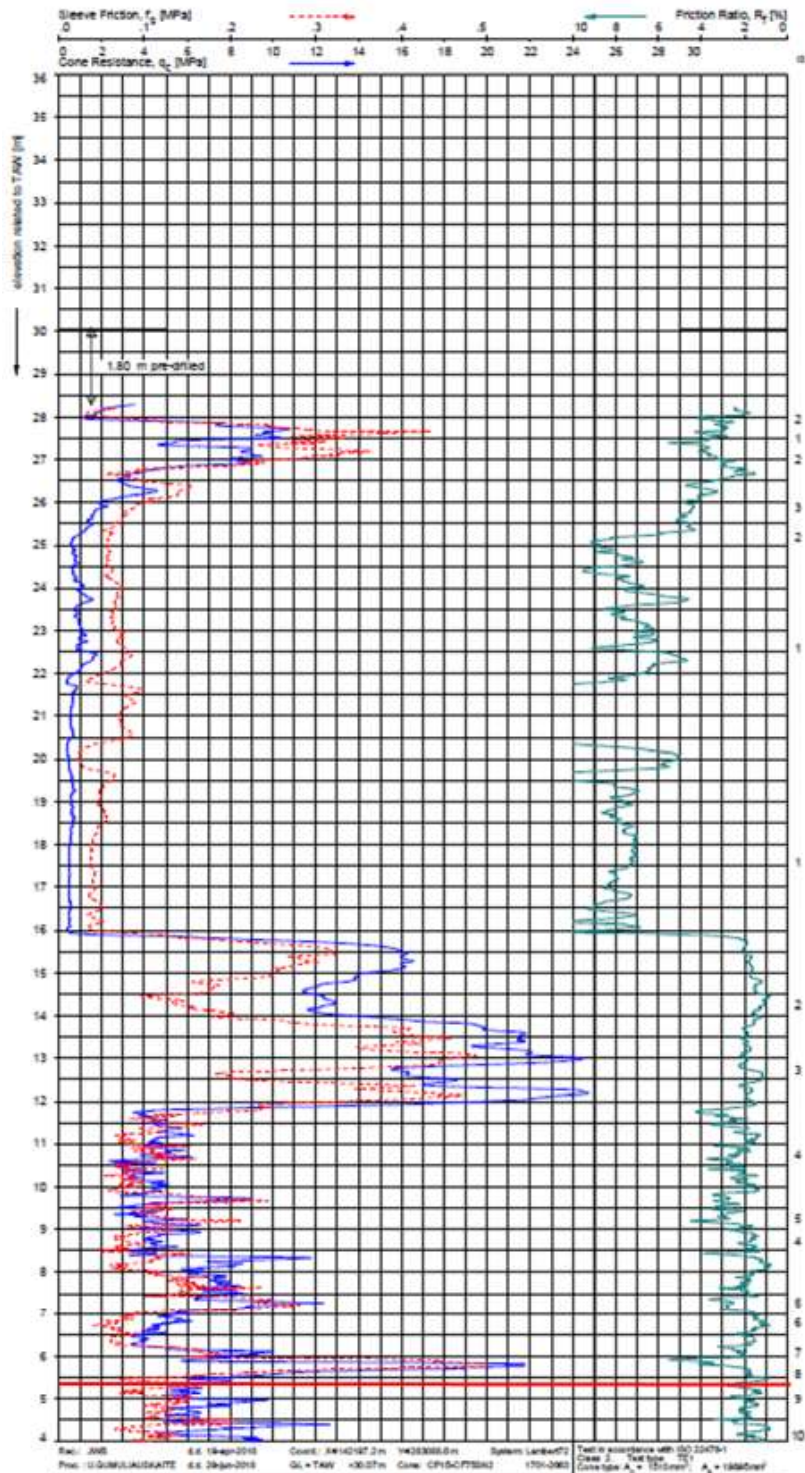
Figure 18. typical CPTE at the job site in the Mons area

A load test program on 8 fully instrumented test piles was carried out by the BBRI on the job site in order to obtain insight in the bearing capacity characteristic in the different soil layers and to verify the design according to the principles of the Belgian design methodology according to EC7 that provides up to now no factors for chalk.

DA piles where installed in 4 pairs at depths of 13.6 m and 17 m below soil surface level in the sand layer (corresponding with absolute levels of +16.7 m TAW and +13.3 m TAW respectively) and at depths of 23.2 m and 24.8 m in the chalk layer (which corresponds with absolute levels of +7 m TAW and +5.4m TAW respectively).

Moreover, for each pair a different DA-tool was used. For one pile of each pair a classical Ø 0.610 m Omega auger, with a relative short auger length of 0.95 m beneath the displacement body was used; for the second pile of a pair an alternative Ø 0.610 m auger with a larger auger length of 1.8 m beneath the displacement body was used(see also the previous Fig. 12).

Figure 19 shows the results of the load distribution for a 24.8 m long pile installed in the direct neighbourhood of the CPT shown in Fig. 18. The load distribution was deduced from the fibre optic sensors (type Fibre Bragg Grating, FBG) that had been integrated in the test pile.

A comparison of the load-settlement behaviour of all the test piles is given in Fig. 20. The full lines in Fig. 20 correspond with the results of the piles executed with the classical DA auger (short auger part), the dashed lines correspond with the results of the piles executed with the alternative DA auger (longer auger part). The reduction of bearing capacity observed between both augers varies between 5 and 20% (pair installed at a depth of 13.6 m). Taking into account the obvious differences and execution particularities, the reduction is considered as rather insignificant.

Anyway, the total pile capacity obtained from testing satisfied largely the predicted values, which were based on the Belgian design methodology according to EC7 and where a safe estimate for the pile resistance in the chalk layers was applied.

These kind of test campaigns on fully instrumented piles are very useful to increase the insight in the behaviour of different types of pile foundations and to improve systematically the design codes. As stated earlier, it isthe author's opinion that design codes should incorporate significant incentives to favour instrumented pile load testing on the job site. We will come back in section 7 on how the Belgian code tries to implement this in practice.
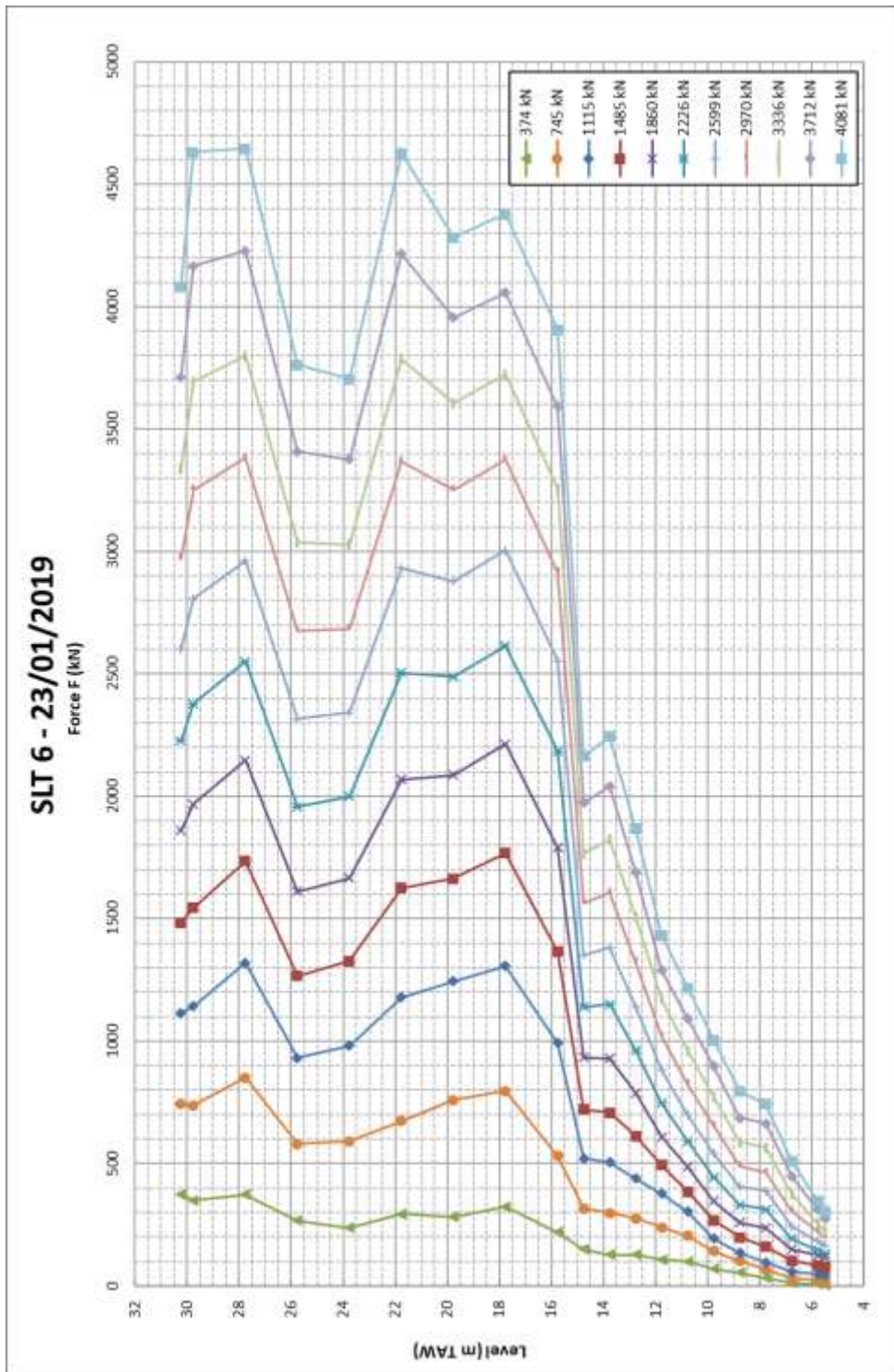
Figure 19. Load distribution of a 24.8 m long test pile deduced from fibre optic sensors (type FBG)
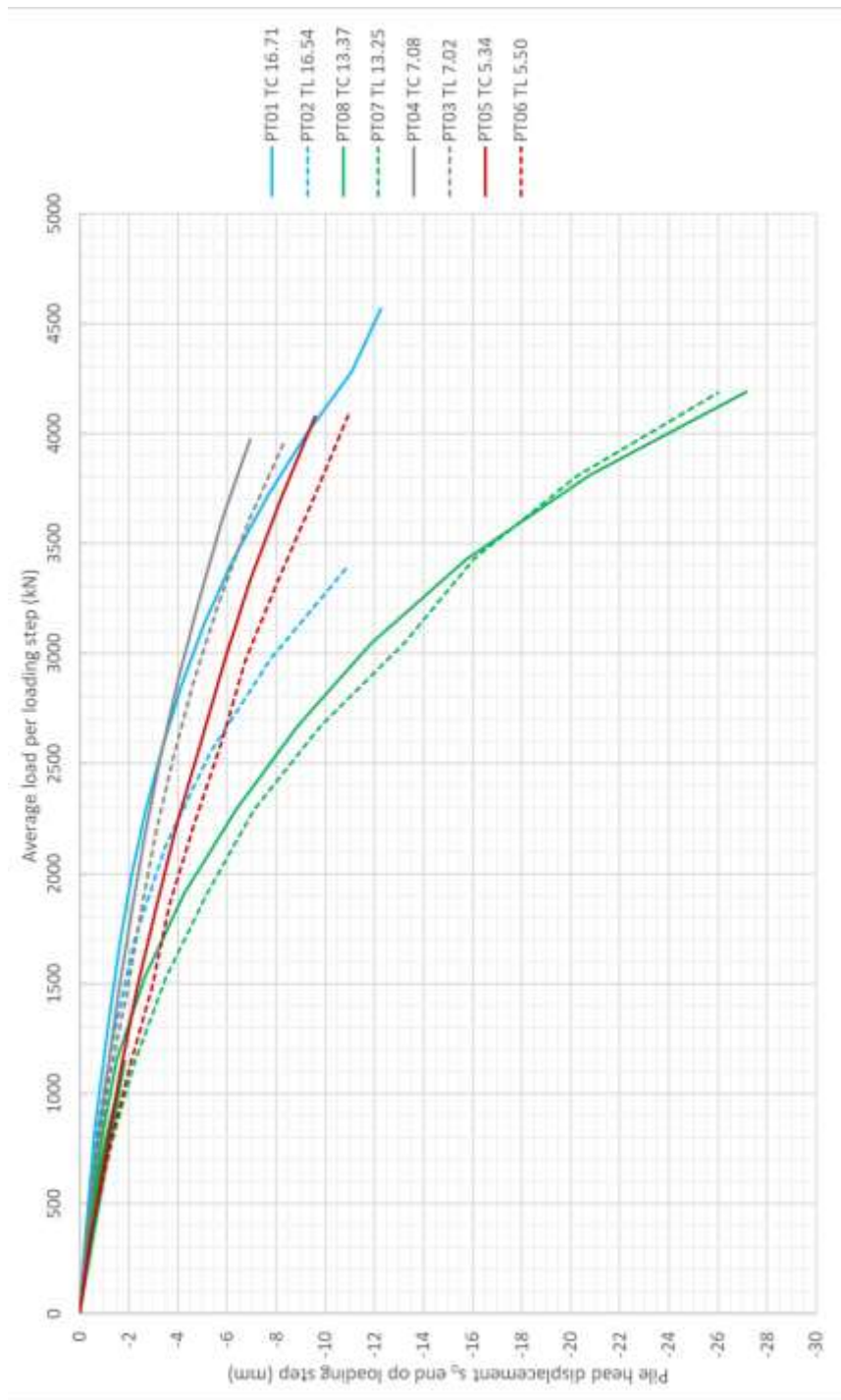
Figure 20. load settlement of the 8 test piles; each colour corresponds with a pair of piles; the full line represent the results of the piles with a classical DA auger, the dashed line correspond with the results of the piles with an alternative auger

3.2.3 Micropiles

The use of micropiles has grown significantly in recent years, together with the development of design and construction guidelines. Many application exist, from the logical underpinning and restricted access projects to even more complex situations where the ability to drill through a large panel of soils, including very variable and hard materials (boulders, karsts, debris,..) where large diameter piling would prove to be unsuccessful.

A large variation of equipment and tools both for drilling and for grouting are used, so that site specific load-testing is usually required to determine the final unit bond strength, certainly for serious structures if one wants to avoid over-conservative design. Here again, the limited dimensions of the foundation elements result in limited loads, and hence easier test setups.

In order to demonstrate the large domain of applicability and the flexibility of micropile systems it is worthwhile to make reference to a recent test campaign on 67 m deep micropiles in the Netherlands. These micropiles will make part of the foundation of a new highway bridge that crosses a high speed railway line.

In order to avoid too large settlements of the high speed railway infrastructure, a foundation system with minimal disturbance of the execution to the surrounding soil had to be applied. Moreover, as compressible clay layers are present at depths between 35 to 50 m, the pile load had to be transferred mainly below a depth of 50 m.

A typical CPTE on the site is given in Fig. 21.

To mitigate this problem the contractor proposed a Ø175-200 mm micropile system with self-drilling rods and with a total pile length of about 67 m, for which he would provide a system to avoid load transfer in the upper 50 m, without compromising the risk on buckling of the micropile system in the upper weak soil layers.

A preliminary compressive load test campaign on instrumented micropiles was performed to prove this concept. Several concepts to realise a "free length" of 50 m were applied by the contractor.

The instrumentation and tests were performed by BBRI. For the instrumentation a prototype with fibre optic sensors that could be installed immediately after the installation of the micropiles was developed (see Fig. 22).

In total 9 test piles were installed of which 6 piles were finally submitted to load tests : 3 compressive load tests on 67m long micropiles and 3 tension load tests on 26 m long micropiles.

Figure 23 illustrates the setup of the compressive load test on a micropile.

Figure 24 illustrates the results of the measured deformations with depth during the compressive load tests on 2 different micropile systems up to a maximum load of 725 kN. The differences between both micropiles exists mainly in the method and means that have been applied to create a "free length" over the upper 50 m.

This figure also shows the results of two different optic sensor technologies that were applied: a multipoint measurement system (Fibre Bragg Grating - FBG) and a distributed measurement system (Brillouin Optical Frequency Domain Analysis – BOFDA).

It can be seen that in the "free length" the measurements are somewhat influenced by variations in the pile section (coupling sleeves each 2 m) and by bending effects on the sensors, which is not surprisingly due to its installation method of the sensors in the fresh grout immediately after pile installation and due to the high length of the pile.

Nevertheless, the measurements allow to deduce a reliable normal load distribution with depth and show very clearly the effect of the load transfer in the upper 50 m. For the pile system on the left side the load transfer seems to be very limited and thus acceptable for the foundation concept. For the pile system on the right side, the applied load at the pile head is completely transferred in the upper 35 m and is thus not acceptable for the envisaged foundation concept.

The results of these test campaign are for the moment still under analysis and will be used to finalize the definite foundation concept of the bridge.

This case shows again the importance and added value of instrumented load test in the realisation and design of innovative but reliable foundation concepts.
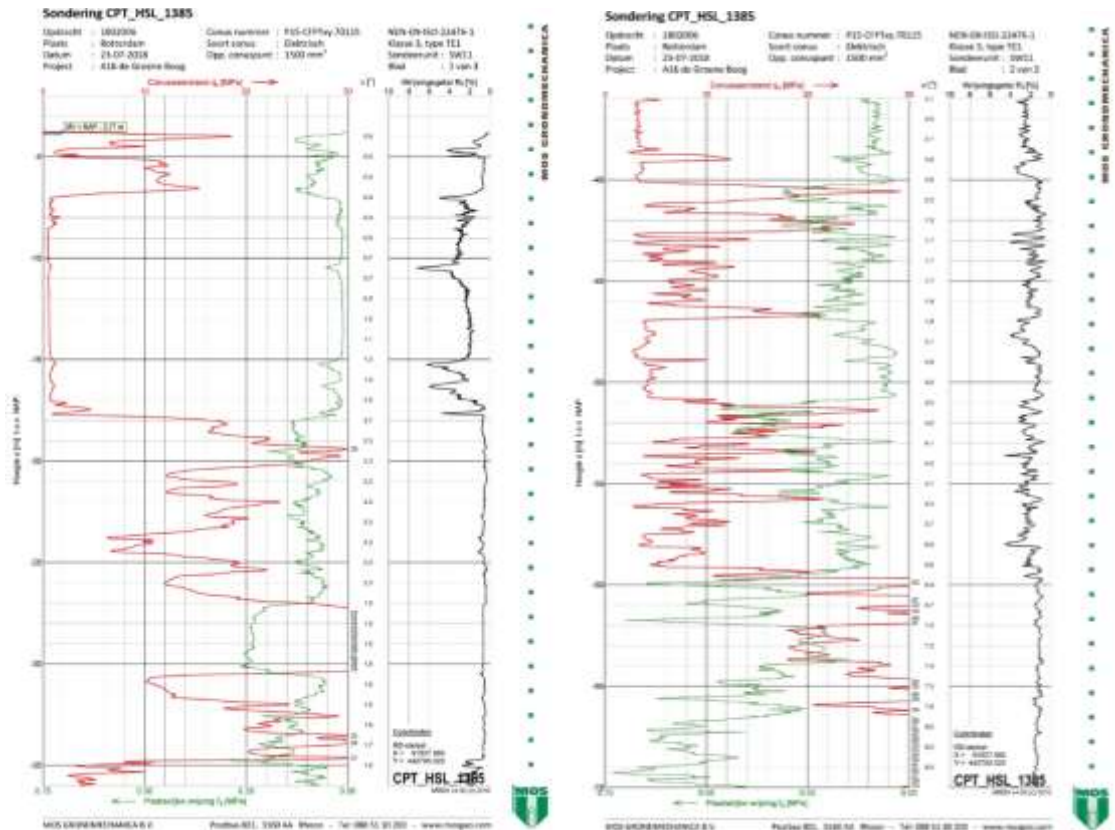
Figure 21. typical CPTE results on the site

Figure 22. Installation of the instrumentation in a 67m deep micropile

Figure 23. Set up of the compressive load test on a micropile
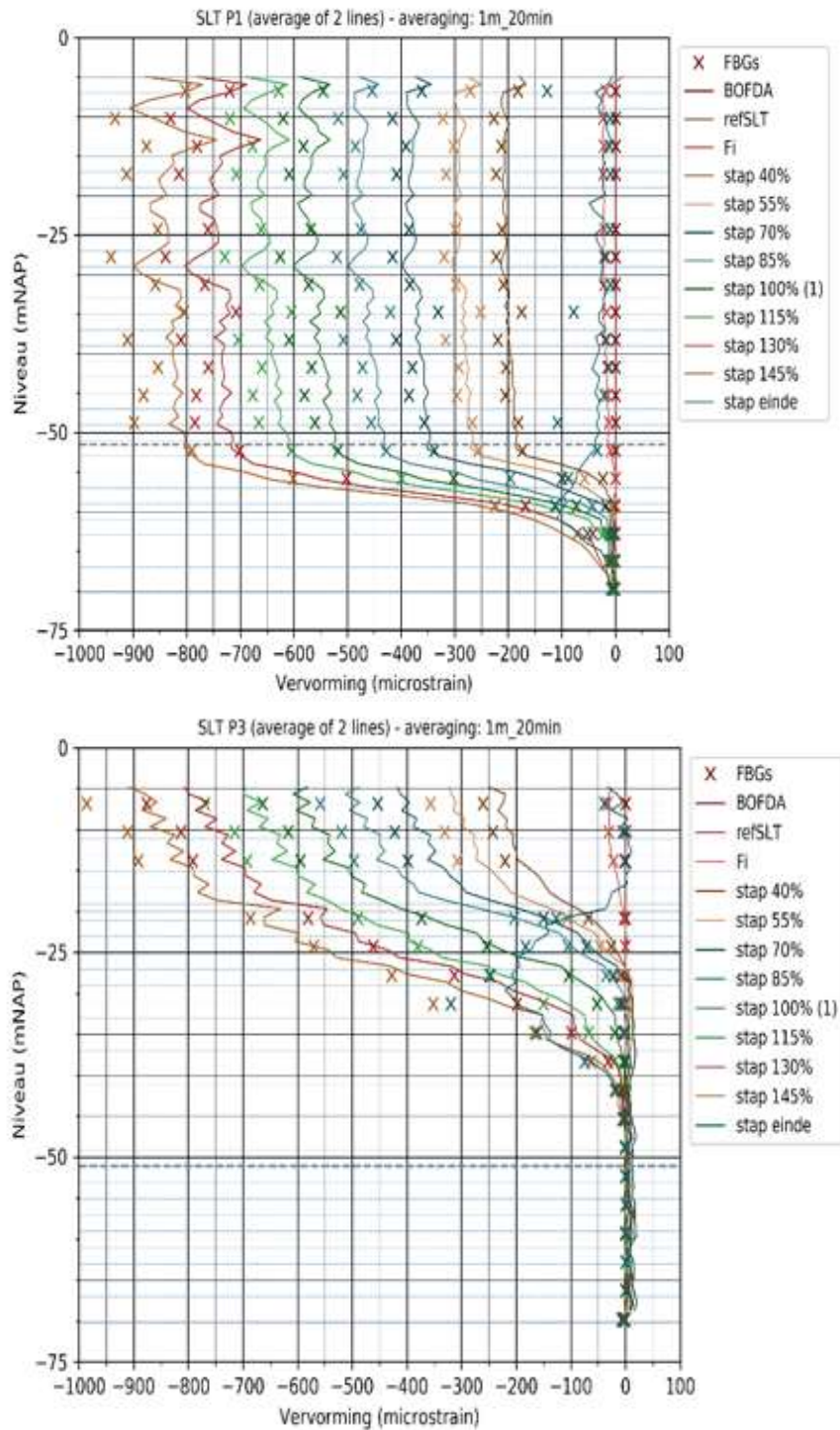
Figure 24. Results of the deformation measurements in 2 different micropile systems during a compressive load test

3.2.4 Bored piles

Tremendous improvements have been made to equipment capabilities (including the use of oscillators, rotators, multi-hammers) enabling to install larger piles at longer depth in harder soils. The use of oscillators or rotators enable to install full length segmental casings which is certainly favourable in loose sands or caving soils. In more extreme rock conditions or challenging working conditions, like limited headroom, Reverse Circulation Drilling is increasingly applied, with full face cutting at the base and removal of the spoil via air-lifting of the drilling fluid.

Because they are usually designed to carry high loads, the reliability of each bored pile is very important, and limited structural weaknesses can have major influence. As we discussed in other papers, many aspects of the pile execution, process may influence the pile capacity : drilling process and drilling tools, cleanliness of the pile bottom, quality of the casting procedure and interaction with the support fluid (bentonite or polymer).

Major advances have been made in the understanding of the critical role of these two fundamental components of the execution process of bored piles:
  - The particular aspects related to tremie concrete.
  - Support fluids

In 2014, the EFFC and DFI started carrying out a joint review of problems in bored piles and diaphragm walls cast using tremie methods. A Task Group was established and the 1st Edition of the "EFFC/DFI Guide to Tremie Concrete for Deep Foundations" was published in 2016. The 2nd Edition was published in 2018. The 1st Edition included some recommendations on support fluid properties, but it rapidly became clear that the preparation, characteristics and testing of support fluids required a dedicated approach. A Support Fluid Task Group was therefore established in 2017 resulting in a Guide presenting good practice in the use of support fluids for the construction of deep foundations and setting out the latest understanding of support fluids.

These two excellent documents have thus recently been made available and provide invaluable information on the topics. It is obviously impossible to summarize these two extensive documents here, but we want to give a few key hints we learned.

EFFC/DFI Guide to Tremie Concrete for Deep Foundations (Beckhaus & Harnan, 2018)

Modern mix designs clearly deviate from those of "classic concrete" (water, aggregates and cement), and consist of comparatively low water contents and low water-cement ratios, often below 0.45, using admixtures such as fly ash or other additions but also chemical admixtures (often as a cocktail of superplasticizers and retarders, sometimes even topped by stabilizers). On the other hand, recent evolution in the design of structures reflects the possibilities of making economic use of building materials, resulting in high strength requests and dramatically dense reinforcement, and increasing durability requirements. Finally, execution processes, as explained before, have resulted in larger and deeper foundation elements, and hence, longer installation and casting periods, requesting highly flowable and set-retarded concrete mixes for several hours if needed.

It is important that the concrete industry and the Deep Foundations specialists realize that this evolution can become dramatic if not taken seriously. A first advance was made when the requirements for Deep Foundation concrete was shifted from the Execution Norms to the Concrete standard EN 206, under the pressure of the Technical Working group of the EFFC. EN 206 in its recent Edition EN 206: 2013 comprises general regulations for the composition and quality of fresh concrete, and, in its normative Annex D, particular rules for deep foundation

concrete used in bored piles and diaphragm walls, taken from the execution standards EN 1536: 2010 and EN 1538: 2010.

Specific restrictions for deep foundations for composition and consistence, according to Annex D, depend on the placement procedure (see Table 1 for bored piles). It is understood that maximum consistency has been standardized on the basis of experiences at the time, to reduce the risk of segregation and associated negative effects. The upper consistency limits appear to disregard the frequent need for higher values corresponding to a sufficient flowability e.g. in order to flow freely around and through the reinforcement.

Accordingly, in terms of pile or wall integrity and quality, it is also important to consider requirements for concrete cover and clearance between reinforcement bars. In this context, the maximum coarse aggregate size is correctly regulated in the European standards, for deep foundations to a maximum of ¼ of the clear space between bars, in order to ease the flow through and around reinforcement.

However, these requirements are insufficient. With modern, five-component concrete the options to individually design the concrete for specific properties are multi-dimensional, i.e. the characterisation of fresh concrete has become more complex and needs at least two rheological parameters to be sufficiently described. One is viscosity and the other is yield stress. The EFFC-DFI Guide helps understanding the concrete's rheology, which is necessary to properly appreciate the main placement characteristics of workability and stability, where:

- workability is simply defined as that "property of freshly mixed concrete which determines the ease with which it can be mixed, poured, compacted, and finished" , and

- stability is simply defined as the "resistance of a concrete to segregation, bleeding and filtration" .

The R&D program has shown that, for tremie concrete, additional requirements for the concrete should be specified in terms of single target values, test methods and acceptance criteria. The Guide usefully comes up with advanced recommendations for testing fresh concrete including the specific, aspects of workability and stability (see Table 2).

Workability:

It is shown that "the fundamental properties characterising concrete workability are yield stress and viscosity. As there are currently no practical field tests to measure these properties directly, indirect measurements are required".

The slump flow test (in accordance with EN 12350-8 and ASTM C1611) was found suitable to reliably measure the yield value of tremie concrete (see Fig. 27).

The viscosity is considered a secondary rheological property of fresh tremie concrete. As the viscosity is usually hard to adjust independently from the yield stress, no discrete range is recommended in the Tremie Guide. Nevertheless, a medium viscosity as shown in Fig. 28 is still considered preferable for tremie concrete. Instead of a direct measurement of viscosity by an outflow test, which can also be found in the Tremie Guide, a rough measure can be derived from the slump flow test by simply recording the time the concrete needs to its final spread, by dividing the average travel distance of the concrete ((slump flow in mm – 200 mm)/2) to the time required (in seconds).

Stability:

The stability of concrete is harder to assess. One of the simpler tests for stability is the Visual Stability Index (VSI) test which can be conducted as part of the slump flow test. It allows the concrete to be visually checked. After slumping, a visual check is made to look for segregation or bleeding i.e. no wet sheen on the surface, no mortar halo or aggregate pile in the centre of the mass (see Fig. 29).

Finally, the Guide gives some interesting research using numerical methods. For discrete site conditions a full scale trial with dyed

concrete could prove such flow patterns but more generally numerical models may be used to explain the relevant dependencies on concrete flow. To cater for this and to prepare for the future opportunities given by modern computational tools a new Section 9 Numerical Modelling of Concrete Flow has been introduced in the new Tremie Guide. Figure 30 indicates how numerical studies can help to understand the flow path of freshly poured concrete and its general consumption over height and time.

Figure 25. Reverse Circulation Drilling – limited headroom and full face drilling tool (Brown , 2012)

Figure 26. Modern five-component substitutes the old three-component concrete technology

Table 1: Requirements for Bored Piles, in accordance with Annex D of EN 206:2013

Placement condition	Cement content [kg/m³]	Water-cement ratio [-]	Slump [mm]	Flow diameter [mm]
Dry	≥ 325	≤ 0.60 and in compliance with provisions valid for specified exposure classes	150 ± 30	500 ± 30
submerged under water,	≥ 375		180 ± 30	560 ± 30
under a stabilizing fluid			200 ± 30	600 ± 30

Table 2: Recommendations for testing tremie concrete

No	TEST	Recommended RANGE for TARGET VALUES	TOLERANCE on specified Target Value	RELEVANCE For SUITABILITY & CONFORMITY	FREQUENCY** of specified ACCEPTANCE testing
A1.1	Slump Flow	400 – 550 mm	± 50 mm	M	Each load
A1.2	Slump Flow Velocity	10 – 50 mm/s	± 5 mm/s	M	At least 1/week
A1.3	VSI	0	-	M	Each load
A4	Modified Cone Outflow	3 – 6 s	± 1 s	R	As required
A6	Workability Retention	to be specified	- 50mm	R/M*	As required
A7	Static Segregation	≤ 10%	+ 2%	R/M*	As required
A9	Bleeding	≤0.1ml/min	+ 0.02 ml/min	R/M*	As required
A10	Bauer Filtration	≤ 22 ml***	+ 3 ml	R/M*	As required
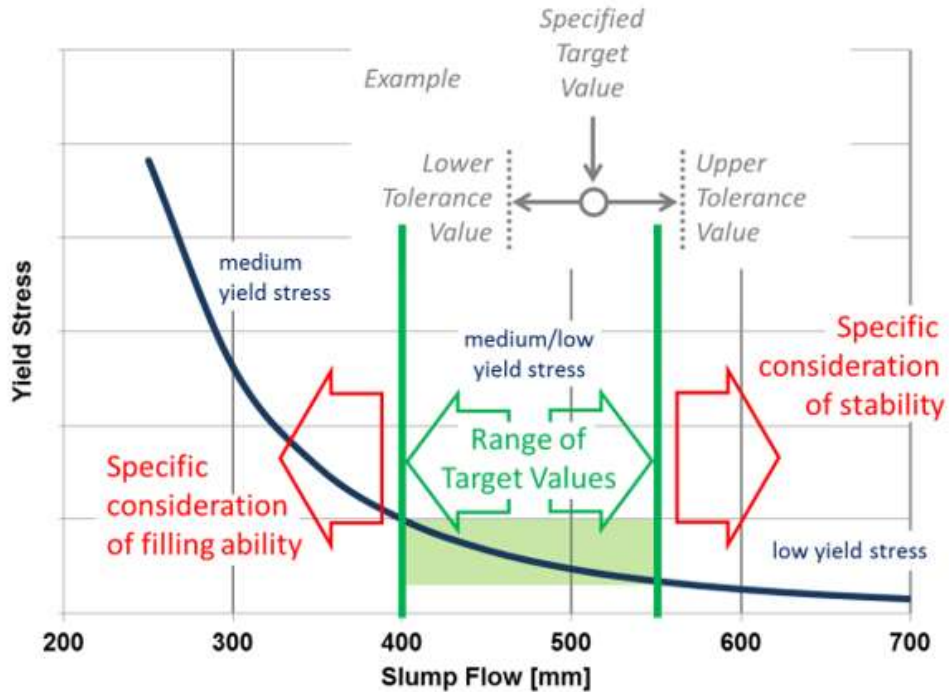
Figure 27. Slump Flow Curve related to yield stress and recommended range for tremie concrete
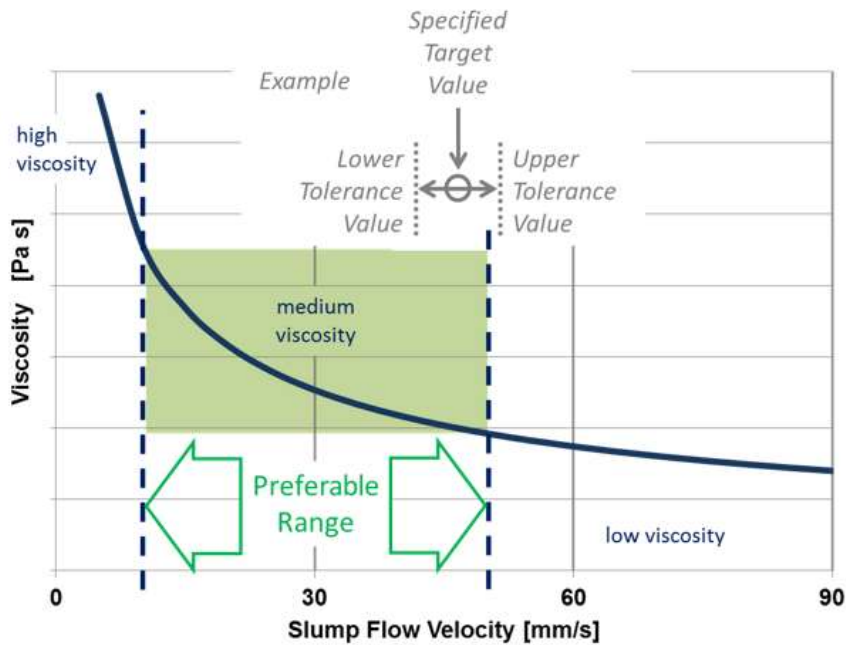
Figure 28. Slump Flow Velocity Curve related to viscosity showing the recommended range of medium viscosity for tremie concrete

Figure 29. Examples of Visual Stability Index Classes [1], photo courtesy of BASF Corporation
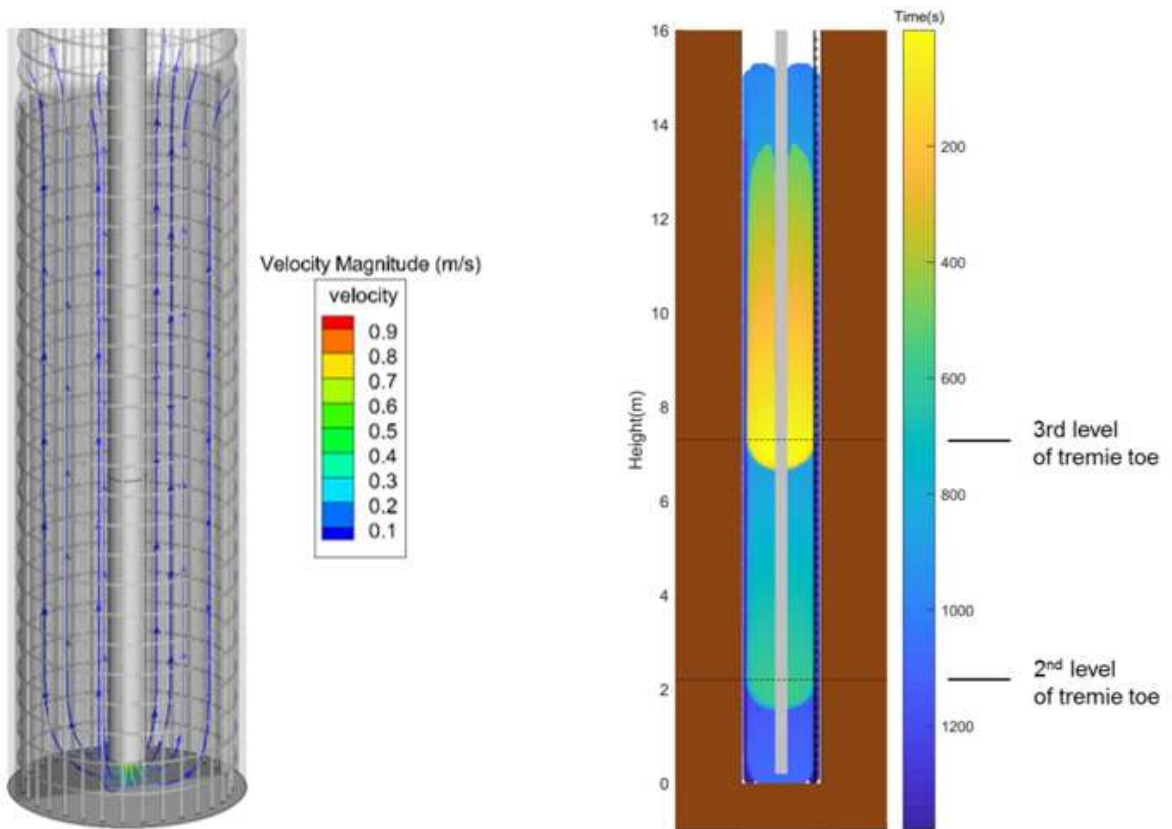
Figure 30. Simulations presenting bulging flow of bulk concrete by velocity streamlines (left), and by dyed concrete following a staged lifting of the tremie pipe [1, 4]

EFFC/DFI Guide to Tremie Concrete for Support Fluids(2019)

Bentonite slurries have been used for over sixty years for the temporary support of excavations such as bored piles and diaphragm walls. Technological developments of drilling methods and enhanced equipment capacities have greatly increased the impact of the soil chemistry and soil fineness on the behaviour of the support fluid.

There have also been advances in support fluid technology. Bentonite properties have evolved and other support fluids (e.g. polymers) have been used in place of bentonite. When used correctly, polymer fluids can offer advantages over their bentonite counterparts, including improved foundation performance, lower environmental impact, smaller site footprint (site area) and also simpler preparation, mixing and final disposal as they are used at much lower concentrations.

The purpose of the Guide is to present current understanding on bentonite, other clays, polymers and blended systems, including the advantages and limitations, in order to allow informed selection of the optimum technical solution(s) for the conditions on each individual worksite.

Three different classes of support fluid are :

- mineral (e.g. bentonite),

- natural (e.g. gum), and modified natural polymer (e.g. CMC and PAC) used alone or blended with bentonite,

- synthetic polymer (e.g. PHPA) – usually used alone.

Bentonite has the beneficial property of forming a filter cake at the excavation sidewall which acts to restrict fluid loss into the surrounding soil and allow a positive hydrostatic head to be maintained within the excavation. The filter cake forms as the bentonite particles are filtered out of the fluid as the hydrostatic head within the excavation drives the fluid into the surrounding permeable soil, as illustrated in Fig. 31.

Polymers perform in a different way to bentonite slurries. **High molecular weight synthetic polymers** are long chain-like hydrocarbon molecules (typically partially hydrolysed polyacrylamides, or PHPA) which interact with each other, with the soil, and with the water to effectively increase the viscosity of the fluid. Although there may be some indication of a polymer membrane at the soil interface, there is no formation of a filter cake as with bentonite. The long polymer chains can be damaged by pumping. Natural modified polymers such as modified celluloses (e.g. polyanionic celluslose, PAC) have been successfully used in the reverse circulation process (e.g. hydromill). They are considered as bio-degradable and produce very thin mud cakes and good fluid loss control.

The flow behaviour of support fluids can be investigated by plotting shear stress as a function of shear rate. Figure 32 shows shear stress-shear rate plots for some idealised flow types with examples of fluids that may show these rheologies.

The three classes call for a separate analysis of their properties and subsequent range of values to be attached to them. The Guide provides target acceptance values and testing methods for the three categories.

The Guide also provides guidance for the correct selection of the adequate support fluid. There is no universal fluid for all projects and selection of the right product(s) has to be made after considering all the parameters. When choosing the preferred support fluid, the following should, as a minimum, be considered:

- project and site dimensions: diameter, width, length and depth of foundation elements to be constructed,

- equipment (excavation, pumping, treatment etc.) and the length of casing (if used),

- excavation method (static drilling or reverse circulation drilling),

- soil conditions: geotechnical profile (e.g. type of soils, permeability, cohesion and chemistry),

- groundwater level and chemistry,

- make-up water quality,

- fluid requirements: ease of use and proven effectiveness in the soil conditions,
- environmental issues (known contaminants and obstacles),
  - disposal requirements/restrictions,
  - supply chain,
  - economics.

Table 3a and 3b present indications of appropriate drilling fluids related to the method of construction and the soil type.

For any given project, the appropriate support fluid will be selected based first on fluid rheology requirements, then availability of resources and previous local experience.

Here again, an excellent way of obtaining important information on the construction aspects of any deep foundation element and thereby ensuring success of the works is to install one or more full-scale trial elements, e.g.:

- Trial pile load tests to assess shaft friction / filter cake performance and base performance,
- Excavations to expose completed panels and stop-end – to assess filter cake thickness and concrete imperfections, see Tremie Guide - Appendix D.
- Pile / panel verticality can be assessed and this is important for circular shafts acting in hoop compression. Various testing methods can be compared.
- Trials can also be undertaken to assess the base cleaning, the initiation of tremie concreting and the development of the interface layer by recording density profiles. When the concreting is undertaken to the ground surface the interface layer can be sampled at ground level (see Appendix A of the guide).

During the execution, properties characterizing a support fluid such as rheology or chemistry are influenced by :

- the ground conditions and environmental considerations,
- the type of foundation system being constructed,
- the proposed construction method,
- the foundation construction cycle.

Those properties, determined by the standard tests described must be conformed to acceptable values in order to ensure the final quality and integrity of the structure.

The life line of the support fluid during the construction process is shown in Fig. 33 and Table 4 with a specific set of tests corresponding to each construction step. The specified properties must be checked and maintained at each step using the standard tests described in Appendix B of the guide to ensure the quality and integrity of the completed works.

During foundation construction it is essential that the contractor complies with the relevant standards for quality assurance and control. The Guide gives the different test methods for each stage for bentonite and polymer fluids with recommended frequencies (Tables 5a and 5b).

The Guide provides a summary of acceptance values for these different methods used in some existing standards.

This first edition presents acceptance values for drilling fluids as given in commonly used Standards. Current acceptance values, though, originate from oil well activities in the middle of the last century. Whilst the values have slowly evolved, there appears to be a lack of technical evidence as to why a certain value is specified. It is clear that the current standards do not adequately cover all the types of fluids available for use in deep foundations or the total tests required. With industry support organized with the help of both EFFC and DFI, a detailed data acquisition study is currently ongoing with visits to sites in both the US and Europe. Based on the findings of this study, it is hoped to give improved recommendations on acceptance values for bentonite, polymer and blended fluids and these will be contained in the second edition which is scheduled for publication in 2020/2021.
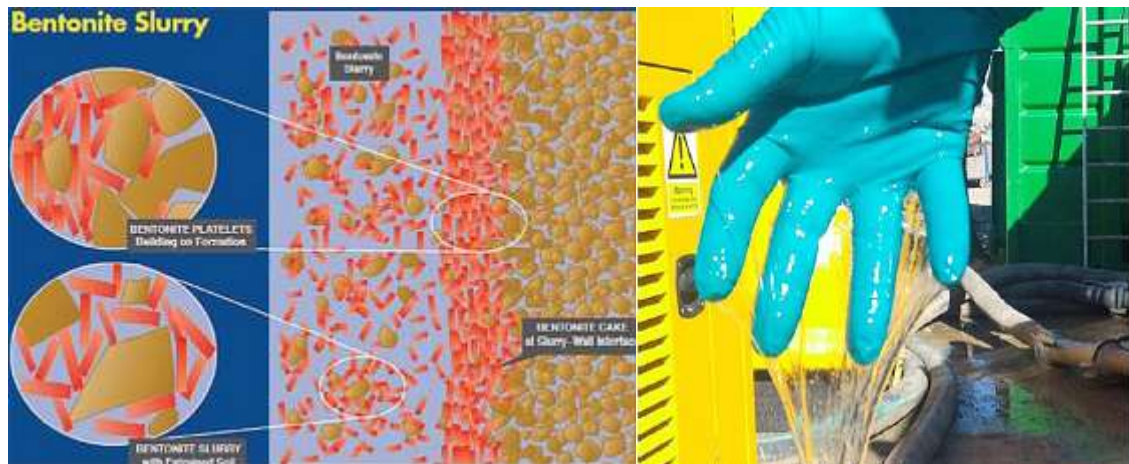
Figure 31. Comparative behaviours of bentonite and polymers
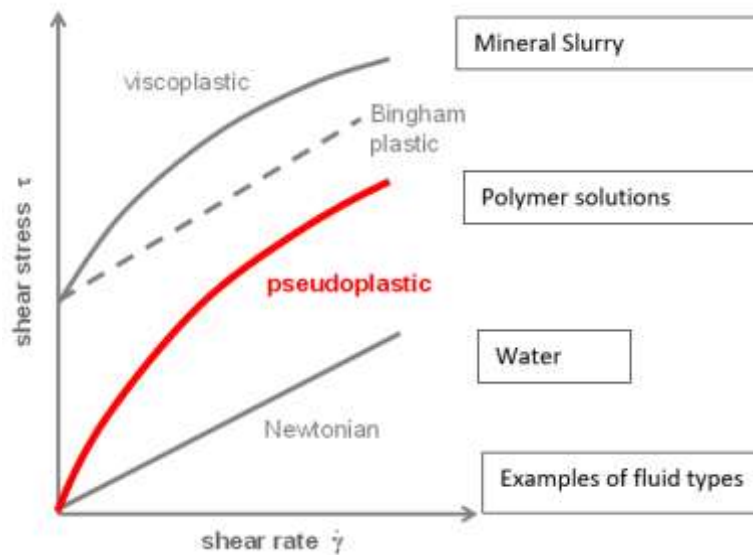
Figure 32. Fluid rheologies

Table 3a: Support Fluid choice related to soil conditions

Fluid Type	Common Examples	Method of Excavation				
		Grab	Hydromill	Auger / Bucket (Kelly)	Reverse or Direct Circulation	Trench Drains
Water		X	X	X	✔✔✔	X
Mineral	Natural Sodium Bentonite Activated Sodium Bentonite	✔✔✔	✔✔✔	✔✔	✔	X
Natural Polymer	Gum Polysaccharide	X	X	X	X	✔✔✔
Modified Natural Polymer	CMC PAC	✔	✔✔	✔	✔	✔✔
Synthetic Polymer	PHPA Vinylic	✔✔✔	–	✔✔✔	✔	✔

✔✔✔ ideal   ✔✔ acceptable   ✔ possible   X not recommended

Table 3b : Support Fluid choice related to the method of construction

Soil Type	Bentonite		CMC/PAC		PHPA		Comments
	Static	Reverse Circulation	Static	Reverse Circulation	Static	Reverse Circulation	
Rock	✔	✔	✔	✔	X	X	no stability issues
Boulders/Cobbles	?	✔	X	X	X	X	fluid loss / head
Gravels	✔	✔	X	?	X	X	fluid loss / head
Coarse Sand/Gravel	✔	✔	?	?	?	X	fluid loss / head
Medium/Fine Sand	✔	✔	✔	✔	?	X	head / low cohesion
Silty/Clayey Sand	✔	✔	✔	✔	✔	X	head / low cohesion
Clay	✔	?	✔	✔	✔	X	head / low cohesion
Hard Clay/Limestone	?	?	✔	✔	✔	X	no stability issues
Swelling Clay	?	?	✔	✔	✔	X	head / soil hydration (sloughing)

✔ applicable   X nonapplicable   ? to be evaluated

Note: Using additives is a way to enhance each type of fluid listed to extend its application in the different soil types (especially those marked with a '?')
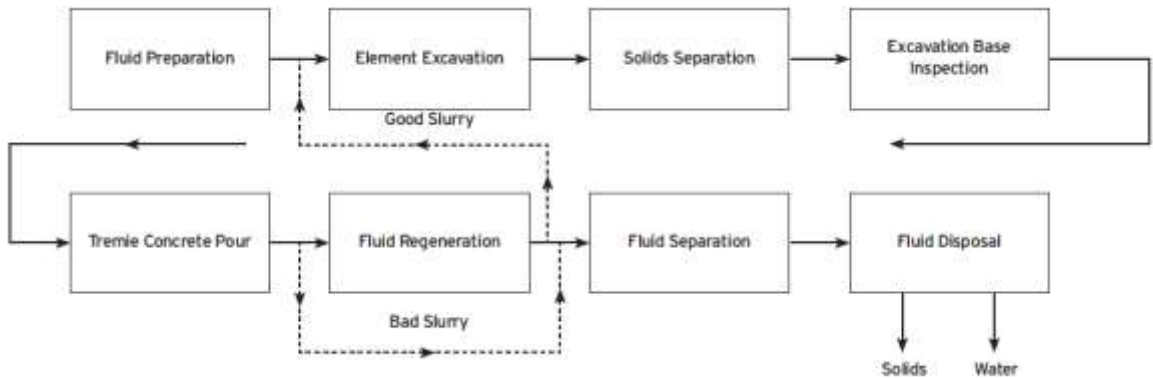
Figure 33. Support Fluid Lifeline During the Construction Process

Table 4 : Construction stages and testing

Stage	Activity	Description	Support Fluid Test
1	Fluid preparation	Mixing of fresh fluid	pH, viscosity, density, filter loss
2	Element excavation	Stabilize excavation	Density, filter loss
3	Solids separation	Mechanical, chemical or gravity treatment of fluid	pH, viscosity, density, sand content, silt content (gel strength)
4	Excavation base inspection	Post rebar placement inspection	Sand & silt content, filter cake
5	Tremie concrete pour	Fluid return from concrete pour	Check for cement contamination
6	Fluid regeneration	Mechanical, chemical or gravity treatment of fluid	pH, viscosity, density, sand content, silt content (gel strength)
7	Fluid separation	Waste fluid separation	Sand & silt content, viscosity
8	Fluid disposal	Waste fluid & solid disposal	pH, sand & silt content, oxygen demand

Table 5a: Applicable Tests and Frequency for Bentonite Support Fluids

Test	Test Method	S1 Fresh Fluid	S2 Excavation Fluid	S3 Before Concreting	S5 & S6 Fluid for Reuse
Frequency		daily	once per element	before pour	daily
Viscosity	Marsh Funnel	M	R	M	M
Density	Mud balance	M	R	M	M
Sand content	Sand content kit	N/A	R	M	R
pH	pH-paper	M	R	M	R
Filter loss	API filter press	M	R	M	M
Filter cake thickness	API filter press	M	R	M	M
Silt content	Calculation	N/A	N/A	O	O
Gel strength	Fann Viscometer	O	N/A	O	O

M : mandatory, R : recommended, O : optional, N/A : not applicable

Table 5b: Applicable Tests and Frequency for Polymer Mud (except for cutter)

Test	Test Method	S1 Fresh Fluid	S2 Excavation Fluid	S3 Before Concreting	S5 & S6 Fluid for Reuse
Frequency		daily	once per element	before pour	daily
Viscosity	Marsh Funnel	M	R	M	M
Density	Mud balance	M	R	M	R
Sand content	Sand content kit	N/A	R	M	R
pH	pH-paper	M	R	R	M
Filter loss	API filter press	N/A	N/A	N/A	N/A
Filter cake thickness	API filter press	N/A	N/A	N/A	N/A
Silt content	Calculation	N/A	N/A	O	O

M : mandatory, R : recommended, O : optional, N/A : not applicable

4 RECENT ADVANCES IN TESTING OF GEOTECHNICAL STRUCTURES

Realizing accurate measurements in deep foundations during testing is not evident, due to the fact that the installation conditions are in most cases very harsh. Often there is also a lack of space to integrate many sensors and their cabling into the foundation elements or it is even not possible to fix/integrate instrumentation at all. These arguments are in many cases valid for classical measurement devices, e.g. strain gauge or vibrating wire sensors. Several reference documents with regard to the more classical type of measurement devices that can be used in geotechnical engineering and piling in particular can be found in the literature, amongst others in Dunicliff (1993) and Hertlein, B. et al. (2006).

The major advances that took place in the ITC sector have found the last decade also their way to the geotechnical sector, leading to significant ameliorations of the classical measurement devices. Miniaturization, integrated electronics, wireless data transmission, real time and online visualization, etc. have been introduced and

applied on regular base, - see e.g. (Soga, 2010) and (Van Alboom, 2012) -, but the most important advancement in the last decade originate, according to the authors' opinion, from the fibre-optics technology.

Optical fibres are very small and fragile materials and the use of them seems on first sight not coherent with the generally required robustness of sensors applied in geotechnical engineering. However, they show some important advantages:

- the optical fibre itself is the sensor and the information carrier for the light waves; generally spoken a fibre optic sensor works by modulating one or more properties of the propagating/reflected light wave (intensity, phase, polarization, frequency, …) in response to the parameter (e.g. deformation, temperature) that is being measured;

- the core of the optical fibres consists of a thin strand of glass (about 10 μm diameter) in which light is transmitted; glass is an inert material so very suitable in harsh and aggressive environment;

- all the sensing and transmitting components of a fibre optic sensor are non-electrical, so disturbance of the measurements due to electro-magnetic interference, stray currents, corrosion or short circuits due to e.g. water infiltration are not an issue; they can also be applied in an explosive environment;

- the measured reflections of the light waves are stable on the long-term (no zero drift);

- in the case of multiplexed or distributed optical sensors a multitude of sensor points are available on one single optical fibre. Above that, the dimensions of optical fibres are so small that they can easily be integrated in all kinds of geotechnical bearing elements. With some basic knowledge of the technology it is possible to find and prototype a measurement solution for almost all types of deep foundation elements at a reasonable cost.

This last point is according to the authors' opinion one of the main advantages when fibre optic sensors are applied in geotechnical engineering.

Figure 34 illustrates the evolution of the use of sensors for pile/anchor load test at BBRI during the last 2.5 decades. Since a few years BBRI applies systematically fibre optic sensors for geotechnical testing of all kind of geotechnical structures: piles, micropiles, anchors, retaining walls (diaphragm walls, secant pile walls, sheet piles …), ground improvement elements (inclusions, soil mix, reinforced earth,…),… In order to validate the optical fibre sensors that are used in geotechnical testing, many comparative tests with classical measurement devices have been carried out in the laboratory as well as in situ.

Some examples where optical fibre sensors have been applied to determine load distribution were already shown in the previous paragraph on displacement auger piles.

In Fig. 35 to 37 some more recent applications are illustrated.

Figure 35 show the examples of a tension load tests on inclined MV-piles. These MV-piles exist out of +50 m long HEB profiles that are driven into the soil under a grout injection from the pile base, in this case in very dense sand layers in the port of Rotterdam, where they will serve as anchorage of a deep quay wall. The steel profiles were instrumented with optical fibre sensors before installation of the piles. Although the driving work was very hard and took a long time, all the sensors survived the driving process, which shows the advantage of optical measurement devices for this case, namely their small dimensions and their low weight resulting in low inertia forces on the measurement devices.

The detailed load distribution obtained out of these instrumented tests were used to validate the design of this case and to optimize the design of other similar applications in the port of Rotterdam.

More details of these test are published by Putteman et al (2017 & 2019).

Figure 34. Evolution at BBRI with regard to the use of instrumentation techniques in deep foundation testing
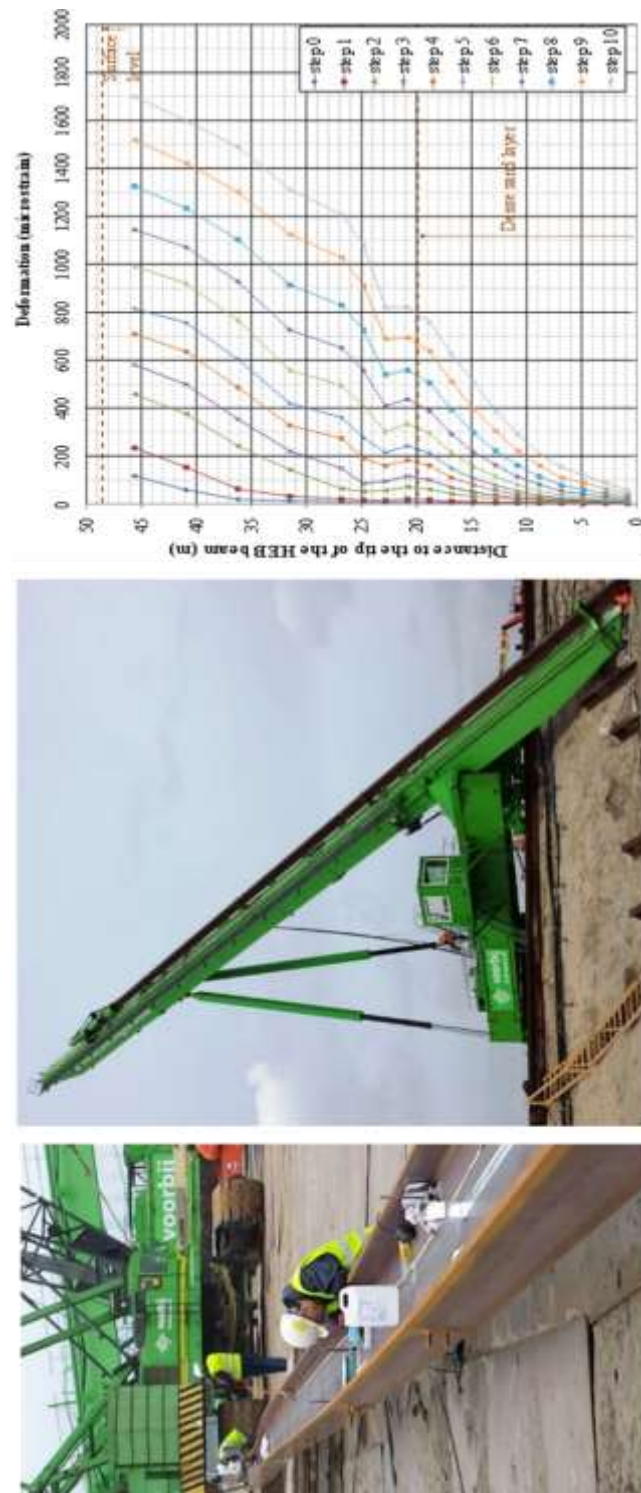
Figure 35. Instrumentation and tension load tests on MV-piles with L>50m (port of Rotterdam)
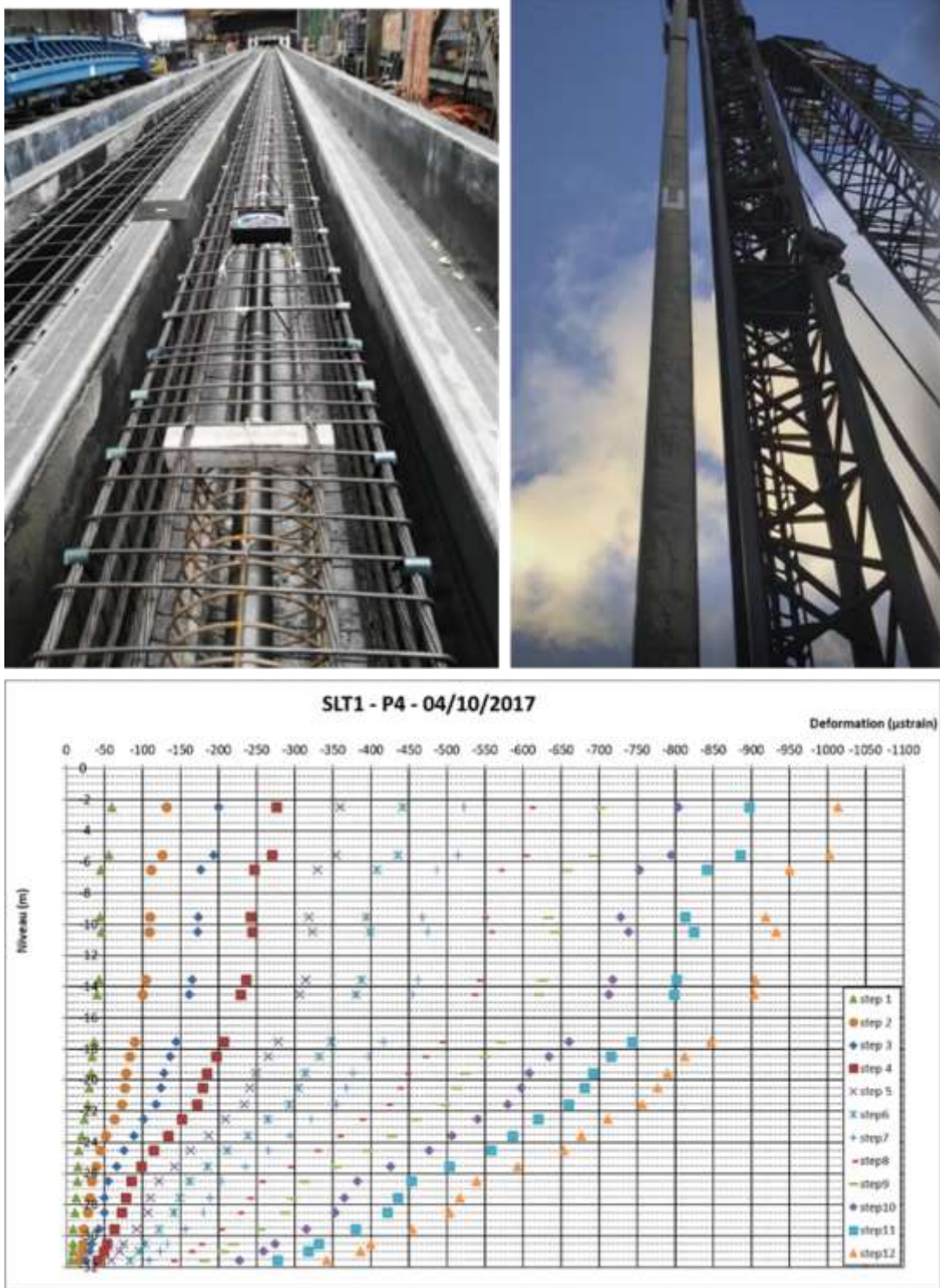
Figure 36. Instrumentation and compressive load tests on precast driven piles (port of Rotterdam)
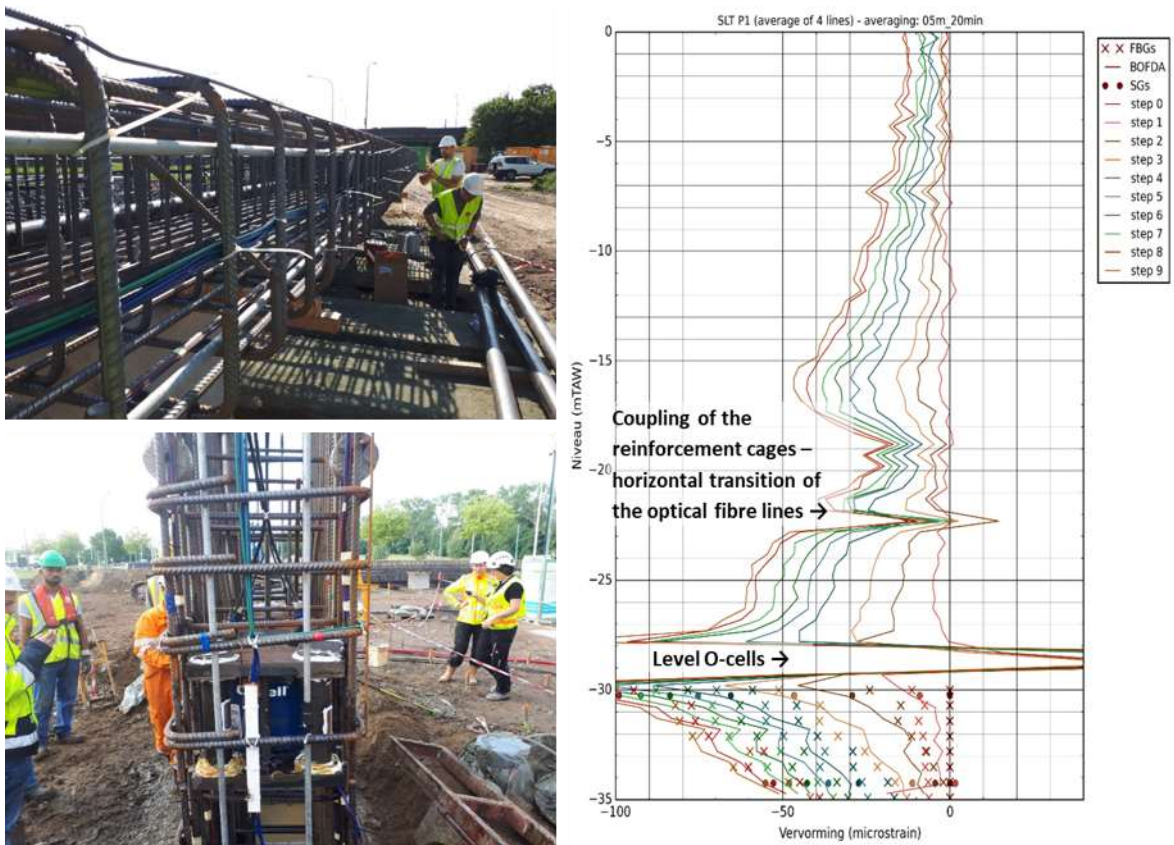
Figure 37. Instrumentation and O-cell load tests on diaphragm walls in Antwerp (Lantis)

Another interesting example is that illustrated in the Fig. 37. It concerns the instrumentation of four 35 m long precast driven piles existing of prestressed concrete in the manufactory. The optical fibre sensors were integrated in the reinforcement cage. Consecutively, the concrete pile was transported to the job site where they were driven into the soil by hydraulic hammering and submitted to load testing.

Also in this case the fibre optical sensors survived the hard driving work and allowed to determine a detailed load distribution with depth during load testing as well as the effect of the residual stresses due to the driving process. The results will be used to optimize installation factors for these kind of piles for future design in the port of Rotterdam.

More details of these test are published by Matic et al (2019) published at this conference.

Figure 37 shows a case were fibre optical sensors have been integrated in the reinforcement cage of four 40 m deep diaphragm walls in the Antwerp area. The diaphragm walls will support the load of a stapled tunnel construction that is planned in the near future in Antwerp (Oosterweel link) and in order to verify the foundation design, a load test program with integrated Osterberg cells was set up. As most interest was going out to the bottom part of the diaphragm wall situated in the stiff over consolidated Tertiary Boom clay, the panels were intensively instrumented with, a.o., optical fibre sensor lines.

The reinforcement cage existed out of three parts and it was a challenge to fix the fibre optical

sensor lines to the reinforcement cage(s) during the installation. For all four diaphragm panels the optical fibre sensors survived the installation. It allowed to determine a detailed view of the load distribution in the diaphragm wall upon testing. An example of the deformation measurements between the level -25 m TAW and -35 m TAW is given in Fig. 37 (at the right).

The results of these tests are under analysis for the moment and are not yet public available.

For more details with regard to the optical fibre technology and more examples of applications, reference is made to Huybrechts et al (2016 and 2017).

Based on the evolution of the measurement techniques and as proven with the previous examples, it is clear that actually a lot more information of the behaviour of foundation elements can be obtained during testing than in earlier days.

This is interesting in the context of design codes, which are still often based on non- or poor instrumented load tests in past.

Anyway, the evolution of the measurement techniques allows to gain more and better insight in the real behaviour of a foundation under test loading and also to link the performance to certain observations with the execution or the soil conditions.

As a conclusion one can state that:
- more load testing is needed to calibrate installation factors,
- economic incentives that favour QC monitoring and testing should be introduced in codes and standards,
- standards and codes should leave the door open and even stimulate innovative techniques and processes,
- in the context of design it is important to have a relation between the risk class of a geotechnical structure and the safety factors.

5 HOW CAN CODES AND TECHNOLOGICAL EVOLUTION BE LINKED WITH EACH OTHER

As we tried to explain in the above sections, the link between installation details and installed pile capacity is tight (see also Bottiau 2014), but is difficult to quantify and to capture this in installation coefficients, which would be valid for all cases:

- Execution systems are in constant evolution, and small details can vary resulting in major differences. The codes are usually not enough up to date to take these new evolutions into account.
- It should be emphasized that all installation methods may prove to be inadequate in function of the local soil conditions, or the installed equipment capacity.
- The response of some types of soils to the solicitation of pile installation procedure, can be dramatically different than expected. This is specifically the case in intermediate soil types or in rapidly changing soil conditions.

For this reason, installation coefficients need to be related to the "real" set of parameters of the specific jobsite. All aspects governing the pile installation should be considered and documented: system details, materials, equipment capacity, monitoring during and after pile installation. In this respect, analysis of modern monitoring data are introducing a completely new paradigm in the way we look at pile performance and documentation.
- Real-time access to all site and equipment related data
- Detailed report with selection of specific data for further analysis and quality documentation
- Focused follow-up by in-house expert team.

For all these reasons, the authors believe that codes should adapt. Installation factors should be aligned on demonstrated performance and model and safety factors should account for proven reliability and reward testing. In this section, we want to show how the Belgian NA of the EC7 is

trying in the recent years to introduce this in the daily practice.

5.1 Belgian procedure for ULS design (simplified)

In Belgium, the ULS design is in most cases based on the cone resistance diagram measured with in situ cone penetration tests. The design methodology to perform ULS design for axially loaded piles based on CPT results is described in the Belgian pile design guide (WTCB-CSTC, 2009/2016), which is referenced in the Belgian national annex of the EC 7 as the reference method.

This is the "GEO"-verification according to Eurocode 7:

$$F_{c,d} \leq R_{c,d} \qquad (2)$$

where $F_{c,d}$ (kN) is the design value of the axial compression load on the pile and $R_{c,d}$ (kN) is the design value of the compressive resistance of the axially loaded pile.

Design value of the pile resistance $R_{c,d}$
Figure 38 gives a schematic overview of the different steps to calculate the design value of the compressive resistance of the pile $R_{c,d}$.
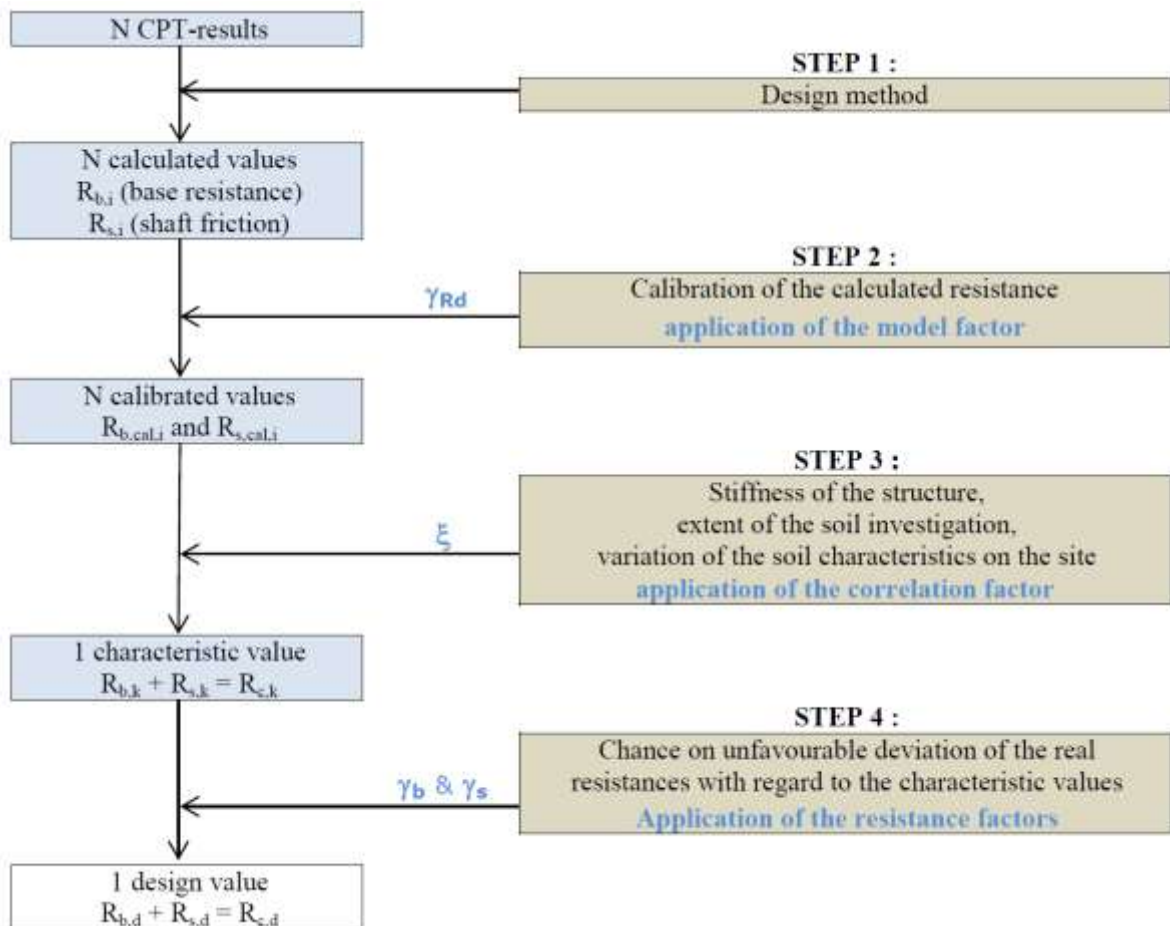
Figure 38. Schematic overview of the different steps to calculate the design value of the pile bearing capacity

In step 1, the compressive resistance of the pile R_c, existing out of the pile base resistance R_b and the shaft friction R_s, is calculated starting from the results of each individual CPT that has been carried out on the job site with the help of the semi-empirical methods, including the installation factors.

The pile base resistance R_b is determined according to the formula:

$$R_b = \alpha_b . \varepsilon_b . \beta . \lambda . A_b . q_b \qquad (3)$$

where q_b (kPa) is the unit pile base resistance calculated with the De Beer Method out of the cone resistance (q_c) diagram of the CPT, α_b (-) is an empirical factor taking into account the installation method of the pile and the soil type, ε_b (-) is a parameter referring to the scale dependent soil shear strength characteristics (e.g. in the case of stiff fissured clay), β (-) is a shape factor, introduced for non-circular nor square-shaped bases, A_b (m²) is the section of the pile base and λ (-) is a reduction factor for enlarged pile bases that generate soil relaxation around the pile shaft during installation of the pile.

The shaft resistance R_s is determined according to the following formula:

$$R_s = \chi_s . \sum (\alpha_{s,i} \, h_{i.} . q_{s,i}) \qquad (4)$$

where $q_{s,i}$ (kPa) is the unit shaft friction:

$$q_{s,i} = 1000 . \eta^*_{p,i} . q_{c,m,i} \qquad (5)$$

with $\eta^*_{p,i}$ (-) an empirical factor, giving the ratio between the unit shaft friction $q_{s,i}$ and the cone resistance q_c for a given soil type, $q_{c,m,i}$ (MPa) the average cone resistance (q_c) for layer i, χ_s (m) the perimeter of the pile shaft, $\alpha_{s,i}$ (-) an empirical factor for layer i, taking into account the installation method of the pile and the roughness of the pile shaft in a given soil type and h_i (m) the thickness of layer i.

In a second step the calculated values of the compressive resistance of the pile are divided with the model factor γ_{Rd} [NBN EN 1997-1 §2.4.1 (6), §2.4.1 (8), §2.4.7.1 (6), §7.6.2.3 (2)]. In this way a calibrated value of the pile resistance $R_{c,cal}$ is obtained for each individual CPT:

$$R_{c,cal} = \frac{R_c}{\gamma_{Rd}} \qquad (6)$$

where $R_{c,cal}$ (kN) is the calibrated bearing capacity of the pile and γ_{Rd} (-) is the model factor.

In step 3, one characteristic value of the pile resistance $R_{c,k}$ is deduced by applying the correlation factors ξ_3 and ξ_4 on the average and the minimum value of the calibrated pile resistances respectively, and by retaining the smallest value of both:

$$R_{c,k} = min \left\{ \frac{(R_{c,cal})_{average}}{\xi_3} ; \frac{(R_{c,cal})_{min}}{\xi_4} \right\} \qquad (7)$$

The correlation factors are applied in order to take the variation on the soil characteristics and the uncertainty on this variation into account.

In step 4, the design value of the pile resistance $R_{c,d}$ is finally obtained by applying the partial safety factors γ_b and γ_s on the characteristic pile base and shaft resistances:

$$R_{c,d} = \frac{R_{b,k}}{\gamma_b} + \frac{R_{s,k}}{\gamma_s} \qquad (8)$$

The values of the partial factors depend on the guarantee that can be given on the quality of the pile installation.

5.2 Current evolution

As mentioned before, it is the authors' opinion that codes and standards should provide incentives in order to encourage Testing, Quality Control and monitoring, with as objective to level up the profession and increase the reliability. For

that reason, the following principles have been provided in the Belgian design methodology as described in WTCB-CSTC, (2009/2016):

- Installation factors α_b and α_s, are function of pile (sub) category. These generic installation factors are rather conservative, but the document provides a methodology (instrumented pile testing program in different soil types) and acceptance criteria to get better installation factors for individual pile systems.

- Model factors γ_{rdi}, are function of the availability of instrumented SLT's.

- Correlation factors $\xi_{3,4}$ are function of the intensity of the soil investigation tests.

- Safety factors $\gamma_{b,s}$ are function of the quality of the QC provided for the production piles.

In order to enforce/facilitate this in practice, a system of Certified Technical Approvals is actually launched in Belgium by BUtgb-UBAtc, which is Belgium's only authority offering technical approval of construction materials, products, systems and installers. In this process, the contractor has to introduce for a particular piling system a dossier based on a formalized installation procedure and a documented PLT campaign in different soil categories. After analysis by an independent expert team of BUtgb-UBAtc,, the piling system and the contractor is granted specific installation factors, as well as model factors and safety factors that account for a period of five years. A renewal procedure is defined, requesting the performance of at least two SLT's on each system in the period.

This process has been discussed and approved by the contractors (ABEF – National Federation of Piling Contractors) and is currently being organized. The impact will be an increased demand for SLT's and will generate a stimulus for contractors to innovate and differentiate from their competitors, as the investment in innovative techniques can be valorised quite fast by means of the Certified Technical Approval procedure, which is in fact a complement to the design standard.

6 CONCLUSION

In this contribution an overview has been given about the situation concerning the harmonization of codes and standards that apply for the design of piles, in particular the Eurocode 7. The great advantage of EC7 is that, at least, the used design terminology is the same throughout Europe. However, some simple design exercise have shown that differences between the output of the different national approaches remain huge. This is not that surprising, as local experience (soil, piling techniques and testing) remain very important in the estimation of pile capacity.

Based on the analysis of the authors, current pile design standards and codes contain several discrepancies, a.o. because they are often based on load tests that were performed several decades ago, they don't account correctly for the real impact of pile installation on its performance. Moreover, they are often not adapted for recent technical evolutions with regard to the piling equipment (new, larger, deeper, faster, with automated registrations, …), the testing and instrumentation possibilities and the advances in numerical modelling. Several of those technical advances have been illustrated in this contribution.

It is the authors' opinion that:

- Standards and codes should reward more efficiently the correct understanding and monitoring of pile execution and the related increase in reliability. They should also integrate methodologies that anticipate on new technical advances, and provide economic incentives for testing, QC and monitoring. The Belgian example, where, complementary to the NA of the Eurocode 7, a system of Certified Technical Approval for pile systems is launched goes in that direction.

- Research is still necessary to better understand some critical issues with regard to the pile installation influence.

- The use of recent monitoring and testing technologies and numerical modelling can help a lot to improve insights in pile behaviour.

Taking into account the previous suggestions could lead on the long term to a significantly better fit between predicted capacity using the codes and the installed capacity in the field.

7   ACKNOWLEDGEMENTS

The authors wish to thank ir. Thomas Wulleman (Franki Foundations Belgium) and dr. ir. Nicolas Denies (Belgian Building Research Institute) for their appreciated help with the establishment and the editing of this paper.

8   REFERENCES

Basu, P., Prezzi, M. and D. Basu, , Drilled Displacement Piles, Current Practice and Design, DFI JOURNAL Vol. 4 No. 1, 2010.

Beckhaus, K. & Harnan, Ch., 2018 EFFC/DFI Guide to Tremie Concrete for Deep Foundations Proceeding of the 2018 DFI-EFFC International Conference on Deep Foundations and Ground Improvement, Rome, Italy, (DFI, EFFC)

Bottiau, M., 2014. Installation parameters, pile performance and importance of testing, DFI-EFFC Int. Conference on Piling and Deep Foundations, May 21–23, 2014, Stockholm, Sweden

Bottiau, M., 2016. Codes, new technologies and quality in Deep Foundations. The importance of pile installation process, DFI-EFFC Int. Conference on Piling and Deep Foundations, 2016, Rome, Italy

Brown, 2012. Recent Advances in the Selection and Use of Drilled Foundations. GeoCongress 2012 , March 25-29, 2012, Oakland, California, United States.

Bustamante, M. & Gianeselli, 1988. L'expérience des LPC en matière de pieux vissés moulés et tarières creuses. Proceedings of the 1st Int. Geotechnical Seminar on Deep Foundations on Bored and Auger piles, Ghent, pp. 35-46

Bustamante, M. & Gianeselli, L. 1993. Design of auger displacement piles from in-situ tests. Proceedings of the 2nd Int. Geotechnical Seminar on Deep Foundations on Bored and Auger piles, Ghent, pp. 193-218

Bustamante, M. 2003. Auger and bored pile monitoring and testing. Deep Foundations on Bored and Auger Piles, Van Impe (ed.). Ghent.

De Vos, M., Huybrechts, N. & Bottiau, M. (eds.), 2016. Proceedings of the int. ETC3 Symposium "Design op piles in Europe – How did Eurocode 7 change daily practice?", 28-19 April 2016, Leuven, Belgium

Day, Peter, 2017. Challenges and shortcomings in geotechnical engineering practice in the context of a developing country. Proceedings of the 19th International Conference on Soil Mechanics and Geotechnical Engineering (Seoul) 2017, Vol. 1, pp 11 -34

Dunnicliff, J. 1993. Geotechnical instrumentation for monitoring field performance. John Wiley & Sons, Inc.

Fellenius, B.H. & Terceros, H., 2014. Response to load for four different types of bored piles. DFI-EFFC Int. Conference on Piling and Deep Foundations, May 21–23, 2014, Stockholm, Sweden

Hertlein, B. and Davis, A. 2006. Nondestructive testing of deep foundations. John Wiley & Sons, UK.

Holeyman, A. (ed.). 2001. Screw piles – Installation and design in stiff clay. Proceedings of the 1st symposium on screw piles, Brussels 15 March 2001. Swets & Zeitlinger, Lisse.

Huybrechts N. 2001. Test campaign at Sint-Katelijne-Waver and installation techniques of screw piles. Screw Piles – Installation and Design in Stiff Clay, Holeyman (ed.). Proceedings of the 1st symposium on screw piles, Brussels 15 March 2001. Swets & Zeitlinger, Lisse.

Huybrechts N., De Vos M. & Van Lysebetten G., 2016. Advances and innovations in measurement techniques and quality control tools. Proc. Int. Symp. Design of Piles in Europe – How did Eurocode 7 change daily practice? Vol. I, pp. 209-233.

Huybrechts, N., Van Lysebetten, G., and De Vos, M. (2017). Advanced monitoring techniques for a wide range of geotechnical applications. ICSMGE 2017 - 19th International Conference on Soil Mechanics and Geotechnical Engineering, 2761–2764.

Maertens, J. & Huybrechts, N. (eds). 2003b. Belgian screw pile technology – design and recent developments. Proceedings of the 2nd symposium on screw piles, Brussels 7 May 2003. Swets & Zeitlinger, Lisse.

Matic, I., deNijs, R., De Vos, M., Roubos, A.A., 2019. Full-scale load testing on long prefabricated concrete piles in the Port of Rotterdam. Proceeding of the European Conference on Soil Mechanics and Geotechnical Engineering, Reykjavik, 2019.

Orr, T.L.L., 2016. Design Examples: Comparison of different national practices, Proceedings of the int. ETC3 Symposium "Design op piles in Europe – How did Eurocode 7 change daily practice?", 28-19 April 2016, Leuven, Belgium

Putteman, J., Imbrechts, T. & Broos, E., 2017. Design of a heavy-duty deep sea quay wall for offshore wind energy. Proceedings of the International Young Geotechnical Engineers' Conference, Seoul 2017.

Putteman, J., Broos, E.J., Brassinga, H.E., Spruit, R., De Vos, M. and Timmermans, A.L.J., 2019. MV tension pile load tests in the Port of Rotterdam: practical aspects and geotechnical behaviour. Proceeding of the European Conference on Soil Mechanics and Geotechnical Engineering, Reykjavik, 2019.

Soga, K. 2010 Innovation in monitoring technologies for tunnels, Jornada Técnica: Instrumentacion de tuneles y excavaciones, Barcelona, 21.10.2010.

Van Alboom, G., De Vos, L., Haelterman, K. & Maekelberg, W. 2012. Innovative monitoring tools for online monitoring of building excavations.Proceedings of the ISSMGE-TC211 International symposium on Ground Improvement, Brussels, Vol. IV pp. 327-338.

Van Impe, W.F., 1988. Considerations on the auger pile design. Proceedings of the 1st Int. Geotechnical Seminar on Deep Foundations on Bored and Auger piles, Ghent pp. 193-218

Van Impe, W.F., 1994. Influence of screw pile installation parameters on the overall pile behaviour, Workshop "Piled Foundations : full scale investigations and design", Naples.

Viggiani, 1993. Further experiences with auger piles in the Naples area. Proceedings of the 2nd Int. Geotechnical Seminar on Deep Foundations on Bored and Auger piles, Ghent, pp. 445-458

Van Weele, A.F., 1988 . Installation methods, soil disturbance and resulting pile behaviour. Proceedings of the 1st Int. Geotechnical Seminar on Deep Foundations on Bored and Auger piles, Ghent pp. 219-226

Van Weele, 1993. Quality assessment foundation piles after installation. Proceedings of the 2nd Int. Geotechnical Seminar on Deep Foundations on Bored and Auger piles, Ghent, pp. 459-468.

WTCB-CSTC, 2009. WTCB Rapport nr. 12. Richtlijnen voor de toepassing van de Eurocode 7 in België – Deel 1: het grondmechanische ontwerp in de uiterste grenstoestand van axiaal op druk belaste funderingspalen/ CSTC Rapport n° 12. Directives pour l'application de l'Eurocode 7 en Belgique – Partie 1: Dimensionnement Géotechnique à l'état limite ultime de pieux sous charge axiale de compression. WTCB-CSTC, Brussels.

WTCB-CSTC, 2016. WTCB Rapport nr. 19 (Revisie WTCB Rapport 12). Richtlijnen voor de toepassing van de Eurocode 7 in België – Deel 1: het grondmechanische ontwerp in de uiterste grenstoestand van axiaal belaste funderingspalen / CSTC Rapport n° 19 (Revision CSTC Rapport 12). Directives pour l'application de l'Eurocode 7 en Belgique – Partie 1: Dimensionnement Géotechnique à l'état limite ultime de pieux sous charge axiale. WTCB-CSTC, Brussels.

XVII European Conference
ECSMGE 2019
Reykjavik
on Soil Mechanics
and Geotechnical Engineering

Landslide hazards and risks to road users, road infrastructure and socio-economic activity

Risques de glissement de terrain et risques pour les usagers de la route, les infrastructures routières et l'activité socio-économique

M. G. Winter
Transport Research Laboratory (TRL), Edinburgh, United Kingdom
University of Portsmouth, Portsmouth, United Kingdom

ABSTRACT: The assessment of landslide hazards and risks forms an essential precursor to landslide risk reduction. This is particularly the case when an authority is responsible for an infrastructure or building portfolio that may be affected by multiple hazards. In this paper semi-quantitative and quantitative assessments of landslide hazards and risks to road networks are considered in terms of the risks that affect road users (fatality), road infrastructure and the socio-economic activities that the network facilitates. A framework for risk acceptance is used to set the context, and the use of a semi-quantitative assessment to determine the sites of highest risk is described. These highest risk sites are subject to the first known quantitative risk assessments for road user fatalities as a result of debris flows. A novel approach is taken to assess the socio-economic risks and the use of fragility curves to articulate the vulnerability of road infrastructure, including the newly-developed approach involving systems of assets, is also described. The effects of climate change are considered alongside likely social and/or demographic change and a strategic approach to landslide risk reduction is presented.

RÉSUMÉ: L'évaluation des dangers et des risques de glissements de terrain constitue un précurseur essentiel de la réduction des risques de glissements de terrain. C'est particulièrement le cas lorsqu'une autorité est responsable d'une infrastructure ou d'un portefeuille de bâtiments pouvant être affectés par de multiples aléas. Dans ce document, les évaluations semi-quantitatives et quantitatives des risques de glissements de terrain et des risques pour les réseaux routiers sont considérées en termes de risques pour les usagers de la route (décès), les infrastructures routières et les activités socio-économiques que le réseau facilite. Un cadre d'acceptation des risques est utilisé pour définir le contexte et l'utilisation d'une évaluation semi-quantitative pour déterminer les sites les plus à risque est décrite. Ces sites présentant les risques les plus élevés font l'objet des premières évaluations quantitatives connues des risques de décès d'usagers de la route par suite de coulées de débris. Une nouvelle approche est adoptée pour évaluer les risques socio-économiques et l'utilisation de courbes de fragilité pour articuler la vulnérabilité des infrastructures routières, y compris l'approche récemment développée impliquant des systèmes d'actifs, est également décrite. Les effets du changement climatique sont pris en compte parallèlement aux évolutions sociales et / ou démographiques probables et une approche stratégique de la réduction des risques de glissements de terrain est présentée.

Keywords: Landslide; hazard; risk; infrastructure; fatality; economic

1 INTRODUCTION

Landslides have formed a major focus of study in the UK for geotechnical engineers, engineering geologists, geomorphologists and other relevant professions. A remarkably wide range of event type including large individual slides (e.g. Mam Tor), large landside complexes (e.g. Undercliff, Isle of Wight), rock falls and debris flows (both of which have significant impact on transport infrastructure) are encountered (e.g. Jones & Lee 1994; Cooper 2007; Bromhead & Winter 2019).

Fatalities due to landslides are, however, relatively rare. The spate of fatalities in south-west England during the period July 2012 to March 2013 (four deaths as a result of three separate landslides) was unusual and such losses, while undoubtedly tragic, are unusual in the context of the UK.

While the morphology of debris flow in Scotland and the Republic of Korea is markedly similar, the annual landslide fatality count is startlingly disparate with the Republic suffering an average of 36 fatalities per annum during the period 1970 to 2017 (Lee & Winter 2019). In this context it seems reasonable to suggest that the UK is generally a low risk environment with respect to landslides (Gibson et al. 2013). Notwithstanding this, significant challenges remain in terms of ensuring the protection and optimal use of assets, minimising risk to road users and ensuring that socio-economic risks are adequately addressed.

Rainfall-induced debris flow events often affect the Scottish strategic road network (Winter et al. 2006; Milne et al. 2009). The risks associated with such events range from damage to the physical infrastructure, through potential injury and fatality to road users, to socio-economic losses associated with the incidents, associated delay and diversion and, potentially, to the loss of business (e.g. Figure 1).

In this paper a framework for risk acceptance is used to set the context for the work undertaken to assess and articulate the risks to road users, the physical infrastructure, and to the socio-economic activities supported by the road network. Issues surrounding the impact of climate and global change are addressed before a strategic approach to landslide risk reduction is detailed.

Figure 1. Debris flow at the A83 Rest and be Thank-ful, Scotland, 28 October 2007.

2 RISK ACCEPTANCE

Landslide hazards are commonplace and affect many parts of the world and the associated risks affect many different cultures.

The elements at risk may include infrastructure (e.g. roads, rail), public service buildings (e.g. hospitals, schools), commercial property (e.g. shops, factories, offices) and residential property (e.g. blocks of flats and houses). Clearly these elements at risk will also include, to a variable degree, the risk to life and limb of the users and occupants of such facilities.

The type of element at risk and the vulnerability of those elements determines what might be described as a reasonable and proportionate response to a given risk profile. However, it can be difficult to compare such responses to different risk profiles in different parts of the world as the varied social (cultural) factors and economic circumstances can mean that the tolerance of the associated risk is very different indeed.
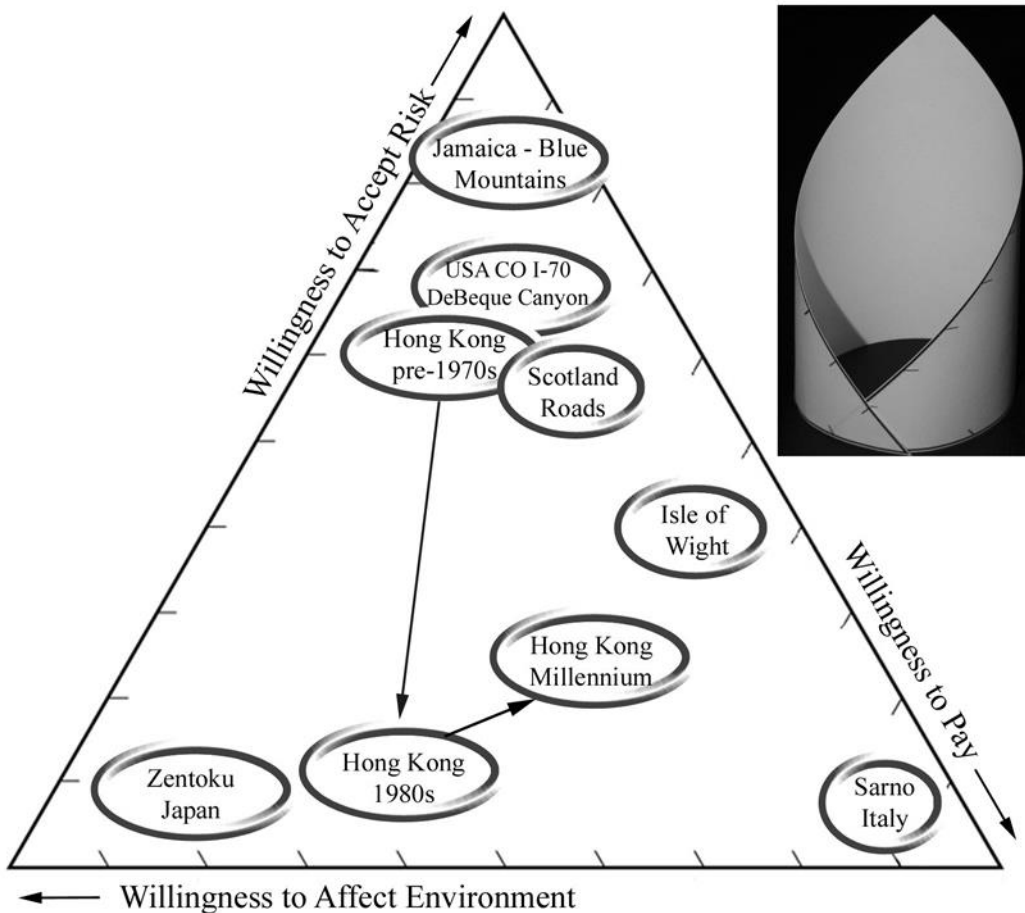
Figure 2. The 'Willingness Diagram' showing the different approaches to landslide risk in the UK and other parts of the World. Inset: The extreme bottom-left and bottom-right corners of the ternary diagram tend to con-verge and the diagram might more strictly be rendered as if wrapped around a cylinder about a vertical axis (from Winter & Bromhead 2012).

It seems clear (Winter et al. 2008; Winter & Bromhead 2012) that such varied approaches to landslide risk are driven not only by the willingness to accept or tolerate) risk, but also by the willingness (or ability) to pay to mitigate risk and the willingness to alter the environment in the process. These factors are interlinked using the ternary 'Willingness Diagram' (Figure 2).

In addition to this geographical variance in culture, the willingness diagram was applied to generic and conceptual approaches to landslide remediation (Section 8). This was not intended to highlight correct, or incorrect, approaches. Instead it reflects different approaches that are the result of a wide range of inputs to the decision-making process including engineering, geological, geomorphological, economic, data and information (particularly the availability of data in a usable format: e.g. GIS), sociological, political, policy-led and cultural factors.

3 SEMI-QUANTITATIVE RISK ASSESSMENT

Hazard and risk assessments can be carried out at a variety of scales and using qualitative, semi-quantitative and quantitative approaches.

Typically, although not exclusively, as assessments move from small-scale (e.g. global or continental) to medium-scale (e.g. national or regional) to large-scale (e.g. site or area) then the availability of quantitative information increases and more detailed assessments are possible. Thus, while small- to medium-scale assessments may typically be conducted in a semi-quantitative framework, large-scale assessments are more typically conducted quantitatively. In addition, it should be noted that even when regional quantitative risk assessments are undertaken (e.g. Redshaw et al. 2017) the nature and resolution of the data is such that the conclusions that can be drawn from the results will still be reflective of the regional nature of the assessment rather than of a quantitative assessment carried out at a larger scale with higher resolution data.

This should not negate the fact that, as Suzanne Lacasse so clearly articulated in her 2015 Rankine Lecture, that [even quantitative risk assessment] "is the systematic application of engineering judgement".

In this section, and in Section 4, semi-quantitative regional and site-scale fully-quantitative risk assessment (QRA), respectively, are described.

The semi-quantitative regional risk assessment was undertaken as the major component of the Scottish Road Network Landslide Study (Winter et al. 2005; 2009; 2013a) that was instigated in direct response to the debris flow events that adversely affected the trunk (strategic) road network in Scotland in August 2004 (Winter et al. 2006; Winter 2019).

The study had the overall purpose of ensuring that the hazards posed by debris flows were systematically assessed and ranked and this was intended to allow all sites to be effectively prioritized for potential action within available budgets (see also Section 8) (Winter et al. 2005).

The hazard and risk assessment Winter et al. (2009) comprised three phases:

- a pan-Scotland, GIS-based, assessment of debris flow susceptibility;
- a desk-/computer-based interpretation of the susceptibility and ground-truthing (to gather field data to either complement or dispute the desk-based data) to determine hazard; and
- a desk-based exposure analysis, primarily focusing upon life and limb risks, but also accounting for socio-economic impacts (traffic levels, and the existence and complexity of the diversionary route were used).
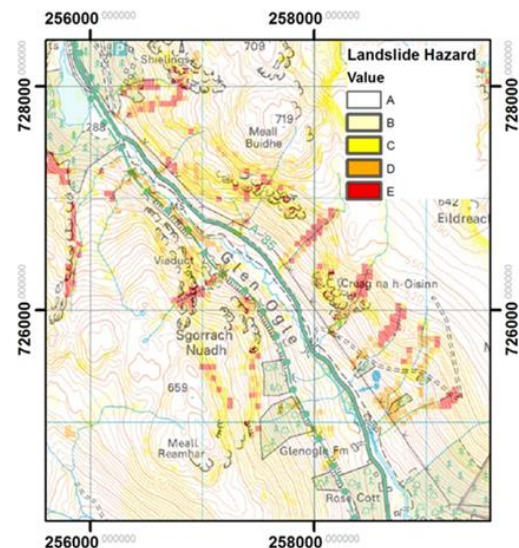
Figure 3. Results of the GIS-based susceptibility assessment for Glen Ogle (from Winter et al. 2009; 2013a). (Base mapping Ordnance Survey 1:50,000 © Crown Copyright. All rights reserved Scottish Government 100046668, 2011.)

These successive stages were used to determine the locations of sites of highest hazard ranking (risk) (Winter et al. 2009; 2013a). The results of the first stage susceptibility analysis for the A85 at Glen Ogle, one of the sites adversely affected in August 2004, are

illustrated in Figure 3. This provides a clear basis for the evaluation of hazard at road level and thus to the determination of risk. Figure 4 illustrates an example of the hazards identified at road level with a ranked priority (red being highest, followed by orange, brown and yellow being the lowest but not illustrated here).

Taking the Cruden & Varnes (1996) definition of risk as follows:

$$R = H \times E \times V \qquad (1)$$

where R is the risk,
   H is the hazard,
   E denotes the elements at risk, and
   V is the vulnerability of the elements at risk to the hazard.
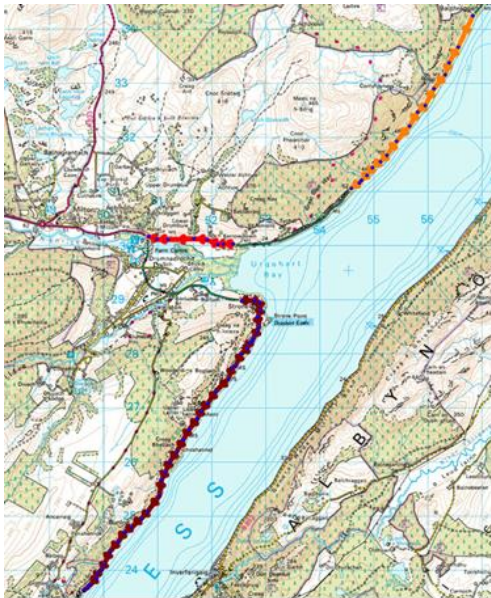
Figure 4. Hazard sections at A82 Loch Ness. Showing lengths categorised, from top to bottom, as Priority 3 (A82-03, orange), Priority 1 (A82-04, red) and Priority 2 (A82-05, brown) (from Winter et a/. 2009; 2013a). (Base mapping Ordnance Survey 1:50,000 © Crown Copyright. All rights reserved Scottish Government 100046668, 2011.)

It is possible to simplify the eq. (1) as the presence of the elements at risk (a road) is binary (it is either present or not) and treat E×V as a weighted function that considers exposure both in terms of the number of vehicles per day

and an evaluation of the potential consequences of a closure and the resulting difficulty and, in some cases, absence of diversionary routes. Clearly this structure, as described by Winter et al. (2013), contains elements of life and limb risk and also socio-economic risk.

The results of the semi-quantitative regional risk assessment are shown in Figure 5 with the 66 sites with the highest semi-quantitative scores overlain on a map of Scotland. The results were also tabulated but the intention was to isolate the highest risk sites rather than to provide a league table.
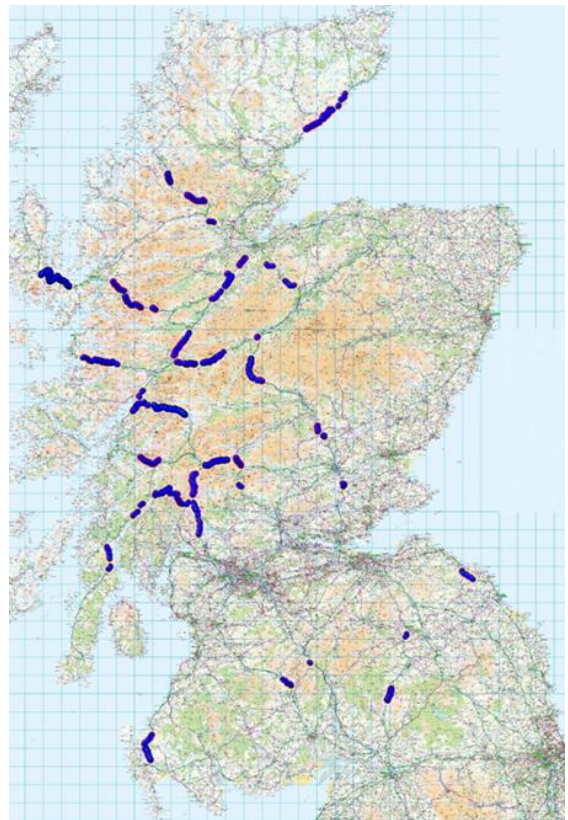
Figure 5. The 66 sites with a hazard ranking (risk) score of 100 or greater (from Winter et al. 2009; 2013a). (Base mapping © Crown Copyright. All rights reserved Scottish Government 100046668, 2011.)

This relatively rapid form of assessment was an effective means of determining the highest

risk sites in Scotland (approximately 78,000 km^2), an area comparable with other extensive assessments (e.g. Castellanos Abella & Van Westen 2007; Dio et al. 2010). Assessments have also been undertaken at the continental scale (e.g. Jaedicke et al. 2014) to inform planning policy at the highest national/trans-national level.

This knowledge can be used to determine those sites that should be targeted for further study and more refined risk assessment (Sections 4, 5 and 6) as well as for landslide risk reduction measures (Section 8).

4 QUANTITATIVE RISK ASSESSMENT

One important benefit of a robust regional assessment is that it allows a more detailed and targeted assessment of sites that pose the highest risks. Typically this involves the use of quantitative risk assessment (QRA) techniques (Corominas et al. 2014). The methodology for QRA for debris flow risk to road users is described by Wong & Winter (2018) in what is believed to be the first full, formal quantitative risk assessment. The methodology was initially applied to the A83 Rest and be Thankful site and a subsequent assessment of the A85 Glen Ogle site was conducted (Winter 2018).

The results from the two sites represent a high frequency-low magnitude site (A83) and a low frequency-high magnitude site (A85).

The form of equation used corresponds to that presented by Lee & Jones (2016) as follows:

$$Risk = P(Event) \times P(Hit|Event) \times P(Damage|Hit) \times C \qquad (2)$$

where *P(Event)* is a measure of the expected likelihood of a landslide event per annum,
P(Hit|Event) is the annual probability of a vehicle 'hit' given that a landslide event occurs which involves both spatial and temporal probabilities of affecting the elements at risk,
P(Damage|Hit) is the annual probability of damage given that a 'hit' has occurred, as a measure of chance between 0 and 1, and
C is the consequences as a result of the landslide event.

For the purposes of this work 'Damage' was taken to represent the fatality of one or more road users and effectively encompasses the concepts of both 'Damage' and 'Consequences' (i.e. *P(Fatality|Hit)*×C).

Two scenarios were considered, that of a vehicle being hit by a debris flow that reaches the road (A) and that of a vehicle hitting a debris flow that has already reached the road (B).

The results for the A83 (Figure 6) demonstrate that for numbers of fatalities N = 1 and 2 lie in the 'Unacceptable' zone with the remaining values being in the 'As Low As Reasonably Practicable (ALARP)' zone. In contrast, those for the A85 (Figure 7) generally lie in the 'Broadly Acceptable' zone with N = 1 and 2 lying in the ALARP zone.

No account of landslide risk reduction measures is made in Figures 6 or 7. This is particularly important at the A83 site, at which a strategic approach has been taken to the reduction of landslide risk (Winter 2014a; 2016a: see also Section 8) including educational leaflets, wig-wag warning signs (Winter et al. 2013b; Winter & Shearer 2017) and the provision of debris flow nets.

The QRA was conducted prior to October 2014 and at that time additional debris flow nets and catch pits were planned along with significant planting of the hillside to improve stability (Winter & Corby 2012; Winter 2016b). Additional nets and catch pits have since been installed and the planting programme is progressing through the planning stages.

This work articulated the effect on societal risk of the landslide risk reduction measures that were in place as of October 2014 and not those measures installed subsequently.
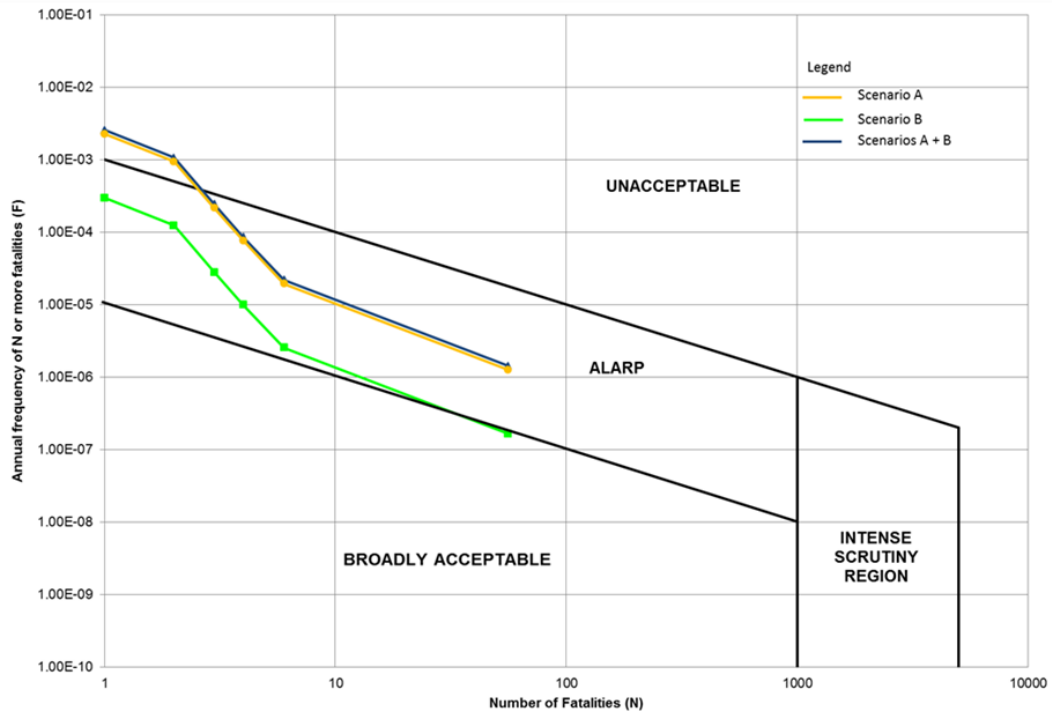
Figure 6. F-N curves based on the Wong et al. (2004) approach for the A83, before mitigation measures (compare to Figure 8).
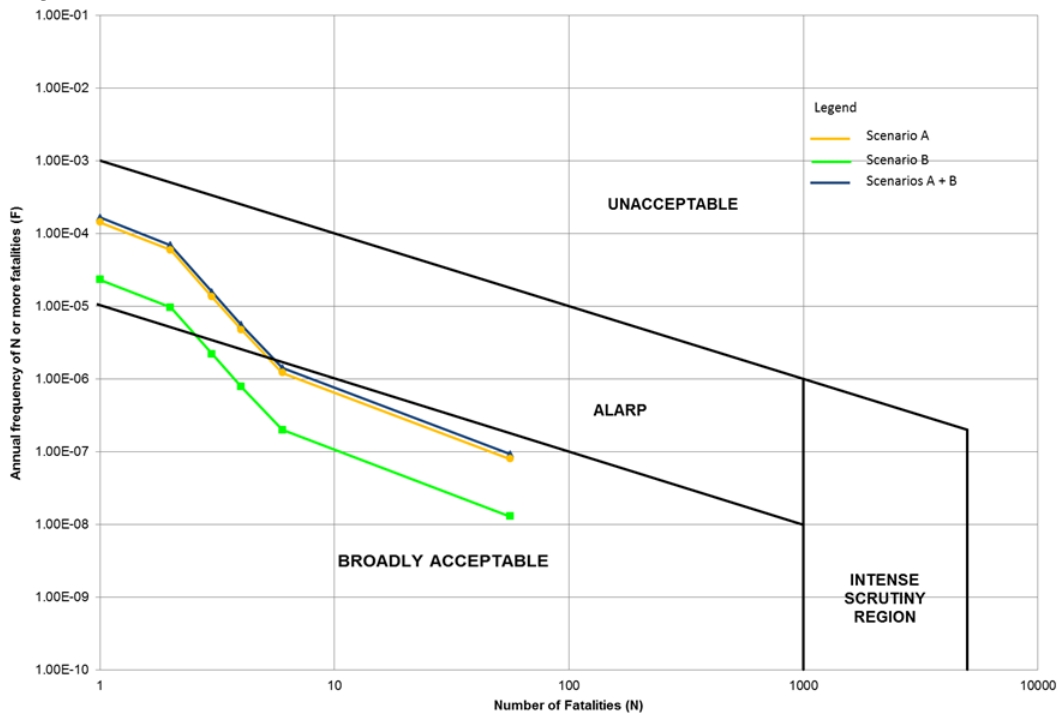
Figure 7. F-N curves based on the Wong et al. (2004) approach for the A85.
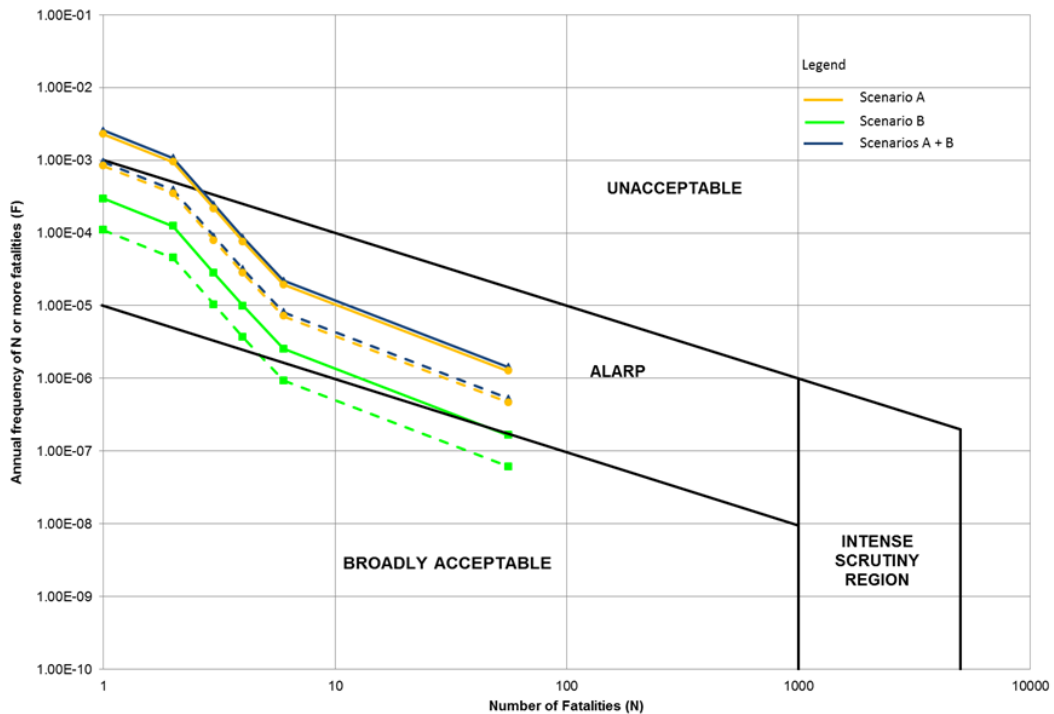
Figure 8. F-N curve showing the risk reduction for the A83 due to the mitigation measures extant as of October 2014 based on the Wong et al. (2004) approach. The dashed lines represent the risk after the mitigation measures are taken into account. Note that the line for Scenarios A and B combined is partly obscured by that for Scenario A.

This was achieved by the use of an event tree diagram and carefully considering (and testing) the contribution to hazard reduction and that each element of the strategic programme made and then calculating the revised risk levels in terms of F-N (Figure 8).

This process was made possible by the detailed evaluation of the wig-wag signs (Winter et al. 2013b) and events that had occurred and tested the efficacy of the debris flow nets. As can be seen in Figure 8, taking account of the landslide risk reduction measures brings the risk back to the ALARP zone for all values of N.

For the F-N (societal/fatality) calculations a notional vehicle speed of 50 mile/h was assigned for the analysis of societal risk. This was considered to be typical of passenger vehicle speeds experienced at the sites (regardless of the speed limit) and is conservative for goods vehicles subject to a lower speed limit.

Wong & Winter (2018) and Winter (2018) also presented results for personal individual risk (PIR), the annual probability of an individual becoming a fatality during a single trip through a site (Lee & Jones 2014). The calculation of such data is an essential precursor and input to the more detailed calculations for the F-N diagrams presented in Figures 6 to 8 and these in turn rely on the calculation of the potential loss of life (PLL). PLL essentially extrapolates PIR based on the amount and type of traffic that uses the site. Thus, rather than being the risk of an individual becoming a fatality at a given site, it is the risk of any individual, taken from those using the route, becoming a fatality; the PLL, and F-N, thus represents a risk to society rather than to the individual.

In the case of PIR the lower of national or posted speed limits were used which are 60

mile/h (97 km/h) at the A83 and 50 mile/h (80 km/h) for passenger vehicles. The results correspond to annual probabilities of fatality of 1.583E-09 at the A83 and 1.147E-10 at the A85, respectively.

The PIR can also be extrapolated to give an annual risk level for both commuters and logistics truck drivers. The national or posted speed limit was used for commuters while the national speed limit for goods vehicles over 7.5 tonnes (maximum laden weight) in Scotland of 40 mile/h (except for the A9 Perth to Inverness) was used for logistics truck drivers.

The annual probability of fatality for commuters at the A83 site was 7.440E-07 and 1.922E-06 for logistics truck drivers; at the A85 site it was 5.391E-08 for commuters and 1.248E-07 for logistics truck drivers. These figures were based on commuters making daily return trips through a site on five days per week for 47 weeks a years, and for logistics truck drivers, making two daily return trips through a site on five days per week for 47 weeks a year.

QRA is an undoubtedly powerful tool to analyse, understand and present the effects of landslides on society. Additionally it can be used to articulate the effects of landslide risk reduction measures as is the case at the A83.

The form of equation used for the QRA (eq. 2) can be directly related to that used for the semi-quantitative regional risk assessment (eq. 1) with hazard (H) in eq. (1) being represented by $P(Event)$ in eq. (2), elements at risk represented by $P(Hit|Event)$ and vulnerability being represented by $P(Damage|Hit) \times C$ (or $P(Fatility|Hit) \times C$). While direct numerical comparisons are not possible the consistency of process does lend confidence to the overall approach, especially when, given the nature of the risks, such work is so often subject to political, media and public scrutiny.

Notwithstanding this the QRA process is, of course, considerably more time-consuming on a site-by-site basis, than the semi-quantitative assessment, and demands significant resources. The associated costs mean that it is not generally possible, or appropriate, to apply QRA to a large number of sites and targeting of the highest risk sites necessary. This means that the existence of a semi-quantitative, regional assessment is an essential precursor to QRA. In addition, a sound knowledge of the infrastructure and its users is required, more so even than for the semi-quantitative regional assessment, in addition to high level knowledge of the physical processes (in this case debris flow).

5   SOCIO-ECONOMIC RISK

The social and economic impacts of landslides are both significant and complex. Roads in Scotland, for example, provide vital communication links to remote communities.

Loss of life and major injuries associated with rainfall-induced landslide events is thankfully rare in Scotland, the real impacts are economic and social. Severance of the access of these communities to services and markets as a result of, for example, a landslide or flooding, has significant economic and social consequences. At an individual level opportunities related to employment, education, health, welfare and social activities may be lost or restricted.

Landslides can occur at almost any time of year, although summer (July and August) and winter landslide seasons (October/November to January) have been identified (Winter et al. 2005; 2009). The Scottish landscape has a high economic value and the most important peak in tourist activity coincides with the summer landslide season.

The qualitative economic impacts of such landslide events include:
- the loss of utility of parts of the road network,
- the need to make often extensive detours in order to reach a destination, and
- the severance of access to and from relatively remote communities for services and markets for goods; employment, health and

educational opportunities; and social activities.

The economic impacts of a landslide event that closes a road, or other form of linear infrastructure were summarized by Winter & Bromhead (2012), in three categories, as follows:

- Direct economic impacts.
- Direct consequential economic impacts.
- Indirect consequential economic impacts.

Direct economic impacts: The direct costs of clean-up and repair/replacement of lost/damaged infrastructure in the broadest sense and the costs of search and rescue. These should be relatively easy to obtain or estimate for any given event, provided that this is done soon after it occurs.

Direct consequential economic impacts: These generally relate to 'disruption to infrastructure' and relate to loss of utility. For example, the costs of closing a road (or implementing single-lane working with traffic lights) for a given period with a given diversion, are relatively simple to estimate using well-established models. The costs of fatal/non-fatal casualties and accidents may also be included here and may be taken (on a societal basis) directly from published figures. While these are set out for the costs of road traffic accidents, or indeed rail accidents, there seems to be no particular reason why they should be radically different to those related to a landslide as both are likely to include the recovery of casualties from vehicles. Indeed, for events in which large numbers of casualties may be expected to occur, data relating to railway accidents may be more appropriate.

Indirect consequential economic impacts: Often landslide events affect access to remote rural areas with economies that are based upon transport-dependent activities, and thus the vulnerability can be extensive and is determined by the transport network rather than the event itself. These impacts include those due to the dependence upon the transport network for incoming and/or outgoing goods, and for the transport of staff and visitors as well as any associated longer term impacts. If a given route is closed for a long period then how does that affect confidence in, and the ongoing viability, and credibility, of local businesses. Manufacturing and agriculture (e.g. forestry in western Scotland) are a concern as access to markets is constrained, the costs of access are increased and business profits are affected and short-term to long-term viability may be adversely affected. Perhaps of even more concern are the impacts on tourist (and other service economies) businesses. It is important to understand how the reluctance of visitors to travel to and within 'landslide areas' is affected after an event that has received publicity and/or caused casualties and how a period of inaccessibility (reduced or complete) affects the short and long-term travel patterns to an area for tourist services. Such costs form a fundamental element of the overall economic impact of such events on society. They are thus important to governments as they should affect the case for the assignation of budgets to landslide risk mitigation and remediation activities. However, these are also the most difficult costs to determine as they are generally widely dispersed both geographically and socially. Additionally, in an environment in which compensation might be anticipated, albeit often erroneously, those that have the best data, the businesses affected by such events, are also those that anticipate such compensatory events.

The above primarily relates to the economic impacts that affect linear infrastructure, particularly roads, Alimohammadlou et al. (2013) describe landslide losses in a more generic sense whilst including many of the elements described in the foregoing.

A similar scheme was presented by Benson (2012) in respect of disaster losses and considered the following:

- Direct losses: Relate to human life and injury and physical damage to productive and social assets.
- Indirect losses: Refer to disruptions to the flow of goods and services stemming from the direct losses.
- Secondary effects: Concern the impacts on socio-economic imbalances and the functioning and performance of an economy.

While closely correlated with the Winter & Bromhead (2012) scheme, these have a broader disaster impact focus than the landslide impacts on a road network.

There is a variety of approaches to determining the economic (and social) risks posed by landslides. Typically these quantify the direct economic losses (e.g. Highland 2006) and occasionally some aspects of direct consequential and/or indirect consequential losses (e.g. Schuster & Highland 2007; Highland 2012). Bespoke methods designed to address a particular set of circumstances are also used to estimate the indirect consequential economic impacts of landslides (MacLeod et al. 2005; Anon. 2013).

Klose et al. (2015) in contrast collected local direct and direct consequential costs for a series and extrapolated these to an entire road network on the basis of a susceptibility survey and infrastructure exposure model, while Eidsvig et al. (2014) used an indicator-based methodology to assess the relative socio-economic vulnerability of communities to landslides at local to regional scale.

The approach developed by Winter & Bromhead (2012) has been used to articulate socio-economic costs of both landslide and flood events that have affected the road network in Scotland. Published and unpublished records were interrogated to obtain direct economic impacts, software used to model delays at roadworks was used to obtain direct consequential economic impacts and questionnaire surveys were used to obtain cost

and, perhaps more importantly, qualitative information on the indirect consequential impacts (Winter et al. 2016). Winter et al. (2018) describe the development and application of the methodology, and the results and their interpretation in detail.

The results indicate a range of total direct economic impact costs of between approximately £400k and £1,700k (2012 prices) for four Scottish landslide events from 2004 to 2014. The corresponding direct consequential costs were between around £180k and £1,400k. Daily costs are presented by Winter et al. (2018), however, the variation in the type of full and partial closure for different events, and their change over time for specific events as repair and remediation work is undertaken defies a simple presentation.

Unsurprisingly the daily direct consequential economic impacts are largely dependent upon traffic levels while the total costs depend upon the traffic and the duration of the disruption. The methods for direct and direct consequential economic impacts have also been applied to flood events that affect the road network; the events generally affect more developed peri-urban parts of Scotland and their rather short duration, transient nature meant that the direct costs were small but the direct consequential costs (c. £3,200k) much greater than for any of the landslide sites considered (Winter et al. 2016).

Surveys of businesses in the areas of events provided cost information that could be interpreted in a number of ways and therefore gave a very wide range of potential results. They did, however, provide useful qualitative information (Winter et al. 2018). For events of lesser impact, descriptors that relate to the hazard are used: 'landslide', 'flooding' and other words that describe the event itself are also to the fore (Figure 9).

In contrast responses to events of greater impact and or repetition such as at the A83 (Figure 10), at which a significant number of events and consequent closures have occurred

over the past 20 years, tend to relate to the effects, risks, or impacts, that derive from the event.

Figure 9. Word map of responses from survey respondents: A85 Glen Ogle, 18 August 2004.

Figure 10. Word map of responses from survey respondents: A83 Rest and be Thankful, 28 October 2014.

In this case the most frequently used word was 'road', with words such as 'closed', 'staff', 'visitors', 'due', 'access', 'tourism', 'minor' and 'island' also coming to the fore. These latter responses seemingly describe the consequences of the hazard, or the economic risks associated with the hazard, rather than the hazard itself, implying a greater economic impact or, at least, a greater awareness of the economic impact.

5.1 Vulnerability Shadow

The vulnerability shadow (Winter & Bromhead 2012) is closely linked to economic impacts and determines their extent and overall magnitude. The vulnerability shadow is a largely qualitative means of expressing the areal extent of the impact of hazards such as landslides and floods (Winter 2014b). It is thus a measure of the area over which the effects of the risks associated

with the hazard are experienced. The magnitude of the vulnerability will not be constant in the area affected and may, as a first level approximation, be expected to decrease with distance from the hazard event.

The vulnerability shadow cast can be extensive and its geographical extent can be determined by the transport network, including closures and diversionary routes, rather than the relatively small footprint of the event itself. In the case of the A83 landslide event at the Rest and be Thankful in 2007, the event itself was of the order of around $400m^3$ with a footprint that closed a few tens of metres of the length of the road (Winter 2014b).

In Scotland the vulnerability shadow has been evaluated using knowledge of the local transport networks and the socio-economic activity associated with the network that has been built up over a period of 30 years. This includes an holistic evaluation of major nodes, origins and destinations and includes both experience and knowledge gleaned from formal surveys (e.g. Winter et al. 2013a). The vulnerability shadow was thus estimated (Figure 11) to be of the order of 2,800km^2 (total area approximately 3,500km^2, 20% allowed for areas of sea).

The area has a population density of approximately 13 people/km^2 (www.argyll-bute.gov.uk) and the event thus had the potential to have had an economic impact upon up to approximately 36,400 people in Argyll & Bute, plus any transient (e.g. tourist) population.

It is instructive to make some simple comparisons with Hong Kong SAR, which has an average population density of around 6,500 people/km^2 (www.gov.hk). This dictates a much greater transport network density. Thus, and purely for the sake of comparison, in order to have an economic impact on the same number of people the vulnerability shadow cast need only be approximately 5.6km^2 (2km by 2.8km, for example).
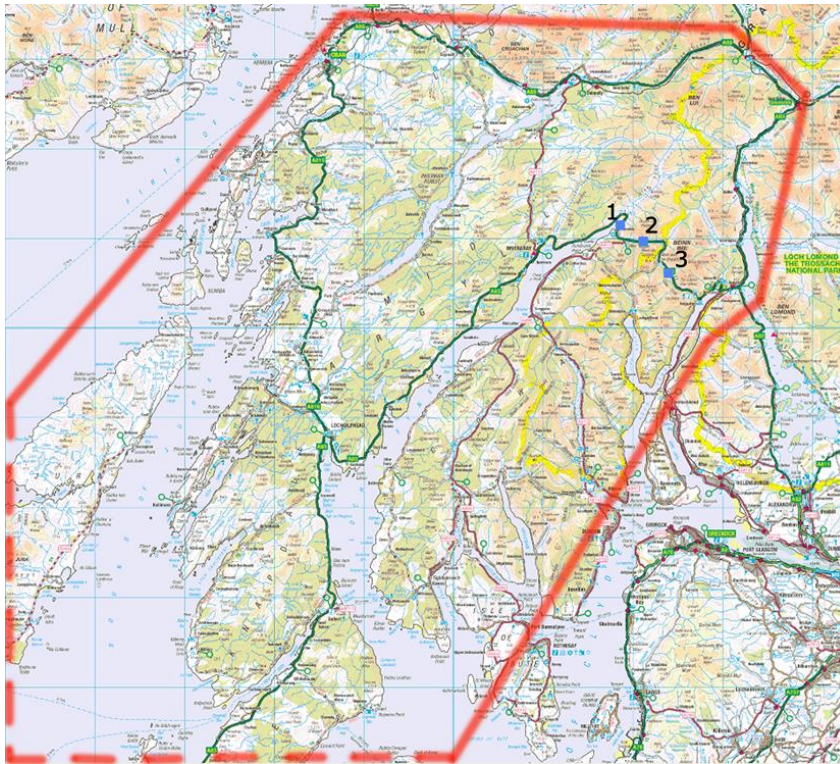
Figure 11. A relatively small debris flow event (blue square '3') closed the A83 at the Rest and be Thankful on 28 October 2007; the vulnerability shadow that was cast (bounded in red) was extensive (Winter 2014a; 2014b). The 2004 events at Cairndow ('1') and Glen Kinglas ('2') are also shown. (Image based on OS 1:250,000 mapping. © Crown Copyright. All rights reserved Scottish Government 100020540, 2018.)

It is not suggested that the economic impacts would be similar for events with vulnerability shadows of these diverse sizes in Argyll & Bute and Hong Kong. However, it is clear that the low density/dispersed network in Argyll & Bute dictates a large vulnerability shadow while the much more dense/less dispersed network in Hong Kong means that vulnerability shadows will be small, with the exception of events that affect critical infrastructure corridors, as more alternative routes will exist and will be more proximal to the event (Winter 2014b).

A landslide on the B1 route in the Blue Mountains of Jamaica (Figure 12) effectively severed the local coffee production industry from the most direct route to the international market for this high value product. As such a single landslide event placed severe constraints on the economy of the Blue Mountains. Again,

while the footprint of the actual event was relatively small, the vulnerability shadow was projected over a much greater area creating tangible economic and social losses.

The economic impact and the vulnerability shadow are concepts that apply equally to other discrete climate-driven events that have the potential to close parts of the road network such as flood events. Like landslides, such flood events are generally thought to be likely to increase in frequency as a result of climate change (Galbraith et al. 2005; Anon. 2011a; Winter et al. 2005; 2010a; 2010b; Winter & Shearer 2013) (see also Section 7). However, it is clear that for some events it is the hazard itself and not the transport network and, more pointedly, its density that determines the location, shape and extent (morphology) of the vulnerability shadow. However, it is important

to recognise that the morphology of the vulnerability shadow related to other types of event (e.g. glacial lake outburst floods), may be determined by the nature of the hazard itself.

Figure 12. Landslide on the B1 road at Section in Portland Parish, Jamaica. This event severed much of the local coffee production industry from the ports used to ship the product to market. (This picture is a photo-collage and some distortion is inevitable.)

An example in which the hazard determines the vulnerability shadow is the Seti River debris flow in Nepal (Figure 13). On 5 May 2012 the event caused significant erosion and deposition in the river channel over a distance of around 40km. The event was initially thought to have resulted from a failed landslide dam. However, subsequent inspection of satellite imagery and aerial photography (Petley & Stark 2012; Petley 2014), and more detailed site inspection and investigation (Dahal & Bhandary 2013) led to the conclusion that the event was a debris flow initiated by part of a 22Mm^3 rock avalanche originating on the slopes of Annapurna IV and entering the upper stream channel at high speed. An estimated 71 people lost their lives at Kharapani, some 20km north of Pokhara. The vulnerability shadow was constrained by the dimensions of the hazard flow within the stream channel, extending beyond these bounds only where infrastructure was damaged, including the footbridge at Kharapani.

Figure 13. Residents of Kharapani located on the platform in the middle distance on the Seti River, Nepal, were among fatalities from the 5 May 2012 debris flow event. The abutment of the suspended footbridge is on the platform.

Similarly, it is entirely possible that the event itself and the transport network may define the vulnerability shadow during different phases of an event. The Zhouqu debris flow disaster (Gansu Province, PR China) occurred at around midnight on 8 August 2010 and claimed the lives of around 1,750 people (Dijkstra et al. 2014; Winter 2019). The vulnerability shadow was initially constrained by the hazard as the debris flow swept through the gorge and the town below (Figure 14). Approximately at the base of the picture, but just out of shot, is the main road that links Zhouqu to the rest of China. As the road was also blocked by the event, the vulnerability shadow spread in both directions along the valley and was thus considerably more extensive than it might otherwise have been if the debris flow run-out had been shorter. Thus, in this case, the morphology of the vulnerability shadow was determined by both the hazard, in the initial phase of transport and deposition, and the transport network (the road), in the latter phase as the run-out zone was reached.

The vulnerability shadow has proven to be a useful and effective means of assessing (semi-quantitatively), presenting and articulating the areal extent of socio-economic landslide (Winter et al. 2016; 2018) and flood hazards (Winter et

al. 2016; 2018; Milne et al. 2016) as exemplified in Figure 11. Indeed, this approach has been extended by Winter et al. (2018), using Figure 11, to enable specific areas within the wider vulnerability shadow to be identified and the economic impact on each area assessed individually.

Figure 14. The channel in which the 8 August 2010 Zhouqu debris flow occurred (Gansu Province, PR China) (from Winter 2019). The road and river that pass through the valley are located just below the bottom of the picture.

6 INFRASTRUCTURE RISK

In the previous sections the primary focus has been the risk to road users and the socio-economic risks. In this section the focus is on the risk to the physical infrastructure elements.

The physical vulnerability of roads to debris flow may be expressed through fragility functions that relate flow volume to damage probabilities. Fragility curves have been produced that indicate the probability of a debris flow of a given volume exceeding each of three damage states. Typically, damage to roads resulting from debris flow may include one or more of the following:

- Debris covering the carriageway, preventing vehicle movements.
- Damage to the carriageway surfacing materials.

- Blockages and other types of damage to the drainage system.
- Damage to vehicle restraint systems.
- Damage to support structures including slopes and retaining walls downhill from the road.

The vulnerability to debris flow for impacted buildings has been expressed using fragility curves and/or probabilities of exceedance of damage states (Haugen & Kaynia 2008; Jakob et al. 2012; Quan Luna et al. 2011; Papathoma-Khöle et al. 2012), while Winter et al. (2014) developed fragility curves for the effects of debris flow on road infrastructure. While several possible approaches were available for the development of fragility curves, including analytical approaches, it was decided that expert engineering judgement should be used due to a lack of a comprehensive empirical dataset as well as the complex nature of the problem

All roads were considered to be relatively stiff and brittle (the low strain stiffness of even an unbound pavement, for example, may be typically up to around one gigapascal) in comparison to most debris materials. In order to further simplify the analysis, roads were divided into low- and high-speed roads, characterized as follows:

- High-speed roads: speed limit between 80 and 110km/h and one or more running lane in each direction, very often in conjunction with a hard strip or hard shoulder.
- Local (or low-speed) roads: speed limit typically <50km/h on a single-carriageway (one lane for each traffic direction) or single-track. This category is intended to encompass both paved (bituminous, unreinforced or reinforced concrete) and unpaved constructions.

Clearly there is a gap between the speed limits of the two classes of road, reflecting the transition between local roads and high-speed roads, which is by no means geographically

consistent. This reflects reality – in some countries and regions certain road geometries are more closely aligned with the definition of local roads, and in others they are more closely aligned with the definition of high-speed roads. Speed limit is not, and should not be, the only determinant of the category of road. In most instances, the category that a particular geometry and speed limit combination will belong to is relatively self-evident, but extending the speed limits between 50 and 80km/h in the category descriptions could lead to uncertainty and potential incorrect categorisation.

Table 1. Damage state definitions

Damage state	High-speed roads	Local (low-speed) roads
P1 (Limited damage)	Encroachment limited to verge/hard strip	Partial blockage of carriageway
P2 (Serious damage)	Blockage of hard strip and one running lane	Complete blockage of carriageway and/or damage to ancillaries
P3 (Destroyed)	Complete blockage of carriageway and/or repairable damage to surfacing	Complete blockage of carriageway and/or damage to surfacing. For unpaved roads the surfacing may remain damaged but passable at reduced speeds post clean-up

Representative damage states associated with the consequences of a debris flow of a given volume intersecting a road were defined. The damage states considered in the questionnaire are defined in Table 1. The damage states range from 'limited damage' which, for high speed roads, is unlikely to significantly affect the passage of vehicles, through 'serious damage', to 'destroyed' involving complete blockage and

damage to the road itself that for, high-speed roads at least, will almost certainly need to be repaired prior to reopening to traffic without restrictions on speed.

The survey was conducted amongst 176 debris flow experts, with a 27% response rate and responses from 17 countries. These represented most parts of the world, but with a significant majority of 83% being received from Europe. The responses were split between those representing academia (32%), the commercial sector (51%) and government bodies (17%).
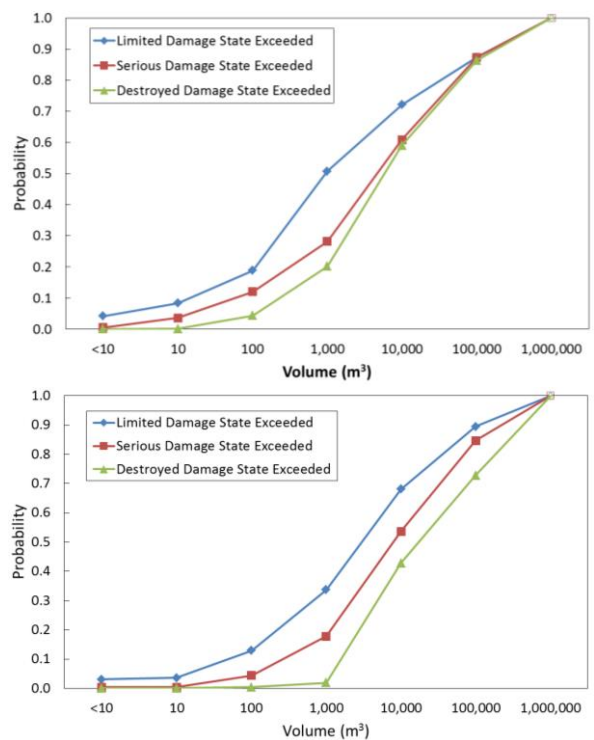
Figure 15. Fragility curves: top, local roads; bottom, high-speed roads.

The data collection, analysis and interpretation is described in detail by Winter et al. (2014) and the resulting curves are illustrated in Figure 15 while Figure 16 explains the probabilities inherent within the fragility curves, in particular the probability of a given damage state being exceeded and the conditional probabilities of a given damage state.
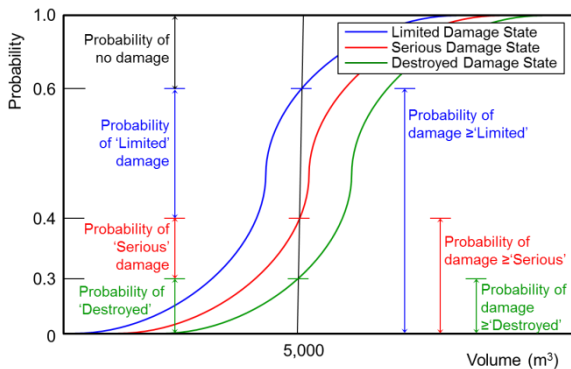
Figure 16 Hypothetical fragility curve illustrating a 5,000m³ event on a high-speed road (Figure 15), illustrating the probabilities of a given damage state being exceeded and the conditional probabilities for damage states.

The experience of the respondents is a critical metric in terms of the data set, and respondents were asked to assess their experience on a scale of zero to 10. The scores of this self-assessment were weighted towards the higher end of the range, as might be expected from a sample of respondents who were selected for their known expertise in this area. As also might be expected, the confidence of respondents for low-volume events is markedly higher than for high-volume events, reflecting the higher frequency, and therefore experience, of low-volume events and the data indicated that for low-volume events, the confidence in the responses is high while for high-volume events (100,000m³) confidence is lower.

The results were tested against events from Scotland (Winter et al. 2006; 2009) and the Republic of Korea (Lee & Winter 2010; 2019). The results from determining the probabilities of a given damage state given the volumes of the events that occurred were found to be broadly consistent with field observations; two examples of the validation work follow.

6.1 A85 Glen Ogle, Scotland

In August 2004, two debris flow events occurred at Glen Ogle (Figure 17). These blocked the A85 strategic road, culverts and other drainage features, and necessitated a full repair to the road pavement, safety barriers and parapets (Winter et al. 2005; 2006). Some 20 vehicles were trapped by the events and 57 people were airlifted to safety; one vehicle was swept away in the latter stages of the event (Winter et al. 2005). The smaller southerly and larger northerly events were estimated to have deposited around 3,200m³ and 8,500m³ in their respective debris lobes, having been triggered by smaller translational slides of around 285m³ and 280m³ (Milne et al. 2009). The depositional figures are believed not to include material deposited on the road, and it seems reasonable therefore to round these figures up to around 5,000m³ and 10,000m³.

Figure 17. The larger northerly of the two August 2004 debris flows at A85 Glen Ogle.

For the smaller (5,000m^3) event, the conditional probabilities for no damage, limited, serious and destroyed damage states are 0.4, 0.2 (0.6), 0.1 (0.4) and 0.3 (0.3) (the probabilities of the damage states being met or exceeded are given in parentheses); for the larger (10,000m^3) event, the conditional probabilities are around 0.3, 0.15 (0.7), 0.15 (0.55) and 0.4 (0.4), in both cases for a high-speed road. Certainly the damage caused by the larger event would have been described as destroyed using the scheme considered here, and the probability of this state, 0.4, seems to be broadly in line with observations made in its immediate aftermath, albeit affecting a road length of around 200m. Similarly, the damage caused by the smaller event, although somewhat less in terms of physical damage to the infrastructure, would also be classified as destroyed and this seems to be broadly reflective of the probability of 0.3 returned from Figure 15.

6.2 Seoul to Chuncheon National Highway Tunnel Portals, Republic of Korea

Landslide deposits at the Chuncheon National Highway tunnel portals (Figure 18) were 500m^3 to 1,000m^3. For an event of this volume (1,000m^3) the conditional probabilities of the damage states no damage, limited, serious, and destroyed are 0.7, 0.1 (0.3), 0.18 (0.2), and 0.02 (0.02), for a high-speed road.

Only very minor damage was incurred at the Seoul to Chuncheon National Highway tunnel portals, and this reflects the small volumes; the probability of either limited damage or no damage (the combined conditional probabilities) is 0.8 (Figure 18). The road was not open at the time of the event, and there is every possibility of both further and larger events that have the potential to meet or exceed higher damage states.

6.3 Systems of Assets

The concept of fragility also lends itself to being based on the results of modelling and in that

sense has been widely applied including damage related to both highway and railway embankments and cut slopes (Argyroudis & Kaynia 2015), cantilever retaining walls (Argyroudis et al. 2013) and to the settlement of bridges (Peduto et al. 2018). The first two of the foregoing examples reflect, to a large degree, the genesis of fragility curves as a tool to understand the severity and potential damage due to seismic activity.

Figure 18. Debris flow site from July 2009 above tunnel portals on the Seoul to Chuncheon National Highway in the Republic of Korea: (top) source area; and (bottom) view from the source area looking out over the tunnel portals.

Infrastructure assets comprise Systems of Assets (SoA) – a combination of interdependent assets exposed not to one, but to multiple hazards, depending on the environment within which these reside (Argyroudis et al. 2018). This multi-element, multi-hazard approach presents a

far more realistic, real-world, approach to understanding and assessing the behaviour and the fragility of assets and SoAs subjected to one or a sequence of similar or disparate hazards.

7 CLIMATE CHANGE AND RESILIENCE

In terms of the potential variability in climate changes, and the subsequent impacts, the statement widely attributed to Donald Rumsfeld, the former US Secretary of Defence at a Defence Department briefing in 2002, is pertinent (Winter et al. 2010b):

"There are known knowns. There are things we know that we know. There are known unknowns. That is to say, there are things that we now know we don't know. But there are also unknown unknowns. There are things we do not know we don't know."

Whatever the merits of the language used – Rumsfeld's statement won the 2003 *Foot in Mouth Award* from the Plain English Campaign and was also hailed as an example of found poetry – the sentiment, if not the precise wordings, has been around for considerably longer. (It arguably has its roots in Socrates' statement "I know that I know nothing", which is often interpreted as a reflection on the confidence levels, and uncertainty inherent, implicit within knowledge and information.) It does, however, provide a useful conceptual and temporal framework for past, current and future climate and the associated potential changes. This may be framed as follows:

- Known knowns: These include historic and recent climate trends, their relation to current patterns and the fact of climate change (the sequence of greenhouse gas emissions, global warming, and climate change and instability).

- Known unknowns: The precise degree and nature of climate change and some of its impacts, particularly in the light of the

variability in climate change forecasts and likely instability in year-on-year climate patterns. These impacts might, for example, include the reaction of vulnerable human populations to both climate change and instability.

- Unknown unknowns: The nature of some other impacts of climate change, although as these are genuinely unknown unknowns these will really have to wait until our knowledge is more complete – that these are unknowns is after all the point. Possibly the real value of this element of the framework is as a reminder that there will always be issues that arrive unexpectedly out of leftfield.

Knowns and unknowns fit well within many geological and geotechnical frameworks with the challenge being to move backwards on the scale from unknown unknowns, through known unknowns to known knowns reducing the risk in the process.

It is also important to bear in mind that one person's known known may be another's known unknown or even unknown unknown; knowns and unknowns may be dependent upon professionalism, specialism, awareness and other factors. This emphasises the need for effective and ongoing communication both within and between the professions.

An integrated data approach was taken to an evaluation of landslide hazard and risk in the light of global change, including climate change by Winter & Shearer (2013; 2014). Data sets describing recent trends (1914 to 2004) in the climate of Scotland (Barnett et al. 2006a; 2006b), current meteorological synoptic data from the national Meteorological Office, and both deterministic climate change forecasts (UKCOP02: Hulme et al. 2002) and probabilistic forecasts (UKCP09: Jenkins et al. 2009; Anon. 2011a; 2011b) were all considered in order to give an holistic view of the potential change in hazard frequency and intensity.

In broad terms the data presented a picture that tended to suggest that landslide frequency and magnitude would increase in Scotland in the future, at least in the winter months. The picture for the summer months was considerably more complex, but one likely outcome was that while the frequency of events would decrease their magnitude, when they do occur, may increase. These conclusions were broadly consistent with those from earlier parts of the work on climate change and the effects on Scotland's road network (Winter et al. 2005).

A consideration of the consequent risks to road users from landslides and climate change concluded that while the effects of climate change were most likely to increase the hazard, increases in the elements at risk and their vulnerability are likely to increase in line with road traffic (and rail passenger) growth. The risk to road users was thus considered likely to increase as a result of both climate change and traffic growth.

A study of the hazards and risks associated with coastal flooding (Milne et al. 2016) concluded that the hazard frequency was likely to increase by a factor of up to around 2.5 between the present and 2100. The economic impacts were also evaluated using the methodology set out by Winter et al. (2016; 2018) and inevitably this demonstrated increased economic impacts on the same scale. However, when projected traffic growth was factored in, this increase in the elements at risk and their vulnerability, produced a much greater impact at around 19 times the present day impacts and around eight times those forecast due to the changing hazard alone.

The conclusion that changes in elements at risk and their vulnerabilities play a key role, and often one that is dominant, driven by social and/or demographic change, is extremely important. Clearly a focus on hazards, with the elements at risk and their vulnerabilities, being treated almost as an afterthought is neither adequate nor acceptable. However, this clearly-demonstrated potential for these oft-neglected components to dominate the risk outcome demonstrates rather graphically that, as interesting as the hazards may be to us as ground engineering professionals and/or geoscientists, it is essential that we engage with other disciplines to adequately assess the elements at risk and their vulnerabilities in order to produce effective risk assessments.

The outcomes of such risk assessments must be balanced against, and be used in the consideration of, opportunities to reduce risk by means of new and renewed infrastructure, albeit this is not a panacea for all ills due to a lack of affordability. In this sense it is essential that resilience of existing and new infrastructure is considered and enhanced where possible.

In terms of resilience, the frequency of events is extremely important relative to the recovery time for an event, and in the coastal flooding case study examined by Milne et al. (2016) for example, the recovery time was around 6.5 weeks (the time from the event occurring to the road being fully open again). This was significantly less than the event frequency allowing full recovery of system resilience between events in that case. However, where the event frequency is less than the recovery time full system resilience may not be recovered before a subsequent event reduces the resilience of the road system further. In such cases the road system resilience is not restored sufficiently before the next event occurs and this can lead to a decrease in system resilience (increase in system vulnerability) over time as illustrated in Figure 19.

Figure 19 is, of course, a simplification of the real situation. For example, in order to keep the diagram relatively straighforward each event is shown at the same magnitude and the frequency is also constant for each of the two scenarios illustrated.
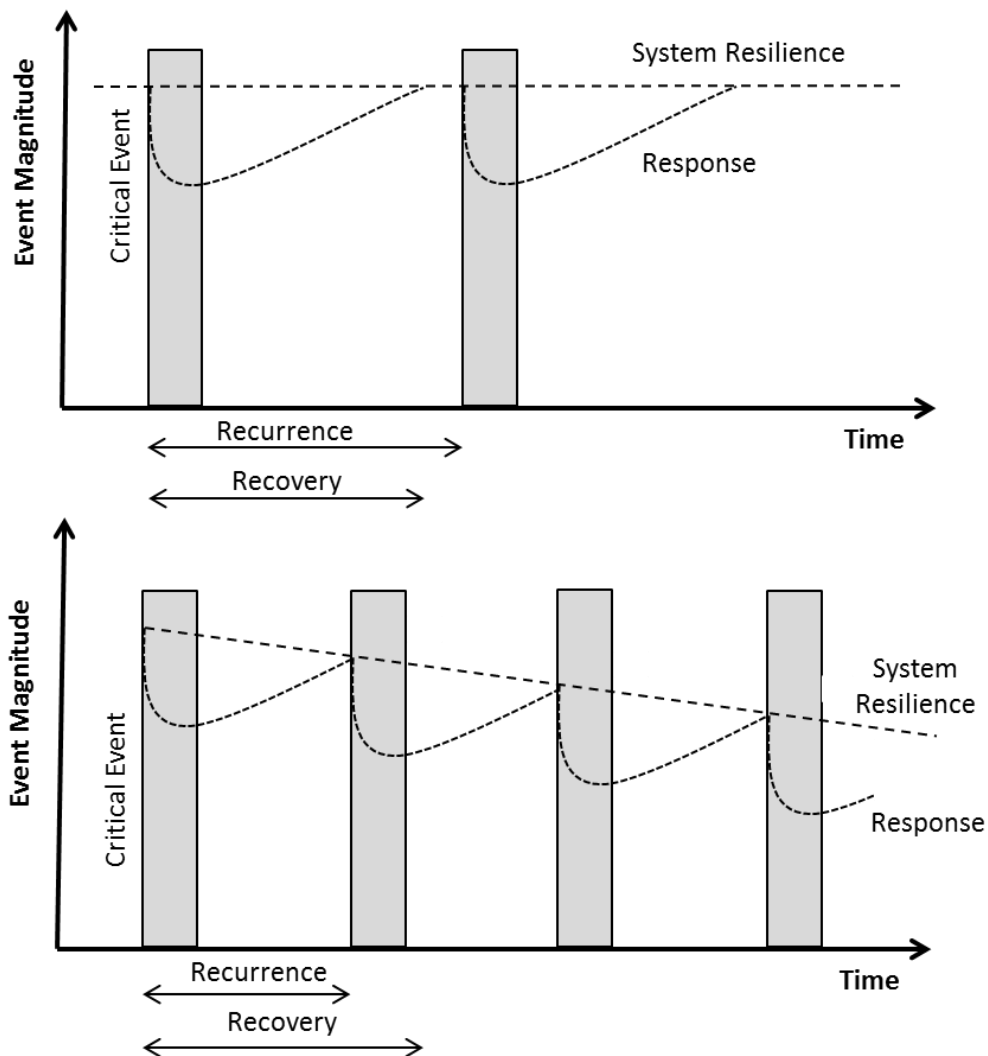
Figure 19. A simplified, conceptual illustration of the effects of repeated hazard events on infrastructure system resilience. Top (sustained resilience): When the event recurrence period is greater than the recovery period then the system resilience, of a road for example, will be retained (i.e. full system resilience recovery is possible between events). Bottom (unsustained resilience): However, if the recovery period is greater than the recurrence period there will be a decrease in system resilience over time (equally this might be considered to be an increase in system vulnerability) (from Milne et al. 2016, adapted from a diagram representing system vulnerability by Dijkstra & Dixon, 2010).

There is also a number of possible responses to the impacts of repeated hazard events on infrastructure and, while these include repeated repair, which is broadly that illustrated in Figure 19, other responses might include repair of the infrastructure in such a way as to build in greater resilience than was previously available or,

indeed, to allow resilience to gradually decline as shown in the lower half of Figure 19, which over time may effectively correspond to a controlled abandonment of the infrastructure.

8   LANDSLIDE RISK REDUCTION

The primary purpose of landslide risk assessment is to enable decisions on risk reduction and, in particular, the prioritization of multiple sites that could potentially be subject to risk reduction through management and/or mitigation in the light of defined budgets.

Bromhead (1997) presented a simple, logical and philosophically consistent framework within which to describe the physical treatment of landslides, providing a useful framework for the interpretation of the detailed methods described by VanDine (1996) and Couture & VanDine (2004) for example. Winter et al. (2005; 2009) developed an approach to landslide risk reduction that accounted for management actions to reduce the vulnerability of mobile (road user) elements at risk as well as mitigation

actions that reduced either the hazard or the vulnerability of the static elements at risk (infrastructure).

Winter & Bromhead (2012) brought many of these elements together in the willingness diagram (see Section 2) for both both generic forms of landslide risk reduction (Figure 20) and conceptual, approaches to landslide risk reduction (Figure 21).

Further development work was reported by Winter (2014a) to articulate a strategic approach to landslide risk reduction. This incorporates a classification scheme for landslide management and mitigation and provides a common lexicon (or group of words) that can be used to describe goals, outcomes, approaches and processes related to risk reduction, and to allow a clear and sequential focus thereon.
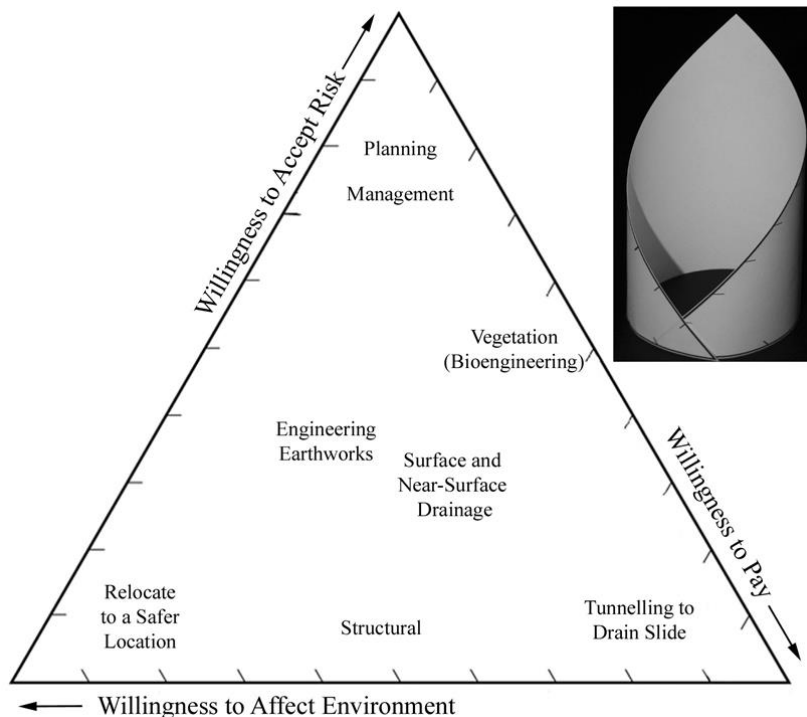
Figure 20. The 'Willingness Diagram' comparing different generic forms of landslide risk reduction. Inset: The extreme bottom-left and bottom-right corners of the ternary diagram tend to converge and the diagram might more strictly be rendered as if wrapped around a cylinder about a vertical axis.
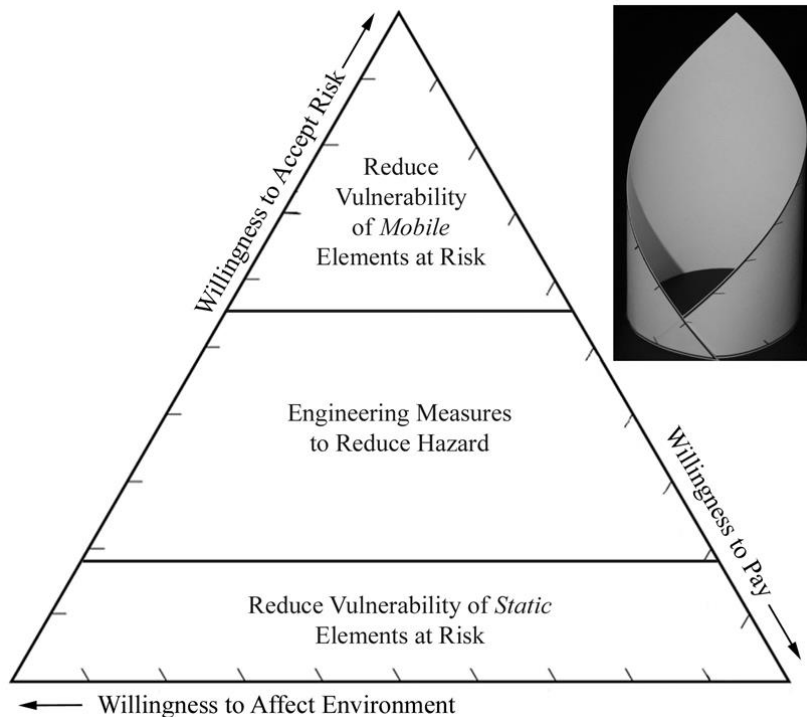
Figure 21. The 'Willingness Diagram' showing conceptual approaches to landslide remediation. Inset: The extreme bottom-left and bottom-right corners of the ternary diagram tend to converge and the diagram might more strictly be rendered as if wrapped around a cylinder about a vertical axis.

To reduce landslide risk to acceptable levels, either the potential exposure or losses (vulnerability) that are likely to arise as a result of an event, and/or the magnitude of the hazard must be addressed. Thus management strategies involve exposure reduction outcomes and mitigation strategies involve hazard reduction outcomes (Figure 22). Further, it is important that those funding such works, including infrastructure owners and local governments, are able to focus clearly on goals of, the outcomes from, and the approaches to such activities rather than the details of individual processes and techniques.

The strategic approach encourages a top-down approach to the selection of management and mitigation processes (specific measures and remedial options). It is intended to aid a focus on the primary goal of landslide risk reduction, the secondary desired outcome(s) and the tertiary generic approach to achieving that outcome rather than, initially at least, the specific measure or options (the process or processes) used to achieve that outcome.

The focus on the secondary desired outcome from risk reduction thus relates to the reduction of the exposure, or vulnerability, of the at-risk infrastructure and people (and their associated socio-economic activities) and/or reduction of the hazard itself. Hazard reduction may be achieved either directly or by reducing the vulnerability of the physical elements at risk. In a road environment the people at risk are road users, whereas in an urban setting they are residents and business people. The tertiary focus is then on the approach(es) to be used to achieve the desired outcome before specific measures and remedial options are considered. By this means a more strategic top-down approach is encouraged rather than a bottom-up approach.
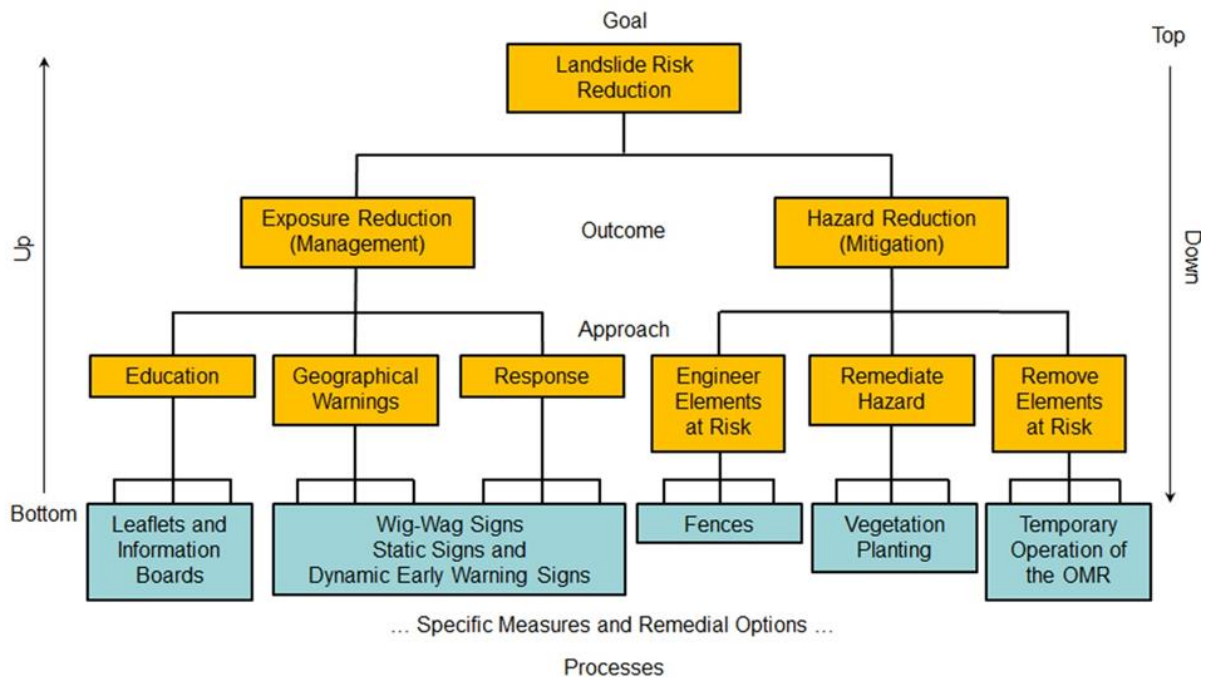
Figure 22. Classification for landslide management and mitigation to enable a strategic approach to risk reduction. The blue boxes illustrated the application of the strategic approach at the A83 Rest and be Thankful.

This approach also provides the aforementioned common lexicon for the description and discussion of landslide risk reduction strategies, which is especially useful in a multi-agency environment. It also renders a multi-faceted (holistic) approach more viable and easier to articulate while helping to ensure that the responses to the hazard and risks in play are appropriate. This approach should be especially useful for infrastructure owners and operators who must deal with multiple landslide, and other, risks, that are distributed across large networks. Such an approach promotes a considered decision-making process that takes account of both costs and benefits. It also encourages careful consideration of the right solution for each location and risk profile, potentially making best use of often limited resources.

The following sections and Figure 22 describe the strategic approach and include limited details of the application of the approach at the A83 Rest and be Thankful site in Scotland (Winter 2016a).

8.1 Exposure Reduction (Management)

Exposure reduction can take three basic forms:
- Education (and information).
- Geographical (non-temporal) warnings.
- Response (including temporal, or early, warnings).

Typically education in its broadest sense may form a key part of an information strategy. It may comprise leaflets, or other forms of communication, that are distributed in both electronic and hardcopy form. The hardcopy also may be available at rest areas for road risks and in retail outlets for urban risks. In addition, information boards may be provided in scenic rest areas, where they can be easily accessed by the public (as well as electronically). The interpretive goals embedded within the communications strategy are critical to success.

These should be specific to the setting and desired outcomes, but may for example consider the development of the landscape (including geological, geomorphological and anthropogenic processes) and set the landslide hazard and risk within that overall picture.

Geographical warning signs may be used in a variety of environments, to demonstrate the presence of landslide hazards. In a road environment they usually follow the standard warning sign form and include a graphic representing rock fall.

The responsive reduction of exposure lends itself to the use of a simple three-part management tool: Detection, Notification and Action (or DNA), providing a simple framework for management responses:

- Detection of either the occurrence of an event (e.g. monitoring, observation: Sparkes et al. 2017; 2018; Winter et al. 2017) or by the forecast of precursor conditions (e.g. rainfall: Winter et al. 2007; 2010b; 2019).
- Notification of the likely/actual occurrence of events to the authorities (e.g. in a roads environment the Police, the road. administration and the road operator).
- Action that reduces the exposure of the elements at risk to the hazard. Again, in a roads environment, this could include media announcements, the activation of geographical signs that also have a temporal aspect (e.g. flashing lights) (e.g. Winter et al. 2013b; Winter & Shearer 2017: Figure 23), the use of variable message signs, 'landslide patrols' in marked vehicles, road closures, and traffic.

8.2 Hazard Reduction (Mitigation)

The challenge with hazard reduction in Scotland often is to identify locations of sufficiently high risk to warrant spending significant sums of money on engineering works. The costs associated with installing extensive remedial works over very long lengths of road may be both unaffordable and unjustifiable and even at discrete locations the costs can be significant. Moreover the environmental impact of such engineering works should not be underestimated. Such works often have a lasting visual impact and, potentially, impact upon the surrounding environment. Such works should be limited to locations where their worth can be clearly demonstrated.

Figure 23. Temporal 'wig-wag' landslide warning signs.

In addition, actions such as ensuring that channels, gullies and other drainage features are clear and operating effectively are important in terms of hazard reduction. This requires that the maintenance regime is both routinely effective and also responsive to periods of high rainfall, flood and slope movement. Planned maintenance and construction should take the opportunity to limit hazards by incorporating suitable measures including higher capacity/better forms of drainage, or debris traps into the design. Critical review of the alignment of culverts (etc.) normally should be carried out as part of any planned maintenance or construction activities.

Beyond such relatively low cost/low impact options three categories of hazard reduction measures may be considered:

- Works to engineer, or protect the elements at risk.

- Remediation of the hazard to reduce failure probability.
- Removal, or evacuation, of the elements at risk.

There are many means of engineering or protecting the elements at risk and this approach accepts that debris flows will occur and makes provision to protect the road, thus limiting the amount of material reaching the elements at risk.

The potential structural forms for protection from debris flow include shelters, barriers and fences (Figure 24), basins, check dams and baffles. Flexible fences absorb the kinetic energy of the debris flow, thus reducing the forces that the structure must accommodate. These systems have been shown to work well, particularly for the arrest of rock fall, but all such systems require maintenance after an impact.

Figure 24. A83 Rest and be Thankful flexible debris fence.

Debris basins are formed as large decant structures, incorporating a downstream barrier that retains debris but allows water to pass. They may be used in association with lined debris channels to move material downslope where potential storage areas on the hillside are limited; lined channels may be used in isolation if storage is limited on the hillside or available only at the foot of the slope. Rigid barriers such as check dams and baffles may slow and

partially arrest flows within a defined channel, and on hillsides may protect larger areas where open hillside flows are a hazard and/or channelised flows may breach the stream course. VanDine (1996) gives design and use guidance for check dams and baffles, including low cost earth mounds. Rigid barriers and debris basins were built as debris flow defence structures at Sarno to the east of Naples in Italy following the events of May 1998 in which 159 people were killed (Versace 2007), at a cost estimated at between €20M and €30M.

The remediation of landslide hazards to reduce the probability of failure may involve alteration of the slope profile by either cut or fill, improvement of the material strength (most often by decreasing pore water pressures), or providing force systems to counteract the tendency to move (Bromhead 1997).

The engineering options available to prevent debris flow depend upon the specific circumstances. Debris flows can be triggered from relatively small source areas, within very large areas of susceptible ground, and be initiated high on the hillside above the road. There may be particular conditions where conventional remedial works and/or a combination of techniques such as gravity retaining structures, anchoring or soil nailing may be appropriate. However, in general terms the cases where these are both practicable and economically viable are likely to be limited. The generic link between debris flows and intense rainfall is well-established and effective runoff management can reduce the potential for debris flow initiation. However, in many circumstances on-hill drainage improvement may have limited impact due to the small scale of many debris flow events. In other locations and situations positive action to improve drainage might well have a more beneficial effect. Such measures could include improving channel flow and forming drainage around the crest of certain slopes to take water away in a controlled manner.

The planting of appropriate vegetation can also contribute to the reduction of instability (Coppin & Richards 2007). Notwithstanding this, the positive effects of such measures can be difficult to quantify but include canopy interception of rainfall and subsequent evaporation, increased root water uptake, and transpiration via leaf cover, and root reinforcement. In addition, the life cycle of the vegetation planted must be considered as, depending upon the species, the climate and other conditions relevant to growth there may be a considerable period before the effects provide a meaningful positive effect on stability. In addition, future deforestation, or harvesting, must also be considered as this is widely recognised as a potential contributor to instability. Such measures do not provide instant solutions and may not always be effective in the long term, especially if commercial forestry is practised. The species planted must be appropriate to the local environment – the planting of non-native species is not allowed in most countries for example. However, the successful application of local knowledge and species can prove successful and a major planting exercise is planned as part of the long-term strategy for the A83 Rest and be Thankful site (Winter & Corby 2012).

Finally, the option of removing the elements at risk from the geographical location of the hazard remains. Typically in an urban or per-urban environment this might involve the abandonment of a settlement (Coppola et al. 2009) or in a transport context the realignment of an infrastructure route, either permanently or on a temporary basis.

It should, of course, be noted that decisions to adopt such extreme options are not taken in isolation. Road realignment might be undertaken as part of a road administration's route improvement activities in order to upgrade both the alignment and the layout of junctions, in particular to reduce road traffic collision risk, and to ensure compliance with current design standards. In cases where the debris flow risk is high and other factors indicate that some degree of reconstruction is required, road realignment may be a viable option. While road realignment has been undertaken in response to landslide activity in Scotland, it was also in response to a genuine need for realignment of the route to increase safety and to ensure compliance with current design standards.

More unusually the Old Military Road in Glen Croe (Figure 25), which is located downslope and therefore somewhat more distant from the hazards at the Rest and be Thankful, has been reopened as an emergency diversion route for periods during which the A83 strategic road is not available; during such periods an alternating, one-way convoy scheme is implemented.

Figure 25. A83 Rest and be Thankful Old Military Road and traffic convoys during a period when the A83 was closed to traffic due to a debris flow, the A83 is to the left-centre and the Old Military Road to the right-centre of the image.

9 SUMMARY AND CONCLUSIONS

In this paper a framework for risk acceptance is used to set the context for a review of the assessment of landslide hazard and risk from the regional scale (small-scale and semi-quantitative) to the site-based scale (large-scale and quantitative).

A regional, semi-quantitative assessment has been used as the basis for further work to assess

the risks related to road users (fatalities), the infrastructure and to the socio-economic activities that the road network supports and facilitates at a larger-scale.

The A83 QRA is believed to be the first full, formal quantitative risk assessment for debris flow risk to road users.

The economic impact assessment uses a bespoke methodology developed to account for all aspects of such economic impacts at specific sites and has been applied to flood events as well as to landslides. The concept of the vulnerability shadow is particularly important to developing a full understanding of such localised events that can have impacts over a significant geographic area.

The use of fragility curves to articulate the vulnerability of physical infrastructure to debris flow is described as it relates to both high-speed and low-speed roads in Scotland and the Republic of Korea. Its potential application to systems of assets, rather than component assets, is set-out in brief.

Climate change is clearly an important consideration when dealing with processes, such as debris flow, that are driven by meteorological events such as rainfall. The understanding of climate impacts is set within the Rumsfeldian context of known knowns, known unknowns and unknown unknowns, which provides a useful framework for articulating the various challenges associated with both climate change and broader issues surrounding global change.

An integrated data approach taken to an evaluation of landslide hazard and risk in the light of global change, including climate change, clearly demonstrates that the elements at risk and their vulnerability are at least as important as the hazard assessment; this conclusion is also supported by the details of the QRA at both the A83 and A85 sites.

The discussion of landslide hazard and risk assessment and of climate change is supported by information derived from assessments of flood (pluvial and coastal). The assessment of the changing economic risk over time clearly demonstrates the potential for the elements at risk and their vulnerability, driven by social and/or demographic change, to be the dominant factors in determining the level of risk rather than: the hazard. The implications of this are clear, a focus on hazards with the elements at risk and their vulnerabilities being treated almost as an afterthought is neither adequate nor acceptable; it is essential that we, as geoprofessionals, engage with other disciplines to adequately assess the elements at risk and their vulnerabilities in order to produce and collaborative effective risk assessments.

Resilience is considered in the context of climate change and the relations between event frequency (recurrence), the time required for recovery and the rate of that recovery are highlighted graphically.

Landslide risk reduction is addressed from a conceptual point of view and a strategic approach is described that offers a logical classification system and encourages a top-down approach to such activities. This helps to avoid a bottom-up approach that can encourage the sometimes inappropriate use of what has worked in the past. The strategic approach provides a common lexicon that can aid clarity of communication in multi-agency risk reduction environments. The application of this approach is demonstrated using the A83 Rest and be Thankful site as an example.

As a profession it is clear that we have some way to go in terms of integrating our approach to landslide hazard assessment with an acceptable form of landslide risk assessment. However, the progress made in the last 15 years should provide encouragement that, with adequate funding and a willingness to engage and collaborate with other professions, this is eminently achievable.

10 ACKNOWLEDGEMENTS

Scotland and NERC. The views presented are those of the author and no agreement or endorsement of those views by any other party is implied.

11 REFERENCES

Alimohammadlou Y., Asadallah N., Yalcin, A. 2013. Landslide processes and impacts: a proposed classification method. *Catena*, **104**, 219-232.

Anon. 2011a. *Scottish road network climate change study: UKCP09 update*. Report prepared by Jacobs for Transport Scotland.

Anon. 2011b. *Paths and climate change – an investigation into the potential impacts of climate change on the planning, design, construction and management of paths in Scotland*. Scottish Natural Heritage Commissioned Report No 436. Scottish Natural Heritage, Inverness.

Anon. 2013. *A83 Trunk Road Route Study: Part A – A83 Rest and be Thankful. Final Report*. Report prepared by Jacobs for Transport Scotland, 212p.

Argyroudis S., Kaynia A.M. 2015. Analytical seismic fragility functions for highway and railway embankments and cuts. *Earthquake Engineering and Structural Dynamics*, **44**(11), 1863–1879.

Argyroudis S., Kaynia A.M., Pitilakis K. 2013. Development of fragility functions for geotechnical constructions: application to cantilever retaining walls. *Soil Dynamics and Earthquake Engineeirng*, **50**, 106-116.

Argyroudis, S., Mitoulis, S., Winter, M.G. & Kaynia, A.M. 2018. Fragility of critical transportation infrastructure systems subjected to geo-hazards. *Proceedings, 16th European Conference on Earthquake Engineering*, CD-Rom Paper No. 11964. Thessaloniki, Greece.

Barnett C., Perry M., Hossell J., Hughes G., Procter, C. 2006a. *A handbook of climate trends across Scotland; presenting changes in the climate across Scotland over the last century*. 62p. Sniffer Project CC03. Edinburgh: Scotland and Northern Ireland Forum for Environmental Research.

Barnett C., Perry M., Hossell J., Hughes G., Procter C. 2006b. *Patterns of climate change across Scotland: technical report*, 102p. Sniffer Project CC03. Edinburgh: Scotland and Northern Ireland Forum for Environmental Research

Benson C. 2012 *Indirect economic impact from disasters*. Commissioned Review, Foresight Programme; Government Office for Science, London, UK.

Bromhead E.N. 1997. The treatment of landslides. *Proceedings, Institution of Civil Engineers (Geotechnical Engineering)*, **125**(2): 85-96.

Bromhead, E.N., Winter, M.G. 2019. A half century of landslide contributions to landslide knowledge in QJEGH. *Quarterly Journal of Engineering Geology & Hydrogeology* **52**(1), 3-16.

Castellanos Abella, E.A., Van Westen, C. J. 2007. Generation of a landslide risk map for Cuba using spatial multi-criteria evaluation. *Landslides* **4**, 311-325.

Cooper, R.G. 2007. *Mass movements in Greta Britain*. Geological Conservation Review Series, No 33, 348p. Joint Nature Conservation Committee, Peterborough.

Coppin N.J., Richards, I.G. 2007. Use of vegetation in civil engineering. *CIRIA Report C708*. CIRIA, London. (Reprinted from CIRIA Report B10, 1990.)

Coppola L., Nardone, R., Rescio, P., Bromhead, E. 2009. The ruined town of Campomaggiore Vecchio, Basilicata, Italy. *Quarterly Journal of Engineering Geology & Hydrogeology*, **42**, 383–387.

Corominas, J., Van Westen, C., Frattini, P., Cascini, L., Malet, J.-P., Fotopoulou, S., Catani, F., Van Den Eeckhaut, M., Mavrouli, O., Agliardi, F., Pitilakis, K., Winter, M.G., Pastor, M., Ferlisi, S., Tofani, V., Hervás, J., Smith, J.T. 2014. Recommendations for the quantitative analysis of landslide risk. *Bulletin of Engineering Geology and the Environment* **73**(2), 209-263.

Couture R. & VanDine D. 2004. Field trip – Guidebook: some geological hazards in North Vancouver and along the Sea-To-Sky Highway, British Columbia. *Open File 4642*. Geological Survey of Canada, Ottawa, ON.

Cruden, D.M., Varnes, D.J. 1996. Landslide types and processes. In: *Special report 247: Landslides: Investigation and Mitigation* (Eds: Turner, A.K., Schuster, R. L.), 36-75. Transportation and Road Research Board, Washington, D. C.: National Academy of Science.

Dahal R.K., Bhandary N.P. 2013. *Excursion guidebook for Pokhara Valley area*. Unpublished.

Dijkstra T.A., Dixon N. 2010. Climate change and slope stability in the UK: challenges and approaches. *Quarterly Journal of Engineering Geology & Hydrogeology*, **43**(4), 371-385.

Dijkstra T.A., Wasowski J., Winter M.G., Meng, X.M. 2014. Introduction to geohazards in Central China. *Quarterly Journal of Engineering Geology & Hydrogeology*, **47**, 195-199.

Dio, S., Forbes, C., Chiliza, G.S. 2010. Landslide inventorization and susceptibility mapping in South Africa. *Landslides* **7**, 207-210.

Eidsvig, U.M.K., McLean, A., Vangelsten, B.V., Kalsnes, B, Ciurean, R.L., Argyroudis, S., Winter, M.G., Mavrouli, O.C., Fotopoulou, S., Pitilakis, K., Baills, A., Malet, J.-P., Kaiser, G. 2014. Assessment of socioeconomic vulnerability to landslides using an indicator-based approach: methodology and case studies. *Bulletin of Engineering Geology and the Environment* **73**(2), 307-324.

Galbraith, R. M., Price, D. J. & Shackman, L. (Eds.) 2005. *Scottish road network climate change study*, 100p. Scottish Executive, Edinburgh.

Gibson A.D., Culshaw M.G., Dashwood C., Pennington C.V.L. 2013. Landslide management in the UK - The problem of managing hazards in a 'low-risk' environment. *Landslides* **10**, 599-610.

Haugen E.D., Kaynia A.M. 2008. Vulnerability of structures impacted by debris flow. *Landslides and Engineered Slopes: From the Past to the Future* (Eds: Chen Z., Zhang J.-M., Ho K., Wu F.Q.), 381-387. CRC Press, London.

Highland L.M. 2006. Estimating landslide losses – preliminary results of a seven-state pilot project. *US Geological Survey Open File Report 2006-1032*. USGS, Reston, VA.

Highland L.M. 2012. Landslides in Colorado, USA: impacts and loss estimation for the year 2010. *US Geological Survey Open File Report 2012-1204*. USGS, Reston, VA.

Hulme M., Jenkins G.J., Lu X., Turnpenny J.R., Mitchell T.D., Jones R.G., Lowe J., Murphy J.M., Hassell D., Boorman P., MacDonald R., Hill, S. 2002. *Climate changes scenarios for the United Kingdom: the UKCIP02 scientific report*. Tyndall Centre for Climate Change research, 120p. Norwich: University of East Anglia.

Jaedicke, C., Van Den Eeckhaut, M., Nadim, F., Hervás, J., Kalsnes, B., Vangelsten, B.V., Smith, J.T., Tofani, V., Ciurean, R., Winter, M.G., Sverdrup-Thygeson, K., Syre, E., Smebye, H. 2014. Identification of landslide hazard and risk 'hotspots' in Europe. *Bulletin of Engineering Geology and the Environment* **73**(2), 325-339.

Jakob M., Stein D., Ulmi M. 2012. Vulnerability of buildings to debris flow impact. *Natural Hazards*, **60**(2), 241-261.

Jenkins G.J., Murphy J.M., Sexton D.S., Lowe J.A., Jones P., Kilsby, C.G. 2009. *UK Climate projections: briefing report*. Exeter: Met Office Hadley Centre.

Jones, D.K.C., Lee, E.M. 1994. Landsliding in Great Britain. Department of the Environment, 361p. London, HMSO.

Klose M., Damn, B., Terhorst, B. 2015. Landslide cost modelling for transportation infrastructures: a methodological approach. *Landslides*, **12**, 321-334.

Lee, E.M., Jones, D.K.C. 2014. *Landslide risk assessment* (Second edition). ICE Publishing, London, 509 p.

Lee S.-G., Winter M.G. 2010 The effects of debris flow in the Republic of Korea and some issues for successful management and mitigation, *Geologically Active: Proceedings, 11th IAEG Congress* (Eds: Williams A.L., Pinches G.M., Chin C.Y., McMorran T.M., Massey C.I.), 1243-1250. CRC Press, London.

Lee, S.-G., Winter, M.G. 2019. The effects of debris flow in the Republic of Korea and some issues for successful risk reduction. *Engineering Geology*, **251**, 1720189.

MacLeod, A., Hofmeister, R.J., Wang, Y., Burns, S. 2005. Landslide indirect losses: methods and case studies from Oregon. *Open File Report O-05-X*. State of Oregon, Department of Geology and Mineral Industries, Portland, OR.

Milne F.D., Werritty A., Davies M.C.R., Browne M.J. 2009. A recent debris flow event and implications for hazard management, *Quarterly Journal of Engineering Geology and Hydrogeology*, **42**, 51-60.

Milne, F.D., Winter, M.G., Reeves, S.J., Knappett, J.K., Dawson, S., Dawson, A., Peeling, D., Peeling J., Brown, M.J. 2016. Assessing the risks to infrastructure from coastal storms in a changing climate.

Published Project Report PPR 800. Transport Research Laboratory, Wokingham.

Papathoma-Khöle M., Keiler M., Totschnig R., Glade T. 2012 Improvement of vulnerability curves using data from extreme events: debris flow event in South Tyrol. *Natural Hazards*, **64**(3), 2083-2105.

Peduto D., Elia F., Rosario Montuori R. 2018. Probabilistic analysis of settlement-induced damage to bridges in the city of Amsterdam (The Netherlands). *Transportation Geotechnics*, **14**, 169–182.

Petley D.N. 2014. The Seti River debris flow in Nepal – what was the role of the smaller landslide downstream? (Accessed February 2014,blogs.agu.org/landslideblog/2014/02/07/seti-river/).

Petley D.N., Stark, C. 2012. Understanding the Seti River landslide in Nepal. (blogs.agu.org/landslideblog/2012/05/23/understanding-the-seti-river-landslide-in-nepal/ Accessed February 2014.)

Quan Luna B., Blahut J., van Westen C.J., Sterlacchini S., van Asch T.W.J., Akbas S.O. 2011. The application of numerical debris flow modelling for the generation of physi-cal vulnerability curves. *Natural Hazards & Earth System Sciences*, **11**, 2047-2060

Redshaw, P., Dijkstra, T., Free, M., Jordan, C., Morley, A., Fraser, S. 2017. Landslide risk assessment for the built environment in sub-saharan Africa. *Advancing Culture of Living with Landslides: Volume 5, Landslides in Different Environments* (Eds: Mikoš, M., Vilímek, V., Yin, Y., Sassa, K.), 5-12, Springer, Switzerland.

Schuster R.L., Highland L.M. 2007. The Third Hans Cloos Lecture. Urban landslides: socioeconomic impacts and overview of mitigative strategies. *Bulletin of Engineering Geology & the Environment*, **66**, 1-27.

Sparkes, B., Dunning, S., Lim, M., Winter, M.G. 2017. Characterisation of recent debris flow activity at the Rest and be Thankful, Scotland. *Advancing Culture of Living with Landslides: Volume 5, Landslides in Different*

Environments (Eds: Mikoš, M., Vilímek, V., Yin, Y., Sassa, K.), 51-58. Springer, Switzerland.

Sparkes, B., Dunning, S.A., Lim, M., Winter, M.G. 2018. Monitoring and modelling of landslides in Scotland: characterisation of slope geomorphological activity and the debris flow geohazard. *Published Project Report PPR 852*. Transport Research Laboratory, Wokingham.

VanDine D.F. 1996. Debris flow control structures for forest engineering. Ministry of Forests Research Program, *Working Paper 22/1996*. Ministry of Forests Victoria, BC.

Versace P. (Ed.) 2007. *La mitigazione del rischio da collate di fango: a Sarno e negli altri comuni colpiti dagle eventi del Maggio 1998*. Commissariato do Governa per l'Emergenze Idrogeologica in Campania, Naples. p 401. (In Italian.)

Winter, M.G. 2014a. A strategic approach to landslide risk reduction. *International Journal of Landslide and Environment* **2**(1), 14-23.

Winter, M.G. 2014b. The vulnerability shadow cast by debris flow events. *Engineering Geology for Society and Territory, Volume 6: Applied Geology for Major Engineering Works* (Eds: Lollino, G., Giordan, D., Thuro, L., Carranza-Torres, C., Wu, F., Marinos, P. Delgado, C.), 641-644. Heidelberg: Springer.

Winter, M.G. 2016a. A strategic approach to debris flow risk reduction on the road network. *Procedia Engineering*, **143**, 759-768.

Winter, M.G. 2016b. Some aspects of the interaction between landslides and forestry operations. *Published Project Report PPR 794*. Transport Research Laboratory, Wokingham.

Winter, M.G. 2018. The quantitative assessment of debris flow risk to road users on the Scottish trunk road network: A85 Glen Ogle. *Published Project Report PPR 799*. Transport Research Laboratory, Wokingham.

Winter, M.G. 2019. Debris flows. In: *Geological Hazards in the UK: their Occurrence,*

Monitoring and Mitigation (Eds: Giles, D.P., Griffiths, J.S.). Engineering Geology Special Publication 29. Geological Society, London. (In Press)

Winter, M.G., Bromhead, E.N. 2012. Landslide risk: some issues that determine societal acceptance. *Natural Hazards*, **62**(2), 169-187.

Winter, M.G., Corby, A. 2012. A83 Rest and be Thankful: ecological and related landslide mitigation options. *Published Project Report PPR 636*. Transport Research Laboratory, Wokingham.

Winter, M.G., Shearer, B. 2013. Climate change and landslide hazard and risk - a Scottish perspective. *Published Project Report PPR 650*. Transport Research Laboratory, Wokingham.

Winter, M.G., Shearer, B. 2014. Climate change and landslide hazard and risk in Scotland. *Engineering Geology for Society and Territory, Volume 1: Climate Change and Engineering Geology* (Eds: Lollino, G., Manconio, A., Clague, J., Shan, W., Chiarle, M.), 411-414. Springer, Heidelberg.

Winter, M.G., Shearer, B. 2017. An extended and updated technical evaluation of wig-wag signs at the A83 Rest and be Thankful. *Published Project Report PPR 743*. Transport Research Laboratory, Wokingham.

Winter, M.G., Macgregor, F., Shackman, L. (Eds.). 2005. *Scottish Road Network Landslides Study*, 119p. The Scottish Executive, Edinburgh.

Winter, M.G., Heald, A.P., Parsons, J.A., Macgregor F., Shackman, L. 2006. Scottish debris flow events of August 2004. *Quarterly Journal of Engineering Geology & Hydrogeology* **39**(1), 73-78.

Winter, M.G., Parsons, J.A., Nettleton, I.M., Motion, A., Shackman. L., Macgregor F. 2007. Proactive debris flow detection in Scotland. *Proceedings, First North American Landslides Conference: Landslides and Society – Integrated Science, Engineering, Management and Mitigation* (Eds: Schaefer, V.R., Schuster, R.L.,Turner, A.K.), 225-233.

Association of Environmental & Engineering Geologists Special Publication 23. OMNI Press, Wisconsin, USA.

Winter, M.G., McInnes, R.G., Bromhead, E.N. 2008. Landslide risk management in the United Kingdom. *Proceedings, 2007 International Forum on Landslide Disaster Management* (Eds: Ho, K., Li, V.), Volume I, 343-374. The Hong Kong Institution of Engineers, Hong Kong.

Winter, M.G., Macgregor, F., Shackman, L. (Eds.). 2009. *Scottish road network landslides study: implementation*, 278p. Transport Scotland, Edinburgh.

Winter, M.G., Dent, J., Macgregor, F., Dempsey, P., Motion, A., Shackman. L. 2010a. Debris flow, rainfall and climate change in Scotland. *Quarterly Journal of Engineering Geology & Hydrogeology* **43**(4), 429-446.

Winter, M.G., Dixon, N., Wasowski, J., Dijkstra, T. 2010b. Introduction to land use and climate change impacts on landslides. *Quarterly Journal of Engineering Geology & Hydrogeology* **43**(4), 367-370.

Winter, M.G., Harrison, M., Macgregor, F., Shackman, L. 2013a. Landslide hazard assessment and ranking on the Scottish road network. *Proceedings, Institution of Civil Engineers (Geotechnical Engineering)*, **166**(GE6), 522-539.

Winter, M.G., Kinnear, N., Shearer, B., Lloyd, L., Helman, S. 2013b. A technical and perceptual evaluation of wig-wag signs at the A83 Rest and be Thankful. *Published Project Report PPR 664*. Transport Research Laboratory, Wokingham.

Winter, M.G., Smith, J.T., Fotopoulou, S., Pitilakis, K., Mavrouli, O., Corominas, J., Argyroudis, S. 2014. An expert judgement approach to determining the physical vulnerability of roads to debris flow. *Bulletin of Engineering Geology and the Environment* **73**(2), 291-305.

Winter, M.G., Shearer, B., Palmer, D., Peeling, D., Harmer, C., Sharpe, J. 2016. The economic impact of landslides and floods on the road network. *Procedia Engineering*, **143**, 1425-1434

Winter, M.G., Sparkes, B., Dunning S.A., Lim, M. 2017. Landslides triggered by Storm Desmond at the A83 Rest and be Thankful, Scotland: panoramic photography as a potential monitoring tool. *Published Project Report PPR 824*. Transport Research Laboratory, Wokingham.

Winter, M.G., Shearer, B., Palmer, D., Peeling, D., Peeling, J., Harmer, C., Sharpe, J. 2018. Assessment of the economic impacts of landslides and other climate-driven events. *Published Project Report PPR 878*. Transport Research Laboratory, Wokingham.

Winter, M.G., Ognissanto, F., Martin, L.A. 2019. Rainfall thresholds for landslides: deterministic and probabilistic approaches. *Published Project Report PPR 901*. Transport Research Laboratory, Wokingham.

Wong, H.N., Ko, F.W.Y., Hui, T.H.H. 2004. Assessment of landslide risk of natural hillsides in Hong Kong. *GEO Report No. 191*, 120p. Geotechnical Engineering Office, Hong Kong.

Wong, J.F.C., Winter, M.G. 2018. The quantitative assessment of debris flow risk to road users on the Scottish trunk road network: A83 Rest and be Thankful. *Published Project Report PPR 798*. Transport Research Laboratory, Wokingham.

XVII European Conference
ECSMGE 2019
Reykjavik
on Soil Mechanics
and Geotechnical Engineering

Recent developments in seismic site response evaluation and microzonation

Développements concernant l'évaluation de la réponse sismique du site et sa microzonation

S. Foti, M. Aimar, A. Ciancimino, F. Passeri
Politecnico di Torino, Turin (Italy)

ABSTRACT: Seismic hazard and seismic actions for the design of buildings are strongly influenced by site response because of significant amplification expected for the specific stratigraphic and topographic conditions. Different approaches can be applied at the scale of the single building, but in complex morphological and geological contexts studies at the urban scale can provide relevant informations to be incorported in the evaluation. The paper builds on the recent experience of seismic microzonation studies in central Italy in the aftermaths of the 2016 seismic sequence to provide an insight on the role of studies at different scales. Within this context, an example is also provided to illustrate recent methodologies that have been conceived to account for uncertainties in the characterization that affects both geophysical tests in situ and geotechnical tests in the laboratory for the assessment of the response of soils to cyclic loadings.

RÉSUMÉ: L'aléa sismique et le chargement sismique utilisé pour le dimensionnement sont fortement influencés par les effets de site, à cause des importantes amplifications qui sont attendues pour des stratigraphies spécifiques et des conditions topographiques. Des différentes approches peuvent être employées à l'échelle d'un seul bâtiment. Cependant, dans un contexte morphologique et géologique complexe, des études à l'échelle de la ville peuvent fournir des informations importantes à prendre en compte dans l'évaluation. Ce papier est basé sur l'expérience récente de microzonage sismique dans l'Italie centrale, développé à la suite de la séquence sismique de 2016, pour montrer l'apport d'études à différente échelle. Dans ce contexte, un exemple est discuté pour présenter des méthodologies récentes qui ont été conçues pour prendre en compte les incertitudes dans la caractérisation qui concerne les essais géophysiques in-situ et les essais géotechniques en laboratoire, réalisés pour l'estimation de la réponse des sols sous chargement cyclique.

Keywords: Earthquake, seismic site response, numerical analyses, microzonation, uncertainties

1 INTRODUCTION

The evaluation of seismic risk for existing buildings and seismic action for the design requires the determination of the expected ground motion, typically termed as *seismic hazard*. The probabilistic framework (Cornell 1968) is widely adopted to account for the related uncertainties with a rational approach.

The prediction of the desired set of intensity measures of the ground motion requires a broad variety of information. The factors that control the predicted ground motions are generally grouped into the *source*, *path*, and *site effects* (Figure 1). Specifically, the site response is primarily a function of the mechanical response of the subsoil and as such it is a primary task of

geotechnical earthquake engineering. Site effects are typically quantified by the difference between the ground motion for the specific site condition and what would have occurred at for a reference condition (Figure 1). Many examples in the literature showed that the site contribution is one of the most influential elements in seismic hazard evaluation (e.g., Bazzurro and Cornell 2004). However, only the source and path effects are usually probabilistically treated adopting the Probabilistic Seismic Hazard Analysis (PSHA) method proposed by Cornell in 1968.

Site effects at a *small-scale* (i.e., for the single building) can be evaluated through the analysis of recorded ground motions and/or 1D numerical simulations. In addition, many International Regulations give the chance for a simplified assessment of the site effects at a small scale by means of a set of amplification factors based on different soil classification schemes. On the other hand, Seismic Microzonation (SM) studies propose an evaluation of the site effects from a *large-scale* different perspective. These studies usually adopt 1D and 2D (rarely, 3D) numerical

simulations to assess the response of a broader investigated area (e.g., for a municipality), compared to small-scale applications.

Evidence of damages in past earthquakes showed the fundamental role of site response with reference to the amplification of the ground motion and to instabilities due to ground shaking. In situ *reconnaissance* surveys are essential to increase the knowledge of the seismic phenomena also in terms of their induced effects. Earthquake-reconnaissance reports date back to several centuries ago. A pioneering example is the report by Sarconi (1784) regarding the earthquake that occurred in Calabria (Italy) with several illustrations documenting the observed damages and the diffuse liquefaction phenomena. Recently a post-event reconnaissance was conducted after the seismic events of Central Italy in 2016 (Stewart et al. 2018). The double sequence of August-October caused significant damages and a huge loss of human lives with 299 casualties. Actually, the strongest earthquake stroke when many villages were abandoned after the initial seismic events. In the aftermaths of the
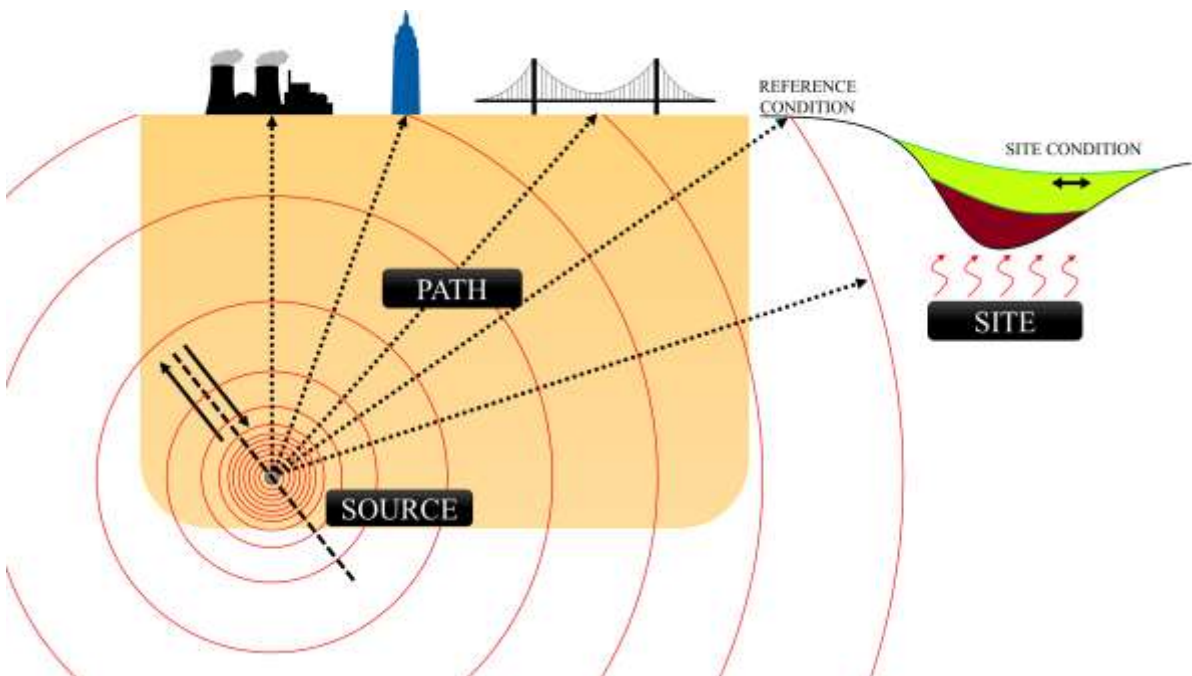
Figure 1 Source, path, and site contributions to the global seismic hazard (modified from Passeri 2019).

main events of the seismic sequences, many teams conducted on-field activities within the framework of the Geotechnical Extreme Events Reconnaissance (GEER) association (Stewart et al. 2017). Specifically, the localization of damages in the different villages showed the evidence of significant site effects (Sextos et al. 2018). Consequently, a large effort was founded by the Italian government for the seismic microzonation of the whole territory which was stroken by the seismic sequence. The whole process is documented in a special issue of the Bulletin of Earthquake Engineering (Hailemikael et al., 2019).

The paper first provides an overview of the procedures for the assessment of site effects on the basis of numerical simulations. Then, it summarizes standard procedures for seismic microzonation in Italy, incorporating examples from the recent experience in Central Italy. Finally, a case history is reported to illustrate a possible strategy to account for experimental uncertainties in site response evaluation.

2   EVALUATION OF SITE EFFECTS

The site response (i.e., site effect) is the process for which considerable modifications of the seismic waves are produced due to the variations of the material properties (i.e., stratigraphical amplification) and/or surface topography (i.e., geometrical amplification) near the Earth's surface (Aki 1993, Kramer 1996, Boore 2004) (Figure 1). Generic site response studies consider the differences in the expected motion in terms of amplitude, frequency content and duration between an established reference condition (typically, for flat and stiff outcropping formations) and the specific site condition. These studies should be performed within a probabilistic framework in order to *Identify, Quantify, and Manage* (i.e., IQM method) all the uncertainties and variabilities involved in the engineering process (Passeri 2019).

The effects of the site response are typically expressed in the frequency domain using Transfer Functions (TFs) defined as the module of the ratio of acceleration Fourier spectra calculated for two specific points of the model. Also, the site response can be described with Amplification Functions (AFs) defined as the ratio of the response spectrum at the surface of the site and the response spectrum of the input motion.

The methodologies and approaches for the evaluation of the site effects can be grouped into two classes depending on the scale of the problem. Small-scale site response studies are usually conducted for a specific single project. In this case, the site response study is dedicated to the design of a specific structure or facility that has a precise location and limited spatial extension. The second class includes large-scale microzonation studies (SM). These are implemented for a wide investigated area for urban planning and seismic risk evaluation.

Site specific studies are usually based on recorded ground motions (i.e., data-based) and/or 1D numerical simulations (i.e., simulation-based, usually termed Ground Response Analyses, GRAs). The data-based methods estimate the site response by collecting a large number of high-quality records, whereas for GRAs a great number of simulations should be performed in a probabilistic framework. Both approaches allow for a consistent prediction of the mean hazard at the site and the estimation of the uncertainties and variabilities in terms of the associated standard deviation (Stewart et al. 2014). Note that simulation-based methods represent the only possible choice when no records or insufficient records are available at the specific site (Olsen 2000, Rodriguez-Marek et al. 2014, Bommer et al. 2015, Faccioli et al. 2015). Therefore, data-based approaches are not covered in the present paper. An alternative approach is proposed in national regulations and building codes (e.g., CEN 2004). It is a simplified deterministic procedure based on a broad ground classification scheme. The categorization is based on synthetic

parameters that represent the average stiffness of the deposit. Site effects are then estimated with a set of amplification factors, depending on the site category and the level of seismicity. This approach provides an estimate of the design ground motions, which can be used for preliminary assessments or for the design of ordinary buildings.

Microzonation studies are well-recognized as a crucial component for the implementation of urban planning management and seismic mitigation strategies in a given area (e.g., Iglesias, 1988; Fah, 1997; Finn et al., 2004; Pitilakis et al., 2006; Ansal et al., 2010; Crespellani, 2014; Pagliaroli et al., 2019). Seismic Microzonation (SM) studies provide maps of the spatial distribution of site response at urban scale with respect to the lithostratigraphic (i.e., mechanical) and morphological (i.e., geometrical) characteristics (e.g., Vinale et al., 2008; Ansal et al., 2009; Pagliaroli, 2018). The studies require expertise of multiple disciplines, namely geotechnical and structural engineering, seismology, geophysics and geology (Pagliaroli, 2018). A crucial element of a SM study is a reliable subsoil model with an overview of the main elements that control the site response. Site response studies for SM purposes are usually based on numerical simulations. 2D and 3D numerical analyses are hereafter termed Site Response Analyses, SRAs. Multidimensional effects can deeply affect the site response in the presence of irregular stratigraphic geometry and/or surface topography (Jibson, 1987). In these circumstances, 2D numerical analyses have been widely adopted in the past (e.g., Fah et al., 1997; Lanzo et al., 2011; Pagliaroli et al., 2019). More recently, some studies have been focused on 3D numerical simulations (e.g., Fah et al., 2006; Lee et al., 2009; Pitilakis et al., 2011; Smerzini et al., 2011; Falcone et al., 2018). Nevertheless, the complexity of the simulations and the high computational demand are still preventing the diffuse application of 3D approaches. The present paper will focus

therefore only on 1D GRAs and 2D SRAs for SM studies.

2.1 Single site applications

Site response studies are usually conducted for specific engineering projects with a limited and precise spatial extension. The inclusion of uncertainties in these types of studies is fundamental for an accurate and consistent hazard study within a probabilistic framework for relevant projects.

2.1.1 Ground Response Analyses

The results of a GRA are affected by uncertainties and variabilities due to the assumption of horizontally stratified medium and to selected *model parameters*, particularly in case of strong nonlinear responses.

The applicability of the 1D assumption of GRAs has been addressed by Faccioli et al. (2002). The authors studied the complex site effects in predicting ground motions, including the topography. They found that, even for complex 2D-3D geological environments, the predominant resonance frequencies are controlled by the 1D simple formulations. However, 1D wave propagation models cannot account for the magnitude of the amplification, and the width of the relevant frequency band observed in weak motion records. For these purposes, an SRA could be required. Baise et al. (2011) and Thompson et al. (2012) stated that an initial assessment of the applicability of GRAs should always be performed by a taxonomic procedure. They classified the investigated sites as "simple" or "complex", depending on the accuracy obtained by 1D GRAs. The analyst can select the most suitable type of analysis (GRA or 2D/3D SRA) depending on the site complexity (Thompson et al. 2012, Afshari and Stewart 2015), always accounting for the nonlinear response of the site (Zalachoris and Rathje 2015, Kim et al. 2016). In fact, preliminary results from GRAs found a general underprediction of the motion, for low periods (i.e., lower than the

model period), possibly due to the difficulty in catching different phenomena (Kwok et al. 2008, Stewart and Kwok 2008, Li and Asimaki 2010). In some particular circumstances, 1D models also show a "base-isolation effect" due to high shear strains (i.e., small stiffness) in a specific layer. This phenomenon is prevented in case of 2D and 3D processes, thanks to the lateral heterogeneity that allows a more realistic spatial spreading of stresses (Makra and Chávez-García 2016).

Besides the model dimension, several studies have addressed the actual capabilities of GRAs in predicting the mean site response (Stewart and Baturay 2001, Baturay and Stewart 2003, Asimaki et al. 2008, Kwok et al. 2008, Stewart 2008, Li and Asimaki 2010, Asimaki and Li 2012, Kaklamanos et al. 2013a, Kaklamanos et al. 2013b, Afshari and Stewart 2015, Kaklamanos et al. 2015, Shi and Asimaki 2017). These results also proved that the user should possess specific expertise and particular knowledge of the global procedures and the physics of the phenomenon. This is particularly true in case of the strong nonlinear responses (Park and Hashash 2005, Hashash et al. 2010, Stewart et al. 2014, Kim et al. 2016, Régnier et al. 2016, Régnier et al. 2018).

Notwithstanding these limitations, GRAs are still the primary choice for the non-ergodic assessment of the site response (Stewart et al. 2014).

It is also recognized that GRAs are a useful tool to investigate the role of *uncertainties* and *variabilities* in site response studies (Field and Jacob 1993). Generally, uncertainties and variabilities are overestimated for low periods and underestimated for long periods (Rodriguez-Marek et al. 2014, Afshari and Stewart 2015, Pehlivan et al. 2016), compared to the results obtained with the data-based approach. However, other examples showed consistency with the variability obtained from recorded data (Papaspiliou et al. 2012a, Papaspiliou et al. 2012b, Kaklamanos et al. 2013b).

The probabilistic philosophy and the IQM method applied to GRAs should account for six main sources of uncertainties on the results, listed thereafter in order of relevance (Foti et al., 2019):

- Shear wave velocity (V_S) profile;
- Modulus reduction and damping (MRD) curves, describing the variations of the normalized shear modulus G/G_0 and the damping D with the cyclic shear strain γ_c;
- Input motions selection;
- Type of non-linear approach;
- Shear strength;
- Small strain damping (D_{min}).

The last two are important in specific conditions and are often not accounted as primary sources of uncertainties (e.g. Idriss 2004, Rathje and Kottke 2011). Specifically, the shear strength may be significant when large strains are expected (e.g. for thick and soft soil deposits).

2.1.2 Simplified methods

The simplified approaches for the assessment of the site effects synthetize the site response through a set of amplification factors that modify the ground motion characteristics evaluated for a reference condition. The amplification factors mainly depend on the local geology of the site accounted via the definition of a number of subsoil categories. Each category clusters different subsoil conditions sharing similar expected amplification. The classification scheme is a function of synthetic parameters representing the features of the soil deposit most affecting the site response (e.g., average stiffness, depth, fundamental frequency).

The main inspiration of the simplified approach is the pioneering study by Seed et al. (1976), which demonstrated the influence of soil conditions on the shape of the surface response spectra. Its results were incorporated into the ATC report (ATC 1978), which firstly introduced prescriptions for the estimate of the site effects. Precisely, it defined specific spectral shapes and amplification coefficients as function of the surface geology. Then, Borcherdt (1994) proposed a quantitative criterion for the classification of sites sharing common response,

based on the $V_{S,30}$ parameter (i.e., the harmonic average of the shear wave velocity in the upper 30 m of the soil profile). This scheme considers a key quantity governing wave propagation and soil response (i.e., the V_S profile), whose characterization is possible without relevant effort, since the investigation is limited to a shallow portion of the soil deposit. Dobry et al. (2000) proposed a $V_{S,30}$-based site categorization system for the National Earthquake Hazard Reduction Program (NEHRP) provisions. A similar scheme was thereafter adopted in several building codes (e.g., CEN 2004, ICC 2015, ASCE 2010), which propose this approach for ordinary and for preliminary assessment studies, in absence of more advanced analyses.

The simplified approach introduced by most current building codes clusters different subsoil conditions into a limited number of site categories, identified by a range of $V_{S,30}$ values. For each site category, the approach prescribes a stratigraphic amplification factor, which is dependent on the characteristics of the specific ground motion (magnitude or peak ground acceleration), in order to account for the soil nonlinear behavior. The prescriptions also provide an estimate of the alterations of the ground motion due to topography by means of a topographic amplification factor.

Despite its ease-of-use, the simplified approach for the estimate of the design ground motions incorporates some drawbacks, due to the small number of parameters for the description of the subsurface geology and the synthesis of a complex phenomenon into a set of amplification factors. Due to these limitations, the field of application is restricted only to stable sites (i.e., not affected by problems of landslides, liquefaction or seismically-induced settlements) where the geology does not include lateral inhomogeneities and strong variations of the mechanical properties with depth (e.g. CEN 2004).

Moreover, several studies (e.g. Castellaro et al. 2008) questioned about the reliability of synthetizing the deposit characteristics into a single parameter, i.e. $V_{S,30}$. This scheme, indeed, cannot model the effect of other relevant elements for the seismic response, for instance the impedance contrast, the thickness of the soil deposit and mechanical parameters governing the nonlinear behavior as the plasticity index (Pitilakis 2004, Pitilakis et al. 2013, Pitilakis et al. 2018, Rodriguez-Marek et al. 2001, Ciancimino et al. 2018, Foti et al. 2018). Another topic of debate is the consistency of the $V_{S,30}$ itself as proxy for stratigraphic amplification, which might be misleading in some conditions (e.g., in presence of shallow velocity inversions, as pointed out by Di Giacomo et al. 2005). Therefore, new site classification schemes proposed to integrate or substitute the $V_{S,30}$ with parameters as the bedrock depth or the fundamental frequency of the soil deposit (e.g., Bouckovalas et al. 2006, Cadet et al. 2012, Pitilakis et al. 2013, Pitilakis et al. 2018).

Finally, the definition of a limited number of site categories can be misleading (Pitilakis 2004) and entails a large degree of variability of the predicted response (Ciancimino et al. 2018). Indeed, each category clusters various soil conditions exhibiting different levels of amplification. The large variability might impact the reliability of the simplified approach, since there may be a number of soil conditions for which the simplified approach does not provide an estimate on the safe side (Foti et al. 2018, Aimar et al. 2019).

For these reasons, the simplified approach is under constant study for its development and improvement, in order to implement a methodology for the assessment of the site response able to provide simultaneously simplicity of application and reliability and robustness of the estimate.

2.2 Urban scale applications

The reduction of the seismic vulnerability of urban areas cannot disregard the evaluation of the amplification phenomena that affect the expected seismic hazard. SM is therefore an essential tool

to implement effective prevention strategies and to manage emergency situations in the aftermath of extraordinary events (Aversa and Crespellani 2016). The main purpose of large-scale applications is identifying zones characterized by homogeneous seismic behaviour in terms of site response and ground instabilities (ISSMGE 1999; Working Group ICMS 2008). The different scale of SM studies and single site studies causes considerable differences for both the intended outcomes and the applied methodologies (Foti et al. 2018). Within this framework, it is clear that SM studies and site-specific analyses are not interchangeable, but rather complementary activities.

In the following, the peculiarities of SM studies are analysed. The attention will be focused on the ground motion estimation, therefore ground instabilities are not treated in the present paper. The two proposed examples have been developed within the framework of the SM studies carried out for the reconstruction of the municipalities struck by the 2016 Central Italy seismic events (Hailemikael et al., 2019).

2.2.1 Guidelines for Seismic Microzonation studies

In the past years, the need to define a common methodology and to standardize SM studies has led to the development of several national and international practical guidelines (a detailed review can be found in Pagliaroli 2018). Among these, a milestone is constituted by the Manual for Zonation on Seismic Geotechnical Hazards developed by the Technical Committee on Earthquake Geotechnical Engineering of the International Society on Soil Mechanics and Geotechnical Engineering (ISSMGE 1999). The manual firstly introduced the concept of three different levels of SM, defined according to the available information and, as a consequence, to the purposes of the studies. The three levels, subsequently incorporated in the Italian Guidelines (Working Group ICMS 2008), are characterized by increasing complexity:

- Level 1: the investigated area is qualitatively subdivided into seismically homogeneous microzones on the basis of the existing data. Within this level, no analyses are carried out to quantitatively estimate site effects.
- Level 2: on the basis of the previous level, preliminary assessments of the site effects are obtained adopting simplified methods (i.e., tables and empirical laws). When necessary, insights for the uncertainties identified in Level 1 are addressed integrating the existing data.
- Level 3: a detailed SM map is developed from the results of specific numerical analyses carried out on areas characterized by high seismic hazard and/or economic and social relevance. The analyses are based on a detailed subsoil model defined by means of available data and additional surveys.

The SM map usually reports synthetic indicators of the site response associated with each seismically homogeneous microzones. For example, the computation can be based on the average amplification over a specific range of spectral periods in the acceleration response spectra (Working Group ICMS 2008), denoted as $\overline{AF}_{T_a-T_b}$ and computed according to the following formulation:

$$\overline{AF}_{T_a-T_b} = \frac{O_{T_a-T_b}}{I_{T_a-T_b}} \tag{1}$$

where T_a and T_b define the interval of spectral periods and $I_{T_a-T_b}$ and $O_{T_a-T_b}$ are, respectively, the mean values, within the spectral periods range, of the pseudo-spectral acceleration for the selected input motion SA_i and for a specific point at the surface of the site SA_o, namely:

$$I_{T_a-T_b} = \frac{1}{T_a-T_b} \cdot \int_{T_b}^{T_a} SA_i(T)dT \tag{2}$$

$$O_{T_a-T_b} = \frac{1}{T_a-T_b} \cdot \int_{T_b}^{T_a} SA_o(T)dT \tag{3}$$

The values of $\overline{AF}_{T_a-T_b}$, computed for a set of input motions, are subsequently logarithmically averaged to get stable estimates.

As for the Italian context, numerous efforts have been made in defining a widely accepted, practical methodology. The history of SM studies in Italy can be divided into three different generations, according to the available knowledge at that time and to the objectives of the studies (Crespellani 2014). The first generation is characterized by studies carried out mainly by researchers for scientific purposes, reference is made to the studies conducted in Tarcento (Brambati et al. 1980) and Ancona (VV. AA. 1981), consequently to the Friuli (1976) and Ancona (1972) earthquakes. Within this period, the first example of quick studies of practical value is given by the SM of 39 urban centres in the aftermath of the Irpinia (1980) earthquake. The project, carried out under the control of the National Geodinamica Project of the National Research Council (CNR 1983), has been intended to be a reference point for the reconstruction of the centres in the aftermath of the seismic event. The growing attention given by researchers and authorities to the SM studies has led, in 1986, to the development of the first example of Italian guidelines (Faccioli 1986).

After the Umbria-Marche seismic sequence (1997), the SM studies of about 80 villages have been undertaken with the prospect of proper planning for the reconstruction. It was clear, from that point forward, the need to introduce site effects into regional codes. As a consequence, a new generation of SM studies (i.e., the second generation) has been developed on a regional scale even with the support of the Italian regions (Crespellani 2014), e.g., the studies promoted by the Emilia Romagna region (Marcellini et al. 1998), the VEL (Evaluation of Local Effects) project promoted by the Toscana region (Ferrini, 1999), and the SM of Fabriano (Marcellini and Tiberi 2000) and Senigallia (Mucciarelli and Tiberi 2007). The importance of the construction of a reliable geological and geotechnical model for the numerical simulations of site response was recognized in this second generation, emphasizing the role of geotechnical laboratory tests and geophysical surveys to define the dynamic properties of the soil (Crespellani 2014). Within this framework, it is worth to mention the case study of L'Aquila (Working Group MS-AQ 2008) for his contribution in addressing both scientific and practical problems.

In 2008, the Italian Civil Protection coordinated a team of researchers and technical representatives of the Italian Regional Government Authorities in order to provide practical guidelines and to establish standard procedures for SM. The final products of the project are the National Guidelines of SM studies (Working Group ICMS 2008), approved by the National Department of Civil Protection and Conference of Regions and Autonomous Provinces.

The third, and last, generation of SM studies is characterized by different perspectives. The main goal of the studies is not of scientific nature: SM studies are not considered merely as post-earthquakes tools for the reconstruction, but they are also recognized to be effective ordinary strategies for the planning of seismic risk mitigation activities (Crespellani 2014). The studies should be carried out by practitioners as quickly as possible, accordingly with administrative needs and consistently to the Italian Guidelines (Working Group ICMS 2008). To provide scientific support to the authorities involved in the SM projects, the CentroMS has been founded in 2015, joining together research institutions and university departments.

2.2.2 GRAs for SM studies

GRAs are generally adopted also for microzonation studies where the one-dimensional hypothesis may be regarded as a reasonable assumption. Nonetheless, the significant spatial variability that characterizes each seismically homogeneus microzone implies the necessity to define an average site response,

without considering the local specific features at the single-project scale. The following example, coming from the SM study of Tino, is presented to better explain the differences between GRAs for small- and large-scale applications (Foti et al. 2018).

Tino is a fraction of the village of Accumoli (Rieti) almost destroyed by the seismic events of Central Italy in 2016 (Stewart et al. 2018). The area has been characterized by means of geological and geotechnical surveys, aiming at defining a reliable subsoil model for site response analyses. Specifically, a Down Hole (DH) test carried out at the Tino site has provided the information regarding the V_S and V_P (i.e., the compression wave velocity) profile. Figure 2.a reports the results of the test, along with the subsoil stratigraphy. The site is characterized by a shallow 5 m thick layer of debris ($V_S{\approx}430$m/s), a yellow sandstone middle layer from slightly weathered ($V_S{\approx}740$m/s, about 9 m thick) to hard

($V_S{\approx}1135$m/s, about 4 m) on an underlying 2-3 m thick layer of grey sandstones ($V_S{\approx}660$m/s) and the seismic bedrock constituted by hard yellow sandstones ($V_S{\approx}930$m/s).

The geological stratigraphy of the whole area is relatively homogenous. Moreover, neither an irregular stratigraphic geometry nor a particular surface topography are present. As a consequence, the area has been identified with a single seismically homogeneus microzone and the site response has been studied by means of GRAs. In order to reflect the large-scale application of the study, a simplified geological model has been developed for the seismically homogeneus microzone (Figure 2.b). The first layer (5-20 m thick) is constituted by debris, the underlying layer is constituted by the weathered sandstones (0-50 m thick) and the deepest part, constituted by hard havana sandstones, is the seismic bedrock of the model. Therefore, the hard sandstones between 14 and 18 m and the
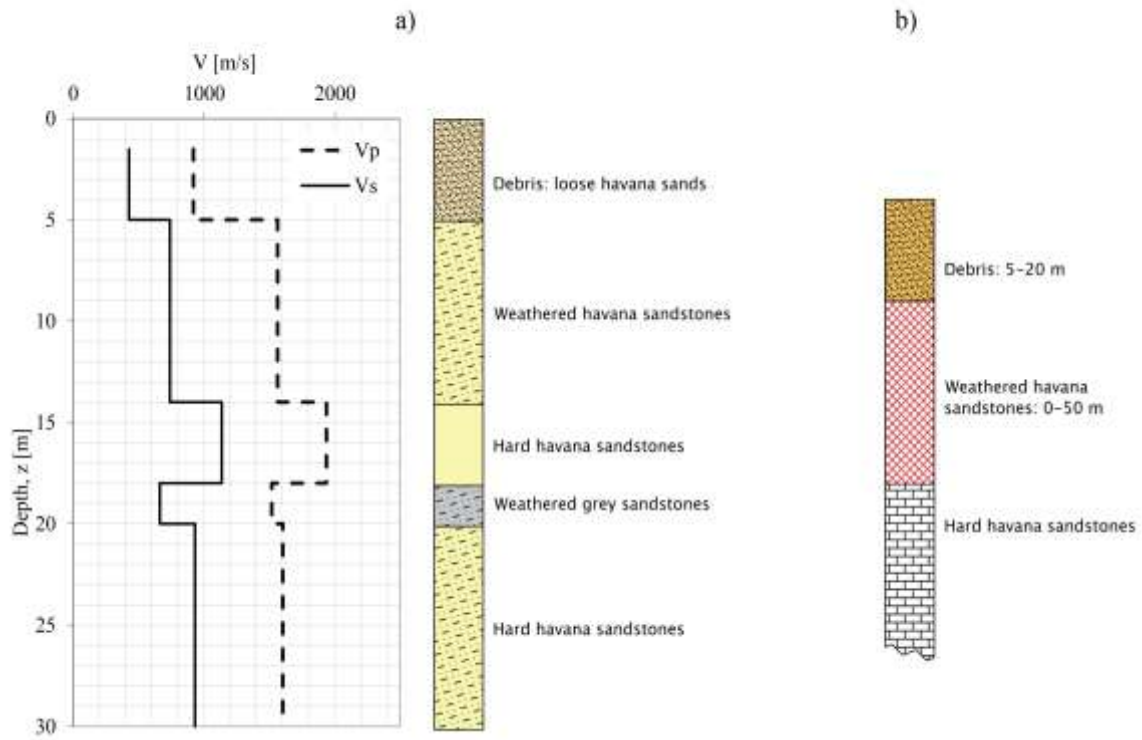
Figure 2 a) V_S and V_P profiles obtained from the DH test along with the subsoil stratigraphy; b) simplified subsoil profile adopted for the GRAs of the SHM (modified from Foti et al. 2018).

underlying grey sandstones have been neglected in the simplified model. Table 1 presents the adopted dynamic properties for each lythotype, i.e. the interval velocity V_S, the unit weight γ and the MRD curves. The V_S profile has been defined on the basis of the DH test, while the MRD curves correspond to literature models derived on similar soils.

The spatial variability of the subsoil geometry within the wide area studied has been considered performing four GRAs, characterized by different thicknesses of the first layer which mainly affect the site response: 5, 10, 15, and 20 m, respectively. For the second layer, a constant thickness of 10 m has been adopted.

Table 1. Dynamic properties of the Tino simplified subsoil model.

Lithotype	V_S (m/s)	γ (kN/m³)	MRD curves
Debris	430	16	Seed and Idriss (1986)
Weathered sandstons	740	21	Rollins et al. (1998) (Upper Limit)
Bedrock	930	22	Linear Elastic D=0.5%

It must be pointed out that the methodology here adopted to take into account the spatial variability is not rigorous; it is just a convenient simplification to explain the differences between GRAs for small- and large-scale studies. The probabilistic assessment of site effects is beyond the scope of this example and will be specifically treated in Section 3.

The input motions consists of seven unscaled horizontal natural records, selected by the ITACA archive (itaca.mi.ingv.it/, Luzi et al. 2017) to be on average compatible, as suggested by the Italian Building Code (MIT 2018), with the Uniform Hazard Spectrum (return period of 475 years) at reference conditions. More details about the selection process are reported in Luzi et al. (2019).

The results of the GRAs are reported in Figure 3.a in terms of average $\overline{AF}s$ for the three spectral periods fields suggested by the Italian Guidelines (Working Group ICMS 2008), i.e., 0.1-0.5 s, 0.4-0.8 s and 0.7-1.1 s. Figure 3.b reports the average input and output SAs.

It is clear that the first layer dominates the site response: the higher is the thickness of the layer, the lower is the resonance frequency and, as a consequence, the higher are the $\overline{AF}s$ in the considered ranges of periods. In absence of specific information about the distribution of the soil stratigraphy in the considered area, the model characterized by the higher $\overline{AF}s$ (i.e., thickness
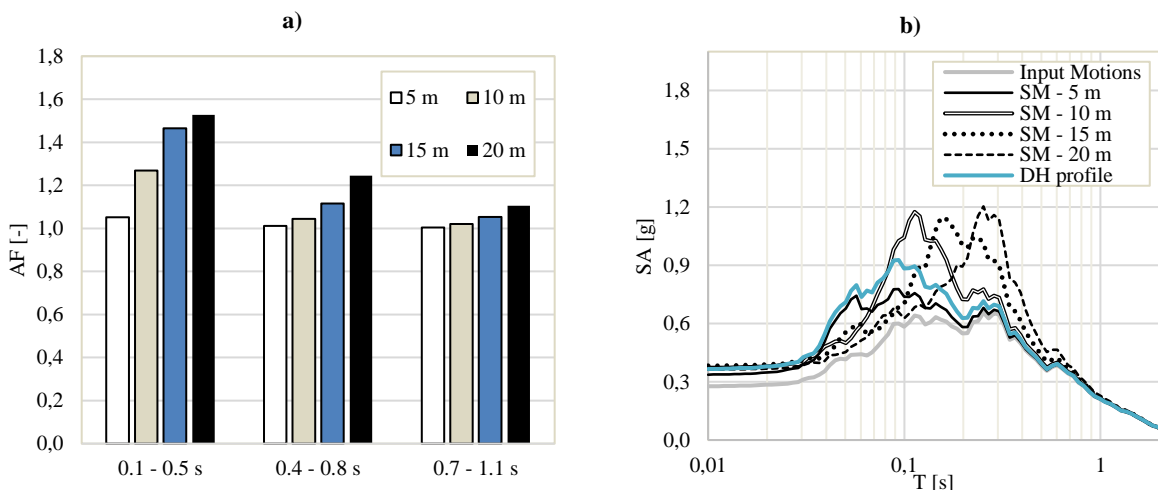
Figure 3. Results of GRAs for the Tino site in terms of a) $\overline{AF}_{T_a - T_b}$ and b) SA (modified from Foti et al. 2018).

equal to 20 m) has been considered as representative of the whole seismically homogeneus microzone.

Figure 3.b also reports the average SA obtained from GRAs performed on the specific V_S profile coming from the DH test (Figure 2.a). The latter would be used to define the site response for a hypothetical project to be realized in the specific investigation site. The site responses are quite different, especially for periods ranging from 0.1 to 0.5 s (typical vibration periods of ordinary buildings in that area). In the case of a site-specific project characterized by a specific natural vibration period of 0.1 s, the SA coming from the SM study would be not on the safe side. Conversely, for large-scale applications involving projects characterized by different vibration periods, the adoption of a simplified model (but able to capture the average site response) prevents that differences related to the specificity of a single-

site influence the $\overline{AFs}$ of the whole seismically homogeneus microzone.

2.2.3 SRAs

The main strengths of SM studies are the opportunity of relying on experts of multiple disciplines and the possibility to build a reliable subsoil model wide enough to capture the multidimensional phenomena. Consequently, SRAs can be carried out for large-scale applications. Conversely, GRAs are sometimes carried out for site-specific analyses also in presence of 2D/3D effects, given the lack of appropriate information to define the subsoil model. Multidimensional effects are subsequently taken into account by means of simplified approaches incorporated in most seismic code provisions (e.g., CEN 2004, MIT 2018). However, these approaches are not always able to capture the site response for complex
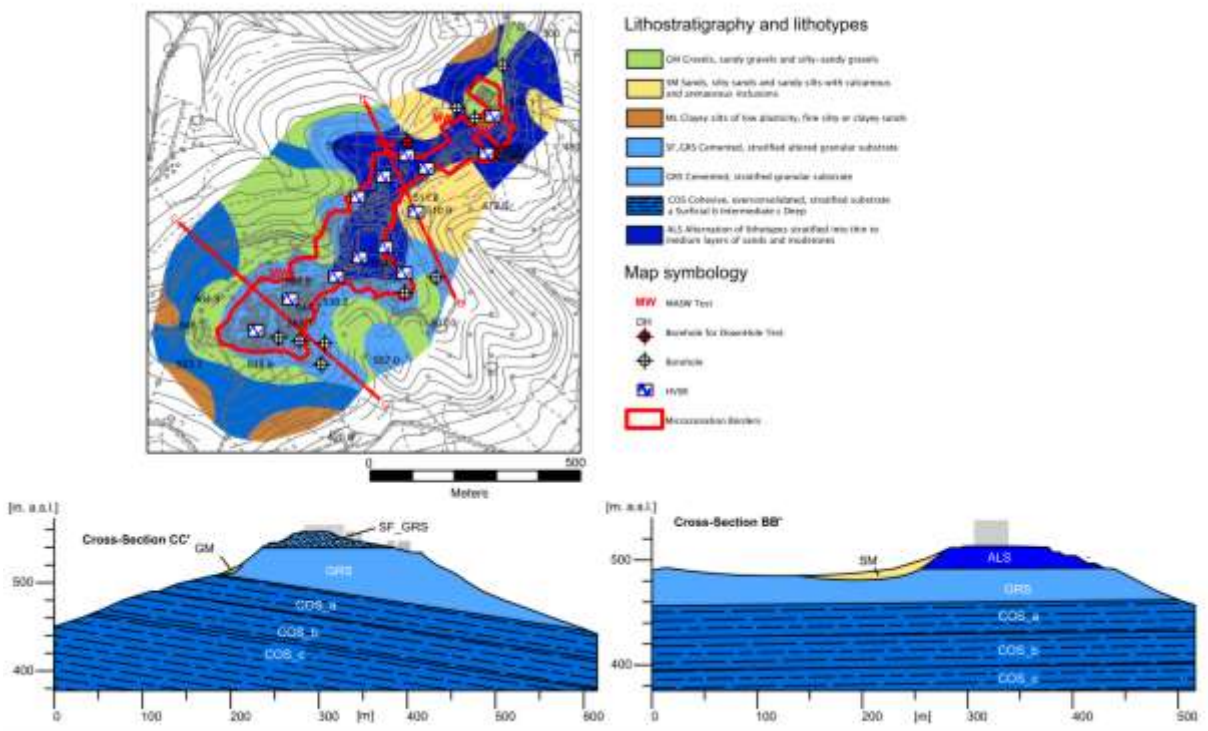
Figure 4. Lithotechnical map and cross-sections of the Montedinove historical centre (from Pagliaroli et al. 2019).

surface topography and morphological conditions.

A case in point is represented by the SM study carried out at the Montedinove site, in the province of Ascoli Piceno, Marche region (further details about the case study can be found in Angelici 2018, Foti et al. 2018 and Pagliaroli et al. 2019). The area is divided into three different zones: the localities of Lapedosa and Croce Rossa and the historical center. The historical center presents a quite interesting stratigraphic condition: it lies mainly on a cemented granular from weathered (SF_GRS) to unweathered (GRS) bedrock, and on an alternation of stratified lithotypes (ALS). The topography of the site is characterized by a NE-SW hilly ridge. The deepest portion is constituted by the Blue Clays Formation with a pelitic lithofacies (hereafter identified as cohesive, overconsolidated stratified bedrock, COS). On the sides of the ridge, there are 3-15 m thick coverings, classifiable as gravels and sandy gravels (GM) and sands and silty sands (SM). Figure 4 reports the lithotechnical map of the Montedinove historical centre and the cross-sections adopted for the SRAs.

The subsoil model has been defined by means of the existing data collected in the level 1 of the SM study and of the additional investigations carried out within the level 3 of the project, i.e. one 35 m deep DH test, five MASW (Multichannel Analysis of Surface Waves) tests, and 24 HVSR (Horizontal to Vertical Spectral Ratio) tests. Figure 5.b reports the results of the DH test in terms of V_S and V_P profiles. The V_S of the lithotypes not inferred by the DH test have been defined by means of non-invasive tests. In particular, the V_S of the COS lithotype has been defined on the basis of the MASW tests carried out in the near Lapedosa locality, where the COS is outcropping. The lithothype has been then subdivided into three different units, with an increasing V_S, i.e. the upper (COS_a, V_S=560 m/s), the intermediate (COS_b, V_S=650 m/s) and the lower (COS_c, V_S=800 m/s). The profile is characterized by a marked V_S inversion between the GRS and the underlying COS_a.

The MRD curves of the COS have been defined on the basis of the Resonant Column test carried out on a sample retrieved for the same soil from the municipality of Monte Rinaldo (Ciancimino et al. 2019). For the other materials,
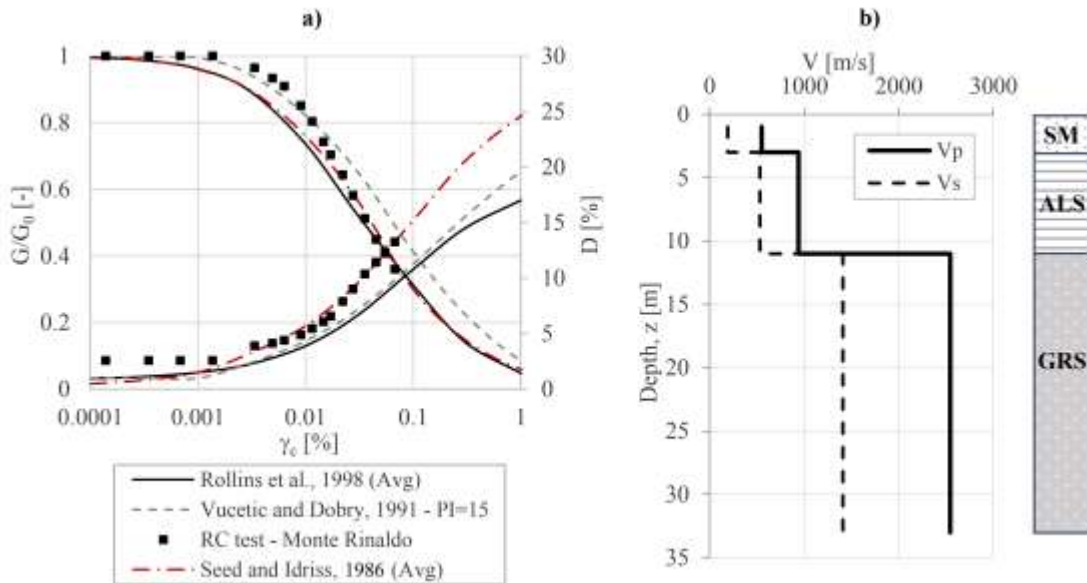
Figure 5. Montedinove subsoil model: a) MRD curves; b) V_P and V_S profiles from the DH test (modified from Pagliaroli et al., 2019).

literature data obtained on similar soils have been adopted. The MRD curves are reported in Figure 5.a and the dynamic properties adopted for the subsoil model are summarized in Table 2.

Table 2. Dynamic properties of the Montedinove sub-soil model.

Lithotype	V_s (m/s)	γ (kN/m³)	MRD curves
SF_GRS	550	19.0	Rollins et al. (1998)
GRS	1400	22.0	Linear Elastic D=0.5%
GM	340	18.6	Rollins et al. (1998)
SM	190	17.6	Seed et al. (1986)
ALS	530	19.6	Vucetic and Dobry (1991) - PI=15
COS_a	560	19.6	Resonant Column test
COS_b	650	19.6	
COS_c	800	19.6	Linear Elastic D=0,5%

SRAs have been performed for the two cross-sections (i.e., BB' and CC') represented in Figure 4. The $\overline{AFs}$ for the three ranges of period here considered are represented in Figure 6.a. Maximum amplifications are observed at the ridge crest, where topographic site effects are expected. A peak is also present on the left edge of the ridge for section BB', where a large impedance contrast between the SM and the underlying GRS is present.

Figure 6.b reports the average output SA obtained from SRAs and from GRAs carried out on 1D models developed on the basis of the stratigraphy at the ridge crest (red dots in the cross-sections). For a direct comparison between GRAs and SRAs, a constant factor has been applied to the SA obtained from GRAs, in order to take into account the topographic effects with the simplified method proposed by Italian Regulations (NTC18). Specifically, both the cross-sections have been classified within the topographic class T4 (i.e., ridge characterized by a slope angle higher than 30°) and, then, a factor of 1.4 has been applied.

The comparison highlights the role of the topographic effects, since the SAs obtained by SRAs are, for this case study, significantly higher than the ones computed through GRAs. In particular, for the cross-section CC', a maximum aggravation factor (defined as the ratio between 2D and 1D analyses) of 3 is observed, in contrast with the lower value predicted by the simplified method. In this situation, the site response is mainly dominated by complex 2D effects that can be captured just performing advanced SRAs. Within the context of large-scale applications, this is possible thanks to the wide subsoil model defined for the whole area of interest.

3 CASE STUDY

The goal of the present case study is to provide some insights about the effects of the uncertainties on the site response and their role in the probabilistic prediction of the design ground motions. The need for a consistent stochastic approach derives from the impossibility of selecting a-priori conservative values of model parameters in dynamic analyses taking into account the role of soil-nonlinearity. For example, an underestimation of soil stiffness would cause large strains and therefore an overestimation of material damping, which could overdamp the actual response of the soil deposit. On the other side, an overestimation of soil stiffness would provide small impedance constrasts and therefore a possible underestimation of stratigraphic amplification.

The example focuses only on the two components of the soil model that mainly affect the uncertainties in the results: the V_S profile and the MRD curves. Field and Jacob (1993) demonstrated that these parameters dramatically influence the ground response. The uncertainties in the input motions are implicitly accounted for by using multiple records for the analyses. The uncertainties due to other parameters (e.g., the nonlinear approach) will not be considered in this example.

a)

b)
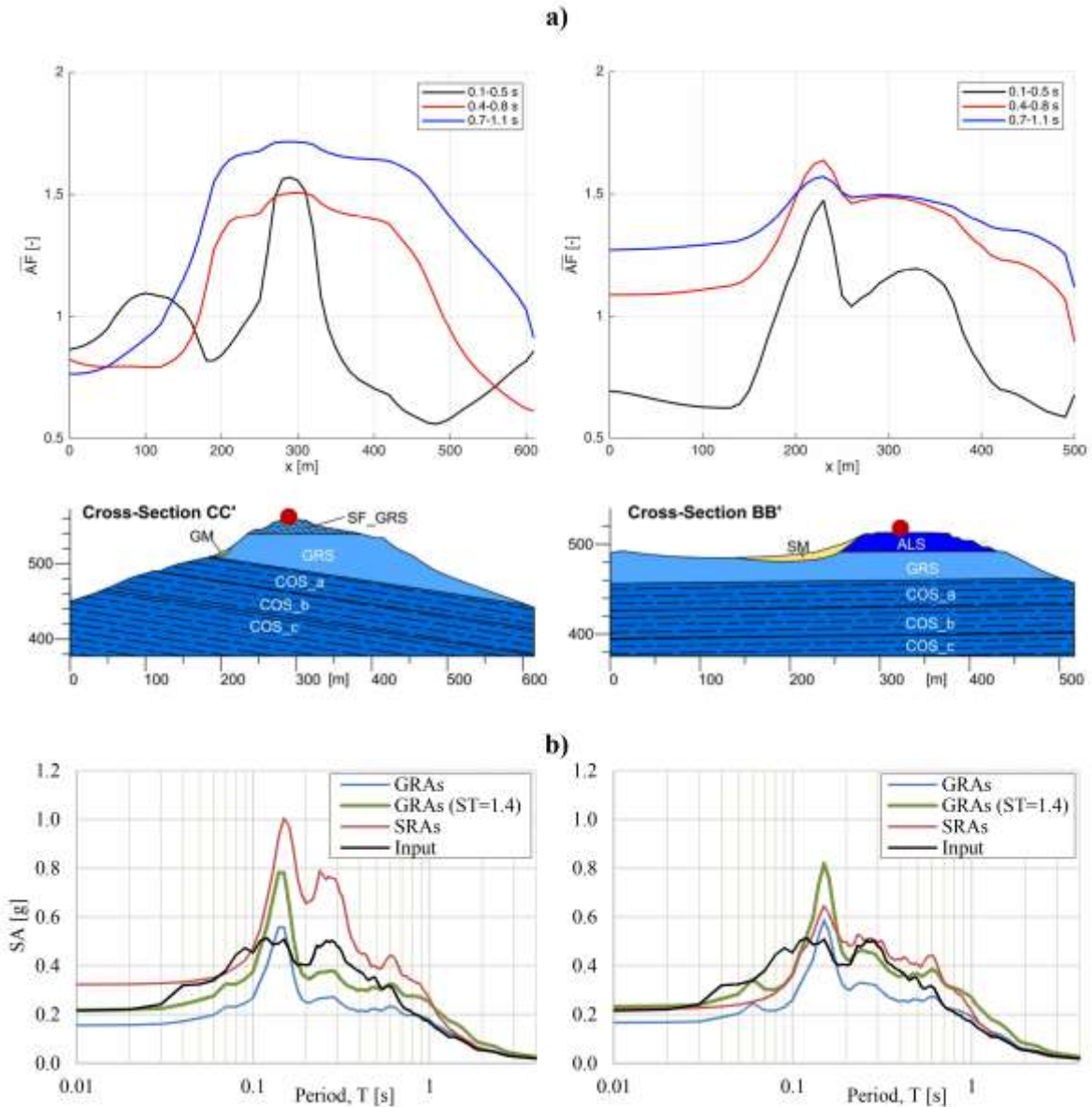
Figure 6 Results for the Montedinove site in terms of a) $\overline{AF}$s and b) SAs from GRAs, SRAs and GRAs with an aggravation topographic factor (as defined by NTC18) of 1.4 (modified from Pagliaroli et al., 2019).

A Monte-Carlo simulation has been conducted to develop a statistical sample of ground models, whose parameters are generated from the results of the geophysical and geotechnical investigations. The nonlinear modeling of the seismic response refers to EQuivalent Linear (EQL) GRAs (Idriss and Seed 1968), which assume linear viscoelastic materials, with time-invariant shear stiffness and damping ratio. The procedure accounts for the nonlinear behavior of the soil by computing strain-compatible quantities derived from the MRD curves at an

effective strain level usually equal to 65% the maximum value. The computation has been performed with the DEEPSOIL v7.0 software (Hashash and Park 2001, Hashash et al. 2017).

3.1 Site description

The village of Marsia falls in the municipality of Roccafluvione (AP), in the Marche region, which has been struck by the seismic sequence started on the 24th August 2016. The site, together with other 140 municipalities, was object of intense geological and geotechnical investigations, resulting into a detailed ground model.

A DH and a MASW tests were conducted at the locations shown in Figure 7 for the definition of the interval velocity (V_S) and the harmonic average ($V_{S,z}$) profile shown in Figure 8.a-b.

The two geophysical surveys provided similar results, but some differences can be observed in terms of depth of the halfspace and thickness of

the shallower layer. A reason of such discrepancies may lie in the different investigated volumes by the two surveys: the DH test focuses on a single vertical, whereas the MASW test detects the wave propagation along the array and its result averages potential lateral heterogeneities of the soil deposit (Passeri 2019). Also, the location of the two surveys is not the same and differences can be due to the 2D local geology of the slight slope. For these reasons, the
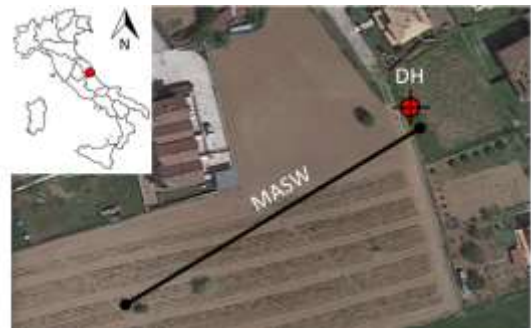
Figure 8. Location of the geophysical surveys.
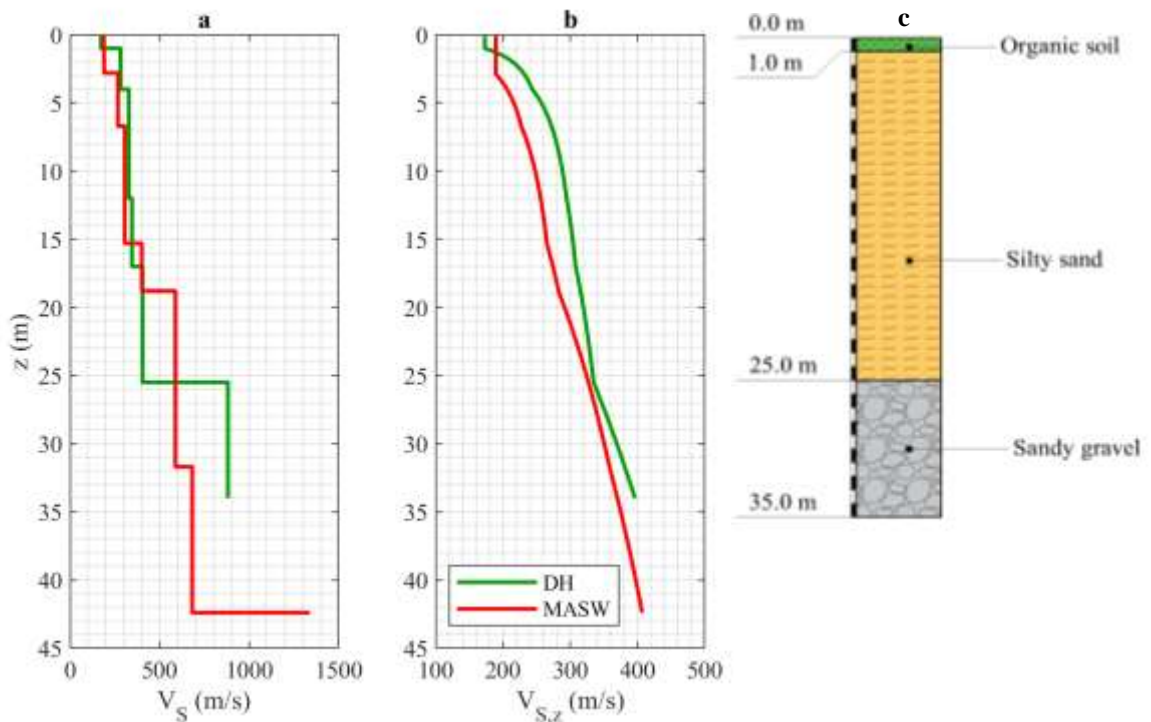
Figure 7 a) V_S profiles obtained from the MASW and the DH survey; b) $V_{S,z}$ profiles obtained from the MASW and the DH survey; c) Simplified stratigraphic profile at the DH borehole.

study followed two parallel analyses based on the two V_S profiles in Figure 8. Then, the results are compared in order to obtain a measure of the effect likely due to spatial variability on the site response.

The stratigraphy obtained from the borehole indicates the presence of a thin layer of organic soil over a 25 m-thick stratification of silty sands, lying over a formation of sands and gravels, which develops down to the bottom of the investigated depth. Figure 8.c shows the simplified stratigraphic model. The deepest layer was identified as the seismic bedrock since it is located in correspondence of a large impedance contrast, where the V_S becomes higher than 800 m/s. Some relevant properties for the GRAs (i.e., the plasticity index PI, the unit weight γ, the over-consolidation ratio OCR and the at-rest lateral pressure coefficient K_0) were derived through literature relationships (Hunter 2003, Massarsh 1979) and Table 3 lists their values.

With regard to the MRD curves, the study adopted the model proposed by Ciancimino et al. (2019), which is a specialized version of the Darendeli (2001) model, adapted to capture the specific behavior of silty and clayey soils from the Central Italy area.

Table 3. Geotechnical parameters of the Roccafluvi-one subsoil model.

Lithotype	Organic soil	Silty sand
PI (%)	40	15
γ (kN/m³)	12	15
OCR (-)	1	1
K_0 (-)	0.64	0.493

The model was calibrated on a database of 72 cyclic tests carried out on low and normal active clays and silts of low plasticity with PI ranging from 0 to 45%. The tests were carried out under effective confining pressures, σ_m', ranging from 30 to 440 kPa. The model also provides information about the statistical dispersion of the results, which can be used as indicator of the uncertainty affecting the MRD curves. Specifically, two relationships were obtained on the basis of the model residuals to estimate the standard deviation as a function of the predicted values (i.e., MRD curves). Figure 9 shows the superposition for the silty clay layer between the distribution of the theoretical MRD curves, represented by the interval defined by one standard deviation, and the experimental points sharing common conditions in terms of plasticity index and confinement level.
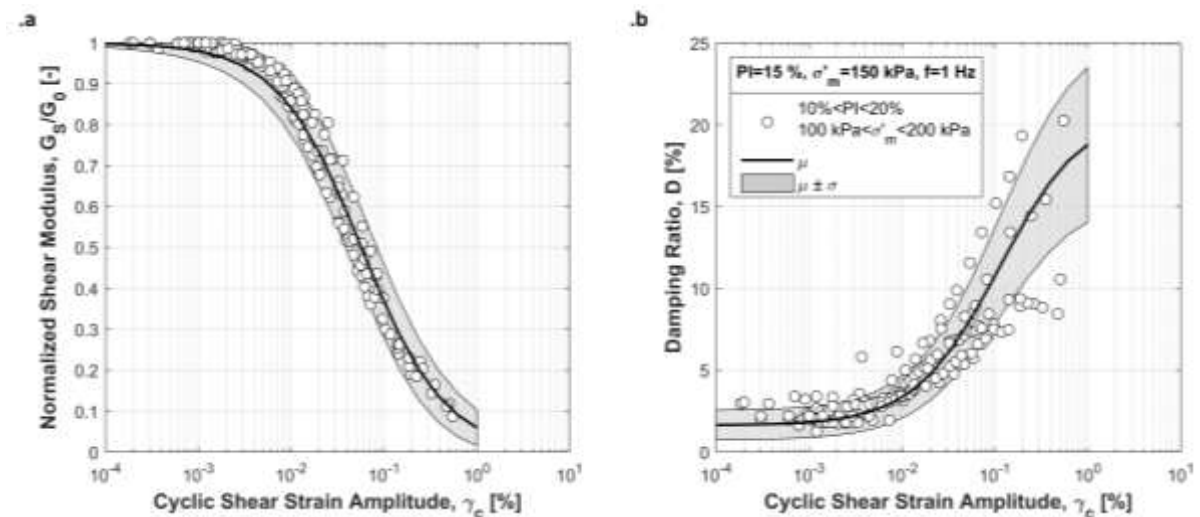
Figure 9 Theoretical distribution and experimental points for a) the MR curve and b) the D curve.

A special remark should be mentioned for the soil small-strain damping ratio D_{min}. Some studies questioned the applicability of a laboratory-based damping measurement to field conditions (Stewart et al. 2014) and proposed alternative approaches for its determination, based on the study of weak motions (e.g., Thompson et al. 2012, Zalachoris and Rathje 2015). On the other side, Stewart and Kwok (2008) observed that the damping-related misfit between theoretical and real response may not be relevant in some shallow soil profiles and the laboratory value is adequate in such situations. Due to the lack of information about the definition of D_{min} and its role on the ground response, the present study assumes as D_{min} the values obtained from the model proposed by Ciancimino et al. (2019).

3.2 Input motions

The input motions consist of seven unscaled seismologically and spectrum-compatible acceleration time histories selected with the web service REXELite (Iervolino et al. 2010). The tool extracts ground motion records from the Italian strong motion database ITACA (itaca.mi.ingv.it/, Luzi et al. 2017), taking into account the compatibility with the expected magnitude and epicentral distance intervals. Then, it checks for an adequate match between the average spectrum and the target Uniform Hazard Spectrum (return period of 475 years) for reference conditions, as provided by the Italian Building Code (NTC, MIT 2018). The average ordinate has to fall between 0.9 and 1.3 times the corresponding value of the code spectrum in the considered interval of vibration periods, ranging from 0.1 to 1.1 s (Figure 10).

More details about the selection process are reported in Luzi et al. (2019).

3.3 Generation of the ground models

The Monte-Carlo generation of the ground models consists in the extraction of two samples of 1000 V_S profiles, each one assuming the resulting profile for the single survey as base-case (Figure 7.a-b). The randomization has been obtained with the geostatistical model proposed by Passeri (2019), which represents an upgrade of the one introduced by Toro (1995). This new geostatistical model provides a physically-based and well-constrained population of soil models, compatible with the common geological features and the experimental site signatures (Passeri et al. 2019). The generation of the layer thicknesses refers to a non-homogeneous Poisson distribution. As for the generation of V_S values, the procedure randomizes the cumulated travel-times from a lognormal distribution, whose statistical parameters derive from a database of geophysical surveys by the Politecnico di Torino (Passeri et al. 2019). The choice of the randomization of the cumulated travel-times (or, equivalently, the harmonic average V_S profiles) is at the same time the most simple and the most crucial innovation of the model. The reader can refer to Passeri et al. (2019) for further details about the model architecture and parameters.
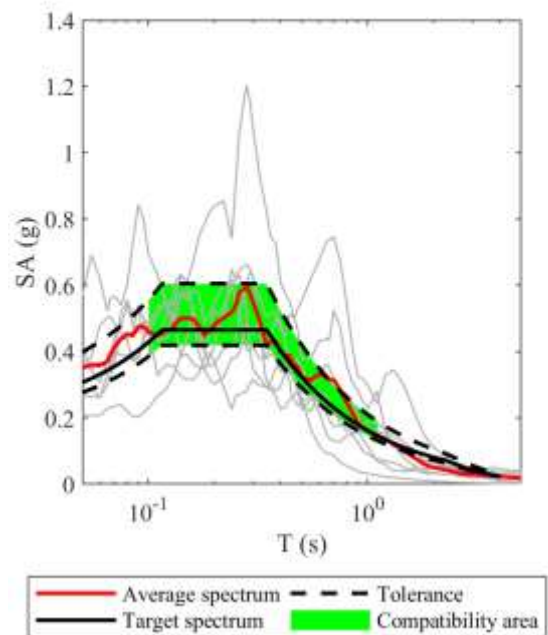
Figure 10. Spectral compatibility of the selected input motions.

Then, the procedure assigns the MRD curves. Thanks to the presence of information about their statistical dispersion, it is possible to simulate different MRD curves for each synthetic ground model, thus incorporating the uncertainties in the soil nonlinear behavior. The generation assumes a negative correlation between the G/G_0 curve and the D curve, by introducing a default correlation coefficient equal to -0.5 (Kottke and Rathje 2008). Furthermore, to avoid physically inconsistent MRD curves, there are some restraints on the possible values: the normalized modulus should not be smaller than 0.05, whereas the damping ratio should be bounded between 0.45% and 24.5% (i.e., the extreme values observed in the laboratory tests on the

soils from Central Italy, normalized to a reference frequency of 1 Hz in order to account for the rate-dependence of this parameter, Ciancimino et al., 2019). Note that the defined minimum value of D_{min} suits the recommendations prescribed in Stewart et al. (2014).

3.4   Results

For each ground model, results are averaged through logarithmic mean with respect to the input motions, obtaining a representative response for every soil profile under the reference ground motion. In order to have synthetic indicators for the distribution of the results, the mean and the standard deviation of the spectral
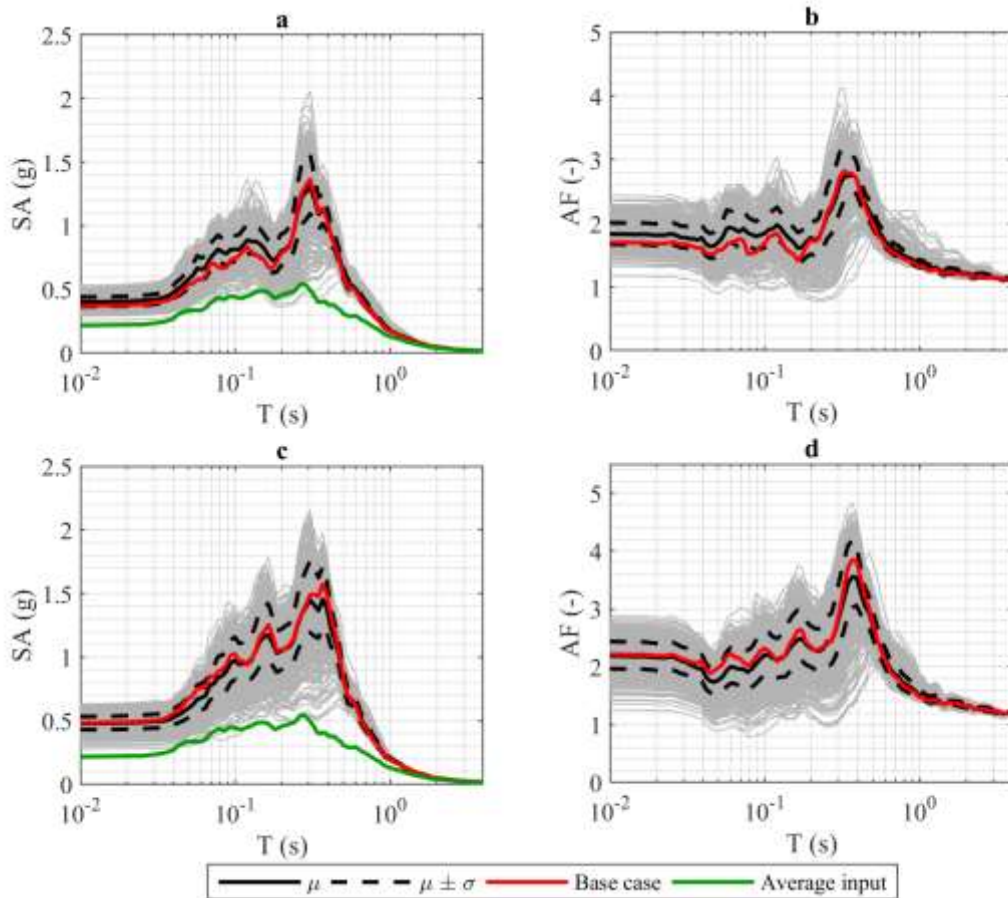
Figure 11 SAs of the a) DH- and c) MASW-based samples, compared with the average spectrum of the input motions; AFs of the b) DH- and d) MASW-based samples.

ordinates with respect to the ground models are computed, assuming lognormal distribution of the data. The procedure is applied for the two populations of ground models. Moreover, the study also reports the ground response of the base-case profile, assuming the mechanical parameters reported in Table 3 and the average MRD curves. This strategy allows for the comparison between the original soil profiles and the distribution of the results.

Figure 11 shows the results in terms of surface SA and AF for the DH-based samples (Figure 11.a and Figure 11.b, respectively) and the ones for the MASW-based models (Figure 11.c and Figure 11.d, respectively). Generally, there is an amplification of the design ground motion at almost all the vibration periods of interest, with a peak at 0.25 s.

On the other side, the response of the two groups of ground models is not the same, as shown in Figure 12.a. The MASW-based models undergo a larger amplification of the spectral ordinates for all the vibration periods of interest

and the difference rises up to 20-30% at short vibration periods and close to 0.25 s (i.e., where the amplification is higher). Moreover, there is a deviation between the two curves for vibration periods ranging between 0.08 s and 0.3 s, since the MASW-based samples exhibit an amplification monotonically increasing together with the period, whereas the amplification function of the DH-based models decreases down to a minimum at 0.15 s. Figure 12.a reports also the AFs obtained from the ground response analyses performed on the DH and MASW base-case profiles, which might be taken as reference. Comparing these results with the mean curves of the samples, a good consistency is observed. The MASW base case exhibits larger amplification with respect to the randomized models, in correspondence of the peak and in the interval of vibration periods between 0.03 s and 0.2 s. Conversely, the amplification observed in the DH-based models is higher than in the correspondent base-case, especially at small vibration periods.
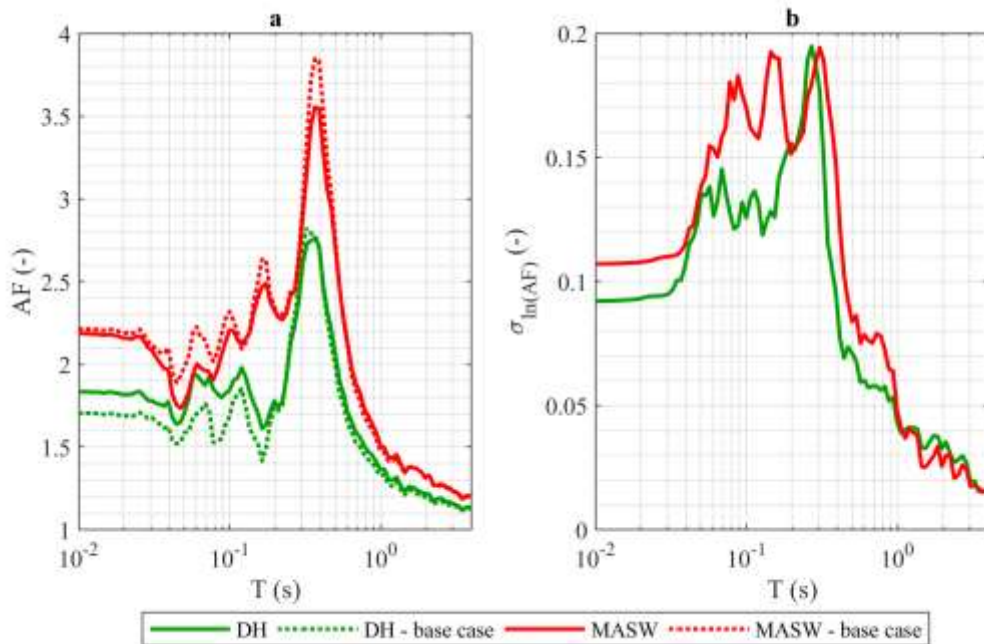
Figure 12 a) Mean AFs of the DH and MASW-based samples and AF of the corresponding base-cases; b) standard deviation (in logarithmic scale) of the AFs of the DH and MASW-based samples.

As for the uncertainty in the ground response of the two sets of samples, the logarithmic standard deviation of the AF is close to 0.1 at small vibration periods, it grows up to a peak a bit smaller than 0.2 for periods close to 0.4 and it gradually decreases at high periods (Figure 12.b). The MASW-based models assume a higher degree of dispersion and the standard deviation keeps its maximum value on a broad range of vibration periods between 0.08 s and 0.2 s, whereas the DH-based models show only a narrow peak.

The observed differences in the response of the two collections highlight the effect of the spatial variability of soil conditions in the site response: the mean value and the uncertainty of the response exhibited by models generated from two surveys performed close to each other and giving similar V_S profiles is not the same and disregarding this discrepancy might lead to errors in the estimate of the seismic action.

4 CONCLUSIONS

The evaluation of seismic hazard at a site requires a detailed assessment of seismic site response to account for the modification of ground motion that are expected as a consequences of the mechanical and geometrical characteristics. In the paper, the main features of site specific and urban scale studies have been considered to show how the two approaches are to be considered complementary rather than alternative. Specifically, urban scale studies allow the adoption of 2D and 3D models, which are most often not feasible at the scale of the single ordinary building.

One of the main issues related to reliability of the results is due to uncertianties in model parameters, which are inevitably propagated into the final assessment of site response. An example of a consistent approach for the identification, quantification and management of the uncertainties is presented with an example based on a recent geostatistical randomization model

and a Montecarlo approach for accounting for uncertainties in laboratory tests. Taking into account that an a-priori selection of conservative values of model parameters in dynamic analyses is not possible, these type of approaches are expected to be widely adopted in the future not only for site response analyses, but also for soil-foundation-structure interaction.

5 ACKNOWLEDGEMENTS

6 REFERENCES

Afshari, K., Stewart, J.P., 2015. Effectiveness of 1D ground response analyses at predicting site response at California vertical array sites.

Aimar M., Ciancimino A., Foti S. 2019. An assessment of the NTC18 simplified procedure for stratigraphic seismic site amplification prediction. *Italian Geotechnical Journal* (submitted to).

Aki, K. 1993. Local site effects on weak and strong ground motion, *Tectonophysics* **218**(1-3), 93-111.

American Society of Civil Engineers (ASCE) 2010. *ASCE/SEI 7-10: Minimum design loads for buildings and other structures*. Reston, Virginia.

Angelici, A. 2018. *Microzonazione Sismica di Livello 3 del Comune di Montedinove ai sensi dell'ordinanza del Commissario Straordinario n°24 registrata il 15 maggio 2017 al n°1065, Comune di Montedinove, Relazione illustrativa* (in Italian).

Ansal, A., Kurtuluş, A., Tönük, G. 2010. Seismic microzonation and earthquake damage scenarios

for urban areas, *Soil Dynamics and Earthquake Engineering* **30**(11), 1319-1328.

Ansal, A., Tönük, G., Kurtulucs, A. 2009. Microzonation for urban planning, *Earthquakes and Tsunamis*, 133-152.

Applied Technology Council (ATC) 1978. *ATC 3-06: Tentative provisions for the development of seismic regulations for buildings*. Palo Alto, California.

Asimaki, D., Li, W. 2012. Site-and ground motion-dependent nonlinear effects in seismological model predictions, *Soil Dynamics and Earthquake Engineering* **32,** 143-151.

Asimaki, D., Li, W., Steidl, J., and Schmedes, J., 2008. Quantifying nonlinearity susceptibility via site-response modeling uncertainty at three sites in the Los Angeles Basin, *Bulletin of the Seismological Society of America* **98**, 2364-2390.

Aversa, S., Crespellani, T. 2016. Seismic microzonation: an essential tool for urban planning in seismic areas, *UPLanD-Journal of Urban Planning, Landscape & environmental Design*, **1**(1), 121.

Baise, L., Thompson, E., Kaklamanos, J., Dorfmann, L. 2011. Complex site response: Does one-dimensional site response work? *Proceedings, 4th IASPEI (International Association of Seismology and Physics of the Earth's Interior)/IAEE (International Association of Earthquake Engineering) International Symposium on the Effects of Surface Geology on Seismic Motion (ESG4)*, 23-26. Santa Barbara, California.

Baturay, M.B., Stewart, J.P. 2003. Uncertainty and bias in ground-motion estimates from ground response analyses, *Bulletin of the Seismological Society of America* **93,** 2025-2042.

Bazzurro, P., Cornell, C.A. 2004. Ground-motion amplification in nonlinear soil sites with uncertain properties. *Bulletin of the Seismological Society of America* **94**, 2090-2109.

Bommer, J.J., Coppersmith, K.J., Coppersmith, R.T., Hanson, K.L., Mangongolo, A., Neveling, J., Rathje, E.M., Rodriguez-Marek, A., Scherbaum, F., Shelembe, R. 2015. A SSHAC level 3 probabilistic seismic hazard analysis for a new-build nuclear site in South Africa, *Earthquake Spectra* **31**, 661-698.

Boore, D.M. 2004. Can site response be predicted?. *Journal of earthquake Engineering* **8**(S.I. 1), 1-41.

Borcherdt, R.D. 1994. Estimates of site-dependent response spectra for design (methodology and justification). *Earthquake spectra* **10**(4), 617-653.

Bouckovalas, G.D., Papadimitriou, A.G., Karamitros, D.K. 2006. Compatibility of EC-8 ground types and site effects with 1D seismic wave propagation theory. *Proceedings, ETC-12 Workshop*, pp. 20-21. Athens (Greece)

Brambati, A., Faccioli, E., Carulli, G., Cucchi, F., Onofri, R., Stefanini, S., Ulcigrai, F. 1980. *Studio di microzonazione sismica dell'area di Tarcento (Friuli)*. CLUET, Trieste (in Italian).

Cabas, A., and Rodriguez-Marek, A., 2018. Toward Improving Damping Characterization for Site Response Analysis.

Cadet, H., Bard, P.Y., Duval, A.M., Bertrand, E. 2012 Site effect assessment using KiK-net data: part 2 – site amplification prediction equation based on f0 and Vsz. *Bulletin of Earthquake Engineering*, **10**(2), 451-489.

Castellaro, S., Mulargia, F., Rossi, P.L. 2008. VS30: Proxy for seismic amplification? *Seismological Research Letters*, **79**(4), 540-543.

Ciancimino, A., Foti, S., Lanzo, G. 2018. Stochastic analysis of seismic ground response for site classification methods verification. *Soil Dynamics and Earthquake Engineering*, **111**, 169-183.

Ciancimino, A., Lanzo, G., Alleanza, G.A., Amoroso, S., Bardotti, R., Biondi, G., Cascone, E., Castelli, F., Di Giulio, A., D'Onofrio, A., Foti, S., Lentini, V., Madiai, C., Vessia, G. 2019. Dynamic characterization of fine-grained soils in Central Italy by laboratory testing, *Bulletin of Earthquake Engineering* (Submitted to)

Consiglio Nazionale delle Ricerche (CNR) 1983. *Indagine di microzonazione sismica, intervento urgente in 39 centri abitati della Campagna e Basilicata colpiti dal terremoto del 23 novembre 1980* (in Italian).

Cornell, C.A. 1968. Engineering seismic risk analysis. *Bulletin of the Seismological Society of America*, **58**(5), 1583-1606-

Crespellani, T. 2014. Seismic Microzoning in Italy: a brief history and recent experiences. *Ingegneria Sismica*, **21**(2), 3-31.

Darendeli, M.B. 2001. *Development of a new family of normalized modulus reduction and material damping curves*, PhD dissertation, University of Texas at Austin, Austin, Texas.

Di Giacomo, D., Gallipoli, M.R., Mucciarelli, M., Parolai, S., Richwalski, S.M. 2005. Analysis and modeling of HVSR in the presence of a velocity inversion: the case of Venosa, Italy. *Bulletin of the Seismological Society of America*, **95**(6), 2364-2372.

Dobry, R., Borcherdt, R.D., Crouse, C.B., Idriss, I.M., Joyner, W.B., Martin, G.R., Power, M.S., Rinne, E.E., Seed, R.B. 2000. New site coefficients and site classification system used in recent building seismic code provisions. *Earthquake spectra* **16**(1), 41-67.

European Committee for Standardization (CEN) 2004. *Eurocode 8: Design of structures for earthquake resistance – Part 1: General rules, seismic actions and rules for buildings*. Brussels, Belgium.

Faccioli, E. 1986. *Elementi per una guida alle indagini di Microzonazione Sismica*. Consiglio nazionale delle ricerche (in Italian).

Faccioli, E., Paolucci, R., Vanini, M., 2015. Evaluation of probabilistic site-specific seismic-hazard methods and associated uncertainties, with applications in the Po Plain, northern Italy, *Bulletin of the Seismological Society of America* **105**, 2787-2807.

Faccioli, E., Vanini, M., Frassine, L. 2002. Complex site effects in earthquake ground motion, including topography. *Proceedings, 12th European Conference on Earthquake Engineering*.

Fäh, D., Rüttener, E., Noack, T., Kruspan, P. 1997. Microzonation of the city of Basel. *Journal of Seismology* **1**(1), 87-102.

Fäh, D., Steimen, S., Oprsal, I., Ripperger, J., Wössner, J., Schatzmann, R., Kästli, P., Spottke I., Huggenberger, P. 2006. The earthquake of 250 AD in Augusta Raurica, A real event with a 3D site-effect? *Journal of Seismology*, **10**(4), 459-477.

Falcone, G., Boldini, D., Amorosi, A. 2018. Site response analysis of an urban area: A multi-dimensional and non-linear approach. *Soil Dynamics and Earthquake Engineering*, **109**, 33-45.

Ferrini, M. 1999. Iniziative regionali per la riduzione del rischio sismico in Toscana, *Ingegneria geotecnica nelle aree sismiche*, 429-447 (in Italian).

Field, E.H., Jacob, K.H. 1993. Monte-Carlo simulation of the theoretical site response variability at Turkey Flat, California, given the uncertainty in the geotechnically derived input parameters, *Earthquake Spectra* **9**(4), 669-701.

Finn, W.L., Onur, T., Ventura, C.E. 2004. Microzonation: developments and applications, *Recent Advances in Earthquake Geotechnical Engineering and Microzonation*, 3-26.

Foti, S., Aimar, M., Ciancimino, A., Passeri, F. 2018. Microzonazione sismica e risposta sismica locale: specificità e aspetti critici. *Analisi e Progetto delle Opere Geotecniche in Zona Sismica: XXV Ciclo di Conferenze di Geotecnica di Torino*, Torino (in Italian).

Foti, S., Passeri, F., Rodriguez-Marek, A. 2019. Uncertainties and variabilities in seismic ground response analyses. *Keynote Lecture, 7ICEGE (Rome, 17-20 June 2019)*.

Hashash, Y.M.A., Musgrove, M.I., Harmon, J.A., Okan, I., Groholski, D.R., Phillips, C.A., Park, D. 2017. *DEEPSOIL 7.0, user manual*. University of Illinois at Urbana-Champaign.

Hashash, Y.M.A., Park, D. 2001. Non-linear one-dimensional seismic ground motion propagation in the Mississippi embayment. *Engineering Geology* **62**(1-3), 185-206.

Hashash, Y.M.A., Phillips, C., Groholski, D.R. 2010. Recent advances in non-linear site response analysis. I*nternational Conferences on Recent Advances in Geotechnical Earthquake Engineering and Soil Dynamics*, 8.

Hunter, J.A. 2003. Some observations of Vp, Vs, depth and porosity from boreholes in water-saturated unconsolidated sediments 2003. *Symposium on the Application of Geophysics to Engineering and Environmental Problems*, 650-661. Society of Exploration Geophysicists.

Idriss, I.M. 2004. Evolution of the state of practice. *International Workshop on the Uncertainties in Nonlinear Soil Properties and Their Impact on Modeling Dynamic Soil Response*, Pacific Earthquake Engineering Research Center. Richmond, California.

Idriss, I.M., Seed, H.B. 1968. Seismic response of horizontal soil layers, *Journal of the Soil Mechanics and Foundations Division* **94**(4), 1003-1031.

Iervolino, I., Galasso, C., Paolucci, R., Pacor, F. 2010. REXELite, online record selection for the ITalian ACcelerometric Archive. *Proceedings of 14th European Conference on Earthquake Engineering*.

Iglesias, J. 1988. Seismic microregionalization of Mexico City after the 1985 earthquake. *Proceedings, 9th World Conference on Earthquake Engineering*, 2, 127-132.

ISSMGE 1999. *Manual for Zonation on Seismic Geotechnical Hazard*. International Society of Soil Mechanics and Geotechnical Engineering, The Japanese Geotechnical Society, Tokyo.

Jibson, R. 1987. *Summary of research on the effects of topographic amplification of earthquake shaking on slope stability*. US Geological Survey, 87-269.

Kaklamanos, J., Baise, L., Dorfmann, L. 2013a Quantification of uncertainty in nonlinear soil models at a representative seismic array. *11th International Conference on Structural Safety and Reliability (ICOSSAR 2013)*.

Kaklamanos, J., Baise, L.G., Thompson, E.M., Dorfmann, L. 2015. Comparison of 1D linear, equivalent-linear, and nonlinear site response models at six KiK-net validation sites, *Soil Dynamics and Earthquake Engineering* **69**, 207-219.

Kaklamanos, J., Bradley, B.A., Thompson, E.M., Baise, L.G. 2013b. Critical parameters affecting bias and variability in site-response analyses using KiK-net downhole array data, *Bulletin of the Seismological Society of America* **103**, 1733-1749.

Kim, B., Hashash, Y.M., Stewart, J.P., Rathje, E.M., Harmon, J.A., Musgrove, M.I., Campbell, K.W., Silva, W.J. 2016. Relative differences between nonlinear and equivalent-linear 1-d site response analyses, *Earthquake Spectra* **32**, 1845-1865.

Kottke, A.R., Rathje E.M. 2009. *Technical Manual for Strata*, PEER Report 2008, University of California, Berkeley, USA.

Kramer, S.L. 1996. *Geotechnical Earthquake Engineering*, Prentice Hall, New Jersey, USA.

Kwok, A.O.L., Stewart, J.P., Hashash, Y.M. 2008. Nonlinear ground-response analysis of Turkey Flat shallow stiff-soil site to strong ground motion, *Bulletin of the Seismological Society of America* **98**, 331-343.

Lanzo, G., Silvestri, F., Costanzo, A., d'Onofrio, A., Martelli, L., Pagliaroli, A., Sica, S., Simonelli, A. 2011. Site response studies and seismic microzoning in the Middle Aterno valley (L'Aquila, Central Italy), *Bulletin of Earthquake Engineering* **9**(5), 1417.

Lee, S.-J., Chan, Y.-C., Komatitsch, D., Huang, B.-S., Tromp, J. 2009. Effects of realistic surface topography on seismic ground motion in the Yangminshan region of Taiwan based upon the spectral-element method and LiDAR DTM. *Bulletin of the Seismological Society of America* **99**(2A), 681-693.

Li, W., Asimaki, D. 2010. Site- and motion-dependent parametric uncertainty of site-response analyses in earthquake simulations, *Bulletin of the Seismological Society of America* **100**, 954-968.

Luzi, L., Hailemikael, S., Bindi, D., Pacor, F., Mele, F., Sabetta, F. 2008. ITACA (ITalian ACcelerometric Archive): a web portal for the dissemination of Italian strong-motion data. *Seismological Research Letters* **79**(5), 716-722.

Luzi, L., Pacor, F., Puglia, R. 2017. *Italian Accelerometric Archive v 2.3*, Istituto Nazionale di Geofisica e Vulcanologia, Dipartimento della Protezione Civile Nazionale (http://itaca.mi.ingv.it).

Luzi, L., Pacor, F., Lanzano, G., Felicetta, C., Puglia, R., D'Amico, M. 2019. 2016-2017 Central Italy seismic sequence: strong-1 motion data analysis and design earthquake selection for seismic microzonation purposes. *Bulletin of Earthquake Engineering*. (submitted)

Makra, K., Chávez-García, F.J. 2016. Site effects in 3D basins using 1D and 2D models: an evaluation of the differences based on simulations of the seismic response of Euroseistest, *Bulletin of Earthquake Engineering* **14**, 1177-1194.

Marcellini, A., Daminelli, R., Pagani, M., Riva, F., Tento, A., Crespellani, T., Madiai, C., Vannucchi, G., Frassineti, G., Martelli, L., Palumbo, D., Viel, G. 1999. Seismic microzonation of some Municipalities of the Rubicone area (Emilia-Romagna Region). *Proceedings of the Eleventh European Conference on Earthquake Engineering*.

Marcellini, A., Tiberi, P. 2000. *La microzonazione sismica di Fabriano*. Biemmegraf, Macerata (in Italian).

Massarsch, K.R. 1979. Lateral Earth pressure in normally consolidated clay, Design Parameters in Geotechnical Engineering. *Proceedings of the 7th European Conference of Soil Mechanics and Foundation Engineering*, 2. Brighton.

Ministero delle Infrastrutture e dei Trasporti (MIT) 2018. *DM 17/01/2018: Aggiornamento delle "Norme Tecniche per le Costruzioni"*.

Mucciarelli, M., Tiberi, P. 2007. *Scenari di pericolosità sismica della fascia costiera*

marchigiana. La microzonazione sismica di Senigallia (in Italian).

Olsen, K. 2000. Site amplification in the Los Angeles basin from three-dimensional modeling of ground motion, *Bulletin of the Seismological Society of America* **90**, S77-S94.

Pagliaroli, A. 2018. Key issues in Seismic Microzonation studies: lessons from recent experiences in Italy, *Italian Geotechnical Journal* **1**(1), 5-48.

Pagliaroli, A., Pergalani, F., Ciancimino, A., Chiaradonna, A., Compagnoni, M., De Silva, F., Foti, S., Giallini, S., Lanzo, G., Lombardi, F., Luzi, L., Macerola, L., Nocentini, M., Pizzi, A., Tallini M., Teramo, C. 2019. Site response analyses for complex geological and morphological conditions: relevant case-histories from 3rd level seismic microzonation in Central Italy. *Bulletin of Earthquake Engineering*. doi:10.1007/s10518-019-00610-7.

Papaspiliou, M., Kontoe, S., Bommer, J.J. 2012. An exploration of incorporating site response into PSHA—Part I: Issues related to site response analysis methods. *Soil Dynamics and Earthquake Engineering*, **42**, 302-315.

Park, D., Hashash, Y.M.A. 2005. Evaluation of seismic site factors in the Mississippi embayment. II. Probabilistic seismic hazard analysis with nonlinear site effects, *Soil Dynamics and Earthquake Engineering* **25**, 145-156.

Passeri, F. 2019. *Development of an advanced geostatistical model for shear wave velocity profiles to manage uncertainties and variabilities in Ground Response Analyses*, Ph.D. dissertation, Politecnico di Torino, Torino.

Passeri, F., Foti, S., Rodriguez-Marek, A. 2019. A new geostatistical model for the management of uncertainties in shear wave velocity profiles, (in preparation).

Pehlivan, M., Rathje, E.M., Gilbert, R.B. 2016. Factors influencing soil surface seismic hazard curves, *Soil Dynamics and Earthquake Engineering* **83**: 180(19).

Pitilakis, K. 2004. Site effects. *Recent advances in earthquake geotechnical engineering and microzonation*, 139-197. Springer, Dordrecht (Netherlands).

Pitilakis, K., Alexoudi, M., Argyroudis, S., Anastasidis, A. 2006. *Seismic risk scenarios for an efficient seismic risk management: the case of Thessaloniki (Greece)*. Dordrecht.

Pitilakis, K., Raptakis, D., Makra, K., Manakou, M., Chávez-García, F.J. 2011. Euroseistest 3D Array for the Study of Complex Site Effects. *In S. Akkar, P. Gülkan, & T. van Eck (Eds.), Earthquake Data in Engineering Seismology: Predictive Models, Data Management and Networks*, 145-166. Springer Netherlands, Dordrecht.

Pitilakis, K., Riga, E., Anastasiadis, A. 2013. New code site classification, amplification factors and normalized response spectra based on a worldwide ground-motion database. *Bulletin of Earthquake Engineering*, **11**(4), 925-966.

Pitilakis, K., Riga, E., Anastasiadis, A., Fotopoulou, S., Karafagka, S. 2018. Towards the revision of EC8: proposal for an alternative site classification scheme and associated intensity dependent spectral amplification factors. *Soil Dynamics and Earthquake Engineering*.

Rathje, E.M., Kottke, A.R. 2011. Relative differences between equivalent linear and nonlinear site response methods. *5th International Conference on Earthquake Geotechnical Engineering (ICEGE)*. Santiago, Chile.

Régnier, J., Bonilla, L.F., Bard, P.Y., Bertrand, E., Hollender, F., Kawase, H., Sicilia, D., Arduino, P., Amorosi, A., Asimaki, D., Boldini, D., Chen, L., Chiaradonna, A., Demartin, F., Elgamal, A., Falcone, G., Foerster, E., Foti, S., Garini, E., Gazetas, G., Gélis, C., Ghofrani, A., Giannakou, A., Gingery, J., Glinsky, N., Harmon, J., Hashash, Y.M.A., Iai, S., Kramer, S., Kontoe, S., Kristek, J., Lanzo, G., Lernia, A.D., Lopez-Caballero, F., Marot, M., Mcallister, G., Mercerat, E.D., Moczo, P., Montoya-Noguera, S., Musgrove, M., Nieto-Ferro, A., Pagliaroli, A., Passeri, F., Richterova, A., Maria, S.S., D'Avila, P.S., Shi, J., Silvestri, F., Taiebat, M., Tropeano, G., Vandeputte, D., Verrucci, L. 2018. PRENOLIN: International Benchmark on 1D Nonlinear Site-Response Analysis - Validation Phase Exercise, *Bulletin of the Seismological Society of America* **108**(2), 876-900.

Régnier, J., Cadet, H., Bard, P.Y. 2016. Empirical quantification of the impact of nonlinear soil behavior on site response, *Bulletin of the Seismological Society of America* **106**, 1710-1719.

Rodriguez-Marek, A., Bray, J.D., Abrahamson, N.A. 2001. An empirical geotechnical seismic site

response procedure. *Earthquake spectra*, **17**(1), 65-87.

Rodriguez-Marek, A., Rathje, E.M., Bommer, J.J., Scherbaum, F., Stafford, P. 2014. Application of single-station sigma and site-response characterization in a probabilistic seismic-hazard analysis for a new nuclear site, *Bulletin of the Seismological Society of America* **104**, 1601-1619.

Rollins, K.M., Evans, M.D., Diehl, N.B., Daily III, W.D. 1998. Shear modulus and damping relationships for gravels. *Journal of Geotechnical and Geoenvironmental Engineering*, **124**(5), 396-405.

Sarconi, M. 1784. *Istoria de fenomeni del tremoto avvenuto delle Calabrie, e nel Valdemone nell'anno 1783*, Campo.

Seed, H.B., Ugas, C., Lysmer, J. 1976. Site-dependent spectra for earthquake-resistant design. *Bulletin of the Seismological society of America*, **66**(1), 221-243.

Seed, H.B., Wong, R.T., Idriss, I.M., Tokimatsu, K. 1986. Moduli and damping factors for dynamic analyses of cohesionless soils. *Journal of geotechnical engineering*, **112**(11), 1016-1032

Sextos, A., De Risi, R., Pagliaroli, A., Foti, S., Passeri, F., Ausilio, E., Cairo, R., Capatti, M. C., Chiarabando, F., Chiaradonna, A., Dashti, S., De Silva, F., Dezi, F., Durante, M. G., Lanzo, G., Sica, S., Simonelli, A. L., Zimmaro, P. 2018. Local site effects and incremental damage of buildings during the 2016 Central Italy earthquake sequence, *Earthquake Spectra* **34**(4), 1639-1669.

Shi, J., Asimaki, D. 2017. From stiffness to strength: Formulation and validation of a hybrid hyperbolic nonlinear soil model for site-response analyses, *Bulletin of the Seismological Society of America* **107**, 1336-1355.

Smerzini, C., Paolucci, R., Stupazzini, M. 2011. Comparison of 3D, 2D and 1D numerical approaches to predict long period earthquake ground motion in the Gubbio plain, Central Italy. *Bulletin of Earthquake Engineering* **9**(6), 2007-2029. doi:10.1007/s10518-011-9289-8.

Hailemikael, S., Amoroso, S., Gaudiosi, I. (Eds.) 2019. Seismic microzonation of Central Italy [Special Issue], *Bulletin of Earthquake Engineering* In press

Stewart, J.P. 2008. *Benchmarking of nonlinear geotechnical ground response analysis procedures*, Pacific Earthquake Engineering Research Center.

Stewart, J.P., Afshari, K., Hashash, Y.M.A. 2014. *Guidelines for performing hazard-consistent one-dimensional ground response analysis for ground motion prediction*, PEER Report 16.

Stewart, J.P., Baturay, M.B., 2001. Uncertainties and residuals in ground motion estimates at soil sites. *International Conferences on Recent Advances in Geotechnical Earthquake Engineering and Soil Dynamics*, 12.

Stewart, J.P., Kwok, A.O.L. 2008. Nonlinear seismic ground response analysis: Code usage protocols and verification against vertical array data. *Geotechnical earthquake engineering and soil dynamics IV*.

Stewart, J.P., Lanzo, G., Ausilio, E., Cairo, R., Bozzoni, F., Capatti, M.C., Della Pasqua, F., Dezi, F., Di Sarno, L., Durante, M., Simonelli, A.L., Foti, S., Chiabrando, F., Dabove, P., Di Pietra, V., Maschio, P., Passeri, F., Sgobio, A., Teppati Losè, L., Zimmaro, P. 2017. *GEER Report: Engineering Reconnaissance following the October 2016 Central Italy Earthquakes – Version 2*.

Stewart, J.P., Zimmaro, P., Lanzo, G., Mazzoni, S., Ausilio, E., Aversa, S., Bozzoni, F., Cairo, R., Capatti, M. C., Castiglia, M. 2018. Reconnaissance of 2016 Central Italy earthquake sequence, *Earthquake Spectra* **34**, 1547-1555.

Thompson, E.M., Baise, L.G., Tanaka, Y., Kayen, R.E. 2012. A taxonomy of site response complexity, S*oil Dynamics and Earthquake Engineering* **41**, 32-43.

Toro, G.R. 1995. *Probabilistic models of site velocity profiles for generic and site-specific ground-motion amplification studies*, Brookhaven National Laboratory, Upton, New York.

Vinale, F., Santucci de Magistris, F., Sica, S., Silvestri, F. 2008. *Indirizzi per studi di microzonazione sismica*. AMRA Scarl Sezione EarlyWarning e Rischio Sismico, a cura di Vinale F, 170.

VV. AA. 1981. Elementi di microzonazione sismica dell'area anconetana (in Italian).

Vucetic, M., Dobry, R. 1991. Effect of soil plasticity on cyclic response. *Journal of geotechnical engineering*, **117**(1), 89-107.

Working Group ICMS 2008. *Indirizzi e criteri per la microzonazione sismica – Guidelines for seismic microzonation*. English version available at http://www.protezionecivile.gov.it/httpdocs/cms/at

tach_extra/GuidelinesForSeismicMicrozonation.p
df.

Working Group ICMS 2011. *Contributi per
l'aggiornamento degli Indirizzi e criteri per la
microzonazione sismica* (in Italian).

Working Group MS-AQ 2010. *Microzonazione
sismica per la ricostruzione dell'area aquilana* (in
Italian).

Zalachoris, G., Rathje, E.M. 2015. Evaluation of one-
dimensional site response techniques using
borehole arrays, *Journal of Geotechnical and
Geoenvironmental Engineering* **141**, 04015053.

XVII European Conference

ECSMGE 2019
Reykjavík

on Soil Mechanics
and Geotechnical Engineering

Geothermal exploitation in Iceland – Success and Challenges

Exploitation de la géothermie en Islande – Succès et Enjeux

Ó.G. Flóvenz

ÍSOR – Iceland GeoSurevy, Reykkjavík, Iceland

ABSTRACT: : Iceland is blessed with favourable geological conditions to produce and utilize geothermal energy. It provides low cost energy to heat about 90% of houses in Iceland and about 27% of the electricity. In addition, the geothermal energy is used for various other applications including swimming pools and spas, fish- and greenhouse-farming and various industrial processes. The geothermal energy is the key to convenient and enjoyable life in Iceland and it affects greatly our culture and living standards. During 90 years of geothermal development in Iceland a lot of challenges has been faced, and problems have always been solved.

The crustal rock in Iceland is usually of low general permeability at reservoir depth and the geothermal fluid flow is confined to subvertical fractures formed by tectonic activity. A well is only productive if it is drilled into an open fracture. The geothermal utilisation has a huge environmental benefit for the society, it has low CO_2 emission and creates local jobs. There are, however, several challenges still to deal with. induced seismicity due to reinjection of fluid, reduction of gas emission from power plants, extraction of energy from superhot roots of the high temperature systems, methods to prevent casing damages due to high thermal stresses in the casing pipes and ways to find a reasonable balance between the renewable geothermal power production and nature protection. Several pioneering projects are now running to address these challenges. The Icelandic success in geothermal utilisation is an incentive for many other countries to increase the share of renewable energy in their energy production.

RÉSUMÉ: L'Islande a la chance de disposer d'un contexte géologique favorable à la production et l'utilisation d'énergie géothermique. L'exploitation de la géothermie fournit une énergie à faible coût, qui permet de chauffer 90% des maisons en Islande et de produire 27% de l'électricité consommée dans le pays. En outre, la géothermie est utilisée pour d'autres applications : piscines et spas, aquaculture et serriculture, ainsi que différents procédés industriels. La géothermie, qui impacte fortement notre culture et notre niveau de vie, est la clef pour une vie confortable et agréable en Islande. De nombreux obstacles ont été rencontrés pendant les 90 années où la géothermie s'est développée en Islande et les problèmes ont toujours été résolus.

La croûte islandaise a, dans l'ensemble, une faible perméabilité aux profondeurs habituelles des réservoirs. Par conséquent, les écoulements de fluides géothermaux sont confinés dans les fractures sub-verticales créées par l'activité tectonique ; un puits n'est productif que s'il est foré dans une fracture ouverte. L'utilisation de la géothermie présente des avantages environnementaux considérables, tels que de faibles émissions de CO_2 et la création d'emplois locaux. Plusieurs enjeux de taille persistent cependant: surveiller la sismicité induite due à la réinjection de fluides, réduire les émissions de gaz à la sortie des centrales géothermiques, extraire l'énergie à la source-même – extrêmement chaude – des systèmes haute-température, limiter l'endommagement des revêtements de forages lié aux fortes contraintes thermiques dans les conduits et enfin trouver un compromis entre la production d'énergie renouvelable par géothermie et la protection de la nature.

Keywords: Geothermal energy, Induced seismicity, CO_2 sequestration, casing damages, superhot systems

1 RENEWABLE ENERGY

Access to energy at affordable prices is a prerequisite for a modern society. Since the first settlement of the island and until the 20th century, people lived mostly in turf houses where peat was the main source of heating and fish oil the main energy source of indoor light. When houses of concrete and wood became common at the end of the nineteenth century the energy for heating changed to imported coal and later oil. Despite numerous hot springs around the country they were only used for bathing and washing but not for house heating, probably due to lack of technical know-how. In the 1920´s drilling for hot water started in Iceland and the first district heating system was operative in 1928. The development was however rather slow until in the 1970s. Figure 1 shows the development of the primary energy use in Iceland and the dominant share of the geothermal in the energy budget. It show that about 80% of the primary energy use in Iceland comes from renewable energy resources, hydro and geothermal. Fossil fuel is only used for cars, ships, mostly the fishing fleet, and for airplanes.

We can identify three jumps in the geothermal development, the first one in the 1940s when large parts of Reykjavík got geothermal water from a resource 15 km away, the second one in from 1970 to 1980 when a major step was taken

Figure 2 Development of the energy used for house heating in Iceland from 1970 to 2018.

by the government to exclude fossil fuel from the heating sector and finally from 1995 to 2010 where major steps were taking in geothermal power production. Figure 2 shows the development in the house heating sector from 1970 when over 50% of the houses were heated by oil to 2018 when the house heating was over 99% from renewable sources, 90% directly from geothermal and 9.3% from electricity. The electricity in Iceland is produced by hydro (73%) and by geothermal energy (27%) with a minor production from wind power.

This development in Iceland was driven by two factors, economy and energy security rather that environmental factors. Figure 3 show comparison of heating cost in the Nordic capitals.

Reykjavík, heated by geothermal energy has far the lowest energy cost which is extremely important when heating is necessary all the year.

Figure 1 The development of primary energy consumption in Iceland from 1940 to 2018. Geothermal energy stands for about 67% of the primary energy. (Source: Orkustofnun)
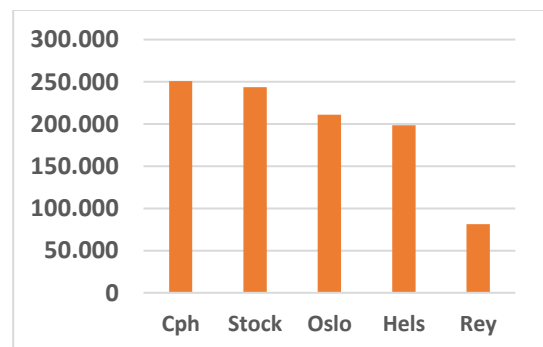
Figure 3 Comparison of calculated cost for heating a 100m² flat in the Nordic capitals, assuming the same energy need everywhere. VAT is not included. Source: Samorka, Federation of Energy and Utility Companies in Iceland www.samorka.is

2 THE GEOTHERMAL SYSTEMS

Iceland is the only place in the world where an active oceanic spreading ridge is above sea level. The reason for this is the presence of a low-density mantle hot spot, centered below central Iceland, that increases the magmatic production rate compared to normal oceanic ridges. This leads to abnormal crustal thickness beneath Iceland of 20-40 km (Bjarnason et al 1993, Kaban et al, 2002) compared to normal oceanic crust of 10 km or less.
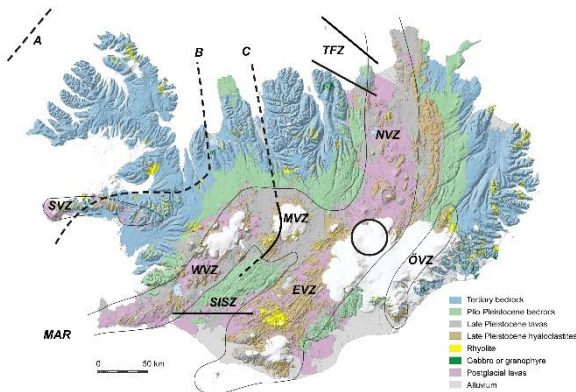
Figure 4 The rift zones of Iceland. The black circle shows the centre of the hot spot and the dotted lines show ancient and extinct rift zones. From Hardarson et al, 2008.

The spreading axis of the Mid-Atlantic Ridge (MAR) crosses the island as a zone of active spreading and volcanism, referred to as the axial volcanic zone (AVZ). It is composed of several segments named the Westeren Volcanic Zone (WVZ), the Eastern Volcanic Zone (EVZ) and the Northern Volcanic Zone (NVZ). The measured half spreading rate in Iceland is close to 1 cm/year. The axis rises from sea on the Reykjanes peninsula on the south-west corner of the country and submerges again at the north-eastern coast (Fig.4). The AVZ does not form a straight line through the country but is shifted about 150 km eastwards, close to the southern coast (The South Iceland Seismic Zone, SISZ) and back in a westerly direction at the northern coast (The Tjörnes Fracture Zone, TFZ). In the southern part of Iceland, the AVZ is composed of two parallel axial segments. Throughout the almost 20 m.y. of the exposed geological history of Iceland the AVZ has shifted eastwards a few times, leaving behind traces of ancient spreading axis and related transform tectonics, especially on the American plate (e.g. Sæmundsson, 1979).

The subaerial volcanism of the country resulted in extensive eruption of flood basalts that characterizes the pre-glacial and interglacial periods. During the glaciation periods, when the country was mostly covered with ice, elongated hyaloclastite ridges or table mountains were formed and accumulated above the volcanic fissures. The glaciation and deglaciation furthermore lead to large vertical crustal movements that might have contributed to the formation of fracture dominated hydrothermal fields outside the rift zones (Böðvarsson, 1982).

The crustal accretion process in Iceland has been modelled and described by Pálmason (1973). His model assumes a simple spreading axis and spreading rate, where new crust is partly formed by dyke injection into the existing crust and partly by surface volcanism. The eruptions cause the lava to accumulate at certain rate, normally distributed around the spreading axis, and the crust subsides by the same amount as the overlying erupted mass. This means that lava that
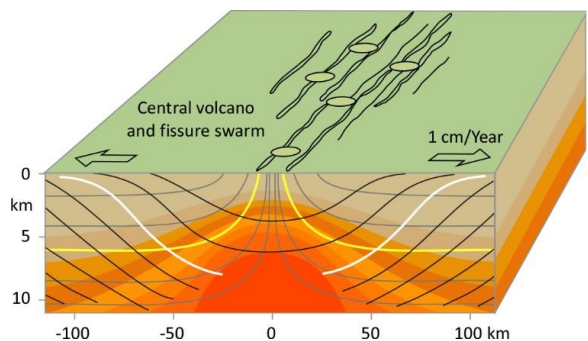
Figure 5. Pálmason´s crustal accretion model. The yellow and the tiny blue lines show the trajectories of the lava material from the surface away from the rift axis and downwards. The white line and the tiny black lines show the isochrones and the temperature is shown with the colour scale.

solidifies on the surface moves horizontally away from the spreading axis, with half spreading rate of 1 cm/year, but simultaneously moves vertically down due to the load of lava that accumulates on the surface at a later time. The trajectories of the lava successions are shown in figure 5. The magma that cool on the surface at the spreading axis move vertically down with time, whilst those which accumulate outside the spreading axis move both laterally and downwards. When lava has left the volcanic zone it only moves laterally away from the spreading axis with time.

A consequence of this process is that the lava becomes reheated as it moves to greater depth, pores close due to external pressure and it undergoes hydrothermal alteration which finally makes the rock almost impermeable. Close to the spreading axis the subsiding crust can even be reheated to solidus of certain minerals so it starts to melt partially and create silicic magma.

Fresh lava on the surface has very high porosity (~30%) and primary permeability. Therefore, there is practically no conductive heat transport in the near surface lava pile, all heat from below is removed by groundwater flow. As the lava becomes buried the porosity and permeability reduce with depth because of the burial pressure and the precipitation of secondary minerals from geothermal fluids. Temperature logs in boreholes in the volcanic zones in Iceland indicate that primary permeability has been reduced enough at around 1 km depth to let thermal conduction dominate the heat transport. A result of this is that the uppermost 1 km of the volcanic crust in Iceland should have very high permeability. But since repeated glacial erosion has removed the uppermost 1-2 km of the crust at present sea level outside the volcanic zone, the general permeability of the basaltic crust outside the volcanic zone is low.
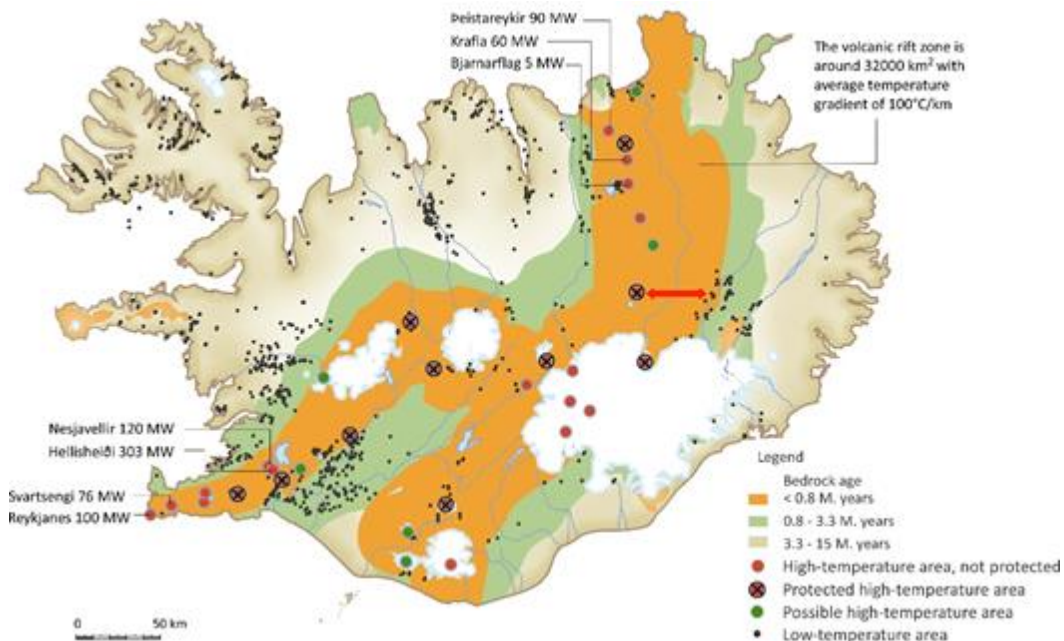
Figure 6. A simplified geological map of Iceland showing the location of the geothermal fields and the present geothermal power plants. The volcanic rift zones are almost identical to zones of bedrock of age less than 0.8 M.Y. The red arrow shows the approximate location of the resistivity section in Figure 11.
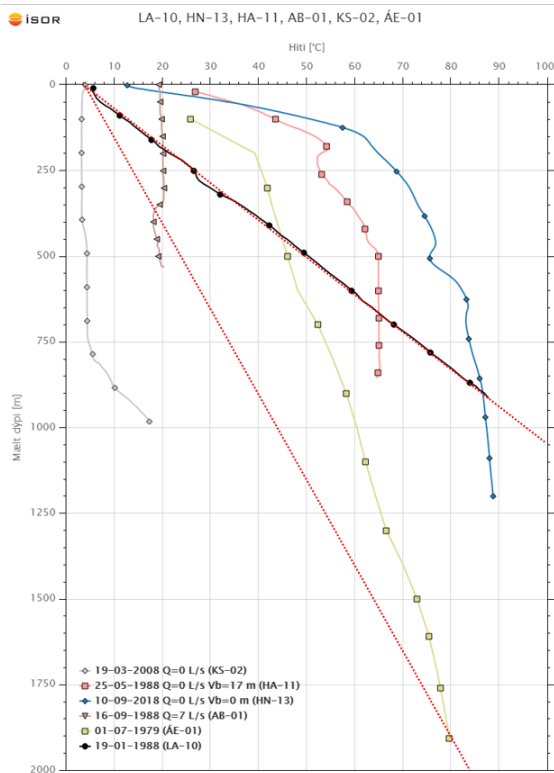
Figure 7. Typical temperature logs from boreholes in Iceland outside the high temperature fields. The background temperature gradient outside geothermal areas is shown by two red dotted straight lines. The other logs are from geothermal fields and show typical convection profiles with different reservoir temperature where the shallow part is abnormally hot but the lower part is abnormally cold. The coldest log is from the volcanic rift zone.

Heat flow in Iceland is high compared to continental areas. The heat flow is basically controlled by two processes. One is a background heat flow, originating from the cooling crust moving away from the spreading axis like at the mid-oceanic ridges. The other is local high or low heat flow anomalies caused by convection of water in vertical fracture systems, the high values corresponds to the upwelling part, while the low values relate to the down flow pattern. Since the crust in Iceland is fairly homogeneous with respect to thermal conductivity (1.6-1.9 W/m°K), the near surface temperature gradient is frequently used as a proxy for heat flow. The

typical background values of the temperature gradient in Iceland is 80-100°C/km at the boarder of the volcanic rift zone to 40-50°C/km in the oldest crust that is farthest away from the rift axis. Within the volcanic zone, however, the uppermost 1 km of the crust consists of highly permeable young volcanics, where all conductive heat from below is transported away by large groundwater currents. Therefore, almost a zero temperature gradient is observed in the uppermost 1 km within the volcanic rift zone (Fig.7), with the exception of the high-temperature hydrothermal fields associated with the volcanic centres.

Geothermal surface manifestations are very common in Iceland. They appear as hot springs, fumaroles, steam vents or simply as geothermal alteration minerals on the ground. Geothermal areas in Iceland are basically of two different types, high-temperature fields and low-temperature fields, but areas with intermediate reservoir temperatures (150-200°C) are rarely found. The locations of the high and low temperature fields in Iceland are shown in figure 6. There are fundamental differences between high and low temperature fields. The high-temperature fields have reservoir temperatures of 200-340°C and are exclusively located within active volcanoes or recent post-glacial volcanism in the axial rift zone. Their surface manifestations are hot springs and fumaroles and high-temperature rock alteration, resulting in colourful and picturesque landscapes (Fig.8). The geothermal fluid is usually acidic and the rather high chemical content prevents direct use of the fluid.

The low-temperature fields in Iceland show quite a different character from those in the high-temperature fields. Their location is also shown in figure 6. The low-temperature geothermal systems are almost all outside the axial rift-zone. Their reservoirs are fracture dominated in otherwise low permeability basaltic lavas or hyaloclastites. The heat is extracted from the relatively high background temperature gradient by fluid convection in permeable fracture

systems (Flóvenz and Sæmundsson, 1993). This is explained in Fig.7. In most cases the surface expressions of the low-temperature fields appear as hot springs on the surface. Sometimes, the low-temperature fields are hidden with no expression of geothermal activity at the surface (Axelsson et al, 2005). In these cases, the geothermal fields are discovered by geophysical measurements of heat flow, or electrical resistivity of the subsurface, or simply by tectonic data.

Figure 8. Hot springs in Krýsuvík, SW-Iceland surrounded by grey and yellow coloured clay minerals formed by hydrothermal alteration.

The tectonic origin of the permeable fractures are not always obvious. In some cases they are clearly linked to the shear zones of the transform faults between rift segments, like in the South Iceland Seismic Zone. There are also examples of low-temperature fields where recent or active fissure swarms of the volcanic centres penetrate the older rocks without any surface volcanism. It has also been suggested that the geothermal fractures are a consequence of the postglacial rebound of the crust (Bödvarsson, 1982).

As expected for a region where the Mid Atlantic Ridge interferes with a hot spot, the overall seismicity in Iceland is high. Figure 9 shows a map of the seismicity of Iceland for the period 1995 to 2016, embedded on a simplified geological map. The seismicity shows clearly the main tectonic and geological patterns of the country; the volcanic centres in the axial rift zones, the axial part of the MAR, and the transform faults and oblique rift zones in North and South Iceland which connect the rift segments in Iceland. The eastern part of Iceland outside axial rift-zone, i.e. that belonging to the European plate, is almost devoid of seismicity as well as surface geothermal activity. On the contrary, the part that belongs to the American plate outside the axial rift-zone, is characterized by both intraplate earthquakes and hydrothermal systems supporting the hypothesis of tectonic origin of the low-temperature systems.

The chemical content of the geothermal fluid within the low-temperature system is usually quite low, typically with total dissolved solids of less than 300 mg/L. At a few places, the reservoir fluid is slightly seawater contaminated giving rise to total dissolved solids of over 1000 mg/L. The quality of the geothermal water is indeed mostly within drinking water standards. The fluid is eminently suitable for domestic use and provides tap water and water for radiator systems.

3 THE BENEFIT OF UTILISATION OF GEOTHERMAL ENERGY

Economy and energy safety have been the primary drivers for the development and use of renewable energy in Iceland. But the side effects are huge, resulting in health, environmental, and social benefits.

3.1 Economical benefit

There are several ways to estimate the economical benefit of the geothermal utilisation in Iceland. Firstly it is the pure effect of the low energy prices compared to alternative energy sources. Orkustofnun, the National Energy Authority, calculates annually the avoided cost of using geothermal instead of oil for house heating. For the year 2014 this amounts around 730 million USD or over 2200 USD per person per year. This avoided cost equals 4,5% of GNP (Orkustofnun 2015). These numbers can vary considerbly with time due to fluctuations in oil

prices and in the exchange rate of the Icelandic krona. This avoided cost might however be an oversetimate as higher prices would eventually lead to lower consumption. Secondly, the geothermal industry creates well paid jobs in Iceland and in many cases rural jobs.

3.2 Environmental benefit

The main environmental impact of the geothermal production in Iceland is the positive influence on the quality of the atmosphere with reduction in carbon dioxide emission and other pollutants from burning of fossil fuel.

The effect on public health was striking in Reykjavík when largest parts of Reykjavík were connected to geothermal district heating system in 1943-1945 (Baldur Johnsen, 1962). Prior to 1940 about 80% of the heating in Reykjavik was by coal that was reduced to about 45% in 1945 and replaced by geothermal and oil. Prior to 1940, the incidences of cold were 50-100% higher in city of Reykjavik compared to rural areas but after the geothermal heating was initiated the incidences in Reykjavik dropped to less than half of the cases in the rural areas. The reason for this positive change is might be a combination of lower air pollution since the smoke from coal heating was strongly reduced and improved indoor heating.

The use of geothermal strongly reduces the CO_2 emission from the energy sector in Iceland. In 2017 the calculated annual CO_2 savings by using geothermal energy for heating and electricity production instead of oil is 8,1 Megatonn. Almost half of is due to the geo-thermal heating (Orkustofnun, 2018)

3.3 Social benefit

Nowadays, geothermal energy is an integrated part of everyday life in Iceland and has created a special culture that marks the society in many ways. About 90% of all buildings in Iceland are heated directly by geothermal energy, both in urban and rural areas and in most cases at very low price. The abundance of hot water affects everyday life. All parts of the houses are heated throughout the year and the typical room temperature is 22°C, even in the garage. You can take a long hot shower with high flow rate without worrying much about your energy bill. And you can, without any additional energy cost, use the return water from your radiator system to heat up the pavement outside your house and keep it free of snow. You can go to the one of the numerous outdoor warm and comfortable geothermally heated public swimming pools and enjoy swimming, both on beautiful summer days as in winter snowstorms; or enjoy sitting outdoors in a hot tub with friends, participating in discussions and debates on politics or simply the life. You can also visit geothermal spas or buy fresh vegetables throughout the year which are grown in geothermally heated greenhouses under lightning produced by renewable electricity. People who enjoy sports can utilise some of the numerous heated sports halls for exercising. In recent years, six full size geothermally heated indoor football grounds have been built, and also numerous large sports halls for football, handball and basketball, providing excellent facilities for the development of youth sport skills.

4 THE MAIN CHALLENGES TO-DAY

4.1 Carbon and sulfur emission

The production of hot water from low-temperature fields is practically without any emission of gasses. The CO_2 emission is negligible. Slight content of hydrogen sulphide (H_2S) is usually observed in the low-temperature geothermal water and gives a faint smell when the hot water is used directly for bathing and washing. The inhabitants are used to this smell and do not even notice it on daily basis, but foreign guests may notice it. The concentration of H_2S is far below all health limits but our nose detects the H_2S in extremely low concentrations. In case of oxygen contamination of the hot water the H_2S in it reacts with the oxygen to produce

sulphate and has therefore a corrosion preventing effect for pipes and radiators. Therefore, H_2S is sometimes deliberately mixed into the hot water if its concentration is negligible.

Emission of CO_2 and H_2S follows the geothermal steam produced in geothermal power plants but in different concentrations from one field to another. In case of Icelandic power plants the emission of CO_2 per electricity produced is in the range 26 -181 g/kWh_e (Ármannsson et al, 2005, Sigurdardottir and Thorgeirsson, 2016). This is of the order of 4-25% of similar values for oil driven power plants. Although the concentration of H_2S from the power plants in the atmosphere is far below environmental limits it may be quite annoying and cause damages to electronic equipment and corrode metals like copper and silver. In case of, the $303MW_e$ Hellisheiði power plant, the largest geothermal power plant in Iceland, ongoing research and demonstration projects called Carbfix and Sulfix show that it is possible to collect and reinject the CO_2 and H_2S into the shallower part of the reservoir where it fixes permanently in minerals as calcite and pyrite. In 2015 over 10% of the emitted CO_2 was reinjected and research indicates that at least 90% of it is fixed in mineral form within a year from reinjection. At the Hellisheidi Power plant about 30% of the H_2S was reinjected in the SulFix project in 2015 whereof about 75-80% is sequestered in the form of minerals like pyrite within six months. (Sigurdardottir and Thorgeirsson, 2016). These leading experiments of Reykjavik Energy are paving the way for future zero emission geothermal power plants. An alternative solution to deal with the CO_2 emission is to use it for production of synthetic fuel or to fix it in plants in greenhouses.

4.2 Induced seismicity

Induced seismicity is commonly a concern for geothermal energy production in the world, especially where hydraulic stimulation is applied. In general, this was not the case for Iceland until

recently. Earthquakes are quite common in Iceland and people living close to the plate boundary and geothermal fields are used to observe small earthquakes now and then (Fig. 9). Therefore, it was generally presumed that induced seismicity would just occur as small additional noise to the background seismicity and not disturb the public seriously.

Monitoring of earthquake have shown that production related earthquakes, usually less than magnitude 2.0, are common at all the high-temperature fields and at the low-temperature fields that are located directly at plate boundaries (Flóvenz et al., 2015).

Larger earthquakes with magnitude in the interval 5.8 to 7.0 have been observed in relation the transform zones where strike slip earthquakes prevail, 21 events in the South Iceland Seismic Zone during the past three centuries (Halldórsson et al, 2013a). and 9 events close to and offshore the north coast over two centuries (Halldórsson et al, 2013b).
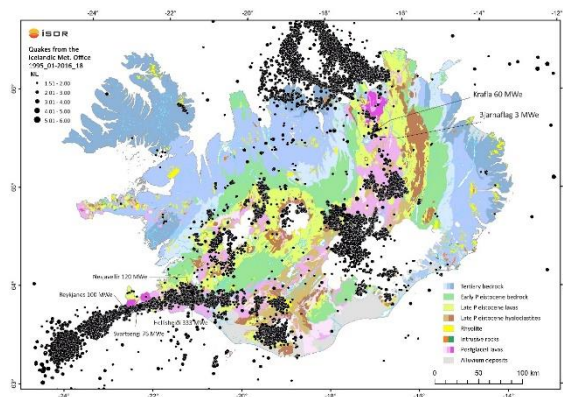
Figure 9. Seismicity in Iceland from 1995 to 2016 showing earthquakes of magnitude 1.5 and larger (Flóvenz and Jónsdóttir, 2016). Data are from the Icelandic Meteorological Office.

The production of geothermal fluid from the ground disturbs the hydraulic pressure in the geothermal reservoir and deforms the local stress field. The production itself lowers the fluid pressure and should therefore increase the overall rock strength and possibly delay impending earthquakes. Sometimes the production is

periodic within the year causing sinusoidal variation in the fluid pressure that might modulate the seismicity and affect the timing of an impending large earthquake. A 6.6 earthquake in Iceland in the year 2000 might have been an example of such an effect. (Flóvenz, et al., 2015). Furthermore, the production itself leads sometimes to land subsidence that might cause earthquakes. On the contrary, fluid injection into the reservoir, elevates the reservoir fluid pressure and can lead to earthquakes. This applies to reinjection of geothermal fluid to counteract the pressure drop caused by the production or to stimulate a reservoir to increase the well productivity or to dispose effluents from the a power plant.

All major geothermal power plants in Iceland are located within high temperature fields that are associated with active volcanoes on the plate boundaries. They all have high natural seismicity due to tectonic and volcanic activity and injection induced earthquakes are recorded in all cases where reinjection is practiced. The level of the induced seismicity is however different from one field to another. The expected maximum magnitude for a natural earthquake is between 4.0 and 6.0 for the different fields. Therefore it is possible that medium to large magnitude earthquakes might be triggered by injection of fluid into the high temperature fields. This happened in the fall of 2011 when a large-scale reinjection was initiated at the Hellisheiði power plant. It triggered repeatedly intense swarms of earthquakes up to magnitude 3.9 (Bessason et al., 2012) that were strongly felt in neighboring village and annoyed people severely but did not cause any damage. Prior to that induced earthquakes up to magnitude 2.5 were observed during circulation loss when the injection wells were drilled (Ágústsson et al., 2015) witnessing that the crust was critically stressed.

The experience has shown us that the presumption of neglecting the potential of annoying or damaging earthquakes triggered by reinjection is not valid. Therefore, the geothermal operators must manage their geothermal

reservoirs with the possibility in mind that their activity can trigger impeding medium to large magnitude earthquakes, especially if injection by hydraulic stimulation is applied. Based on this experience the authorities have introduced guidelines for reinjection operations in line with what is being done in the international community.

To deal with this challenges ÍSOR has in co-operation with Reykjavík Energy and other energy companies participated in international projects. They aim to mitigate the risk of damaging induced seismicity and perform well stimulation under strict control using a sort of traffic light system to manage the stimulation. Example of such projects are the EU-supported projects GEISER (see geiser-fp7.fr/default.aspx), DESTRESS (destress-h2020.eu/en/home/) and COSEISMIQ (geothermica.eu/projects/coseismiq/).

4.3 Thermal casing damages

High temperature wells might experience large variation in temperature during their lifetime. The temperature is often 300-340°C in conventional reservoirs but can be 450-500°C in superhot wells that exploits the deeper part of the high temperature systems. Conventional high temperature wells are typically cased with steel casing to 1000-1500m dept and in extreme cases to 3000m depth. The steel casings are cemented to the surrounding rock. When they heat up the steel pipes are subject to large thermal stresses that may lead to irreversible plastic deformation of the casings and even cause a collapse with buckling of the casing itself. If the casing is cooled down again, which sometimes is necessary, it contracts, and large tensile stresses occur which can lead to tensile rupture of the casing that mostly occur at casing joints. Consequently, the wells might be destroyed and abandoned as they might leak and cause steam explosions in the wellfield. Such casing damages are common and is one of the main obstacles for

utilization of superhot geothermal systems in the roots of the high temperature fields.

It is of utmost importance for the geothermal industry to solve this casing problem if superhot systems are going to be exploited in the future. The most promising concept is that of flexible couplings that are used to connect individual casing pipes (Thorbjörnsson et al. 2017). This solution was proposed and patented by the expert team of ISOR. It enables well designers to account for thermal axial stresses without designing for plastic strain and thereby reduce the risk of plastic deformation or collapse during warm up and production of the well. The basic concept is to allow each casing segment to expand into the coupling during the warm-up of the well and the coupling will close after reaching calculated temperature for the given coupling and build up pressure to ensure tight connection. If the wells cool down later the coupling will open again and prevent tensile rupture.

The casing damage problem is presently being dealt with by several collaboration projects supported by the Horizon 2020 program of the European Union. (e.g. projects GEOWELL http://geowell-h2020.eu/, DEEPEGS https://deepegs.eu/work-packages/, GeConnect https://www.geothermalresearch.eu/geconnect/about/) The laboratory tests of the concept have been quite successful and a full-scale demonstration test will be performed in the near future.

4.4 Nature conservation

The geographic location of Iceland together with its spectacular landscape formed by interaction between glaciers, water, plate movements and volcanic activity make the Icelandic nature unique. This applies not the least to the high temperature areas of Iceland that are usually a part of a magnificent landscape of the volcanic zone where the surface expression of geothermal activity forms of colourful alteration minerals, hot springs, mud pools and steam vents.

Figure 10 Boiling ground in Grensdalur in S-Iceland, a popular tourist attraction.

Consequently, the Icelanders faces the dilemma of the nature conservation versus exploitation of benign renewable energy resources. Harnessing the high temperature fields has considerable visual impact in form of power plants, drilling pads, pipelines, roads and powerlines. The production itself has only minor effect on the surface and visible geothermal activity will rather increase than decrease. Therefore it is important to design the constructions, pipes and power lines with respect to the landscape, avoid to damage geological formations or vegetation, reduce the number of drill pads by drilling several wells from each pad, and minimize the effect of hot brine and gas disposal.

Already seven major high-temperature fields have been harnessed, most of them close the habituated areas and outside the central highlands. To build power plants in the central highlands will be controversial as there is a strong will to protect the highlands from further human activity apart from tourism. Some of the larges known high temperature fields are already in protected areas and there are plans to extent the present national parks to cover most of the central highlands. This will put tight constraints on possible new geothermal power plants in Iceland. The main challenge for the future is to find a reasonable balance between nature conservation and harnessing the renewable energy resources of Iceland.

5 THE FUTURE OF GEOTHERMAL ELECTRICITY PRODUCTION

5.1 *The geothermal potential in Iceland*

The volcanic rift zone of Iceland (Fig.6) covers 32,000 km^2 where only 600 km^2 belongs to known high temperature geothermal systems. The remaining part of the volcanic rift zone was defined as 2,150 km^2 of active areas with recent tectonic or volcanic activity and 29,250 km^2 belong to non-active areas. Pálmason et al. (1985) made a volumetric assement of the geothermal potential in Iceland and by taking into account the accessibility factor, likely recovery and utilization factors, the stored energy above 3 km depth was estimated to give 3500 MW$_e$ for 50 years from the known high temperature sytems alone. Similar values are 8400 MW$_e$ for the active areas and 24,100 MWe for the non-active areas within the volcanic rift-zone (Pálmason et al. 1985). Until now power production has been limited to the known high temperature fields where the total installed power is presently 752 MW$_e$ from 7 power stations in 6 defined high temperature fields. The limits of 3 km depth in the assessment in 1985 was based on the geothemal drilling technology at that time. Now, over thirty years later, it is quite possible to drill to 5 km depth or even greater in Icelandic geothermal areas. This almost double the potential of the volcanic riftzone (Flóvenz, 2018).

There are in principle four ways to increase the electricity production from geothemal resources in the volcanic zone of Iceland:

Firstly, to increase production in the presently utilized fields and their pheriphery. This is a possibility in some cases but it is considered only to offer a moderate increase in the energy production.

Secondly, to start production in new and unexploited fields. This could lead to considerable increase in electricity production but as most of these fields are on areas that are already protected or are likely to be protected soon this possibility is not realistic.

Thirdly, to extract energy from deep roots of the present utilized systems by drilling to 4-5 km depth for superhot steam, even at near-magmatic temperature.

Fourthly to drill to 4-5 km depth in the active areas of the volcanic riftzone but in areas outside the known high temperature fields.

The two last possibilities are discussed in the following sections.

5.2 *Exploiting the deep roots og volcanoes*

The Icelandic geothermal industry has put considerable effort into exploration of the deeper part of the already harnessed high temperature fields. There, very high temperatures are expected, even close to magmatic conditions, and the extracted fluid might be superheated or in supercritical state. Alternatively, the deep superhot wells could be used as reinjection wells where the cold injected fluid extracts the energy from 3-5 km depth and is captured in shallower wells. The aim is to respond to the increasing environmental awareness and to utilize better the infrastructure at each power plant. The Iceland Deep Drilling Project (IDDP), a joint effort of the main power companies and the government of Iceland, has been the core of this development. Friðleifsson et al (2014) have described the concept of IDDP. The project has gained high international attention where a large number of scientist and international funding bodies have participated.

Two wells have already been drilled under the IDDP project, the IDDP-1 in Krafla (Friðleifsson et al. 2015) and the IDDP-2 in Reykjanes (Friðleifsson et al. 2017). Although number of problems rose during drilling and testing of the wells, these projects have tough many lessons. They have visualized challenging problems and confirmed that it is a realistic option to extract energy from the superhot roots of the high temperature geothermal systems.

The main lesson learned are at present:

- It is possible to drill into magma bodies beneath the high temperature reservoirs.

Well IDDP-1 penetrated a magma body just below 2 km depth.

- A zone of high permeability was found at the top of the magma body yielding 450°C hot superheated steam that could give up to 36 MW$_e$ from the single well. (Friðleifsson et al. 2015)

- The steam contained chlorine gas that makes the fluid extremely corrosive when it starts to condense into small droplets. Experiments to scrub the fluid at the surface were promising (Markusson and Hauksson, 2015).

- Due to corrosive failure in wellhead equipment, it was necessary to kill the well after 28 months of flow testing. Then serious casing damages were observed that are most likely due to thermal expansion and contraction of the casing, probably also due to corrosion and improper cementing of the casing. It was not possible to repair the well and it was cemented and abandoned.

- Well IDDP-2 was successfully drilled to a depth of 4.6 km. No magma was detected which was in agreement with the geophysical exploration prior to drilling.

- Loss of circulation or feed zones were observed as deep as 4.5 km in IDDP-2 according to temperature logs (Friðleifsson et al. 2017).

- Casing damages occurred also in IDDP-2, most likely due to thermal stresses in the casing. This has prevented further testing of the well and reliable measurement of the bottom hole temperature, but it is clearly well above 430°C (Friðleifsson et al. 2017). These lessons are source of optimism for future energy extraction from the deep roots of the high temperature fields in Iceland and have a world-wide relevance. At the same time, they tell us that we have technical and scientific challenges to

meet in order to realize the dream of this kind of projects.

5.3   Exploring the deep volcanic riftzone

The idea of exploring for applicable geothermal resource at 2-5 km depth in the volcanic rift zone is based on the assumption of high temperature gradients of (>100°C/km) beneath the permeable zone that cover the uppermost 1-2 km within the volcanic rift-zone. Furthermore, the existence of active fault systems within the volcanic rift-zone indicate high possibilities for considerable fracture permeability. If this is true the ideal reservoir temperature of 230-300°C can be expected between 2 and 5 km depth. Then the obvious question is how we can estimate the real temperature in this depth interval and its spatial variations within the rift-zone. To do it by drilling numerous 1-2 km wildcat exploration wells would be far too expensive so it is necessary to rely on the geophysics, especially resistivity measurements and earthquake seismology.

The best method to measure the resistivity of the crust down to 5-10 km depth in the volcanic rift-zone is to use a combination of time-domain electromagnetic soundings (TEM) and magnatotelluric soundings (MT).

Assuming that the inversion process of the TEM/MT data gives us reliable resistivity models, the next step is to interpret the resistivity structure in terms of relevant geothermal parameters. It is a complicated task and requires understanding of the still debated conduction mechanisms in porous rock and its dependence on various parameters. The process of electrical conduction in basaltic crust has been investigated for a long time, both experimentally and theoretically and still is (e.g. Levy et al. 2018 and references there in). The highlights of these research activities are the complex role of smectite and other clay minerals (e.g. Levy et al. 2018, Flóvenz et al. 1985, Árnason et al. 2000), the dominance of surface or interface conduction
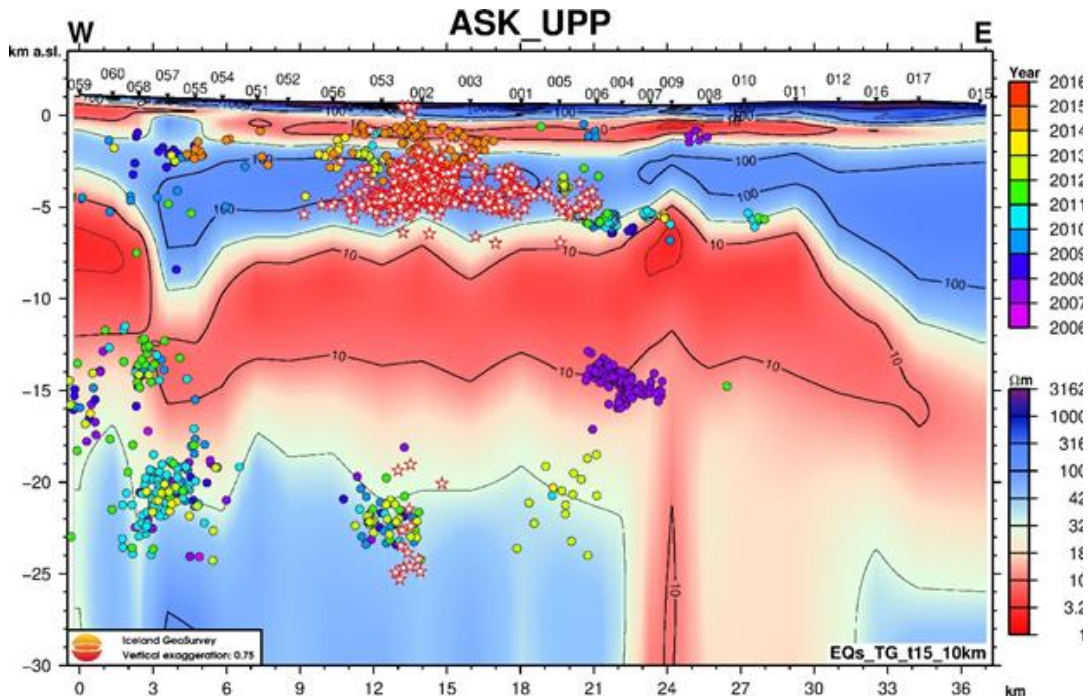
Figure 11. A West-East resistivity cross section from the Askja high temperature field in the west to the eastern border of the volcanic rift-zone. The dots are the seismic events. Note the absence of seismicity within the deep conductive layer and up-doming of it under the high temperature field in Askja. Figure from Vilhiálmsson and Flóvenz (2017).

and its high temperature dependence (e.g. Kristinsdóttir et al, 2010) and the measurements of resistivity of porous rock above 300°C (e.g. Nono et al. 2018).

Most of the known high temperature fields in Iceland have been mapped by resistivity soundings (e.g. Árnason et al. 2010). They show generally a very typical structure of a shallow up-doming layer of very low resistivity covering a core of higher resistivity. It has been explained as a layer of high smectite content of the basaltic rock caused by hydrothermal activity. The increase in resistivity below corresponds to the top of the more resistive chlorite alteration zone (e.g. Árnason et al. 2000). It is known that this change in mineralogy occur at temperature close 230°C. Therefore, we can map the 230°C isothermal surface in the high temperature system provided that it has not cooled at later time.

Outside the known high temperature fields but within the volcanic rift-zone, another layer of low resistivity has been observed at 5-10 km depth, deepening further away from the rift axis. (e.g. Beblo and Björnsson, 1980). This structure has been mapped in more details in a small part of the volcanic rift zone of NE-Iceland as shown in Figure 6 (Vilhjálmsson and Flóvenz, 2017). It extends eastwards from the eastern boarder of the Askja central volcano and high temperature system to the boarder of the volcanic rift-zone.

The section shows the typical resistivity structure of the volcanic rift-zone;

• High near surface resistivity of the ~1 km thick permeable fresh basaltic material,

• A conductive layer at roughly 2 km depth showing the smectite alteration zone,

• A more resistive layer, starting from 2-3 km depth, corresponding to the chlorite alteration zone.

• A deep conductive layer at roughly 7-15 km depth, doming up below Askja.

• Elevated resistivity below roughly 15 km dept.

• Possible a column of low resistivity extending further downwards.

The dots on the figure denote hypocenters of microearthquakes (Soosalu 2009 and Greenfield 2016). They show that the deep conductive layer appears aseismic but at the same time S-waves from location beneath the layer propagate normally through it. This can be interpreted as the layer is close to the brittle ductile boundary but far below the solidus of the material. The estimated temperature of the top of the deep conductive layer is therefore likely to be close to or above 500°C (Vilhjálmsson and Flóvenz, 2017). Hence, mapping the top of the deep conductive layer puts constraints on the temperature in the upper crust of the volcanic rift-zone.

Another constraint on the temperature distribution can be estimated from the top of the chlorite zone as represented by the bottom of the upper conductive layer. This temperature is close to 230°C provided that the alteration minerals are in thermal equilibrium (Flóvenz et al, 2012).

These two constraints on the temperature distribution open up the possibility to use TEM/MT soundings to map the spatial temperature distribution within the volcanic rift zone. By systematic mapping of the resistivity it is possible to explore for the best sites for future development of the geothermal power sector in Iceland.

6 CONCLUSIONS

Almost one century of geothermal development in Iceland has led to great success where 90% of houses in the country are heated by geothermal water at very low cost. The households in Iceland pays only 30-40% of what they would have to pay for same amount of energy in the other Nordic Capitals. Geothermal energy is also used to produce 27% of the electricity produced in Iceland at competitive cost. The success in Iceland is a result of combination of favourable geological conditions and continuous research and development activity over long time.

The Icelandic geothermal industry has faced many challenges on its way to the present stage and has still challenges to meet. They include development of methods to extract energy from the superhot roots of the volcanic geothermal systems where magmatic conditions might be faced, sequestration of CO_2 and H_2S in order to create zero emission power plants, mitigation of induced seismicity, development of methods to prevent casing damages in high temperature wells and finding ways to combine geothermal energy production with nature conversation..

7 ACKNOWLEDGEMENTS

8 REFERENCES

Ágústsson, K., Kristjánsdóttir, S., Flóvenz., Ó.G., Guðmundsson, Ó. 2015. Induced Seismic Activity during Drilling of Injection Wells at the Hellisheiði Power Plant, SW Iceland. *Proceedings World Geothermal Congress 2015 Melbourne, Australia*, 10p.

Ármannsson, H., Fridriksson, Th.,. Kristjánsson, B.R., 2005. CO_2 emissions from geothermal power plants and natural geothermal activity in Iceland. *Geothermics* **34**. 286–296

Árnason, K., Karlsdóttir, R., Eysteinsson, H., Flóvenz, Ó.G. and Gudlaugsson, S.T. 2000. The resistivity structure of high temperature geothermal systems in Iceland. *Proceedings: The World Geothermal Congress*, 923-928.

Axelsson, G., Bjornsson, G., Egilson, Th., Flovenz, Ó.G., Gautason, B., Hauksdottir, S., Olafsson, M., Smarason, O.B., Saemundsson, K. 2005. Nature and Properties of Recently Discovered Hidden Low-Temperature

Geothermal Reservoirs in Iceland. 2005 Anatlya, Turkey, 10p.

Beblo, M. and Björnsson, A. 1980. Model of electrical resistivity beneath NE-Iceland and correlation with temperature. *Journal of Geophysics*, **47**, 184-190

Bessason, B., Ólafsson, E.H., Gunnarsson, G., Flóvenz, Ó.G., Jakobsdóttir, S.S., Björnsson, S., Árnadóttir,Þ. 2012: Verklag vegna örvaðrar skjálftavirkni í jarðhitakerfum. *Orkuveita Reykjavíkur, report*, 108p.

Bjarnason, I.Th., Menke, W., Flóvenz, Ó.G., Caress, D., 1993. Tomographic image of the mid-Atlantic plate boundary in southwestern Iceland. *J. Geophys. Res*., **98**, 6607–6622.

Bödvarsson, G, 1982. Glaciation and geothermal processes in Iceland. *Jökull*, **32**, 21-28.

Flóvenz, Ó.G., Georgsson, L.S. and Árnason, K. 1985. Resistivity structure of the upper crust in Iceland. *Journal of Geophysical Research*, **90**, 10136-10150.

Flóvenz, Ó.G., Sæmundsson, K, 1993. Heat flow and geothermal processes in Iceland. *Tectonophysics*, **225**, 123-138,

Flóvenz, Ó.G., Hersir, G.P., Sæmundsson, K., Ármannsson, H. and Friðriksson Þ., 2012. Geothermal Energy Exploration Techniques. In:. (ed) *Comprehensive Renewable Energy*, (ed.: Sayigh A) **7**, 51-95, Elsevier, Oxford.

Flóvenz, Ó.G., Ágústsson, K, Guðnason, E.Á., Kristjánsdóttir, S. 2015. Reinjection and Induced Seismicity in Geothermal Fields in Iceland. *Proceedings World Geothermal Congress 2015 Melbourne, Australia*, 15p.

Flóvenz, Ó.G., Jónsdóttir, B. 2016. The Icelandic Experience on Integrated Geothemal Utilization. *Perspectives for Geothermal Energy in Europe* (Ed. Bertani, R.) 77-126. World Scientific Publishing Europe, Ltd, London.

Flóvenz, Ó.G. 2018. Expanding the resource base for high temperature geothermal power production in Iceland. GRC Transactions, **42**, 15p.

Friðleifsson G.Ó., Elders, W.A. and Albertsson, A., 2014 "The concept of the Iceland deep drilling project." *Geothermics*, **49**, 2–8.

Friðleifsson G.Ó., Pálsson B., Albertsson, A., Stefánsson, B., Gunnlaugsson, E., Ketilsson, J. and, Gíslason, Þ., 2015. IDDP-1 Drilled Into Magma – World's First Magma-EGS System Created. *Proceedings World Geothermal Congress*, 12p

Friðleifsson G.Ó. and Elders, W.A., 2017. "Successful Drilling for Supercritical Geothermal Resources at Reykjanes in SW Iceland." *GRC Transactions*, **41**, 1095-1107.

Halldórsson, P., Björnsson, S., Sólnes, J., Bessason, B. 2013a. Suðurland. *Náttúrvá á Íslandi* (Eds. Sólnes, J., Sigmundsson, F., Bessason, B.), 591-609 Viðlagatrygging Íslands/Háskólaútgáfan.

Halldórsson, P., Brandsdóttir, B., Sólnes, J., Stefánsson, R. 2013b. Norðurland. *Náttúrvá á Íslandi* (Eds. Sólnes, J., Sigmundsson, F., Bessason, B.), 591-609 Viðlagatrygging Íslands/Háskólaútgáfan.

Harðarson, B.S., Fitton, J.G., Hjartarson, Á. 2008. Tertiary volcanism in Iceland. *Jökull* **58**, 161-178.

Johnsen, B. 1962. Úr heilbrigðisskýrslum. *Fréttabréf um heilbrigðismál*, **11**, 3-5.

Kaban,M.K., Flóvenz, Ó.G., Pálmason, G., 2002. Nature of the crust-mantle transition zone and the thermal state of the upper mantle beneath Iceland from gravity modelling. *Geophys. J. Int.* **149**, 281–299.

Kristinsdóttir, L.H., Flóvenz, Ó.G., Árnason, K., Bruhn, D., Milsch, H., Spangenberg, E. and Kulenkampff, J. 2010. Electrical conductivity and P-wave velocity in rock samples from high temperature Icelandic geothermal fields. *Geothermics*, **39**, 94-105

Levy, L., Gibert, B., Sigmundsson, F., Flóvenz, Ó.G., Hersir, G.P., Briole, P. and Pezard, P. 2018. The role of smectites in the electrical conductivity of active hydrothermal systems: electrical properties of core samples from Krafla volcano, Iceland. *Geophys. J. Int*. **214**, 1558-1552.

Markusson, S.H. and Hauksson, T., 2015. Utilization of the Hottest Well in the World, IDDP-1 in Krafla. *Proceedings World Geothermal Congress*, 6p.

Nono, F., Gibert, B., Parat, F., Loggia, D., Cichy, S.B. and Violay, M. 2018. Electrical conductivity of Icelandic deep geothermal reservoirs up to supercritical conditions: Insight from laboratory experiments. J.Volcanol.Geotherm.Res.,15p. https://doi.org/10.1016/j.jvolgeores.2018.04.021.

Orkustofnun, 2015. OS-2015-T009-01: Economic benefits of using geothermal energy instead of oil for space heating [data file].

Orkustofnun, 2018. OS-2018-T004-01: CO_2 savings using renewable energy instead of oil [data file].

Pálmason, G., 1973. Kinematics and heat flow in a volcanic rift zone, with application to Iceland. *Geophys. J. R. Astr. Soc.*, **33**, 451–481.

Pálmason, G., Johnsen, G.V., Torfason, H., Sæmundsson, K., Ragnars, K., Haraldsson G.I. and Halldórsson, G.K., 1985. Mat á jarðvarma Íslands (Geothermal Assessment of Iceland). *Orkustofnun Report, OS-085/JHD-076*, (1985), 136p. (In Icelandic with English summary).

Sæmundsson, K. 1979, Outline of the geology of Iceland, *Jökull* **29**, 7-28.

Sigurdardóttir, H., Thorgeirsson, Th.A. (ed), 2016. OR Environmental Report 2015. Orkuveita Reykjavíkur, 91 p

Soosalu, H., Key, J., White, R.S., Knox, C., Einarsson, P. and Jakobsdóttir, S.S. 2009. Lower-crustal earthquakes caused by magma movement beneath Askja volcano on the north Iceland rift. *Bulletin of Volcanology*, **72(1)**, 55.

Thorbjornsson, I., Kaldal, G.S., Gunnarsson, B.S. and Ragnarsson, Á., 2017. A New Approach to Mitigate Casing failures in High-Temperature Geothermal Wells. *GRC Transactions*, **41**, 585-591.

Vilhjálmsson, A.M., Flóvenz, Ó.G. 2017. Geothermal implications from a Resistivity Survey in the Volcanic Rift Zone of NE-Iceland and Comparison with Seismic Data." *Iceland GeoSurvey, Report ÍSOR-20017/065*, 46p.

XVII European Conference
ECSMGE 2019
Reykjavík
on Soil Mechanics
and Geotechnical Engineering

The CarbFix project: Carbon capture and subsurface mineralisation in basalt.

Sigurður Reynir Gíslason
Reasearch Professor, University of Iceland: https://notendur.hi.is/~sigrg/
One of three directors of CarbFix: https://www.carbfix.com/
President of the European Association of Geochemistry http://www.eag.eu.com/

ABSTRACT: All the carbon in the atmosphere, living creatures, and dissolved in the oceans is derived from rocks and will eventually end up in rocks, the largest carbon reservoir on Earth. The carbon moves from one reservoir to another in what is called the carbon cycle. Humans have accelerated this cycle by mining and burning fossil fuel since the beginning of the industrial revolution, causing rising atmospheric carbon dioxide (CO_2) concentrations that are the main cause of global warming. If we burn all fossil fuel on Earth at the past decades rate increase and do nothing about it, most of it will be finished in 250 years and all in 500 years. The peak concentration after 250 years will be greater than 1500 ppm, resulting in acidification of the oceans, climate warming, runaway melting of glaciers and sea-level rise.

The Intergovernmental Panel on Climate Change released a special report last October. There, modelled pathways with no or limited overshoot of 1.5°C rise in temperature above pre-industrial level, call on rapid global net anthropogenic CO2 emissions decline, reaching net zero around 2050, followed by a large-scale carbon dioxide direct removal from the atmosphere. The direct CO2 removal from air will be done by growing plants that turn CO2 into biomass, which is then burned under controlled conditions in power plants, where the CO2 is captured and stored in rocks. This is referred to as BECCS, (Bioenergy with Carbon Capture and Storage). Engineered Direct Air Capture and Storage in rocks will also be employed (DACS).

Carbon dioxide has been captured from concentrated gas streams since 1996. The captured CO_2 is compressed to a liquid stage and injected into sedimentary rocks were it can be stable for centuries and even millions of years. In 2012 the CarbFix research group developed a method where the carbon dioxide is mineralised in basaltic rocks. This is the safest way of storing carbon. This method has been employed since 2014 at the Hellisheidi geothermal power plant in SW-Iceland. In 2017, the CarbFix group employed an engineered Direct Air Capture unit at the Hellisheidi power plant where the captured CO2 was eventually mineralized in the basaltic rocks (DACS). Again, this was the first in the world direct air capture where the CO2 was stored as mineral (DACS). If humanity will be forced to "clean" the atmosphere in the latter half of this century, Iceland could play a significant role in the clean-up.

XVII European Conference
ECSMGE 2019
Reykjavík
on Soil Mechanics
and Geotechnical Engineering

Input of advanced geotechnical modelling to the design of offshore wind turbine foundations

Apport de la modélisation géotechnique avancée au dimensionnement de fondations d'éoliennes offshore

F. Pisanò

Faculty of Civil Engineering & Geosciences / Delft University of Technology, Delft, The Netherlands

ABSTRACT: The offshore wind sector is skyrocketing worldwide, with a clear trend towards wind farms installed in increasingly deep waters and harsh marine environments. This is posing significant engineering challenges, including those regarding the design of support structures and foundations for offshore wind turbines (OWTs). Substantial research efforts are being devoted to the geotehnical design of monopile foundations, currently supporting about 80% of OWTs in Europe. This paper overviews recent work carried out at TU Delft on the numerical integrated modelling of soil-monopile-OWT systems, and its input to the improvement of geotechnical design approaches. The benefits of incorporating advanced soil constitutive modelling in three-dimensional finite element simulations are highlighted, with emphasis on the interplay of cyclic soil behaviour and dynamic OWT performance. Ongoing research on high-cyclic soil plasticity modelling is also presented, and related to the analysis of monopile tilt under irregular environmental loading.

RÉSUMÉ: Le secteur de l'éolien offshore grimpe en flèche partout dans le monde, avec une tendance claire pour les parcs installés à de plus en plus grandes profondeurs et dans des environnements marins particulièrement compliqués. Ces conditions posent d'importants enjeux d'ingénierie, notamment liés au dimensionnement des structures de support et des fondations des turbines éoliennes offshores (OWTs). Des efforts de recherche significatifs sont consacrés au dimensionnement de fondation pour monopieux, qui supportent près de 80% des OWTs en Europe. Ce papier présente un aperçu des travaux réalisés à TU Delft sur la modélisation numérique intégrée de systèmes sol – monopieux – OWTs. Les bénéfices de modèles constitutifs avancés de sol sont mis en évidence, avec une attention particulière sur les interactions entre le comportement cyclique des sols et la dynamique des OWTs. Les recherches en cours sur la modélisation d'un grand nombre de cycles sont aussi présentées, et associées à l'analyse du basculement de monopieux sous chargement environnemental non-monotone.

Keywords: offshore wind energy; numerical modelling; monopile foundations; cyclic loading; dynamics

1 INTRODUCTION

The gradual depletion of hydrocarbon reserves is shifting the global energy mix towards clean and sustainable sources, with solar and wind energies gradually gaining larger shares. The wind energy sector is skyrocketing worldwide, especially with respect to installations in the ocean. Recent technological advances have fostered impressive growth in size and power

output of offshore wind turbines (OWTs) (Fig. 1), along with remarkable reduction of fabrication and installation costs. To date, Europe remains the main player in offshore wind, with the North Sea hosting most wind farms in the continent (~70%), and the Irish Sea, Baltic Sea and Atlantic Ocean witnessing new developments (WindEurope, 2018). Discussions about extending offshore wind farming to the Mediterranean Sea are also ongoing (Balog et al., 2016).

Owing to extensive research started in the late 1990s, offshore wind technology is nowadays mature in many areas, and constantly looking forward to new challenges. Reportedly, latest offshore wind projects are developing in waters of increasing depth and distance from the shore, as illustrated in Fig. 2 for bottom-fixed wind farms in Europe (WindEurope, 2018). The trend towards "deeper & farther" is instrumental to building wind farms with larger power output, or sometimes simply unavoidable in presence of large water depths close to the shore (Rodrigues et al., 2015). The latter case is relevant, for instance, to recent offshore wind plans in the United States and Japan (Jacobson et al., 2015; Ushiyama, 2018), and has promoted in the last decade considerable studies regarding floating wind farms (Castro-Santos & Diaz-Casas, 2016) – not considered in this paper.

Installations in deeper waters imply harsher environments and loading conditions, and thus serious technical challenges regarding the design of support structures and foundations. Restricting attention to the case of bottom-founded (i.e. non-floating) OWTs, a number of foundation setups have been proposed over the years, including deep and shallow foundations assembled as either single or compound units (Byrne & Houlsby, 2003) (Fig. 3). Discussions about their suitability still take place at most international geo-events, during themed sessions dedicated to the testing, analysis and design of OWT foundation systems – see for instance Pisanò & Gavin (2017).
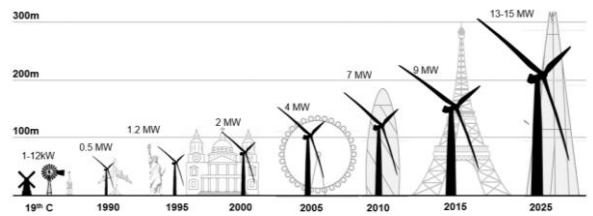
Fig. 1. Evolution of wind turbine size and power output (from Bloomberg New Energy Finance)

About 80% of all OWTs in Europe are founded on monopiles (MPs), tubular steel piles of large diameter (~5-10 m) and embedment ratio (embedded length/diameter) in the range from 3 to 6 (Fig. 4). Bigger OWTs in deeper waters require larger monopiles – expected to reach up to 15 m diameter in the future – depending on site-specific soil conditions and environmental loading from wind and waves. Furthermore, recent developments in south-eastern Asia, e.g. in Taiwan (Zhang et al., 2017), are drawing attention to the design of earthquake-resistant structures and foundations (Kaynia, 2018).

At current state of practice, monopiles of 8-10 m diameter for 30 m water depth can easily require for their fabrication more than 1000 tonnes of steel. As foundation costs still amount
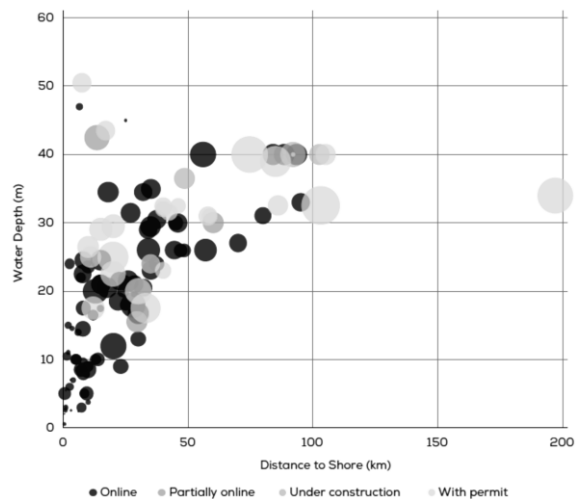
Fig. 2. Water depth and distance to shore of bottom-fixed offshore wind farms, organised by development status (modified after WindEurope, 2018)
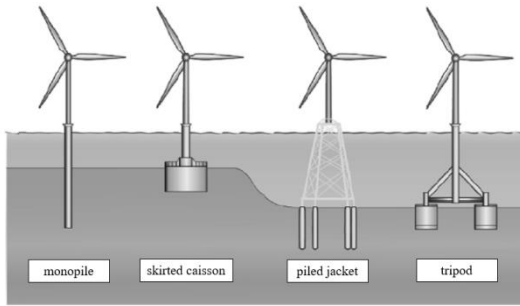
Fig. 3. Most common foundation concepts for bottom-fixed OWTs (modified after Kaynia, 2018)

to 30-40% of the capital expenditure, the industry is strongly driven towards optimisation (Doherty & Gavin, 2011).

The present paper summarises recent TU Delft research regarding OWT foundations and their analysis via advanced numerical modelling. After introducing geotechnical drivers for MP design (Section 2), theory and set-up of 3D finite element (FE) models for OWT-MP-soil systems are overviewed in Section 3, with focus on the case of MPs in sandy soils; Section 4 illustrates how advanced 3D FE modelling can fruitfully serve the non-linear dynamic analysis of OWTs,
and provide precious input to improve existing design tools; the open issue of predicting MP tilt under environmental loading is addressed in Section 5, and related to ongoing research on the constitutive modelling of high-cyclic sand behaviour. The main goal of the paper is to point

out how advanced numerical modelling can impact the understanding of soil-structure interaction in OWTs, and promote enhanced geotechnical design for further cost-reduction.

2 DESIGN OF MP FOUNDATIONS

Monopile dimensions (length, diameter, wall thickness) must be designed to guarantee safe performance under OWT loads, in presence of surrounding soil reactions (Arany et al., 2017; Bhattacharya, 2019). At present, the main industry guidelines for MP design are those in the DNVGL-ST-0126 document (DNV-GL, 2016), prescribing the following design checks:

1. the first natural frequency of the global OWT-MP-soil system must fall within prescribed limits, and ensure *soft-stiff* behaviour (Fig. 5);
2. MPs must not fail under prolonged loading during the whole OWT operational life (FLS, Fatigue Limit State);
3. MPs must not fail under loads of exceptional magnitude (ULS, Ultimate Limit State);
4. MPs must remain fully usable under ordinary loading, i.e. only limited deformations are allowed (SLS, Serviceability Limit State).

While checks 2-4 underlie usual limit states for offshore structures, check 1 is a peculiar design requirement for OWTs. Undesired resonances are to be avoided by keeping f_0 (global natural frequency associated with the first bending mode) within the f_{1P}-f_{3P} range – f_{1P} is the rotor revolution frequency, while f_{3P} (for three-bladed OWTs) the frequency of the aerodynamic pulses induced by the passage of each blade (*shadowing effect*). Setting $f_{1P} < f_0 < f_{3P}$ is commonly referred to as *soft–stiff* design, as it combines a stiff superstructure with a more compliant foundation.

Checks 1 and 2 are mostly dictated by soil behaviour at small strains, whereas check 3 relates to the non-linear, near-failure regime. Check 4 is transversal to different conditions, though mostly relevant to normal operations.

Fig. 4. OWT MP at Port of Rotterdam (Netherlands)
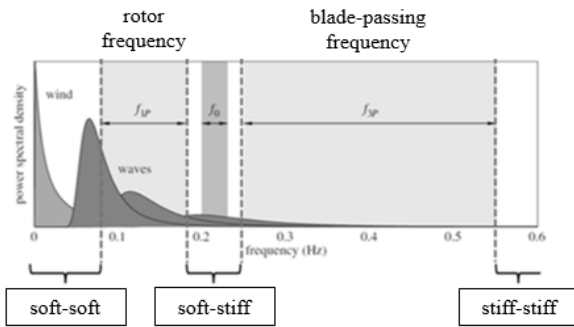
Fig. 5. Excitation ranges in the frequency-domain and design set-ups associated with different OWT and foundation stiffness (modified after Kallehave et al., 2015)

Performing the above design checks is highly challenging in presence of realistic environmental cyclic loading (ECL). ECL is known to mobilise non-trivial aspects of soil behaviour, such as variations in stiffness and strength, energy dissipation, build-up of pore water pressures, and accumulation of permanent deformations (di Prisco and Wood, 2012). For instance, cyclic soil deformations may induce unacceptable monopile tilt (Abadie et al, 2018), a serviceability issue (check 4) that is often mitigated through larger MP embedment depth. Uncertainties about cyclic soil behaviour lead to conservatism in design, i.e. non-optimal use of steel.

MP design for offshore wind projects is commonly performed via *p-y modelling*, i.e. by lumping soil reactions along the MP into distributed spring elements. The DNVGL-ST-0126 document (DNV-GL, 2016) questions the suitability of existing p-y models (e.g. from API, 2014) for stiff piles, and recommends more advanced experimental and numerical studies to "*better assess the possible failure modes, drainage mechanisms, effective stresses and the effects of high- or low-level cyclic loading*". Although the PISA project has recently released new monotonic p-y curves for MPs (Byrne et al., 2019), further work seems still needed for geotechnically sound design of MPs under ECL.

About filling such knowledge gaps, the research agenda by the European Academy of Wind Energy (EAWE) indicates the road for moving offshore wind geotechnics forward (van Kuik et al., 2016). In Section 8 (*Hydrodynamics, soil characteristics and floating turbines*) the Authors observe: ''*What is the amount of soil damping for an offshore turbine? Is it possible to estimate soil damping from first principles, like from numerical simulation with solid elements? Improved insight could lead to major breakthroughs like a possible pile eigenfrequency fine tuning through varying ramming depth as a function of soil characteristics and other key variables*''. At a first glance, the EAWE agenda points to the chance of studying soil mechanisms and energy dissipations in OWTs (*damping*) through 3D numerical models (*solid elements*). Ultimately, van Kuik et al. (2016) support the use of advanced numerical analysis as a way to gain deeper insight into governing mechanics, and promote the improvement of design methods.

The EAWE agenda inspired the research thread overviewed herein, about the advanced numerical modelling of OWT foundations.

3 INTEGRATED 3D FE MODELLING OF OWT-MP-SOIL SYSTEMS

This section covers the set-up of integrated 3D FE models of OWTs, including turbine tower, foundation and soil. The developments presented hereafter are aligned with the EAWE research agenda (van Kuik et al., 2019), in an effort to help unveil the role of several geotechnical factors in OWT design. The importance of integrated modelling is nowadays widely acknowldged in relation to complex structural systems, among which bottom-founded offshore structures offer a notable example (Bienen and Cassidy, 2006; Aasen et al., 2017; Pisanò et al., 2019).

The highest level of OWT model integration – i.e. including structure, water, air and soil – is not pursued herein. Emphasis is on building 3D

FE models with advanced representation of non-linear soil behaviour and cyclic/dynamic soil-MP interaction.

3.1 Governing equations and model set-up

Fig. 6a illustrates the idealisation of a MP-supported OWT subjected to wind/wave loading. As full integration of water and air in the modelling is not considered, aero- and hydro-dynamic loads are to be provided as an input, with no two-way interaction between such loads and structural vibrations. Established approaches for determining external loads on OWTs are described in Bhattacharya (2019). In the lack of fluid-structure interaction modelling, water added mass effects (inertial interaction) can be simplistically introduced through water lumped masses, e.g. as proposed by Newman (1977).

The same system in Fig. 6a is presented in its discretised FE version in Fig. 6b, formed by the following components (Corciulo et al., 2017a):

- OWT tower plus the portion of the pile above the mudline modelled as a Timoshenko beam. For realistic OWT modelling, beam elements with mass density and stiffness variable along the elevation are normally used, with the addition of lumped masses for RNA (Rotor-Nacelle Assembly) and equipment (flanges, transition piece, working platforms, etc.) (Kementzetzidis et al., 2019a);
- embedded length of the pile modelled through either 3D solid elements or 2D shells. The use of 1D embedded beams is not recommended, as it would hinder proper representation of 3D soil-MP interaction (e.g. effect of distributed shear stresses, presence of soil plug, bottom shear/moment fixity);
- soil around the foundation represented as a 3D domain discretised via solid elements. Underwater soils are normally water-saturated. They respond to external loading

(a)

(b)
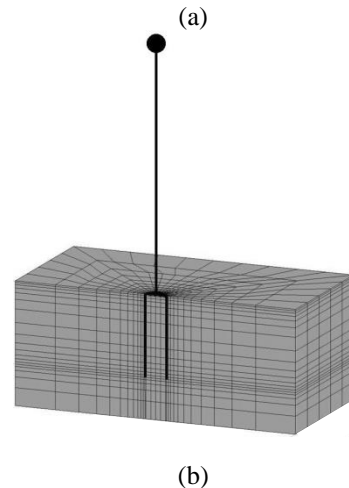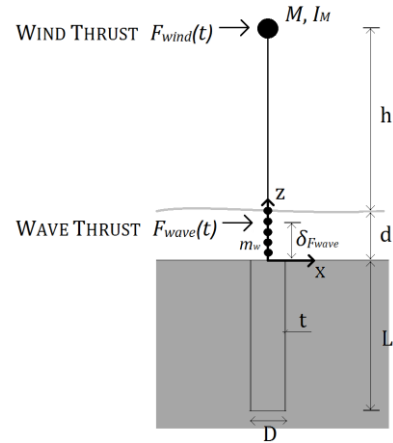
Fig. 6. (a) Idealisation of a MP-supported OWT subjected to wind/wave loading, and (b) associated 3D FE model (modified after Corciulo et al., 2017a)

under drainage conditions that approach the drained or undrained limit depending on their hydraulic/mechanical properties. The dynamic consolidation of saturated soils has been widely studied in the literature after Biot's pioneering work (Biot, 1956a-b). Zienkiewicz et al. (1980) discussed significance and applicability of different mathematical formulations, in relation to the interplay of loading frequency and soil permeability. Based on linear elastic analysis, Ziekiewicz et al. concluded that many problems in earthquake geotechnics – i.e. involving frequencies mostly lower than 10 Hz – can be

tackled through the so-called *u-p formulation* of relevant conservation laws (balance of linear momentum and pore water mass). Based on the assumption of no relative acceleration between pore water and solid skeleton, the u-p formulation is the most economical among all options, as it only requires in 3D domains the determination of three displacement components for the soil (***u***) and a scalar field for the pore pressure (p). Details regarding formulation and numerical solution of dynamic problems in saturated soils can be found in Zienkiewicz et al. (1999); more recent discussions about the suitability of different formulations in two-phase soil dynamics are provided by Jeremić et al. (2008) and Staubach & Machacek (2019). As environmental/mechanical loads on OWTs are rather slow (frequencies lower than 1 Hz, Fig. 4), the use of the u-p formulation in offshore wind problems is not to be questioned.

After space discretisation, the model in Fig. 6a can be used for time-domain simulations under given initial and boundary conditions. To date, dynamic FE models of OWT-MP-soil systems (Fig. 6b) have found only limited application in offshore wind geotechnics, for instance in the works by Cuéllar et al. (2014), Corciulo et al. (2017a), Barari et al. (2017), Kementzetzidis et al. (2019a).

A number of set-up choices can impact the accuracy and computational burden of a 3D FE model of the type in Fig. 6a:

Soil element type. Two-phase soil elements are needed to obtain both displacements and pore pressures in the soil domain. In this respect, it is well-known that only certain types of elements are suitable for hydro-mechanical simulations. To avoid instabilities in the pore pressure field (checker-board modes) under (nearly) undrained conditions, using stabilised elements with linear interpolation for both diplacements and pressures seems the best option. Stabilisation techniques for mixed elements with equal order interpolation have been widely studied for incompressible problems, (Zienkiewicz et al., 1999), as a way to circumvent the so-called LBB

condition and minimise the number of degrees-of-freedom in FE models. Recently proposed *H1P1ssp* elements (stabilised single point) elements (McGann et al., 2015) have been exploited to reduce computational burdens in the present thread of work. As explained in the original publication, *H1P1ssp* brick elements do not only remedy undrained pore pressure instabilities, but can also mitigate inaccuracies related to volumetric locking effects;

Boundary conditions. Hydraulic and mechanical boundary conditions must be set along the lateral surface of the 3D soil domain (Fig. 6b). Since neither the mechanical soil response nor the flow of pore water depend on the absolute water depth, it is possible to set nil pore pressure at the mudline. This is a simplification enabled by the assumption of no-interaction between free and interstitial water (Jeng, 2003). Regarding mechanical boundary conditions, it is worth noting that in presence of low-frequency cyclic loading (Fig. 5), typical concerns about absorbing outgoing waves become less relevant. Indeed, since MP vibrations occurr at frequencies usually lower than the so-called *cut-off threshold* (Graff, 1975), no real waves can be generated and propagated through the soil domain – only *evanescent*, spatially decaying waves can exist. As a consequence, static node fixities work properly as long as lateral boundaries are sufficiently far from the structure – in the order of 5-6 pile diameters (Corciulo et al., 2017a, Kementzetzidis et al., 2019a).

Soil-MP interface modelling. Following the approach by Griffiths (1985), the simplest way to model soil-MP interface is to introduce around the pile a thin layer (~5% MP diameter) of solid two-phase elements, to be assigned material parameters that represent changes (often degradation) in soil properties induced by pile installation – which is not explicitly simulated in the considered *wished-in-place* approach. Better representation of sliding and detachment along the soil-pile interface, as well as of water flow through discontinuities, may be achieved by using widthless interface elements

of the kind proposed by Cerfontaine et al. (2015). A drawback often associated with widthless interface elements is their relatively simplistic formulation from a constitutive standpoint, usualy based on perfect elasto-plasticity and hardly suitable to capture the complex cyclic behaviour of soil-steel interfaces – an interesting remedy to this issue has been recently proposed by Stutz et al. (2017).

Time integration algorithm. Standard algorithms for time integration in solid dynamics are suitable, such as the well-known Nermark's or HHT methods (Hughes, 1987). Algorithmic energy dissipation in time marching is usually beneficial in non-linear computations to damp spurious (non-physical) high-frequencies modes out of the calculated response (Kontoe et al., 2008). It should also be noted that, while implicit time integration combined with Newton-type iterations helps fulfilling global equilibrium, the selection of appropriate time-step size is most often driven by accuracy and stability of stress-strain integration at Gauss points – this aspect stands out most severely when sophisticated non-linear soil models are adopted (Watanabe et al., 2017).

3.2   Modelling of cyclic soil behaviour

The analysis of soil-MP interaction under ECL can only be as accurate as the constitutive modelling of cyclic soil behaviour, obviously a very relevant ingredient in integrated OWT models. Great efforts have been devoted in the past four decades to conceiving plasticity theories for cyclically loaded soils, e.g. in the frameworks of multi-surface plasticity (Mroz, 1967), bounding surface plasticity (Dafalias & Popov, 1975), generalised plasticity (Zienkiewicz & Mroz, 1984), hypoplasticity (Mašín, 2018) and hyperplasticity (Houlsby & Puzrin, 2007). Readers interested in these developments may refer to Prévost and Popescu (1996), Zienkiewicz et al. (1999) and di Prisco and Wood (2012).

The research overviewed in this paper focuses on OWTs in medium-dense/dense sandy soils, a case relevant to offshore wind developments in the North Sea. Special care has been taken about adopting state-of-the-art soil modelling, as shown in Corciulo et al. (2017a,b) and Kementzetzidis et al. (2018, 2019a). Despite fundamental differences in their formulations (Prévost, 1982), both multi-surface and bounding surface models can capture several aspects of cyclic sand behaviour, including stiffness degradation, hysteresis and deviatoric-volumetric coupling (leading to pore pressure build-up when drainage is hindered). However, after testing the performance of the UCSD multi-surface model (Elgamal et al., 2003; Yang et al., 2008), conceptual motivations have later led to embrace the family of SANISAND bounding surface models developed by Dafalias and co-workers. Since the launch of the first SANISAND model (Manzari & Dafalias, 1997), intensive work has been spent to overcome certain limitations of the original formulation, regarding fabric effects, hysteretic small-strain behaviour, response to radial stress paths, influence of principal stress axes rotation (Papadimitriou et al., 2001; Dafalias & Manzari, 2004; Taiebat & Dafalias, 2008; Petalas et al., 2019).

To date, the SANISAND version by Dafalias & Manzari (2004) – SANISAND04 – is still the most widespread with the following features:

- bounding surface formulation with kinematic hardening and Lode-angle dependence;
- adoption of the 'state parameter' concept (Been & Jefferies, 1985; Muir Wood et al., 1994). The model can capture the effects of varying effective confinement and void ratio, and thus simulate the response of loose to dense sands with a single set of parameters;
- contraction-to-dilation transition when the stress path crosses the *phase transformation surface*;
- *fabric tensor* to phenomenologically represent fabric effects triggered by load

reversals following stages of dilative deformation.

As discussed in Section 4, the above model features impact altogether the numerical solution of initial-boundary value problems. However, the conceptual advances fostered by SANISAND developments are not yet conclusive. Current research on offshore foundations (and not only) is continually stimulating the enhancement of cyclic modelling approaches – for example regarding SLS requirements threatened by the accumulation of soil deformations under long-lasting (high-cyclic) ECL. This matter is further addressed in Section 5.

From the standpoint of numerical integration, explicit stress-point algorithms are usually preferred over implicit methods for applications involving cyclic/dynamic loading and, therefore, frequent stress increment reversals. While the Forward Euler algorithm is the simplest in this area, adaptive Runge-Kutta methods with automatic error control should be adopted to combine accuracy and efficiency (Sloan, 1987; Tamagnini et al., 2000).

4 FROM NON-LINEAR SOIL–MP INTERACTION TO OWT DYNAMICS

The modelling concepts introduced in the previous section have been applied to the dynamic analysis of a real 8 MW OWT under different loading and geotechnical scenarios. The main structural details of the OWT – courtesy of Siemens Gamesa Renewable Energy – are provided in Fig. 7; the original design of the foundation – a monopile of 8 m diameter, 27 m embedded length and 62 mm wall thickness – was conceived for installation in North Sea dense sand. Due to the lack of thorough laboratory test data, a homogeneous deposit of Toyoura sand has been assumed, characterised by SANISAND04 model parameters provided by Dafalias & Manzari (2004). This deviation from reality, however, is not believed to prevent

realistic conclusions regarding cyclic soil-MP interaction in water-saturated sand.

The following subsections address different aspects of OWT-MP-soil dynamics as emerging from 3D FE simulations of the 8 MW structure shown in Fig. 7. All results have been obtained through the open-source FE platform OpenSees[1] (McKenna, 1997; Mazzoni et al., 2007) – more details about OWT model set-up are available in Kementzetzidis et al. (2019a). Beyond its proven suitability for dynamic soil-structure modelling, OpenSees includes accessible implementations of stabilised *H1P1ssp* brick elements (McGann et al., 2015) and SANISAND04 (Ghofrani & Arduino, 2018).
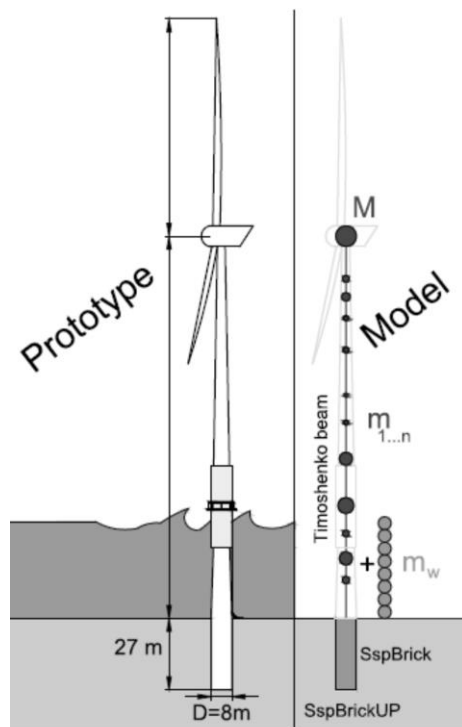
Fig. 7. Structural idealisation of the considered 8 MW OWT (modified after Kementzetzidis et al., 2019a).

---

[1] http://opensees.berkeley.edu

4.1 OWT natural frequency shifts due to storm loading and seabed scour

After setting up the 3D FE model of the OWT-MP-sand system in Fig. 7, the dynamic response of the structure has been numerically analysed in relation to severe environmental loading. In particular, the 10 minutes time histories of wind/wave thrust forces in Fig. 8 have been considered[2] as representation of a 50-years return period storm (average wind speed of 47 m/s), including a 10 m-tall rogue wave hitting the structure after about 70 s. Under such loading conditions it is appropriate to assume the OWT to be in idling state, so that wind loading is mostly due to viscous drag along the structure. As mentioned in Section 2, an important design driver for OWTs is the tuning of the first bending eigenfrequency f_0 of the OWT over its compliant foundation (MP + soil). Advanced 3D modelling can be fruifully employed to foresee deviations of the structural performance from the desired *soft-stiff* range, for instance during exceptional storm events. For this purpose, it is beneficial to inspect the OWT response by means of time-frequency transformation. A suitable option is provided by the so-called S(Stockwell)-transform (Stockwell et al., 1996), e.g. applied by Kramer et al. (1996) to study the cyclic liquefaction of sandy sites.
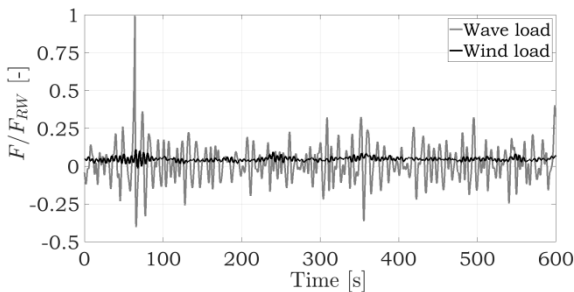
Fig. 8. Wind/wave thrust forces associated with a 50-years return period storm – average wind speed equal to 47 m/s (modified after Kementzetzidis et al., 2019a)

2 Force amplitudes in Fig. 8 are normalised with respect to the rogue wave amplitude (F_{RW}).
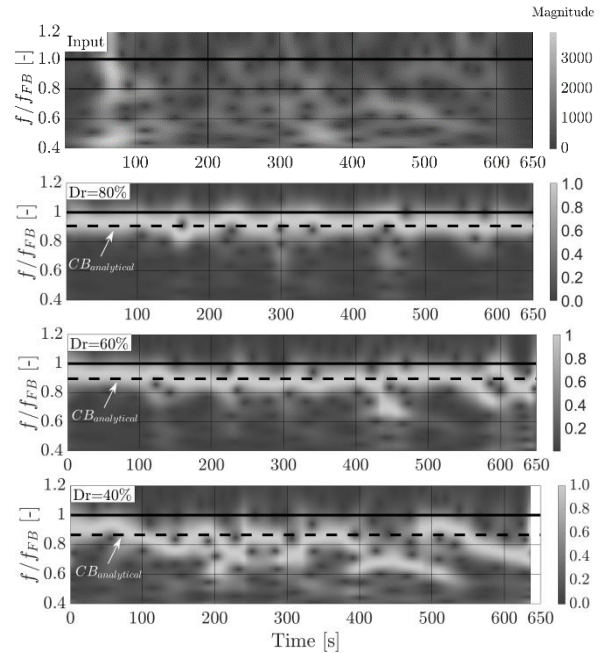
Fig. 9. S-plots of (top) input load (Fig. 8) and (up to bottom) hub displacement for Dr= 80%, 60%, 40%. Fixed-base natural frequency $f_0/f_{FB} = 1$. Colourbars indicate the amplitude of harmonics in the range (0.4–1.2)×f_0/f_{FB}. (modified after Kementzetzidis et al., 2019a)

S-transformation can show how the frequency content (and associated energy levels) of a signal evolves in time, which is here instrumental to tracking f_0 for an OWT subjected to severe ECL.

Fig. 9 reports S-plots of the total horizontal load applied to the OWT (top), and of the OWT hub displacement histories emerging from three different initial conditions – sand relative density (D_r) equal to 80, 60, 40%. Although unrealistic, the case $D_r = 40\%$ is purposely considered to mobilise high soil non-linearity, and thus warn about the detriments of poor geotechnical design. S-amplitudes in Fig. 9 relate the colourbars on the side, and normalised at each step with respect to the maximum value across the frequency axis – this allows to

emphasise the peak frequency[3] with the same light-grey colour along the 10 minutes history. Plotted for the three cases are are also analytical estimates of f_0 on compliant base ($CB_{analytical}$) as per Arany et al. (2017) – dashed lines, see calculation details in Kementzetzidis et al. (2019a). S-plots reveal strong dependence of the OWT response on the initial relative density, as well as on the amplitude and frequency content of the input loading. When the OWT is founded on stiff sand ($D_r = 80\%$), its response in the frequency domain exhibits a single main peak at the first eigenfrequency, with only modest transient shifts; similar conclusions are mostly applicable to the $D_r = 60\%$ case as well. In other words, f_0-shifts should not be a concern when the monopile is designed according to current practice. In this case, even analytical predictions (Arany et al., 2017) return robust lower-bound estimates of the f_0 values resulting from 3D FE simulations.

The OWT response becomes quite different for $D_r = 40\%$. Fig. 9 (bottom) shows in this case a very irregular evolution of the peak frequency. Such a response marks a transition from "resonance-dominated" to "input-dominated" regime – note that the most evident drops in peak frequency at the hub occur at frequencies associated with high energy content in the input S-transform. This kind of structural performance is clearly undesired, and may be regarded here as the outcome of poor geotechnical design.

The global picture emerging from Fig. 9 can be further understood through its relation to the hydro-mechanical response of the soil around the MP. With reference to the check-point B_R in Fig. 10a, Fig. 10b illustrates the time evolution of the local pore pressure u at varying initial D_r (u is normalised with respect to the current total mean pressure p). It is interesting to note that the inception of "chaotic" time-frequency response for $D_r = 40\%$ correlates very well with the time

(t = 300 s) at which the pore pressure ratio u/p goes beyond 0.9 – at point B_R and, it could be
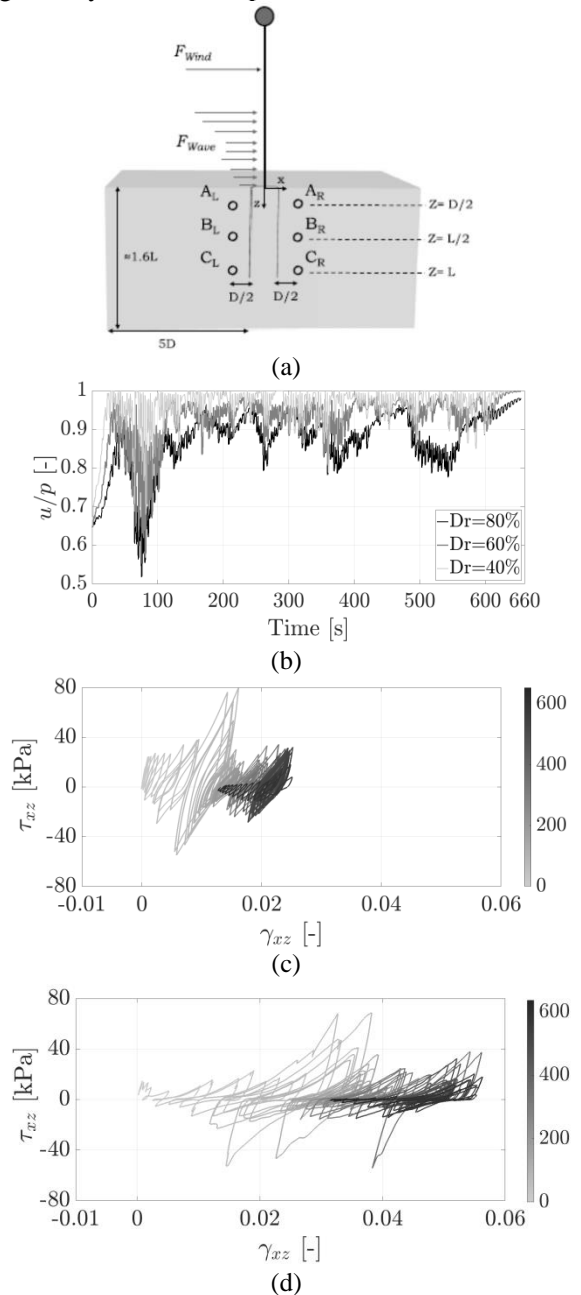
Fig. 10. (a) 8MW OWT model and location of control points; (b) pore pressure evolutions at point B_R; shear stress-strain plots at B_R for (c) Dr = 80% and (d) D_r = 40% (modified after Kementzetzidis et al., 2019a)

---

[3] Frequencies in Fig. 9 are normalised with respect to the natural frequency of the OWT on a fixed base (f_{FB}).

verified, at all other control points in Fig. 10a (see Kementzetzidis et al., 2019a). From that time onward the soil around the pile can only mobilise very low stiffness due to the reduced effective confinement, with an obvious effect on the global compliance of the foundation. The stress-strain response predicted by SANISAND04 is in turn consistent with pore pressure build-up: although significant non-linearity and dissipative behaviour are already evident in Fig. 10c for $D_r = 80\%$, the $D_r = 40\%$ case displays the same features more extremely, with severe loss in stiffness/strength and accumulation of irreversible shear strains. Partial liquefaction (Fig. 10b), however, does not extend to the whole soil deposit: the resistance available at farther soil locations is not fully compromised, with positive impact on the OWT performance.

The mentioned transition from resonance- to input-dominated OWT response (Fig. 9) is also affected by the amount of energy dissipated at the foundation. Large values of foundation damping promotes quick dissipation of transient "eigen-motion" components of the structure, letting external loading dominate structural vibrations. The numerical rotor-stop tests documented in Kementzetzidis et al. (2019a) confirm the high damping generated at the foundation during the 50-years storm in Fig. 8. It is also worth recalling that accurate analysis of dissipative phenomena is highly relevant to FLS checks (Section 2), as they affect the amplitude of the stress levels experienced by the steel during the OWT life.

The numerical results discussed so far support the conjecture of Kallehave et al. (2012): pore pressure effects may negatively impact the OWT dynamic performance, especially in presence of under-designed foundations. However, current design practice would hardly result in a structural response as poor as in the $D_r = 40\%$ case (Fig. 9), unless "unexpected" circumstances arise during operations. A possible event of this kind may be the erosion of
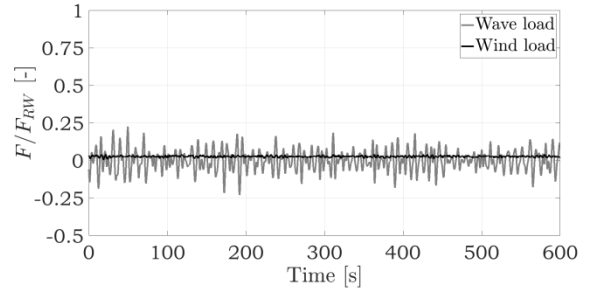
Fig. 11. Wind/wave thrust forces associated with a storm without rogue wave – average wind speed equal to 24 m/s (modified after Kementzetzidis et al., 2019a)

soil around the monopile, also termed *seabed scour*. Scour takes place when near-bed shear stresses are such that soil sediments can be displaced from the original location (Prendergast et al., 2015). DNV-GL design guidelines recommend to perform ULS and SLS checks accounting for likely scour scenarios (scour depth up to 1.3 MP diameters), perhaps caused by ineffective scour protection.

To study the impact of scour on f_0, the same OWT in Fig. 7 has been numerically analysed in combination with the wind/wave loading history in Fig. 11, associated with an average wind speed of 24 m/s – for better comparison, forces are again normalised with respect to the amplitude of the rogue wave in Fig. 8. For simplicity, three scenarios of uniform scour have been considered –removal in the FE model a superficial layer of sand ($D_r = 80\%$) of thickness $H_{scour} = 0$ (no scour), 0.5, 1.25 MP diameters.

In Fig. 12a S-plots are used again to visualise in the time-frequency domain the response at the OWT hub at varying scour depth. Looking at the S-transform of the load input (Fig. 12a-top), it is apparent that increasing H_{scour} has a twofold effect: (i) it causes a reduction of the average ratio between f_0 and the reference fixed-base value f_{FB}; (ii) as H_{scour}/D approaches 1.25, the previous transition towards input-dominated vibrations is observed. These two effects are interrelated sides of the same coin. As soil confinement around the monopile reduces due to

(a)

(b)
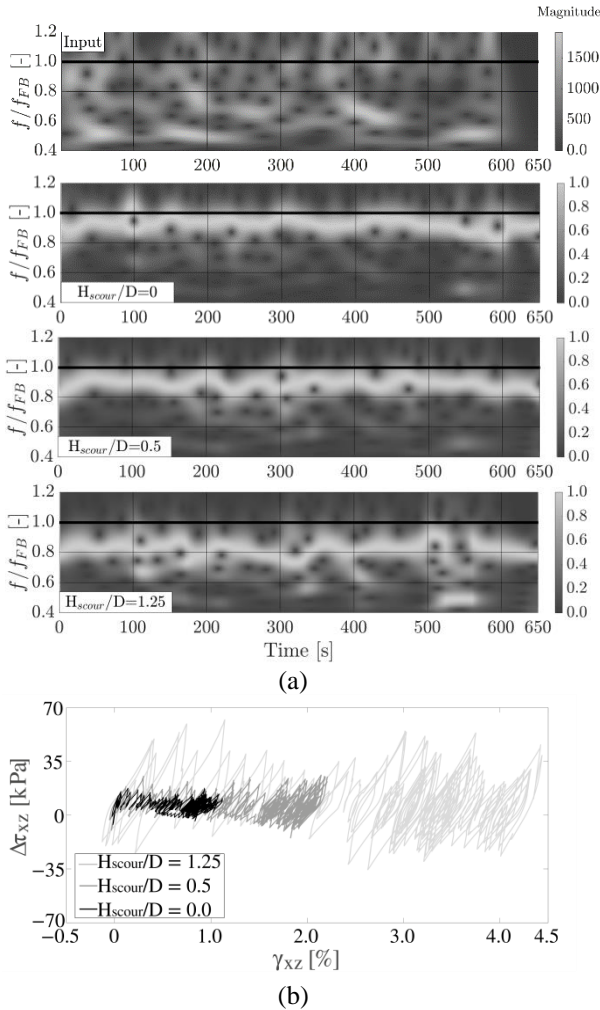
Fig. 12. (a) S-plots of (top) input load (Fig. 11) and (up to bottom) hub displacement for $H_{scour}/D = 0$, 0.5, 1.25 (Dr = 80%); (b) shear stress-strain plots for a soil location next to the MP tip at varying H_{scour}/D

erosion, the remaining soil is strained more severely under the storm in Fig. 11. The hydro-mechanical response of the soil reaches levels of non-linearity that keep the structure from functioning in the intended *soft-stiff* range. This fact is elucidated by Fig. 12b, reporting the local shear stress-strain response in the soil close to the MP tip: increasing dissipation and strain accumulation occur at higher H_{scour}. The results in Fig. 12 appear in line with recent experimental evidence (Li et al., 2018), and

raise design concerns that may not be properly addressed through simplistic models.

4.2 Effects of long-term re-consolidation

In Section 4.1 transient shifts in f_0 have been numerically investigated as a result of short storm events (duration equal to 10 mins), inducing pore-pressure build-up and related cyclic softening of the soil. As a further step, it is relevant to explore whether losses in soil confinement will be permanent or not after the storm. For this purpose, the numerical case presented in Kementzetzidis et al. (2018) is summarised herein. The same reference 8 MW OWT is subjected to the more complex load history in Fig. 13, comprising multiple loading sub-events and after-storm reconsolidation, during which excess pore pressure dissipation can take place. In this spirit, the load history (sum of wind and wave loads) illustrated in Fig. 13 is considered – total duration of more than 2 hours:

1. 150 s of weak loading, mobilising relatively small strains in the soil around the pile;
2. 1200 s of strong storm loading (average wind speed of 24 m/s), inducing transient f_0-drops;
3. 150 s of the previous weak loading to explore after-storm effects on f_0;
4. 1.7 hours (6000 s) of no loading to allow for excess pore pressure dissipation;
5. 150 s of weak loading to detect regains in f_0 enabled by soil re-consolidation. As previous excess pore pressures are mostly dissipated at the beginning of this stage, any differences with respect to pre-storm OWT response can only be due to permanent effects of plastic straining and void ratio changes.

To reduce the burden of a long (sequential) 3D FE simulation, the mesh in Fig. 14, coarser than the instance in Fig. 5b, has been adopted – the soil control points A, B, C are also highlighted in the same figure. The evolution of the frequency content in the OWT response has been monitored through the S-transform of the
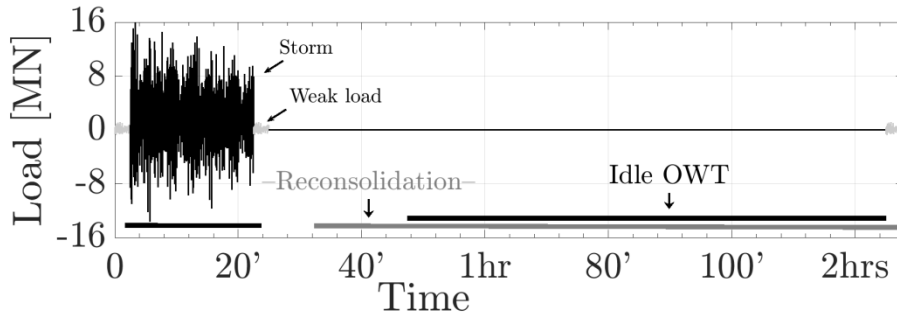
Fig. 13. Assumed load time history – sum of wind and wave thrusts (modified after Kementzetzidis et al., 2018)
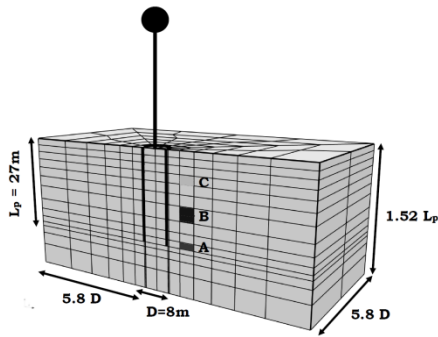
Fig. 14. 3D coarser soil mesh (~950 H1P1ssp bricks) adopted for ~2hrs FE simulation – A, B, C are control points considered for post-processing (modified after Kementzetzidis et al., 2018)
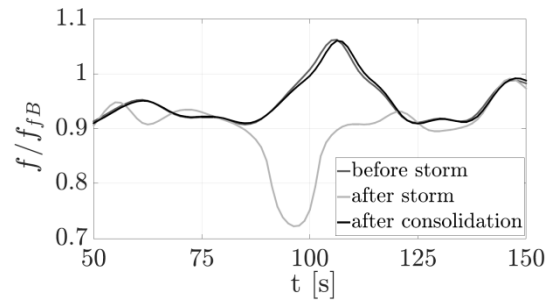
Fig. 16. Time evolution of the OWT peak frequency during the three weak loading stages in the compound load history in Fig. 13 (modified after Kementzetzidis et al., 2018)
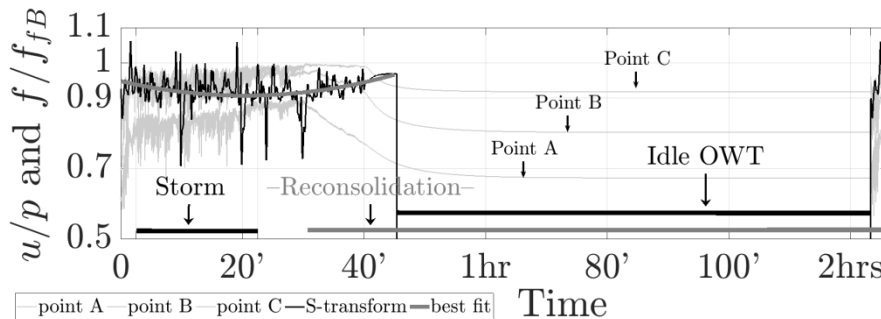
Fig. 15. Thick black line: normalised OWT peak frequency, along with best quadratic fit; dotted lines: u/p ratios at the control points in Fig. 14 (modified after Kementzetzidis et al., 2018)

horizontal displacement at the hub. Since the S-transform returns (time-varying) frequency content within a relevant band, the outcrop values related to the maximum (normalised) S-amplitude at each time-step can be used to track f_0-drops with respect to the fixed-base value f_{FB}. It is evident in Fig. 15 that the OWT experiences transient natural frequency shifts during the storm – as also underlined by the quadratic time-fit of the peak frequency extracted from the S-transform. At the same time, an increase in pore pressure ratio u/p is observed at the three control points indicated in Fig. 14. The local minimum of the fitting parabola lies close to the time of load removal, which hints that f_0 recovery starts at the end of a storm. When free structural vibrations are entirely damped out after the storm, soil re-consolidation starts to dominate the response (Fig. 15). It is noted that f_0 tends to recover its pre-storm value as re-consolidation proceeds. When excess pore pressures are dissipated up to the shallowest control point C, the natural frequency of the OWT appears to be completely restored. As a further confirmation, Fig. 16 shows that pre-storm and after-consolidation responses of the OWT are practically identical as to their S-representation. This leads to claim the existence of a sort of "self-healing" mechanism associated, in the considered analysis framework, to soil re-consolidation.

Obviously, the conclusions drawn after this application example are not only specific of geometrical and loading settings, but also of the adopted SANISAND04 model calibrated for Toyoura sand.

4.3 Towards MP-soil macro-modelling

The examples discussed so far give an impression of the possibilities of advanced geotechnical modelling in offshore wind research. At the same time, however, it should be acknowledged that its direct application to engineering practice is exactly straightforward, due to computational burdens, intrinsic model

limitations, dearth of experimental data for parameter calibration, etc. These and other factors hinder daily use of 3D FE modelling in engineering design, normally based on more user-friendly p-y 1D methods.

It is also possible to formulate "0D" macro-models, in which soil-foundation interaction is lumped into a small number – 6 at most for 3D problems – of constitutive relationships between the forces and displacements describing the statics/kinematics of the considered foundation. This approach – also known as *macroelement modelling* – was first devised for the integrated modelling of mobile jack-up platforms (Schotman, 1989), then applied to a variety of shallow foundation problems (Nova & Montrasio, 1991; Pisanò et al., 2014, Houlsby, 2016), also including dynamic/seismic loading conditions (di Prisco and Pisanò, 2011). More recently, advanced macroelements have been proposed to capture the complex behaviour of piled foundations (Li et al., 2016), with some instances of application to OWT monopiles (Houlsby et al., 2017; Page et al., 2019a,b). Regardless of the specific foundation type, macroelement models need accurate description of soil-structure interaction, including – in cyclic loading problems – stiffness degradation and energy dissipation effects. In presence of higher loading frequencies, such macro-interaction will be also "dynamic", i.e. frequency-dependent.

All the mentioned ingredients are not only challenging to lumpt into a simple 0D (plasticity) formulation, but also to investigate through experimental or numerical studies. Integrated 3D FE models can positively inspire such developments, as shown by Corciulo et al. (2017b) in relation to MP-supported OWTs – Fig. 17a illustrates a simplified OWT model, with soil-monopile interaction condensed into two (uncoupled) springs. With reference to the results discussed in Section 4.1 for the input storm in Fig. 8, it is shown in Figs. 17b-c how the moment-rotation response at the MP head evolves in time, with average stiffness (dashed lines) decreasing as more severe plastic straining

(a)

(b)

(c)
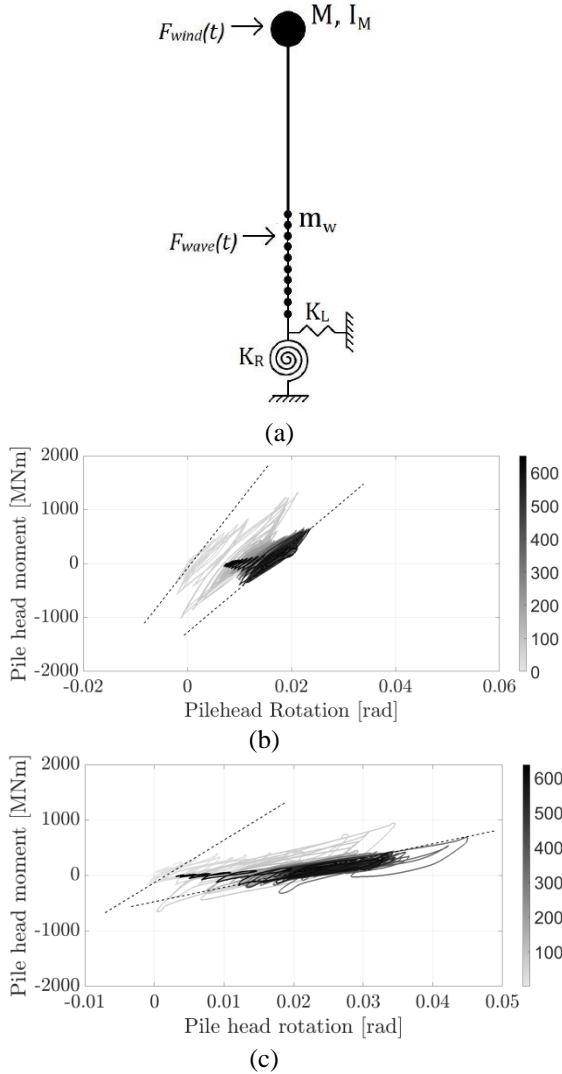
Fig. 17. (a) simplified structural model of a MP-supported OWT (modified after Corciulo et al., 2017b); time-evolution of the rotational MP head stiffness for the storm input in Fig. 8 with Dr equal (b) 80% and (c) 40% (modified after Kementzetzidis et al., 2019a)

takes place in the soil around the foundation. In particular, rotational stiffness degradation[4] from 99 to 79 GNmrad^{-1} and from 60 to 34 GNmrad^{-1} are observed in the cases $D_r = 80\%$ (Fig. 17b)

---

[4] In this illustrative example it was not attempted to distinguish rotational-translation stiffness couplings.

and $D_r = 40\%$ (Fig. 17c), respectively – see details in Kementzetzidis et al. (2019a). This kind of input to macroelement modelling seems particularly valuable, as it already includes non-linear hydro-mechanical effects hard to account for otherwise. It seems prudent to say that, when the soil is strained beyond the *volumetric shear threshold* (i.e. beyond the onset of deviatoric-volumetric deformation coupling), macro-models that neglect pore pressure effects cannot reproduce aspects of MP-soil interaction clearly emerging from advanced 3D FE modelling.

3D FE simulations and derived macro-models can also aid the analysis of OWTs under seismic loading (Kaynia, 2018; Vacareanu et al., 2019), although with additional complexity arising from dynamic amplification and, in sandy soils, cyclic liquefaction. Even when disregarding soil instabilities, the problem of properly representing frequency-dependence in MP-soil dynamic interaction is still open. Work on this specific subject is presently ongoing at TU Delft (Versteijlen et al., 2017; Kementzetzidis et al., 2019b), although not covered here for brevity.

5 HIGH-CYCLIC SAND MODELLING FOR SLS CHECKS IN MP DESIGN

The serviceability of monopiles is also related to preventing their excessive deformation under long-lasting environmental loading – see check 4 in Section 2 (Kuo et al., 2011). The problem of predicting cyclic deformations of laterally loaded piles is not new in geotechnical engineering, but is presently receiving renewed attention with reference to offshore wind developments. In recent years, a number of experimental studies have been devoted to studying the cyclic lateral tilting of stiff piles (Leblanc et al, 2010; Rudolph et al., 2014; Li et al., 2015; Nicolai et al, 2017; Truong et al., 2018, Abadie et al., 2018). Still with reference to monopiles in sandy soils, tilt accumulation laws have been empirically derived from small-scale tests. New insight into the evolution of soil stiffness and post-cyclic MP capacity has

emerged, sometimes contraddicting "traditional beliefs" regarding presumed "degradation" phenomena in cyclically loaded foundations (API, 2014; DNV-GL, 2016).

In parallel with experimental activities, several researchers are also exploring methods for numerically predicting cyclic MP tilt. One of the main challenges in this area is the high number of loading cycles experienced by OWTs during their operational life – up to 10^{7-8} (Leblanc et al., 2010). As a consequence, MP tilt predictions are non-trivial to obtain for at least two reasons: (a) time-domain, step-by-step analysis (*implicit*, in the terminology of Niemunis et al., 2005) is computationally very demanding; (b) even if implicit computations were viable, the literature still lacks fully reliable models reproducing soil behaviour under so-called *high-cyclic* loading. Alternatively, *explicit* methods have also been considered, in which permanent soil straining is directly linked to the number of loading cycles *N*. In this framework, the relationship between accumulated strains and N is given by empirical laws derived from high-cyclic laboratory test results. Valuable examples of explicit methods adopted in the 3D FE analysis of tilting monopiles are provided e.g. by Achmus et al. (2009), Jostad et al. (2014), Wichtmann et al. (2017), Chong & Pasten (2018).

Regarding implicit approaches based on cycle-by-cycle analysis, the experimental evidence provided by the aforementioned studies is being mainly reproduced via special macro-models, as proposed e.g. by Houlsby et al. (2017). However, most recent studies are making a clear point about the need to link global MP-soil interaction to the local high-cyclic behaviour of the soil subjected to a variety of loading and boundary conditions (Cuéllar et al., 2009). Such a need is clearly noted, for instance, by Abadie et al., (2018):
"*It would be of great interest to analyse the soil behaviour down the pile and correlate the macro response observed in this paper to the local pile behaviour, and also to soil element behaviour.*"
or by Truong et al. (2018):
"*It is of interest to examine whether standard cyclic triaxial testing can be used to provide guidance to designers on the likely value of α in other sand types. […] Triaxial cyclic testing can provide insights for designers into expected lateral cyclic response in sands for which no previous experience exists.*".

These statements have been the premises to the TU Delft research on the (implicit) modelling of high-cyclic sand behaviour, and its ongoing application to the 3D FE analysis of pile tilt.

5.1 SANISAND-MS: a memory-enhanced model capturing cyclic sand ratcheting

The SANISAND04 model described in Section 3.2 (Dafalias & Manzari, 2004) allows to look deep into MP-sand interaction, including the interplay of dynamics, sand porosity and pore pressure effects. Owing to this conceptual tool, the performance of OWTs in presence of exceptional external conditions (severe storms, seabed scour, etc.) can be analysed and grasped in a way not allowed by simplified engineering methods. However, despite its notable merits, SANISAND04 is clearly quite far from perfection, with some of its drawbacks being most incovenient for offshore wind foundation problems. Among them, it is important to reliably predict high-cyclic strain accumulation (*soil ratcheting*), as well as the timing and extent of pressure build-up when water drainage is hindered. Regarding the former issue, none of the abovementioned SANISAND models can quantitatively reproduce the high-cyclic (drained) ratcheting of sands (Houlsby & Puzrin, 2007), nor its dependence on input loading parameters. To mitigate this limitation Liu et al. (2018a) recently proposed a new SANISAND model with ratcheting control. Liu et al.'s model is built upon the parent SANISAND04 model, and enhanced according to the notion of *memory*

surface (Corti et al., 2016) – hence the name SANISAND-MS. The memory locus is introduced to phenomenologically track fabric effects at the micro-scale, and thus improve the simulation of cyclic sand behaviour.

Compared to Dafalias & Manzari's model, SANISAND-MS adopts a third circular locus in the normalised deviatoric stress ratio plane, the memory surface (Fig. 18), which evolves during soil straining so as to (i) modify its size/position in reflection of fabric changes, (ii) always enclose the yield surface, (iii) influence changes in sand stiffness and dilatancy. Other ingredients of SANISAND04 are mostly unchanged. Continual efforts are being devoted to validating the model against laboratory test data from the literature, trying to address as many loading conditions as possible – including cyclic triaxial, simple shear and oedometer tests (Liu at al., 2018a).

The performance of SANISAND-MS in drained cyclic triaxial tests on anisotropically consolidated specimens (Fig. 19a) is compared to SANISAND04's in Fig. 19b-c. It is self-apparent that SANISAND-MS can prevent the irrealistic overestimation of sand ratching yielded by the parent model, and thus capture cyclic strain accumulation as observed in laboratory tests.

Fig. 20 supports the quantitative accuracy of the new model in light of comparisons to measured strain accumulation trends at varying governing factors (Wichtmann, 2005), namely initial mean pressure (Fig. 19a), initial void ratio (Fig. 19b) and cyclic stress deviator amplitude (Fig. 19c).
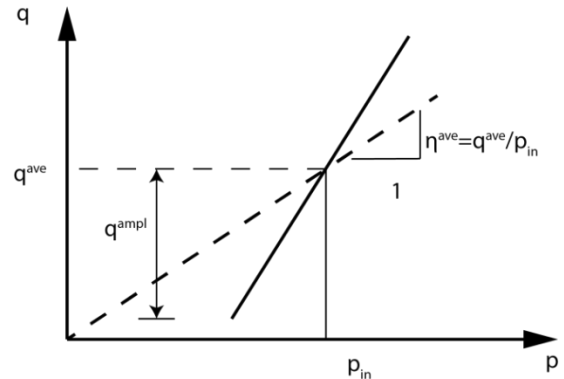
(a)
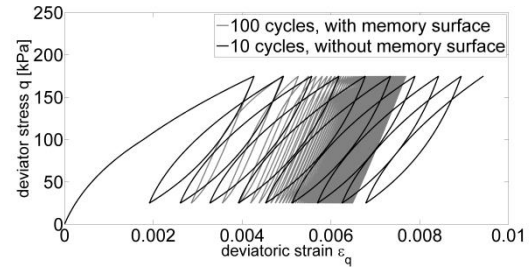
(b)
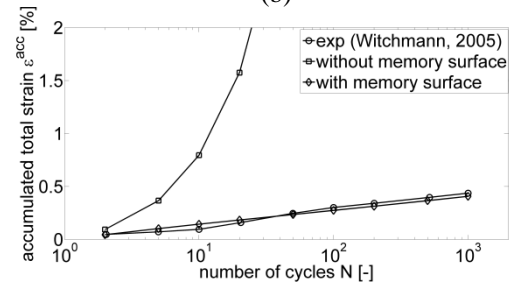
(c)

Fig. 19. (a) Stress path in cyclic triaxial tests on anisotropically consolidated specimens; (b) influence of the memory surface formulation on the response to asymmetric drained triaxial loading, and (c) comparison to laboratory test results in terms of accumulated total strain (experimental data from Wichtmann, 2005).

Fig. 18. Relevant model loci, stress ratios and directions in SANISAND-MS (modified after Liu & Pisanò, 2019)

(a)

(b)

(c)
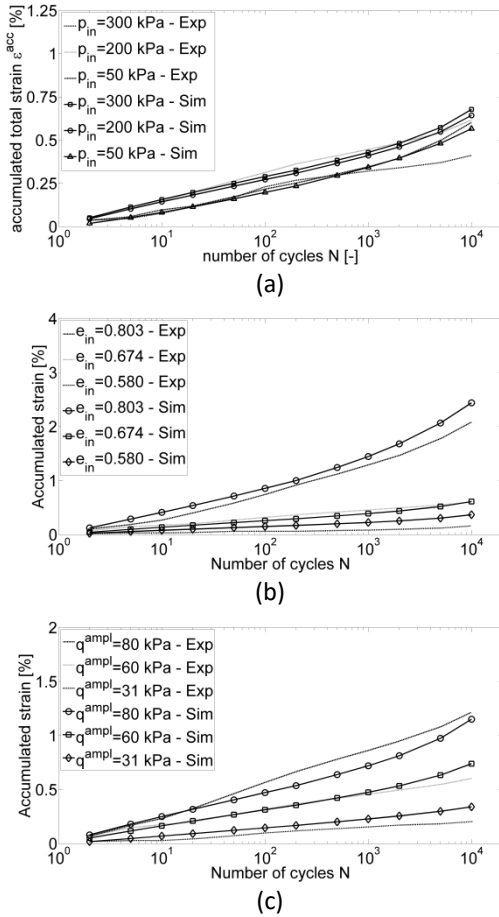
Fig. 20. Comparison between SANISAND-MS and laboratory test results about the influence of (a) initial mean pressure, (b) initial void ratio, and (c) cyclic deviatoric stress amplitude – same stress path as in Fig. 19a (test data from Wichtmann, 2005).
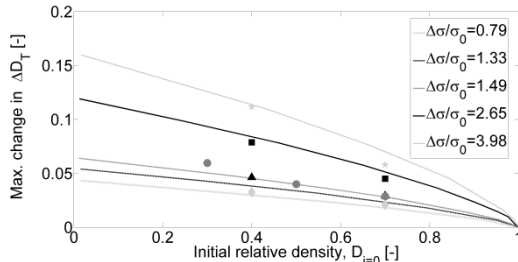
Fig. 21. Maximum changes in relative density (ΔD_T) against initial/pre-cyclic values $D_{i=0}$ – dash lines: interpolation of Park & Santamarina's data; markers: SANISAND-MS simulations (modified after Liu and Pisanò, 2019)

More recently, the suitability of SANISAND-MS has also been investigated with respect to cyclic oedometer tests on dry sand, particularly about the ability to predict so-called *terminal densities* – which refers to sands eventually approaching under cyclic loading an asymptotic void ratio, depending on mechanical properties, loading programme and boundary conditions.
In Liu & Pisanò (2019a) the cyclic oedometer tests results from Park & Santamarina (2018) are successfully reproduced through SANISAND-MS for Ottawa sand specimens subjected to different combinations of initial void ratio and cyclic axial stress amplitude (Fig. 21).

The suitability of the memory surface approach is not limited to drained ratcheting behaviour, but seems also extremely promising in relation to undrained response and cyclic pore pressure build-up. Research on this aspect is currently ongoing at TU Delft (Liu et al., 2018b; Liu et al., 2019b).

5.2 3D FE analysis of cyclic monopile tilt

The SANISAND-MS model described above is suitable to reproduce (drained) sand ratcheting over thousands of loading cycles and diverse stress paths (Liu et al., 2018a; Liu & Pisanò, 2019a). This confidence about the performance of the model suggests to attempt its use in the 3D FE analysis of MP tilt. As previously noted, the adoption of 3D modelling for long-lasting cyclic loading histories may not (yet) be viable in daily engineering practice, due to computational costs. Nevertheless, advanced modelling approaches can certainly add to the understanding of complex soil-structure interaction mechanisms, and inspire the conception of engineering methods.

In the examined case, it should be recognised that the tilting response of MPs is most likely affected by the complexity of environmental loading, featuring variable amplitude, spatial orientation and frequency spectrum. Such features should be expected to induce in the soil loading conditions not commonly investigated in

(a)

(b)
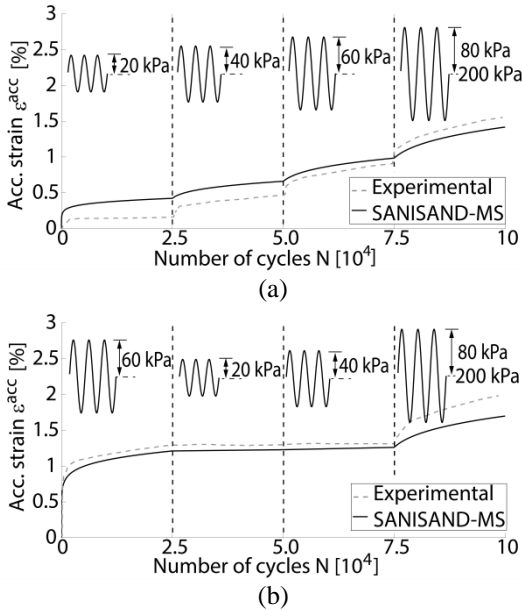
Fig. 22. Relationship between cyclic strain accumulation and sequence of cyclic load packages in biased one-way triaxial tests. Comparison between experimental results (data from Wichtmann, 2005) and SANISAND-MS simulations (Liu, 2020)

laboratory tests, and hardly considered in the validation of constitutive models. An exception in this area is the experimental work carried out in Germany by Wichtmann and co-workers (Wichtmann, 2005; Wichtmann et al., 2010; Wichtmann & Triantafyllidis, 2017), who studied how the specific sequence of different cyclic load packages can influence the ratching behaviour. The resulting experimental evidence supports at the material level the well-known *Miner's rule*, originally devised in relation to metal fatigue (Miner, 1945). Accordingly, the specific sequence of cyclic load packages only slightly affects final strain accumulation, also in sand specimens. Fig. 22 provides an instance of this observation, regarding two medium-dense sand specimens subjected to 10^5 biased one-way triaxial cycles (as in Fig. 19a) of either increasing (Fig. 22a) or alternating (Fig. 22b) deviatoric stress amplitude. The same figure also shows SANISAND-MS simulations obtained

with material parameters calibrated for the Karlsruhe sand tested in the laboratory (Liu et al., 2018a). Owing to the memory surface mechanism, SANISAND-MS can reproduce the Miner-like response observed in the experiments (Liu, 2020). Particularly, the transition from higher to lower cyclic load amplitude seems to inhibit strain accumulation, an occurrence captured by the model through the higher cyclic stiffness associated with stress state within the memory surface. Significant ratcheting is predicted upon expansion of the memory domain, which happens when the stress path hits new absolute maxima. These considerations have important engineering implications, e.g. about identifying the loading events that in reality will cause significant MP tilt – seemingly, only the most severe.

SANISAND-MS' performance is not only encouraging at the sand specimen level. Currently, the model is being tested in the 3D FE simulation of cyclic MP tilt (Liu, 2020). Preliminary results are presented herein for the problem illustrated in Fig. 23, regarding a monopile (diameter $D = 4$ m) in Karlsruhe dry sand (initial $D_r = 57\%$) subjected to cyclic lateral loading applied at the soil surface level. After space discretisation and soil gravity loading, quasi-static horizontal cyclic loading has been applied according to two loading programmes: (1) monotonic lateral loading up to 0.8 MN, followed by two cyclic load packages (100 cycles each) of 0.4 MN and 1.2 MN amplitude; (2) same monotonic loading, followed by a cyclic load sequence with reversed amplitudes.
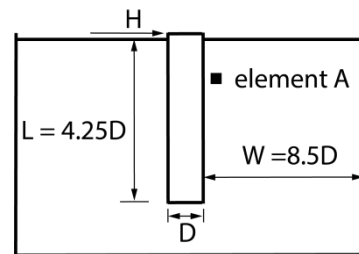
Fig. 23. Case example selected for the 3D FE simulation of cyclic MP tilt based on SANISAND-MS

Lateral displacement trends at the MP head are plotted in Fig. 24 for both cyclic load sequences. Displacement accumulation plots are aligned with the multi-amplitude ratcheting behaviour exemplified for single sand specimens in Fig. 22. The MP tilting rate evolves with the number of cycles depending on the load package sequence, and decreases significantly as packages of decreasing cyclic amplitude are considered (Fig. 24b). 3D FE results support the idea that the final accumulated displacement is mostly determined by strongest packages, a fact also corroborated by the experimental results in Li et al. (2015), Troung et al. (2018), Abadie et al. (2018). It appears that the aforementioned Miner's rule upscales from the level of soil specimen to the global foundation level. The use of a cyclic soil model with ratcheting control, SANISAND-MS, is key to capturing such behaviour in 3D simulations, and can help unveil relevant relationships among external loading, evolution of soil state and resulting MP tilt (Liu, 2020).
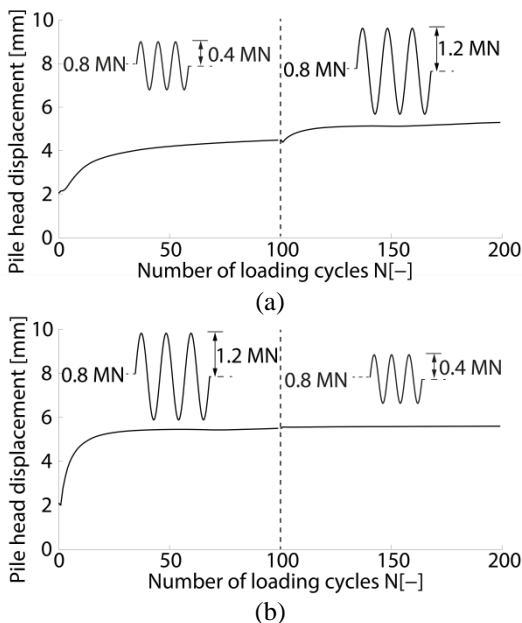
Fig. 24. Lateral displacement accumulation at MP head for cyclic load sequence (a) 1 and (b) 2 (Liu, 2020)
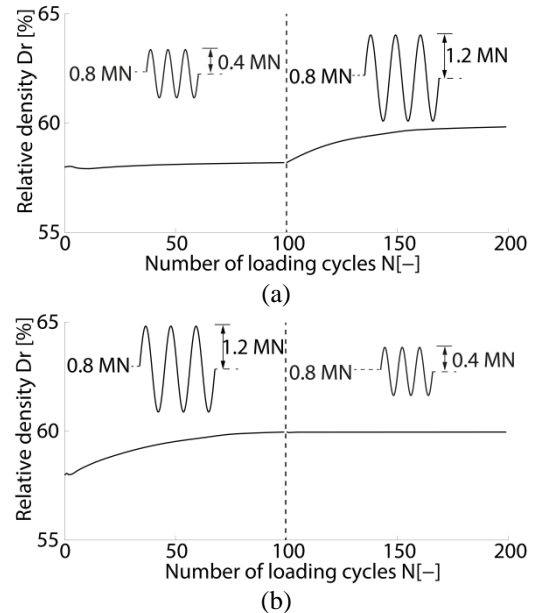
Fig. 25. Variation in relative density obtained at element A in Fig. 23 for cyclic load sequence (a) 1 and (b) 2 (Liu, 2020)

Local sand response is illustrated in terms of relative density evolution in Fig. 25 for the control element A in Fig. 23. Sand densification takes place around the pile in a Miner-like manner, confirming the occurrence of soil mechanisms described by Cuéllar et al. (2009).

Although preliminary, the results in Figs. 24-25 open to a whole thread of numerical modelling research, focused on the 3D analysis of sand ratcheting effects in laterally loaded monopiles. This line of work will contribute in the near future to quantifying the influence of different governing factors on monopile tilt.

6 CONCLUDING REMARKS

This paper presented an overview of recent research carried out at TU Delft on the numerical modelling of soil-structure interaction in offshore wind turbines, particularly for the common case of monopile foundations in sandy soils.

Modelling concepts and practical set-up issues were covered in relation to 3D FE models

capable of integrating the response of wind turbine, foundation and surrounding soil. The relevance of effective-stress-based analysis with advanced modelling of soil behaviour was stressed as a way to adequately reproduce dynamic consolidation processes in the seabed induced by structural vibrations. Despite significant complexity and computational burdens, 3D FE modelling was recognised as a powerful addition to traditional engineering methods, allowing for deeper design checks after preliminary foundation sizing.

The approaches discussed herein appear suitable to investigate possible shifts in OWT natural frequency caused by environmental loading and/or seabed scour; at the same time, modes and governing factors of energy dissipation around the foundation (damping) can be inspected and quantified. Beyond enabling more detailed analysis, the outcomes of 3D FE models can also support the conception and calibration of more efficient lumped models of soil-foundation interaction (macro-models), particularly useful for long-lasting time-domain calculations.

The problem of prolonged environmental loading was also linked to a specific monopile serviceability check, namely the accumulation of permanent lateral tilt. In order to complement experimental and macro-modelling studies, the problem of high-cyclic monopile tilt was addressed from a 3D FE modelling perspective. In this context, the memory-enhanced plasticity sand model developed at TU Delft, SANISAND-MS, was briefly described, and its performance demonstrated against experimental data from the literature. It was clarified that accumulating soil deformations during cyclic loading (ratcheting response) are major responsible for monopile tilt, in a way that 3D FE computations can help explore at a more detailed scale than allowed by macro-models. Ongoing work on improving and validating SANISAND-MS is foreseen to impact the understanding of monopile tilting in offshore environments.

The work summarised in this overview opens to numerous developments, such as extension to offshore wind structures interacting with different soil types (clays, silts, calcareous sands) and more realistic loading conditions. Further studies about seismic soil-foundation interaction issues are becoming increasingly relevant as new offshore wind farms are installed in seismically active regions. Further opportunities for high-fidelity integrated 3D FE modelling also lie in the explicit inclusion of sea-wave loading in fully coupled structure-fluid-soil analysis.

7 ACKNOWLEDGEMENTS

8 REFERENCES

Aasen, S., Page, A. M., Skau, K. S., & Nygaard, T. A. 2017. Effect of foundation modelling on the fatigue lifetime of a monopile-based offshore wind turbine. *Wind Energy Science*, 2(2), 361-376.

Abadie, C. N., Byrne, B. W., & Houlsby, G. T. 2018. Rigid pile response to cyclic lateral loading: laboratory tests. *Géotechnique*, 1-14, DOI: 10.1680/jgeot.16.P.325.

Achmus, M., Kuo, Y. S., & Abdel-Rahman, K. 2009. Behavior of monopile foundations under

cyclic lateral load. *Computers and Geotechnics*, 36(5), 725-735.

API. 2014. Recommended Practice 2A-WSD. Planning, Designing, and Constructing Fixed Offshore Platforms - Working Stress Design. American Petroleum Institute, 22 edition.

Arany, L., Bhattacharya, S., Macdonald, J. H., & Hogan, S. J. 2015. A critical review of serviceability limit state requirements for monopile foundations of offshore wind turbines. In Proc. Offshore Technology Conference. Houston (USA).

Arany, L., Bhattacharya, S., Macdonald, J., & Hogan, S. J. 2017. Design of monopiles for offshore wind turbines in 10 steps. *Soil Dynamics and Earthquake Engineering*, 92, 168-152.

Barari, A., Bagheri, M., Rouainia, M., & Ibsen, L. B. 2017. Deformation mechanisms for offshore monopile foundations accounting for cyclic mobility effects. *Soil Dynamics and Earthquake Engineering*, 97, 439-453.

Been, K., & Jefferies, M. 1985. A state parameter for sands. *Géotechnique*, 35(2), 99–112.

Biot, M. A. 1956a. Theory of propagation of elastic waves in a fluid-saturated porous solid. II. Low frequency range. *The Journal of the Acoustical Society of America*, 28(2), 168-178.

Biot, M. A. 1956b. Theory of propagation of elastic waves in a fluid-saturated porous solid. II. Higher frequency range. *The Journal of the Acoustical Society of America*, 28(2), 179-191.

Balog, I., Ruti, P. M., Tobin, I., Armenio, V., & Vautard, R. 2016. A numerical approach for planning offshore wind farms from regional to local scales over the Mediterranean. *Renewable energy*, 85, 395-405.

Bhattacharya, S. 2019. *Design of foundations for offshore wind turbines*. Wiley.

Bienen, B., & Cassidy, M. J. 2006. Advances in the three-dimensional fluid–structure–soil interaction analysis of offshore jack-up structures. *Marine Structures*, 19(2-3), 110-140.

Byrne, B. W., & Houlsby, G. T. 2003. Foundations for offshore wind turbines. *Philosophical Transactions of the Royal Society of London. Series A: Mathematical, Physical and Engineering Sciences*, 361(1813), 2909-2930.

Byrne, B. W., Burd, H. J., Zdravkovic, L., Abadie, C. N., Houlsby, G. T., Jardine, R. J., ... & Potts, D. M. 2019. PISA Design Methods for Offshore Wind Turbine Monopiles. In *Offshore Technology Conference*. Offshore Technology Conference, Houston (USA).

Castro-Santos, L., & Diaz-Casas, V. (Eds.). (2016). Floating offshore wind farms. Springer.

Cerfontaine, B., Dieudonné, A. C., Radu, J. P., Collin, F., & Charlier, R. 2015. 3D zero-thickness coupled interface finite element: Formulation and application. *Computers and Geotechnics*, 69, 124-140.

Chong, S. H., & Pasten, C. 2018. Numerical study on long-term monopile foundation response. *Marine Georesources & Geotechnology*, 36(2), 190-196.

Corciulo, S., Zanoli, O., & Pisanò, F. 2017a. Transient response of offshore wind turbines on monopiles in sand: role of cyclic hydro–mechanical soil behaviour. *Computers and Geotechnics*, 83, 221-238.

Corciulo, S., Zanoli, O., & Pisanò, F. 2017b. Supporting the engineering analysis of offshore wind turbines through advanced soil-structure 3D modelling. In Proc. 36th Int. Conf. on Ocean, Offshore and Arctic Engineering (OMAE2017). June 25-30, 2017, Trondheim (Norway)

Corti, R., Diambra, A., Wood, D. M., Escribano, D. E., & Nash, D. F. 2016. Memory surface hardening model for granular soils under repeated loading conditions., 142(12), 04016102.

Cuéllar, P., Baeßler, M., & Rücker, W. 2009. Ratcheting convective cells of sand grains around offshore piles under cyclic lateral loads. *Granular Matter*, 11(6), 379.

Cuéllar, P., Mira, P., Pastor, M., Merodo, J. A. F., Baeßler, M., & Rücker, W. 2014. A numerical model for the transient analysis of offshore foundations under cyclic loading. *Computers and Geotechnics*, 59, 75-86.

Dafalias, Y. F., & Popov, E. P. 1975. A model of nonlinearly hardening materials for complex loading. *Acta mechanica*, 21(3), 173-192.

Dafalias, Y. F., & Manzari, M. T. 2004. Simple plasticity sand model accounting for fabric

change effects. *Journal of Engineering mechanics*, 130(6), 622-634.

di Prisco, C., & Pisanò, F. 2011. Seismic response of rigid shallow footings. *European Journal of Environmental and Civil Engineering*, 15(sup1), 185-221.

di Prisco, C. G., & Wood, D. M. (2012). *Mechanical Behaviour of Soils Under Environmentallly-Induced Cyclic Loads*. Springer Science & Business Media.

DNV-GL. 2016. Support structures for wind turbines - Standard DNV-GL-ST-0126. DNV-GL AS.

Doherty, P. & Gavin, K. 2011. Laterally loaded monopile design for offshore wind farms. Proceedings of the Institution of Civil Engineers, 165(EN1):7-17.

Elgamal, A., Yang, Z., Parra, E., & Ragheb, A. 2003. Modeling of cyclic mobility in saturated cohesionless soils. *International Journal of Plasticity*, 19(6), 883-905.

Ghofrani, A., & Arduino, P. 2018. Prediction of LEAP centrifuge test results using a pressure-dependent bounding surface constitutive model. *Soil Dynamics and Earthquake Engineering*, 113, 758-770.

Graff, K. F. 1975. *Wave motion in elastic solids*. Oxford University Press.

Griffiths, D. V. 1985. Numerical modelling of interfaces using conventional finite elements. In *Proc. of the 5th Int. Con on Numerical Methods in Geomechanics*, Nagoya (Japan).

Houlsby, G. T., & Puzrin, A. M. 2007. *Principles of hyperplasticity: an approach to plasticity theory based on thermodynamic principles*. Springer Science & Business Media.

Houlsby, G. T. 2016. Interactions in offshore foundation design. *Géotechnique*, 66(10), 791-825.

Houlsby, G. T., Abadie, C. N., Beuckelaers, W. J. A. P., & Byrne, B. W. 2017. A model for nonlinear hysteretic and ratcheting behaviour. *International Journal of Solids and Structures*, 120, 67-80.

Hughes, T. J. 1987. *The Finite Element Method: linear static and dynamic finite element analysis.* Prentice-Hall.

Jacobson, M. Z., Delucchi, M. A., Bazouin, G., Bauer, Z. A., Heavey, C. C., Fisher, E., ... &

Yeskoo, T. W. 2015. 100% clean and renewable wind, water, and sunlight (WWS) all-sector energy roadmaps for the 50 United States. *Energy & Environmental Science*, 8(7), 2093-2117.

Jeng, D. S. 2003. Wave-induced sea floor dynamics. *Applied Mechanics Reviews*, 56(4), 407-429.

Jeremić, B., Cheng, Z., Taiebat, M., & Dafalias, Y. 2008. Numerical simulation of fully saturated porous materials. *International Journal for Numerical and Analytical Methods in Geomechanics*, 32(13), 1635-1660.

Jostad, H. P., Grimstad, G., Andersen, K. H., Saue, M., Shin, Y., & You, D. 2014. A FE procedure for foundation design of offshore structures–applied to study a potential OWT monopile foundation in the Korean Western Sea. *Geotechnical Engineering Journal of the SEAGS & AGSSEA*, 45(4), 63-72.

Kallehave, D., Thilsted, C. L., & Liingaard, M. A. 2012. Modification of the API py formulation of initial stiffness of sand. In *Offshore site investigation and geotechnics: integrated technologies-present and future*. Society of Underwater Technology.

Kallehave, D., Byrne, B. W., LeBlanc Thilsted, C., & Mikkelsen, K. K. 2015. Optimization of monopiles for offshore wind turbines. *Philosophical Transactions of the Royal Society A: Mathematical, Physical and Engineering Sciences*, 373(2035), 20140100.

Kaynia, A. M. (2018). Seismic considerations in design of offshore wind turbines. *Soil Dynamics and Earthquake Engineering*. DOI: 10.1016/j.soildyn.2018.04.038

Kementzetzidis, E., Versteijlen, W. G., Nernheim, A., & Pisanò, F. 2018. 3D FE dynamic modelling of offshore wind turbines in sand: natural frequency evolution in the pre–to after-storm transition. In *Proc. 9th European Conf. on Numerical Methods in Geotechnical Engineering (NUMGE 2018)*, June 25-27, 2018, Porto (Portugal).

Kementzetzidis, E., Corciulo, S., Versteijlen, W. G., & Pisanò, F. 2019a. Geotechnical aspects of offshore wind turbine dynamics from 3D non-linear soil-structure simulations. *Soil*

Dynamics and Earthquake Engineering, 120, 181-199.

Kementzetzidis, E., Metrikine, A. V., Versteijlen, W. G., & Pisanò, F. 2019b. Frequency effects in the dynamic lateral stiffness of monopiles in sand: insight from field tests and 3D FE modelling. Under Review.

Kontoe, S., Zdravkovic, L., & Potts, D. M. 2008. An assessment of time integration schemes for dynamic geotechnical problems. *Computers and Geotechnics*, 35(2), 253-264.

Kramer, S. L., Sideras, S. S., & Greenfield, M. W. 2016. The timing of liquefaction and its utility in liquefaction hazard evaluation. *Soil Dynamics and Earthquake Engineering*, 91, 133-146.

Kuo, Y. S., Achmus, M., & Abdel-Rahman, K. 2011. Minimum embedded length of cyclic horizontally loaded monopiles. *Journal of Geotechnical and Geoenvironmental Engineering*, 138(3), 357-363.

LeBlanc, C., Houlsby, G. T., & Byrne, B. W. 2010. Response of stiff piles in sand to long-term cyclic lateral loading. *Géotechnique*, 60(2), 79-90.

Li, W., Igoe, D., & Gavin, K. 2015. Field tests to investigate the cyclic response of monopiles in sand. *Proceedings of the Institution of Civil Engineers-Geotechnical Engineering*, 168(5), 407-421.

Li, Q., Prendergast, L. J., Askarinejad, A., & Gavin, K. 2018. Effect of scour on the behavior of a combined loaded monopile in sand. In *Proc. 9th European Conf. on Numerical Methods in Geotechnical Engineering (NUMGE 2018)*, June 25-27, 2018, Porto (Portugal).

Li, Z., Kotronis, P., Escoffier, S., & Tamagnini, C. 2016. A hypoplastic macroelement for single vertical piles in sand subject to three-dimensional loading conditions. *Acta Geotechnica*, 11(2), 373-390.

Liu, H. Y., Abell, J. A., Diambra, A., & Pisanò, F. 2018a. Modelling the cyclic ratcheting of sands through memory-enhanced bounding surface plasticity. *Géotechnique*, 1-18. DOI: 10.1680/jgeot.17.P.307

Liu, H. Y., Zygounas, F., Diambra, A., & Pisanò, F. 2018b. Enhanced plasticity modelling of high-cyclic ratcheting and pore pressure accumulation in sands. In *Proc. 9th European Conf. on Numerical Methods in Geotechnical Engineering (NUMGE 2018)*, June 25-27, 2018, Porto (Portugal).

Liu, H. Y., & Pisanò, F. 2019a. Prediction of oedometer terminal densities through a memory-enhanced cyclic model for sand. *Géotechnique Letters*, 9(2), 1-8.

Liu, H. Y., Abell, J. A., Diambra, A., & Pisanò, F. 2019b. Capturing cyclic mobility and preloading effects in sand using a memory-surface hardening model. In *Proc. of 7th Int. Conf. on Earthquake Geotechnical Engineering (7ICEGE)*, June 17-20, 2019, Rome (Italy).

Liu, H. Y., Diambra, A., Abell, J. A., & Pisanò, F. 2019c. Memory-enhanced plasticity modelling of sand behaviour under undrained cyclic loading. Under review.

Liu, H. Y. 2020. *Constitutive modelling of cyclic sand behaviour for offshore foundations*. PhD Thesis, Delft University of Technology.

Manzari, M. T., & Dafalias, Y. F. 1997. A critical state two-surface plasticity model for sands. *Géotechnique*, 47(2), 255-272.

Mazzoni, S., McKenna, F., Scott, M, & Fenves, G. 2007. *OpenSees command language manual*.

Mašín, D. 2018. *Modelling of Soil Behaviour with Hypoplasticity: Another Approach to Soil Constitutive Modelling*. Springer.

McGann, C. R., Arduino, P., & Mackenzie-Helnwein, P. 2015. A stabilized single-point finite element formulation for three-dimensional dynamic analysis of saturated soils. *Computers and Geotechnics*, 66, 126-141.

McKenna, F. T. 1997. *Object-oriented finite element programming: frameworks for analysis, algorithms and parallel computing*. Ph.D. Thesis, University of California Berkeley.

Miner, M. 1945. Cumulative damage in fatigue. *Transactions of the American Society of Mechanical Engineering*, 67:A159–64.

Mroz, Z. 1967. On the description of anisotropic workhardening. *Journal of the Mechanics and Physics of Solids*, 15(3), 163-175.

Muir Wood, D., Belkheir, K., & Liu, D. 1994. Strain softening and state parameter for sand modelling. *Géotechnique*, 44(2), 335-339.

Newman, J. N. 1977. *Marine hydrodynamics*. MIT press.

Nicolai, G., Ibsen, L. B., O'Loughlin, C. D., & White, D. J. 2017. Quantifying the increase in lateral capacity of monopiles in sand due to cyclic loading. *Géotechnique Letters*, 7(3), 245-252.

Niemunis, A., Wichtmann, T., & Triantafyllidis, T. 2005. A high-cycle accumulation model for sand. *Computers and Geotechnics*, 32(4), 245-263.

Nova, R., & Montrasio, L. (1991). Settlements of shallow foundations on sand. *Géotechnique*, 41(2), 243-256.

Page, A. M., Grimstad, G., Eiksund, G. R., & Jostad, H. P. 2019a. A macro-element model for multidirectional cyclic lateral loading of monopiles in clay. *Computers and Geotechnics*, 106, 314-326.

Page, A. M., Næss, V., De Vaal, J. B., Eiksund, G. R., & Nygaard, T. A. 2019b. Impact of foundation modelling in offshore wind turbines: Comparison between simulations and field data. *Marine Structures*, 64, 379-400.

Papadimitriou, A. G., Bouckovalas, G. D., & Dafalias, Y. F. 2001. Plasticity model for sand under small and large cyclic strains. *Journal of Geotechnical and Geoenvironmental Engineering*, 127(11), 973-983.

Park, J., & Santamarina, J. C. 2018. Sand response to a large number of loading cycles under zero-lateral-strain conditions: evolution of void ratio and small-strain stiffness. *Géotechnique*, 1-13.

Petalas, A. L., Dafalias, Y. F., & Papadimitriou, A. G. 2019. SANISAND-FN: An evolving fabric-based sand model accounting for stress principal axes rotation. *International Journal for Numerical and Analytical Methods in Geomechanics*, 43(1), 97-123.

Pisanò, F., di Prisco, C. G., & Lancellotta, R. 2014. Soil-foundation modelling in laterally loaded historical towers. *Géotechnique*, 64(1), 1.

Pisanò, F., & Gavin, K. G. 2017. General report for TC209 – Offshore Geotechnics, In *Proc. 19th Int. Conf. on Soil Mechanics and Geotechnical Engineering (ICSMGE 2017)*, September 17-22, 2017, Seoul (South Korea)

Pisanò, F., Schipper, R., & Schreppers, G. J. 2019. Input of fully 3D FE soil-structure modelling to the operational analysis of jack-up structures. *Marine Structures*, 63, 269-288.

Prendergast, L. J., Gavin, K., & Doherty, P. 2015. An investigation into the effect of scour on the natural frequency of an offshore wind turbine. *Ocean Engineering*, 101, 1-11.

Prévost, J. H. 1982. Two-surface versus multi-surface plasticity theories: a critical assessment. *International Journal for Numerical and Analytical Methods in Geomechanics*, 6(3), 323-338.

Prévost, J. H., & Popescu, R. 1996. Constitutive relations for soil materials. *Electronic journal of geotechnical engineering*, 1.

Rodrigues, S., Restrepo, C., Kontos, E., Pinto, R. T., & Bauer, P. (2015). Trends of offshore wind projects. *Renewable and Sustainable Energy Reviews*, 49, 1114-1135.

Rudolph, C., Bienen, B., & Grabe, J. 2014. Effect of variation of the loading direction on the displacement accumulation of large-diameter piles under cyclic lateral loading in sand. *Canadian Geotechnical Journal*, 51(10), 1196-1206.

Schotman, G. J. M. 1989. The effects of displacements on the stability of jackup spud-can foundations. In *Offshore Technology Conference*. Offshore Technology Conference.

Sloan, S. W. 1987. Substepping schemes for the numerical integration of elastoplastic stress–strain relations. *International Journal for Numerical Methods in Engineering*, 24(5), 893-911.

Staubach, P., & Machacek, J. 2019. Influence of relative acceleration in saturated sand: analytical approach and simulation of vibratory pile driving tests. *Computers and Geotechnics*, 112, 173-184

Stockwell, R. G., Mansinha, L., & Lowe, R. P. 1996. Localization of the complex spectrum: the S transform. *IEEE transactions on signal processing*, 44(4), 998-1001.

Stutz, H., Mašín, D., Sattari, A. S., & Wuttke, F. 2017. A general approach to model

interfaces using existing soil constitutive models application to hypoplasticity. *Computers and Geotechnics*, 87, 115-127.

Taiebat, M., & Dafalias, Y. F. 2008. SANISAND: Simple anisotropic sand plasticity model. *International Journal for Numerical and Analytical Methods in Geomechanics*, 32(8), 915-948.

Tamagnini, C., Viggiani, G., Chambon, R., & Desrues, J. 2000. Evaluation of different strategies for the integration of hypoplastic constitutive equations: Application to the CLoE model. *Mechanics of Cohesive frictional Materials*, 5(4), 263-289.

Truong, P., Lehane, B. M., Zania, V., & Klinkvort, R. T. 2018. Empirical approach based on centrifuge testing for cyclic deformations of laterally loaded piles in sand. *Géotechnique*, 69(2), 133-145.

Ushiyama, I. (2018). Present status and target of Japanese wind power generation. In *Transition Towards 100% Renewable Energy* (pp. 433-440). Springer, Cham.

van Kuik, G. A. M., Peinke, J., Nijssen, R., Lekou, D., Mann, J., Sørensen, J. N., ... & Polinder, H. 2016. Long-term research challenges in wind energy–a research agenda by the European Academy of Wind Energy. *Wind Energy Science*, 1(1), 1-39.

Vacareanu, V., Kementzetzidis, E., & Pisanò, F. 2019. 3D FE seismic analysis of a monopile-supported offshore wind turbine in a non-liquefiable soil deposit. In Proc. of 2nd Int. Conf. on Natural Hazards & Infrastructure (ICONHIC2019), 23-26 June 2019, Chania (Greece).

Versteijlen, W. G., Renting, F. W., van der Valk, P. L. C., Bongers, J., van Dalen, K. N., & Metrikine, A. V. 2017. Effective soil-stiffness validation: Shaker excitation of an in-situ monopile foundation. *Soil Dynamics and Earthquake Engineering*, 102, 241-262.

Watanabe, K., Pisanò, F., & Jeremić, B. 2017. Discretization effects in the finite element simulation of seismic waves in elastic and elastic-plastic media. *Engineering with Computers*, 33(3), 519-545.

Wichtmann, T. (2005). *Explicit accumulation model for non-cohesive soils under cyclic loading*.

PhD thesis, Institut für Grundbau und Bodenmechanik, Bochum University.

Wichtmann, T., Niemunis, A., & Triantafyllidis, T. 2010. Strain accumulation in sand due to drained cyclic loading: on the effect of monotonic and cyclic preloading (Miner's rule). *Soil Dynamics and Earthquake Engineering*, 30(8), 736-745.

Wichtmann, T., Triantafyllidis, T., Chrisopoulos, S., & Zachert, H. 2017. Prediction of Long-Term Deformations of Offshore Wind Power Plant Foundations Using HCA-Based Engineer-Oriented Models. *International Journal of Offshore and Polar Engineering*, 27(04), 346-356.

Wichtmann, T., & Triantafyllidis, T. 2017. Strain accumulation due to packages of cycles with varying amplitude and/or average stress–On the bundling of cycles and the loss of the cyclic preloading memory. *Soil Dynamics and Earthquake Engineering*, 101, 250-263.

WindEurope. 2019. Offshore wind in Europe: key trends and statistics 2018. Via internet: *https://windeurope.org/about-wind/statistics/offshore/european-offshore-wind-industry-key-trends-statistics-2018/*.

Yang, Z. & Elgamal, A. 2008. Multi-surface cyclic plasticity sand model with Lode angle effect. *Geotechnical and Geological Engineering*, 26(3), 335-348.

Zhang, Y., Zhang, C., Chang, Y. C., Liu, W. H., & Zhang, Y. 2017. Offshore wind farm in marine spatial planning and the stakeholders engagement: opportunities and challenges for Taiwan. *Ocean & coastal management*, 149, 69-80.

Zienkiewicz, O. C., Chang, C. T., & Bettess, P. 1980. Drained, undrained, consolidating and dynamic behaviour assumptions in soils. *Géotechnique*, 30(4), 385-395.

Zienkiewicz, O. C., & Mroz, Z. 1984. Generalized plasticity formulation and applications to geomechanics. *Mechanics of engineering materials*, 44(3), 655-680.

Zienkiewicz, O. C., Chan, A. H. C., Pastor, M., Schrefler, B. A., & Shiomi, T. 1999. *Computational geomechanics*. Wiley.

XVII European Conference
ECSMGE 2019
Reykjavík
on Soil Mechanics
and Geotechnical Engineering

Pile penetration in crushable soils: Insights from micromechanical modelling

Pénétration des pieux dans les sols concassables: informations tirées de la modélisation micromécanique

M. O. Ciantia
University of Dundee, School of Science and Engineering, Dundee, UK

C. O'Sullivan and R. J. Jardine
Imperial College, Dept. Civil and Environmental Engineering, London, UK

ABSTRACT: A 3D discrete element model (DEM) was used to simulate calibration chamber experiments of a cone shaped tip pile penetrating into crushable granular media. Both monotonic and cyclic jacking are considered. Particle crushing is simulated by employing a rigorous breakage criterion applied to elasto-brittle spheres. Particle scaling is used to limit the number of particles considered and it is shown that, above a threshold limit, the penetration curves become scale independent, provided a scalable crushing model is used. The particle crushing model parameters were calibrated by matching triaxial and one-dimensional compression tests. The DEM model could capture the stress measurements made around a model pile during and after its penetration into sand relatively well. The particle-scale mechanics that underlie the observed macroscopic responses are analysed, placing emphasis on the distribution of crushing events around the pile tip and distributions of particle stresses and forces around the shaft. Comparing simulations made with crushable and uncrushable grains, and analysing the particle displacement fields, provides insights into one of the mechanisms proposed for the well-known, yet not fully understood, marked shaft capacity increases developed over time by piles driven in sands.

RÉSUMÉ: Un modèle 3D d'éléments discrets (DEM) est utilisé pour prédire les expériences en chambre d'étalonnage de la pénétration de cônes et de pieux dans des supports pouvant être écrasés, à la fois par fonçage monotone et cyclique. Un modèle de broyage de particules basé sur un critère de rupture rigoureux pour les sphères élasto-fragiles est utilisé. Une mise à l'échelle des particules est réalisée pour limiter le nombre total de particules. Il est montré qu'au-delà d'un nombre minimum de particules, les courbes de pénétration deviennent indépendantes de leur taille, à condition qu'un modèle de broyage évolutif soit utilisé. Le modèle, calibré en faisant correspondre les tests de compression triaxiale et unidimensionnelle, fournit de bonnes prévisions pour les mesures de contrainte effectuées lors d'essais de pieux, pendant et après les phases de pénétration. Les caractéristiques micromécaniques expliquant les réponses macroscopiques observées sont analysées. Il s'agit notamment d'identifier la répartition de l'intensité de broyage autour de la pointe du pieu et d'analyser en détail les contraintes exercées par les particules et les chaînes de force autour du fût du pieu. La comparaison de simulations réalisées avec ou sans grains broyables, ainsi que l'analyse des champs de déplacement de particules, offrent une explication possible de l'impact bien connu, mais pas encore bien compris, du vieillissement sur la capacité du fût de pieux battus dans le sable.

Keywords: Discrete-element modelling, Piles, Particle crushing/crushability, Stress path, Stress analysis

1 INTRODUCTION

Improvements have been achieved in driven pile design through approaches such as those set out by Jardine et al., (2005) and Lehane et al., (2005). However, the full effective stress regime developed around piles driven in sands and the factors that control features such as their cyclic loading responses, group action and strong shaft capacity growth over time, remain incompletely fully understood; see Jardine (2013), (2019).

Calibration chamber experiments (Tehrani et al., 2018; Yang et al., 2014) and centrifuge tests (Bolton et al., 1999; Coop et al., 2005; Klotz and Coop, 2001) have highlighted the intense stress concentrations that develop below the pile tips, and also shown that pile geometry and driving cycles affect the final stress regime. Particle breakage, which is known to affect sands' mechanical behaviour significantly (Lade et al., 1996) also occurs during driving. Physical tests with highly instrumented piles and calibration chambers have identified aspects of the evolution of ground displacements and stresses around penetrating piles (Arshad et al., 2014; Doreau-Malioche et al., 2018; Jardine et al., 2013a; White and Bolton, 2004; White and Lehane, 2004). These programmes have provided benchmarks to test continuum modelling approaches for penetration problems (Gens et al., 2016; Monforte et al., 2017; Phuong et al., 2016) including treatments that consider particle breakage (Zhang et al., 2014, 2013).

The discrete element method (DEM), which considers individual soil particles and their interactions explicitly, can also be used to study large displacement contact problems and so provide fundamental insights into the mechanisms that underlie macroscopic behaviour (Santamarina, 2003). DEM has been applied to model monotonic 2D steady pile penetration (Huang and Ma, 1994; Jiang et al., 2014) as well as 3D cases (Arroyo et al., 2011; Butlanska et al., 2014; Butlanska and Arroyo, 2015; Janda and Ooi, 2016; Zhang and Wang, 2015). DEM analyses of

dynamic penetration problems have also been reported (Tran et al., 2016; Zhang et al., 2018; Zhang and Evans, 2019) as have simulations of penetration in crushable media (Ciantia et al., 2016; Falagush et al., 2015; Zhang et al., 2018), pressurised grout injection (Boschi et al., 2019), and screw pile installation (Sharif et al., 2019).

This paper describes novel 3D DEM simulations that: a) are validated against experimental observations of the stress fields set up by pile penetration; b) test the hypothesis that arching forms around the pile shafts; c) examine the impact of cyclic jacking and particle crushing on the piles' micro-and macro mechanical behaviour. A computationally efficient DEM crushing model was employed to capture the load-deformation behaviour of the sand at high stresses, including grain crushing during one-dimensional compression (Ciantia et al., 2015) and shearing (Ciantia et al., 2019b). Parallel simulations involving crushable and unbreakable grains reveal how crushing accentuates stress relaxation close to the shaft and facilitates arching. Additional insights are given through analyses of the incremental radial displacements particles experience over each jacking cycle. The calibration chamber experiments reported by Rimoy et al. (2015), Jardine et al. (2013a), (2013b) and Yang et al. (2010), in which highly instrumented model piles were jacked into dense, pressurised, Fontainebleu NE34 sand, are adopted as a benchmark to test the simulations.

2 DEM PARTICLE CRUSHING MODEL AND NUMERICAL ANALYSES

2.1 DEM crushing model

The crushable DEM grain model of Ciantia et al. (2015, 2019b) was employed, which adopts a simplified Hertz-Mindlin contact law and spherical particles whose rotation is inhibited to capture the rotational resistances of angular grains (Arroyo et al. 2011; Calvetti 2008; Ting et al. 1989). The model's particle failure criterion follows Russell and Muir Wood (2009) and

Russell et al. (2009). Particles crush when any interparticle contact force reaches the limit:

$$F = \sigma_{lim} \cdot A_F \qquad (1)$$

where σ_{lim} is the limit strength of the material and A_F is the contact area. Hertzian theory for smooth sphere contacts provides an expression for the contact area to give:

$$F \leq \left\{ \sigma_{lim} \pi \left[\frac{3}{4} \frac{\left(\frac{1-v_1^2}{E_1} + \frac{1-v_2^2}{E_2} \right)}{\left(\frac{1}{r_1} + \frac{1}{r_2} \right)} \right]^{\frac{2}{3}} \right\}^3 \qquad (2)$$

where r_i (i=1,2) are the radii of the contacting spheres and E_i, v_i are the Young's Moduli and Poisson's ratios respectively. To incorporate experimentally observed variability into the model, the limit strength, σ_{lim}, for a given sphere size is assumed to be normally distributed, which is incorporated through a correction factor, $f(var)$, that is applied to σ_{lim}. The coefficient of variation of the distribution, var, is considered to be a material parameter. A particle size dependency is also introduced to capture the relatively higher strength of smaller particles; this takes a Weibull-like form, where the limit strength is given by:

$$\sigma_{lim} = \sigma_{lim} f(var) \left(\frac{d}{Nd_0} \right)^{\frac{-3}{m}} \qquad (3)$$

where m is a material constant, σ_{lim0} is the mean limit strength at the reference diameter, d_0, (taken to be 2 mm here) and N is the scaling factor. The failure criterion remains unchanged for particle-wall contacts; the wall is considered as particle 2 so that the elastic properties of the wall are used to select E_2 and v_2 and the ratio $1/r_2$ is taken as 0 as the wall radius far exceeds that of the particles.

Once the crushing limit condition is reached, the spherical particles are split into smaller inscribed tangent spheres, corresponding to the first steps of an Apollonian series. The spawned frag-

ments assume the velocity and material parameters of the original particle apart from the intrinsic strength (σ_{lim}) which is reassigned using eq. (3).To track the evolution of the PSD, the breakage index Br (Einav, 2007), is computed continuously. The limit grading is given by a fractal distribution with fractal dimension ω=2.6, which (Einav, 2007) expressed as:

$$\frac{M_{(L<d)}}{M_T} = \frac{d^{3-\omega} - d_{min}^{3-\omega}}{d_{max}^{3-\omega} - d_{min}^{3-\omega}} \qquad (4)$$

where M_T is the total mass, $M_{(L<d)}$ the mass of particles smaller than d, d_{max} and d_{min} are, respectively, the maximum and minimum particle sizes assumed for the limit distribution. Following Ciantia et al. (2015) a numerically motivated comminution limit, d_{comm}, is imposed to halt the production of excessively small particles. The crushing model was implemented in PFC3D-V5 (Itasca, 2016).

Table 1. Calibrated model parameters for FS grains

d_{50}	μ	G	v	$\sigma_{lim,0}$	m
mm	-	GPa	-	GPa	-
0.21	0.275	9	0.2	1.9	10
d_0	var	d_{comm}/d_{50}	d_{max}	d_{min}	D_{loc}
mm	-	-	mm	mm	-
2	0.36	0.55	0.27	0.01	0.05

The model parameters used in the current study, listed on Table 1 are those obtained in an extensive calibration exercise that considered Fontainebleau sand, Figure 1 (Ciantia et al., 2019b). Comparisons are given in (a) of the experimental and numerical particle size distributions. Simulations and outcomes from triaxial tests performed from $p' = 100$ kPa are compared in (b), while parallel oedometer test conditions are presented in (c) and the corresponding evolutions of particle size distributions are shown in (d). In line with the proposal made by Muir Wood (2007) and Muir Wood & Maeda (2008), Altuhafi et al., (2018b) show that Fontainebleu sand develops an infinite possible family of critical state lines as its particle distribution profile evolves under high pressure shearing that together constitute a

unique critical state plane (CSP). Ciantia et al., (2019b) show that the adopted DEM model can reproduce the experimental trends found by Altuhafi et al. (2018a). The ability to capture the behaviour of highly overconsolidated, pre-crushed, sand is important to the pile simulations as particles near the axis experience extreme loading as the tip penetrates into any given layer within the sand mass, and then undergo very significant unloading as the pile tip advances to greater depth

a)

b)

c)

d)
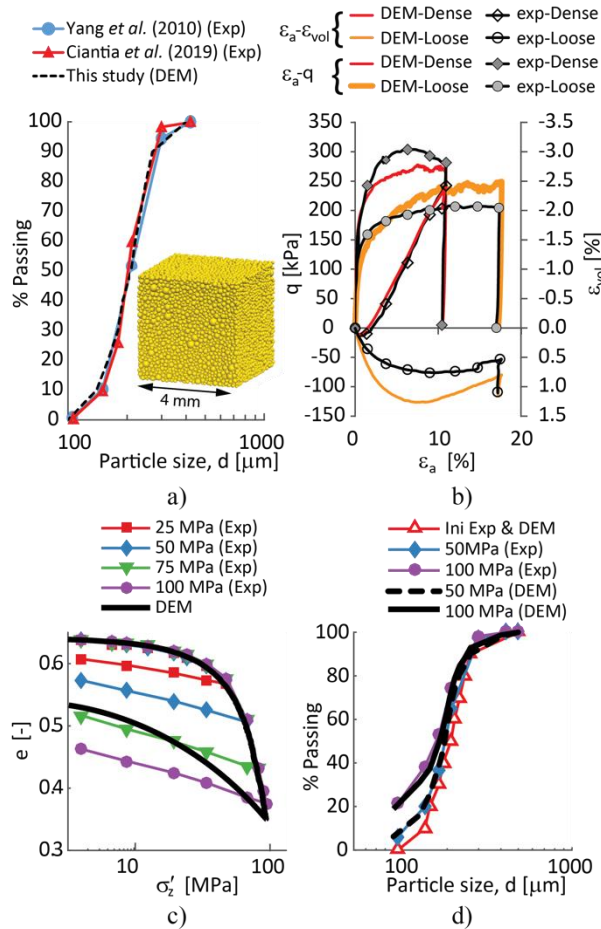
Figure 1 Contact model calibration from Ciantia et al. (2019a): a) Experimental and numerical PSD and DEM model at 5kPa isotropic compression pressure, b) DEM simulation of drained triaxial compression test (cell pressure 100 kPa; experimental data from Seif El Dine et al., 2010). Crushing model validation by DEM simulation of high-pressure oedometer tests in terms of c) effective vertical stress vs void ratio and d) PSD evolution.

3 ANALYSIS OF CONE-ENDED PENETRATION TEST IN FONTAINEBLEAU SAND

The calibrated DEM crushing model was adopted to simulate the cone-ended model pile tests described by Yang et al. (2010). An important feature to emerge from the physical experiments was the considerable difference between the sand stresses developed during steady penetration (the push phases of jacking cycles) and those that applied when the pile was stationary without any pile head load during the jacking-cycle pause phases; see (Jardine et al., 2013b). The DEM analyses considered both cases. Where possible, the results of the FEM steady penetration conditions simulated by Zhang et al. (2013) are compared with the DEM predictions.

3.1 DEM Model Construction

A DEM 'model calibration chamber' was developed to match the physical experiments by Yang et al. (2010) as closely as was feasible, as summarised in Table 2 and illustrated in Figure 2(a). Noting that Coetzee (2019) showed that particle scaling is a viable approach when using DEM to model large scale boundary value problems, the particles were scaled up by a factor of 39, while adhering to the Fontainebleau sand's particle size distribution curve's normalised shape. This allowed the analyses to proceed with four orders of magnitude fewer particles than in the experiments and led to a computationally feasible 442,335 particles. Falagush et al. (2015) showed that when using a non-scalable crushing law and adjusting particle sizes leads to unphysical results because of particle strength size effects. In the present analyses the crushing law used is scalable and so avoids the unrealistic results possible when scaling is not considered.

The calibration chamber (CC) instrumented pile tests were performed under a no-strain, low friction, radial lateral condition. The experimental chamber's vertical boundaries were located 33.7R, where R is the pile radius, R from
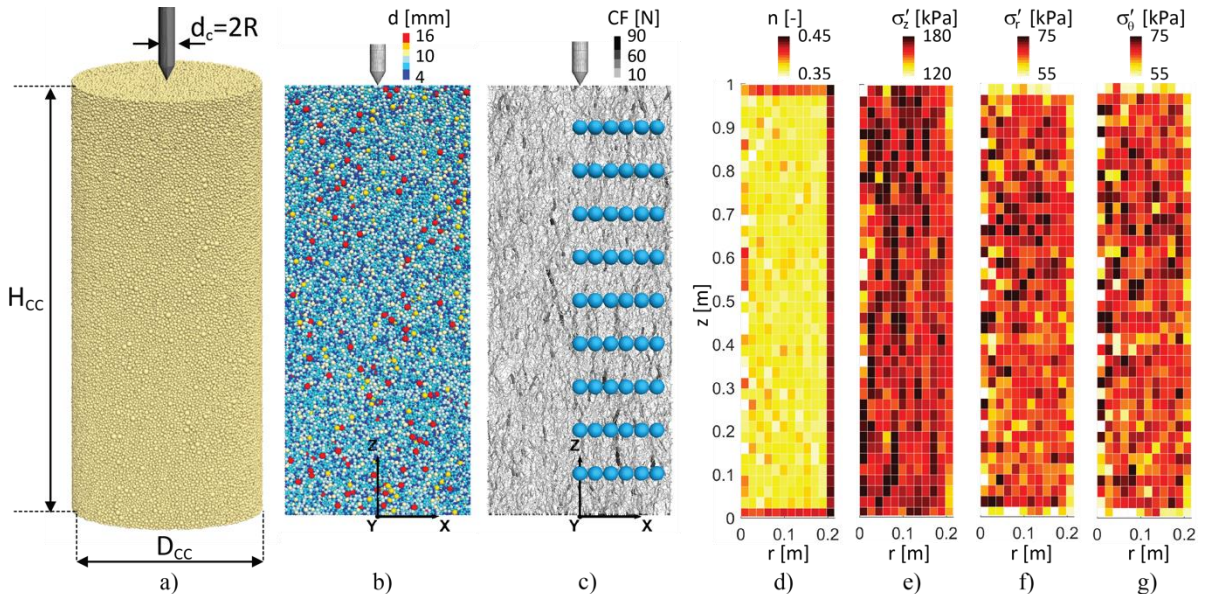
Figure 2 Initial condition of DEM model: a) 3D view, b) 2D cross section showing particle diameter, c) contact forces and position of measurement spheres (MSs), initial porosity (d), vertical stress (e) radial stress (f) and circumferential stress (g) contours.

the pile axis; still larger ratios are required to simulate field behaviour accurately (Pournaghiazar et al., 2013; Salgado et al., 1998). To make the DEM modelling feasible, frictionless radial walls preventing circumferential motion of particles were placed at a smaller radial distance $12R$ from the centre of the pile noting that the experimentally measured radial, vertical and tangential stresses during penetration were relatively stable at this distance from the pile axis (Jardine et al., 2013a). Adopting a larger radial distance for the modelling would have been more representative. However, capturing even the test chamber dimensions would have required approximately 3 million extra (scaled-up) particles and rendered the analyses impossible to achieve with the adopted software and available computers.

Techniques employed to decrease boundary effects in DEM models include the particle refinement method, using larger radial walls (McDowell et al., 2012) and coupled DEM-FEM approaches (Tu et al., 2017). The former was not used, as the model was designed to have the same level of resolution across the whole chamber. Unfortunately, coupled software was not available

to follow the second route. Instead, the particle-lateral chamber wall contacts where assigned a stiffness equal to the particle stiffness to mimic the far-field response. The match shown later between the DEM and the experimental penetration resistance and stress profiles indicate that this step led to reasonable overall outcomes, although other approaches could also have been followed.

Table 2. Comparative geometrical characteristics of experimental and simulated (DEM) calibration chamber.

Variable (unit)	Symbol	Experiments	DEM Model
Chamber diameter (mm)	D_{CC}	1200	432
Cone diameter (mm)	d_c	36	36
Chamber height (mm)	H_{CC}	1500	1000
Particle median size (mm)	d_{50}	0.21	8.19
Initial number of particles	N_p	$3 \times 10^{11*}$	442335
Chamber/cone ratio D_C/d_c	R_d	33.7	12
Cone /particle ratio d_c/d_{50}	n_p	171.4	4.4
Stress cell diameter/particle ratio d_{cell}/d_{50}	n_s	28-31	4.4
Number of stress cells	N_{cells}	36	54
Average porosity	n	0.382	0.38
Average CC σ_z' (kPa)	$\bar{\sigma}_z'$	150	152.9
Initial CC σ_r' (kPa)	$\bar{\sigma}_r'$	76	76.7

*approximate

The experiments employed sand air-pluviated to an initial porosity $n=0.382$, and relative density $Dr=72\%$. Simulating such a procedure in DEM is computationally very demanding (Ciantia et al., 2017), so the 'DEM chamber' was filled with scaled-up grains using the radius expansion method (Itasca, 2016) as described by Ciantia et al. (2018). In the experiments a constant 150 kPa vertical stress was maintained along the top boundary and there was a rigid wall at the base. In the DEM model, the top (frictionless) horizontal boundary was servo-controlled to apply the desired vertical stress level while both the bottom (frictionless) wall was fixed. To match the initial stress conditions in the experiments, the DEM specimen was first formed at a target initial porosity of 0.385 at 5 kPa of isotropic pressure followed by an axial compression to the 150 kPa target vertical stress. The exterior horizontal stress was adjusted to match the experimental 76 kPa value by using radial wall servo-control, giving a mean effective stress $p'=101$ kPa and a final average porosity of 0.383 (Figure 2(d)).

The pile shaft and tip were modelled using rigid frictional cylindrical walls with the interface friction coefficient set equal to the critical state value ($\tan\delta =0.5$) measured in interface ring-shear tests conducted against surfaces composed of the same stainless steel as the pile and with the same surface roughness (Yang et al., 2010). The particle-pile contacts employed a simplified Hertz-Mindlin contact model with the pile shear modulus (G_{pile}) and Poisson's ratio (ν_{pile}) set to 85 GPa and 0.2 respectively (Young Modulus of 200 GPa); the pile was therefore effectively rigid relative to the particulate assembly. The pile-to-median particle diameter ratio, n_p, was 4.4 in the DEM model which this is much smaller than the experimental value of 36 but larger than other published 3D DEM penetration simulations (Table 3). The low n_p ratio increased the scatter (or fluctuations) in the stress predictions made for the penetrating pile (Arroyo et al. (2011); Butlanska et al. (2014)).

Such scatter can only be avoided by employing smaller particles, which then render the analysis computationally unfeasible. However, the fluctuations can be filtered out by fitting appropriate penetration trend lines through the scatter. The exponential expression applied in Arroyo et al., (2011) was used in the present analyses to establish smooth pile end-bearing pressure versus tip-depth trend $q_{c,trend}$ where:

$$q_{c,trend}(h_p) = a[1 - exp(-bh_p)] \qquad (5)$$

where h_p is the penetration depth and a and b are fitting parameters. The parameter a gives the asymptotic or steady state value of cone resistance. The influence of the cone penetration velocity was investigated to ensure quasi-static conditions were achieved during penetration. The inertial

Table 3. 3D DEM numerical penetration model characteristics

Symbol	This study	(Arroyo et al., 2011)	(Ciantia et al., 2016)	(Janda and Ooi, 2016)	(Zhang and Wang, 2015)	(Zhang and Evans, 2019)	(Zhang et al., 2019)
D_C (mm)	432	1200	760	101	12	20000	760
d_c (mm)	36	71.2	36	12.83	1	2100	50.8
H_{cc} (mm)	1000	700	760	250	24	25000	500
d_{50} (mm)	8.19	26.5	15	5	0.172	500	16.6
N (-)	39	50	15	-	1	-	79
N_p (-)	442,335	65,000	203,000	15,000	608,088	-	60,000
R_d (-)	12	16.9	21	7.87	12	11.9	15
n_p (-)	4.4	2.7	2.4	2.57	5.8	4.2	3.06
n_s (-)	4.4	1.89*	-	-	2.9	-	-
N_{cells} (-)	54	45*	-	-	2	-	-

*Reported in Butlanska et al. (2009)

number, I, can be used to characterize dynamic effects in systems under shear:

$$I = \dot{\gamma} d_{50} \sqrt{\rho/P} \qquad (6)$$

Where $\dot{\gamma}$ is the shear strain rate, d_{50} is the median diameter of the particles, ρ is the particle density and P is the confining pressure. In their penetration simulations Janda and Ooi (2016) assumed $I<10^{-2}$ for quasi-static conditions; giving $\dot{\gamma}<7.6\text{s}^{-1}$ when P is taken as the initial p' (101 kPa), ρ as the particle density (2600 kg/m^3) and d_{med} as 8.9mm. The cone penetration velocity was then calculated as:

$$v_{pile} = \dot{\gamma} L_p \qquad (7)$$

where L_p is the width of the plastic zone formed under the tip which, following Lu et al. (2004), was assumed to be $3d_c$. Assuming $\dot{\gamma}=7.6\text{s}^{-1}$ gives $v_{pile}=$ 0.8 m/s. Since Butlanska et al. (2010) showed that for similar particle masses rates between 0.02 and 0.50 m/s do not change the simulation results, an optimum value of 0.50 m/s was adopted. This is below the 1 m/s limit where dynamic effects have been documented as appearing by Janda and Ooi (2016), Quezada et al. (2014) and Tran et al. (2016b).

To simulate cyclic pile jacking, after each 100 mm of penetration, the pile was unloaded by slowly displacing it upwards until the vertical head force was zero. These jack strokes were repeated until 1m penetration was achieved. Two monotonic simulations (where no unloading was simulated) were also performed, one of which was run without invoking particle breakage.

As illustrated in Figure 2(c), thirty six measurement spheres (MS) each with a diameter equal to the cone diameter, were placed in the DEM model domain to allow frequent measurement of the average soil stresses. In each sphere the stress is computed as (Christoffersen et al., 1981):

$$\boldsymbol{\sigma}' = \frac{1}{V_{MS}} \sum_{N^c} \boldsymbol{F}^c \otimes \boldsymbol{L}^c \qquad (8)$$

where N^c is the number of contacts that lie in the measurement region of volume V_{MS}, $\boldsymbol{F}^c$ is the contact force vector, $\boldsymbol{L}^c$ is the branch vector joining the centroids of the two bodies in contact, $\otimes$ denotes the outer (tensor) product.

The particle and contact model data were saved and processed externally at the end of each push and pause (unload) period, enabling the stresses to be calculated within any portion of the model domain. To do so, the particle Cartesian stress tensor ($\overline{\boldsymbol{\sigma}}^p$) was calculated following Luding, (2004):

$$\overline{\boldsymbol{\sigma}}^p = \frac{1}{V_p} \sum_{c=1}^{Nc,p} \boldsymbol{s}^c \otimes \boldsymbol{F}^c \qquad (9)$$

where the superscripts indicate particle (p) or contact (c). $N^{c,p}$ is the number of contacts involving particle p, $\boldsymbol{s}^c$ is the vector connecting the element centre with the contact point and $\boldsymbol{F}^c$ is the contact force vector. These data can be used to compute the average stress for a volume V containing of N^p particles (each having volume V^p) as follows:

$$\boldsymbol{\sigma}' = \frac{1}{V} \sum_{N^p} \overline{\boldsymbol{\sigma}}^p V^p \qquad (10)$$

The mean effective stress p' and the deviatoric stress q are given by

$$p' = \frac{1}{3} tr(\boldsymbol{\sigma}') \qquad (11)$$

$$q = \sqrt{\frac{2}{3}} \|\boldsymbol{s}\| \qquad (12)$$

where $\boldsymbol{s} = \boldsymbol{\sigma} - p\boldsymbol{I}$, $\|\boldsymbol{s}\|$ denotes the Euclidian norm of $\boldsymbol{s}$ and $\boldsymbol{I}$ is the second order identity tensor. Assuming axisymmetric conditions, the stress state of the soil can be described using the radial stress σ_r', the circumferential stress σ_θ', the vertical stress σ_z' and the shear stress τ_{zr}'.

The homogeneities of initial sand chamber porosities and stresses were considered before commencing pile penetration by considering 480 annular rings each having a width equal to the pile radius and a height of 25 mm. The ring size was chosen to give an optimal balance between resolution, which decreases with increasing ring size, and achieving a statistically representative volume which requires a minimum number of particles. The minimum number of particles in any averaging ring was 65. Stresses were calculated using equation (10) taking care that only the portions of the particle volumes (V^p) inside each averaging volume V were considered. Sections were taken through these rings and the average stress or porosity in each ring was displayed according to a colour scale. As expected and represented in Figure 2(d) higher porosity values are measured near to the rigid walls (Huang et al., 2014) while the internal mass is more homogeneous. As shown in Figure 2(e-g) the DEM sample also experienced relatively homogenous initial stresses: the mean vertical, radial, and circumferential stresses are 152.9 kPa, 76.7 kPa and 76.8 kPa with a standard deviation of 12 kPa, 4.9 kPa and 5.1 kPa respectively. Table 2 compares these averages with the experimental target values.

3.2 Macroscale results

Figure 3(a) gives the penetration data from both the monotonic and the cyclically jacked DEM simulations and their corresponding fitted penetration curves. The cyclic and monotonic DEM numerical simulations give very similar curves, suggesting that the cycling process has little influence on the end bearing capacity q_c, as found in the calibration chamber experiments by Yang et al. (2010). However, when crushing is disabled the cone resistance rises 50% above the crushable model response (around 20 MPa). These results are combined with those from other DEM and experimental studies and plotted as q_c (uncrushable particles)/q_c(crushable) versus initial relative density in Figure 3(b). The analyses described herein conform with the trends from the earlier experimental studies and DEM simulations cited above.
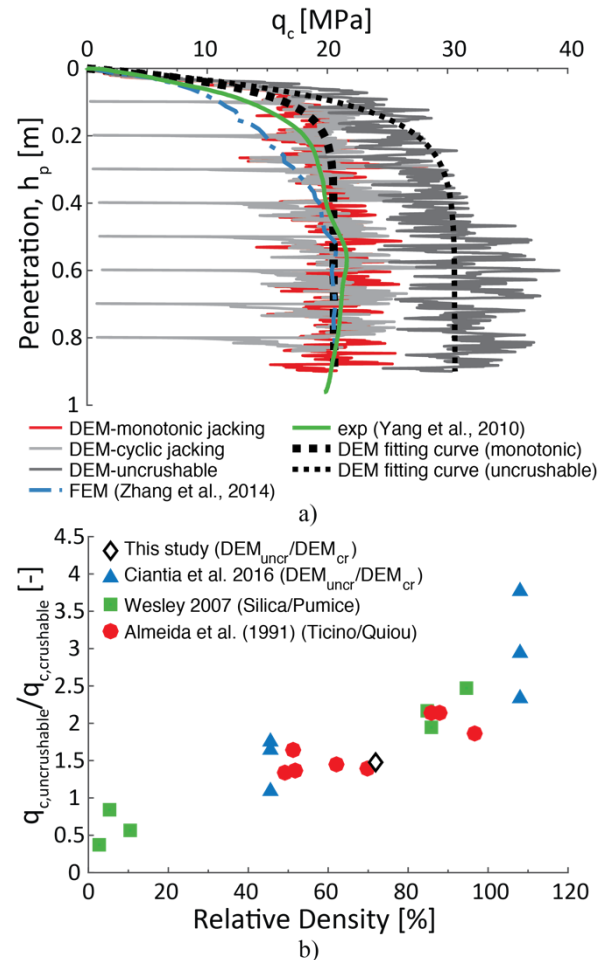
Figure 3 a) End-bearing capacity q_c versus penetration: Comparison between DEM (raw data and fitting curve), FEM (Zhang et al., 2014) (steady state q_c = 21 MPa)and experimental results (Yang et al., 2010) and b) effect of crushability on tip resistance (Ciantia et al., 2016).

3.3 Stress distributions: comparison of DEM model predictions with experiments and FE simulations

Figure 4 compares the experimental and DEM outcomes for σ'_r considering stress measurements at $r=2R$ (R=pile radius) and three depths below the sand surface during the push phase of the jacking cycle. There is generally good agreement

between the experimental stresses the model predictions. However, the agreement becomes less satisfactory once the tip has penetrated 50 mm below the measurement point. Given that the displacement fields are largely controlled by the pile tip geometry, the stress discrepancy may be due to the contact model predicting that the DEM model's unloading response is softer (see Figure 1c) than is seen experimentally.
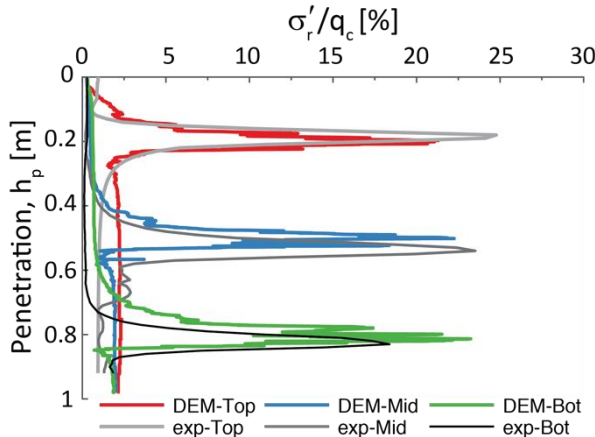
Figure 4 DEM and experimental (Jardine et al., 2013a) normalised radial stresses measured at r =2R for three different locations in the soil (20cm, 50cm and 80cm from the top boundary) as the pile is installed.

The radial stress regime developed in the sand beneath and above the moving pile tip is further explored in Figure 5. To be consistent with (Jardine et al., 2013a) the data are represented as a function of relative pile tip depth h normalized by pile radius R. Note that h/R is initially negative, and becomes positive when the penetrating tip reaches each stress measurement particular level. Data are plotted for Three r/R positions and the circumferential (σ'_θ) and vertical (σ'_z) stresses are also reported. Over the r/R ranges considered, the DEM predictions are in good agreement with the experimental profile shapes, their positions and peak magnitudes.
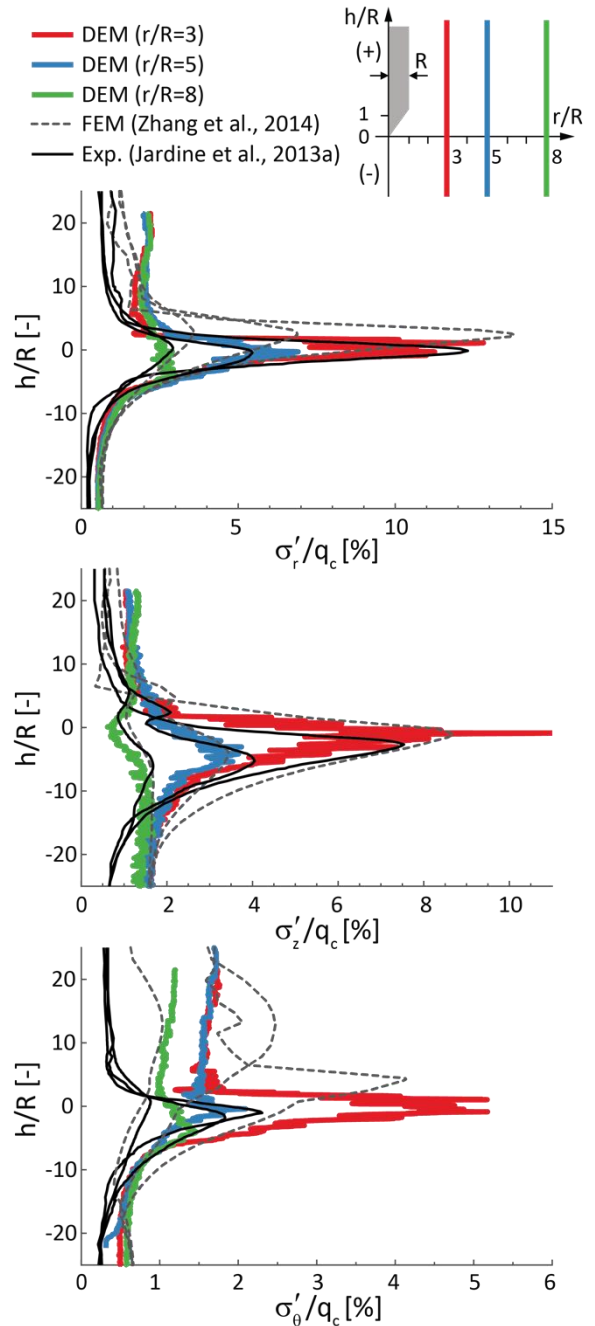
Figure 5 DEM, FEM (Zhang et al., 2014) and experimental (Jardine et al., 2013a) comparison of stresses developed as pile tip advances. The radial (b) circumferential (c) and vertical (d) stresses are normalized by q_c and refer to lines having at a distance r/R=3,5 and 8 from the pile axis as sketched in (a).
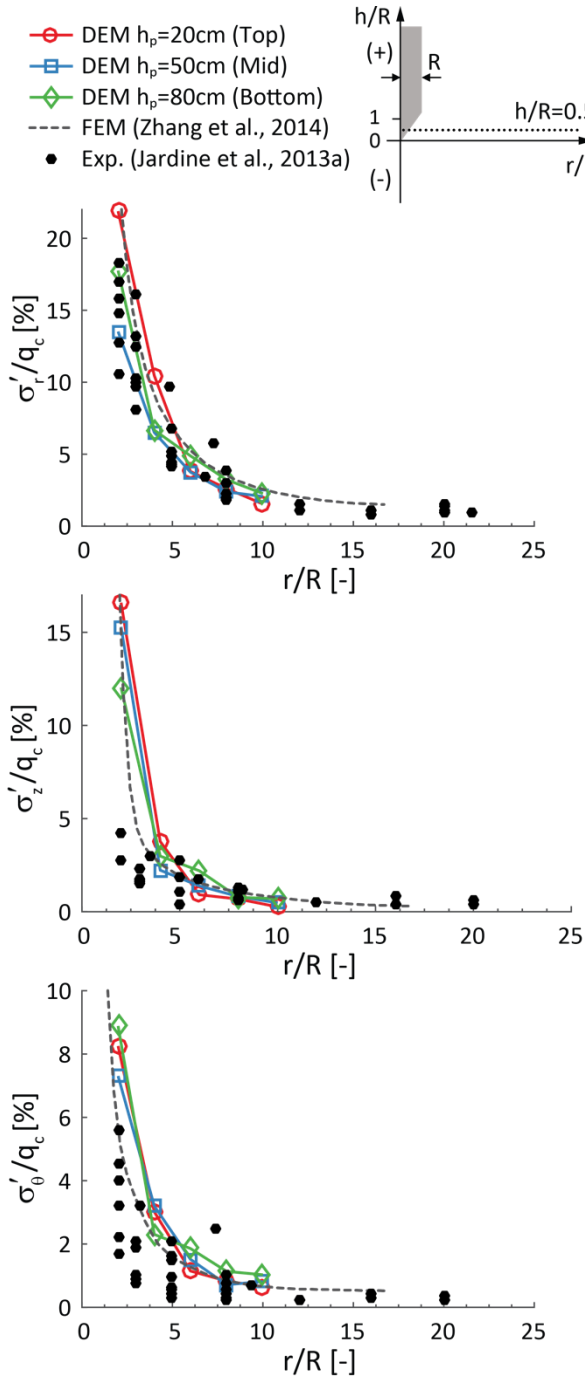
Figure 6 DEM, FEM (Zhang et al., 2014) and experimental (Jardine et al., 2013a) comparison of normalized radial (b) tangential (c) and vertical (d) effective stress evolutions along the radial axis at h=0.5R above the tip.

Figure 6 considers the decay of the σ_r', σ_θ' and σ_z' stresses (normalized by q_c) with increasing r/R during the penetrating phases of the jacking cycles. These values are established at $h/R=0.5$ at three penetration stages (all three in the steady state regime) and compared with the Jardine et al. (2013a) experimental data. The same experiments were simulated using the finite element method (FEM) by Zhang et al. (2014). It is interesting that the FEM and DEM analyses both show similar exponential decays to the experiments, even close to the tip where numerical analyses predictions are most difficult to predict accurately (Gupta,1991).

As with the numerical simulation data, Jardine et al. (2013a) report that measurements made close to the pile tip are subject to relatively high coefficients of variation (COVs). While the DEM σ_r' trend follows the experimental data at all plotted r/R ratios, the σ_θ'/q_c and σ_z'/q_c predictions tend to exceed the experimental trends, especially close to the pile shaft ($r/R<3$).

Figure 7 summarises the spatial variation of radial effective stress normalized by q_c at three stages of penetration, considering both loaded push period (push) and zero-load pause period (pause) phases of the cyclic jacking process. In line with the results presented in Figure 5, the stress distributions below and around the tip appear to depend principally on h/R and r/R and to be independent of the absolute penetration depths for the conditions considered. However, the stresses applying around the shaft are influenced by the top boundary condition over the first 200-300 mm below the sand surface, after which the end-bearing penetration curve achieves its quasi-steady state regime (see Figure 3). This is more evident in the 'pause' contours (Figure 7b) where a peak of radial stresses develops at about 50-60 mm out from the axis (at $r/R\approx3$) along the shaft length below the region that is influenced by the top boundary ($0.0< z <0.2$).

a) loaded push period

b) zero-load pause period
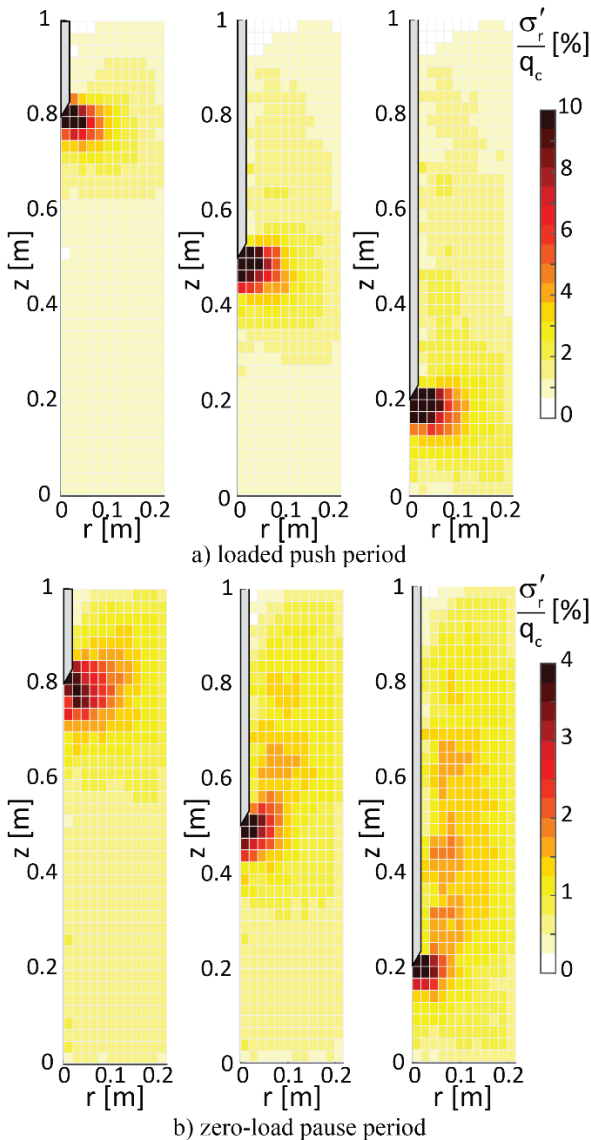
Figure 7 Illustration of radial stress spatial distribution, normalised by q_c, shown in %, during installation for three penetration depths: (a) 'penetrating' conditions at end of push; (b) 'unloaded' at end of each corresponding pause.

Figure 8 Illustration of DEM stress spatial distribution of stresses normalised by q_c during the loaded push period. Experimental contours are reported in Jardine et al. (2013b).
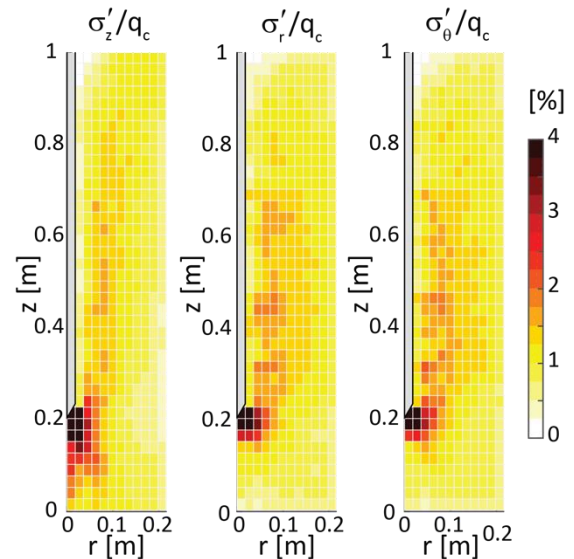
Figure 9 Illustration of DEM stress spatial distribution of stresses normalised by q_c during zero-load pause period. Experimental contours are reported in Jardine et al. (2013b).

To better investigate the stress evolution around the pile tip, the spatial variations of σ_r', σ_θ' and σ_z' around the shaft are presented in Figures 8 and 9 (normalised by q_c) for the penetrating and (unloaded) pause conditions. The numerical predictions are in broadly good agreement with the experimental contour plots given by Jardine et al. (2013b).

This is confirmed in Figure 10 where radial profiles of the stresses are represented for three positions above the shaft and compared when possible with experimental data (from Jardine et al. (2013b)) and FEM predictions by Zhang et al.

(2014), who did not consider the pause stages explicitly. The FEM and (smoothed) DEM analyses led to similar peak stress ratios and generally comparable trends. The DEM predictions for the pause periods also show fair agreement with the experimental data, particularly for the radial stress cases for which there were more sensors and lower potential measurement errors and scatter; Jardine et al (2013a).

Further insight into the extreme stress changes that apply around pile shafts during penetration into sand is given by considering the stresses experienced at the h/R=0.5 stage (Figure 10). The soil around the shaft (r/R<5) unloads very significantly as the pile tip passes, while further way (at r/R>5) the stress relaxation is relatively modest. These opposing trends leads to the stress profiles presenting their maxima at $3R$-$5R$ from the pile axis.

Figure 10 DEM vertical radial and circumferential stresses acting above pile tip during: (a) steady penetration and (b) (unloaded) pause conditions. Where possible FEM and experimental results are also shown.
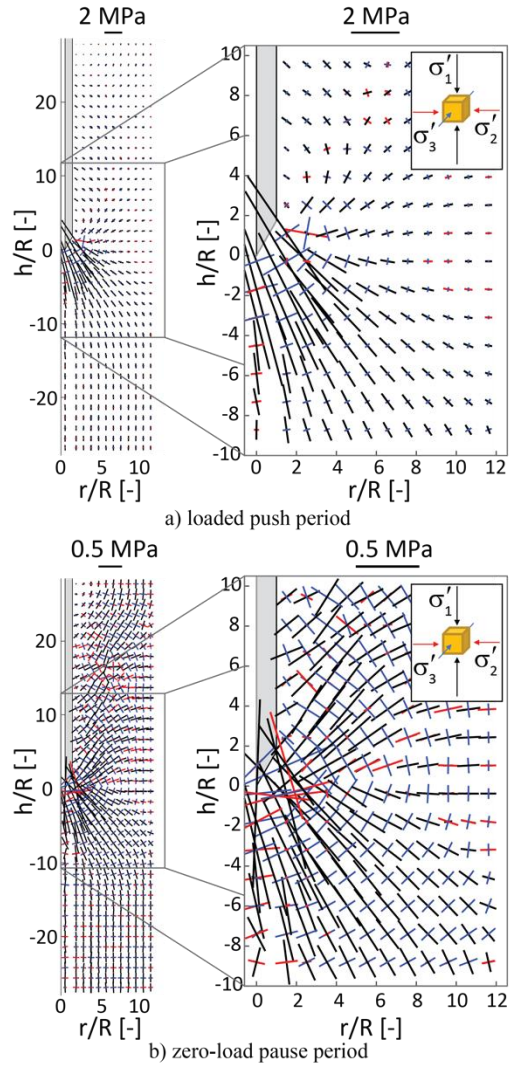
Figure 11 Major (σ'_1 in black), intermediate (σ'_2 in red) and minor (σ'_3 in blue) principal stress vectors for (a) 'penetrating' conditions at end of the h_p=0.5 push phase; (b) 'unloaded' at end of the corresponding pause period.

The stress analyses presented above considered only the σ'_r, σ'_θ and σ'_z cylindrical components. While the initial stress regime has $\sigma'_z = \sigma'_1$ and $\sigma'_r = \sigma'_\theta = \sigma'_2 = \sigma'_3$ as its principal stresses Figure 11a demonstrates the intensive rotation (up to 250°) of the major principal stress axes that take place in the sand mass as the pile penetrates. Jiang et al. (2006) report similar overall trends from their 2D DEM simulations.

As depicted in Figure 11(b), the unloading associated with the jacking pauses induces further rotations of the principal stress axes close to the shaft. Interestingly, the spatial distribution of the major principal stress axis directions resemble closely the principal strain increment axis directions interpreted by Galvis-Castro et al. (2019) from model pile calibration chamber experiments through digital image correlation. While closer correlation checks are required between the principal stress and strain axes' directions, it appears that pile penetration in sands provokes a largely co-axial mechanical behavioural response.

The spatial variations in σ'_1 shown in Figure 12b) and c) confirm that the major principal stress significantly reduces around the pile tip shoulder as h/R grows. The marked stress axis rotation is induced by the change in direction of the vertical shaft shear stresses, which are represented in Figure 12(c) normalised by the radial (effective) stress.

3.4 Microscale insights: particle breakage and arching

Comparisons between DEM simulations performed with and without particle breakage allow evaluation of the separate impacts on the stress relaxation experienced around the shaft of grain crushing. Considering a measurement sphere whose origin is positioned at $r/R = 2$ and $z = 0.5$m, at the chamber mid-height. Figure 13 tracks how the mobilised stress ratio q/p' varies with h/R.

Figure 12 spatial distributions of a) changes of normalized vertical shear stress between 'push' and 'pause' stages. Parts b) and c) present magnitudes of major principal stress (σ'_1) normalized by q_c covering the penetration and (unloaded) conditions respectively.
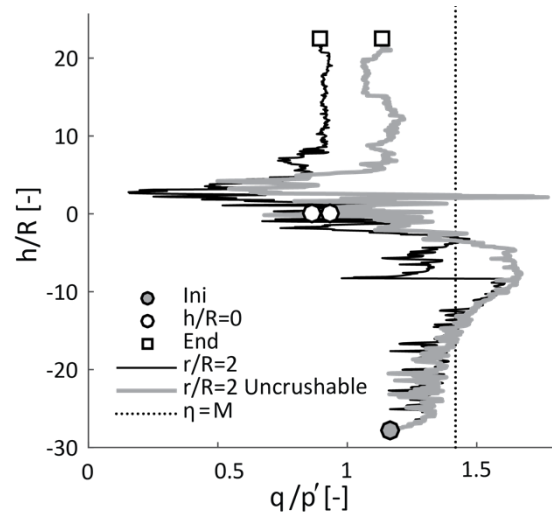
Figure 13 Evolution of stress ratio (q/p') measured during pile monotonic penetration at r=2R form pile axis for MS at z=0.5 for the crushable (black) and uncrushable (grey) case.

With crushable grains, the q/p' ratio reaches its peak at $h/R = -8$ after which it falls, passing through critical state at $h/R = -1$ and then starts to decrease, indicating shear unloading. The uncrushable grain analysis does not show the
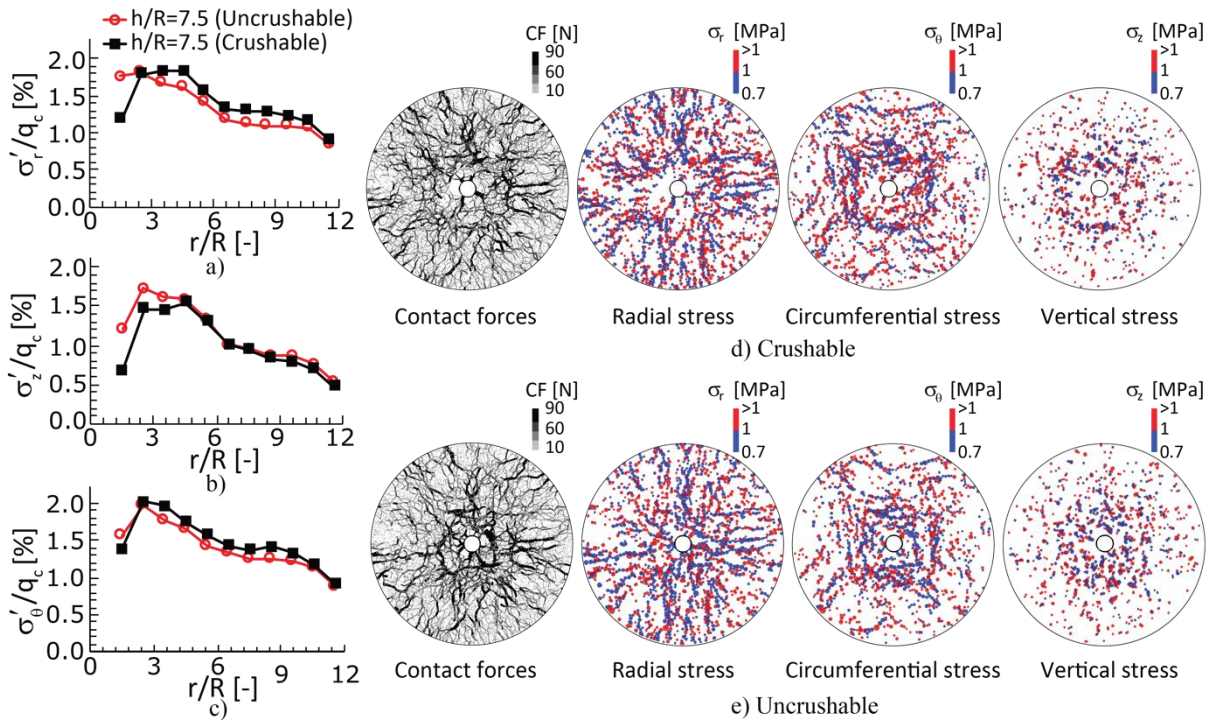
Figure 14 Radial profiles of (a) radial, (b) circumferential and (c) vertical stresses acting at h/R=7.5, comparing crushable and uncrushable simulations of the (unloaded) pause phases and demonstrating arching around the pile shaft: d) Uncrushable e) Crushable. Only particles with circumferential, radial and vertical stress>0.7MPa are shown: blue > 1MPa and red<1MPa

same sharp drop in q/p' when h/R passes the maximum (peak q/p' value). Nevertheless, q, p' and q/p' decrease as the pile tip penetrates to give h/R >0.6 in both cases and shear unloading reaches a minimum once h/R reaches ≈3.

The stress ratio subsequently increases slightly until a stationary value is obtained. However, the crushable grain case involves a greater degree of shear unloading further from the tip (at h/R>5) than is predicted to apply to unbreakable grains.

Parts (a), (b) and (c) of Figure 14 compare the radial profiles of the cylindrical stress components (normalised by q_c of the crushable response) given from analyses with crushable and unbreakable grains at h/R=7.5 above the tip, considering a zero-load pause period jacking stage of a cycle. Crushing accentuates the unloading close to the shaft and promotes the arching action.

It is possible to construct images of the associated contact force network by representing each

contact force as a line (with thickness proportional to its force) that joins the centres of contacting particles. Vertical plan views of the force networks predicted around the shaft at h/R=7.5 for the uncrushable and crushable cases are shown in Figures 14(d) and (e), which are broken down into radial, circumferential and vertical sets to highlight how crushing affects the force chain systems. Circumferentially arching force networks are more clearly developed around the shaft in the crushable case that shield the pile shaft surface (at r/R=1) from the higher radial stresses developed at greater r/R and lead to more weekly developed radial force networks close to the shaft.

Figure 15 provides further insights into the arch development by showing the incremental particle displacements developed during the penetration and (unloaded) pause phases of the jacking cycle that advanced the pile tip from 0.7 to

0.8 m depth. Particles located below the tip experience large radial displacements away from the axis tip, while those just above the tip move radially inwards (by far smaller degrees) and promote radial stress relaxation (see Figure 11a) in both the crushable and uncrushable simulations although more inward radial displacement applies in the uncrushable case during the zero-load pause period.

a) loaded push period (h_p from 0.7 to 0.8)

b) zero-load pause period (h_p=0.8)
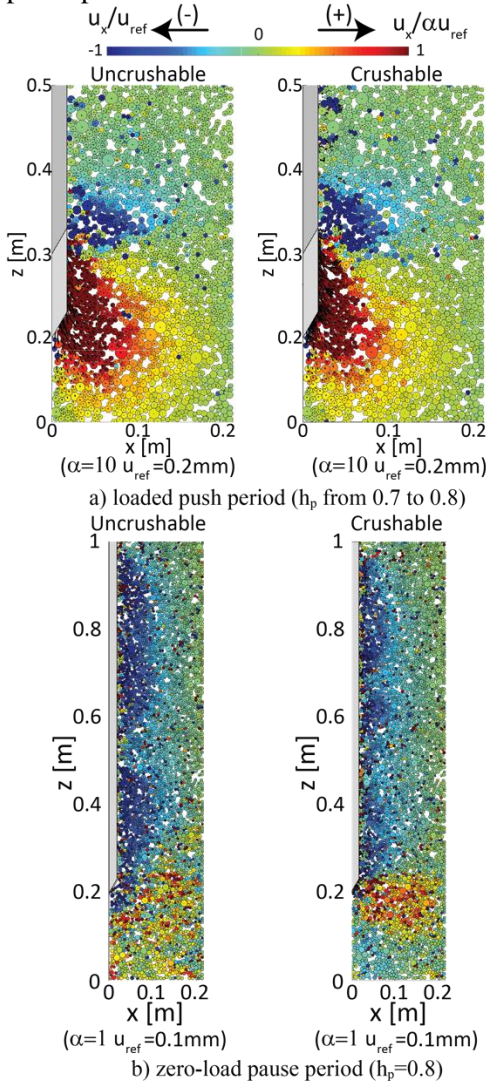
Figure 15 Comparison of particle radial displacement increments for the crushable and uncrushable models during a) 10cm of penetration (0.7 to 0.8m of penetration dept h_p) and b) the following zero-load pause period: the negative values (towards the shaft) are normalised by u_{ref}, the positive values (away from the pile) are normalised by αu_{ref}.

Jardine et al (2006) and Jardine (2019) argue that the non-uniform stress distributions set up by driven pile installation provide one of the potential mechanisms for the marked growth of shaft capacity over time developed by piles driven in sand. Creep could weaken circumferential arching and lead to radial stresses (and shaft resistances) rising. Corrosion reactions and other processes can also be important, particularly with small diameter piles: see Carroll et al (2019).

Particle breakage clearly affects the particle movements and stress redistributions around the pile shafts. Recent acoustic emission (AE) and signal processing (Mao et al., 2018, 2016) studies have revealed that, for flat ended piles, particle breakage develops principally under the pile tip within an area located between 0.5-1.5 pile diameters below the tip. Doreau-Malioche et al. (2018) by means of X-Ray imaging show that it is possible to identify the location of crushed fragments around a small-scale displacement pile penetrating through a crushable carbonate sand and show that crushing develops principally around the tip.
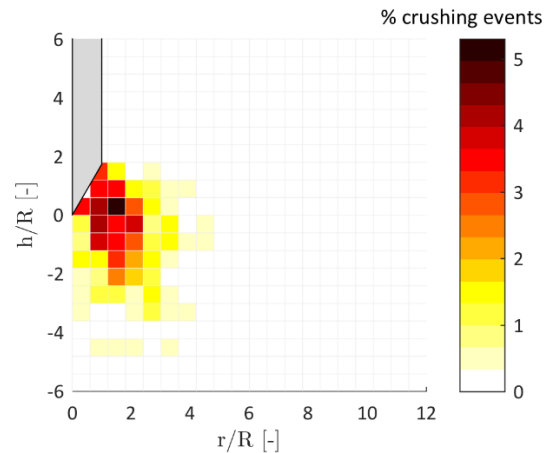
Figure 16 Particle crushing location during pile penetration represented as % of crushing events with respect to tip position.

Figure 16 provides a representation in h/R, r/R coordinates of the positions at which all particle breakage is predicted in the DEM analyses of pile penetration. The DEM model predicts that most

crushing occurs close to the cone, within a volume described by a triangular, convex shaped, solid of revolution with characteristic length of about $1.5R$. In line with the experimental evidence mentioned above, no crushing events are predicted at distances $5R$ below the tip or above the pile tip shoulder. The crushed fragments are first pushed away from the axis and then move back towards the shaft after the tip passes, as observed experimentally by Arshad et al. (2014) and Doreau-Malioche et al. (2018).
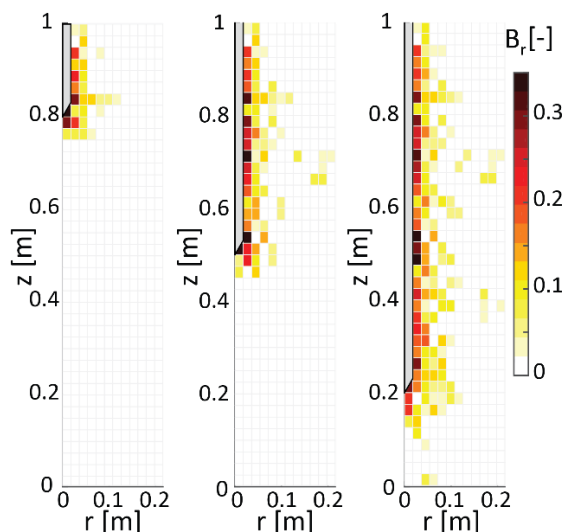
Figure 17 . DEM breakage distributions corresponding to three penetration depths.

The crushing profiles corresponding to three penetration depths are depicted in Figure 17, showing similar profiles to those obtained in crushable grain FEM analyses by Zhang et al. (2013). Both numerical approaches are in agreement with experiments reported by (Yang et al., 2010) and predict that the crushing-influenced zone is mainly confined close to the shaft.

Yang et al (2010) report that breakage ratios B_r=0.2 applied within their most highly crushed Zone 1, which extends over the $1< r/R <1.6$ range from the pile axis, with ratios of 0.09 and 0.07 ratios applying in their more distant Zones 2 and 3 respectively. The necessary particle scaling and the resulting limited number of particles make it

difficult to distinguish such zones from the DEM analysis, as the sampling volumes are too small to give representative results. Nevertheless, analysis of Figure 17 shows average B_r ratios of 0.22 in the $1< r/R <2$ and 0.09 over the $2 < r/R < 3$ range that match the experimental findings. Zhang et al's (2014) continuum FEM simulation captures the spatially varying evolution of B_r better than the DEM treatment.

Galvis-Castro et al. (2019) suggested that any constant thickness of the crushed particle band width provides an indirect indication that particle crushing occurs mostly at, or below, the pile tip during installation. Comparing Figures 16 and 17 shows the DEM results supporting this hypothesis. We recognise, however, that Yang et al (2010) observed in their experiments that the crushed sand became concentrated into annular areas that adhered to the piles' shafts as penetration continued, forming 'crusts' whose thickness grew gradually with h/R. Yang et al (2010) argued that surface shear abrasion, which is not captured in the DEM analysis, fed this growth and note that similar 'fractured sand crusts' have been observed in the field around piles driven in sands. Yang et al (2010) and Jardine (2019) argue that such abrasion and the very large number of load cycles applied during field driving contribute to shaft radial stresses continuing to decay at larger h/R ratios than is expected by current FEM or DEM analyses.

4 CONCLUSIONS

DEM simulations offer new insights into the stress conditions developed around piles penetrating in sand. The analyses reported both match and help explore the pile calibration chamber experiments reported by Jardine et al. (2013a) and Yang et al. (2010). The crushable DEM model employed was calibrated to match element test conducted on the same NE34 Fontainebleau sand before being employed to study how grain crushing, and monotonic versus cyclic jacking, affected the micromechanical mechanisms that

give rise to key macro-scale features of pile behaviour. The main findings are:

1) Quasi-static DEM simulations indicated pile tip resistances q_c that followed similar profiles, independently of whether piles advanced by monotonic or cyclic jacking.

2) In line with recent experimental evidence (Doreau-Malioche et al., 2018; Mao et al., 2016) particle crushing occurred within a limited volume that extended to ≈ 4 radii below the pile base.

3) The degree of crushing predicted by the DEM model was broadly compatible with that observed experimentally. No crushing was predicted along the shaft, although it is recognised that surface abrasion may add to the thickness of any crushed sand crust seen in physical experiments or pile driving in the field.

4) The average stresses determined within volumes of the modelled soil particle arrays at given depths below the pile tip rose sharply as the tip approached from above, and declined sharply as it penetrated below to greater depth. They also varied with radial distance from the pile axis.

5) The DEM analysis predictions are broadly comparable to both the experimental observations and earlier independent FEM analyses undertaken with an advanced crushable soil model.

6) The DEM simulations show a strongly non-uniform stress regime developing around the pile shaft, with marked arching above the pile tip and stress maxima over the $2<r/R<6$ range that match the experiments, as interpreted by Jardine et al. (2013b). However, the DEM analysis indicates more clearly visible peaks in the vertical and circumferential stresses than were seen in the experiments, where the latter were harder to measure and therefore subject to greater scatter.

7) The penetration simulations identified key aspects of the stress paths provoked in the sand around the pile tip and shaft. The latter include large rotations of the principal stress axes (by as much as 250^0) during penetration as well extreme stress peaks as the tip arrives and decrease massively as it passes, leaving the sand mass around the shaft in a state of arching.

8) Arching was accentuated by grain crushing but did not appear to be as strongly influenced by cyclic changes in the jack's pile head loads.

9) Close similarities were noted between the directions of the principal strain axis directions observed experimentally by (Galvis-Castro et al. 2019) and the DEM model principal stress axis, showing an apparently nearly co-axial global material response in the sand.

10) The insights provided by the DEM into interparticle stresses, force chains and particle incremental displacements highlight how circumferential arching develops around the shaft through local unloading. Variations over time in such arching offers one potential explanation for the shaft capacity growth with age that occurs around industrial piles driven in sand.

5 ACKNOWLEDGEMENTS

6 REFERENCES

Altuhafi, F.N., Jardine, R.J., Georgiannou, V.N., Moinet, W.W., 2018a. Effects of particle breakage and stress reversal on the behaviour of sand around displacement piles. *Géotechnique* **68**, 546–555.

Altuhafi, F.N., Jardine, R.J., Georgiannou, V.N., Moinet, W.W., Ciantia, M.O., Arroyo, M., Gens, A., 2018b. Effects of particle breakage and stress reversal on the behaviour of sand around displacement piles. *Géotechnique* 1–2 https://doi.org/10.1680/jgeot.18.D.010.

Arroyo, M., Butlanska, J., Gens, A., Calvetti, F., Jamiolkowski, M., 2011. Cone penetration tests in a virtual calibration chamber. *Géotechnique* **61**, 525–531.

Arshad, M.I., Tehrani, F.S., Prezzi, M., Salgado, R., 2014. Experimental study of cone penetration in silica sand using digital image correlation. *Géotechnique* **64**, 551–569.

Bolton, M.D., Gui, M.W., Garnier, J., Corte, J.F., Bagge, G., Laue, J., Renzi, R., 1999. Centrifuge cone penetration tests in sand. *Géotechnique* **49**, 543–552.

Boschi, K., di Prisco, C., Ciantia, M.O., 2019. Micromechanical investigation of grouting in soils. *Int. J. Solids Struct*. https://doi.org/10.1016/j.ijsolstr.2019.06.013.

Butlanska, J., Arroyo, M., 2015 Discussion of "Stresses Developed around Displacement Piles Penetration in Sand" by Z. X. Yang, R. J. Jardine, B. T. Zhu, and S. Rimoy. J. Geotech. Geoenvironmental Eng.**141**(3), 1-3.

Butlanska, J., Arroyo, M., Gens, A., (2009). *Homogeneity and Symmetry in DEM Models of Cone Penetration*. AIP Conf. Proc 425–428.

Butlanska, J., Arroyo, M., Gens, A., O'Sullivan, C., (2014). Multi-scale analysis of cone penetration test (CPT) in a virtual calibration chamber. *Can. Geotech. J.* **51**, 51–66.

Butlanska, J., de Toledo, M., Gens Solé, A., (2010). *Size effects on a virtual calibration chamber.* In: Seventh European Conference on Numerical Methods in Geotechnical Engineering. pp. 225–230.

Calvetti, F., (2008). Discrete modelling of granular materials and geotechnical problems. *Eur. J. Environ. Civ. Eng.* **12**, 951–965.

Carroll, R., Carotenuto, P., Dano, C., Salama, I., Silva, M., Gavin, K. and Jardine, R. 2019. Field experiments at three sites to investigate the effects of age on steel piles driven in sand. *Géotechnique*.

Christoffersen, J., Mehrabadi, M.M., Nemat-Nasser, S., 1981. A Micromechanical Description of Granular Material Behavior. *J. Appl. Mech.* **48**, 339.

Ciantia, M., Arroyo, M., Zhang, N., Emam, S., 2017. *Periodic cells for large-scale problem initialization*. In: EPJ Web of Conferences.

Ciantia, M.O., Arroyo, M., Butlanska, J., Gens, A., 2016. DEM modelling of cone penetration tests in a double-porosity crushable granular material. *Comput. Geotech*. **73**, 109–127.

Ciantia, M.O., Arroyo, M., Calvetti, F., Gens, A., 2015. An approach to enhance efficiency of DEM modelling of soils with crushable grains. *Géotechnique* **65**, 91–110.

Ciantia, M.O, Arroyo, M., O'Sullivan, C., Gens, A., 2019a. Micromechanical Inspection of Incremental Behaviour of Crushable Soils. *Acta Geotech.* 1–20. https://doi.org/10.1007/s11440-019-00802-0

Ciantia, M.O., Arroyo, M., O'Sullivan, C., Gens, A., Liu, T., 2019b. Grading evolution and critical state in a discrete numerical model of Fontainebleau sand. *Géotechnique* 1–15. https://doi.org/10.1680/jgeot.17.P.023

Ciantia, M.O., Boschi, K., Shire, T., Emam, S., 2018. Numerical techniques for fast generation of large discrete-element models. *Proc. Inst. Civ. Eng. - Eng. Comput. Mech*. **171**(4), 147–161.

Coetzee, C.J., 2019. Particle upscaling: Calibration and validation of the discrete element method. *Powder Technol.* **344**, 487–503.

Coop, M.R., Klotz, E.U., Clinton, L., 2005. The influence of the in situ state of sands on the load–deflection behaviour of driven piles. *Géotechnique* **55**, 721–730.

Doreau-Malioche, J., Combe, G., Viggiani, G., Toni, J.B., 2018. Shaft friction changes for cyclically loaded displacement piles: an X-ray investigation. *Géotechnique Lett.* **8**, 66–72.

Einav, I., 2007. Breakage mechanics—Part I: Theory. *J. Mech. Phys. Solids* **55**, 1274–1297.

Falagush, O., McDowell, G. R., Eng, C., Yu, H.-S., 2015. Discrete Element Modeling of Cone Penetration Tests Incorporating Particle Shape and Crushing. *I. J. Geomech.* **15**(6), 04015003

Galvis-Castro, A.C., Tovar-Valencia, R.D., Salgado, R., Prezzi, M., 2019. Effect of loading direction on the shaft resistance of jacked piles in dense sand. *Géotechnique* **69**(1)16–28.

Gens, A., Arroyo, M., Butlanska, J., Carbonell, J.M., Ciantia, M., Monforte, L., O'Sullivan, C., 2016. Simulation of the cone penetration test: Discrete and continuum approaches.

Aust. Geomech. J. **51**.

Gupta, R.C., 1991. Finite Strain Analysis for Deep Cone Penetration. *J. Geotech. Eng.* **117**, 1610–1630.

Huang, A.-B., Ma, M.Y., 1994. An analytical study of cone penetration tests in granular material. *Can. Geotech. J.* **31**, 91–103.

Huang, X., Hanley, K.J., O'Sullivan, C., Kwok, F.C.Y., 2014. Effect of sample size on the response of DEM samples with a realistic grading. *Particuology* **15**, 107–115.

Itasca, C.G.I., 2016. Particle Flow Code, V. 5.0.

Janda, A., Ooi, J., 2016. DEM modeling of cone penetration and unconfined compression in cohesive solids. *Powder Technol*. **293**, 60–8.

Jardine, R.J., Chow, FC, Overy, RF and Standing, J.R., 2005. *ICP design methods for driven piles in sands and clays*". Thomas Telford Ltd, London p. 105.

Jardine, R.J, Standing, J.R and Chow, F.C. 2006 Some observations of the effects of time on the capacity of piles driven in sand. *Géotechnique* **55**(4), 227-244

Jardine, R.J., Zhu, B.T., Foray, P., Yang, Z.X., 2013a. Interpretation of stress measurements made around closed-ended displacement piles in sand. *Géotechnique* **63**, 613–627.

Jardine, R.J., 2013. Advanced laboratory testing in research and practice. *2nd Bishop Lecture*. Proc. ICSMGE, Eds Delage et al., Presses des Ponts, Paris, Vol 1, pp. 35-55.

Jardine, R.J., Zhu, B.T., Foray, P., Yang, Z.X., 2013b. Measurement of stresses around closed-ended displacement piles in sand. *Géotechnique* **63**, 1–17.

Jardine, R.J., 2019. Geotechnics, Energy and Climate Change. 56th Rankine Lecture, *Géotechnique*.https://doi.org/10.1680/jgeot.18.RL.001

Jiang, M., Dai, Y., Cui, L., Shen, Z., Wang, X., 2014. Investigating mechanism of inclined CPT in granular ground using DEM. *Granul. Matter* **16**, 785–796.

Jiang, M.J., Yu, H.S., Harris, D., 2006. Discrete element modelling of deep penetration in granular soils. *Int. J. Numer. Anal. Methods Geomech.* **30**, 335–361.

Klotz, E.U., Coop, M.., 2001. An investigation of the effect of soil state on the capacity of driven piles in sands. *Géotechnique* **51**, 733–751.

Lade, P. V., Yamamuro, J.A., Bopp, P.A., 1996. Significance of Particle Crushing in Granular Materials. *J. Geotech. Eng.* **122**, 309–316.

Lehane, B.M., Schneider, J.A., Xu, X., 2005. A review of design methods for offshore driven piles in siliceous sand. UWA Rep. GEO 5358.

Lu, Q., Randolph, M.F., Hu, Y., Bugarski, I.C., 2004. A numerical study of cone penetration in clay. *Géotechnique* **54**, 257–267.

Luding, S., 2004. Micro–macro transition for anisotropic, frictional granular packings. *Int. J. Solids Struct.* **41**, 5821–5836.

Mao, W., Towhata, I., Aoyama, S., Goto, S., 2016. Grain crushing under pile tip explored by acoustic emission. *Geotech. Eng. J.* SEAGS AGSSEA 47.

Mao, W., Yang, Y., Lin, W., Aoyama, S., Towhata, I., 2018. High Frequency Acoustic Emissions Observed during Model Pile Penetration in Sand and Implications for Particle Breakage Behavior. *I. J. Geomech.* **18**(11), 04018143

McDowell, G.R., Falagush, O., Yu, H.-S., 2012. A particle refinement method for simulating DEM of cone penetration testing in granular materials. *Géotechnique Lett*. **2,** 141–147.

Muir Wood, D. 2007. The magic of sands – the 20th Bjerrum Lecture presented in Oslo, 25 November 2005. *Can. Geotech. J.* **44**(11), 1329–1350.

Monforte, L., Arroyo, M., Carbonell, J.M., Gens, A., 2017. Numerical simulation of undrained insertion problems in geotechnical engineering with the Particle Finite Element Method (PFEM). *Comput. Geotech.* **82**, 144–156.

Phuong, N.T.V., van Tol, A.F., Elkadi, A.S.K., Rohe, A., 2016. Numerical investigation of pile installation effects in sand using material point method. *Comput. Geotech.* **73**, 58–71.

Pournaghiazar, M., Russell, A.R., Khalili, N., 2013. Drained cavity expansions in soils of finite radial extent subjected to two boundary conditions. I*nt. J. Numer. Anal. Methods Geomech.* **37**, 331–352.

Quezada, J.C., Breul, P., Saussine, G., Radjai, F., 2014. Penetration test in coarse granular material using Contact Dynamics Method. *Comput. Geotech.* **55**, 248–253.

Rimoy, S., Silva, M., Jardine, R., Yang, Z.X., Zhu, B.T., Tsuha, C.H.C., 2015. Field and model investigations into the influence of age on axial capacity of displacement piles in silica sands. *Géotechnique* **65**, 576–589.

Russell, A.R., Muir Wood, D., 2009. Point load tests and strength measurements for brittle spheres. *I. J. Rock Mech. Min. Sci.* **46**, 272–280.

Russell, A.R., Muir Wood, D., Kikumoto, M., 2009. Crushing of particles in idealised granular assemblies. *J. Mech. Phys. Solids* **57**, 1293–1313.

Salgado, R., Mitchell, J.K., Jamiolkowski, M., 1998. Calibration Chamber Size Effects on Penetration Resistance in Sand. *J. Geotech. Geoenvironmental Eng.* **124**, 878–888.

Santamarina, J.C., 2003. *Soil Behavior at the Microscale: Particle Forces.* In: Soil Behavior and Soft Ground Construction. American Society of Civil Engineers, Reston, VA, 25–56.

Seif El Dine, B., Dupla, J.C., Frank, R., Canou, J., Kazan, Y., 2010. Mechanical characterization of matrix coarse-grained soils with a large-sized triaxial device. *Can. Geotech. J.* **47**, 425–438.

Sharif, Y., Brown, M., Ciantia, M.O., Knappett, J., Davidson, C., Cerfontaine, B., Robinson, S., 2019. *Numerically modelling the installation and loading of screw piles using DEM*. In: Davidson, et al. (Eds.), Proceedings of the 1st International Screw Pile Symposium on Screw Piles for Energy Applications. Dundee, 101-8.

Tehrani, F.S., Arshad, M.I., Prezzi, M., Salgado, R., 2018. Physical Modeling of Cone Penetration in Layered Sand. *J. Geotech. Geoenvironmental Eng.* **144**, 04017101.

Ting, J.M., Corkum, B.T., Kauffman, C.R., Greco, C., 1989. Discrete Numerical Model for Soil Mechanics. *J. Geotech. Eng.* **115**, 379–398.

Tran, Q.A., Chevalier, B., Breul, P., 2016. Discrete modeling of penetration tests in constant velocity and impact conditions. *Comput. Geotech.* **71**, 12–18.

Tu, F., Ling, D., Hu, C., Zhang, R., 2017. DEM-FEM analysis of soil failure process via the separate edge coupling method. *Int. J. Numer. Anal. Methods Geomech.* **41**, 1157–1181.

White, D., Bolton, M.D., 2004. Displacement and strain paths during plane-strain model pile installation in sand. *Géotechnique* **54**, 375-397.

White, D., Lehane, B.M., 2004. Friction fatigue on displacement piles in sand. *Géotechnique* **54**, 645–658.

Yang, Z.X., Jardine, R.J., Zhu, B.T., Foray, P., Tsuha, C.H.C., 2010. Sand grain crushing and interface shearing during displacement pile installation in sand. *Géotechnique* **60**, 469–482.

Yang, Z.X., Jardine, R.J., Zhu, B.T., Rimoy, S., 2014. Stresses Developed around Displacement Piles Penetration in Sand. *J. Geotech. Geoenvironmental Eng.* **140**, 04013027.

Zhang, C., Nguyen, G.D., Einav, I., 2013. The end-bearing capacity of piles penetrating into crushable soils. *Géotechnique* **63**, 341–354.

Zhang, C., Yang, Z.X., Nguyen, G.D., Jardine, R.J., Einav, I., 2014. Theoretical breakage mechanics and experimental assessment of stresses surrounding piles penetrating into dense silica sand. *Géotechnique Lett.* **4**,11–16.

Zhang, N., Arroyo, M., Ciantia, M., Gens, A., 2018. *DEM Investigation of Particle Crushing Effects on Static and Dynamic Penetration Tests*. In: Wu, W., Yu, H.-S. (Eds.), Proceedings of China-Europe Conf. on Geotech.Engineering. Springer, Cham, Vienna. 274–278.

Zhang, N., Arroyo, M., Ciantia, M.O., Gens, A., Butlanska, J., 2019. Standard penetration testing in a virtual calibration chamber. *Comput. Geotech.* **111**, 277–289.

Zhang, N., Evans, M., 2019. Discrete numerical simulations of torpedo anchor installation in granular soils. *Comput. Geotech.* **108**, 40–52.

Zhang, Z., Wang, Y.-H., 2015. Three-dimensional DEM simulations of monotonic jacking in sand. *Granul. Matter* **17**, 359–376.

List of authors of submitted papers

All papers accessible at the ISSMGE Online Library:

https://www.issmge.org/publications/online-library

Adinolfi, Livia
 A conceptual model to demonstrate the role of suction in the formation of head-cut in fine-grained embankments subjected to overflow, 400

Afshani, Alireza
 Numerical investigation of a close underground excavation, 914

Akçakal, Önder
 Aspects of design and monitoring of deep excavations – a case study, 854

Al Heib, Marwan
 Etude expérimentale du renforcement d'une cavité par géosynthétique en présence d'un remblai cohésif, 719

Alamanis, Nikolaos
 Effect of spatial variability of soil properties on the stability and permanent seismic displacements of highway slopes, 10

Alekhin, Alexey Nikolaevich
 Features of application of non-liner soil model in geotechnical design, 82

Alencar, Ana
 The influence of the dilatancy on the ultimate bearing capacity of the rock mass., 447

Allani, Malek
 Full-scale tests and three-dimensional finite element analysis on micropile groups, 169

Al-Madhlom, Qais Hatem
 Literature Review and perspective Use of UTESS in Arid Region, study area Karbala Province Iraq, 983

Altun, Selim
 Small and large strain dependence on cyclic behavior of silts and silt-clay mixtures, 563

Amoroso, Sara
 From the seismic microzonation studies to the site scale: the case of Arpino (Italy), 80

Andresen, Lars
 Slope failure in sensitive clay, a case study, 714

Antão, Armando
 Nunes Upper and lower bounds for the bearing capacity of foundations on soft soils with reinforcement columns, 345

Araújo Santos,
 Luis Characterization of liquefiable sands using the Hollow Cylinder Apparatus, 429

Araújo Santos, Luis
 Difficulties of using the Harvard miniature compaction apparatus as a reference test in the study of soil compaction, 620

Arnold, André
 Evaluating the reliability of back analysed shear strengths in slopes, 554

ARROYO, MARCOS
 Enhanced cone penetration test interpretation with the Particle Finite Element Method (PFEM), 190

Askarinejad, Amin
 Physical and numerical modelling of the effect of scouring on the lateral stiffness of monopiles, 636

Atalar, Cavit
 Prediction of modified Proctor compaction characteristics using Atterberg limit tests for laterite soils, 425

Atalar, Cavit
 Comparison of Multiple Regression and Artificial Neural Networks in Estimating Compaction Characteristics of Lateritic Soils, Ghana, 422

Atalay, Fikret
 A comparison between thermal conductivity of undisturbed and remolded soil samples, 950

Attari, Yeganeh
 Predicting Pile Driving Induced Movements in Gothenburg Soft Clay, 344

Auverny-Bennetot, Charles
 Yamal LNG: retour d'expérience d'un méga projet pétrolier battis sur le permafrost, 217

Avar, B. Burcin
 Geological and geotechnical considerations for seismic hazard for Penang Island, Malaysia, 39

Avar, B. Burcin
 Design and construction of an excavation under railway bridges at Reading, UK, 270

Gibbon, Dominic

The innovative use of fabric formwork for tunnel infilling, Battersea Power Station Redevelopment, London., 224

Gilder, Charlotte Elizabeth

Ground Investigations in Developing Countries: A study to inform Earthquake Hazard Assessment in the Kathmandu Valley, 110

Giridharan, Shreyas

Modelling liquefaction problems in saturated sand with application to sea dike failure under seismic loading, 192

Gluchowski, Andrzej

Pore pressure behavior of compacted clay under long-term cyclic loads in undrained conditions, 330

Glushkov, A.V.

Investigation of the bored pile work with thermochemical broadening in the basis, 838

Gobbi, Stefania

Influence of geometrical and mechanical properties of soils on numerically computed response spectra for 1D stratigraphies, 644

Godlewski, Tomasz

Determining G-? decay curve in overconsolidated clays from Seismic Dilatometer Test, 281

Golchin, Ali

A thermodynamically based thermo-mechanical model for fine-grained soils, 712

Gomes, Rui Carrilho

Importance of small-strain stiffness on the prediction of the displacements of a flexible retaining wall, 386

González-Gallego, Javier

San Bernabe's hermitage and Ojo Guareña Karst Complex. An inusual slope stability case., 277

Goodey, Richard James

Design and development of a large shear box for testing working platform material, 267

Gottardi, Guido

From geological and historical data to the geotechnical model of the Two Towers in Bologna (Italy), 269

Gottardi, Guido

Experimental study on a river embankment silty soil in partially saturated conditions, 175

Gowda, Sujith

Parameter study for an effective pile installation method in saturated soil using Material Point Method (MPM), 200

Grasso, Salvatore

A comparative study of seismic response analysis of soils using different numerical codes, 904

Grava, Martins

Slope stability issues close to local road P130 near the town Sabile, in Latvia - case story, 289

Green, Russell A.

Quality Assurance Criteria for Cyclic Direct Simple Shear Tests for Evaluating Liquefaction Triggering Characteristics of Cohesionless Soils, 470

GRESS, Jean-Claude

Preconsolidation pressure, CPT'u tip resistance and MENARD net limit pressure, 804

Griffiths, Mark

Geosynthetic cementitious composite mats - essential characteristics and properties, 360

Grizi, Athina

Surface Wave Development during Impact Pile Driving, 464

Günther, Helen

Resistance of fine-grained soil against hydraulic failure, 55

Haas, Sonja

Soil improvement with quicklime - quantification of the carbonation rate in an embankment after 34 years, 868

Haasnoot, Jacco

Macro-stability assessment of dikes using two different probabilistic models, 58

Habert, Julien

Abaques complets synthétiques pour la prévision du comportement des pieux géothermiques, 576

Hailemariam, Henok

'Effect of stress on the thermal conductivity of porous media, 1079

Halder, Prasun

Numerical Study of Load Carrying Capacity of Piled Raft Foundation Embedded in Sand, 730

KIRICHEK, YURIY
Reducing the vibration level of the footings for equipment by viscoelastic connections, 812

Kirstein, Joachim Maaløe
Foundation Subgrade Reactions, 430

Kissane, Paul
Back-analysis of Static Load Tests on Bored Piles Founded in Glacial Soils and Weak Rocks Overlain by Peat/Lacustrine Soils in Northern Ireland, 371

Knopp, Julia
Classification of the weathering-dependent decay behaviour of weak rocks, 334

Knudsen, Jannie
Design of bored piles in Denmark – a historical perspective, 732

Knudsen, Siren
Effect of reconstitution techniques on the triaxial stress-strength behaviour of a very dense sand, 575

Knut, Alexander
Influence of the momentum and the energy on the performance of dynamic compaction technologies – recent field and laboratory tests, 487

Koch, Edina
Finite element analysis of bridge transition zone for investigating the effect of moving loads, 137

Koda, Eugeniusz
Landfill containment system as an effective method of preventing heavy metal pollution, 312

Koedel, Uta
A CPT-based seismic tomographic system for geotechnical subsurface investigations and site assessment, 168

Koivisto, Kirsi
Effect of pore water pressure on the rutting of low-volume roads with varying pavement structures, 747

Koivulahti, Marjo Susanna
Deep soil mixing – Finnish guideline for stabilisation tests, 738

Kokošin, Jure
The designing of a Three-levels Excavation Pit in Soft and Sensitive Clays in Oslo, Norway., 315

Konon, Anastasia
Test results of railway ballast for bearing capacity calculations, 558

KORFF, MANDY
Combined subsidence phenomena in high-rise built urban areas: numerical study for Frankfurt am Main, 370

Koroleva, Irina
Deformation of clay soils under regime long-term static loading, 956

Korzec, Aleksandra Paulina
Procedure of design accelerogram deconvolution in 2D FEM analysis, 828

Kostal, Jiri
Research of the redevelopment spoil heap for construction of the homogenization coal deposit, 96

Koungelis, Dimos
Findings from a dewatering trial used to densify loosened natural soils, 191

Kovacevic, Meho Sasa
Developing correlations between the soil fines content and CPT results using neural networks, 244

Krawczyk, Dorota Anna
Determination of liquidity index of glacial tills based on the fall cone single point methods, 171

Kristinof, Ross Edward
Use of Neural Networks to Predict Pile Driving Performance, 139

Kristinsson, Vilbergur
Sigalda dam leakage – a 40-year review, 1078

Krogsbøll, Anette
Application of associated or non-associated flow rule on typical failure problems, 870

Kumar, Ashutosh
Damage assessment at World Heritage Monument zone in Kathmandu valley after 2015 Gorkha Earthquake, 1018

Kumar, Sachin
Challenges of Design and Constriction of Passenger Terminal Building Foundation, New Mexico City International Airport, Mexico City, 618

Kummerer, Clemens
Recent developments with the use of the BIM method in Europe, 890

Kumor, Lukasz Aleksander
Geotechnical problems of extensive highway embankment slope failures , 179

Matsuda, Hiroshi
Effects of drainage by the sheet pipe on the suction and volume water content of subsurface layer, 1017
Matziaris, Vasileios
Development of a dynamic simple shear apparatus with confining pressure, 999
Mavroulidou, Maria
Innovative cementing agents, used as alternatives to conventional soil stabilisers, 556
Mavroulidou, Maria
Geotechnical properties of paper recycling waste streams, 560
Mayne, Paul Wesley
Analytical CPTu model for sensitive clay at Tiller-Flotten, 153
Mazzieri, Francesco
In situ testing of a composite GM – GCL barrier against emission of gaseous Hg from polluted soil, 394
Mehdizadeh, Amirhassan
Cyclic performance of a new concrete-free driven minipile footing system in a non-cohesive material, 928
Meissner, Simon Robin
An innovative dewatering system to reduce the environmental impact, 441
MELENTIJEVIC, SVETLANA
Failure mechanisms developed in rock masses under circular footing, 537
Mendes, Lucas Oliveira
Confining Layer Influence on Capacity of Offshore Caisson Foundations, 4
Mendoza, Cristhian
Geotechnical behavior of Bogotá lacustrine soil through its geological history, 17
Mevoli, Federica Angela
Thermo-mechanical load-transfer analysis of heating-cooling cycles in energy piles, 380
Mevoli, Federica Angela
Load-transfer versus transient axisymmetric finite element thermo-mechanical analysis of energy piles, 376
Mickovski, Slobodan B.
Practical methodology for the design and management of instability in hard rock tunnels, 294
Mihaljevic, Ivan
Remediation measures for motorway bridge piers damaged by rock sliding in the Republic of Kosovo, 892
Mirsayapov, Ilizar
Calculation model of bearing capacity plate-pile foundations under cyclic loading, 957
Mitrosz, Oskar
Complex foundation analysis of network arch bridge and adjacent embankments founded on grouted columns, 21
Mitrosz, Oskar
Preliminary field tests as a method of geotechnical design risk mitigation, 22
Mohyla, Tomáš
Undrained strength of unsaturated fill for stability analysis, 352
Moormann, Christian
Investigation of hydraulic heave in excavations using the material point method, 501
Moormann, Christian
Angle of incidence on geothermal tunnel plants – a calculation concept, 198
Moormann, Christian
Lateral bearing behaviour of vibratory-driven monopiles: a modified p-y approach based on experimental observations of scaled model tests, 350
Moretti, Sabrina
Geosynthetics-reinforced barriers impacted by flow-like landslides, 646
Mortensen, Niels
Effects of tangential surface load component on earth pressure coefficients, 871
MOUSSAI, BELKACEM
Effect of salts on Atterberg limits of saline soils, 937
Muguda, Sravan
Geotechnical characterisation of recycled biopolymer-stabilised earthen material, 164
Möller, Paula
Weak rocks of varying strength as earthworks materials, 152
Nadimi, Sadegh
A laboratory-based technique for grain shape characterisation, 157
Nagaraj, H.B A
Review of factors affecting undrained strength of fine-grained soils, 472

NAGULA, SPARSHA SINDURI
Numerical simulation of vibroflotation based on CEL approach, 1021

Nagy, Gábor
Dispersive clays – approach, assessment, connections, 1039

Nagy, Peter
Quality control of deep vibro compaction based on the vibrator movement, 78

NEJJAR, Khadija
Performance and modelling of a deep excavation in the context of the Grand Paris project, 415

NEJJAR, Khadija
Accounting for nonlinear behavior of soil for the prediction of settlements due to deep excavation, 852

Nepelski, Krzysztof
Comparative analysis of the CPTs results obtained with the use of electric and mechanical penetrometer cone, 877

Nespereira, José
Modelling the behaviour of stiff clays from continental origin in tunnel construction: back analysis of the first stage of the El Almendro Tunnel, 282

Nettleton, Ian M
On the nexus of engineering failures in the ground, 866

Nocilla, Alessandra
The role of particle mineralogy in mixtures of sands, 824

Norbury, David
Tomorrow's geotechnical toolbox: EN 1997-2:202x Ground investigation, 946

Nordal, Steinar
The cause of the soil sildes of 1st and 2nd April 2016 in Tosbotn, Norway, 290

Nuttall, Jonathan David
Site Spatial Correlation Estimation from CPT Data using Neural Networks and Random Fields, 572

Nyambayo, Vincent
Overcoming design challenges for an urban railway interacting with fragile 19th century infrastructure in London, UK, 59

O'Brien, Anthony
Geotechnical characterisation of fine-grained alluvial & proluvial soils for a motorway project in Kosovo, 128

O'Brien, Anthony
Some observations on the design and construction of wet soil mixing in the UK, 233

O'Brien, Anthony
Statistical inferences from a database of lime and cement modified soil in earthworks for residential construction in the UK, 234

O'Connor, Emer
Determining the extents and material effects of a buried pre-glacial channel on underground construction in Dublin, Irelan, 211

Ofrikhter, Vadim
Field testing of municipal solid waste, 68

Okkels, Nik
New consistent guidelines for classification of fine-grained soils, 651

Okkels, Nik
Introduction of a fast multi-soil test to field vane standards, 990

Olinic, Ernest-Daniel
Soil-mix compacted cushion for land rising and loads distribution to highly compressible foundation soil, 993

Oliveira, José Renato
Evaluation of the behavior of the mixtures of soil with sludge from wastewater treatment plants for liner purpose using physical modeling, 609

Ortuta, Juraj
Determination of global stability for a group of geotechnical objects in complicated geological conditions, 986

Osman, Ashraf
Numerical analysis of cavity propagation in deep trapdoor experiments, 408

Oudhof, Jessica
Reassessment of the combined caisson-pile foundation of the van Brienenoordbrug in Rotterdam for increased selfweight due to deck retrofit, 919

Ólafsdóttir, Elín Ásta
Benchmarking of an open source MASW software using data from four GeoTest sites in Norway, 772

Ólafsdóttir, Elín Ásta
Geophysical investigation of earth dams using the MASW technique, 788
Ólafsdóttir, Elín Ásta
Open source MASW software and open MASW results database, 771
Panchal, Jignasha P
Centrifuge modelling to determine the influence of pile stiffness on pile capacity, 36
Pandrea, Paul
The revised execution standard EN 12716 for jet grouting – amendments and changes explained, 368
Paniagua, Priscilla
Comparison of three Norwegian clays from a mineralogical, chemical and geotechnical approach, 265
Pap, Miklós
Estimation of permeability function for concrete, 844
Papadopoulou, Konstantina
Surface settlements from excavations retained with prestressed anchors, 329
Papic, Jovan Branislav
Applicability of relations between results from field and laboratory tests on sands from tailing dams, 991
Pastor, Jose Luis
Influence of limestone powder waste on the geotechnical behaviour of a soft soil: Preliminary results, 897
Pastor, Jose Luis
Geological-geotechnical characterization of a deep-seated landslide affecting a road-bridge in Alcoy (southern Spain), 896
Pálmason, Pálmi Ragnar
An overview of fuse plug design embedded in earthfill dams in Iceland, 923
Pedro, Antonio M. G.
Numerical analysis of the lining forces induced by the sequential excavation of twin tunnels in different soil conditions, 391
Peduto, Dario
Probabilistic analysis of vulnerability of buildings to slow-moving landslides: a study in three municipalities in southern Italy., 446
Pelecanos, Loizos
Nonlinear seismic response of earth dams due to dam-reservoir interaction, 389
Pelecanos, Loizos
Statistical analysis of long-term earth dam settlements, 739
Pelecanos, Loizos
Finite element analysis of earth dam settlements due to seasonal reservoir level changes, 740
Peranic, Josip
Rainfall infiltration and stability analysis of an unsaturated slope in residual soil from flysch rock mass, 906
Perdikou, Skevi
Landslide risk evaluation in Cyprus using satellite radar interferometry, 488
Pereira, Gustavo
Overview of the dual foundation system of the Dubai Creek Tower, 703
Peri, Elena
Interpretation of consolidation and creep on chalk, 147
Peri, Elena
Evaluation of Preparation Techniques of Chalk Samples for Oedometer Testing, 242
Petriaev, Andrei
Behavior of geogrid reinforced ballast in a triaxial shear strength tests, 660
Peuchen, J.
Strength of chalk derived from on-site needle penetration testing, 117
Peuchen, J.
Challenges for CPT accuracy classes, 49
Pérez Herreros, Jesús
Centrifuge modelling of a pile group foundation in a multilayered soil under sinusoidal and seismic loadings, 206
Pfaffhuber, Andreas Aspmo
Large scale & efficient geotechnical soil investigations - applying machine learning on airborne geophysical models, 398
Pinto, Alexandre
Landslide risk mitigation of "São Pedro de Alcântara Viewpoint Slope" in Lisbon Historical Center, 527